SYNTHESIS, STRUCTURAL CHARACTERISATION BY X-RAY DIFFRACTOMETRY AND BIOLOGICAL STUDIES OF SOME NITROGENOUS COMPOUNDS AND THEIR CORRELATIONS WITH COMPUTATIONAL MODELLING

A THESIS SUBMITTED TO THE

NATIONAL INSTITUTE OF TECHNOLOGY WARANGAL

FOR THE DEGREE OF

DOCTOR OF PHILOSOPHY

IN

CHEMISTRY

BY

THANDRA DHANANJAY RAO
(Roll No. 716190)

under the guidance of
Prof. A. Ramachandraiah
Professor – HAG (Retd)

DEPARTMENT OF CHEMISTRY
NATIONAL INSTITUTE OF TECHNOLOGY
WARANGAL-506 004, TELANGANA, INDIA

February, 2023

CERTIFICATE

This is to certify that the thesis entitled **"SYNTHESIS, STRUCTURAL CHARACTERIZATION BY X-RAY DIFFRACTOMETRY AND BIOLOGICAL STUDIES OF SOME NITROGENOUS COMPOUNDS AND THEIR CORRELATIONS WITH COMPUTATIONAL MODELLING"** is the record of the bonafide original work carried out in the Department of Chemistry, National Institute of Technology Warangal by **Thandra Dhananjay Rao** under my supervision and the same has not been submitted anywhere for the award of any degree or diploma.

Prof. A. RAMACHANDRAIAH
(Supervisor)
Professor (HAG) of Chemistry (Retd, 2021)
Department of Chemistry
National Institute of Technology Warangal
Warangal, 506 004, Telangana, India

Warangal

February, 2023

STATEMENT

I hereby declare that the subject matter, embodied in this thesis, entitled, **"SYNTHESIS, STRUCTURAL CHARACTERISATION BY X-RAY DIFFRACTOMETRY AND BIOLOGICAL STUDIES OF SOME NITROGENOUS COMPOUNDS AND THEIR CORRELATIONS WITH COMPUTATIONAL MODELLING",** is an outcome of the investigations and research work carried out by me in the Department of Chemistry, National Institute of Technology Warangal, under the guidance of Prof. A. Ramachandraiah, Professor (HAG) of Chemistry, and the same has not been submitted elsewhere either in part or in full for any degree or diploma.

T. DHANANJAY RAO
Author of the Thesis

Warangal
February, 2023

ACKNOWLEDGMENTS

The work presented in this thesis would not have been possible without my close association with many people. I take this opportunity to extend my sincere gratitude and appreciation to all those who made this Ph.D. thesis possible.

It gives me an immense pleasure and delight to express my deep sense of gratitude to my research supervisor **Prof. A. Ramachandraiah (HAG, Retd)**, Department of Chemistry, National Institute of Technology Warangal for his inspiring and valuable guidance. His unfailing attention, unmitigated encouragement and co-operation have helped me in attaining my goal. It would have been impossible to achieve this goal without his able support and valuable advice. I consider myself fortunate that he has given me a decisive tune, a significant acceleration to my career. I will be thankful to him throughout my lifetime.

I am greatly indebted to Prof. **N. V. Ramana Rao**, Director, National Institute of Technology Warangal for providing me an Institute Research Fellowship and for allowing me to use the Institute's infrastructure and now to submit my research work in the form of a thesis. I express my gratitude to **Prof. G. R. C. Reddy**, former Director, National Institute of Technology Warangal for admitting me as a Full Time Research Scholar with institute Fellowship.

My special words of thanks are to **Dr. Vishnu Shanker**, Head, Department of Chemistry and to the former Heads, **Prof. P. V. Srilakshmi**, **Prof. K. V. Gobi** and **Prof. V. Rajeswar Rao**, for their valuable advice, help and support.

I express my sincere thanks to the Doctoral Scrutiny Committee (DSC) Members, **Prof. K. Laxma Reddy**, **Dr. D. Kashinath**, Department of Chemistry and **Prof. A. Venu Vinod**, Department of Chemical Engineering for their constant encouragement and valuable suggestions during the DSC Proceedings.

I take this opportunity to express thanks to **Dr. Venkatathri Narayanan**, **Dr. Raghu Chitta**, **Dr. S. Nagarajan**, **Dr. M. Raghasudha**, **Dr. Ch. Jugun Prakash**, **Dr. Mukul Pradhan**, **Dr. Rajeshkhanna Gaddam**, **Dr. V. Rajeshkumar** for their suggestions and encouragement.

The financial assistance from the Ministry of Education (MoE), Government of India, in the form of an Institute Fellowship at the National Institute of Technology Warangal, is gratefully acknowledged.

My sincere thanks are to **Prof. M. Sathiyendiran**, School of Chemistry, University of Hyderabad, for providing single crystal XRD (SCXRD) data. I also acknowledge with thanks **Dr. Podeti Srinivas**, Department of Biotechnology, Kakatiya University, Warangal, for providing biological activities of the compounds, I have synthesized.

My special thanks are to **Dr**. **B. Srinivas** and **Dr. Ravinder Pawar**, Department of Chemistry, National Institute of Technology Warangal for useful discussions on the XRD data and the DFT/B3LYP calculations, respectively. I am also thankful to **Dr. B. Rajeswara Rao**,

Senior Chemist (Retd), Kakatiya Thermal Power Project (O&M), Chelpur, Telangana, for obtaining some AM1 computational data on one of the compounds, modelled.

I am very delighted to work with my colleagues **A. Ramesh**, **Ms. Pooja**, **Dr. A. Bhargava Sai**, **G. Sivaparwathi**, **M. Shireesha, B. Prashanth, K. Madhu**, **V Rukya Naik** and **S. Akanksha** for their support and encouragement during my Ph.D. work.

It gives me a great pleasure to fondly remember my campus life with my research colleagues in the Department, **Dr. G. Srinivasa Rao**, **A. Naveen Kumar**, **G. Srinath**, **Dr. G. Ramesh**, **Dr. K. Vimal Kumar**, **Ms. P. Soumya**, **Dr. T. Sanjeeva, Dr. Ch. Suman, Dr. V. Sunil Kumar, Dr. M. Venkanna, Dr. Ms. K. Sujatha, Dr. J. Parameswara Chary, Dr. M. Srikanth, Dr. P. Babji, Dr. G. Ambedkar, K. Vijendar Reddy, N. Satyanarayana, Dr. Ms. R. Hithavani, Dr. K. Sathish, Dr. K. Shekar, Ch. Raju, Dr. S. Suresh, R. Venkatesh, G. Sripal reddy, P. Venkatesham, K. Sampath, T. Shirisha, R. Vara Prasad, B. Anjaiah, R. Arun, Ms. J. Swathi, B. Srikanth, Anindya Roy, Ms. Khushboo Agarwala, Ms. Tohira Banoo, Ms. M. Sasi Sree, Akash Kumar, Avinash Sharma, B. Apurba, M. Subir, M. Faizan, M. Arokiaraj, M. Vijay, Aarti Gautam, B. Srikanth, Ch. Vijay Kumar**, **Ms. B. Divya**, **Dr. Ms. N. Manjula** and **Dr. G. Rama Rao** and many of the research scholars from other Departments for their good company and nice atmosphere in and outside the laboratory and their encouragement and help during my research period.

I express my gratitude to my friends, **J. Rajesh**, **K. Praveen, Ch. Venkatesh**, **Ms**. **K. Sowjanya**, **G. Chaitanya**, **B. Krishna**, **D. Shankaramma** for their encouragement and support.

It would be an understatement to say that I would not be the person what I am today without the affection and sacrifices from my family. I am extremely grateful to my beloved father **Sri. Narasimha Rao** for his moral support and inspiration to never give up. My heartfelt thanks are to my beloved mother **Smt. Savithri** for her best wishes and blessings for my success. I would never forget the motivational, inspiring, enthusiastic behavior of my brothers **Sridhar Rao** and **Shasi Vardhan Rao** for their constant support, cooperation, encouragement, inspiration, love and affection whose blessings made this journey, worthy one. I owe a lot to them.

Finally, I thank one and all those who have helped me, all through my research work at the Department of Chemistry, NIT Warangal, in various capacities, ways and means.

Thandra Dhananjay Rao

ABSTRACT

This PhD Thesis, entitled, "***Synthesis, Structural Characterization by X-Ray Diffractometry and Biological Studies of Some Nitrogenous Compounds and Their Correlations with Computational Modelling***', deals with the synthesis, characterization, molecular structure determination and computational modeling of some structurally interesting nitrogenous organic compounds along with their coordination compounds. Both, ligands and their complexes have been exposed to molecular docking on some biomolecules and were tested for possible anti-fungal, anti-bacterial, anti-cancer and anti-oxidant *in vitro* applications.

The contemporary research on the correlation of empirical molecular structural studies by XRD and those obtained from advanced computational modeling, is highlighted with examples is presented in **Chapter I** of the Thesis. The Chapter concludes with the Scope and objectives.

Chapter II is titled as '**Materials and Methods**' and it describes the procedures of the synthesis and characterization of compounds studied along with the details of characterization by various wet, spectral and other instrumental methods. It also briefly introduces the current computational chemistry procedures.

In **Chapter III**, entitled, **Spectral, Electrochemical, Molecular Modelling, Protein Docking and Biological Activity Studies of Fluoxetine Dithiocarbamate (FLXDTC) and Its Bivalent Metal Complexes**, I have presented the details of investigations of the title compounds. The studies indicate the formation **M(FLXDTC)$_2$** type complexes [M = Zn(II), Cd(II), Co(II), Ni(II), Mn(II) and Cu(II)]. The antimicrobial, antioxidant, antifungal, anti-malarial and antitumor capabilities have been tested for both **FLXDTC** and **M(FLXDTC)$_2$** complexes.

Chapter IV of the Thesis is entitled, **Synthesis and Spectral, Electrochemical, Single Crystal X-Ray Diffractometric, Computational Chemistry and Biological Studies of 1-(((3-Fluoro-4-morpholinophenyl)-imino)methyl)-napthalen-2-ol (FMIMN) and Its Bivalent Metal Complexes.** The characterization of the **FMIMN**, and it metal complexes besides the single crystal X-ray diffraction studies are discussed It is found that **FMIMN** crystallizes in the $P_{21/n}$ monoclinic space group. The comparison of experimental XRD crystal data of **FMIMN** with those evaluated by computational analysis from fully optimized semi empirical AM1 calculations by MOPAC, MM2 and DFT/B3LYP calculations is presented and discussed. An excellent agreement of the computationally evaluated data with the empirical data obtained by single crystal XRD data was found. Biological docking studies and the antimicrobial, antifungal, anticancer and anti-oxidant biological activity studies of **FMIMN** ligand and its metal complexes are also presented. **Zn(FMIMN)$_2$** was found to show a better antimicrobial activity while **Cd(FMIMN)$_2$** a promising anticancer activity.

Chapter V is titled as, **Synthesis, Characterization and Single Crystal X-Ray Diffractometric, Computational Chemistry and Biological Studies of a Pair of Phenyl**

Quinolinium Salts. The two are **FMPC** and **FMMC** salts. Both **FMPC** and **FMMC** crystallize in their centrosymmetric monoclinic $P_{21/c}$ space groups. The crystal structure analysis data and molecular modelling studies on the platforms of AM1, MM2 and B3LYP calculations and the data have been found to be in excellent agreement with the single crystal XRD data. These new heterocyclic compounds exhibit certain level of anti-cancer property.

In **Chapter VI**, entitled, **Spectral Characterization, and Single Crystal X-Ray Diffractometric, Computational and Biological Studies of Mono- and Di-Aza Derivatives of a Pair of Malonaldehydes**, the studies of 4 distinct compounds have been described.

Single crystals could be generated only for **FMAPA** and **FFMMMC. FMAPA** crystallizes in a centrosymmetric monoclinic P21/c space group but with four molecules in one-unit cell whereas **FFMMMC** crystallizes in a centrosymmetric triclinic P_{-1} space group with only two molecules in a one-unit cell. The XRD molecular structural data of **FMAPA** and **FFMPMC** obtained through single crystal XRD studies have been compared with the molecular modelled structural of all the four compounds in this Chapter. Finally, this Chapter presents briefly the biological applications of the title compounds.

In the last, **Chapter VII**, entitled, **Synthesis and Spectral, Electrochemical, Computational and Biological Studies of 2,2'-(((1E,3E)-2-Phenylpropane-1,3-diylidene)-bis-(azaneylylidene))-dibenzoic Acid (PDBAD) and Its Bivalent Metal Complexes [M(PDBAD)X_2],** the studies of **PDBAD**, and **[M(PDBAD)X_2]** are presented.

CONTENTS

CERTIFICATE

STATEMENT

ACKNOWLEDGEMENTS

ABSTRACT

LIST OF SYMBOLS AND ABBREVATIONS

LIST OF FIGURES

LIST OF TABLES

CHAPTER-I	**INTRODUCTION**	**Page No**
1.1	Importance of Nitrogenous Organic Ligands	3
1.2	General Introduction to Schiff Bases and Their Metal Coordination	5
1.3	General Introduction to Dithiocarbamate and their Metal Binding	8
1.4	Introduction to Quinolines	11
1.5	Computational Chemistry and Molecular Modelling Paradigms	13
1.6	Scope for the Present Work	27
1.7	Objectives of the Present Work	28
	References	30
CHAPTER-II	**MATERIALS AND METHODS**	
PART A	**MATERIALS**	
2A.1	Synthesis of Fluoxetine Dithiocarbamate, **FLXDTC**	41
2A.2	Synthesis of the **FLXDTC** Complexes, **M(FLXDTC)$_2$**	41
2A.3	Synthesis of (E)-1-(((3-fluoro-4-morpholinophenyl)imino)methyl)naphthalene-2-ol, **FMIMN**	42
2A.4	Synthesis of the Complexes, **M(FMIMN)$_2$**	42
2A.5	Synthesis of 2-Phenylmalonaldehyde	43

2A.6	Cyclization and Adduction to Schiff Bases of the 2-Phenylmalonaldehyde	44
2A.7	Synthesis of 2,2'-(((1E,3E)-2-phenylpropane-1,3-diylidene)bis(azaneylylidene))dibenzoic acid, **PDBAD** and its Metal Complexes	46
PART B	**METHODS**	
2B.1	Sampling Methods and Instrumental Operations	47
2B.2	Crystallographic Data Collections	49
2B.3	Molecular Modelling	49
2B.4	Biological Studies Procedures	50
2B.5	Functional Principles of Some Important Techniques	51
	References	67
CHAPTER-III	**SPECTRAL, ELECTROCHEMICAL, MOLECULAR MODELLING, PROTEIN DOCKING AND BIOLOGICAL ACTIVITY STUDIES OF FLUOXETINE DITHIOCARBAMTE (FLXDTC) AND ITS BIVALENT METAL COMPLEXES**	
PART A	**SPECTRAL AND ELECTROCHEMICAL STUDIES FLXDTC AND M(FLXDTC)$_2$**	
3A.1	Elemental Analysis	72
3A.2	Infrared Spectroscopic Studies	73
3A.3	Electronic Spectral Studies	76
3A.4	NMR Spectral Studies	78
3A.5	Metal to Ligand Ratio; Job's Monovariation Spectrophotometric Titration	82
3A.6	Electron Spin Resonance Spectroscopy of **Cu(FLXDTC)$_2$**	84
3A.7	Cyclic Voltammetric Studies of **M(FLXDTC)$_2$**	86
PART B	**COMPUTATIONAL MOLECULAR MODELLING AND MOLECULAR DOCKING STUDIES**	
3B.1	Molecular Modelling Studies of **FLXDTC** and **M(FLXDTC)$_2$** Complexes	91
3B.2	Molecular Docking Studies of **FLXDTC** and **M(FLXDTC)$_2$**	101
PART C	**BIOLOGICAL ACTIVITY STUDIES OF THE TITLE COMPOUNDS**	
3C.1	*In vitro* Antimicrobial Activity	109
3C.2	*In vitro* Antioxidant Property	109
3C.3	*In vitro* Antifungal Activity	111

3C.4	*In vitro* Anticancer Activity	112
	References	114
CHAPTER-IV	**SYNTHESIS AND SPECTRAL, ELECTROCHEMICAL, SINGLE CRYSTAL X-RAY DIFFRACTOMETRIC, COMPUTTIONAL CHEMISTRY AND BIOLOGICAL STUDIES OF 1-(((3-FLUORO-4-MORPHOLINOPHENYL)IMINO)METHYL)-NAPTHALEN-2-OL (FMIMN) AND ITS BIVALENT METAL COMPLEXES**	
PART A	**SPECTRAL, ELECTROCHEMICAL CRYSTALLOGRAPHIC STUDIES OF FMIMN AND [M(FMIMN)$_2$]**	
4A.1	Elemental Analysis	119
4A.2	Mass Spectrum of **FMIMN**	119
4A.3	IR Spectral Studies	120
4A.4	Electronic Spectral Studies	122
4A.5	NMR Spectral Studies of **FMIMN**	123
4A.6	Electron Spin Resonance Spectroscopy of **Cu(FMIMN)$_2$**	125
4A.7	X-Ray Crystal Structure of **FMIMN**	126
4A.8	Cyclic Voltammetric Studies of **FMIMN** and **Cu(FMIMN)$_2$**	129
PART B	**COMPUTATIONAL AND DOCKING STUDIES OF FMIMN AND [M(FMIMN)$_2$] AND CORRELATION WITH CRYSTALLOGRAPHIC DATA**	
4B.1	Computational Methods	134
4B.2	Comparison of the X-Ray Data with Computational Data	138
4B.3	Hirshfeld Surface Analysis	144
4B.4	Molecular Modelling and Docking Studies of **FMIMN** and **M(FMIMN)$_2$**	150
PART C	**BIOLOGICAL ACTIVITY STUDIES OF FMIMN AND [M(FMIMN)$_2$]**	
4C.1	*In vitro* Antimicrobial Activity	158
4C.2	*In vitro* antioxidant property	158
4C.3	*In vitro* antifungal activity	160
4C.4	*In vitro* anticancer activity	161
	References	163

CHAPTER-V	**SYNTHESIS, CHARACTERIZATION AND SINGLE CRYSTAL X-RAY DIFFRACTOMETRIC, COMPUTATIONAL CHEMISTRY AND BIOLOGICAL STUDIES OF A PAIR OF PHENYL QUINOLINIUM SALTS**	
PART A	**CHARACTERIZATION AND SINGLE CRYSTAL X-RAY DIFFRACTOMETRIC STUDIES OF FMPC AND FMMC**	
5A.1	Analytical Characteristics of **FMPC** and **FMMC**	168
5A.2	Electronic Spectral Studies of **FMPC** and **FMMC**	169
5A.3	FTIR Spectral Studies of **FMPC** and **FMMC**	170
5A.4	NMR Spectral Analysis of **FMPC** and **FMMC**	171
5A.5	Fluorescence Spectral Studies of **FMPC** and **FMPC**	173
5A.6	Electrochemical Studies of **FMPC**	174
5A.7	Crystal Structure Analysis of **FMPC** and **FMMC**	176
PART B	**MOLECULAR MODELLING AND MOLECULAR BIOLOGICAL DOCKING STUDIES OF FMPC AND FMMC AND CORRELATION OF THE COMPUTATIONAL DATA WITH THE X-RAY DIFFRACTION DATA**	
5B.1	Correlation of the X-Ray Crystallographic Data of **FMPC** and **FMMC** Molecular Modelled Data of These Cations	180
5B.2	Hirshfeld Surface Analysis of **FMPC** and **FMMC**	198
5B.3	Biological Studies of **FMPC** and **FMMC**	204
5B.4	Molecular Docking Studies of **FMPC** and **FMMC**	205
	References	208
CHAPTER-VI	**SPECTRAL CHARACTERIZATION, AND SINGLE CRYSTAL X-RAY DIFFRACTOMETRIC, COMPUTATIONAL AND BIOLOGICAL STUDIES OF MONO- AND DI-AZA DERIVATIVES OF A PAIR OF MALONALDEHYDES**	
PART A	**SPECTRAL, SINGLE CRYSTAL X-RAY DIFFRACTOMETRIC AND COMPUTATIONAL CHEMISTRY STUDIES OF FMAPA AND FMAMA**	
6A.1	Physical and Analytical Characterization of **FMAPA** and **FMAMA**	211
6A.2	IR Spectral Studies of **FMAPA** and **FMAMA**	212
6A.3	NMR Spectral Analysis of **FMAPA** and **FMAMA**	213
6A.4	Fluorescence Studies of **FMAPA** and **FMAMA**	215

6A.5	Crystal Structure Analysis of **FMAPA**	216
6A.6	Correlation of the X-Ray Crystallographic Data with the Molecular Modelled Data of FMAPA	219
6A.7	Hirshfeld Surface Analysis	236
6A.8	Molecular Docking Studies of **FMAPA** and **FMAMC**	241
PART B	**SPECTRAL, SINGLE CRYSTAL X-RAY DIFFRACTOMETRIC AND COMPUTATIONAL CHEMISTRY STUDIES OF FFMPMC AND FFMMMC**	
6B.1	Analytical Characterization of **FFMPMC** and **FFMMMC**	243
6B.2	Mass Spectra of **FFMPMC** and **FFMMMC**	243
6B.3	IR Spectral Studies of **FFMPMC** and **FFMMMC**	244
6B.4	NMR Spectral Studies of **FFMPMC** and **FFMMMC**	245
6B.5	Fluorescence Studies of **FFMPMC** and **FFMMMC**	247
6B.6	Tautomerization and Potentiometric Titration of **FFMPMC** and **FFMMMC**	248
6B.7	Crystal Structure Analysis of **FFMMMC**	250
6B.8	Correlation of the X-Ray Crystallographic and Computational Molecular Modelled Data of **FFMMMC** and **FFMPMC**	253
6B.9	Hirshfeld Surface Analysis	278
6B.10	Molecular Docking Studies of **FFMPMC** and **FFMMMC**	283
	References	285
CHAPTER-VII	**SYNTHESIS AND SPECTRAL, ELECTROCHEMICAL, COMPUTATIONAL AND BIOLOGICAL STUDIES OF 2,2'-(((1E,3E)-2-PHENYLPROPANE-1,3-DIYLIDENE)-BIS-(AZANEYLYLIDENE))-DIBENZOIC ACID (PDBAD) AND ITS BIVALENT METAL COMPLEXES [M(PDBAD)X_2]**	
PART A	**SPECTRAL, ELECTROCHEMICAL AND COORDINATION CHEMISTRY STUDIES OF PDBAD and [M(PDBAD)X_2]**	
7A.1	Analytical Characteristics of the **PDBAD** and **[M(PDBAD)X_2]**	288
7A.2	IR Spectral Studies	289
7A.3	Electronic Spectral Studies	290
7A.4	Fluorescence Spectral Studies of **PDBAD** and **[M(PDBAD)X_2]**	294
7A.5	Fluorescence Spectrophotometric Titration of **PDBAD** Against Cu^{+2} ion (Job's Plot)	295
7A.6	Electron Spin Resonance Spectroscopy of **[Cu(PDBAD)]**	296

7A.7	Cyclic Voltammetric Studies of **PDBAD** and **[M(PDBAD)X_2]**	297
PART B	**MOLECULAR MODELING AND MOLECULAR DOCKING STUDIES OF PDBAD AND ITS METAL COMPLEXES**	
7B.1	Molecular Modelling Studies of **PDBAD** and **[M(PDBAD)X_2]**	301
7B.2	Molecular Docking Studies of **PDBAD** and **[M(PDBAD)X_2]**	314
PART C	**BIOLOGICAL ACTIVITIE STUDIES OF PDBAD AND [M(PDBAD)X_2]**	
7C.1	*In vitro* Antimicrobial Activity	318
7C.2	*In vitro* Antioxidant Property	318
7C.3	*In vitro* Antifungal Activity	319
7C.4	*In vitro* Anticancer Activity	320
	References	323
	SUMMARY AND SCOPE FOR FURTHER WORK	325
	PUBLICATIONS ARISING FROM THE WORK PRESENTED IN THIS THESIS	329
	CONFERENCES AND WORKSHOPS ATTENDED	329
	BIO-DATA	332

LIST OF SYMBOLS AND ABBREVATIONS

°	Degree
Å	Angstrom
°C	Degree centigrade
g	gram
mg	Microgram
L	Litre
mL	Mille Liter
µL	Micro Liter
M	Molar
µM	Micro Molar
mM	Milli Molar
cm	Centimeter
mm	Millimeter
nm	Nanometer
Å	Angstrom
MHz	Mega Hertz
i	Current
µA	microampere
ν	Scan rate
mV	Millivolt
E	Potential
sec	Second
min	Minute
eV	Electron volt
h	Hour
M	Molarity
N	Normality
µM	Micro molar
mM	Mill molar
B.M	Bohr Magneton
M.P	Melting point
FTIR	Fourier Transform Infrared
NMR	Nuclear Magnetic Resonance
TMS	Trimethylsilane
UV	Ultra-Violet
ESR	Electron Spin Resonance

EPR	Electron Paramagnetic Resonance
ESI-MS	Electrospray Ionization Mass Spectrometry
SCE	Saturated Calomel Electrode
Ex	Excitation
AM1	Austin Modeling-1
DFT	Density Functional Theory
HF	Hartee-Fock
B3LYP	Becke-3-Parameter-Lee–Yang–Parr
SCF	Self Consistent field
QM	Quantum Mechanics
MD	Molecular Dynamics
HOMO	Highest Occupied Molecular Orbital
LUMO	Lowest Occupied Molecular Orbital
ORTEP	Oak Ridge Thermal Ellipsoid Plot
DPPH	1,1-diphenyl-2-picrylhydrazyl
DMSO	Dimethyl Sulfoxide
DMF	Dimethylformamide
TEAP	Tetraethylammonium perchlorate
MTT	3-(4,5-dimethylthiazol-2-yl)-2,5-diphenyltetrazolium bromide
Calcd	Calculated
ADT	Auto Dock Tools
CV	Cyclic Votammogram
LSV	Linear Sweep Voltammogram
DNA	Deoxyribonucleic acid
PDB	Protein Data Bank
ppm	Parts Per Million
sp	Syn periplanar
sc	Syn-clinical
ac	Anti-clinical
ap	Anti periplanar
PHE	Phenylalanine
ALA	Alanine
ARG	Arginine
GLU	Glutamic acid
ASP	Aspartic acid
VAL	Valine
LEU	Leucine

PRO	Proline
CYS	Cysteine
GLY	Glycine
SER	Serine
ASN	Asparagine
GLN	Glutamine
THR	Threonine
TRP	Tryptophan
TYR	Tyrosine
HIS	Histidine
EGFR-TK	Epidermal growth factor receptor tyrosine kinase

LIST OF FIGURES

Figure No.	Caption	Page No
Figure 1.1	Selected examples for biologically active Schiff bases	4
Figure 1.2	General structure of a Schiff base	5
Figure 1.3	Variable number of donor atoms in Schiff base complexation	6
Figure 1.4	Canonical resonance forms of dithiocarbamate anion	9
Figure 1.5	Monodentate and bidentate metal-binding modes of dithiocarbamate	10
Figure 1.6	Schematic of Dithiocarbamate as a bridge to form adducts with Lewis bases	10
Figure 1.7	Structures of ferbam and ziram	10
Figure 1.8	The Schematic of the ab initio sequence of molecular modelling	15
Figure 1.9	**(a)** fabricated and a **(b)** commercial low-cost	22
Figure 1.10	Discosoma coral chromophore shown in stereographic projection	23
Figure 1.11	A typical anaglyph spectacle to view anaglyph pictures	23
Figure 1.12	The anaglyph picture of phenylalanine (one has to wear the anaglyph spects for a 3-D perception)	24
Figure 2B.1	Three-electrode electrochemical cell system	49
Figure 2B.2	Typical triangular potential programme in a cyclic voltammetric run (eg. between -1.5 and +1.5 vs SCE)	52
Figure 2B.3	Shape of a typical reversible cyclic voltammogram	52
Figure 2B.4	Schematic of an X-Ray diffractometer	56
Figure 2B.5	The 3D (left) Surfer plot and (right) Grapher plot for the equation, $z = x^2-y^2+xy$, for the range of $-20<x<20$ and $-20<y<20$ with a gridding increment of 0.5 on each of x and y domains	64
Figure 2B.6	Normal (left) and SCF-Energy-Minimized stereographic structures of 2-(2-aminophenoxy)-5-methylphenol	65
Figure 2B.7	Dihedral-driven conformational energy plot (left)of 2-(2-aminophenoxy)-5-methylphenol and its plot (right) truncated for clarity for the torsion overC6-O7 bond	65
Figure 2B.8	Dihedral-driven conformational energy plot (left)of 2-(2-aminophenoxy)-5-methylphenol and its plot (right) truncated for clarity for the torsion over O7-C8 bond	66
Figure 2B.9	Double dihedral-driven conformational energy plot of 2-(2-aminophenoxy)-5-methylphenol over the bond sequence, C6-O7-C8; (top left) contour plot from the Chem3D; (top right) and its plot by Surfer and (bottom left) Grapher platforms; (bottom right) Grapher plot truncated beyond 400 units for clarity	66
Figure 3A.1	Mass spectrum of **FLXDTC**	73
Figure 3A.2	FTIR Spectrum of **FLXDTC**	74
Figure 3A.3	FTIR Spectrum of **Cu(FLXDTC)$_2$**	74
Figure 3A.4	FTIR Spectrum of **Zn(FLXDTC)$_2$**	75

Figure 3A.5	FTIR Spectrum of **$Mn(FLXDTC)_2$**	75
Figure 3A.6	FTIR Spectrum of **$Ni(FLXDTC)_2$**	75
Figure 3A.7	FTIR Spectrum of **$Co(FLXDTC)_2$**	75
Figure 3A.8	Electronic Spectra of FLX (—) and **FLXDTC** (—) in methanol (each at $1.25x10^{-3}$ M)	76
Figure 3A.9	Electronic spectrum of **$Cu(FLXDTC)_2$** in methanol ($4x10^{-4}$ M); inset ($2x10^{-2}$ M)	76
Figure 3A.10	Electronic spectrum of **$Ni(FLXDTC)_2$** in methanol ($4x10^{-4}$ M**);** inset ($2x10^{-2}$ M)	77
Figure 3A.11	Electronic spectrum of **$Co(FLXDTC)_2$** in methanol ($4x10^{-4}$ M**));** inset ($2x10^{-2}$ M)	77
Figure 3A.12	^{1}H-NMR Spectrum of Fluoxetine.HCl in $CDCl_3$	78
Figure 3A.13	^{1}H-NMR Spectrum of **FLXDTC** in $CDCl_3$ and DMSO	79
Figure 3A.14	^{1}H-NMR Spectrum of **$Zn(FLXDTC)_2$** in $CDCl_3$ and DMSO mixture	79
Figure 3A.15	^{1}H-NMR Spectrum of **$Cd(FLXDTC)_2$** in $CDCl_3$	80
Figure 3A.16	^{13}C-NMR Spectrum of **FLX** in $CDCl_3$	80
Figure 3A.17	^{13}C-NMR Spectrum of **FLXDTC** in $CDCl_3$ and DMSO mixture	81
Figure 3A.18	^{13}C-NMR Spectrum of **$Zn(FLXDTC)_2$** in $CDCl_3$ and DMSO mixture	81
Figure 3A.19	^{13}C-NMR Spectrum of **$Cd(FLXDTC)_2$** in $CDCl_3$	82
Figure 3A.20	**(a)** Monovariation Job's plot for the spectrophotometric titration of **FLXDTC** ($c = 4x10^{-4}$ M) against $NiCl_2$ **(b)** Monovariation Job's plot for the spectrophotometric titration	82
Figure 3A.21	Sulfur bridged binuclear **$[Cu_2(FLXDTC)_2Cl_2]$**	83
Figure 3A.22	Spectrophotometric titration of **FLXDTC** ($c = 1x10^{-4}$ M) against $CuCl_2$ (in jc concentrations where $0 \leq j \leq 1.9$); (—) $CuCl_2$ ($0.5x10^{-4}$ M) alone; (—) **FLXDTC** ($0.5x\ 10^{-4}$ M) alone	84
Figure 3A.23	Monovariation Job's plot for the spectrophotometric titration of **FLXDTC** ($c = 1x\ 10^{-4}$ M) against $CuCl_2$	84
Figure 3A.24	X-band electron spin resonance spectrum of **$Cu(FLXDTC)_2$** in solid state	85
Figure 3A.25	X-band electron spin resonance spectrum of **$Cu(FLXDTC)_2$** in toluene (ν = 9.191GHz)	86
Figure 3A.26	Cyclic voltammograms of $5x\ 10^{-4}$ M **(a)** **$Cu(FLXDTC)_2$** **(b)** **$Co(FLXDTC)_2$** at 120 mVs^{-1} scan rate in acetone solvent	87
Figure 3A.27	**(a)** Cyclic voltammograms of **$Cu(FLXDTC)_2$** in Acetone at different concentrations **(b)** Variation of anodic and cathodic currents of **$Cu(FLXDTC)_2$** with respect to various concentrations	88
Figure 3A.28	**(a)** Cyclic voltammogram of **$Cu(FLXDTC)_2$** ($5x10^{-5}$ M) in acetone at different scan rates **(b)** Effect of scan rate on the anodic current of **$Cu(FLXDTC)_2$**	88

Figure 3A.29	Plot of scan rate-dependent E_p vs log i for **Cu(FLXDTC)$_2$**	89
Figure 3A.30	**(a)** Cyclic voltammograms of **Co(FLXDTC)$_2$** in Acetone at different concentrations **(b)** Variation of anodic currents of **Co(FLXDTC)$_2$** with respect to concentration	89
Figure 3A.31	**(a)** Cyclic voltammogram of $5x10^{-4}$ M **Co(FLXDTC)$_2$** ($5x10^{-5}$ M) in acetone at different scan rates **(b)** Effect of scan rate on the anodic current of **Co(FLXDTC)$_2$**	89
Figure 3A.32	Plot of scan rate-dependent E_p vs log i for **Co(FLXDTC)$_2$**	90
Figure 3B.1	MM2-energy-minimized structure of **FLXDTC** with numbered atoms	91
Figure 3B.2	Anaglyph structure of **FLXDTC** obtained from ChemDrawPro	92
Figure 3B.3	Stereographic projection of **FLXDTC** obtained from ChemDrawPro	92
Figure 3B.4	Conformational analysis over O8-C9	92
Figure 3B.5	Conformational analysis over O8-C7	92
Figure 3B.6	Conformational analysis over C6-C7	93
Figure 3B.7	Conformational analysis over C7-C19	93
Figure 3B.8	Conformational analysis over C19-C20	93
Figure 3B.9	Conformational analysis over C20-N21	93
Figure 3B.10	Double dihedral torsional energy Surfer plot of **FLXDTC** over C19-C20 (on axis shown in red) and C20-N21 (on axis shown in blue) bonds (Refer **Figure 3B.1** for numbering of the atoms)	93
Figure 3B.11	Double dihedral torsional energy Grapher plot of **FLXDTC** over C19-C20 (on axis shown in blue) and C20-N21 (on axis shown in red) bonds (Refer **Figure 3B.1** for numbering of the atoms)	94
Figure 3B.12	Double dihedral torsional energy Surfer plot of **FLXDTC** over C7-O8 (on axis shown in blue) and O8-C9 (on axis shown in red) bonds (Refer **Figure 3B.1** for numbering of the atoms	94
Figure 3B.13	Double dihedral torsional energy Grapher plot of **FLXDTC** over C7-O8 (on axis shown in blue) and O8-C9 (on axis shown in red) bonds (Refer **Figure 3B.1** for numbering of the atoms)	95
Figure 3B.14	Double dihedral torsional energy Surfer plot of **FLXDTC** over C7-C9 (on axis shown in blue) and C9-C20 (on axis shown in red) bonds (Refer **Figure 3B.1** for numbering of the atoms)	95
Figure 3B.15	Double dihedral torsional energy Grapher plot of **FLXDTC** over C7-C9 (on axis shown in blue) and C9-C20 (on axis shown in red) bonds (Refer **Figure 3B.1** for numbering of the atoms)	96
Figure 3B.16	Double dihedral torsional energy Surfer plot of **FLXDTC** over C6-C7 (on axis shown in blue) and C7-O8 (on axis shown in red) bonds (Refer **Figure 3B.1** for numbering of the atoms)	96

Figure 3B.17	Double dihedral torsional energy Grapher plot of **FLXDTC** over C6-C7 (on axis shown in blue) and C7-O8 (on axis shown in red) bonds (Refer **Figure 3B.1** for numbering of the atoms)	97
Figure 3B.18	Double dihedral torsional energy Surfer plot of **FLXDTC** over C6-C7 (on axis shown in blue) and C7-C19 (on axis shown in red) bonds (Refer **Figure 3B.1** for numbering of the atoms)	97
Figure 3B.19	Double dihedral torsional energy Grapher plot of **FLXDTC** over C6-C7 (on axis shown in blue) and C7-C19 (on axis shown in red) bonds (Refer **Figure 3B.1** for numbering of the atoms)	98
Figure 3B.20	Global minimized ball-stick models of **(a) $Cu(FLXDTC)_2$ (b) $Ni(FLXDTC)_2$ (c) $Co(FLXDTC)_2$ (d) $Mn(FLXDTC)_2$ (e) $Zn(FLXDTC)_2$** and **(f) $Cd(FLXDTC)_2$** (The hydrogen atoms are hidden for clarity)	99
Figure 3B.21	HOMO and LUMO molecular orbitals of **FLXDTC** in wire mesh format (H-atoms and lone pairs of electrons are excluded for clarity)	99
Figure 3B.22	HOMO and LUMO molecular orbitals of **$Cu(FLXDTC)_2$** in wire mesh format (H-atoms and lone pairs of electrons are excluded for clarity)	100
Figure 3B.23	HOMO and LUMO molecular orbitals of **$Ni(FLXDTC)_2$** in wire mesh format (H-atoms and lone pairs of electrons are excluded for clarity)	100
Figure 3B.24	HOMO and LUMO molecular orbitals of **$Mn(FLXDTC)_2$** in wire mesh format (H-atoms and lone pairs of electrons are excluded for clarity)	100
Figure 3B.25	HOMO and LUMO molecular orbitals of **$Zn(FLXDTC)_2$** in wire mesh format (H-atoms and lone pairs of electrons are excluded for clarity)	101
Figure 3B.26	HOMO and LUMO molecular orbitals of **$Cd(FLXDTC)_2$** in wire mesh format (H-atoms and lone pairs of electrons are excluded for clarity)	101
Figure 3B.27	Molecular docking interactions of **FLXDTC** with EGFR protein; (a) 3D depiction of ligand-receptor binding interactions and (b) 2D representation of different forms of interactions with amino acid residues	102
Figure 3B.28	Molecular docking interactions of **$Cu(FLXDTC)_2$** with EGFR protein; (a) 3D depiction of ligand-receptor binding interactions and (b) 2D representation of different forms of interactions with amino acid residues	102

Figure 3B.29	Molecular docking interactions of **Ni(FLXDTC)$_2$** with EGFR protein; (a) 3D depiction of ligand-receptor binding interactions and (b) 2D representation of different forms of interactions with amino acid residues	103
Figure 3B.30	Molecular docking interactions of **Co(FLXDTC)$_2$** with EGFR protein; (a) 3D depiction of ligand-receptor binding interactions and (b) 2D representation of different forms of interactions with amino acid residues	103
Figure 3B.31	Molecular docking interactions of **Mn(FLXDTC)$_2$** with EGFR protein; (a) 3D depiction of ligand-receptor binding interactions and (b) 2D representation of different forms of interactions with amino acid residues	104
Figure 3B.32	Molecular docking interactions of **Zn(FLXDTC)$_2$** with EGFR protein; (a) 3D depiction of ligand-receptor binding interactions and (b) 2D representation of different forms of interactions with amino acid residues	104
Figure 3B.33	Molecular docking interactions of **Cd(FLXDTC)$_2$** with EGFR protein; (a) 3D depiction of ligand-receptor binding interactions and (b) 2D representation of different forms of interactions with amino acid residues	105
Figure 3C.1	Histographical representation of the IC_{50} inhibition values of DPPH radical scavenging activity of **FLXDTC** and **M(FLXDTC)$_2$**	110
Figure 3C.2	Cell viability assay; dose-response curves of **FLXDTC** and its metal complexes with different concentrations on MCF7 cells	110
Figure 3C.3	Cell viability assay; dose-response curves of **FLXDTC** and its metal complexes with different concentrations on HepG-2 cells	111
Figure 4A.1	The chemical structure of **FMIMN** and **M(FMIMN)$_2$**	120
Figure 4A.2	Mass spectrum of **FMIMN**	120
Figure 4A.3	FT-IR Spectrum of **FMIMN**	121
Figure 4A.4	FT-IR Spectrum of **Cu(FMIMN)$_2$**	121
Figure 4A.5	FT-IR Spectrum of **Ni(FMIMN)$_2$**	121
Figure 4A.6	FT-IR Spectrum of **Zn(FMIMN)$_2$**	121
Figure 4A.7	Electronic Spectra of **FMIMN** (—) and **Cu(FMIMN)$_2$** (—) in DMSO ($5x10^{-5}$ M); inset ($2x10^{-2}$ M)	122
Figure 4A.8	^{1}H-NMR spectrum of **FMIMN** in $CDCl_3$	124
Figure 4A.9	^{13}C-NMR spectrum of **FMIMN** in $CDCl_3$	124
Figure 4A.10	^{1}H-NMR spectrum of **Zn(FMIMN)$_2$** in DMSO-d6	125
Figure 4A.11	ESR spectrum of **Cu(FMIMN)$_2$**	126
Figure 4A.12	XRD- Platon diagram of **FMIMN** with atom-numbering	126
Figure 4A.13	X-Ray crystallographic stick diagram of **FMIMN** showing intramolecular hydrogen bonding	127

Figure 4A.14	X-Ray diffraction intensity as a function of angle (^{o}) of reflection	127
Figure 4A.15	ORTEP diagram of the XRD structure of **FMIMN** molecule	127
Figure 4A.16	Unit cell crystal packing diagram of **FMIMN** showing the two dimesitional layer structure with O-H…N intramolecular hydrogen bonding	128
Figure 4A.17	Cyclic Voltammogram of **FMIMN** ($5x10^{-4}$ M) in DMSO at different scan rates	130
Figure 4A.18	Cyclic Voltammogram of **FMIMN** ($5x10^{-4}$ M) in DMSO at different concentration	130
Figure 4A.19	Effect of scan rate on the anodic current of **FMIMN** in cyclic voltammogram	131
Figure 4A.20	Variation of anodic currents of **FMIMN** with respect to various concentrations	131
Figure 4A.21	Cyclic Voltammogram of **Cu(FMIMN)$_2$** in DMSO at different scan rates	131
Figure 4A.22	Linear Sweep Voltammogram of **Cu(FMIMN)$_2$** in DMSO at different scan rates	132
Figure 4A.23	Cyclic Voltammogram of **Cu(FMIMN)$_2$** in DMSO at different concentrations	132
Figure 4A.24	Effect of scan rate on the anodic current of **Cu(FMIMN)$_2$** in cyclic voltammogram	132
Figure 4A.25	Effect of scan rate on the anodic current of **Cu(FMIMN)$_2$** in linear sweep voltammetry	133
Figure 4A.26	Variation of anodic currents of **Cu(FMIMN)$_2$** with respect to concentration	133
Figure 4B.1	Stereographic projections of MM2-energy-minimised **FMIMN** obtained from ChemDraw Pro	135
Figure 4B.2	Dihedral angles over various locations of energy-minimized structure of **FMIMN**	136
Figure 4B.3	Conformational Analysis over C-C Bond	137
Figure 4B.4	Conformational Analysis over N-C Bond	137
Figure 4B.5	Double Angle Torsional Energy Plot Over –C(Naphth)-C=N- Moiety of **FMIMN**. Full z-scale (left, wireframe) and truncated z-scale (right, surface)	137
Figure 4B.6	AM1- Structure along with atom-numbering	138
Figure 4B.7	Hirshfeld d_{norm} surface of **FMIMN**	144
Figure 4B.8	Hirshfeld d_{norm} surface of **FMIMN** showing intermolecular hydrogen bonding interactions	145
Figure 4B.9	Hirshfeld finger print plots of **FMIMN**	146
Figure 4B.10	Intermolecular Hirshfeld inter-atomic interaction percentages	146
Figure 4B.11	Pair-wise intermolecular interactions in **FMIMN** (viewed along the c axis)	147
Figure 4B.12	Crystallographic axis-wise modes of intermolecular energies in **FMIMN**	149

Figure 4B.13	Hirshfeld surface maps of **FMIMN** represented by modes	149
Figure 4B.14	Global minimized ball-stick models of (a) **FMIMN** (b) **Cu(FMIMN)$_2$** (c) **Ni(FMIMN)$_2$** (d) **Mn(FMIMN)$_2$** and (e) **Zn(FMIMN)$_2$** (The hydrogen atoms are hidden for clarity)	151
Figure 4B.15	HOMO and LUMO molecular orbitals of **FMIMN** in wire mesh format (H-atoms and lone pairs of electrons are excluded for clarity)	152
Figure 4B.16	HOMO and LUMO molecular orbitals of **M(FMIMN)$_2$** in wire mesh format (H-atoms and lone pairs of electrons are excluded for clarity)	152
Figure 4B.17	Molecular docking interactions of **FMIMN** with EGFR protein; (a) 3D depiction of ligand-receptor binding interactions and (b) 2D representation of different forms of interactions with amino acid residues	153
Figure 4B.18	Molecular docking interactions of **Cu(FMIMN)$_2$** with EGFR protein; (a) 3D depiction of ligand-receptor binding interactions and (b) 2D representation of different forms of interactions with amino acid residues	153
Figure 4B.19	Molecular docking interactions of **Co(FMIMN)$_2$** with EGFR protein; (a) 3D depiction of ligand-receptor binding interactions and (b) 2D representation of different forms of interactions with amino acid residues	154
Figure 4B.20	Molecular docking interactions of **Mn(FMIMN)$_2$** with EGFR protein; (a) 3D depiction of ligand-receptor binding interactions and (b) 2D representation of different forms of interactions with amino acid residues	154
Figure 4B.21	Molecular docking interactions of **Ni(FMIMN)$_2$** with EGFR protein; (a) 3D depiction of ligand-receptor binding interactions and (b) 2D representation of different forms of interactions with amino acid residues	155
Figure 4B.22	Molecular docking interactions of **Zn(FMIMN)$_2$** with EGFR protein; (a) 3D depiction of ligand-receptor binding interactions and (b) 2D representation of different forms of interactions with amino acid residues	155
Figure 4C.1	Histographical representation of the IC_{50} inhibition values of DPPH radical scavenging activity of **FMIMN** and **M(FMIMN)$_2$**	159
Figure 4C.2	Cell viability assay; dose-response curves of **FMIMN** and its metal complexes with different concentrations on MCF7 cells	159
Figure 4C.3	Cell viability assay; dose-response curves of **FMIMN** and its metal complexes with different concentrations on HepG-2 cells	160
Figure 4C.4	Graphical representation MIC values of antifungal activity of **FMIMN** and its metal complexes	161
Figure 4C.5	Graphical representation MIC values of anti-cancer activity of **FMIMN** and **M(FMIMN)$_2$**	162

Figure 5A.1	Structure of **FMPC** and **FMMC**	168
Figure 5A.2	MASS Spectra of **FMPC** and **FMMC**	169
Figure 5A.3	Electronic Spectra of **FMPC** and **FMMC**	169
Figure 5A.4	UV-Visible spectra of **FMPC** and its complexes in DMSO	170
Figure 5A.5	FT-IR spectra of **FMPC** and **FMMC**	170
Figure 5A.6	^{1}H and spectra of **FMPC** and **FMMC** in DMSO-d6	171
Figure 5A.7	^{13}C NMR spectra of **FPMC** and **FMMC** in DMSO-d6	172
Figure 5A.8	Absorption (black) and emission (red) spectra of **FMPC** and **FMMC** in DMSO	173
Figure 5A.9	Fluorosence emission spectra of **FMPC** and its complexes (in their powder form)	174
Figure 5A.10	Cyclic voltammograms of **FMPC** (3.5×10^{-4} mM**)** on glassy carbon electrode at scan rates of **(a)** 40 mVs^{-1} and **(b)** at different scanrates and (**c**) the plot of the effect of the scan rate on the anodic peak current (in DMSO; pH= 4 buffer as the supporting electrolyte)	175
Figure 5A.11	XRD-Platon diagrams of **FMPC** and **FMMC** with atom numbering	176
Figure 5A.12	X-Ray crystallographic stick diagrams of **FMPC** and **FMMC** showing intramolecular hydrogen bonding (The atom numbering here is different from that in the manuscript)	177
Figure 5A.13	Unit cells of **FMPC (A)** and **FMMC (B)** seen along crystallographic **(a)** a-axis **(b)** b-axis **(c)** c-axis	177
Figure 5A.14	Parquet floor structure of **FMPC** with C–H···Cl, N–H···Cl and C–H···O hydrogen bond intermolecular interactions (shown in blue dotted lines)	177
Figure 5A.15	Parquet floor structure of **FMMC** with N–H···Cl and H_2O···Cl hydrogen bond intermolecular interactions (shown in blue and red dotted lines)	178
Figure 5A.16	X-Ray diffraction intensity as a function of angle (^{o}) of reflection of **FMPC** and **FMMC**	178
Figure 5B.1	Energy-minimized (38.07 kcal mol^{-1}) cationic form of **FMPC** (by MM2) in **(a)** stereo view and **(b)** its lateral view with the line joining N9 and C8 atoms perpendicular to the plane of the page (H-atoms are hidden for clarity)	183
Figure 5B.2	Torsional energy plots of **FMPC** over (a) C-C and (b) C-N bonds	183
Figure 5B.3	Torsional energy plots of **FMMC** over (a) **C-C** and (b) **C-N** bonds	184
Figure 5B.4	HOMO-LUMO orbitals of **FMPC** obtained from (a) B3LYP and (b) MM2	184
Figure 5B.5	HOMO-LUMO orbitals of **FMMC** obtained from (a) B3LYP and (b) AM1 (c) MM2	184
Figure 5B.6	Hirshfeld surface maps (a) with d_{norm} neighboring molecules associated with close contacts among **FMPC**, (b) two-dimensional fingerprint plot and (c) deconvolution of two-dimensional fingerprint plot illustrating percent interactions	198

Figure 5B.7	Graphical visuals of the Hirshfeld surface for **FMPC** mapped over as (a) shape index property (b) curve index flat region (rings, referred to, are marked in red) (c) diffuse color graphical portrayal (positive electrostatic potential is shown in blue shade and negative in red) (d) color coded interactions with in 3.8 Å	199
Figure 5B.8	Hirshfeld d_{norm} surface of **FMMC** showing intermolecular hydrogen bonding interactions	200
Figure 5B.9	Hirshfeld finger print plots of **FMMC**	200
Figure 5B.10	Hirshfeld surface maps of **FMMC** represented by modes	200
Figure 5B.11	Histogram of percentage contributions of various intermolecular interactions **FMPC** and **FMMC**	201
Figure 5B.12	Hirshfeld energy frameworks calculated for **FMPC** and as viewed along the c-axis showing the **(a)** electrostatic potential force, **(b)** dispersion force and **(c)** total energy diagram and (d) its annotated total energy diagram	202
Figure 5B.13	Crystallographic axis-wise modes of intermolecular energies in **FMMC**	203
Figure 5B.14	Pair-wise intermolecular interactions in **FMMC** (viewed along the c axis)	203
Figure 5B.15	Cell viability graph of **FMPC** using FaDu cells by MTT assay	204
Figure 5B.16	Cell viability graph of **FMMC** using FaDu cells by MTT assay	205
Figure 5B.17	Molecular docking interactions of **FMPC** with EGFR-TK protein; (a) 3D depiction of ligand-receptor binding interactions and (b) 2D representation of different forms of interactions with amino acid residues	206
Figure 5B.18	Molecular docking interactions of **FMMC** with EGFR-TK protein; (a) 3D depiction of ligand-receptor binding interactions and (b) 2D representation of different forms of interactions with amino acid residues	206
Figure 6A.1	Structures of **FMAPA** and **FMAMA**	211
Figure 6A.2	Mass Spectra of **FMAPA** and **FMAMA**	212
Figure 6A.3	FT-IR Spectra of **FMAPA** and **FMAMA**	212
Figure 6A.4	Overlay ^{1}H-NMR spectra of **FMAPA** and **FMAMA**	214
Figure 6A.5	Overlay ^{13}C-NMR spectra of **FMAPA** and **FMAMA**	214
Figure 6A.6	The absorptive (black) and emission (red) spectra of **FMAPA** and **FMAMA**	215
Figure 6A.7	XRD- Platon diagram of **FMAPA** with atom-numbering	216
Figure 6A.8	X-Ray diffraction intensity as a function of angle (^{o}) of reflection	216
Figure 6A.9	Crystal packing diagram of **FMAPA** showing the two dimesitional layer structure with O-H…N intramolecular hydrogen bonding	217

Figure 6A.10	Unit cell of **FMAPA** seen along crystallographic **(a)** a-axis **(b)** b-axis **(c)** c-axis	217
Figure 6A.11	MM2-energy-minimized structure of **FMAPA** (keto form) with numbered atoms	221
Figure 6A.12	Anaglyph structure of **FMAPA** (enamine form) obtained from ChemDrawPro	222
Figure 6A.13	Anaglyph structure of **FMAPA** (keto form) obtained from ChemDrawPro	222
Figure 6A.14	Conformational analysis over C6-C7	223
Figure 6A.15	Conformational analysis over C7-C8	223
Figure 6A.16	Conformational analysis over N9-C12	223
Figure 6A.17	Conformational analysis over C15-N18	223
Figure 6A.18	Conformational analysis over C6-C7-C8-N9	223
Figure 6A.19	Conformational analysis over C7-C8-N9-C12	223
Figure 6A.20	Conformational analysis over C8-N9-C12-C12	224
Figure 6A.21	Conformational analysis over C5-C6-C7-C8	224
Figure 6A.22	Double dihedral torsional energy Surfer plot of **FMAPA** (enamine form) over C19-C20 (on axis shown in red) and C20-N21 (on axis shown in blue) bonds (Refer **Figure 6A.11** for numbering of the atoms)	224
Figure 6A.23	Double dihedral torsional energy Surfer plot of **FMAPA** (keto form) over C6-C7 (on axis shown in blue) and C7-C8 (on axis shown in red) bonds (Refer **Figure 6A.11** for numbering of the atoms)	225
Figure 6A.24	Double dihedral torsional energy Grapher plot of **FMAPA** (keto form) over C6-C7 (on axis shown in blue) and C7-C8 (on axis shown in red) bonds (Refer **Figure 6A.11** for numbering of the atoms)	225
Figure 6A.25	Double dihedral torsional energy Surfer plot of **FMAPA** (keto form) over C6-C7 (on axis shown in blue) and C7-C10 (on axis shown in red) bonds (Refer **Figure 6A.11** for numbering of the atoms)	226
Figure 6A.26	Double dihedral torsional energy Grapher plot of **FMAPA** (keto form) over C6-C7 (on axis shown in blue) and C7-C10 (on axis shown in red) bonds (Refer **Figure 6A.11** for numbering of the atoms)	226
Figure 6A.27	Double dihedral torsional energy Surfer plot of **FMAPA** (keto form) over C8-C7 (on axis shown in blue) and C7-C10 (on axis shown in red) bonds (Refer **Figure 6A.11** for numbering of the atoms)	227

Figure 6A.28	Double dihedral torsional energy Grapher plot of **FMAPA** (keto form) over C8-C7 (on axis shown in blue) and C7-C10 (on axis shown in red) bonds (Refer **Figure 6A.11** for numbering of the atoms)	227
Figure 6A.29	HOMO and LUMO orbitals of **FMAPA** obtained from different modelling platforms	236
Figure 6A.30	Hirshfeld d_{norm} surface of **FMAPA** showing intermolecular hydrogen bonding interactions	237
Figure 6A.31	Hirshfeld finger print plots of **FMAPA**	237
Figure 6A.32	Relative contributions of different intermolecular contacts to the Hirshfeld surface area of **FMAPA**	238
Figure 6A.33	Hirshfeld surface maps of **FMAPA** represented by modes	238
Figure 6A.34	Pair-wise intermolecular interactions in **FMAPA** (viewed along the c axis)	239
Figure 6A.35	Crystallographic axis-wise modes of intermolecular energies in **FMAPA**	241
Figure 6A.36	Molecular docking interactions of **FMAPA** and **FMAMC** with EGFR-TK protein; (a) 3D depiction of ligand-receptor binding interactions and (b) 2D representation of different forms of interactions with amino acid residues	242
Figure 6B.1	Structures of **FFMPMC** and **FFMMMC**	243
Figure 6B.2	Mass Spectra of **FFMPMC** and **FFMMMC**	244
Figure 6B.3	IR Spectra of **FFMPMC** and **FFMMMC**	245
Figure 6B.4	^{1}H-NMR Spectra of **FFMPMC** and **FFMMMC**	246
Figure 6B.5	^{13}C-NMR Spectra of **FFMPMC** and **FFMMMC**	247
Figure 6B.6	The solid state absorption (black) and emission (red) spectra of **FFMPMC** and **FFMMMC**	248
Figure 6B.7	Acid-base pH metric titration curve for the titration of **FFMPMC** ($5x10^{-4}$ M)	249
Figure 6B.8	XRD- Platon diagram of **FFMMMC** with atom-numbering	250
Figure 6B.9	X-Ray diffraction intensity as a function of angle (^{o}) of reflection	250
Figure 6B.10	Unit cells of **FFMMMC (A)** and **FMMC (B)** seen along crystallographic **(a)** a-axis **(b)** b-axis **(c)** c-axis	251
Figure 6B.11	Crystal packing diagram of **FFMMMC** showing the two dimesitional layer structure with O-H…N intramolecular hydrogen bonding	251
Figure 6B.12	MM2-energy-minimized structure of **FFMPMC** (keto form)	255
Figure 6B.13	MM2-energy-minimized anaglyph structure of **FFMPMC** (keto form)	256

Figure 6B.14	Stereographic projection of MM2-minimized structure of **FFMPMC** (enamine form) obtained from ChemDrawPro	256
Figure 6B.15	Conformational analysis over C6-C7	257
Figure 6B.16	Conformational analysis over C7-C9	257
Figure 6B.17	Conformational analysis over N10-C13	257
Figure 6B.18	Conformational analysis over C21-N25	257
Figure 6B.19	Conformational analysis over C5-C6-C7-C9	257
Figure 6B.20	Conformational analysis over C5-C6-C7-C8	257
Figure 6B.21	Conformational analysis over C9-N10-C13-C23	258
Figure 6B.22	Conformational analysis over C22-C21-N25-C31	258
Figure 6B.23	Double dihedral torsional energy Surfer plot of **FFMPMC** (keto form) C8-C7 (on axis shown in blue) and C7-C9 (on axis shown in red) bonds (Refer **Figure 6B.12** for numbering of the atoms)	258
Figure 6B.24	Double dihedral torsional energy Grapher plot of **FFMPMC** (keto form) C8-C7 (on axis shown in blue) and C7-C9 (on axis shown in red) bonds (Refer **Figure 6B.12** for numbering of the atoms)	259
Figure 6B.25	Double dihedral torsional energy Surfer plot of **FFMPMC** (keto form) C6-C7 (on axis shown in blue) and C7-C8 (on axis shown in red) bonds (Refer **Figure 6B.12** for numbering of the atoms)	259
Figure 6B.26	Double dihedral torsional energy Grapher plot of **FFMPMC** (keto form) C6-C7 (on axis shown in blue) and C7-C8 (on axis shown in red) bonds (Refer **Figure 6B.12** for numbering of the atoms)	260
Figure 6B.27	Double dihedral torsional energy Surfer plot of **FFMPMC** (keto form) C6-C7 (on axis shown in blue) and C7-C9 (on axis shown in red) bonds (Refer **Figure 6B.12** for numbering of the atoms)	260
Figure 6B.28	Double dihedral torsional energy Grapher plot of **FFMPMC** (keto form) C6-C7 (on axis shown in blue) and C7-C9 (on axis shown in red) bonds (Refer **Figure 6B.12** for numbering of the atoms	261
Figure 6B.29	Double dihedral torsional energy Surfer plot of **FFMPMC** (enamine form) C8-N11 (on axis shown in red) and N11-C12 (on axis shown in blue) bonds (Refer **Figure 6B.12** for numbering of the atoms)	261
Figure 6B.30	Double dihedral torsional energy Grapher plot of **FFMPMC** (enamine form) C8-N11 (on axis shown in blue) and N11-C12 (on axis shown in red) bonds (Refer **Figure 6B.12** for numbering of the atoms)	262
Figure 6B.31	HOMO-LUMO orbitals of **FFMMMC** obtained from (a) AM1 (b) B3LYP (c) MM2	262
Figure 6B.32	Core structure of **FFMMMC** molecule	276
Figure 6B.33	Hirshfeld finger print plots of **FFMMMC**	279

Figure 6B.34	Relative contributions of different intermolecular contacts to the Hirshfeld surface area of **FFMMMC**	280
Figure 6B.35	Hirshfeld surface maps of **FFMMMC** represented by modes	280
Figure 6B.36	Pair-wise intermolecular interactions in **FFMMMC** (viewed along the c axis)	281
Figure 6B.37	Crystallographic axis-wise modes of intermolecular energies in **FFMMMC**	283
Figure 6B.38	Molecular docking interactions of **FFMPMC** and **FFMMMC** with EGFR-TK protein; (a) 3D depiction of ligand-receptor binding interactions and (b) 2D representation of different forms of interactions with amino acid residues	284
Figure 7A.1	Schematic of the synthesis of **PDBAD** and **[M(PDBAD)X_2]**	289
Figure 7A.2	IR spectrum of **PDBAD**	291
Figure 7A.3	IR spectrum of **[Cu(PDBAD)]**	291
Figure 7A.4	IR spectrum of **[Ni(PDBAD)]**	292
Figure 7A.5	IR spectrum of **[Co(PDBAD)(H_2O)]**	292
Figure 7A.6	IR spectrum of **[Mn(PDBAD)(H_2O)]**	292
Figure 7A.7	IR spectrum of **[Zn(PDBAD)(H_2O)]**	292
Figure 7A.8	Overlay UV-Visible spectra of **PDBAD** and **[Cu(PDBAD)]**	293
Figure 7A.9	Overlay UV-Visible spectra of **PDBAD** and **[Ni(PDBAD)]**	293
Figure 7A.10	Overlay UV-Visible spectra of **PDBAD** and **[Zn(PDBAD)(H_2O)]**	293
Figure 7A.11	Overlay UV-Visible spectra of **PDBAD** and **[Co(PDBAD)(H_2O)]**	293
Figure 7A.12	The solid state Absorption (black) and emission (red) spectra of **PDBAD**	294
Figure 7A.13	The solid state Absorption (black) and emission (red) spectra of [**Cu(PDBAD)]**	294
Figure 7A.14	The solid state absorption (black) and emission (red) spectra of **[Mn(PDBAD)(H_2O)]**	295
Figure 7A.15	The solid state absorption (black) and emission (red) spectra of **[Ni(PDBAD)]**	295
Figure 7A.16	The solid state absorption (black) and emission (red) spectra of **[Zn(PDBAD)(H_2O)]**	295
Figure 7A.17	The solid state absorption (black) and emission (red) spectra of **[Co(PDBAD)(H_2O)]**	295
Figure 7A.18	Spectrophotometric titration of **PDBAD** (c = $1x10^{-4}$ M) against **$CuCl_2$** (c = $1x10^{-4}$ M) with variation metal volume	296
Figure 7A.19	Monovariation Job's plot for the spectrophotometric titration of **PDBAD** (c = $1x10^{-4}$ M) against $CuCl_2$	296
Figure 7A.20	X-band electron spin resonance spectrum of **[Cu(PDBAD)]** in solid state	297

Figure 7A.21	**(a)** Cyclic voltammogram of **PDBAD** ($5x10^{-5}$ M) in DMSO at different scan rates **(b)** Effect of scan rate on the anodic current of **PDBAD**	298
Figure 7A.22	**(a)** LSV of **PDBAD** in DMSO at different concentrations **(b)** Variation of anodic and cathodic currents of **PDBAD** with respect to various concentration	299
Figure 7A.23	**Figure 7A.23: (a)** Cyclic voltammogram of **[Zn(PDBAD)(H_2O)$_2$]** ($5x\ 10^{-5}$ M) in DMSO at different scan rates **(b)** Effect of scan rate on the anodic current of **[Zn(PDBAD)(H_2O)$_2$]**	299
Figure 7A.24	**(a)** LSV of **[Zn(PDBAD)(H_2O)$_2$]** ($5x10^{-5}$ M) in DMSO at different scan rates **(b)** Effect of scan rate on the anodic current of **[Zn(PDBAD)(H_2O)$_2$]**	300
Figure 7B.1	MM2-energy-minimized structure of **PDBAD** (enamine form)	302
Figure 7B.2	MM2-energy-minimized anaglyph structure of **PDBAD** (Enamine form)	302
Figure 7B.3	Stereographic projection of MM2-minimized structure of **PDBAD** (enamine form) obtained from ChemDrawPro	303
Figure 7B.4	Conformational analysis over C6-C7	303
Figure 7B.5	Conformational analysis over C7-C9	303
Figure 7B.6	Conformational analysis over C8-N11	303
Figure 7B.7	Conformational analysis over N11-C12	303
Figure 7B.8	Conformational analysis over C1-C6-C7-C8	304
Figure 7B.9	Conformational analysis over C1-C6-C7-C9	304
Figure 7B.10	Conformational analysis over C7-C8-N11-C12	304
Figure 7B.11	Conformational analysis over C7-C9-N10-C13	304
Figure 7B.12	Double dihedral torsional energy Surfer plot of **PDBAD** (keto form) over C6-C7 (on axis shown in red) and C7-C9 (on axis shown in blue) bonds (Refer **Figure 7B.1** for numbering of the atoms)	304
Figure 7B.13	Double dihedral torsional energy Grapher plot of **PDBAD** (keto form) over C6-C7 (on axis shown in blue) and C7-C9 (on axis shown in red) bonds (Refer **Figure 7B.1** for numbering of the atoms)	305
Figure 7B.14	Double dihedral torsional energy Surfer plot of **PDBAD** (keto form) over C8-C7 (on axis shown in red) and C7-C9 (on axis shown in blue) bonds (Refer **Figure 7B.1** for numbering of the atoms)	305
Figure 7B.15	Double dihedral torsional energy Grapher plot of **PDBAD** (keto form) over C8-C7 (on axis shown in blue) and C7-C9 (on axis shown in red) bonds (Refer **Figure 7B.1** for numbering of the atoms)	306

Figure 7B.16	Double dihedral torsional energy Surfer plot of **PDBAD** (keto form) over C7-C8 (on axis shown in red) and C8-N11 (on axis shown in blue) bonds (Refer **Figure 7B.1** for numbering of the atoms)	306
Figure 7B.17	Double dihedral torsional energy Grapher plot of **PDBAD** (keto form) over C7-C8 (on axis shown in blue) and C8-N11 (on axis shown in red) bonds (Refer **Figure 7B.1** for numbering of the atoms)	307
Figure 7B.18	Double dihedral torsional energy Surfer plot of **PDBAD** (enamine form) over C7-C8 (on axis shown in red) and C8-N11 (on axis shown in blue) bonds (Refer **Figure 7B.1** for numbering of the atoms)	307
Figure 7B.19	Double dihedral torsional energy Grapher plot of **PDBAD** (enamine form) over C7-C8 (on axis shown in blue) and C8-N11 (on axis shown in red) bonds (Refer **Figure 7B.1** for numbering of the atoms)	308
Figure 7B.20	Double dihedral torsional energy Surfer plot of **PDBAD** (enamine form) over C6-C7 (on axis shown in red) and C7-N9 (on axis shown in blue) bonds (Refer **Figure 7B.1** for numbering of the atoms)	308
Figure 7B.21	Double dihedral torsional energy Grapher plot of **PDBAD** (enamine form) over C7-C8 (on axis shown in blue) and C8-N11 (on axis shown in red) bonds (Refer **Figure 7B.1** for numbering of the atoms)	308
Figure 7B.22	Double dihedral torsional energy Surfer plot of **PDBAD** (enamine form) over C8-C7 (on axis shown in red) and C7-C9 (on axis shown in blue) bonds (Refer **Figure 7B.1** for numbering of the atoms)	309
Figure 7B.23	Double dihedral torsional energy Grapher plot of **PDBAD** (enamine form) over C8-C7 (on axis shown in blue) and C7-C9 (on axis shown in red) bonds (Refer **Figure 7B.1** for numbering of the atoms)	309
Figure 7B.24	Double dihedral torsional energy Surfer plot of **PDBAD** (enamine form) over C7-C8 (on axis shown in red) and C8-N11 (on axis shown in blue) bonds (Refer **Figure 7B.1** for numbering of the atoms)	310
Figure 7B.25	Double dihedral torsional energy Grapher plot of **PDBAD** (enamine form) over C7-C8 (on axis shown in blue) and C8-N11 (on axis shown in red) bonds (Refer **Figure 7B.1** for numbering of the atoms)	310
Figure 7B.26	HOMO and LUMO molecular orbitals of **PDBAD**	311
Figure 7B.27	HOMO and LUMO molecular orbitals of **[CuPDBAD)]**	311

Figure 7B.28	HOMO and LUMO molecular orbitals of **[NiPDBAD)]**	311
Figure 7B.29	HOMO and LUMO molecular orbitals of **[Co(PDBAD)(H_2O)$_2$]**	311
Figure 7B.30	HOMO and LUMO molecular orbitals of **[Mn(PDBAD)(H_2O)$_2$]**	311
Figure 7B.31	HOMO and LUMO molecular orbitals of **[Zn(PDBAD)(H_2O)$_2$]**	311
Figure 7B.32	Molecular docking interactions of **PDBAD** with EGFR-TK protein; (a) 3D depiction of ligand-receptor binding interactions and (b) 2D representation of different forms of interactions with amino acid residues	314
Figure 7B.33	Molecular docking interactions of **[Cu(PDBAD)]** with EGFR-TK protein; (a) 3D depiction of ligand-receptor binding interactions and (b) 2D representation of different forms of interactions with amino acid residues	314
Figure 7B.34	Molecular docking interactions of **[Ni(PDBAD)]** with EGFR-TK protein; (a) 3D depiction of ligand-receptor binding interactions and (b) 2D representation of different forms of interactions with amino acid residues	315
Figure 7B.35	Molecular docking interactions of **[Co(PDBAD)(H_2O)$_2$]**with EGFR-TK protein; (a) 3D depiction of ligand-receptor binding interactions and (b) 2D representation of different forms of interactions with amino acid residues	315
Figure 7B.36	Molecular docking interactions of **[Mn(PDBAD)(H_2O)$_2$]**with EGFR-TK protein; (a) 3D depiction of ligand-receptor binding interactions and (b) 2D representation of different forms of interactions with amino acid residues	315
Figure 7B.37	Molecular docking interactions of **[Zn(PDBAD)(H_2O)$_2$]**with EGFR-TK protein; (a) 3D depiction of ligand-receptor binding interactions and (b) 2D representation of different forms of interactions with amino acid residues	315
Figure 7C.1	Histographical representation of the IC_{50} inhibition values of DPPH radical scavenging activity of **PDBAD** and **[M(PDBAD)X_2]**	319
Figure 7C.2	Histographical representation of the IC_{50} inhibition values of Asperegillusniger, Pencilliumnotatum antifungal activity of **PDBAD** and **[M(PDBAD)X_2]**	320
Figure 7C.3	Histographical representation of % inhibition values of MCF-7, HepG-2, HEK-293 of cytotoxicity activity of **PDBAD** and its metal complexes	321
Figure 7C.4	Cell viability assay; dose-response curves of **PDBAD** and its metal complexes with different concentrations on MCF7 cells	321
Figure 7C.5	Cell viability assay; dose-response curves of **PDBAD** and its metal complexes with different concentrations on HepG-2 cells	322

LIST OF TABLES

Table No.	Caption	Page No.
Table 1.1	Structures of the compounds investigated	3
Table 1.2	A few examples for molecular modelling software	16
Table 1.3	Some popular molecular modelling software	19
Table 1.4	Comparison of the structures evaluated experimentally by XRD and theoretically by modelling	24
Table 1.5	Selected bond distances (Å) and bond angles (◦) by X-ray diffraction and theoretical (DFT) calculations for **(N-(4-(dimethylamino)benzyl)-Npropyldithiocarbamato-S,S′)(thiocyanato-N)(triphenylphosphine)nickel(II)** complex (Numbering of the atoms is in relation to the structure shown at **Table 1.4, S.No. 1**)	25
Table 1.6	Selected bond distances (Å) and bond angles (◦) by X-ray diffraction and theoretical (DFT) calculations for **[Co(L)$_3$],** where **L** = **Ethylaminoethanol dithiocarbamate.** (Numbering of the atoms is in relation to the structure shown at **Table 1.4, S.No. 2)**	26
Table 1.7	Selected bond distances (Å) and bond angles (◦) by X-ray diffraction and theoretical (DFT) calculations for **[Zn(L)$_2$],** where **L = (E)-1-(2-Aminophenyl) ethanone oxime.** (Numbering of the atoms is in relation to the structure shown at **Table 1.4, S.No. 3)**	26
Table 1.8	Selected bond distances (Å) and bond angles (◦) by X-ray diffraction and theoretical (DFT) calculations for **[Zn(L)$_2$],** where **L = (E)-2-methoxy-6-(((3-methoxypropyl)imino)methyl)phenol**. (Numbering of the atoms is in relation to the structure shown at **Table 1.4, S.No. 4)**	27
Table 3A.1	Analytical data of **FLXDTC** and **[M(FLXDTC)$_2$]**	72
Table 3A.2	IR spectral data of **FLXDTC** and **[M(FLXDTC)$_2$]**	74
Table 3A.3	Physical, spectral and magnetic data of **FLX**, **FLXDTC** and **[M(FLXDTC)$_2$]**	77
Table 3A.4	Electrochemical data of various metal complexes in acetone medium	90
Table 3B.1	Some of the important bond lengths and bond angles of **ML$_2$ (L=FLXDTC)** (Refer **Figure 3B.20** for numbering of the atoms)	105
Table 3B.2	Some of the important dihedral angles of **ML$_2$ (L=FLXDTC)** (Refer **Figure 3B.20** for numbering of the atoms)	106
Table 3B.3	Docking data of **FLXDTC** and its metal complexes with the EGFR protein	107

Table 3C.1	MIC values of antifungal activity of **FLXDTC** and **[M(FLXDTC)$_2$]** (μg/ml)	109
Table 3C.2	Anti-scavenging activity MIC values of **FLXDTC** and **[M(FLXDTC)$_2$]** (μg/ml)	111
Table 3C.3	Antifungal activity MIC values of **FLXDTC** and **[M(FLXDTC)$_2$]** (μg/ml)	112
Table 3C.4	Anticancer activity MIC values of **FLXDTC** and **[M(FLXDTC)$_2$]** (μg/ml)	112
Table 4A.1	Analytical data# of **FMIMN** and **[M(FMIMN)$_2$]**	119
Table 4A.2	IR data# of the **FMIMN** and **[M(FMIMN)$_2$]**	120
Table 4A.3	Physical, spectral and magnetic data of **FMIMN** and **[M(FMIMN)$_2$]**	122
Table 4A.4	^{1}H NMR data of **FMIMN** and **Zn(FMIMN)$_2$**	123
Table 4A.5	Crystallographic data of **FMIMN**	128
Table 4A.6	Data of hydrogen bonding of **FMIMN**#	129
Table 4A.7	Electrochemical data of **FMIMN** and **Cu(FMIMN)$_2$** in DMSO medium	133
Table 4B.1	Important molecular energy data evaluated by AM1 and B3LYP calculations on **FMIMN**	138
Table 4B.2	Comparative list of selected bond lengths (A^o) between experimental XRD and AM1, MM2 and B3LYP Calculations of **FMIMN**	139
Table 4B.3	Comparative list of selected bond angles (^{o}) between experimental XRD and calculated AM1, MM2 and B3LYP studies of **FMIMN**	141
Table 4B.4	Comparative list of selected Dihedral angle (^{o}) of Schiff base, from experimental XRD and AM1, MM2, B3LYP calculations of **FMIMN**	142
Table 4B.5	Pair-wise intermolecular interaction energies of **FMIMN**	148
Table 4B.6	Some of the important bond lengths and bond angles of **ML$_2$ (L=FMIMN)** (Refer **Figure 4B.13** for numbering of the atoms)	155
Table 4B.7	Some of the important dihedral angles of **ML$_2$ (L=FMIMN)** (Refer **Figure 4B.13** for numbering of the atoms)	156
Table 4B.8	Docking data of **FMIMN** and its metal complexes with the EGFR protein	157
Table 4C.1	Antibacterial MIC values of **FMIMN** and **[M(FMIMN)$_2$]** (μg/ml)	158
Table 4C.2	Anti-scavenging activity MIC values of **FMIMN** and **[M(FMIMN)$_2$]** (μg/ml)	159
Table 4C.3	Antifungal activity MIC values of **FMIMN** and **[M(FMIMN)$_2$]** (μg/mL)	160
Table 4C.4	MIC values of anticancer activity of **FMIMN** and **[M(FMIMN)$_2$]** (μg/ml)	161
Table 5A.1	Analytical data# of **FMPC** and **FMMC**	168
Table 5A.2	X-ray crystallographic data for **FMPC** and **FMMC**	179

Table 5B.1	Important molecular energy data evaluated by AM1, B3LYP and MM2 calculations on the cation of **FMPC** and **FMMC**	182
Table 5B.2	Comparative list of selected bond lengths of **FMPC** (block), **FMMC** (RED) in (Å)	185
Table 5B.3	Comparative list of selected bond angles of **FMPC** (block), **FMMC** (RED) in (^{o})	188
Table 5B.4	Comparative list of selected torsional angles of **FMPC** (block), **FMMC** (RED) in (^{o})	194
Table 5B.5	Intermolecular Hirshfeld inter-atomic interaction percentages	201
Table 6A.1	Physical data$^{\#}$ of **FMAPA** and **FMAMA**	211
Table 6A.2	IR data$^{\#}$ of **FMAPA** and **FMAMA (**in cm^{-1}**)**	212
Table 6A.3	X-Ray crystallographic data for **FMAPA**	218
Table 6A.4	Important molecular energy data evaluated by AM1, B3LYP and MM2 calculations on the cation of **FMAPA**	221
Table 6A.5	Comparative list of selected bond lengths (Å) of **FMAPA**	228
Table 6A.6	Comparative list of selected bond angles (^{o}) of **FMAPA**	230
Table 6A.7	Comparative list of selected torsional angles (^{o}) of **FMAPA**	233
Table 6A.8	Intermolecular Hirshfeld inter-atomic interaction percentages	238
Table 6A.9	Pair-wise intermolecular interaction energies of **FMAPA**	240
Table 6B.1	Analytical data$^{\#}$ of **FFMPMC** and **FFMMMC**	243
Table 6B.2	X-ray crystallographic data of **FFMMMC**	252
Table 6B.3	Important molecular energy data evaluated by AM1, B3LYP and MM2 calculations on **FFMMMC**	263
Table 6B.4	Comparative list of selected bond lengths(Å) of **FFMMMC**	263
Table 6B.5	Comparative list of selected bond angles (^{o}) of **FFMMMC**	266
Table 6B.6	Comparative list of selected torsional angles (^{o}) of **FFMMMC**	271
Table 6B.7	Selected geometric and delocalization parameters for **FFMMMC**	277
Table 6B.8	Sum of bond angles around selected atoms in **FFMMMC**	277
Table 6B.9	Intermolecular Hirshfeld inter-atomic interaction percentages of **FFMMMC**	279
Table 6B.10	The molecular pair-wise interaction energies of **FFMMMC**	281
Table 7A.1	Analytical data$^{\#}$ of **PDBAD** and **[M(PDBAD)X_2]**	288
Table 7A.2	IR data$^{\#}$ of **PDBAD** and **[M(PDBAD)X_2]**	289
Table 7A.3	Physical, electronic spectral and magnetic data of **PDBAD** and **[M(PDBAD)$(H_2O)_2$]**	290
Table 7A.4	Electrochemical data of **PDBAD** and **[Zn(PDBAD)$(H_2O)_2$]** various metal complexes in acetone medium	300
Table 7B.1	Some of the important bond lengths and bond angles of **[M(PDBAD)X_2]**	312
Table 7B.2	Some of the important torsional angles of **[M(PDBAD)X_2]**	313
Table 7B.3	Docking results of **PDBAD** and its metal complexes with the EGFR protein	317

Table 7C.1	Antibacterial activity MIC values of **PDBAD** and **[M(PDBAD)X_2]** (μg/ml)	318
Table 7C.2	Anti-scavenging activity MIC values of **PDBAD** and **[M(PDBAD)X_2]** (μg/ml)	319
Table 7C.3	Antifungal activity MIC values of **PDBAD** and **[M(PDBAD)X_2]** (μg/ml)	320
Table 7C.4	Anticancer activity MIC values of **PDBAD** and **[M(PDBAD)X_2]** (μg/ml)	320

CHAPTER I

INTRODUCTION

Chemistry is known as the Central Science. Any new development in science and technology finds chemistry as the quickest customer to be applied for. Chemical sciences conventionally investigate the relationship between structure of molecules and materials and their macroscopic properties (applications). Ultimately, it is how the atoms occupy the space while to get the bond by some quantum mechanical discipline, resulting in the molecules that make the latter manifest certain unique properties. Further, structural sets of bond lengths, bond angles and dihedral angles alone are the only three spatial characteristics that distinguish one isomer from the other. While single crystal X-Ray diffraction (XRD) enabled invisible molecules to be virtually magnified to be seen vividly on a monitor or a sheet of paper, computational chemistry has been cultivated on the virtual terrain of quantum mechanics. The most advanced theoretical development of quantum mechanics, with the latest developments in the computer technology, have enabled chemists to visualize and model known and unknown compounds and to evaluate their physicochemical properties without even truly characterizing them experimentally either by wet or instrumental methods of chemical analysis. The power of computational chemistry[1] has become a potential tool in the hands of modern chemists to first predict the properties of the materials by modeling techniques before considering to really synthesizing them for real applications and biological applications[2] by molecular docking studies[3].

A great deal of research is going on in the world these days to understand the reliability and authenticity of the modelled structural properties by computational chemical methods in juxtaposition with those obtained from molecular structures obtained experimentally by single crystal X-Ray diffractometery[4,5]. Different levels of sophistication are attached to different versions of computational chemistry software. As to how much deeper and most modern quantum mechanical attributes are used in the development of the software is the factor that would decide the degree of agreement between the real and modelled properties of molecules. PH4, PC MODEL, ACD Labs, etc. were very primitive molecular modelling software which provide only very rudimentary spatial structure of the molecules. Software such as Chem 3D, marketed by Perkin Elmer, AM1 promoted by WinMOPAC, Gaussian, generated by Sun, Sybil from Certara, DFT

based software from VASP, ABINIT, CASTEP, CP2K etc. from other commercial outlets with varied levels of reliability of agreement of the modelled properties with the experimental ones, are presently used by various research groups all over the world[6,7,8,9]. A few representative examples of computational chemistry software, routinely in current applications are provided in **Table 1.2.**

It is our primary objective to consider synthesizing some new organic compounds with a molecular formula weight of 300 to 500 amu and with 20 to 30 distinct atoms, then to obtain their single crystals or of their extended derivatives and obtain their molecular structure by single crystal XRD methods before modelling the molecules with a few computational chemistry software to ascertain the degree of agreement of the structural data. It was also our objective to characterize the synthesized compounds by various spectral, electro chemical and other instrumental methods and to correlate the same with the XRD structures and the properties obtained by molecular modelling and with the orbital energies and shapes. Conformational analysis by both single bond dihedral torsion and dual bonds by double dihedral torsion was also considered to ascertain the most stable single molecules by global minimum Eigen values. The compounds would be also exposed to evaluate their biological applications and molecular docking studies.

In case the XRD and modelled data are in good agreement and the compounds are proven to be potential ligands for metal-coordination, the complexes would also be attempted for XRD studies and molecular modelling. If we would be unable to develop single crystals for the complexes or some chosen ligands, suitable enough for the XRD, such molecules would be modelled and their structural properties would be estimated based on the XRD properties of their ligands and of their structural analogues, respectively.

New classes of Schiff bases and dithiocarbamate systems have been considered for our studies as nitrogen and sulfur compounds have potential biological applications.

The azomethine functionality or the sulfur functionality bearing compounds, were edificed on various aromatic skeletons, such as substituted phenyl, naphthyl and quinolinyl aromatic rings.

The following are the compounds chosen and studied in detail.

Table 1.1: *Structures of the compounds investigated*

Nature/Type	Nitrogen exocyclic	Nitrogen endocyclic; Sulfur exocyclic	Nitrogen-exo and endo
Ligand Type	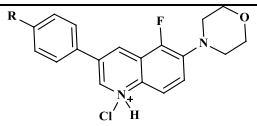 R = -H, -OMe **FMPC**	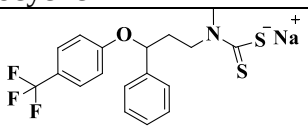 **FLXDTC** 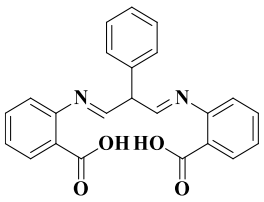 **PDBAD**	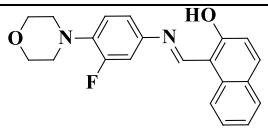 **FMIMN** 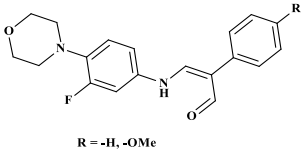 R = -H, -OMe **FMAPA** 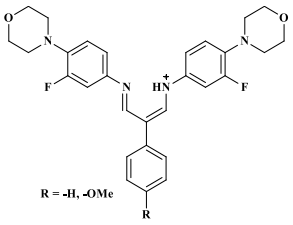 FFMMMC
Complex Type	**[M(FMPC)$_4$]**	**[M(FLXDTC)$_2$]** **[Cu$_2$(FLXDTC)$_2$Cl$_2$]** **[M(PDBAD)X$_2$]**	**[M(FMIMN)$_2$]** **[M(FMAPA)]$_2$** **[M(FFMMMC)$_2$]**

The state of the art of nitrogenous and thio-organic compounds is briefly outlined hereunder:

1.1 Importance of Nitrogenous Organic Ligands:

Nitrogen compounds are important because they are key in metabolic activities. Nitrogen compounds have various physicochemical and biological applications. Urea, amine, and guanidine are nitrogen compounds that denature proteins, giving them antibacterial properties[10]. quaternary ammonium salts are a type of nitrogen molecules that can be used to treat bacteria[11,12,13] (Coleman, 2005; Shahidi and Wiener, 2012; Windler et al., 2013). Nitrogen compounds [nitrites (NO_2^-) and nitrates (NO_3^-)] are frequently utilized in the fertilizer sector and by the food industry to extend the shelf life of food goods. In both nature and synthetic organic chemistry, nitrogen compounds, in general, and amines, in particular, are extremely significant molecules[14].

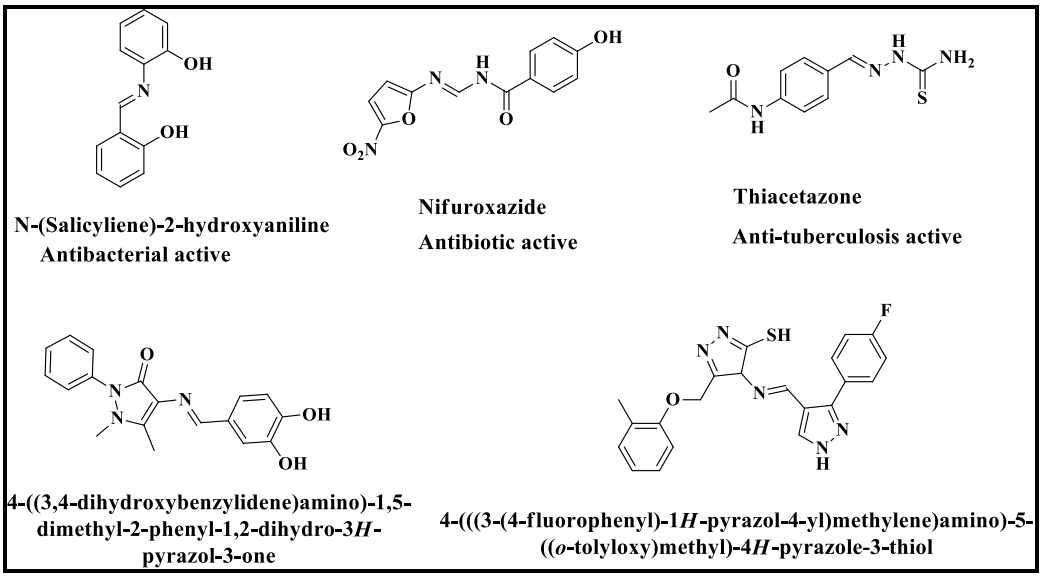

Figure 1.1: *Selected examples for biologically active Schiff bases*

Amines have a unique niche in organic chemistry. These are found in amino acids, peptides, proteins (enzymes and glycoproteins), lactams, porphyrins, chlorophyll, nucleosides, nucleotides, DNA, RNA, alkaloids, and many other naturally occurring, biologically significant compounds. They are also present in a lot of the synthetic substances that are used to make medications for commercial applications. Amines are not only crucial building components in many common polymers, such as nylons and polyamides, but also are used as bases in many synthetic transformations. They also serve as key intermediates in organic synthesis, especially to be adducted as Schiff bases, in which them convert carbonyl groups (–C=O) in to azomethine (-C=N) moieties. Schiff bases, or azomethine compounds have become as unique class of compounds by themselves to possess a most of biological application and in coordination chemistry as potential ligands. Compounds with proven biological applications, possessing an azomethine group (R_1R_2**C=N**R_3) are presented in **Figure 1.1**.

Primary amines and secondary amines are also very potential precursors in their extension to result in thio-organic compounds. A special class thio-organic compounds are dithiocarbamate R_1R_2**N-CSS**$^-$. These -N-CS_2^- based compounds have a unique character of resulting in a quadricyclic chelation as

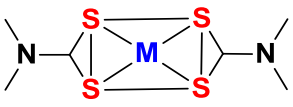

whose analogue of

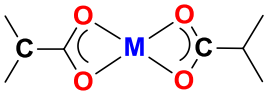

is hardly present in nature.

1.2 General Introduction to Schiff Bases and Their Metal Coordination:

Schiff base ligands have a significant impact on coordination transitional metal chemistry and organic chemical synthesis. Hugo Schiff discovered the interaction of carbonyl compounds with primary amines to generate imines, or Schiff base compounds, in 1864[15]**.** These can form stable metal complexes with metal atoms in a variety of oxidation states[16]. Schiff bases bind to metal ions via donating lone pair electrons to the nitrogen atom and a variety of donor groups to the Schiff bases, such as hydroxyl (-OH), carboxyl ($-COO^-$), thionyl (-SH), and many more. The Schiff base is depicted structurally in **Figure 1.2**.

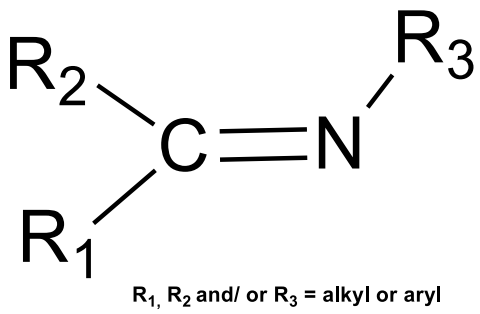

Figure 1.2: *General structure of a Schiff base*

Aryl group substituted Schiff bases are more stable than aliphatic group substituted Schiff bases because imine causes resonance due to effective conjugation with aromatic rings[17]. Due to steric hindrance concerns, aldehydes are more reactive with amines to produce Schiff bases than ketones. The general approach for synthesizing Schiff bases is shown in **Scheme 1.1**.

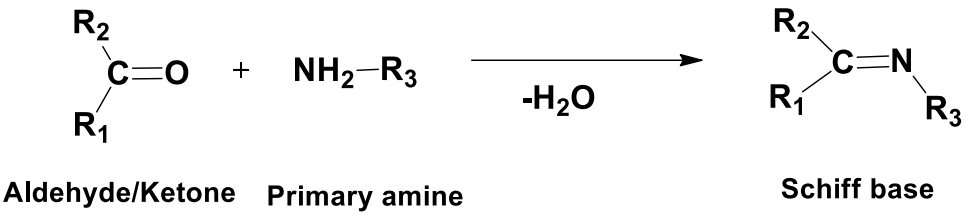

Scheme 1.1: *The general schematic of the synthesis of a Schiff Base*

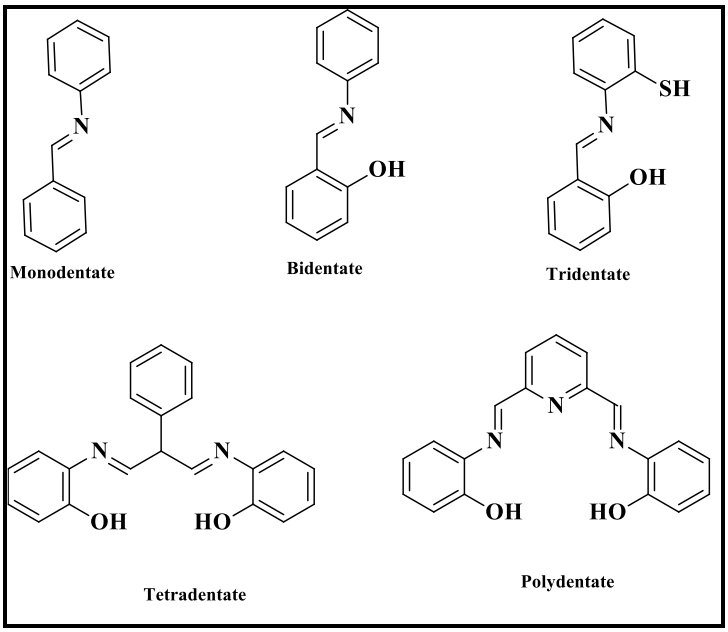

Figure 1.3: *Variable number of donor atoms in Schiff base complexation*

Schiff base ligands are effective chelating agents in metal complexation because they have a lone pair of electrons in the sp^2 orbital of the nitrogen atom in the azomethine group[18]. Schiff bases comprising a variety of donor atoms have been reported frequently. Depending on the number of donating moieties on the Schiff base, Monodentate (one contributing site), bidentate (two donating sites), tridentate (three donating sites), tetra dentate (four giving sites), and polydentate ligands generate metal-coordinated complexes. In stable metal complexes, numerous functional groups play a role in addition to the Schiff base nitrogen donor. **Figure 1.3** shows the structures of different donor functional group ligands.

Schiff base's chemical, electrical, electrochemical, and structural expressions are based on the molecular skeleton with various electron-donating or electron-withdrawing groups (R_1, R_2 and

R_3 in **Scheme 1.1**)[19]. Researchers continue to be drawn to them due to their significance in a wide range of technological and biological activities. Schiff bases have a significant impact on coordination chemistry and have played a pivotal role in the evolution of inorganic chemistry. Because of their variety, synthetic flexibility, and sensitivity to the central metal atom, Schiff bases are an important family of ligands.

Schiff bases and their metal complexes are extremely important for biological systems due to their preparative accessibility and structural arrangements. They have applications in polymers[20], dyes[21], catalysis[22], agriculture[23], pigments[24] and industry[25]. Schiff bases have become extremely important in the fields of medicine and pharmacology[26]. Antifungal[27], antibacterial[28], antioxidant[29], anticancer[30], analgesic[31], inflammatory[32], antitubercular[33] and allergy[34] effects have been reported in metal complexes derived from several Schiff bases. Some of the biologically active Schiff-bases are shown in **Figure 1.1**. In the solid state, crystal packing and intermolecular interactions of diverse azomethine species might provide significant information for the design and fabrication of innovative device materials. Because of their wide range of analytical, commercial, and biological applications, research on Schiff base ligands and their metal complexes is continuing.

Murukan *et al.* reported the formation of a bishydrazone by synthesizing 2-hydroxy-1-naphthaldehyde with isatin monohydrazone[35]. Metal complexes of Mn(II), Fe(II), Co(II), Ni(II), Cu(II), and Zn(II) with the ligand bishydrazone were synthesized and characterized. The results show that the complexes are more effective at killing bacteria than the ligand. V. Barve *et al.* reported the synthesis of 3-formylchromone Schiff base derivatives and their copper complexes. The synthesized compounds were characterized and studied for their anticancer activity. The IC_{50} values of the complexes were far less than the ligands[36]. M. Kalanithi *et al.* reported the synthesis of metal complexes with the ligand derived from 3-formylchromone with 2-aminothiazole. The ligand and its metal complexes were characterized by different analytical tools. The antimicrobial activity against the species *A. niger, S. aureus, C. albigans, P. aeruginosa, E. coli* and *B. subtilis*, was tested and compared with the ligand activity. The metal complexes showed more activity due to the chelation process[37]. The synthesis and characterization of Cu(II) and Zn(II) complexes with the new Schiff base ligand derived from 2-amino-3-formylchromone with (R)-2-amino-2-phenylethanol have been reported by F. Arjmand *et al.* The DNA binding results showed that both

the metal complexes bind to CT-DNA by electrostatic groove binding mechanism. The Cu(II) complex shown efficient cleavage activity of plasmid pBR322 DNA[38].

C. Anitha *et al.* reported the synthesis and characterization of VO(II), Co(II), Ni(II), Cu(II) and Zn(II) complexes of Schiff base synthesized from 5-(4-chloro-phenylazo)-2-hydroxybenzaldehyde, 3-formylchromone and *p*-phenylenediamine. The antibacterial activity results showed that Cu(II) and Zn(II) complexes were more active. The synthesized compounds showed higher luminescence efficiency[39]. T. Jeewoth *et al.* reported the synthesis and characterization of Cu(II), Fe(III), Ni(II), Ru(II) and Zn(II) complexes with the new Schiff base ligand derived from 2-hydroxy-1- naphthaldehyde with 2,3-diaminopyridine[40].

V. Mahalingam *et al.* reported some new Ru(III) complexes by using the Schiff bases formed by the reaction between 2-hydroxy-1-naphthaldehyde with some derivatives of aniline. Some of the Ru(II) complexes have been tested for the catalytic activity in the oxidation of benzaldehyde[41]. Trivalent lanthanide complexes with Schiff base derived from 2-hydroxy-1-naphthaldehyde and 1,3-propyldiamine have been reported by Ziyad A. Taha *et al*. Results presented in this study indicated that Sm and Tb complexes with *N*,*N'*-bis(2- hydroxynaphthyl-methylidene)-1,3-propanediamine can be considered as promising candidates in the design of photoluminescence devices[42]. M. Macit *et al.* reported crystal structure, spectroscopic properties and DFT studies on Cu(II) complex of the Schiff base compound derived from the reaction of 2-hydroxy-1- naphthaldehyde with 3-chloro-4-methylaniline. This study demonstrated that Cu(II) complex can be used as a good nonlinear optical material[43].

A few of the above ligands and complexes have been structurally investigated by both XRD experimentally and by computational molecular modeling followed by correlating the structural data.

1.3 General Introduction to Dithiocarbamate and their Metal Binding:

In dithiocarbamate, both of the carbamate's oxygen atoms have been replaced with sulfur atoms. They were originally used as rubber vulcanization accelerators. The tetra methyl thiuram disulphide, often known as thiuram, was the first dithiocarbamate derivative to be patented as a fungicide in 1934[44]. Dithiocarbamates have drawn a lot of attention because of their soft binding nature and acute biting angles[45] as well as their uses in pharmacy[46], electrochemistry[47], industry[48],

agriculture, and other sectors. Through thioureide tautomerism (**Figure 1.4),** the dithiocarbamate moiety can stabilize the oxidation states of numerous transitional metal ions[49]. They use Monodentate or bidentate chelating modes to bind to metal ions as shown in **Figure 1.5.**

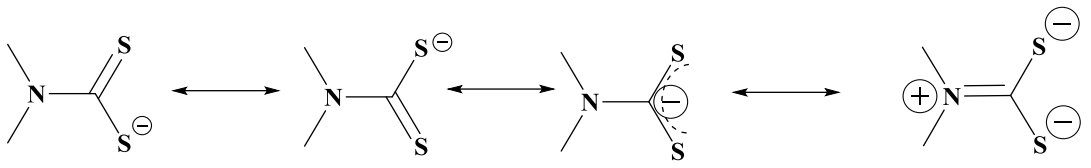

Figure 1.4: *Canonical resonance forms of dithiocarbamate anion*

Primary and secondary amines reacted with carbon disulfide in cold conditions to synthesize dithiocarbamate ligands. Any sodium or potassium base can be used to produce dithiocarbamate ligand salts, and a general scheme for the preparation of dithiocarbamate is shown in **Scheme 1.2.**

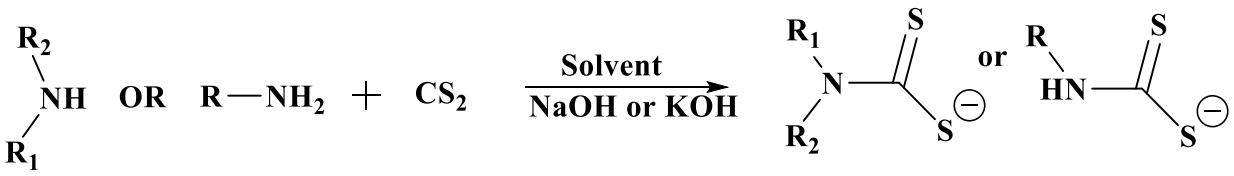

Scheme 1.2: *General schematic for the synthesis of dithiocarbamate*

Dithiocarbamate coordination compounds, comprising divalent transition metals with a partially coordinated central metal atom, can reverse the binding molecules of organic sulfur-nitrogen-phosphorous donor bases, resulting in intermolecular heteroleptic coordination complexes known as adducts[50]. Because one or two Lewis base molecules are present, adducts have a higher coordination number. **Figure 1.6** shows the adduct formation through bidentate dithiocarbamate with Lewis base. Ekennia et al. say that forming adducts with Lewis bases doesn't change the oxidation state of the metal atom, but it does increase the coordination number of the metal ion. The physical properties of the adducts are also different from those of the parent complex, which helps with the development of different photosensitizer applications and biological activities[51].

Figure 1.5: *Monodentate and bidentate metal-binding modes of dithiocarbamate*

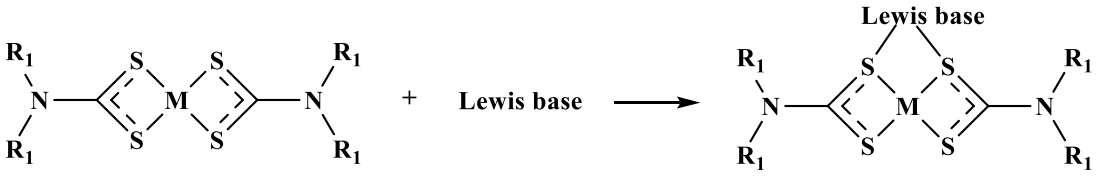

Figure 1.6: *Schematic of Dithiocarbamate as a bridge to form adducts with Lewis bases*

Anderson discovered ferric dimethyl dithiocarbamate (ferbam) for the first time[52]. Ziram (zinc dimethyl dithiocarbamate) has been proven to be more effective in vegetable crops than in fruit trees, and has been used to prevent orchard diseases as well as an ornamental spray[53]. The structures of ferbam and ziram are shown in **Figure 1.7**.

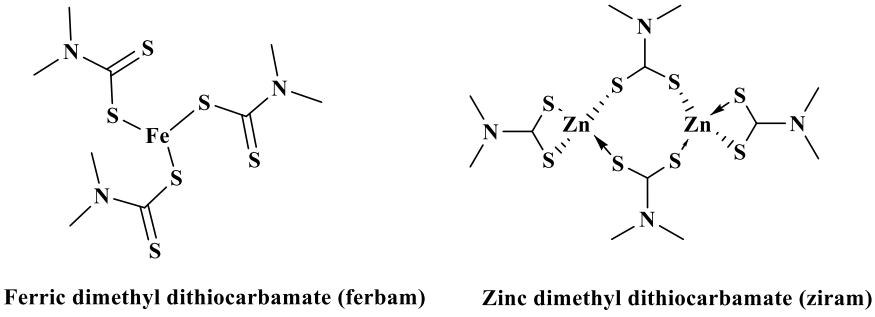

Figure 1.7: *Structures of* ***ferbam*** *and* ***ziram***

Many of the reported studies of dithiocarbamate describe the effectiveness of dithiocarbamate as potential bidentate ligands and the stability of the four-membered MSCS chelates. There are no extensive studies of the influence of complexation on the otherwise reversible cyclic voltammetric behavior and magnetic resonance spectra of dithiocarbamates in non-aqueous environments. In addition, how the complexes serve for further extension of

complexation with dithiocarbamate sulfurs serving as bridging atoms is also not considerably documented, though in biology, ferredoxins exhibit such instances. In the case of stable metals, dithiocarbamate binds with another metal ion with no further consumption of an additional dithiocarbamate ligand. Such a phenomenon would be reflected in spectral studies. Thus, more metal centers can be bound by the conservation of dithiocarbamate ligand.

1.4 Introduction to Quinolines:

Quinoline is an aromatic heterocyclic family of organic compounds having a double-ring system consisting of a benzene and a pyridine ring joined at two carbon atoms adjacent to each other [54]**.** It forms salts when it reacts with acids in the same way as benzene and pyridine do. It can perform both electrophilic and nucleophilic substitution reactions[55]. 1-azanapthalene and benzo [b] pyridine are other names for quinoline. Quinoline is an essential element that can be found in both natural and synthetic compounds. The pyranoquinoline ring system has drawn a lot of interest because it's a significant structure that makes up the basic skeleton of numerous alkaloids[56]. Quinolines are generated from quinine, an alkaloid extracted from the Cinchona tree's bark[57].

Quinoline is primarily used in the production of nicotinic acid, which is used to treat pellagra in humans as well as other compounds[58]. The synthesis of polysubstituted quinoline derivatives has received a lot of attention and interest because of their wide variety and-vast range of biological applications[59]. Montelukast and Skimmianine are two natural chemicals that contain the quinoline moiety[60]. Polysubstituted quinolines, in particular, are important chemicals with antimalarial[61], anti-inflammatory[62], antiasthmatic[63]**,** and antibacterial activities[64], as well as a variety of commercial uses. Substituted quinolines are alkaloids found in many plants belonging to the Rutaceae family[65]**.** Quinoline's structure is essential for the development of novel pharmacological compounds with broad biological effects. Chloroquine, which was the frontline treatment for treating P. falciparum malaria until the 1950s, is an example of the quinoline structure[66]. Its use has now been phased out in several endemic locations owing to parasite resistance, which has rendered the treatment ineffective. Quinolines cause Plasmodium cytotoxicity by binding to heme and preventing the formation of hemozoin. Nitroxoline (antibacterial action), chloroquine and hydroxychloroquine (antimalarial action), and bedaquiline (antimalarial action) are all commercially accessible quinoline structural component medicines (multidrug-resistant tuberculosis action). So far, several synthesis processes have been published

in the literature for the creation of this scaffold. Traditional synthesis approaches, including Gould–Jacob[67], Friedländer[68], Pfitzinger[69], Skraup[70], Doebner–von Miller[71], and Conrad–Limpach[72], have been used to create the primary quinoline scaffold in the past. Transition metal-catalyzed reactions, metal-free ionic liquid assisted procedures, ultrasonic irradiation reactions, and green reaction protocols are all suitable for the synthesis and functionalization of this molecule. The majority of literature focuses on and emphasizes the synthesis methods and findings stated above to address the shortcomings of the syntheses as well as their environmental side effects. Even though there are many well-known ways to make substituted quinoline derivatives, which are important in medicine and industry, developing new ways to make more potent derivatives is still an active area of research.

1.4.1 *General Synthetic Method for Quinoline Derivatives:*

As we have synthesized a novel compound, **FMPC** (**Table 1.1**) by cyclization, the general procedure of obtaining quinoline synthesis by reported Combes cyclization method is briefly described here.

The Combes quinoline synthesis was first reported by Combes in 1888[73]. It involves the condensation of unsubstituted anilines **(1)** with β-diketones **(2)** to form substituted quinolines **(4)** after an acid-catalyzed ring closure of an intermediate Schiff base **(3).** The Combes quinoline synthesis is often used to prepare the 2,4-substituted quinoline backbone and is unique in that it uses a β-diketone substrate. **Scheme 1.3** shows the synthetic procedure of quinoline from the Combes method.

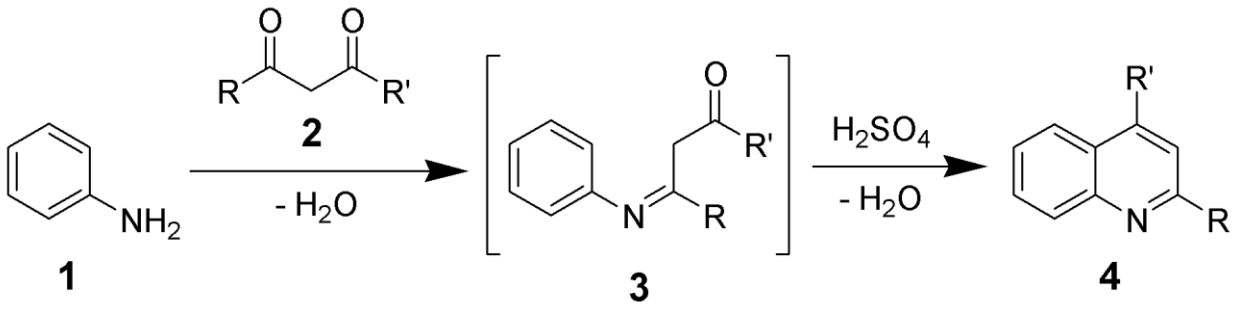

Scheme 1.3: *General scheme of the Combes quinoline synthesis*

1.5 Computational Chemistry and Molecular Modelling Paradigms:

When a mathematical method is sufficiently well developed that it may be automated for computer implementation, it is referred to as "computational chemistry." The application of chemical, mathematical, and computing skills to the solving of interesting chemical issues is known as "computational chemistry." It makes use of computers to generate data such as molecular attributes or simulated experimental outcomes. Even though only a few parts of chemistry can be calculated exactly, almost every part has been described in a qualitative or close-to-quantitative way.

The development of theoretical and computational approaches to model and investigate the behavior of molecules, from small chemical systems to huge biological molecules and material assemblies, is the basis of molecular modeling. Molecular modeling has applications in computational chemistry, drug design, computational biology, and materials research. Simulation is the most basic computer tool for molecular modeling. Ebejer et al. (2013) say that molecular simulation approaches need more processing power and software[74]. Understanding the structure, stability, and response qualities of molecular crystals at specific pressures and temperatures is essential for crystal engineering and applications. For a long time, classical mechanistic force-field approaches have dominated the field of crystal structure prediction and modeling of molecular crystals. First-principles techniques based on density functional theory may now be applied to realistically relevant molecular crystals in view of growing processing capacity and the development of increasingly sophisticated quantum-mechanical approximations. Computational chemistry has proven to be a beneficial tool for researching compounds that are either difficult to get or incredibly expensive. It also helps chemists make predictions before they do real experiments, which makes it easier for them to make observations. Computer software can calculate a variety of molecular unit properties. Geometry optimization is the most important of these calculations. Geometry optimization is the process of observing the molecular potential energy surface and finding equilibrium between the molecule and the resulting energy. The potential energy surface is a representation of the relationship between bond distance and energy associated with nuclear locations. When a global minimum is found, which indicates the lowest energy of repulsion and attraction between the atoms in the structure, the structure is said to be optimized. The gradient, or first derivative of the potential energy surface, aids the program in locating the global minimum by describing the slope and identifying the direction in which the

energy declines the most rapidly from the original input. When the convergence requirements are met, the optimization process is complete. These requirements entail bringing the forces and their root-mean-squares as near to zero as possible, as well as bringing the calculated atom displacement and its root-mean-square to zero.

Bond energies, bond lengths, bond angles, and dihedral angles can all be calculated using an optimized geometry. In order to calculate any other parameter correctly, geometry optimization must be performed to a basis level that is equivalent to or higher than the parameter to be calculated. Each structural unit is subjected to a vibrational frequency calculation once the geometry has been adjusted. The nuclei's motion directions and amplitudes in the ground and excited states, as well as the modes of vibration, are calculated. The equation 3n-6 calculates the number of modes of vibration for nonlinear molecules, where n is the number of atoms. Because there is no change in dipole moment as a linear molecule rotates around its molecular axis, it has 3n–5 normal modes of vibration.

As mentioned above computational chemistry as reached such an advanced stage that contemporary chemist is not only able to visualize the molecular spatial geometry (with all the structural parameters viz., bond lengths, bond angles and dihedral angles) but also predict their macroscopic properties based on quantum mechanical molecular modelling without having to synthesize the compounds and characterize. The usual procedure follows the following steps (**Figure 1.8**).

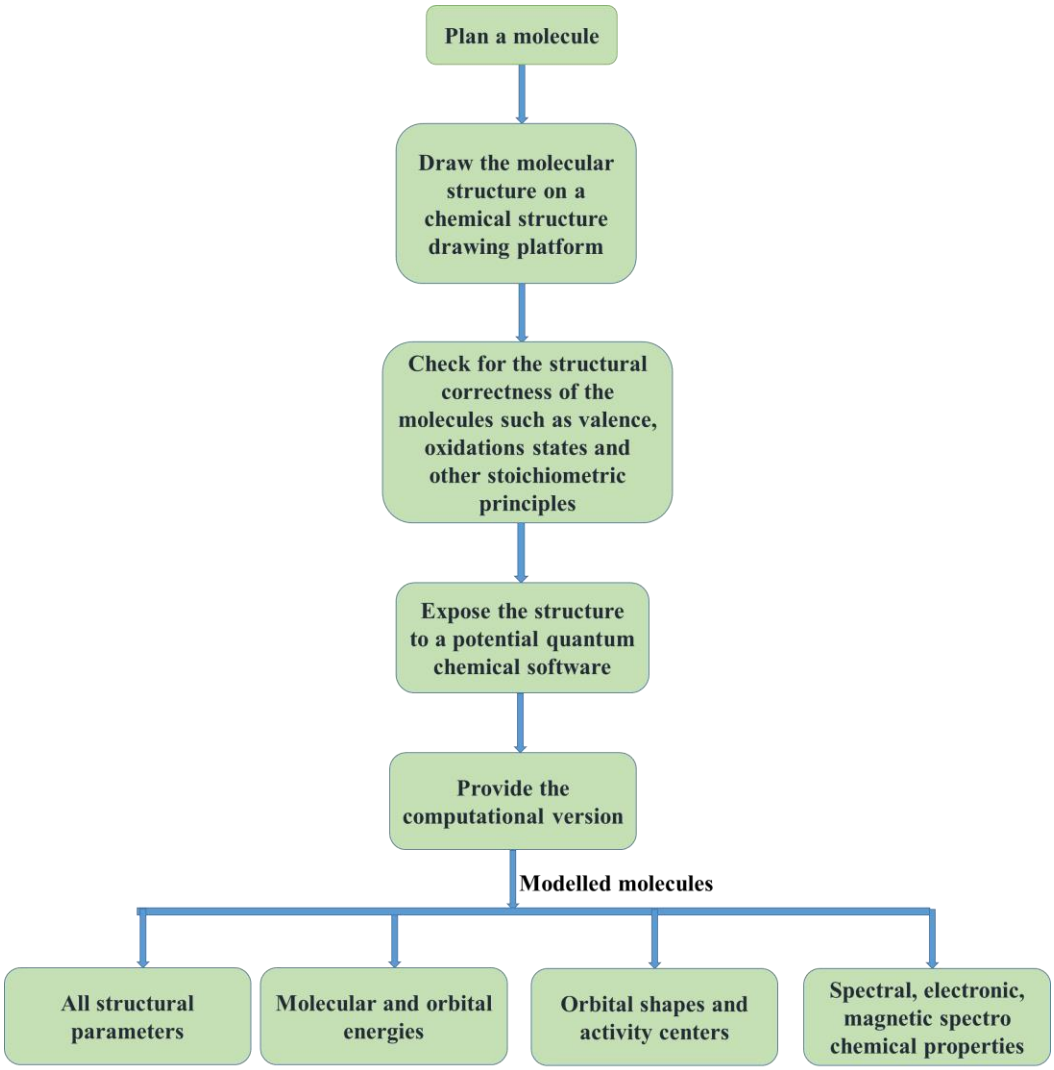

***Figure 1.8*:** *The Schematic of the ab initio sequence of molecular modelling*

A variety of skeletal structural drawing software for molecular structure drawing, quantum mechanical computational chemistry software for molecular modelling and molecular docking software for inter molecular interactions and bio-molecular docking, are available both in open access and proprietary domains.

A few versions of software to achieve the above various tasks are mentioned here under:

Table 1.2: *A few examples for molecular modelling software*

		Proprietary:	Free Software:
(a)	**Structural Drawing:**	ACD/ChemSketch, BIOVIA Draw, ChemDraw, ChemWindow, Marvin Sketch, etc.	BKChem, JChemPaint, Molsketch, XDrawChem etc.
(b)	**Quantum Mechanical Molecular Modelling:**	CPMD, CHEMKIN, Discovery Studio, Desmond, Glide, Gaussian, MOPAC, Spartan, GAMESS, Q-Chem, Chem3D, AMBER, MODELLER, UCSF Chimera etc.	BigDFT, CONQUEST, MPQC, ORCA, Quantum ESPRESSO, GROMACS, OpenMM, CP2K, AutoDock, AutoDock Vina, Avogadro, Jmol, Cantera, Chemistry Development kit, RasMol, Open Babel etc.
(c)	**Molecular Docking:**	Glide, LeDock, MOE etc.	AutoDock, AutoDock Vina, FlexAID, rDock etc.

The above various versions of molecular modelling software employ a blend of classical mechanics and quantum mechanics to varied degrees of advancement and sophistication.

Whereas medium range and low-cost software utilized Hartree-Fock method based on self-consistent theory (SCF) on many body systems advance theories such as Density Functional Theory (DFT), Time-dependent Density Functional Theory (TD-DFT), use frontier molecular orbital functional and inter electronic interactions wherein electron cloud of the whole molecule is taken as localized density variation on the basis of Thomas-Fermi model developed by Walter Kohn (1998, Nobel prize) and Lu Jeu Sham.

Irrespective of the modernity, any of the above molecular modelling software uses Born-Oppenheimer approximation, which treats the positively charged nuclei of the molecules or clusters as fixed in space which generate a static external potential ($\hat{V}$) over the moving electrons. Then a time independent function describing stationary electronic state Ψ ($r_1, r_2, \ldots r_N$) is generated followed by its Hamiltonian operation through Schrodinger equation,

$$\hat{H}\Psi = [\hat{T} + \hat{V} + \hat{U}]\,\Psi = \left[\sum_{i=1}^{N}\left(-\frac{\hbar^2}{2m_i}\nabla_i^2\right) + \sum_{i=1}^{N} V(r_i) + \sum_{i<j}^{N} U(r_i, r_j)\right]\Psi = E\Psi \qquad \textbf{(1.1)}$$

where,

$\hat{H}$ = Hamiltonian operator for the wave function (Ψ) of the N electron system, $\hat{T}$ is the total kinetic energy of all the electrons.

$\hat{V}$ is the inter electronic interactions energy

h = Plank constant

m_i = mass of the i^{th} electron

∇_i^2 = Laplacian operator

E = Total energy of the system (sum of potential and kinetic energies)

Here r_i is the radial distance of the i^{th} electron from the origin of the Cartesian coordinate system

While medium range molecular modelling software use the simplest Hartree-Fock methods, use Kohn-Sham equations on normalized wave functions (Ψ) along with the electron density functional, $n_i(r_i)$ given by (for arbitrary first electron)

$$n_1(r_1) = N\int d^3 r_2 \ldots, \int d^3 r_N \Psi^*(r_1, r_2, \ldots, r_N)\, \Psi(r_1, r_2, \ldots, r_N) \quad \textbf{(1.2)}$$

With certain local density approximations, (LDA)

$$E_{XCi}^{LDA}[n_i] = \int \epsilon_{XCi}(n_i)\, n_i(r_i)\, d^3 r_i \quad \textbf{(1.3)}$$

and local spin density approximations [LSDA]

$$E_{XCi}^{LSDA}[n_{i\uparrow}, n_{j\downarrow}] = \int \epsilon_{XCi}(n_{i\uparrow,} n_{j\downarrow})\, n_i(r_i)\, d^3 r_i \quad \textbf{(1.4)}$$

where

ϵ_{XCi} = is the sum of the inter electronic exchange part (ϵ_{Xi}) and correlation part (ϵ_{Ci})

along with generalized gradient approximations (GGA)

$$E_{XCi}^{GGA}[n_{i\uparrow}, n_{j\downarrow}] = \int \epsilon_{XCi}(n_{i\uparrow,} n_{j\downarrow,}\ \nabla_{ni\uparrow,} \nabla_{nj\downarrow})\, n_i(r_i)\, d^3 r_i \quad \textbf{(1.5)}$$

and Thomas-Fermi model, Hohenberg-Kohn theorem have developed an equation for the lowest eigen value (global minimum) of the n electron system has given below

$$E_{(V,N)}[n] = F[n] + \int V(r_i) n_i(r_i) d^3 r_i \quad \textbf{(1.6)}$$

In molecular modeling, one generates a 3-D structure of the most stable molecule (with the least possible Eigen value) by exposing the molecule to a quantum mechanical machinery as mentioned above.

Occasionally, some of the properties of the compounds (molecules) depend simultaneously on more than one independent variable. Though there are a variety of graphical software are available to generate plot of the functions like, y = f (x) where y is the domain of the dependent variable (property) and the x is that of the independent. In order to picture plots of the kind, z = f (x, y) where z is the domain of the data of the dependent variable (property) and x and y are those of the dependent ones, one may have to depend on some special software. One may be interested in the conformational analysis of the molecule over an important single bond or over a pair of bonds. Plots of molecular energy as a function of torsional angle over a bond can be obtained by incremental twisting of the molecular segments connected by the bond and by obtaining the respective Eigen value at each of the twists. A 2-D plot can, then, be obtained for the conformational energy diagram. However, if two major molecular moieties are linked at 1,3 carbons, the conformational energy diagram may have to be obtained as the plot of Eigen value vs the angle of torsion over 1-2 carbon bond and also as a simultaneous function of the torsional angle over the 2-3 carbon atoms. In such cases, a 3-D plotting is necessary. There are commercial and open access software which generate data-set of z domain, as a simultaneous function of x-data-set and y-data-set, in case one has experimental data of the z as independently function of x and y variables. This process is called, Gridding. The grid files can be transformed in to 3-dimensional images in various formats, mostly as wire-frame diagrams or surfaces. Commercial software such as GoldenSoft's Surfer and Grapher can execute such operations.

A few routinely used chemistry software, available both in open access and commercial markets for molecular modelling are presented in **Table 1.2.**

Table 1.3: *Some popular molecular modelling software*

Program	Organization	Function
ChemDoodle	iChemLabs	Producing chemical 3D structures, graphics, animations, molecular masses, and elemental analysis calculations. The optimizations were performed using a MMFF94 force field with a conjugate gradient search direction and Newton line search to convergence. It comes with a visualization tool called ChemDoodle 3D that transforms the 2D chemical structures into unique 3D models.
Hypercube	HyperChem Site Licenses	With single point, geometry optimization, or transition state search computations, use HyperChem to examine the potential energy surfaces of quantum or classical models. Include the effects of thermal mobility in simulations using Metropolis Monte Carlo, Langevin dynamics, or molecular dynamics. It is possible to incorporate user-defined structural restrictions.
Avogadro	Avogadro Chemistry. Powered by Jekyll & Minim al Mistakes.	Avogadro is a program that creates various computational chemistry packages and facilitates the import of chemical data. It is utilized by beginning and experienced chemists alike in a variety of scientific disciplines, including computational chemistry, molecular modeling, bioinformatics, and materials science. This software's powerful features for molecular editing and flexible, high-quality rendering are some of its main benefits.
ChemAxon	ChemAxon	Tools for drug research, chemical database searching, and management are all included in the Chemaxon Products line. For academic use, products come with free licenses. The desktop applications from Chemaxon include JChem for Excel, which combines the structure handling capabilities of JChem and Marvin within a Microsoft Excel environment; Instant JChem, a desktop application for end-user scientists; and Marvin, free chemistry software for drawing and visualizing chemical structures. The program can be used to forecast logP values and pKa values. Using Markush structures from the Thomson Reuters Derwent World Patents Index (DWPISM) database, the business built Markush structure storage and search capabilities (without enumeration). Many Pearson Mastering Chemistry courses use Chemaxon's JChem, MarvinSketch, and MarvinView as its chemistry tools.
BIOVIA Draw		An application for drawing molecules called BIOVIA Draw is primarily intended for chemists and other professional members of the chemical industry. It provides them with an entire range of tools for designing and manipulating intricate molecules, chemical processes, and biological sequences. It has an easy-to-use interface that makes it possible to look at, share, and keep scientific knowledge.

MolView	MolView AGPL Free Software	The chemistry modeling program MolView has a very unique interface compared to the other programs described before. Its primary distinction is that it is a free, accessible web application. In comparison to the other packages described above, MolView has a very distinct interface and is a modeling tool for chemistry. The key distinction between a molecular editor and a viewer for 3D models is that both are available in this open-source web application. We may upload molecules from significant databases, including PubChem, the RCSB Protein Data Bank, and the Crystallography Open Database as a user. In addition to establishing structural formulas, MolView also allows for the depiction of chains, modeling and simulation of protein assembly, and protein display. Additionally, you can export several types of data in the JCAMP file format or the PNG format (as a snapshot from the interactive spectrum) (JCAMP-DX file of the current spectrum).
ACD/ChemSketch	ACD/Labs	It is available as free and commercial. However, it is a rather complete piece of software that either high school pupils or university chemistry students can use for educational purposes. You may create Markush structures, polymer structures, organometallic structures, and organic chemical structures using this software. Calculations for molecular weight, density, molar refractivity, etc. can be made. It can provide 3D structures.
ChemDraw Professional	PerkinElmer	single drawing solution that is reliable for handling and representing organic, organometallic, polymeric, and biopolymer materials (including amino acids, peptides, DNA, and RNA sequences) as well as working with sophisticated stereochemistry. Chemists can draw and submit chemical compound and reaction searches automatically to SciFinder using ChemDraw Professional instead of spending time laboriously cutting and pasting. Using a wide variety of biological templates and drawing tools to produce dynamic drawings of cells and metabolic pathways, incorporating live chemical items when necessary, scientists can rapidly, effectively, and precisely communicate findings and ideas. ChemDraw Professional helps scientists forecast characteristics, create spectra, create accurate IUPAC names, and determine reaction stoichiometry while speeding up the process and improving data quality. It offers molecular mechanics, molecular dynamics calculations, and 3D structures.
Gaussian	Gaussian, INC	Chemists, chemical engineers, biochemists, physicists, and other scientists utilize the computer application Gaussian. To anticipate energies, chemical structures, spectroscopic data (NMR, IR, UV, etc.), and much more complex calculations, it makes use of the fundamental laws of quantum mechanics. You can simulate molecular systems of increasing scale with more precision and under a wider range of real-world situations, leading to the

		advanced capabilities and performance improvements offered by Gaussian09. One of these features is the ability to model the reaction of very large systems using ONIOM. Examine the gas phase's and the solution's excited states. Forecasts for future spectra performance enhancements, user-friendly features, and new and improved methods IR and Raman, NMR, UV/Visible, Vibrational Circular Dichroism (VCD), Raman Optical Activity (ROA), Electronic Circular Dichroism (ECD), Optical Rotary Dispersion (ORD), Hyperfine Spectra (Microwave Spectroscopy), Franck-Condon, Herzberg-Teller, and Franck-Condon/Herzberg-Teller analyses are just a few of the spectra that Gaussian09 gives you a choice of very accurate energy methods for estimating thermochemical quantities, photochemistry and other excited state processes, and solvent effects when we are optimizing structures and making predictions about most molecular properties.
CrystalExplorer	School of Biomedical and Chemical Sciences, University of Western Australia, Nedlands 6009, Australia	Free software named CrystalExplorer (CE) is designed to examine crystal structures in the *.cif file format. For example, Hirshfeld surface analysis, intermolecular interactions, polymorphism, the impact of pressure and temperature on crystal structure, single-crystal to single-crystal interactions, void analysis, and structure-property relationships are all solid-state chemistry topics that can be studied using CE. CE's graphical interface for 3D crystal structure visualization has greatly improved.
Grapher	GOLDEN SOFTWARE, USA	Grapher is a graphing calculator that can produce both 2D graphs in the following coordinate systems: standard system, cylindrical system, and spherical system, as well as 3D graphs in the following coordinate systems: polar coordinates, linear-logarithmic, log-log, and polar log. It is one of the few high-end graphing apps that can export clear vector drawings for usage in printed documents with ease (although exporting 3D graphs to vector is not possible). Both 2D and 3D graph animation are supported, and a QuickTime file is produced.
Surfer		Microsoft Windows is required to operate Surfer, a full-featured 3D visualization, contouring, and surface modelling application by Golden Software. In addition to many other things, Surfer is widely used for terrain modelling, landscape visualization, surface analysis, contour mapping, 3D surface mapping, gridding, and volumetric.

Recent structural studies of organic molecules by single crystal X-Ray diffractometric and molecular modeling on DFT theoretical platforms have proven an amazing success for the modeling methods. A few examples of Schiff bases and dithiocarbamates are presented along with their molecular structural data obtained experimentally (by single crystal diffractometry) and computational methods evaluated by DFT/B3LYP[75,76,77,78] in **Table 1.4** through **Table 1.8**. The molecular structures of the compounds mentioned in these tables are presented in **Table 1.4**.

Since 3-dimensional images (and molecular structures) cannot be placed on a 2-dimensional stationery or screens, a few gadgets have been invented to visualize 3-dimensionality by optical illusion to get a virtual binocular perception. Two of the most popular methods are (i) Stereography and (ii) Anaglyphy. In Stereography, the left-eye view and the right-eye view of the true 3-D picture in 2-D format are placed side by side at a distance of about 5 cms (typical human eye separation distance and each figure is viewed separately by the respective eye by a gadget called, stereograph (shown in **Figure 1.9)** and the brain synthesizes the 3-D perception.

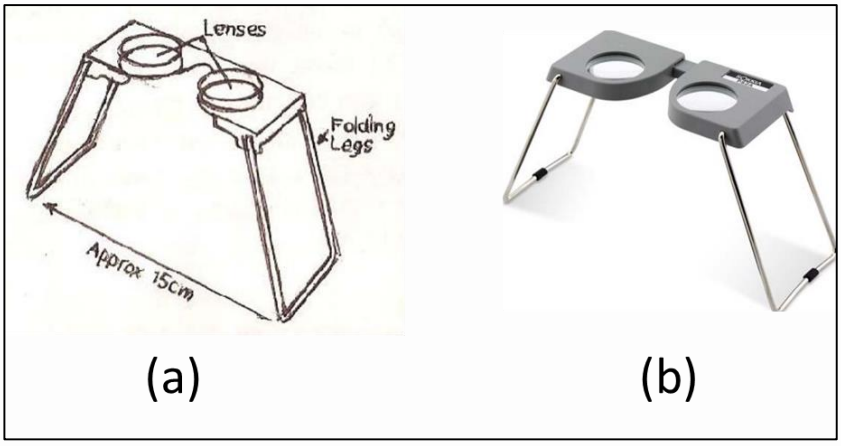

Figure 1.9: (a) *fabricated and a* ***(b)*** *commercial low-cost stereograph*[78]

Almost all commercially available Molecular modeling software generates a pair of molecular structures that can be viewed by a stereograph. Similarly, any single crystal X-Ray Diffractometer also offers this provision. An example of stereographically generated molecular structure is shown in **Figure 1.10.**

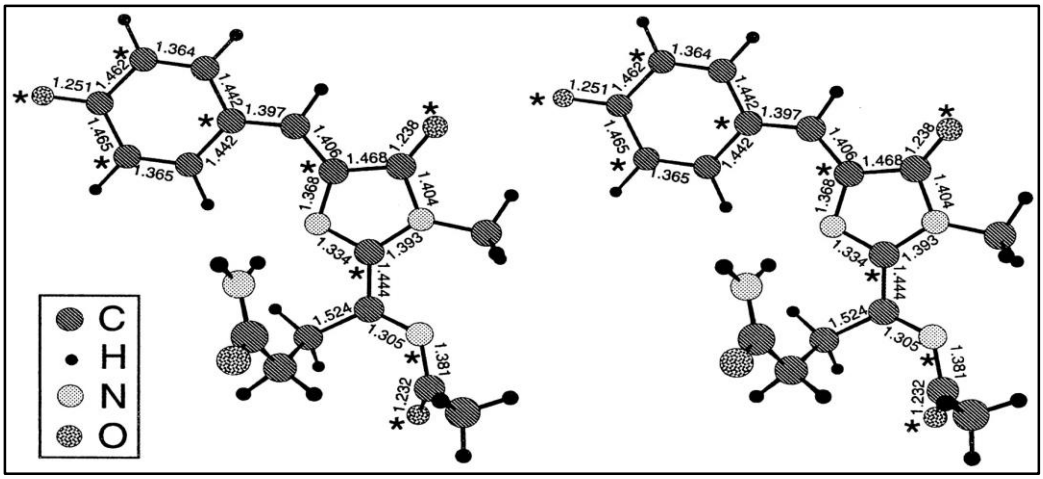

***Figure 1.10*: *Discosoma coral chromophore shown in stereographic projection*[79]**

In the Anaglyphy, the left and right eye views of the true 3-D picture (molecular structure) is split into 2 differently colored (usually cyan and blue) 2-D graphical pictures aligned slightly staggered as it would have been by the two eyes. An unusual goggle (spectacles) with left side cyan and right side blue is used to see the above mentioned anaglyph picture. The picture in cyan color is seen by left eye only and the blue one by the right eye only. Thereby the brain is able to synthesize the two different images into one 3-D picture.

The image of a typical anaglyph spectacles (goggle) is shown in **Figure 1.11**.

***Figure 1.11:** A typical anaglyph spectacle to view anaglyph pictures*

The anaglyph image of phenylalanine is shown in **Figure 1.12**

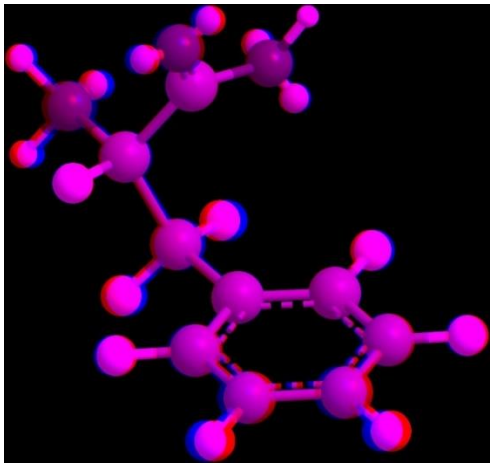

Figure 1.12: *The anaglyph picture of phenylalanine (one has to wear the anaglyph spects for a 3-D perception)*

Table 1.4: *Comparison of the structures evaluated experimentally by XRD and theoretically by modelling*

S.No	Structure	Molecular structure from XRD	Molecular structure from DFT
	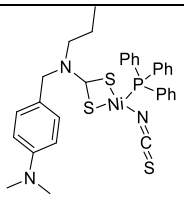	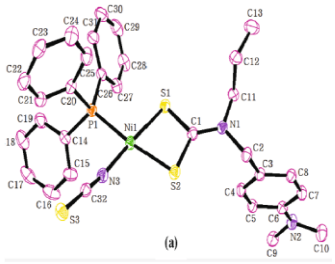	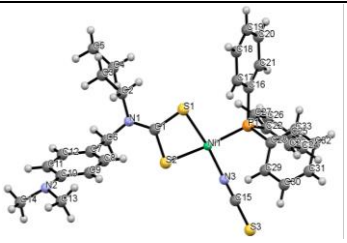
	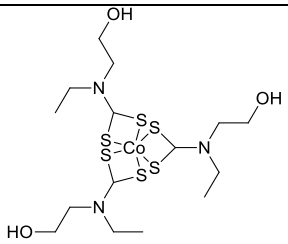	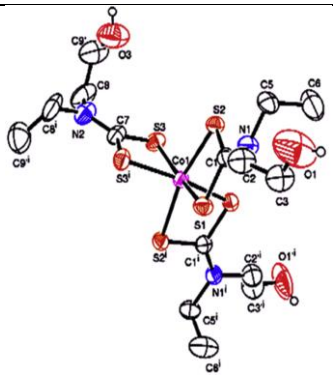	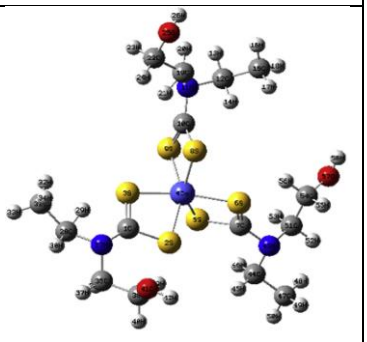

	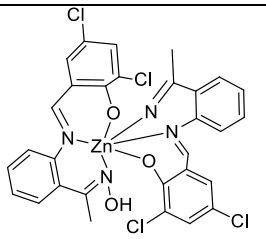	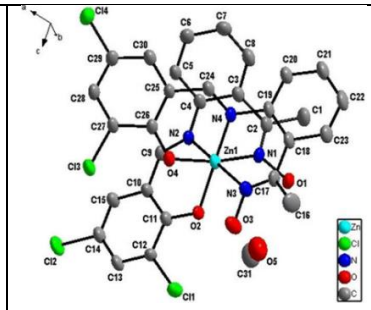	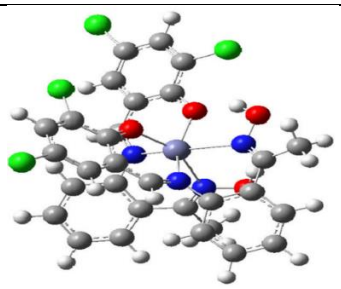
	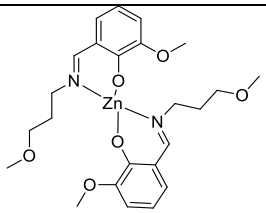	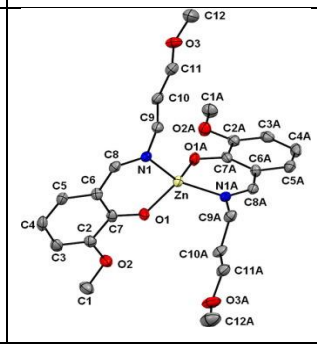	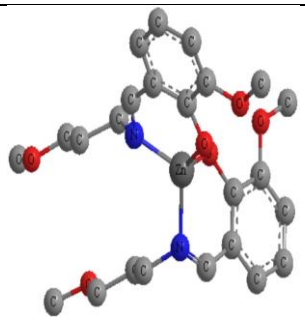

Table 1.5: *Selected bond distances (Å) and bond angles (◦) by X-ray diffraction and theoretical (DFT) calculations for* ***(N-(4-(dimethylamino)benzyl)-Npropyldithiocarbamato-S,S')(thiocyanato-N)(triphenylphosphine)nickel(II)*** *complex (Numbering of the atoms is in relation to the structure shown at* ***Table 1.4, S.No. 1****)*

Bond lengths				**Bond angles**			
	XRD	**DFT**	**XRD-DFT**		**XRD**	**DFT**	**XRD-DFT**
N1-C1	1.3130	1.3494	-0.0364	**N1-C1-S1**	124.22	124.19	0.03
C1-S1	1.7310	1.8616	-0.1306	**N1-C1-S2**	126.82	125.00	1.82
C1-S2	1.7180	1.8593	-0.1413	**S1-C1-S2**	108.96	110.80	-1.84
S1-Ni1	2.1664	2.3927	-0.2263	**C1-C1-Ni1**	86.66	85.66	1.00
S2-Ni1	2.2314	2.4293	-0.1979	**C1-S2-Ni1**	84.93	84.65	0.28
Ni1-P1	2.1857	2.4006	-0.2149	**S1-Ni1-S2**	79.32	78.86	0.46
Ni1-N3	1.8639	1.8404	0.0235	**S1-Ni1-P1**	95.26	94.74	0.52
N3-C32	1.1690	1.2080	-0.039	**S2-Ni1-N3**	94.86	94.90	-0.04
C32-S3	1.6200	1.7762	-0.1562	**S1-Ni1-N3**	171.15	173.76	-2.61
				S2-Ni1-P1	174.24	173.61	0.63
				Ni1-N3-C32	161.65	169.98	-8.33
				N3-C32-S3	178.61	199.93	-21.32

P1-Ni1-N3	90.29	91.48	-1.19

Table 1.6: *Selected bond distances (Å) and bond angles (◦) by X-ray diffraction and theoretical (DFT) calculations for* ***[Co(L)$_3$],*** *where* ***L = Ethylaminoethanol dithiocarbamate.*** *(Numbering of the atoms is in relation to the structure shown at* ***Table 1.4, S.No. 2)***

Bond lengths				**Bond angles**			
	XRD	**DFT**	**XRD-DFT**		**XRD**	**DFT**	**XRD-DFT**
S1-Co1	2.2857	2.3945	-0.1088	**S3-Co1-S3^i**	76.45	76.09	0.36
S2-Co1	2.2812	2.3986	-0.1174	**S2-Co1-S2^i**	165.91	166.58	-0.67
S3-Co1	2.2861	2.4025	-0.1164	**S1-Co1-S1^i**	95.99	96.12	-0.13
C1-N1	1.337	1.3081	0.0289	**S1^i-Co1-S2^i**	76.23	75.98	0.25
C7-N2	1.371	1.4730	-0.102	**S3-Co1-S2**	95.20	95.74	-0.54
C1-S1	1.720	1.7784	-0.0584	**S3-Co1-S1**	166.95	166.44	0.51
C1-S2	1.729	1.7802	-0.0512	**N2-C7-S3**	124.4	124.22	0.18
C7-S3	1.715	1.7794	-0.0644	**N1-C1-S1**	125.7	123.76	1.94
C3-O1	1.200	1.4315	-0.2315	**O1-C3-C2**	109.00	109.85	-0.85

Table 1.7: *Selected bond distances (Å) and bond angles (◦) by X-ray diffraction and theoretical (DFT) calculations for* ***[Zn(L)$_2$],*** *where* ***L = (E)-1-(2-Aminophenyl) ethanone oxime.*** *(Numbering of the atoms is in relation to the structure shown at* ***Table 1.4, S.No. 3)***

Bond lengths				**Bond angles**			
	XRD	**DFT**	**XRD-DFT**		**XRD**	**DFT**	**XRD-DFT**
Zn1-O2	1.999	2.039	-0.04	**O2-Zn1-O4**	87.6	90.35	-2.75
Zn1-N2	2.129	2.208	-0.079	**O2-Zn1-N2**	89.8	87.67	2.13
Zn1-N3	2.046	2.155	-0.109	**O2-Zn1-N4**	166.6	164.77	1.83
Zn1-O4	2.042	2.060	-0.018	**O4-Zn1-N2**	91.1	87.47	3.63
Zn1-N2	2.010	2.099	-0.089	**O4-Zn1-N4**	84.6	84.34	0.26
Zn1-N4	2.041	2.109	-0.068	**N1-Zn1-N3**	94.4	94.64	-0.24
				N2-Zn1-N3	172.9	169.51	3.39
				N3-Zn1-N4	83.1	80.65	2.45

O2-Zn1-N1	97.5	100.3	-2.8

Table 1.8: *Selected bond distances (Å) and bond angles (◦) by X-ray diffraction and theoretical (DFT) calculations for* ***[Zn(L)$_2$], where L = (E)-2-methoxy-6-(((3-methoxypropyl)imino)methyl)phenol****. (Numbering of the atoms is in relation to the structure shown at* ***Table 1.4, S.No. 4)***

Bond lengths				**Bond angles**			
	XRD	**DFT**	**XRD-DFT**		**XRD**	**DFT**	**XRD-DFT**
Zn-O1	1.937	1.953	-0.016	**O1-Zn-N1**	95.31	93.25	2.06
Zn-N1	2.001	2.086	-0.085	**O1-Zn-O1A**	110.93	131.80	-20.87
O1-C7	1.309	1.297	0.012	**O1-Zn-N1A**	116.84	109.1	7.74
O2-C1	1.421	1.413	0.008	**N1-Zn-N1A**	122.64	123.67	-1.03
O2-C2	1.362	1.363	-0.001				
O3-C11	1.424	1.413	0.011				
O3-C12	1.421	1.409	0.012				
N1-C8	1.293	1.301	-0.008				
N1-C9	1.455	1.466	-0.011				
C2-C7	1.423	1.443	-0.02				
C6-C8	1.434	1.438	-0.004				

1.6 Scope for the Present Work:

- Search for new molecules as candidates for applications in various fields of medicine, energy storage, communication, defense, agriculture, cosmetics, nutrition, optoelectronics, etc. is one of the prime and active areas of research. Hence, new molecules are first computationally modelled and their Quantitative Structure-Activity Relationships (QSARs) are obtained before a computationally discovered potential molecule is taken up for actual synthesis.

- Correlation of actual and modelled molecular properties of a synthesized molecule is a new and highly relevant area of chemical research before that molecule is truly adopted for any actual application in real life. Agreement of various structural parameters of the molecule

upon such correlation would vindicate suitability of the molecule for the intended real life application.

- Nitrogenous and thio organic compounds and their metal complexes are known for their potential pharmaceutical applications. Hence, a set of a few of such compounds, that has not yet been investigated and reported from QSARs points of view and that, that has not yet been crystallographically and computationally investigated and correlated, could be a good set to be investigated.
- The compounds are chosen on the basis of their distinct and varied structural characteristics that have some analogous structural relationship with some compounds that are proven to have biological applications
- The compounds are chosen with a viability for green chemistry and for possibility of crystallization for actual XRD measurements and also to be computationally administrable.

1.7 Objectives of the Present Work:

i) To synthesize by known and novel methods a few nitrogenous and thio organic compounds and their metal complexes that are likely to have potential pharmaceutical applications

ii) To characterize the synthesized ligands and complexes by various spectral, electrochemical and other relevant methods to assess their bulk and solution properties and to evaluate their biological applications

iii) To develop single crystals of the chosen ligands and metal complexes and determine their molecular structures by single-crystal X-ray diffractometry (XRD)

iv) To perform molecular modelling and do computational chemical evaluation of the compounds on different computational platforms

v) To correlate the molecular structural properties of the compounds obtained by the XRD studies with those of the modelled molecules and to assign reasons of chemistry for the agreement or deviations of these structural parametric sets.

vi) To perform conformational analysis on the modelled molecules by dihedral and double-dihedral driving to know the spatial geometry of the free molecules and thereby to

understand the mechanism of computational molecular docking on chosen proteins or biomolecules adopted from bioinformatics data base

Keeping in view the above Scope and Objectives, we have synthesized and studied a few nitrogenous organic compounds besides one with a dithiocarbamate moiety, shown in **Table 1.1**, as examples, to meet the objectives of my thesis. Some of these compounds have been extended for metal coordination. Suitable crystals for a considerable number of these organic compounds could be isolated for single crystal X-Ray Diffractometric. Despite repeated attempts with change in solvents, temperature radiance and other experimental conditions, single crystals suitable for XRD could not be developed for the complexes and for the dithiocarbamate series. In the light of the excellent correlation between the XRD data and the computationally modelled data of the other successful compounds, the molecular structural data of the ligands in the modelled complexes, both as isolated systems and in their biological docking studies, have been justified. Almost all the ligands and their complexes were investigated for their biological applications.

The procedures of the synthesis of the chosen compounds and the details of the experimental methods used, are presented in Chapter II and the results of laboratory investigations, crystallographic studies, molecular modeling and docking and biological studies of these compounds, form the contents of the subsequent chapters.

References

(1). Wormer, P. E. S.; Avoird, A. van der. Forty Years of Ab Initio Calculations on Intermolecular Forces. In *Theory and Applications of Computational Chemistry*; Elsevier, 2005; pp 1047–1077. https://doi.org/10.1016/B978-044451719-7/50080-9.

(2). Gould, I. R. Computational Chemistry: Application to Biological Systems. *Molecular Simulation* **2001**, *26* (1), 73–83. https://doi.org/10.1080/08927020108024201.

(3). Stanzione, F.; Giangreco, I.; Cole, J. C. *Use of Molecular Docking Computational Tools in Drug Discovery*, 1st ed.; Elsevier B.V., 2021; Vol. 60. https://doi.org/10.1016/bs.pmch.2021.01.004.

(4). Kumar, R.; Obrai, S. Comparison of Computational Studies with the X-Ray Crystal Structure of Directly Synthesized Bis(D,L-Aminobutyric)Copper(II) Complex. *Journal of Structural Chemistry* **2014**, *55* (2), 241–247. https://doi.org/10.1134/S0022476614020073.

(5). Kumar, R.; Obrai, S. Comparison of Computational Studies with the X-Ray Crystal Structure of Directly Synthesized Bis(D,L-Aminobutyric)Copper(II) Complex. *Journal of Structural Chemistry* **2014**, *55* (2), 241–247. https://doi.org/10.1134/S0022476614020073.

(6). Abdul Jaleel, U. C.; Rakhila, M.; Parameswaran, G. Comparison between Investigational IR and Crystallographic Data with Computational Chemistry Tools as Validation of the Methods. *Advances in Physical Chemistry* **2010**, *2010*, 1–5. https://doi.org/10.1155/2010/787813.

(7). Gao, T.; Andino, J. M.; Alvarez-Idaboy, J. R. Computational and Experimental Study of the Interactions between Ionic Liquids and Volatile Organic Compounds. *Physical Chemistry Chemical Physics* **2010**, *12* (33), 9830. https://doi.org/10.1039/c003386c.

(8). Pöhls, J.-H.; Heyberger, M.; Mar, A. Comparison of Computational and Experimental Inorganic Crystal Structures. *Journal of Solid State Chemistry* **2020**, *290*, 121557. https://doi.org/10.1016/j.jssc.2020.121557.

(9). Pöhls, J.-H.; Heyberger, M.; Mar, A. Comparison of Computational and Experimental Inorganic Crystal Structures. *Journal of Solid State Chemistry* **2020**, *290*, 121557. https://doi.org/10.1016/j.jssc.2020.121557.

(10). Pace, C. N.; Grimsley, G. R.; Scholtz, J. M. Denaturation of Proteins by Urea and Guanidine Hydrochloride. In *Protein Science Encyclopedia*; Wiley-VCH Verlag GmbH & Co. KGaA: Weinheim, Germany, 2008. https://doi.org/10.1002/9783527610754.sf03.

(11). Jiao, Y.; Niu, L.; Ma, S.; Li, J.; Tay, F. R.; Chen, J. Quaternary Ammonium-Based Biomedical Materials: State-of-the-Art, Toxicological Aspects and Antimicrobial Resistance. *Progress in Polymer Science* **2017**, *71* (January), 53–90. https://doi.org/10.1016/j.progpolymsci.2017.03.001.

(12). Cavallito, C. J. Quaternary Ammonium Salts — Advances in Chemistry and Pharmacology since 1960. In *Progress in Drug Research / Fortschritte der Arzneimittelforschung / Progrès des recherches pharmaceutiques*; Birkhäuser Basel: Basel, 1980; Vol. 24, pp 267–373. https://doi.org/10.1007/978-3-0348-7108-2_6.

(13). Shao, H.; Jiang, L.; Meng, W.-D.; Qing, F.-L. Synthesis and Antimicrobial Activity of a Perfluoroalkyl-Containing Quaternary Ammonium Salt. *Journal of Fluorine Chemistry* **2003**, *124* (1), 89–91. https://doi.org/10.1016/S0022-1139(03)00193-3.

(14). Compounds, N. Nitrogen Compounds. *Enological Chemistry* **2012**, 183–193. https://doi.org/10.1016/b978-0-12-388438-1.00012-1.

(15). (a) Schiff, H. Mittheilungen Aus Dem Universitätslaboratorium in Pisa: Eine Neue Reihe Organischer Basen. Justus Liebigs Annalen der Chemie 1864, 131 (1), 118–119. https://doi.org/10.1002/jlac.18641310113.

(b) Tidwell, T. T. Hugo (Ugo) Schiff, Schiff Bases, and a Century of β-Lactam Synthesis. Angewandte Chemie - International Edition 2008, 47 (6), 1016–1020. https://doi.org/10.1002/anie.200702965.

(16). More, M. S.; Joshi, P. G.; Mishra, Y. K.; Khanna, P. K. Metal Complexes Driven from Schiff Bases and Semicarbazones for Biomedical and Allied Applications: A Review. Materials Today Chemistry 2019, 14 (January), 100195. https://doi.org/10.1016/j.mtchem.2019.100195.

(17). Sheikhshoaie, I. Synthesis and Characterization of Oxovanadium (Iv) Complexes and Metal (Ii) Schiff Base Complexes. International Journal of Advanced Research in Chemical Science 2018, 5 (4), 942–946. https://doi.org/10.20431/2349-0403.0504003.

(18). Majid, S. A.; Mir, J. M.; Paul, S.; Akhter, M.; Parray, H.; Ayoub, R.; Shalla, A. H. Experimental and Molecular Topology-Based Biological Implications of Schiff Base Complexes: A Concise Review. Reviews in Inorganic Chemistry 2019, 39 (2), 113–128. https://doi.org/10.1515/revic-2018-0023.

(19). (a) Feng, Z. Q.; Yang, X. L.; Ye, Y. F.; Hao, L. Y. The Effect of Electron-Withdrawing Group Functionalization on Antibacterial and Catalytic Activity of Palladium(II) Complexes. Bulletin of the Korean Chemical Society 2014, 35 (4), 1121–1127. https://doi.org/10.5012/bkcs.2014.35.4.1121.

(b) Iftikhar, B.; Javed, K.; Khan, M. S. U.; Akhter, Z.; Mirza, B.; Mckee, V. Synthesis, Characterization and Biological Assay of Salicylaldehyde Schiff Base Cu(II) Complexes and Their Precursors. Journal of Molecular Structure 2018, 1155, 337–348. https://doi.org/10.1016/j.molstruc.2017.11.022.

(c) Hung, W. C.; Lin, C. C. Preparation, Characterization, and Catalytic Studies of Magnesium Complexes Supported by NNO-Tridentate Schiff-Base Ligands. Inorganic Chemistry 2009, 48 (2), 728–734. https://doi.org/10.1021/ic801397t.

(d) Xiao, Y.; Cao, C. Influence of Substituents on the Structure of Schiff Bases Cu(II) Complexes. Journal of Molecular Structure 2020, 1209, 127916. https://doi.org/10.1016/j.molstruc.2020.127916.

(20). (a) Fuchs, M.; Schmitz, S.; Schäfer, P. M.; Secker, T.; Metz, A.; Ksiazkiewicz, A. N.; Pich, A.; Kögerler, P.; Monakhov, K. Y.; Herres-Pawlis, S. Mononuclear Zinc(II) Schiff Base Complexes as Catalysts for the Ring-Opening Polymerization of Lactide. European Polymer Journal 2020, 122 (Ii), 109302. https://doi.org/10.1016/j.eurpolymj.2019.109302.

(b) Drozdzak, R.; Allaert, B.; Ledoux, N.; Dragutan, I.; Dragutan, V.; Verpoort, F. Ruthenium Complexes Bearing Bidentate Schiff Base Ligands as Efficient Catalysts for Organic and Polymer Syntheses. Coordination Chemistry Reviews 2005, 249 (24), 3055–3074. https://doi.org/10.1016/j.ccr.2005.05.003.

(21). Nejati, K.; Rezvani, Z.; Massoumi, B. Syntheses and Investigation of Thermal Properties of Copper Complexes with Azo-Containing Schiff-Base Dyes. Dyes and Pigments 2007, 75 (3), 653–657. https://doi.org/10.1016/j.dyepig.2006.07.019.

(22). (a) Gupta, K. C.; Sutar, A. K. Catalytic Activities of Schiff Base Transition Metal Complexes. Coordination Chemistry Reviews 2008, 252 (12–14), 1420–1450. https://doi.org/10.1016/j.ccr.2007.09.005.

(b) Liu, X.; Manzur, C.; Novoa, N.; Celedón, S.; Carrillo, D.; Hamon, J. R. Multidentate Unsymmetrically-Substituted Schiff Bases and Their Metal Complexes: Synthesis, Functional Materials Properties, and Applications to Catalysis. Coordination Chemistry Reviews 2018, 357, 144–172. https://doi.org/10.1016/j.ccr.2017.11.030.

(c) Gupta, K. C.; Sutar, A. K. Catalytic Activities of Schiff Base Transition Metal Complexes. Coordination Chemistry Reviews 2008, 252 (12–14), 1420–1450. https://doi.org/10.1016/j.ccr.2007.09.005.

(23). Akelah, A.; Kenawy, E. R.; Sherrington, D. C. Agricultural Polymers with Herbicide/Fertilizer Function-III. Polyureas and Poly(Schiff Base)s Based Systems. European Polymer Journal 1993, 29 (8), 1041–1045. https://doi.org/10.1016/0014-3057(93)90306-Z.

(24). Wahba, O. A. G.; Hassan, A. M.; Naser, A. M.; Hanafi, A. M. Preparation and Spectroscopic Studies of Some Copper and Nickel Schiff Base Complexes and Their Applications as Colouring Pigments in Protective Paints Industry. Egyptian Journal of Chemistry 2017, 60 (1), 25–40. https://doi.org/10.21608/ejchem.2017.517.1000.

(25). Abu-Dief, A. M.; Mohamed, I. M. A. A Review on Versatile Applications of Transition Metal Complexes Incorporating Schiff Bases. Beni-Suef University Journal of Basic and Applied Sciences 2015, 4 (2), 119–133. https://doi.org/10.1016/j.bjbas.2015.05.004.

(26). Uddin, M. N.; Ahmed, S. S.; Alam, S. M. R. REVIEW: Biomedical Applications of Schiff

Base Metal Complexes. Journal of Coordination Chemistry 2020, 73 (23), 3109–3149. https://doi.org/10.1080/00958972.2020.1854745.

(27). Abdallah, S. M.; Zayed, M. A.; Mohamed, G. G. Synthesis and Spectroscopic Characterization of New Tetradentate Schiff Base and Its Coordination Compounds of NOON Donor Atoms and Their Antibacterial and Antifungal Activity. Arabian Journal of Chemistry 2010, 3 (2), 103–113. https://doi.org/10.1016/j.arabjc.2010.02.006.

(28). Da Silva, C. M.; Da Silva, D. L.; Modolo, L. V.; Alves, R. B.; De Resende, M. A.; Martins, C. V. B.; De Fátima, Â. Schiff Bases: A Short Review of Their Antimicrobial Activities. Journal of Advanced Research 2011, 2 (1), 1–8. https://doi.org/10.1016/j.jare.2010.05.004.

(29). Kumar, M.; Padmini, T.; Ponnuvel, K. Synthesis, Characterization and Antioxidant Activities of Schiff Bases Are of Cholesterol. Journal of Saudi Chemical Society 2017, 21, S322–S328. https://doi.org/10.1016/j.jscs.2014.03.006.

(30). Malik, M. A.; Dar, O. A.; Gull, P.; Wani, M. Y.; Hashmi, A. A. Heterocyclic Schiff Base Transition Metal Complexes in Antimicrobial and Anticancer Chemotherapy. MedChemComm 2018, 9 (3), 409–436. https://doi.org/10.1039/c7md00526a.

(31). Deivanayagam, P.; Bhoopathy, P.; Thanikaikarasan, S. Synthesis, Characterization, Antimicrobial, Analgesic and CNS Studies of Schiff Base Cu(II) Complex Derived from 4-Choro-o-Phenylene Diamine. International Journal of Advanced Chemistry 2014, 2 (2), 166. https://doi.org/10.14419/ijac.v2i2.3338.

(32). (a) Azam, M.; Al-Resayes, S. I.; Trzesowska-Kruszynska, A.; Kruszynski, R.; Shakeel, F.; Soliman, S. M.; Alam, M.; Khan, M. R.; Wabaidur, S. M. Zn(II) Complex Derived from Bidentate Schiff Base Ligand: Synthesis, Characterization, DFT Studies and Evaluation of Anti-Inflammatory Activity. Journal of Molecular Structure 2020, 1201, 127177. https://doi.org/10.1016/j.molstruc.2019.127177.

(b) Ki, J.; Mukherjee, A.; Rangasamy, S.; Purushothaman, B.; Song, J. M. Insulin-Mimetic and Anti-Inflammatory Potential of a Vanadyl-Schiff Base Complex for Its Application against Diabetes. RSC Advances 2016, 6 (62), 57530–57539. https://doi.org/10.1039/c6ra11111d.

(33). Budhani, P.; Iqbal, S. A.; Bhattacharya, S. M. M.; Mitu, L. Synthesis, Characterization and Spectroscopic Studies of Pyrazinamide Metal Complexes. Journal of Saudi Chemical Society 2010, 14 (3), 281–285. https://doi.org/10.1016/j.jscs.2010.02.009.

(34). Natsch, A.; Gfeller, H.; Haupt, T.; Brunner, G. Chemical Reactivity and Skin Sensitization Potential for Benzaldehydes: Can Schiff Base Formation Explain Everything? Chemical Research in Toxicology 2012, 25 (10), 2203–2215. https://doi.org/10.1021/tx300278t.

(35). Murukan, B.; Mohanan, K. Synthesis, Characterization and Antibacterial Properties of Some Trivalent Metal Complexes with [(2-Hydroxy-1-Naphthaldehyde)-3-Isatin]-Bishydrazone. Journal of Enzyme Inhibition and Medicinal Chemistry 2007, 22 (1), 65–70. https://doi.org/10.1080/14756360601027373.

(36). Barve, V.; Ahmed, F.; Adsule, S.; Banerjee, S.; Kulkarni, S.; Katiyar, P.; Anson, C. E.; Powell, A. K.; Padhye, S.; Sarkar, F. H. Synthesis, Molecular Characterization, and Biological Activity of Novel Synthetic Derivatives of Chromen-4-One in Human Cancer Cells. *Journal of Medicinal Chemistry* **2006**, *49* (13), 3800–3808. https://doi.org/10.1021/jm051068y.

(37). Kalanithi, M.; Kodimunthiri, D.; Rajarajan, M.; Tharmaraj, P. Synthesis, Characterization and Biological Activity of Some New VO(IV), Co(II), Ni(II), Cu(II) and Zn(II) Complexes of Chromone Based NNO Schiff Base Derived from 2-Aminothiazole. Spectrochimica Acta - Part A: Molecular and Biomolecular Spectroscopy 2011, 82 (1), 290–298. https://doi.org/10.1016/j.saa.2011.07.051.

(38). Siddiqi, K. S.; Arjmand, F.; Tabassum, S.; Zaidi, S. A. A. Schiff Base Complexes as Ligands. Bimetallic Chelates of $[M(SB\text{-}H_2)]Cl_2$ with Group IV Metal Tetrachlorides. Synthesis and Reactivity in Inorganic and Metal-Organic Chemistry 1995, 25 (6), 0955–0964. https://doi.org/10.1080/15533179508218273.

(39). Anitha, C.; Sheela, C. D.; Tharmaraj, P.; Johnson Raja, S. Synthesis and Characterization of VO(II), Co(II), Ni(II), Cu(II) and Zn(II) Complexes of Chromone Based Azo-Linked Schiff Base Ligand. Spectrochimica Acta - Part A: Molecular and Biomolecular Spectroscopy 2012, 98, 35–42. https://doi.org/10.1016/j.saa.2012.08.022.

(40). Jeewoth, T.; Li Kam Wah, H.; Bhowon, M. G.; Ghoorohoo, D.; Babooram, K. Synthesis and Anti-Bacterial/Catalytic Properties of Schiff Bases and Schiff Base Metal Complexes Derived from 2,3-Diaminopyridine. Synthesis and Reactivity in Inorganic and Metal-Organic Chemistry 2000, 30 (6), 1023–1038. https://doi.org/10.1080/00945710009351817.

(41). Mahalingam, V.; Chitrapriya, N.; Fronczek, F. R.; Natarajan, K. New Ru(II)-DMSO Complexes of ON/SN Chelates: Synthesis, Behavior of Schiff Bases towards Hydrolytic Cleavage of CN Bond, Electrochemistry and Biological Activities. Polyhedron 2010, 29 (18), 3363–3371. https://doi.org/10.1016/j.poly.2010.09.019.

(42). Ajlouni, A. M.; Taha, Z. A.; Al Momani, W.; Hijazi, A. K.; Ebqa'ai, M. Synthesis, Characterization, Biological Activities, and Luminescent Properties of Lanthanide Complexes with N,N′-Bis(2-Hydroxy-1-Naphthylidene)-1,6-Hexadiimine. Inorganica Chimica Acta 2012, 388, 120–126. https://doi.org/10.1016/j.ica.2012.03.029.

(43). Toprak, Ş.; Tanak, H.; Macit, M.; Dege, N.; Orbay, M. Experimental and Theoretical Studies of Bis[(E)-1-((3-Chloro-4-Methylphenylimino)Methyl)Naphthalen-2-Olate-N,O]Copper(II). Journal of Molecular Structure 2018, 1174, 184–191. https://doi.org/10.1016/j.molstruc.2018.03.082.

(44). Lazo, C. R.; Miller, G. W. Thiram. Encyclopedia of Toxicology: Third Edition 2014, 4, 558–559. https://doi.org/10.1016/B978-0-12-386454-3.00201-3.

(45). (a) Kartina, D.; Wahab, A. W.; Ahmad, A.; Irfandi, R.; Raya, I. In Vitro Antibacterial and

Anticancer Activity of Zn(II)Valinedithiocarbamate Complexes. Journal of Physics: Conference Series 2019, 1341 (3). https://doi.org/10.1088/1742-6596/1341/3/032042.

(b) Andrew, F. P.; Ajibade, P. A. Metal Complexes of Alkyl-Aryl Dithiocarbamates: Structural Studies, Anticancer Potentials and Applications as Precursors for Semiconductor Nanocrystals. Journal of Molecular Structure 2018, 1155, 843–855. https://doi.org/10.1016/j.molstruc.2017.10.106.

(c) Lawal, M. M.; Lawal, I. A.; Klink, M. J.; Tolufashe, G. F.; Ndagi, U.; Kumalo, H. M. Density Functional Theory Study of Gold(III)-Dithiocarbamate Complexes with Characteristic Anticancer Potentials. Journal of Inorganic Biochemistry 2020, 206 (Iii), 111044. https://doi.org/10.1016/j.jinorgbio.2020.111044.

(d) Nami, S. A. A.; Ullah, I.; Alam, M.; Lee, D. U.; Sarikavakli, N. Synthesis, Characterization, Molecular Docking and Biological Studies of Self Assembled Transition Metal Dithiocarbamates of Substituted Pyrrole-2-Carboxaldehyde. Journal of Photochemistry and Photobiology B: Biology 2016, 160, 392–399. https://doi.org/10.1016/j.jphotobiol.2016.05.010.

(46). Al-Obaidy, G. S.; Ibraheem, K. R.; Mesher, M. F. Metal Complexes Derived from Dithiocarbamate Ligand: Formation, Spectral Characterization and Biological Activity. Systematic Reviews in Pharmacy 2020, 11 (6), 360–368. https://doi.org/10.31838/srp.2020.6.57.

(47). (a) Verma, S. K.; Singh, V. K. Synthesis, Electrochemical, Fluorescence and Antimicrobial Studies of 2-Chloro-3-Amino-1,4-Naphthoquinone Bearing Mononuclear Transition Metal Dithiocarbamate Complexes [M{κ 2 S,S-S 2 C–Piperazine–C 2 H 4 N(H)ClNQ} N]. RSC Advances 2015, 5 (65), 53036–53046. https://doi.org/10.1039/C5RA08065G.

(b) Singh, N.; Kumar, A.; Prasad, R.; Molloy, K. C.; Mahon, M. F. Syntheses, Crystal, Photoluminescence and Electrochemical Investigation of Some New Phenylmercury(Ii) Dithiocarbamate Complexes Involving Ferrocene. Dalton Transactions 2010, 39 (10), 2667. https://doi.org/10.1039/b917871f.

(48). Rubino, F. M.; Mrema, E. J.; Colosio, C. Pesticide Residues: Dithiocarbamates. In Encyclopedia of Food Safety; Elsevier, 2014; Vol. 3, pp 5–10. https://doi.org/10.1016/B978-0-12-378612-8.00240-7.

(49). (a) Hogarth, G. Metal-Dithiocarbamate Complexes: Chemistry and Biological Activity. Mini-Reviews in Medicinal Chemistry 2012, 12 (12), 1202–1215. https://doi.org/10.2174/138955712802762095.

(b) Adokoh, C. K. Therapeutic Potential of Dithiocarbamate Supported Gold Compounds. RSC Advances 2020, 10 (5), 2975–2988. https://doi.org/10.1039/C9RA09682E.

(50). Odularu, A. T.; Ajibade, P. A. Dithiocarbamates: Challenges, Control, and Approaches to

Excellent Yield, Characterization, and Their Biological Applications. Bioinorganic Chemistry and Applications 2019, 2019, 1–15. https://doi.org/10.1155/2019/8260496.

(51). Ekennia, A. C.; Onwudiwe, D. C.; Ume, C.; Ebenso, E. E. Mixed Ligand Complexes of N -Methyl- N -Phenyl Dithiocarbamate: Synthesis, Characterisation, Antifungal Activity, and Solvent Extraction Studies of the Ligand. Bioinorganic Chemistry and Applications 2015, 2015 (2), 1–10. https://doi.org/10.1155/2015/913424.

(52). Gullino, M. L.; Tinivella, F.; Garibaldi, A.; Kemmitt, G. M.; Bacci, L.; Sheppard, B. Mancozeb: Past, Present, and Future. Plant Disease 2010, 94 (9), 1076–1087. https://doi.org/10.1094/PDIS-94-9-1076.

(53). Thind, T. S.; Hollomon, D. W. Thiocarbamate Fungicides: Reliable Tools in Resistance Management and Future Outlook. Pest Management Science 2018, 74 (7), 1547–1551. https://doi.org/10.1002/ps.4844.

(54). Jain, S.; Chandra, V.; Kumar Jain, P.; Pathak, K.; Pathak, D.; Vaidya, A. Comprehensive Review on Current Developments of Quinoline-Based Anticancer Agents. Arabian Journal of Chemistry 2019, 12 (8), 4920–4946. https://doi.org/10.1016/j.arabjc.2016.10.009.

(55). Garrido Montalban, A. Quinolines and Isoquinolines. In Heterocycles in Natural Product Synthesis; Wiley-VCH Verlag GmbH & Co. KGaA: Weinheim, Germany, 2011; pp 299–339. https://doi.org/10.1002/9783527634880.ch9.

(56). Shang, X.-F.; Morris-Natschke, S. L.; Liu, Y.-Q.; Guo, X.; Xu, X.-S.; Goto, M.; Li, J.-C.; Yang, G.-Z.; Lee, K.-H. Biologically Active Quinoline and Quinazoline Alkaloids Part I. Medicinal Research Reviews 2018, 38 (3), 775–828. https://doi.org/10.1002/med.21466.

(57). Patten, A. M.; Vassão, D. G.; Wolcott, M. P.; Davin, L. B.; Lewis, N. G. Trees: A Remarkable Biochemical Bounty. In Comprehensive Natural Products II; Elsevier, 2010; Vol. 3, pp 1173–1296. https://doi.org/10.1016/B978-008045382-8.00083-6.

(58). Woodward, C. F.; Badgett, C. O.; Kaufman, J. G. Chemical-Catalytic Liquid-Phase Oxidation of Nicotine, β-Picoline, and Quinoline to Nicotinic Acid. Industrial & Engineering Chemistry 1944, 36 (6), 544–546. https://doi.org/10.1021/ie50414a012.

(59). (a) Marella, A.; Tanwar, O. P.; Saha, R.; Ali, M. R.; Srivastava, S.; Akhter, M.; Shaquiquzzaman, M.; Alam, M. M. Quinoline: A Versatile Heterocyclic. Saudi Pharmaceutical Journal 2013, 21 (1), 1–12. https://doi.org/10.1016/j.jsps.2012.03.002.

(b) Kumar, R.; Mazumder, A.; Kumar, A.; Tiglani, D. Updates on Synthesis and Biological Activities of Quinoline Derivatives: A Review. International Journal of Pharmaceutical Research 2021, 13 (01). https://doi.org/10.31838/ijpr/2021.13.01.472.

(60). Matada, B. S.; Pattanashettar, R.; Yernale, N. G. A Comprehensive Review on the Biological Interest of Quinoline and Its Derivatives. Bioorganic & Medicinal Chemistry

2021, 32 (August 2020), 115973. https://doi.org/10.1016/j.bmc.2020.115973.

(61). (a) Theeraladanon, C.; Arisawa, M.; Nishida, A.; Nakagawa, M. A Novel Synthesis of Substituted Quinolines Using Ring-Closing Metathesis (RCM): Its Application to the Synthesis of Key Intermediates for Anti-Malarial Agents. Tetrahedron 2004, 60 (13), 3017–3035. https://doi.org/10.1016/j.tet.2004.01.084.

(b) Foley, M. Quinoline Antimalarials Mechanisms of Action and Resistance and Prospects for New Agents. Pharmacology & Therapeutics 1998, 79 (1), 55–87. https://doi.org/10.1016/S0163-7258(98)00012-6.

(62) (a) Evaluation of the Anti-Inflammatory Activity of Quinoline Derivatives. Medicinal Chemistry Research 2015, 24 (6), 2591–2603. https://doi.org/10.1007/s00044-015-1323-y.

(b) Pinz, M. P.; Reis, A. S.; de Oliveira, R. L.; Voss, G. T.; Vogt, A. G.; Sacramento, M. do; Roehrs, J. A.; Alves, D.; Luchese, C.; Wilhelm, E. A. 7-Chloro-4-Phenylsulfonyl Quinoline, a New Antinociceptive and Anti-Inflammatory Molecule: Structural Improvement of a Quinoline Derivate with Pharmacological Activity. Regulatory Toxicology and Pharmacology 2017, 90, 72–77. https://doi.org/10.1016/j.yrtph.2017.08.014.

(c) Shaheen, F.; Badshah, A.; Gielen, M.; Croce, G.; Florke, U.; Vos, D. de; Ali, S. In Vitro Assessment of Cytotoxicity, Anti-Inflammatory, Antifungal Properties and Crystal Structures of Metallacyclic Palladium(II) Complexes. Journal of Organometallic Chemistry 2010, 695 (3), 315–322. https://doi.org/10.1016/j.jorganchem.2009.10.048.

(63). (a) Paris, D.; Cottin, M.; Demonchaux, P.; Augert, G.; Dupassieux, P.; Lenoir, P.; Peck, M. J.; Jasserand, D. Synthesis, Structure-Activity Relationships, and Pharmacological Evaluation of Pyrrolo[3,2,1-Ij]Quinoline Derivatives: Potent Histamine and Platelet Activating Factor Antagonism and 5-Lipoxygenase Inhibitory Properties. Potential Therapeutic Application I. Journal of Medicinal Chemistry 1995, 38 (4), 669–685. https://doi.org/10.1021/jm00004a013.

(b) Cairns, H.; Cox, D.; Gould, K. J.; Ingall, A. H.; Suschitzky, J. L. New Antiallergic Pyrano[3,2-g]Quinoline-2,8-Dicarboxylic Acids with Potential for the Topical Treatment of Asthma. Journal of Medicinal Chemistry 1985, 28 (12), 1832–1842. https://doi.org/10.1021/jm00150a014.

(c) Gaurav, A.; Singh, R. Pharmacophore Modeling, 3DQSAR, and Docking-Based Design of Polysubstituted Quinolines Derivatives as Inhibitors of Phosphodiesterase 4, and Preliminary Evaluation of Their Anti-Asthmatic Potential. Medicinal Chemistry Research 2014, 23 (12), 5008–5030. https://doi.org/10.1007/s00044-014-1048-3.

(64). (a) dos Santos Chagas, C.; Fonseca, F. L. A.; Bagatin, I. A. Quinoline-Derivative Coordination Compounds as Potential Applications to Antibacterial and Antineoplasic Drugs. Materials Science and Engineering: C 2019, 98 (January), 1043–1052.

https://doi.org/10.1016/j.msec.2019.01.058.

(b) Kaminsky, D.; Meltzer, R. I. Quinoline Antibacterial Agents. Oxolinic Acid and Related Compounds. Journal of Medicinal Chemistry 1968, 11 (1), 160–163. https://doi.org/10.1021/jm00307a041.

(c) Pham, T. D. M.; Ziora, Z. M.; Blaskovich, M. A. T. Quinolone Antibiotics. MedChemComm 2019, 10 (10), 1719–1739. https://doi.org/10.1039/C9MD00120D.

(65). Grundon, M. F. Quinoline, Quinazoline, and Acridone Alkaloids. Natural Product Reports 1990, 7 (2), 131. https://doi.org/10.1039/np9900700131.

(66). Tse, E. G.; Korsik, M.; Todd, M. H. The Past, Present and Future of Anti-Malarial Medicines. Malaria Journal 2019, 18 (1), 93. https://doi.org/10.1186/s12936-019-2724-z.

(67). Dave, C. G.; Joshipura, H. M. ChemInform Abstract: Microwave Assisted Gould-Jacob Reaction: Synthesis of 4-Quinolones under Solvent-Free Conditions. ChemInform 2010, 33 (28), no-no. https://doi.org/10.1002/chin.200228178.

(68). Cheng, C.-C.; Yan, S.-J. The Friedländer Synthesis of Quinolines. In Organic Reactions; John Wiley & Sons, Inc.: Hoboken, NJ, USA, 1982; Vol. 35, pp 37–201. https://doi.org/10.1002/0471264180.or028.02.

(69). Knight, J. A.; Porter, H. K.; Calaway, P. K. The Synthesis of Quinolines by the Pfitzinger Reaction. Journal of the American Chemical Society 1944, 66 (11), 1893–1894. https://doi.org/10.1021/ja01239a029.

(70). Denmark, S. E.; Venkatraman, S. On the Mechanism of the Skraup−Doebner−Von Miller Quinoline Synthesis. The Journal of Organic Chemistry 2006, 71 (4), 1668–1676. https://doi.org/10.1021/jo052410h.

(71). Doebner, O.; v. Miller, W. Ueber Eine Dem Chinolin Homologe Base. *Berichte der deutschen chemischen Gesellschaft* **1881**, *14* (2), 2812–2817. https://doi.org/10.1002/cber.188101402258.

(72). Wang, Z. Conrad-Limpach Quinoline Synthesis. In Comprehensive Organic Name Reactions and Reagents; John Wiley & Sons, Inc.: Hoboken, NJ, USA, 2010; pp 692–696. https://doi.org/10.1002/9780470638859.conrr152.

(73). Graham, A.; Robinson, M. Tricyclic Systems: Central Carbocyclic Ring with Fused Five-Membered Rings. In *Comprehensive Heterocyclic Chemistry III*; Elsevier, 2008; Vol. 10, pp 1135–1199. https://doi.org/10.1016/B978-008044992-0.00921-4.

(74). Ebejer, J.-P.; Fulle, S.; Morris, G. M.; Finn, P. W. The Emerging Role of Cloud Computing in Molecular Modelling. Journal of Molecular Graphics and Modelling 2013, 44, 177–187. https://doi.org/10.1016/j.jmgm.2013.06.002.

(75). Chai, L. Q.; Zhang, J. Y.; Chen, L. C.; Li, Y. X.; Tang, L. J. Synthesis, Crystal Structure, Spectroscopic Properties and DFT Calculations of a New Schiff Base-Type Zinc(II) Complex. *Research on Chemical Intermediates* 2016, *42* (4), 3473–3488. https://doi.org/10.1007/s11164-015-2226-8.

(76). Wang, Z. Conrad-Limpach Quinoline Synthesis. In Comprehensive Organic Name Reactions and Reagents; John Wiley & Sons, Inc.: Hoboken, NJ, USA, 2010; pp 692–696. https://doi.org/10.1002/9780470638859.conrr152.

(77). Ghorai, P.; Saha, R.; Bhuiya, S.; Das, S.; Brandão, P.; Ghosh, D.; Bhaumik, T.; Bandyopadhyay, P.; Chattopadhyay, D.; Saha, A. Syntheses of Zn(II) and Cu(II) Schiff Base Complexes Using N,O Donor Schiff Base Ligand: Crystal Structure, DNA Binding, DNA Cleavage, Docking and DFT Study. *Polyhedron* **2018**, *141*, 153–163. https://doi.org/10.1016/j.poly.2017.11.041.

(78). Devi, S. Stereoscopic Vision, Stereoscope, Selection of Stereo Pair and Its Orientation. *International Journal of Science and Research (IJSR) ISSN (Online Impact Factor* **2012**, *3* (9), 2319–7064.

(79). Gross, L. A.; Baird, G. S.; Hoffman, R. C.; Baldridge, K. K.; Tsien, R. Y. The Structure of the Chromophore within DsRed, a Red Fluorescent Protein from Coral. *Proceedings of the National Academy of Sciences* **2000**, *97* (22), 11990–11995. https://doi.org/10.1073/pnas.97.22.11990.

CHAPTER II

MATERIALS AND METHODS

This Chapter, entitled, '**Materials and Methods'**, describes the experimental aspects such as the procedures of synthesis, purification and crystallization of the materials investigated, sampling techniques and methods of measurements involved in the instrumental analysis of the compounds, data management, computational procedures, biological assaying details, etc. among others.

This Chapter is divided into two parts, **Part A** and **Part B,** out of which **Part A** deals with the synthesis, purification, crystallization of the chosen compounds and other wet methods of materials, while **Part B** deals with the instrumental details of characterization of the compounds besides the computational chemistry procedures on the modelled compounds. **Part B** also introduces the principles, instrumentation and applications of some modern methods used during the studies, for the general benefit of the readers of this thesis.

PART A

MATERIALS

2A.1 Synthesis of Fluoxetine Dithiocarbamate, FLXDTC (See **Scheme 2A.1):**

High purity Fluoxetine Hydrochloric acid was purchased from Pharma Company and was purified by recrystallization before use. For this, AR grade salts of Cd, Zn, Ni, Cu, Co, and MN were used. Tetra Ethyl Ammonium Perchlorate (TEAP) and CDCl3 (99.9% D with 0.03% TMS) were purchased from Aldrich (USA). Spectroscopic grade carbon disulfide and other solvents were employed during the investigations.

To a solution of 1.210 g (3.5 mm) of fluoxetine hydrochloride (FLX) in 20 ml of diethyl ether, 2.66 g of carbon disulfide (3.5 mm) was added at a temperature of 5 ˚C with stirring. After 5 minutes, 2 ml of sodium hydroxide solution (3.5 mm) was added to this mixture, with stirring continued for 5 hours. The yellow-colored solution, thus obtained, was reduced to one third of its volume in a rotovapour under reduced pressure and mild heating before eluting the reaction mixture from a polystyrene column chromatograph with a mixture of 20% hexane and 80% ethyl acetate as the mobile phase. Finally, the yellow-colored solid was separated by suction filtration, dried in vacuum desiccators over fused calcium chloride, and purified by recrystallization from a mixture of methanol and dichloromethane. The synthesis procedure of the **FLXDTC** ligand and its metal complexes is shown in **Scheme 2A.1.**

2A.2 Synthesis of the FLXDTC Complexes, M(FLXDTC)$_2$ (See **Scheme 2A.1):**

This section outlines a typical method for preparing **Cu(FLXDTC)$_2$**. An aqueous solution of cupric chloride in 10 ml of water (26.89 mg, 0.2 mM) was added to a methanol solution of 81.49 mg **FLXDTC** ligand (0.2 mM) while stirring on a water bath. The brown colored precipitate that formed was filtered and washed with a hexane-ethyl acetate (1:4 v/v) solvent mixture (**Scheme 2A.1)**. The same procedure is followed for the remaining metal complex synthesis.

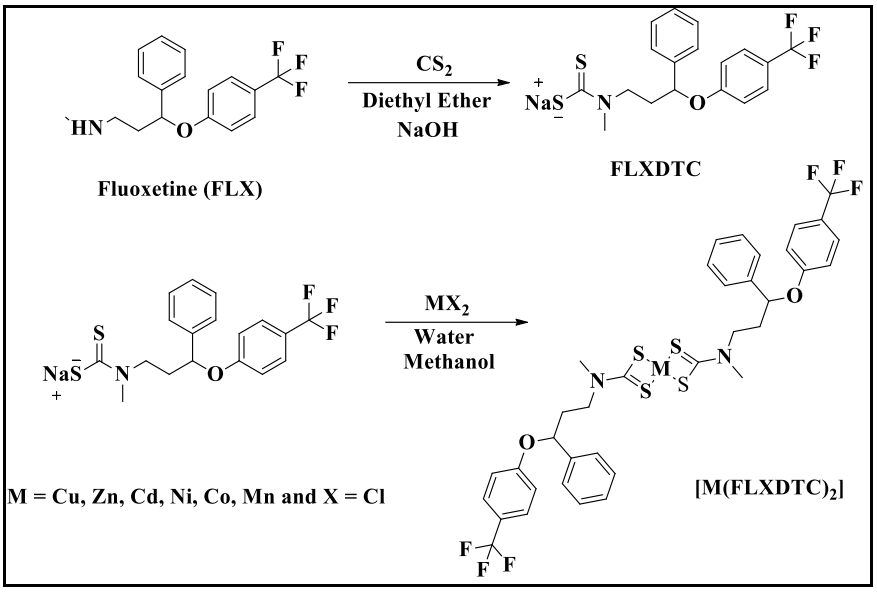

Scheme 2A.1: *Schematic of the synthesis of* ***FLXDTC*** *and* ***[M(FLXDTC)$_2$]***

Studies of **FLXDTC** and its complexes are presented in **Chapter-III**

2A.3 Synthesis of (E)-1-(((3-fluoro-4-morpholinophenyl)imino)methyl)naphthalene-2-ol, FMIMN (See **Scheme 2A.2):**

All of the needed chemicals, including 2-hydroxy-1-napthaldehyde, 3-fluoro-4-morpholinoaniline, methanol, chloroform, and 35% hydrochloric acid, were of analytical grade and used as received.

A mixture of 2-hydroxy-1-napthaldehyde (0.172 g, 1 mM) and 3-fluoro-4-morpholinoaniline, (0.196 g, 1 mM) was dissolved in methanol and refluxed for an hour after being spiked with 2 drops of **HCl** to yield a yellow-colored compound, **FMIMN** which was filtered, washed several times with cold methanol and dried. Crystals were grown for this Schiff base in methanol and a chloroform mixture (1:3 v/v).

2A.4 Synthesis of the Complexes, M(FMIMN)$_2$ (See **Scheme 2A.2):**

A typical procedure for the preparation of **Cu(FMIMN)$_2$** is briefly described below. A methanol solution of 140.15 mg (0.4 mM) of the ligand **FMIMN** was added to a methonolic solution of cupric chloride in 10 ml (26.89 mg, 0.2 mM) while stirring on a water bath. The

resulting brown precipitate was filtered and washed in an ethanol solvent. The remaining metal complexes were synthesized using the same process. The sequential procedure of the synthesis of both **FMIMN** and its complexes is depicted in **Scheme 2A.2.** The studies of these complexes are presented in **Chapter IV**.

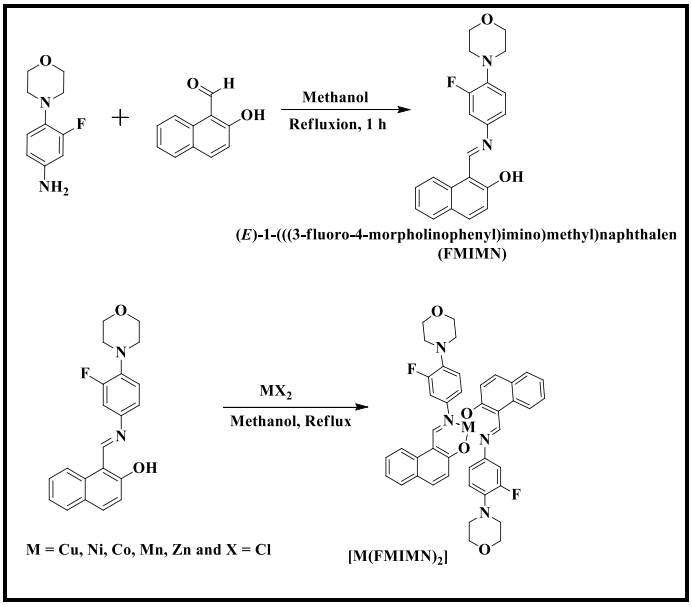

Scheme 2A.2: *Schematic of the synthesis of* ***FMIMN*** *and* ***[M(FMIMN)$_2$]***

2A.5 Synthesis of 2-Phenylmalonaldehyde (See **Scheme 2A.3):**

A procedure reported elsewhere was used to prepare 2-phenyl malonaldehyde[1,2]. To the solution of phenyl acetic acid in dry DMF, was added small drops of $POCl_3$ under overnight reflux. The dark brown colored mixture was treated with an excess saturated sodium perchlorate solution to obtain the white colored crystalline solid, N-(3-(dimethylamino)-2-phenylallylidene)-N-methylmethanaminium **(DPM).** The white colored compound, 2-phenylmalonaldehyde was obtained by adding 20 mL warm sodium hydroxide (28 mmol) to 13.5 mmol of **DPM** and upon heating at 95 °C for 20 min, after the mixture was acidified to pH = 2 by dropwise 10% HCl. The procedure is briefly depicted in **Scheme 2A.3.**

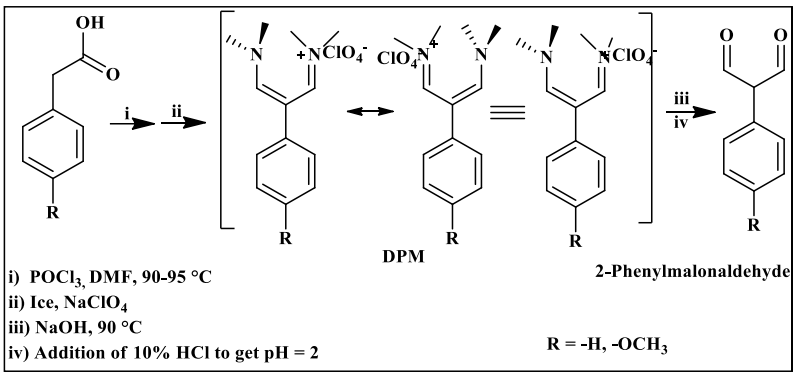

Scheme 2A.3: *Schematic of the synthetic sequence of the 2-phenylmalonaldehyde*

2A.6 Cyclization and Adduction to Schiff Bases of the 2-Phenylmalonaldehyde (See **Scheme 2A.4):**

Very interesting synthesis facts are found from the 2-Phenylmalonaldehyde. Dissolving on the reaction constituents with mild variation in reagents, we got 3 different compounds from the 2-phenylmalonaldehyde as shown in **Scheme 2A.4.**

2A.6a ***Synthesis of 7-Fluoro-6-morpholino-3-phenylquinolin-1-ium Chloride (FMPC):***

The 7-fluoro-6-morpholino-3-phenylquinoline-1-ium chloride salt **(FMPC)** was prepared by Combe's quinoline procedure[3]. It was formed by refluxion of the ethanolic mixture of 2-phenylmalonaldehyde and 3-fluoro-4-morpholinoaniline, spiked with a few drops of HCl (**Scheme 2A.4**). The precipitated **FMPC** was suction-filtered, washed with ethanol, and air-dried. Crystals were grown for this salt in methanol and a chloroform mixture (1:3 v/v).

2A.6b ***Synthesis of 5-Fluoro-3-(4-methoxyphenyl)-6-morpholinoquinolin-1-ium Chloride (FMPMC):***

5-fluoro-3-(4-methoxyphenyl)-6-morpholinoquinolin-1-ium chloride salt, **(FMPMC)** was prepared by refluxion of the ethanolic mixture of 2-(4-methoxyphenyl)malonaldehyde and 3-fluoro-4-morpholinoaniline spiked with a few drops of HCl (**Scheme 2A.4**).

2A.6c ***Synthesis of (E)-3-Fluoro-N-((Z)-3-((3-fluoro-4-morpholinophenyl)amino)-2-(4-methoxyphenyl)allylidene)-4-morpholinobenzenaminium (FFMMMC):***

(E)-3-fluoro-N-((Z)-3-((3-fluoro-4-morpholinophenyl)-amino)-2-phenylallylidene)-4-morpholinobenzenaminium, **FFMPMC** and (E)-3-fluoro-N-((Z)-3-((3-fluoro-4-morpholinophenyl)-amino)-2-phenylallylidene)-4-morpholinobenzenaminium, **FFMMMC** were synthesized after a mixture of substituted phenyl malonaldehydes and 3-fluoro-4-morpholinoaniline was dissolved in ethanol, spiked with 3 drops of glacial acetic acid, and refluxed for an hour **(Scheme 2A.4)** before the contents were filtered, washed several times with cold ethanol, and dried. Investigations of these compounds are presented in **Chapter IV.** Single crystals could be generated only for (Z)-3-((3-fluoro-4-morpholinophenyl)amino)-2-phenylacrylaldehyde **(FMAPA),** with one of the carbonyl groups converted to azomethine, and 3-fluoro-N-((1E,2Z)-3-((3-fluoro-4-morpholinophenyl)amino)-2-(4-methoxyphenyl)allylidene)-4-morpholinobenzenaminium **(FFMMMC)**, with both the carbonyl groups converted to azomethines, whereas we could not obtain single crystals of 3-fluoro-N-((1Z,3E)-3-((3-fluoro-4-morpholinophenyl)imino)-2-phenylprop-1-en-1-yl)-4-morpholinobenzenaminium (**FFMPMC)** and (Z)-3-((3-fluoro-4-morpholinophenyl)amino)-2-(4-methoxyphenyl)acrylaldehyde (**FMAMA)** in a chloroform-methanol solvent mixture.

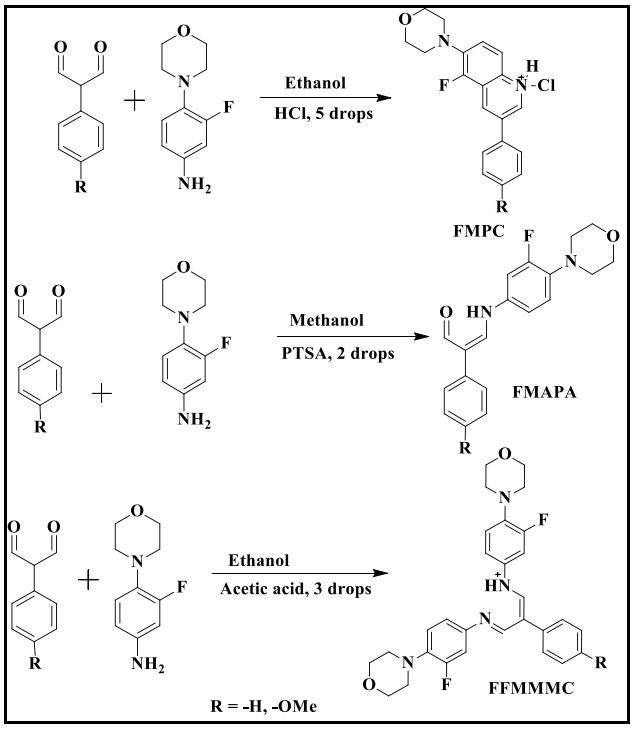

Scheme 2A.4: *Schematic for the synthesis of various compounds from 2-phenyl malonaldehyde and 3-fluoromorpholino aniline*

2A.7 Synthesis of 2,2'-(((1E,3E)-2-phenylpropane-1,3-diylidene)bis(azaneylylidene))dibenzoic acid, PDBAD and its Metal Complexes (See **Scheme 2A.5):**

The yellow color compound, 2,2'-(((1E,3E)-2-phenylpropane-1,3-diylidene)bis(azaneylylidene))dibenzoic acid **(PDBAD)** was obtained after a mixture of 2-phenyl malonaldehyde (0.74 g, 5 mM) and anthranalic acid (1.37 g, 10 mM) was resulted in ethanol, spiked with 3 drops of acetic acid for 2 hours (**Scheme 2A.5**).

A typical procedure followed for the preparation of the **[Cu(PDBAD)]** is presented here: An ethonolic solution of cupric chloride in 10 ml (26.89 mg, 0.2 mM) was added to a methanol solution of 77.28 mg **PDBAD** ligand (0.2 mM) while stirring on a water bath. The brown colored precipitate, formed, was filtered and washed with a methanol solvent mixture. Same procedure is followed for remaining metal complexes synthesis. The simplified chemical equations are shown in **Scheme 2A.5.**

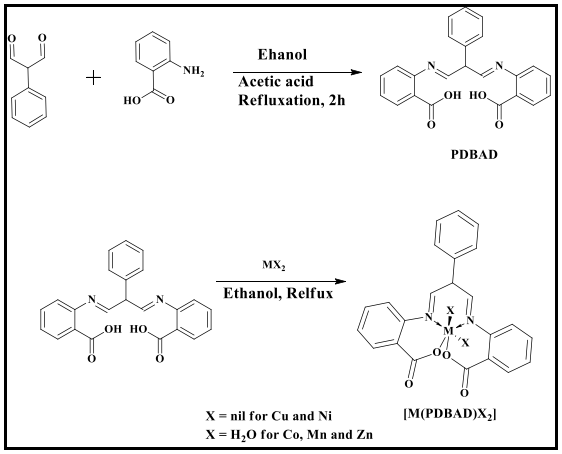

Scheme 2A.5: *Scheme for the synthesis of* ***PDBAD*** *and* ***[M(PDBAD)X_2]***

The recrystallized pure compounds suitable for single crystal XRD studies were obtained from dilute solutions of theirs in test tubes, sealed with aluminium foil with one or two perforations. To avoid temperature variations, the test tubes were enclosed under a thick sheet of thermocoal, which was then sealed inside a wooden chest for 3–10 days. After a few weeks, the tubes were removed to identify single crystals of various shapes and sizes. Through the use of a compound microscope, these crystals were sorted. For single crystal XRD studies, the best crystal was carefully chosen and washed with pure relevant solvents to get rid of any solvent residues.

PART B

METHODS

This part covers the sample procedures for measurements and characterization of various instruments and instrumental techniques. A brief introduction to the principles of some modern research methods that we have used is provided at the end of this chapter for the benefit of the readers of this thesis.

2B.1 Sampling Methods and Instrumental Operations:

2B.1.1 *Melting Point Determination:*

The Stuart SPM30 Digital Melting Point Apparatus was used to measure the melting points of various solid materials and other purifications. The results are now corrected where ever glass thermodynamics was followed. Mostly these readings are digital.

2B.1.2 *Elemental Analysis:*

The C, H, N, and S elemental analysis of the ligands and complexes was done using a Carlo Erba Fisons Model EA 1108 CHNS-O Elemental Analyzer with a DP 200 Data Processor and a microgram-sensitive Sartorius MC5 Microbalance.

2B.1.3 *Mass Spectral Analysis:*

A Perkin Elmer Model (SCIEX API-2000, ESI-MS) Spectrometer was used to determine the electrospray ionization mass spectra (ESI-MS). The Agilent model 6530 Q-TOF LC-HRMS was also used.

2B.1.4 *Infrared Spectral Studies:*

The FT-IR spectra of the compounds in their KBr pellets were recorded on a Perkin Elmer Model Spectrum 100S spectrophotometer that has a resolution of 1 cm^{-1}.

2B.1.5 ***NMR Spectral Studies:***

The ligands and some of the soluble diamagnetic complexes were characterized using ^{1}H and ^{13}C NMR spectra recorded on a Bruker Advance 400 MHz NMR spectrometer at room temperature using TMS as an internal reference. Solutions suitable for the studies were prepared in approximately deuterated solvents. The deuterated solvents were also used as the locking isotopes during the NMR studies.

2B.1.6 ***ESR Spectral Studies:***

In the powder and solution states, EPR spectra were measured with a JEOL FA 100 X-Band Spectrometer. 2,2-diphenyl-1-picrylhydrazyl (DPPH) radical compound was the external standard taken in a small capillary.

2B.1.7 ***UV-Visible Absorption Spectral Methods:***

The electronic spectra of all substances were recorded on a Thermo Scientific Evolution 600 or on a Perkin Elmer Lambda 25 Spectrophotometer in the wavelength range of 200-1100 nm at a band width of 1 nm or lower. It has been used to monitor pH-metric and spectrophotometric titrations, which are used to investigate protonation, deprotonation, and chemical kinetics.

2B.1.8 ***Fluorescence Emission Spectral Methods:***

The UV-Visible fluorescence emission spectra of all compounds were recorded on a Horiba Instruments Incorporated, USA model FL-1000 Fluorescence spectrophotometer in the wavelength range of 900-200 nm. As per the nature of each compound, the excitation wavelength and its intensities were altered.

2B.1.9 ***Electrochemical Investigations:***

A result, a variety of electroanalytical procedures were applied in our research. An Orion Model EA 940 Expandable Ion Meter equipped with an Ag|AgCl combined glass electrode was used to test the pH of buffers, stock solutions, and reaction mixtures. Electrochemical measurements were carried out using a CHI workstation (Model 6132E, USA). The voltammograms were obtained from a three-electrode electrochemical cell system with either a glassy carbon electrode or platinum disc as the working electrode, either Ag|AgCl|Cl (sat) or SCE

as the reference electrode and platinum wire as the auxiliary electrode. pH buffers and Tetra ethyl ammonium perchlorate solutions were used as electrolytes. **Figure 2B.1** shows the three-electrode assembly. To activate the glass carbon electrode surface, polish the electrode with a 0.05 m alumina slurry. Several scoops of alumina can be mixed with a small wash bottle of high purity water, such as NanopureTM, and sprayed onto a clean, ground glass plate.

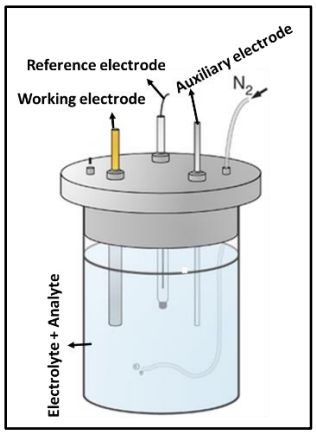

Figure 2B.1: *Three-electrode electrochemical cell system*

2B.2 Crystallographic Data Collections:

The single crystal X-ray data is collected on a Bruker-Nonius SMART APEX CCD diffractometer at 293 (2) Kα using graphite-monochromated Mo K radiation (= 0.71073), after getting a suitable crystal for an X-ray experiment. This device is used to direct X-ray beams through a crystal, record where they diffract, and quantify the intensity of the reflection.

2B.3 Molecular Modelling:

We have run computational studies on it under a few modeling platforms, viz., MM2 (ChemSoft), AM1 (Austin Model-1) and DFT (B3LYP). MM2 uses a force field to produce energy-minimized molecules, based on the Self Consistent Field (SCF) approach and the semi-empirical Austin Model-1 (AM1). Becke-3-Parameter-Lee–Yang–Parr (B3LYP) Density Functional Theory (DFT/B3LYP) is predominantly applied to molecular systems with a large number of electrons and atoms and operates on the nature and extent of inter-electronic interactions that manifest as hybrid functional instead of simple electronic wave functions. The chemicals were

molecularly modeled using ChemOffice Ultra. This molecular modelling software was used to obtain important thermochemical and molecular energy data, as well as HOMO-LUMO energy values. Single and double dihedral conformation analyses were performed on the energy minimized structures. Golden Software's Surfer 10 was used to make 3-D counter plots of double-dihedral conformational analysis charts.

2B.4 Biological Studies Procedures:

2B.4.1 *Antimicrobial and Antifungal Screening:*

Two gram-negative bacteria, *Klebsiella pneumoniae* and *Escherichia coli*, and two gram positive bacteria, *Staphylococcus aureus* and *Bacillus subtilis*, as well as a few fungus strains, *Aspergillus niger* and *Pencilliumnotatum*, were employed in this study. For bacteria and fungi, the reference drugs were streptomycin and ketoconazole, respectively. The MIC values of the investigated compounds and reference drugs were measured in μM.

2B.4.2 *Antioxidant Screening:*

The antioxidant activity of the synthesized compounds has attracted people's interest, and it's been tested predominantly in vitro systems. The antioxidant activity of the ligand and its metal complexes was investigated using the DPPH (1,1-diphenyl-2-picrylhydrazyl) radical as a reagent in a spectrophotometric test. The antioxidant ascorbic acid is used as a standard. The substances were tested in triplicate, and the standard deviation was computed.

2B.4.3 *Anticancer Screening:*

Following the successful evaluations of antimicrobial and scavenging activity, we used the 3-(4,5-dimethylthiazol-2-yl)-2,5-diphenyltetrazolium bromide (MTT) method to investigate anticancer activity against MCF-7 (breast), HepG-2 (liver), HEK293 (embryonic kidney), and FaDU (head and neck) cancer cell lines. Cisplatin is used as a standard of comparison.

2B.4.4 *Molecular Protein Docking Interaction Studies:*

The objective of molecular docking approaches is to anticipate a ligand's optimal binding mode to a macromolecular partner (here just proteins are considered)[3]**.** It entails the creation of a variety of potential ligand conformations and orientations, or poses, within the protein binding

site[4]. As a result, the presence of the molecular target's three-dimensional structure is needed; it can be an experimentally solved structure (such as via X-ray crystallography or NMR) or a structure produced by computational techniques. The graphical user interface tool AutoDock Tools was used to perform intermediate stages such as creating pdbqt files for protein and ligand preparation and creating grid boxes (ADT)[5]**.** The protein was modified using ADT by adding polar hydrogens, Kollman charges, solvation parameters, and fragmental volumes[6]. The prepared file was saved in PDBQT format by AutoDock. An AutoGrid was used to create a grid map using a grid box. To reduce computing time, a score grid is calculated using the ligand structure[7]**.** The protein and ligand information, as well as grid box attributes in the configuration file, were used to dock AutoDock/Vina. An accelerated local search global optimizer is used by AutoDock/Vina. Both the protein and the ligands are treated as rigid during the docking phase. The findings with a positional root-mean-square deviation (RMSD) of less than 1.0 were grouped together and represented by the result with the lowest binding free energy. For further analysis, the posture with the lowest binding energy or binding affinity was extracted and aligned with the receptor structure. EGFR-TK (pdb id: 1m17) belongs to the epidermal growth factor receptor family. Excess EGFR expression results in anal cancer and epithelial malignancies of the neck and head. The DockVina[8] software was used to perform docking calculations. Using AutoDockTools-1.5.6, the ligand is prepared by eliminating water molecules and adding polar hydrogens, as well as ascribing Kollman and Gasteiger partial charges. The AutoGrid application was used to create affinity maps with 60×60×60 grid points and 0.575 spacing. The discovery studio visualizer software was used to help people understand the 2D structure and figure out how the binding interactions worked.

2B.5 Functional Principles of Some Important Techniques:

Here is a brief breakdown of some of the modern methods for ligand and complex characterization that we have studied. In spite of the fact that excellent books, review articles, and reference material are available on these strategies, a quick overview may suffice. Only those methods are talked about here that help us understand the compounds better in terms of their electrical, structural, redox, geometric, and spectral properties.

2B.5.1 *Cyclic Voltammetry as Tool for Material Diagnostics:*

Cyclic voltammetry (CV) has become an important and widely used voltammetric technique in a number of fields, such as chemical engineering, material science, and chemical sciences. CV is done by changing the potential of an electrode linearly as a function of time and watching the current signal at each potential. This is usually done with a three-electrode electrochemical cell. In this method, the voltage at the working electrode changes both forward and backward while the current is being measured. **Figure 2B.2** depicts a typical waveform applied to the working electrode.

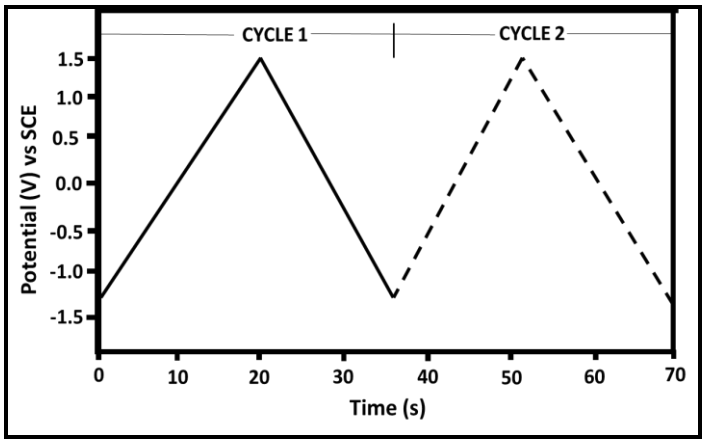

Figure 2B.2: *Typical triangular potential programme in a cyclic voltammetric run (eg. between -1.5 and +1.5 vs SCE)*

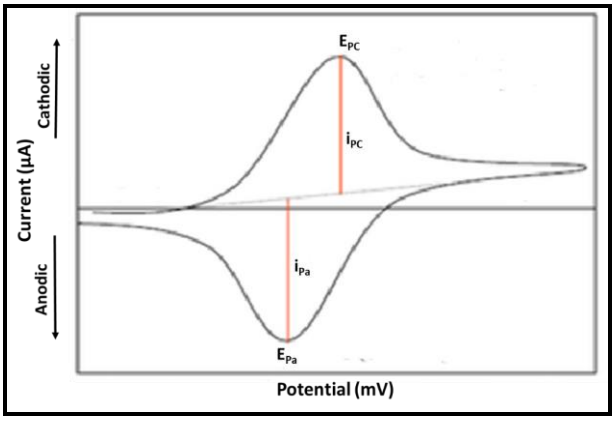

Figure 2B.3: *Shape of a typical reversible cyclic voltammogram*

However, repetitive cyclic voltammograms can be used for a variety of applications, such as determining the Nernstian (reversible) and non-Nernstian (irreversible) behavior of a redox couple, the stability of reaction products, the number of electrons transferred in an electrochemical event, reaction kinetics, and so on. The Randles-Sevcik equation explains the effect of scan rate and electrode area[9]**.** On the other hand, a chemical event that happens at the same time as the electrochemical event can make a big difference in the ratio of peak currents.

Shain and collaborators provide a detailed theory of cyclic voltammetry[10,11,12]. Randles established the utility of the approaches for reversible processes, while Delahey determined the significance of the techniques for irreversible processes[13].

The net current at the peak of the cathodic response, the potential at the peak of the cathodic response, the net current at the peak of the anodic response, and the potential at the peak of the anodic response are all measured by the current potential wave. A typical cyclic voltammogram for reversible charge transfer is shown in **Figure 2B.3.**

For a general electrode process,

$$i_p = 2.99 \times 10^5 \, n(\alpha_{na})^{1/2} A D^{1/2} v^{1/2} C \qquad \textbf{(2.1)}$$

where

i_p = peak current in μA

n = number of electrons

A = area of working electrode in cm^{-1}

D = diffusion coefficient in cm^2

C = concentration in mol lit^{-1}

ν = scan rate in volts

α = transfer coefficient (usually 0.5)

n_a = number of electrons involved in the rate determining step.

The value of α_{na} is given through

$$E_{p_{\frac{1}{2}}} - E_p = \frac{0.048}{\alpha_{na}} \qquad \textbf{(2.2)}$$

Where E_p and $E_{p1/2}$ are the peak and half peak potentials, respectively.

For a reversible system,

$$|E_{pa} - E_{pc}| = \frac{0.059}{n} \quad \textbf{(2.3)}$$

$$\frac{i_{pc}}{i_{pa}} = 1 \quad \textbf{(2.4)}$$

The peak current in reversible process is given by Randel-Sevcik equation

$$i_p = kn^{3/2}AD^{1/2}cv^{1/2} \quad \textbf{(2.5)}$$

where

i_p = peak current in μA

n = number of electrons

A = area of working electrode in cm^{-1}

D = diffusion coefficient in cm^2

C = concentration in mol lit^{-1}

ν = scan rate in volts

k = Randel-Sevcik constant

The peak current in irreversible process is given by equation

$$i_p = 0.227nFAc^o k_f \exp[\frac{\alpha_n F}{RT}]\{E_p - E_o\} \quad \textbf{(2.6)}$$

A plot of log i_p vs $E_p - E^\circ$ of different scan rates yields, α from the slope and k from the intercept, provide E° is known.

Shain and Nicholson calculated the peak potentials for an irreversible response

$$E_p = E_o - \frac{RT}{\alpha_n F}[0.780 + \ln(D_\circ \alpha_a)^{1/2} - \ln k_s] \quad \textbf{(2.7)}$$

There is 30/αn mV cathodic shift in peak potential for every 10-fold increase in scan rate and this criterion can be used to characterize an irreversible response.

The heterogeneous forward rate constant (k_o f, h) values can be calculated using the equation,

$$E_p = \frac{RT}{\alpha_n F}\{(\ln(k^o_f, h/D^{1/2}) - 1.14) - (0.5\ln(\alpha_{na}V)\} \quad \textbf{(2.8)}$$

where R is the gas constant, F is the Faraday constant and T is the absolute temperature.

Eqns. 2.3 and 2.4 are commonly used to check an electrochemical process's reversibility. Eqn 2.1 indicates that ip is proportional to $\nu^{1/2}$ for a specific ion and other experimental conditions. As a result, a straight line should be drawn between the square root of the scan rate and the peak current, i_p, of the respective cyclic voltammograms. In organic voltammetry, deviations from this rule are fairly common.

Usually, the shape of the peak of irreversible response is independent of scan rate and the separation of E_p and $E_{p1/2}$ is given by

$$E_P - E_{P_{1/2}} = \frac{-1.857RT}{\alpha_n F} \quad \textbf{(2.9)}$$

If the electron transfer is a diffusion-controlled process with a faster scan rate than the chemical reaction, the kinetics of the chemical reaction can be determined by analyzing the variation of peak current and peak potential over time and concentrations.

2B.5.2 ***X-Ray Crystallographic Technique for Elucidation of Crystal and Molecular Structures:***

The experimental science of determining the arrangement of atoms in crystalline substances is known as crystallography. These techniques are used by material scientists, biologists, astronomers, and other scientists to determine the structure and other geometrical properties of crystalline materials[14]. The examination of the diffraction patterns of a sample targeted by an X-ray beam generated from an anodic material such as Cu, Mo, etc. is now used in crystallographic procedures[15]**.** X-rays interact with the spatial structure of crystals to produce diffraction patterns of sharp Bragg reflection spots[16]**,** making this approach perfect for examining solid structures. In this Thesis, we discussed some Schiff base and quinoline derivative crystal structures that were used in the current research, as well as the relationship between X-ray diffraction data and molecular modeling data. **Figure 2B.4** depicts the schematic diagram of a single crystal XRD method.

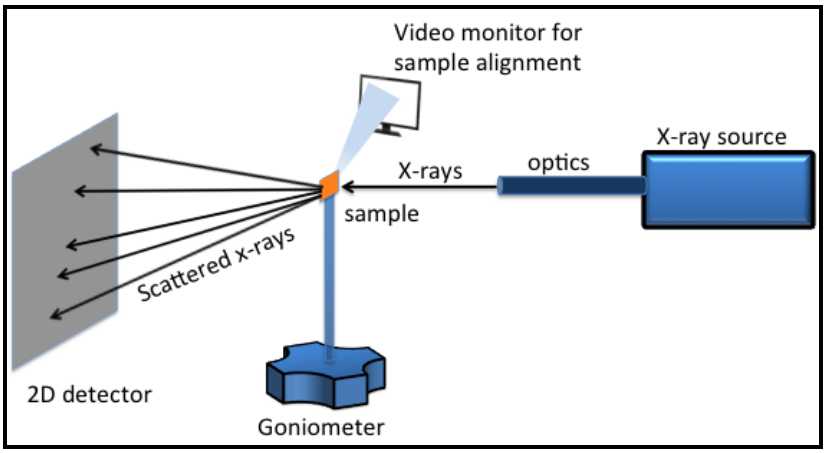

Figure 2B.4: *Schematic of an X-Ray diffractometer*

2B.5.3 *Molecular Modelling:*

"Computational Chemistry" is the science of representing molecular structures computationally and simulating their behavior with quantum and classical physics equations[17]. Computational chemistry, often known as molecular modelling, is the simulation of chemical processes and computation of chemical characteristics employing computer-based models. The combination of two mathematical methodologies, Molecular Mechanics (MM) and Quantum Mechanics (QM), is molecular modelling. ChemOffice Ultra, HyperChem, Gaussian, Spartan, Sybyl, and other molecular modelling tools are used to calculate single point energy, geometrical optimization, and property calculations (prediction of certain physical and chemical properties like heat of formation, HOMO-LUMO, dipole moment)[18]**.** All methods are not capable of performing all types of calculations, and no single approach is ideal for all applications. The following is a quick overview of four major computational chemistry approaches.

2B.5.3a *Ab Initio Methods:*

Quantum mechanics underlies these methods (i.e., solving the Schrodinger equation)[19]**.** In ab initio calculations, the wave functions Hartree-Fock and Quantum Monte Carlo (QMC) are commonly used[20]. Another type of ab initio calculation is density functional theory, which is based on total electron density rather than wave functions[21]**.** It's the most promising methodology for quantum chemical calculations. For simple molecules, ab initio calculations produce excellent quantitative results.

The theory that all chemistry can be described in terms of interaction between electronic charges within molecules is the basis of electronic structure approaches. As a result, chemical bonding can be roughly defined as a redistribution of electrical charge that stabilizes a molecule with respect to a group of its (isolated) constituent atoms. The relative stability of a system is shown by its total energy, which is given by a differential equation.

$$\hat{H} = \hat{T} + \hat{V} \tag{2.10}$$

where $\hat{H}$ denotes the Hamiltonian operator that sums the kinetic ($\hat{T}$) and potential ($\hat{V}$) energies. The kinetic energy of a particle in quantum mechanical systems is

$$\hat{T} = \frac{-\hbar^2}{2m} \nabla^2 \tag{2.11}$$

where m is the mass of the particle, ħ is the Plank constant and

$$\nabla^2 = \frac{\partial^2}{\partial x^2} + \frac{\partial^2}{\partial y^2} + \frac{\partial^2}{\partial z^2} \tag{2.12}$$

The potential energy of electrostatic systems is commonly described as the pairwise interaction between charged particles.

$$\hat{V} = \frac{q_1 q_2}{4\pi\varepsilon_o} \frac{1}{|r1 - r2|} \tag{2.13}$$

where

ε_o is permittivity of free space and $|r_1\text{-}r_2|$ is the distance between the charges q_1 and q_2.

The Schrödinger equation cannot be solved exactly for systems with more than two interacting particles. As a result, all ab initio calculations for many-body systems (e.g., molecules) involve a variety of approximations. However, ab initio methods for molecular calculations must meet a number of specific requirements:

- Both the structure and electronic states of the molecule must be well defined and specified in order for solutions to be very well defined and specified.
- With respect to atomic nuclei displacements, the molecule's potential energy must vary smoothly and continuously.

- The model can't be skewed in any way, like by assuming that there is a chemical bond between two atoms.
- The model must be "size-consistent," implying that the solutions and errors must scale in proportion to the molecule's size.
- The model must be "variational," which means that approximate solutions must put an upper bound on the system's "actual" energy. So, within the limits of the method, the closest fit to the real wave function is the approximate solution with the lowest energy.

2B.5.3b *Semi-Empirical Methods:*

Ab initio approaches are substantially slower than semi-empirical methods. These calculations involve a number of approximations and constraints, including the use of experimental data[22]**.** Various semi-empirical approaches are optimized according to necessity. The NDDO, MNDO, AM1, and PM3 methods are some of the approaches used to reproduce the formation temperatures and structures of massive organic compounds[23]**.** Some methods, like ZINDO/S, are made to predict electronic transitions in the UV/VIS range[24]**.**

In semi-empirical calculations, the basis sets are specifically optimized minimal basis sets made up of Slater-type orbitals. Hartree-Fock theory uses a simple point charge model to figure out the energy of nuclear repulsion. However, this model is not good enough for semi-empirical calculations because it only takes into account valence electrons and treats core electrons and nuclei as one effective core potential. The core-core potential employed in NDDO methods extends further the use of simple point charge modelling with lowered nuclear charges to account for some of the approximations employed in computing the attractive core-electron energies.

$$E_{AB} = Z'_A Z'_B e^{2/R_{AB}} \quad \textbf{(2.14)}$$

R_{AB} represents the inter-nuclear separation, while Z'_A represents the effective core charge, which includes the nuclear charge as well as all core electrons. In NDDO methods, a general equation for figuring out the energy of core-core repulsion between nuclei A and B at a distance of R_{AB} is:

$$E_{AB} = Z'_A Z'_B < S_A S_A, \; S_B S_B > [1 + F(A) + F(B)] \quad \textbf{(2.15)}$$

The core repulsion energy is a result of both the electron-electron repulsion integral S_AS_A and S_BS_B atom-type dependent functions F(A) and F(B), both of which are dependent on the inter-nuclear spacing R_{AB}. In MNDO, the functions F(A) and F(B) have a relatively simple form:

$$F_A = \exp(-\alpha_A R_{AB}) \quad \textbf{(2.16)}$$

Some of MNDO's flaws, especially those that had to do with hydrogen bonds, were fixed by giving AM1 a slightly more complex function:

$$F_A = \exp(-\alpha_A R_{AB}) + \Sigma\, K_{Ai} \exp[L_{Ai}(R_{AB} - M_{Ai})^2] \quad \textbf{(2.17)}$$

The sum over supplementary exponential functions includes three or four components and provides three new parameters for each element, KAi, LAi, and MAi, which are the main differences between AM1 and MNDO (aside from the actual appropriate technique).

2B.5.3c *Molecular Mechanics Methods:*

Within those molecular mechanics (MM) calculations, Newtonian mechanics (classical physics) is used to predict the structures and properties of molecules**.** In this approach, nuclei are considered as spheres, and connected bonds are treated as springs. These MM techniques can be used to simulate biomolecules like DNA or proteins[25]**.**

The potential energy (E) of a molecular system in a particular conformation is calculated as a sum of individual energy terms using the following functional approximation, known as an interatomic state equations or force field in chemistry.

$$E = E_{Covalent} + E_{Noncovalent} \quad \textbf{(2.18)}$$

where the following summations derive the portions of the covalent and non - covalent interaction contributions:

$$E_{Covalent} = E_{Bond} + E_{Angle} + E_{Dihedral} \quad \textbf{(2.19)}$$

$$E_{Noncovalent} = E_{Electrostatic} + E_{Van\ der\ Waals} \quad \textbf{(2.20)}$$

2B.5.3d *Molecular Dynamics (MD):*

To mimic the time-dependent behavior of molecules, molecular dynamics simulations are

used[26]**.** The MD method is used to investigate how a solute molecule diffuses across a liquid. This method can be applied to computations involving big biomolecules in solutions[27]**.**

Where the following summations derive the portions of the covalent and non-covalent interaction contributions: The variation of a set of interacting particles is quantified in MD simulations using the solution of Newton's equations of motion, eqn 2.21, wherein $r_i(t) = (x_i(t), y_i(t), z_i(t))$ is the position vector of the i^{th} particle, F_i is the force acting on the ith particle at time t, and m_i is the particle's mass.

$$F_i = m_i \frac{d^2 r_i(t)}{dt^2} \tag{2.21}$$

The simultaneous forces acting on the particles, as well as their initial locations and velocities, must be provided in order to incorporate the above second-order partial differential equation. The differential equations are normalized and solved numerically due to the many nature of the case. MD trajectories reflect the time system dynamics in phase space and are described by both position and velocity vectors. As a result, numerical integrators, such as the Verlet method, are used to propagate the locations and velocities over a finite time interval. $r_i(t)$ determines the (changing over time) position of each particle in space, whereas $v_i(t)$ determines the kinetic energy and temperature in the system.

The objective of numerical integration of Newton's equations of motion is to discover an expression that specifies locations $r_i(t + \Delta t)$ at time $t + \Delta t$ in terms of positions known at time t. The Verlet algorithm is widely utilized in MD simulations due to its simplicity and stability. The essential formula for this technique is eqn 2.22, which is obtained from the Taylor expansion for the positions $r_i(t)$.

$$r_i(t + \Delta t) \cong 2r_i(t) - r_i(t - \Delta t) + \frac{F_{i(t)}}{m_i} \Delta t^2 \tag{2.22}$$

2B.5.4 ***Hirshfeld Surface Analysis:***

a) Hirshfeld Surface and Finger Print Plots:

Hirshfeld surface analysis is a valuable technique for visualizing molecular crystal interactions[28]. CrystalExplorer 17.5 is a computer program that uses calculated Hirshfeld surfaces of molecules within a crystal structure to calculate intermolecular interactions between specific

molecules or for the entire crystal structure[29]. An extension of the weight function describing an atom in a molecule included the function of a molecule in a crystal producing Hirshfeld surfaces[30]. The isosurface derived from these calculations surrounds the molecule and delineates the space occupied by a molecule in a crystal by partitioning the electron density of the molecular fragments[31]. It has a weight function with the formula w(r) = 0.5. Because the surface is made up of both the molecules that are inside and their closest neighbors, Hirshfeld surfaces can show how the crystal's molecules interact with each other.

The electron densities employed in *CrystalExplorer* to compute the HS surfaces are tabulations of atomic wave functions enlarged with exponential-type basis functions (Clementi & Roetti, 1974; Koga et al., 1993, 2000). The resulting (spherical) atomic electron densities ρ_A (r) are used to construct the promolecule electron density ρ_{promol} (r) and the procrystal electron density $\rho_{procryst}$ (r), which are then used to define the weight function, inspired by Fred Hirshfeld's 'stockholder' partitioning of atoms in molecules (Hirshfeld, 1977).

$$w_A(r) = \frac{\rho_{promol}(r)}{\rho_{procryst}(r)} = \frac{\Sigma_{A \in molecule} \, pi_A(r)}{\Sigma_{C \in crystal} \, pi_C(r)} \qquad \textbf{(2.23)}$$

In all space, this constant scalar function has $0 < w_A$ (r), and the HS is the 0.5 isosurface of all this function.

The fused sphere van der Waals and smoothed Connolly surfaces, which are used to visualize and quantify molecular geometries, do not have this advantage because they are exclusively specified by the molecule itself. The essential requirement for extracting excellent data about intermolecular interactions from Hirshfeld surfaces is that the crystal structures input into the computer are well-characterized, with all hydrogen atoms identified and arranged precisely. In crystal space, the HS is the zone around a molecule that separates two regions: the inner reference molecule and the outer neighboring molecules[32]**.** The HS enables the investigation of fingerprint intermolecular interactions in a crystalline environment by separating space[33]**.** HS analysis can be used to visualize and quantify non-covalent interactions that help to maintain the crystal packing stable. d_{norm}, electrostatic potential, shape index, and curvature are all qualities that can be mapped to HS[34]**.** The d_{norm} property is a symmetric function of the nuclei's surface distances (di and de) in relation to their van der Waals radii[35].

The red and blue colored regions on the d_{norm} represent shorter and longer inter-contacts, respectively, whereas the white colored regions represent contacts around the van der Waals radii[36]**.** Two-dimensional fingerprint plots in the crystal provide useful information on intermolecular contacts. The use of HS analysis to describe the nature of intermolecular interactions that affect the packing of molecules in crystals has been shown to be very effective. Hirshfeld surface analysis[37] is used to investigate polymorphism and crystallization. It also talks about the importance of small molecules in macromolecule cavities, as well as how the strength of interactions and the melting point are linked.

The Hirshfeld surface is a smooth, continuously differentiable three-dimensional manifold with two major curvatures. Using the distances from the surface to atomic nuclei inside and outside the surface, these can be used to figure out a lot of important things about any spot on the surface.

b) Intermolecular Interaction Energies:

Because it provides a computationally tractable way to obtain reliable intermolecular energies constructed from a non-empirical electrostatic energy and semi-empirical polarization, dispersion, and repulsion contributions, PIXEL has become popular for investigating molecular crystals in terms of pairwise interaction energies[38]. CrystalExplorer calculates pairwise intermolecular interaction energies using a method that is based on Gavezzotti's work but differs in several ways[39]. The basic expression used by Gavezzotti and others is $E_{tot} = k_{ele}E_{ele} + k_{pol}E_{pol} + k_{dis}E_{dis} + k_{rep}E_{rep}$, with the exception that each energy term is multiplied by a different scale factor[40]. The following are the definitions of the terms used in this expression: E_{ele} is the classical electrostatic energy of interaction between monomers with non-affected quantum mechanical charge distributions; E_{pol} is the polarization energy, calculated as a sum over nuclei with terms of the kind, where the electric field at each nucleus is due to the quantum mechanical charge distribution of the other monomer. E_{rep} is the exchange-repulsion energy calculated between unperturbed quantum mechanical charge distributions of the monomers; E_{dis} is Grimme's D2 dispersion correction, summed over all intermolecular atom pairs. Because it provides a computationally tractable way to obtain reliable intermolecular energies constructed from a non-empirical electrostatic energy and semi-empirical polarization, dispersion, and repulsion contributions, PIXEL has become popular for investigating molecular crystals in terms of pairwise

interaction energies[41]. CrystalExplorer calculates pairwise intermolecular interaction energies using a method that is based on Gavezzotti's work but differs in several ways[42].

c) Energy Frameworks:

The pairwise interaction energies for a nearest neighbor cluster of molecules can be used to build and view a molecular crystal's "energy framework"[43]**.** By integrating intermolecular interaction energies with a graphical representation of their significance, these innovative images were created in order to better comprehend crystal packing. The pairwise interaction energies for a cluster of molecule's closest neighbors. This method was developed and used on a range of organic molecular crystals with known bending, shearing, and brittle behavior to show how it can be used to explain mechanical behavior at the molecular level[44]**.** In crystals, anisotropy of the interaction topology in the form of strongly bonded molecular columns, sheets, or slabs can be linked to mechanical properties like bending and shearing. The energies between molecular pairs are depicted as cylinders interconnecting the centroids of pairs of molecules in an energy framework diagram, with the cylinder radius corresponding to the size of the interaction energy. E_{ele} (red cylinders), E_{dis} (green), and E_{tot} can all have their own frameworks (blue).

Energy frameworks are a strong and unique technique to explore molecular crystal structures' supramolecular architecture. The framework's cylinders depict the relative strengths of molecular packing in various directions. Lattice energies are found by adding up the total interaction energies of all molecules B that interact with a central molecule A until E_{lat} is close to a minimum energy threshold using a cut-off based on the distance between molecule's centers of mass.

$$E_{lat} = \frac{1}{2} \sum_{R_{AB<R}} E_{Tot}^{AB} \qquad \textbf{(2.24)}$$

To adjust for duplicate counting of all pairs in the summing, a factor of 1/2 is required. Comparing E_{lat}'s convergent value to an experimental estimate derived from sublimation enthalpy data is enlightening.

$$H_{sub}(T) = E_{lat} + E_{vib} + 4RT = E_{lat} - 2RT \qquad \textbf{(2.25)}$$

where approximating the thermal effects by 2RT assumes no difference between gas and crystal intramolecular vibrations and that the intermolecular vibrational energy is at the high-temperature limit of 6RT.

2B.5.5 ***Data Processing, 2D and 3D Graphical Presentation:***

MS EXCEL was routinely used for initial data processing and curve fitting. Origin was used for drawing plots. GoldenSoft's Surfer (version 12) and Grapher (version 10) were extremely used for gridding, surfaces and wireframe mesh 3D plots of data of the z = f (x, y) kind where z is the domain of the acquired data for the x and y binary conditions or variables[45].

The Surfer can generate a 'z' data set for any mathematical function, z = f (x, y), where 'x' and 'y' form sets of real numbers within any range that never makes the value of 'z' undefined.

The graphical forms, in 'wire frame' format from Surfer and in 'surface mat' format from Grapher platforms for the equation, $z = x^2-y^2+xy$, are shown in **Figure 2B.5**. It may be noted that Grapher has MOE versatile features to manipulate with the presentation and appearances of the plots.

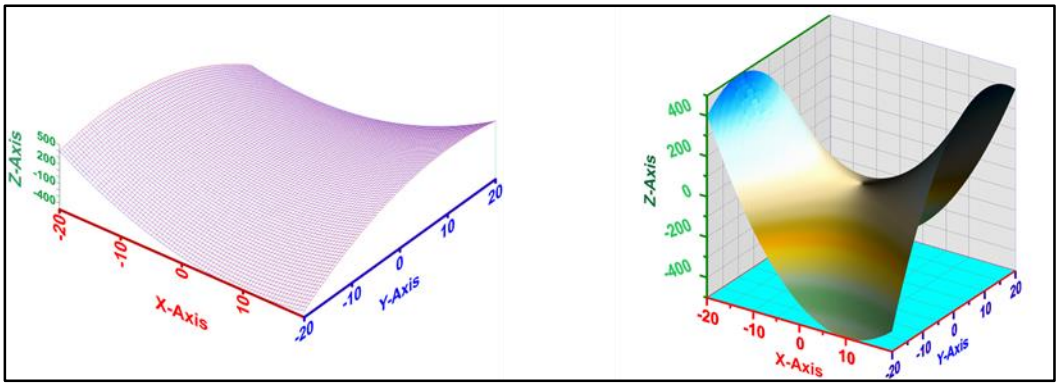

Figure 2B.5: *The 3D (left) Surfer plot and (right) Grapher plot for the equation,* $z = x^2-y^2+xy$, *for the range of -20<x<20 and -20 <y <20 with a gridding increment of 0.5 on each of x and y domains*

In molecular modeling, these graphical platforms can be used to obtain similar 3D plots for double dihedral driven conformational analysis though single dihedral driven plots can be easily generated from MS EXCEL or from Origin. Consider the sample molecule, 2-(2-aminophenoxy)-5-methylphenol, shown in **Figure 2B.6** with multiple intramolecular hydrogen

bonds possible. Its stereographic projection, modelled and energy-minimized by an Hartree–Fock SCF (Self Consistent Field) method (ΔH^{o}_{f} =-9.7 kcal/mol) is also shown in that figure which confirms the multiple intramolecular hydrogen bonds. Dihedral driven conformational analysis plots over C6-O7 bond and O7-C8 bonds worked out are presented in **Figure 2B.7** and **Figure 2B.8**, respectively. The 3D plots of the double dihedral driven conformational analysis over C6-O7-C8 bonds.

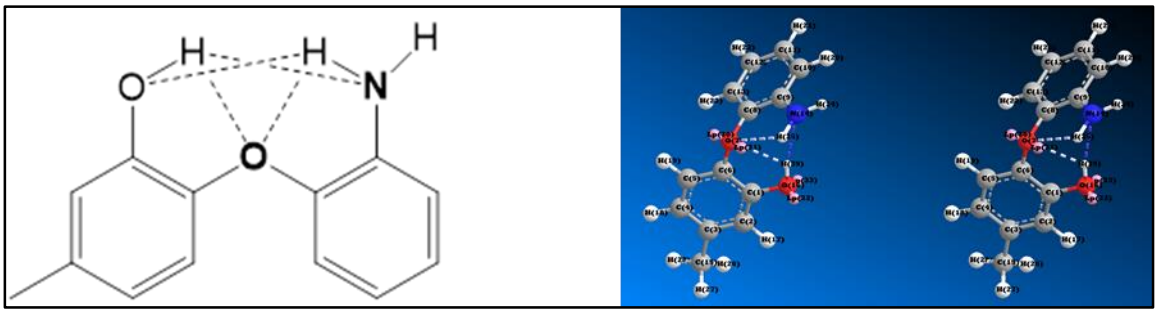

Figure 2B.6: *Normal (left) and SCF-Energy-Minimized stereographic structures of 2-(2-aminophenoxy)-5-methylphenol*

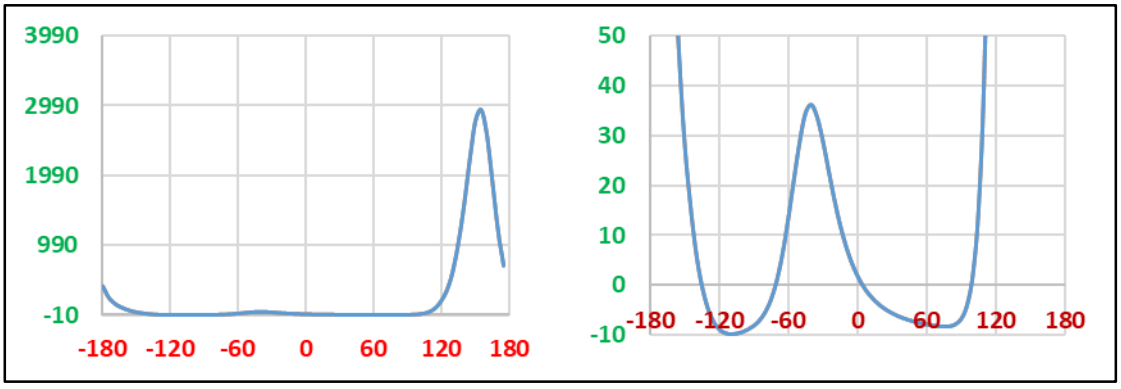

Figure 2B.7: *Dihedral-driven conformational energy plot (left)of 2-(2-aminophenoxy)-5-methylphenol and its plot (right) truncated for clarity for the torsion overC6-O7 bond*

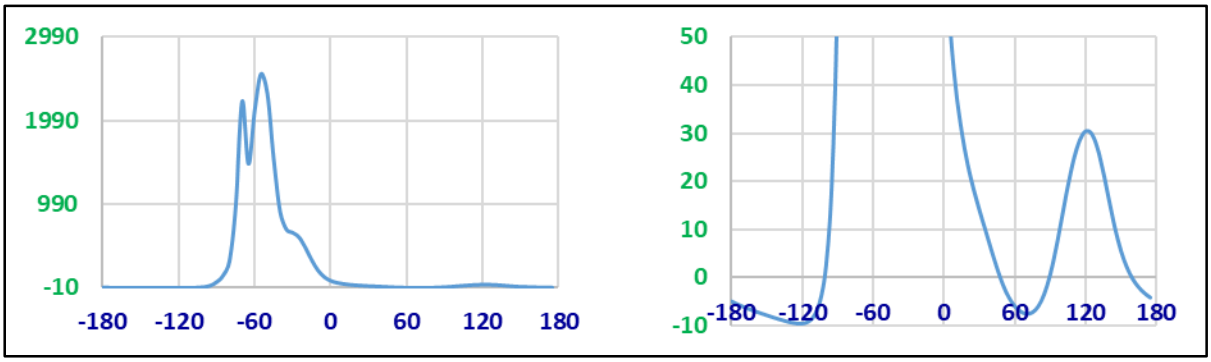

Figure 2B.8: *Dihedral-driven conformational energy plot (left)of 2-(2-aminophenoxy)-5-methylphenol and its plot (right) truncated for clarity for the torsion over O7-C8 bond*

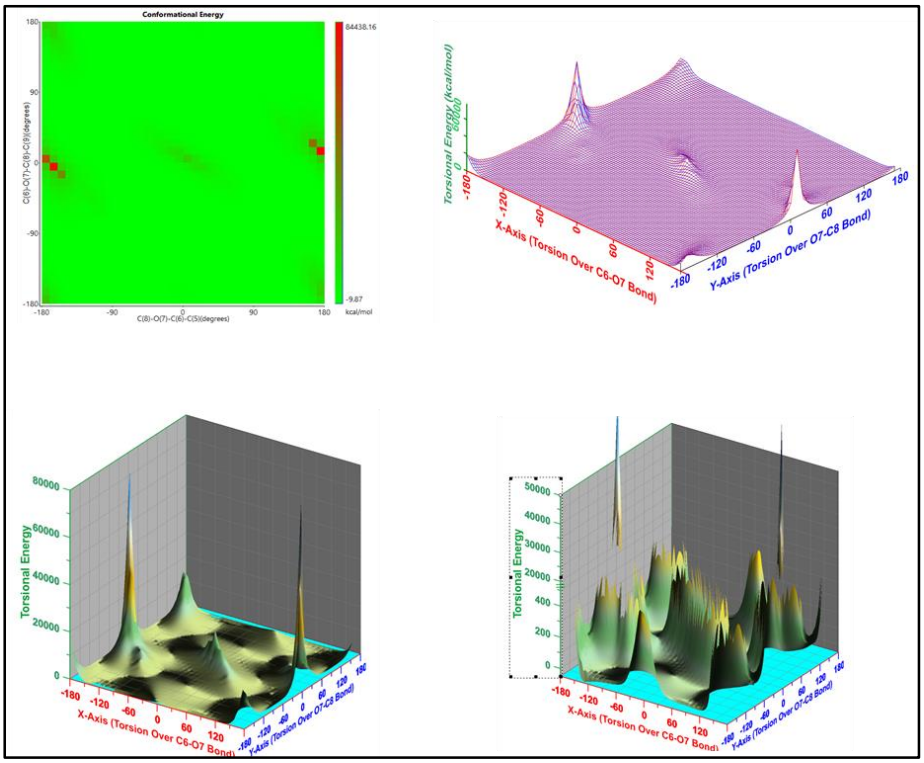

Figure 2B.9: *Double dihedral-driven conformational energy plot of 2-(2-aminophenoxy)-5-methylphenol over the bond sequence, C6-O7-C8; (top left) contour plot from the Chem3D; (top right) and its plot by Surfer and (bottom left) Grapher platforms; (bottom right) Grapher plot truncated beyond 400 units for clarity*

References

(1). Chen, H.-J.; Chew, C. Y.; Chang, E.-H.; Tu, Y.-W.; Wei, L.-Y.; Wu, B.-H.; Chen, C.-H.; Yang, Y.-T.; Huang, S.-C.; Chen, J.-K.; Chen, I.-C.; Tan, K.-T. S - Cis Diene Conformation: A New Bathochromic Shift Strategy for Near-Infrared Fluorescence Switchable Dye and the Imaging Applications. Journal of the American Chemical Society 2018, 140 (15), 5224–5234. https://doi.org/10.1021/jacs.8b01159.

(2). Siegl, S. J.; Vrabel, M. Probing the Scope of the Amidine-1,2,3-Triazine Cycloaddition as a Prospective Click Ligation Method. *European Journal of Organic Chemistry* **2018**, *2018* (37), 5081–5085. https://doi.org/10.1002/ejoc.201800530.

(3). Meng, X.-Y.; Zhang, H.-X.; Mezei, M.; Cui, M. Molecular Docking: A Powerful Approach for Structure-Based Drug Discovery. Current Computer Aided-Drug Design 2011, 7 (2), 146–157. https://doi.org/10.2174/157340911795677602.

(4). Pinzi, L.; Rastelli, G. Molecular Docking: Shifting Paradigms in Drug Discovery. International Journal of Molecular Sciences 2019, 20 (18), 4331. https://doi.org/10.3390/ijms20184331.

(5). Forli, S.; Huey, R.; Pique, M. E.; Sanner, M. F.; Goodsell, D. S.; Olson, A. J. Computational Protein–Ligand Docking and Virtual Drug Screening with the AutoDock Suite. Nature Protocols 2016, 11 (5), 905–919. https://doi.org/10.1038/nprot.2016.051.

(6). Sivaramakrishnan, M.; Kandaswamy, K.; Natesan, S.; Devarajan, R. D.; Ramakrishnan, S. G.; Kothandan, R. Molecular Docking and Dynamics Studies on Plasmepsin V of Malarial Parasite Plasmodium Vivax. Informatics in Medicine Unlocked 2020, 19, 100331. https://doi.org/10.1016/j.imu.2020.100331.

(7). Feinstein, W. P.; Brylinski, M. Calculating an Optimal Box Size for Ligand Docking and Virtual Screening against Experimental and Predicted Binding Pockets. Journal of Cheminformatics 2015, 7 (1), 18. https://doi.org/10.1186/s13321-015-0067-5.

(8). Valdés-Tresanco, M. S.; Valdés-Tresanco, M. E.; Valiente, P. A.; Moreno, E. AMDock: A Versatile Graphical Tool for Assisting Molecular Docking with Autodock Vina and Autodock4. *Biology Direct* **2020**, *15* (1), 12. https://doi.org/10.1186/s13062-020-00267-2.

(9). (a) Gulaboski, R.; Pereira, C. M. Electroanalytical Techniques and Instrumentation in Food Analysis. In Handbook of Food Analysis Instruments; CRC Press, 2016; pp 395–418. https://doi.org/10.1201/9781420045673-22.

(b) Wiley, N. Y. Allen J . Bard and Larry R . Faulkner , Electrochemical Methods : 2002, 38 (12), 1505–1506. https://doi.org/org/10.1023/A:1021637209564.

(10). Olmstead, M. L.; Nicholson, R. S. Double Potential Step Method for Measuring Rate Constants of Dimerization Reactions. *Analytical Chemistry* **1969**, *41* (6), 851–852. https://doi.org/10.1021/ac60275a033.

(11). A J Bard, Larry Faulkner, "*Electrochemical methods-Fundamentals and Applications"* John Wiley & Sons Inc, **1980**.

(12). Lawrence, M. A. W.; Lorraine, S. C.; Wilson, K.-A.; Wilson, K. Review: Voltammetric Properties and Applications of Hydrazones and Azo Moieties. *Polyhedron* **2019**, *173*, 114111. https://doi.org/10.1016/j.poly.2019.114111.

(13). P Delahay, "*New Instrumental Methods in Electrochemistry"* Inter Science, New York, **1954,** 132

(14). Li, J.; Sun, J. Application of X-Ray Diffraction and Electron Crystallography for Solving Complex Structure Problems. Accounts of Chemical Research 2017, 50 (11), 2737–2745. https://doi.org/10.1021/acs.accounts.7b00366.

(15). Hendrickson, W. A. Anomalous Diffraction in Crystallographic Phase Evaluation. Quarterly Reviews of Biophysics 2014, 47 (1), 49–93. https://doi.org/10.1017/S0033583514000018.

(16). Petkov, V. Nanostructure by High-Energy X-Ray Diffraction. Materials Today 2008, 11 (11), 28–38. https://doi.org/10.1016/S1369-7021(08)70236-0.

(17). Genheden, S.; Reymer, A.; Saenz-Méndez, P.; Eriksson, L. A. Chapter 1. Computational Chemistry and Molecular Modelling Basics; 2017; pp 1–38. https://doi.org/10.1039/9781788010139-00001.

(18). (a) Pimentel, A. S.; Guimarães, C. R. W.; Miller, Y. Molecular Modeling: Advancements and Applications. Journal of Chemistry 2013, 2013 (001), 1–2. https://doi.org/10.1155/2013/875478.

(b) Pimentel, A. S.; Guimarães, C. R. W.; Miller, Y. Molecular Modeling: Advancements and Applications. Journal of Chemistry 2013, 2013 (001), 1–2. https://doi.org/10.1155/2013/875478.

(19). Defranceschi, M.; Le Bris, C. Mathematical Models and Methods for Ab Initio Quantum Chemistry; Lecture Notes in Chemistry; Springer Berlin Heidelberg: Berlin, Heidelberg, 2000; Vol. 74. https://doi.org/10.1007/978-3-642-57237-1.

(20). Bickmore, B. R.; Wander, M. C. F. Encyclopedia of Geochemistry; White, W. M., Ed.; Encyclopedia of Earth Sciences Series; Springer International Publishing: Cham, 2018. https://doi.org/10.1007/978-3-319-39312-4.

(21). Grabowski, I.; Teale, A. M.; Śmiga, S.; Bartlett, R. J. Comparing Ab Initio Density-Functional and Wave Function Theories: The Impact of Correlation on the Electronic Density and the Role of the Correlation Potential. The Journal of Chemical Physics 2011, 135 (11), 114111. https://doi.org/10.1063/1.3636114.

(22). (a) Lewars, E. G. Semiempirical Calculations. In Computational Chemistry; Springer Netherlands: Dordrecht, 2011; pp 391–444. https://doi.org/10.1007/978-90-481-3862-3_6.

(b) Stewart, J. J. P. Optimization of Parameters for Semiempirical Methods VI: More Modifications to the NDDO Approximations and Re-Optimization of Parameters. Journal of Molecular Modeling 2013, 19 (1), 1–32. https://doi.org/10.1007/s00894-012-1667-x.

(23). Hofmann, M.; Schaefer, H. F. Computational Chemistry. In Encyclopedia of Physical Science and Technology; Elsevier, 2003; pp 487–506. https://doi.org/10.1016/B0-12-

227410-5/00129-0.

(24). Anouar, E. H.; Osman, C. P.; Weber, J. F.; Ismail, N. H. UV/Visible Spectra of a Series of Natural and Synthesised Anthraquinones: Experimental and Quantum Chemical Approaches. SpringerPlus 2014, 3 (1), 233. https://doi.org/10.1186/2193-1801-3-233.

(25). van der Kamp, M. W.; Shaw, K. E.; Woods, C. J.; Mulholland, A. J. Biomolecular Simulation and Modelling: Status, Progress and Prospects. Journal of The Royal Society Interface 2008, 5 (suppl_3), 173–190. https://doi.org/10.1098/rsif.2008.0105.focus.

(26). Adcock, S. A.; McCammon, J. A. Molecular Dynamics: Survey of Methods for Simulating the Activity of Proteins. Chemical Reviews 2006, 106 (5), 1589–1615. https://doi.org/10.1021/cr040426m.

(27). Durrant, J. D.; McCammon, J. A. Molecular Dynamics Simulations and Drug Discovery. BMC Biology 2011, 9 (1), 71. https://doi.org/10.1186/1741-7007-9-71.

(28). Batsanov, A. S. X-Ray Diffraction, Small Molecule Applications ☆. In Encyclopedia of Spectroscopy and Spectrometry; Elsevier, 2017; pp 656–666. https://doi.org/10.1016/B978-0-12-409547-2.11370-8.

(29). Price, S. (Sally) L. Quantifying Intermolecular Interactions and Their Use in Computational Crystal Structure Prediction. CrystEngComm 2004, 6 (61), 344. https://doi.org/10.1039/b406598k.

(30). Barbour, L. J. Single-Crystal X-Ray Diffraction. In Comprehensive Supramolecular Chemistry II; Elsevier, 2017; Vol. 2, pp 23–43. https://doi.org/10.1016/B978-0-12-409547-2.12493-X.

(31). Jelsch, C.; Ejsmont, K.; Huder, L. The Enrichment Ratio of Atomic Contacts in Crystals, an Indicator Derived from the Hirshfeld Surface Analysis. IUCrJ 2014, 1 (2), 119–128. https://doi.org/10.1107/S2052252514003327.

(32). Tojiboev, A.; Zhurakulov, S.; Englert, U.; Wang, R.; Kalf, I.; Vinogradova, V.; Turgunov, K.; Tashkhodjaev, B. Hirshfeld Surface Analysis and Energy Framework for Crystals of Quinazoline Methylidene Bridged Compounds. Proceedings 2020, 62 (1), 1. https://doi.org/10.3390/proceedings2020062001.

(33). Shamsuzzaman; Khanam, H.; Mashrai, A.; Asif, M.; Ali, A.; Barakat, A.; Mabkhot, Y. N. Synthesis, Crystal Structure, Hirshfeld Surfaces, and Thermal, Mechanical and Dielectrical Properties of Cholest-5-Ene. Journal of Taibah University for Science 2017, 11 (1), 141–150. https://doi.org/10.1016/j.jtusci.2016.01.001.

(34). Pook, N.-P. Supramolecular Architecture in a Ni(II) Complex with a Weakly Bonded N,N′-(1,4-Phenylenedi- Carbonyl)Diglycinate Counter-Anion: Crystal Structure Investigation and Hirshfeld Surface Analysis. Crystals 2019, 9 (12), 615. https://doi.org/10.3390/cryst9120615.

(35). Tojiboev, A.; Zhurakulov, S.; Englert, U.; Wang, R.; Kalf, I.; Vinogradova, V.; Turgunov, K.; Tashkhodjaev, B. Hirshfeld Surface Analysis and Energy Framework for Crystals of Quinazoline Methylidene Bridged Compounds. Proceedings 2020, 62 (1), 1.

https://doi.org/10.3390/proceedings2020062001.

(36). Luo, Y.; Sun, B. An Investigation into the Substituent Effect of Halogen Atoms on the Crystal Structures of Indole-3-Carboxylic Acid (ICA). CrystEngComm 2013, 15 (37), 7490. https://doi.org/10.1039/c3ce40952j.

(37). Balić, T.; Perdih, F.; Počkaj, M.; Molnar, M.; Komar, M.; Balić, I. Polymorphism of Coumarin Thione-Triazole-4-Methyl-7-[(4-Phenyl-5-Thioxo-4,5-Dihydro-1H-1,2,4-Triazol-3-Yl)Methoxy]-2H-Chromen-2-One. Journal of Molecular Structure 2021, 1231, 129957. https://doi.org/10.1016/j.molstruc.2021.129957.

(38). Turner, M. J.; Grabowsky, S.; Jayatilaka, D.; Spackman, M. A. Accurate and Efficient Model Energies for Exploring Intermolecular Interactions in Molecular Crystals. The Journal of Physical Chemistry Letters 2014, 5 (24), 4249–4255. https://doi.org/10.1021/jz502271c.

(39). Gavezzotti, A. Calculation of Lattice Energies of Organic Crystals: The PIXEL Integration Method in Comparison with More Traditional Methods. Zeitschrift für Kristallographie - Crystalline Materials 2005, 220 (5–6), 499–510. https://doi.org/10.1524/zkri.220.5.499.65063.

(40). Spackman, P. R.; Turner, M. J.; McKinnon, J. J.; Wolff, S. K.; Grimwood, D. J.; Jayatilaka, D.; Spackman, M. A. CrystalExplorer : A Program for Hirshfeld Surface Analysis, Visualization and Quantitative Analysis of Molecular Crystals. Journal of Applied Crystallography 2021, 54 (3), 1006–1011. https://doi.org/10.1107/S1600576721002910.

(41). Delgado, G. E.; Mora, A. J.; Seijas, L. E.; Almeida, R.; Chacón, C.; Azotla-Cruz, L.; Cisterna, J.; Cárdenas, A.; Brito, I. N-Acetyl-5-Isopropyl-2-Tioxoimidazolidin-4-One: Synthesis, Spectroscopic Characterization, Crystal Structure, DFT Calculations, Hirshfeld Surface Analysis and Energy Framework Study. Journal of Molecular Structure 2020, 1219, 128630. https://doi.org/10.1016/j.molstruc.2020.128630.

(42). Devarapalli, R.; Kadambi, S. B.; Chen, C.-T.; Krishna, G. R.; Kammari, B. R.; Buehler, M. J.; Ramamurty, U.; Reddy, C. M. Remarkably Distinct Mechanical Flexibility in Three Structurally Similar Semiconducting Organic Crystals Studied by Nanoindentation and Molecular Dynamics. Chemistry of Materials 2019, 31 (4), 1391–1402. https://doi.org/10.1021/acs.chemmater.8b04800.

(43). Meng, X.-Y.; Zhang, H.-X.; Mezei, M.; Cui, M. Molecular Docking: A Powerful Approach for Structure-Based Drug Discovery. Current Computer Aided-Drug Design 2011, 7 (2), 146–157. https://doi.org/10.2174/157340911795677602.

(44). Pinzi, L.; Rastelli, G. Molecular Docking: Shifting Paradigms in Drug Discovery. International Journal of Molecular Sciences 2019, 20 (18), 4331. https://doi.org/10.3390/ijms20184331.

(45). Urszula Litwin, Jacek M. Pijanowski, A. S.; Zygmunt, M. Application of Surfer Software in Densification of Digital Terrain Model (DTM) Grid with The Use. **2013**, No. 1, 51–61.

CHAPTER III

SPECTRAL, ELECTROCHEMICAL, MOLECULAR MODELLING, PROTEIN DOCKING AND BIOLOGICAL ACTIVITY STUDIES OF FLUOXETINE DITHIOCARBAMTE (FLXDTC) AND ITS BIVALENT METAL COMPLEXES

In this Chapter, the studies of dithiocarbamate ligand, **FLXDTC** are reported along with those of its complexes with some bivalent metal ions such as Zn(II), Cd(II), Hg(II), Co(II), Ni(II), Mn(II) and Cu(II). The ligand and the complexes have been characterized by various analytical and spectroscopic methods in addition to voltammetry. The studies propose **M(FLXDTC)$_2$** stoichiometry to the complexes. Antimicrobial, antioxidant, antifungal, anti-malarial and antitumor capabilities have been tested for both **FLXDTC** and **M(FLXDTC)$_2$** complexes along with molecular docking studies.

This Chapter is divided into three Parts based on structural variety as **PART A**, **PART B**, and **PART C**

PART A describes the physical, analytical, spectroscopic, electrochemical, and coordination chemistry studies of the fluoxetine dithiocarbamate ligand **(FLXDTC)**

In **PART B** are placed the results and discussion of the studies of **FLXDTC** ligand and its metal complexes besides those of the molecular modelling and protein molecular docking investigations.

PART C describes the biological activity studies of **FLXDTC** ligand and its metal complexes.

PART A

SPECTRAL AND ELECTROCHEMICAL STUDIES FLXDTC AND M(FLXDTC)$_2$

3A.1 Elemental Analysis:

The analytical characteristics of the **FLXDTC** ligand and its metal complexes are shown in **Table 3A.1**. The chemical structures shown in the **Scheme 3A.1** are in good agreement with the results of the elemental analysis. The mass spectrum of **FLXDTC** shown in **Figure 3A.1** confirms the molecular weight of it as 408.

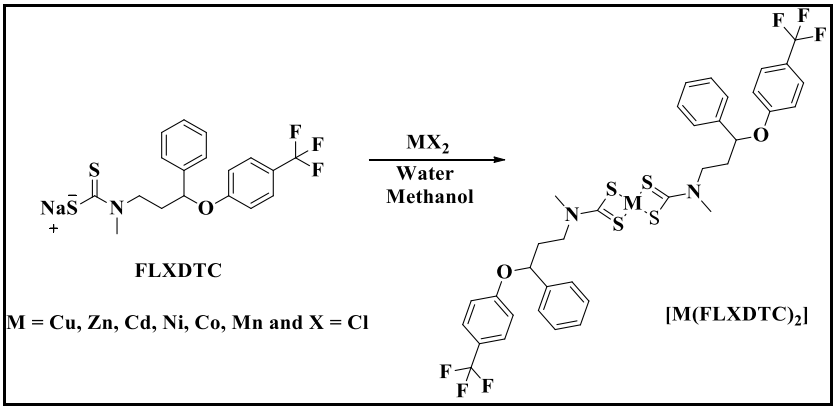

Scheme 3A.1: *Schematic of the synthesis of* ***M(FLXDTC)$_2$*** *from* ***FLXDTC***

Table 3A.1: *Analytical data of* ***FLXDTC*** *and* ***[M(FLXDTC)$_2$]***

Compound	M.P (°C)	Molecular formula	Molecular Weight*	Elemental analysis#			
				%C	%H	%N	%S
FLXDTC	121-123	$C_{18}H_{18}F_3NNaOS_2$	408	53.16 (53.06)	4.25 (4.21)	3.38 (3.44)	15.78 (15.74)
Cu(FLXDTC)$_2$	143-145	$C_{36}H_{34}CuF_6N_2O_2S_4$	832	51.94 (51.85)	4.12 (4.16)	3.37 (3.30)	15.41 (15.40)
Ni(FLXDTC)2	136-138	$C_{36}H_{34}NiF_6N_2O_2S_4$	826	52.24 (52.32)	4.14 (4.18)	3.38 (3.42)	15.50 (15.54)

Co(FLXDTC)$_2$	142-144	$C_{36}H_{34}CoF_6N_2O_2S_4$	827	52.23 (52.15)	4.14 (4.18)	3.38 (3.32)	15.49 (15.43)
Mn(FLXDTC)$_2$	143-145	$C_{36}H_{34}MnF_6N_2O_2S_4$	823	52.48 (52.38)	4.16 (4.21)	3.40 (3.31)	15.57 (15.52)
Zn(FLXDTC)$_2$	146-147	$C_{36}H_{34}ZnF_6N_2O_2S_4$	834	51.83 (51.72)	4.11 (4.16)	3.36 (3.31)	15.37 (15.32)
Cd(FLXDTC)$_2$	120-122	$C_{36}H_{34}CdF_6N_2O_2S_4$	881	49.06 (49.15)	3.89 (3.83)	3.18 (3.22)	14.55 (14.49)

[#] data in parenthesis are calculated ones; [*] data limited to integral values

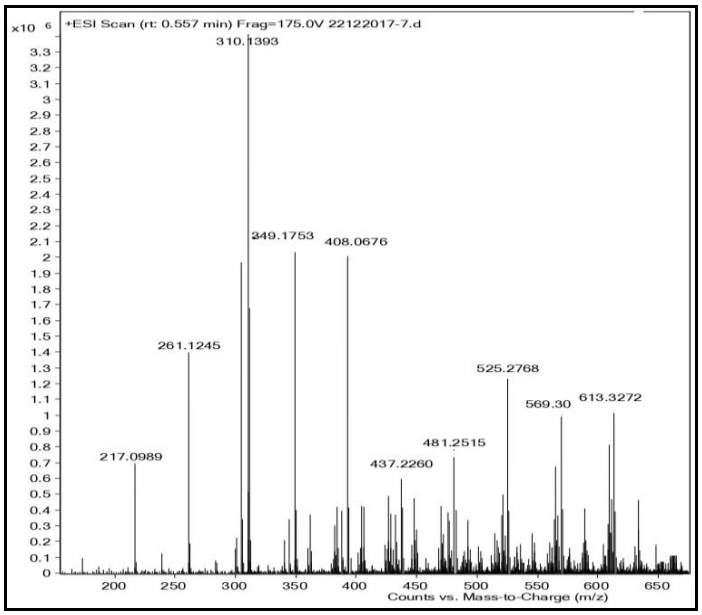

Figure 3A.1: *Mass spectrum of* ***FLXDTC***

3A.2 Infrared Spectral Studies:

The FTIR spectra in KBr pellet of **FLXDTC** ligand and a few of its complexes are shown in **Figures 3A.2** through **Figure 3A.7.** The ligand's aliphatic C-H stretching frequency comes in the range of 2810-2910 cm^{-1} and that of aromatic C-H stretching bands at 3020-3080 cm^{-1}. The **FLXDTC** ligand's ν (C-N) stretching band at 1424 decreases by ~ 25 cm^{-1} on complexation. The negative shift on complexation is due to near loss of the –C=N- tautomeric character.

Table 3A.2: *IR spectral data of* ***FLXDTC*** *and* ***[M(FLXDTC)$_2$]***

Compounds	IR spectral data (cm^{-1})#		
	ν [N-H (str)]	ν [N-C (str)]	ν [C-S (sym)]
FLXDTC	3524	1386	945
Cu(FLXDTC)$_2$	3451	1403	962
Ni(FLXDTC)$_2$	3468	1404	952
Co(FLXDTC)$_2$	3507	1405	947
Zn(FLXDTC)$_2$	3444	1401	975
Cd(FLXDTC)$_2$	3500	1394	971
Mn(FLXDTC)$_2$	3483	1404	952

#, in KBr pellet

The ν (C-S) stretching band for free ligand appears at 970 cm^{-1} and it decreases by ~40 to 60 cm^{-1} on complexation. The negative shift of ν (C-S) stretching band frequency is due to the formation of complexes through the bidentate mode[1]. Important infrared spectral data are provided in **Table 3A.2.**

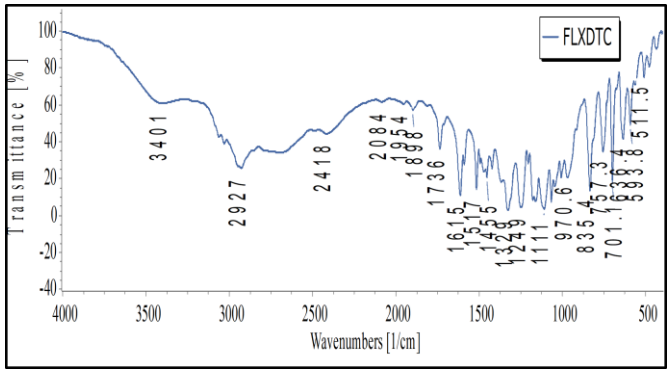

Figure 3A.2: *FTIR Spectrum of* ***FLXDTC***

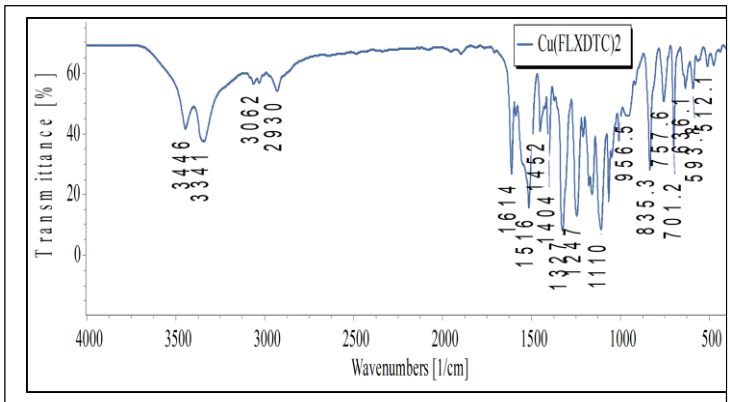

Figure 3A.3: *FTIR Spectrum of* ***Cu(FLXDTC)$_2$***

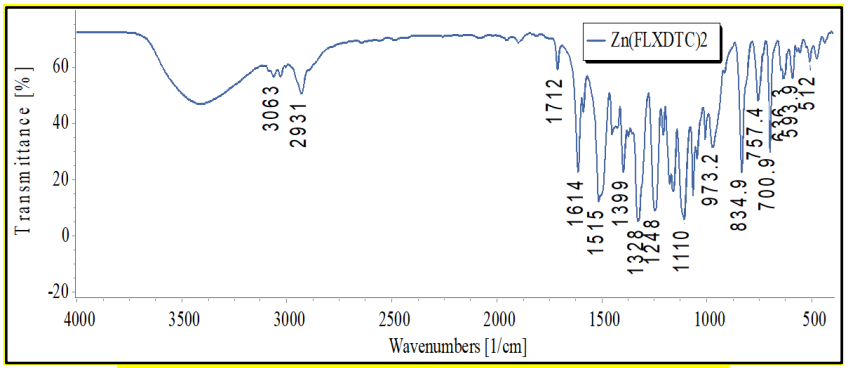

Figure 3A.4: *FTIR Spectrum of* ***Zn(FLXDTC)$_2$***

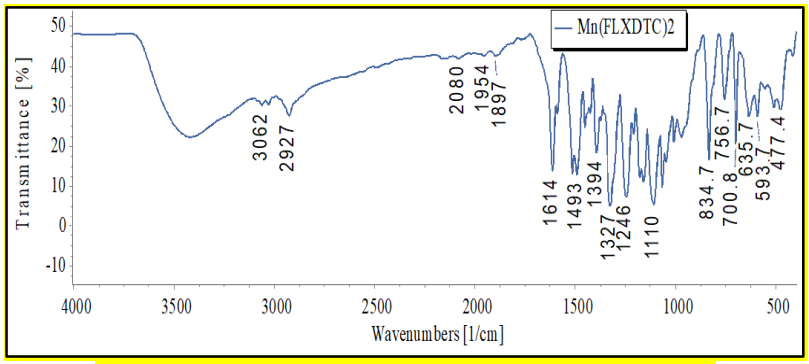

Figure 3A.5: *FTIR Spectrum of* ***Mn(FLXDTC)$_2$***

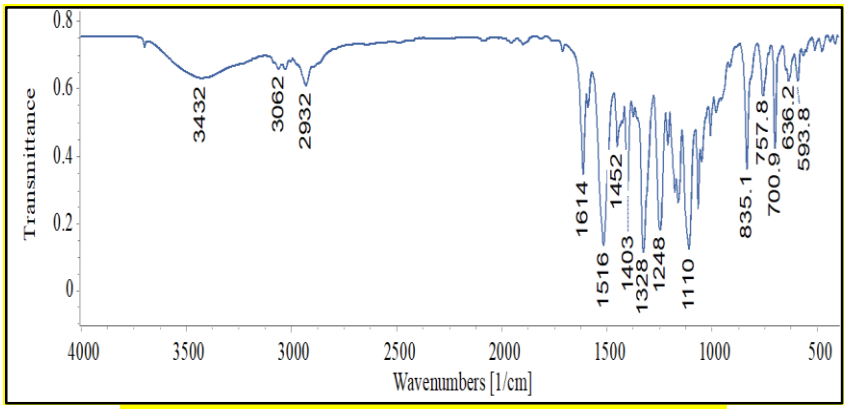

Figure 3A.6: *FTIR Spectrum of* ***Ni(FLXDTC)$_2$***

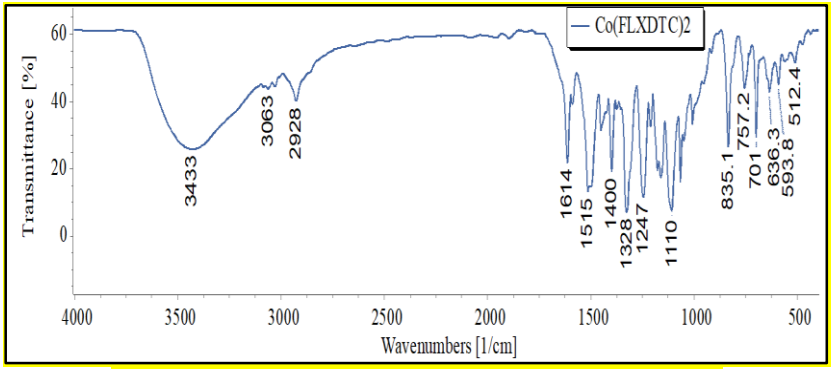

Figure 3A.7: *FTIR Spectrum of* ***Co(FLXDTC)$_2$***

3A.3 Electronic Spectral Studies:

The electronic spectra of **FLX** and **FLXDTC** are shown in **Figure 3A.8.** The drug, **FLX**, exhibits only two transitions at ~296 and 263 nm whereas its dithiocarbamate, **FLXDTC**, shows three peaks at 320, 289 and 260 nm. Further, the spectral intensities of **FLXDTC** are found to be 2 to 3 times higher than those of the drug. The electronic spectrum of the drug matches well with the values reported for similar compounds in literature[2]**.** The two peaks for **FLX** are attributed to $n\rightarrow\pi^*$ (of the ethereal oxygen) and $\pi\rightarrow\pi^*$ (aromatic) transitions. When the drug gets adducted to become the **FLXDTC**, an extra $n\rightarrow\pi^*$ transition of N-C=S moiety is expected. The new peak at 289 nm is assigned to this transition. The $n\rightarrow\pi^*$ of the drug is observed to be considerably red-shifted whereas the $\pi\rightarrow\pi^*$ transition is hardly altered in energy. The spectral data of **FLX** and **FLXDTC** are presented in **Table 3A.3**.

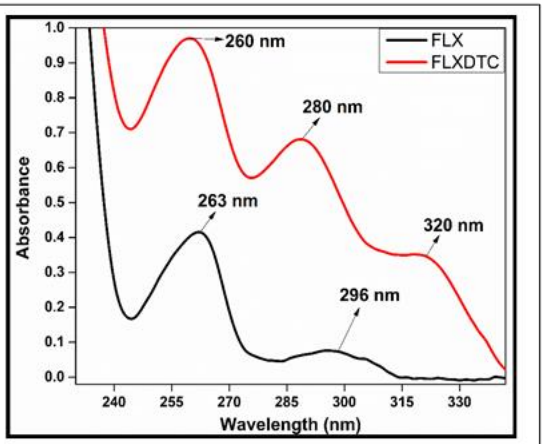

Figure 3A.8: *Electronic Spectra of FLX (—) and* ***FLXDTC*** *(—) in methanol (each at 1.25 x10^{-3} M)*

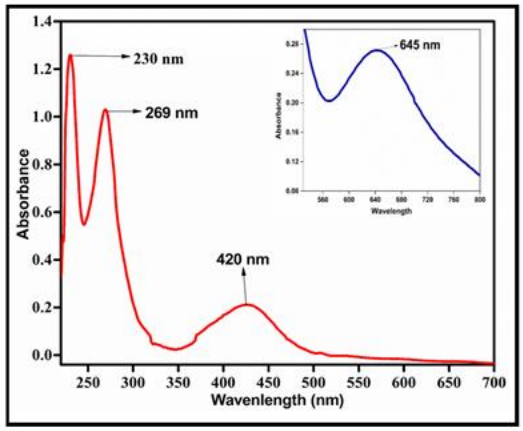

Figure 3A.9: *Electronic spectrum of* ***Cu(FLXDTC)$_2$*** *in methanol (4x10^{-4} M); inset (2x10^{-2} M)*

The electronic spectra of **M(FLXDTC)$_2$** show considerable variation with that of their ligand, **FLXDTC**. A selected few of the spectra of the complexes are shown in **Figure 3A.9** through **Figure 3A.11**. The relevant electronic spectral data of **M(FLXDTC)$_2$** are collected in **Table 3A.3**. The weak and broad band observed for **Cu(FLXDTC)$_2$** at 645 nm is assigned to the $^1B_{1g} \rightarrow 2E_g$ d-d transition[3] whereas that at ~420 nm is to metal to ligand charge transfer. These data suggest a square planar geometry for **Cu(FLXDTC)$_2$.** The band found for **Ni(FLXDTC)$_2$** at ~481 nm and at 633 nm are assigned to $^1A_{1g} \rightarrow {}^1B_{1g}$ and $^1A_{1g} \rightarrow {}^1A_{2g}$ transitions respectively which

indicate a square planar structure to **Ni(FLXDTC)$_2$** also[4]**. Co(FLXDTC)$_2$** shows two bands at ~638 nm and 324 nm, attributed to the $^4A_2(F) \rightarrow {}^4T_1(P)$ and $^4A_2(F) \rightarrow {}^4T_1(F)$ d-d transitions. All of these results together suggest a tetrahedral geometry for **Co(FLXDTC)$_2$**[5]**.** The **Mn(FLXDTC)$_2$** is a d^5 high spin system with Laporte and spin-forbidden d-d transitions[6]**.** No d-d transitions are found for **Zn(FLXDTC)$_2$** and **Cd(FLXDTC)$_2$** as expected for d^{10} systems.

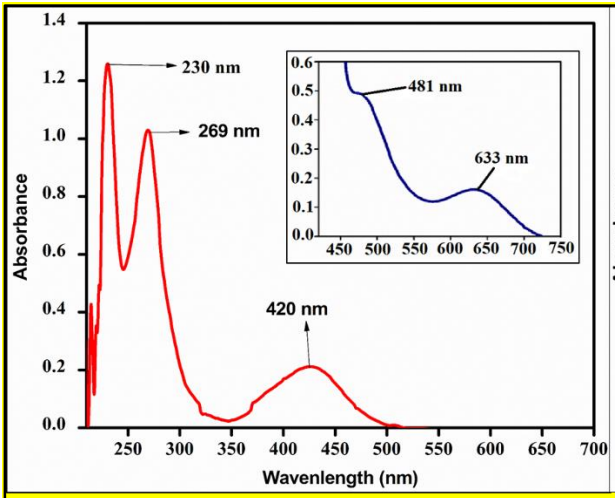

Figure 3A.10: *Electronic spectrum of* ***Ni(FLXDTC)$_2$*** *in methanol (4x10^{-4} M); inset 2x10^{-2} M*

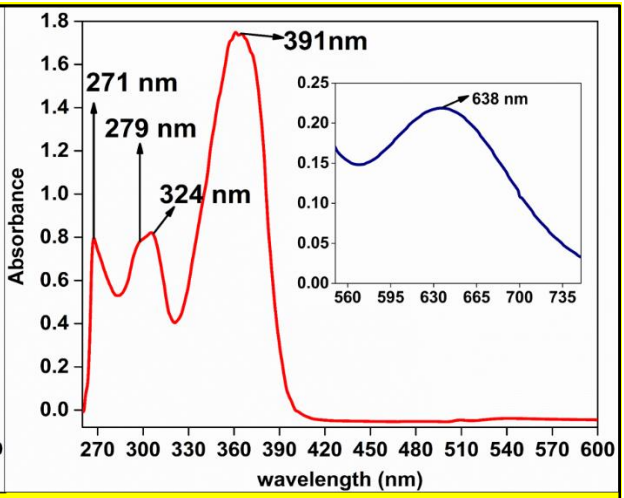

Figure 3A.11: *Electronic spectrum of* ***Co(FLXDTC)$_2$*** *in methanol (4x10^{-4} M); inset 2x10^{-2} M*

Table 3A.3: *Physical, spectral and magnetic data of* ***FLX***, ***FLXDTC*** *and* ***[M(FLXDTC)$_2$]***

Compound	Color	Electronic spectral data λ (ε)*	μ_{eff} (BM)
FLX	White	263 (336); 297 (65)	-
FLXDTC	Yellow	228 (784); 289 (545); 321 (296)	-
Cu(FLXDTC)$_2$	Brown	230 (3250); 269 (2400); 420 (500); 635 (15)	1.82
Ni(FLXDTC)$_2$	Green	247 (1270); 323 (2875); 391 (150); 481 (24); 633 (8)	2.95
Co(FLXDTC)$_2$	Green	271 (1875); 279 (1950); 324 (2000); 391(4250); 638 (12)	4.37
Mn(FLXDTC)$_2$	Brown	230 (4125); 280 (1125)	5.62

Zn(FLXDTC)$_2$	White	234 (3250); 259 (2985); 288 (2375); 320 (1125)	-
Cd(FLXDTC)$_2$	White	232 (4625); 252 (2750); 279 (2200)	-

* λ in nm, ε in lt mol^{-1}cm^{-1}

3A.4 NMR Spectral Studies:

The ^{1}H NMR spectra of **FLX** and **FLXDTC** are presented in **Figure 3A.12** and **Figure 3A.13** respectively. The methylene protons of the -NH–CH_2- are NMR-distinguishable by geometric isomerism in relation to their position with the bonds around the nitrogen. They are found to show their individual chemical shifts at ~4.25 ppm and 4.37 ppm. The ^{1}H NMR spectra of **Zn(FLXDTC)$_2$** and **Cd(FLXDTC)$_2$** are presented in **Figure 3A.14** and **Figure 3A.15** respectively. Though the methylene protons of the -NH–CH_2- are NMR-distinguishable in **FLXDTC**, they seem to get indistinguishable upon complexation to give their common chemical shift at ~3.95 ppm. The positions of the other protons of **FLXDTC** hardly undergo any contact shift upon complexation as they are considerably away from the coordination sphere. The ^{13}C NMR spectra of **FLX** and **FLXDTC** are presented in **Figure 3A.16** and **Figure 3A.17** respectively. A similar non-contact shift is observed for the ^{13}C peaks of the **FLXDTC,** the position of the C-S carbon in **FLXDTC** is shifted from ~209 in **FLXDTC** to ~204 ppm in **M(FLXDTC)$_2$** (M = Zn or Cd). The enhanced shielding suffered by this carbon is attributed to the diffusion of the electron cloud of the nitrogen's lone pair towards the C-S carbon through ligand-to-metal-charge transfer (LMCT) upon complexation[7]**.**

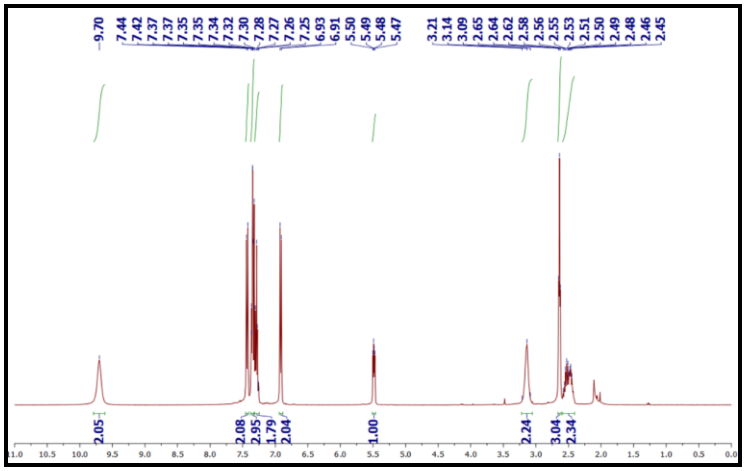

Figure 3A.12: *^{1}H-NMR Spectrum of Fluoxetine.HCl in $CDCl_3$*

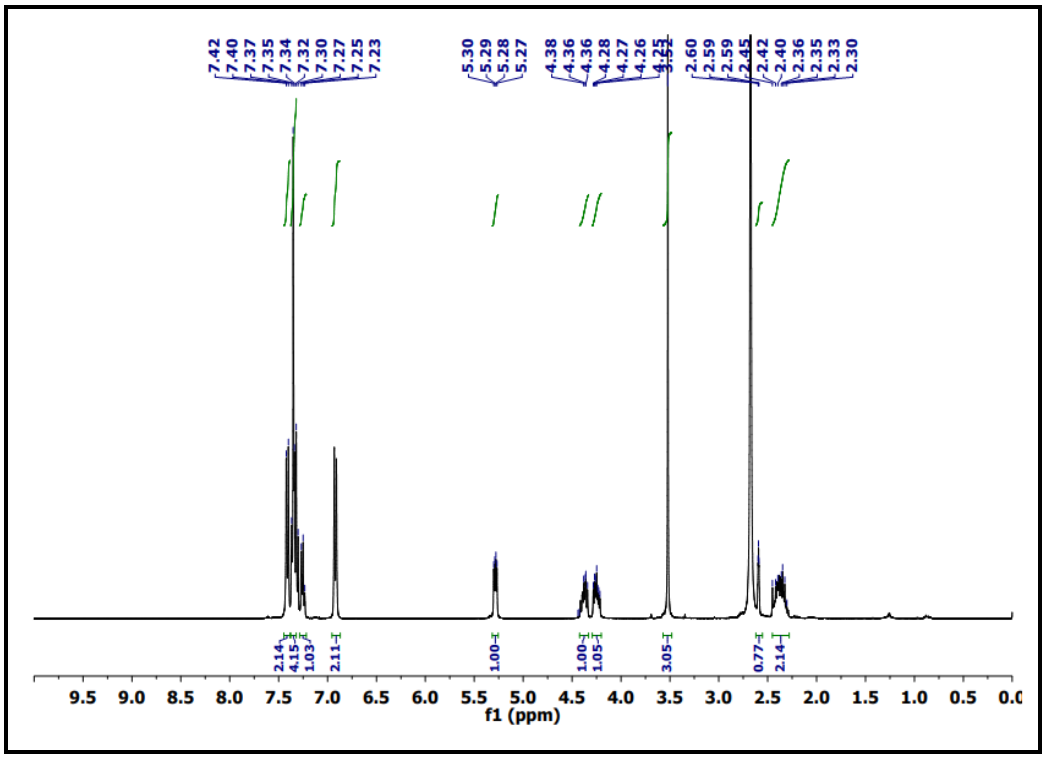

Figure 3A.13: *^{1}H-NMR Spectrum of* ***FLXDTC*** *in DMSO*

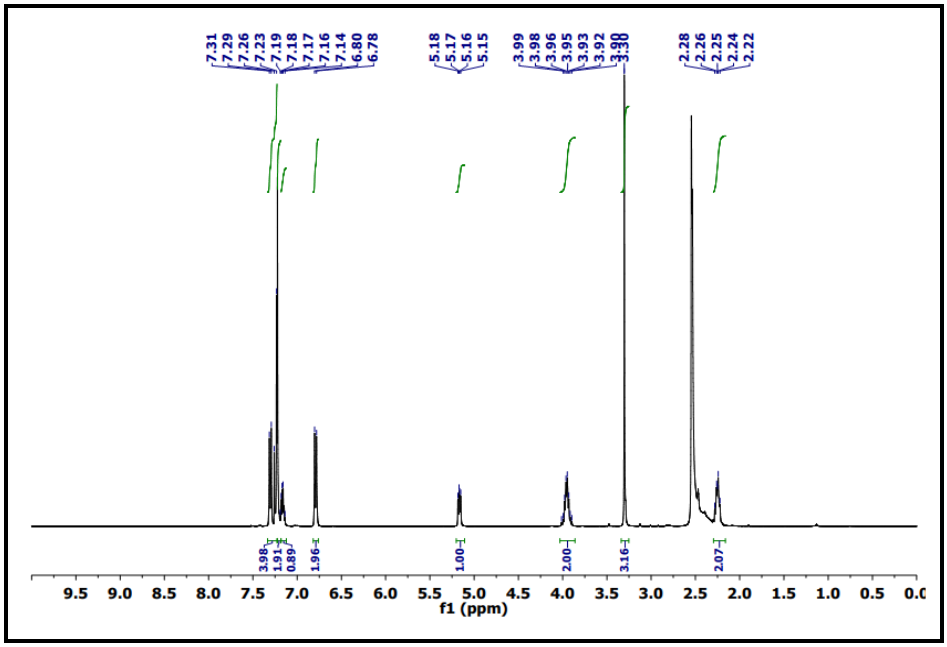

Figure 3A.14: *^{1}H-NMR Spectrum of* ***Zn(FLXDTC)$_2$*** *in $CDCl_3$ and DMSO mixture*

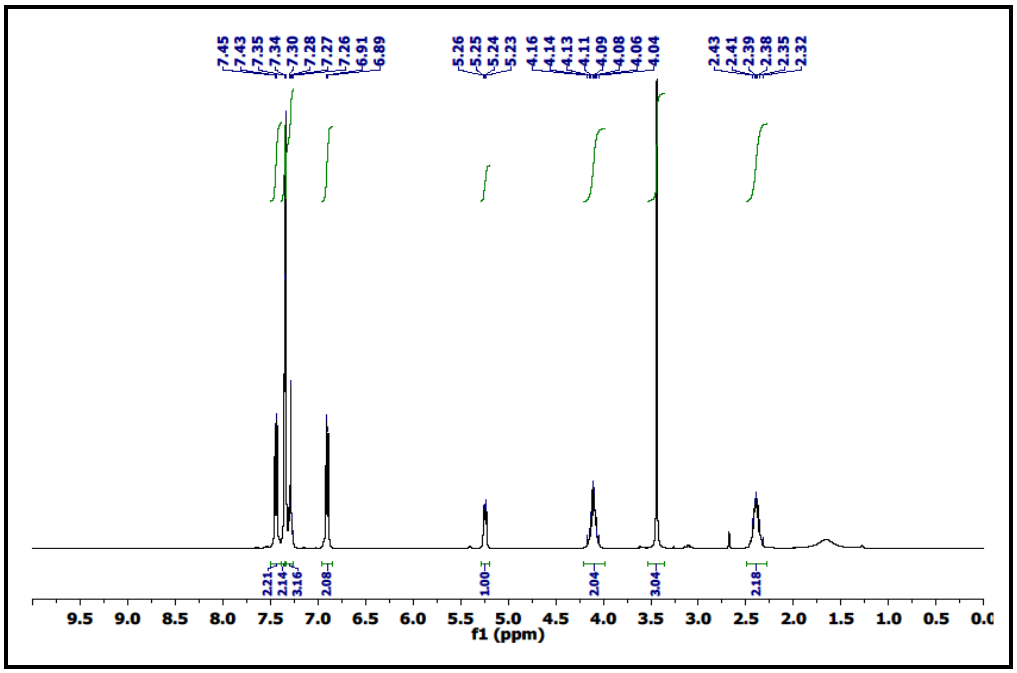

Figure 3A.15: *^{1}H-NMR Spectrum of* ***Cd(FLXDTC)$_2$*** *in $CDCl_3$*

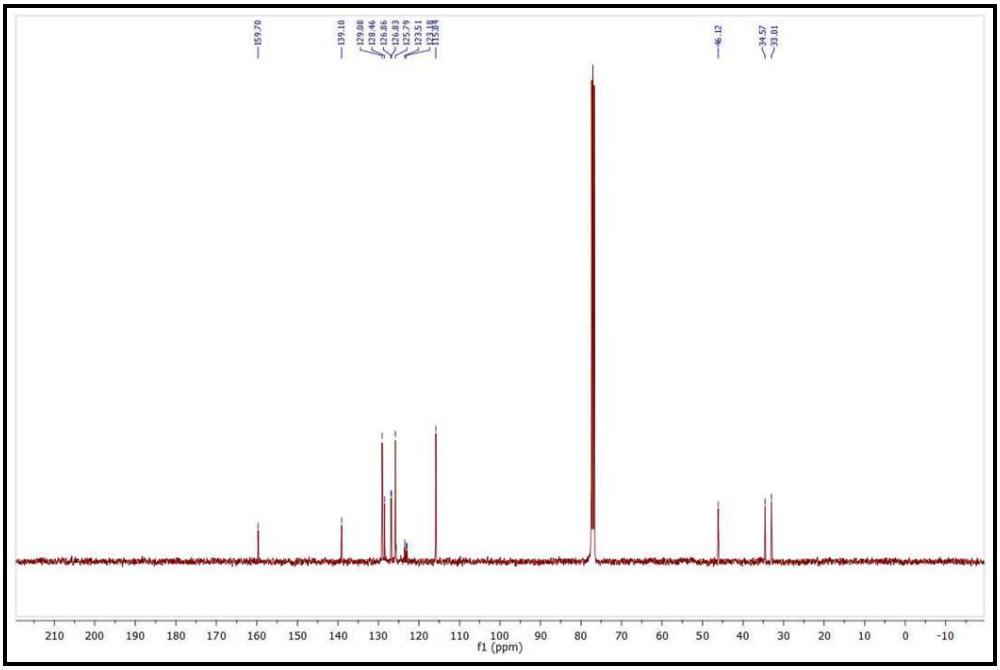

Figure 3A.16: *^{13}C-NMR Spectrum of* ***FLX*** *in $CDCl_3$*

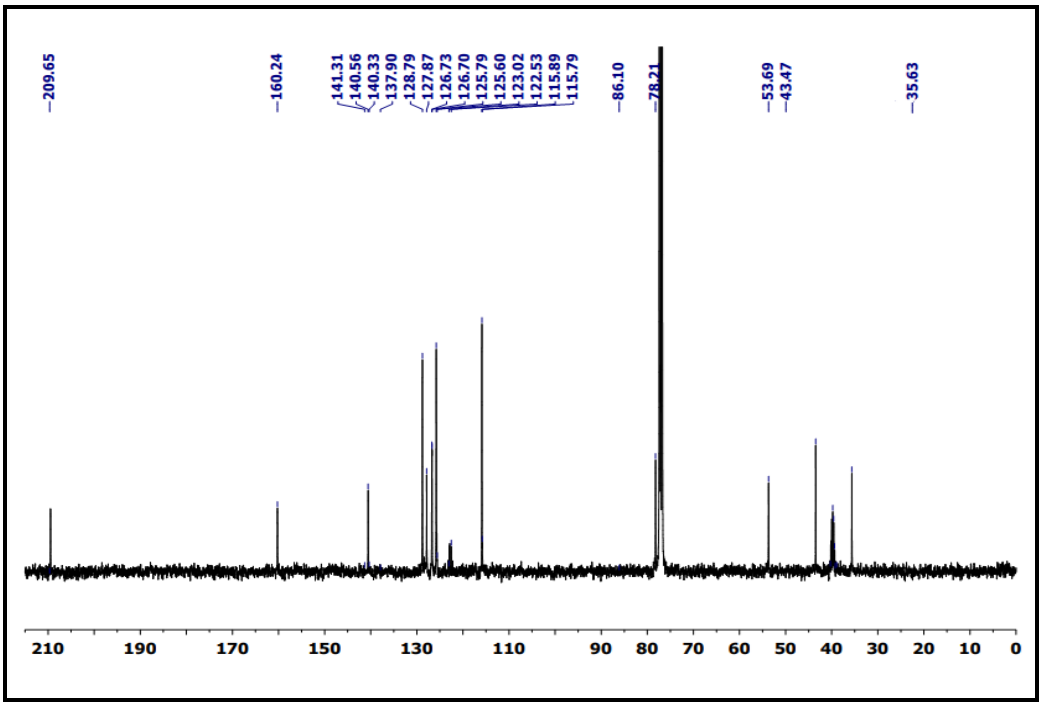

Figure 3A.17: *^{13}C-NMR Spectrum of **FLXDTC** in $CDCl_3$ and DMSO mixture*

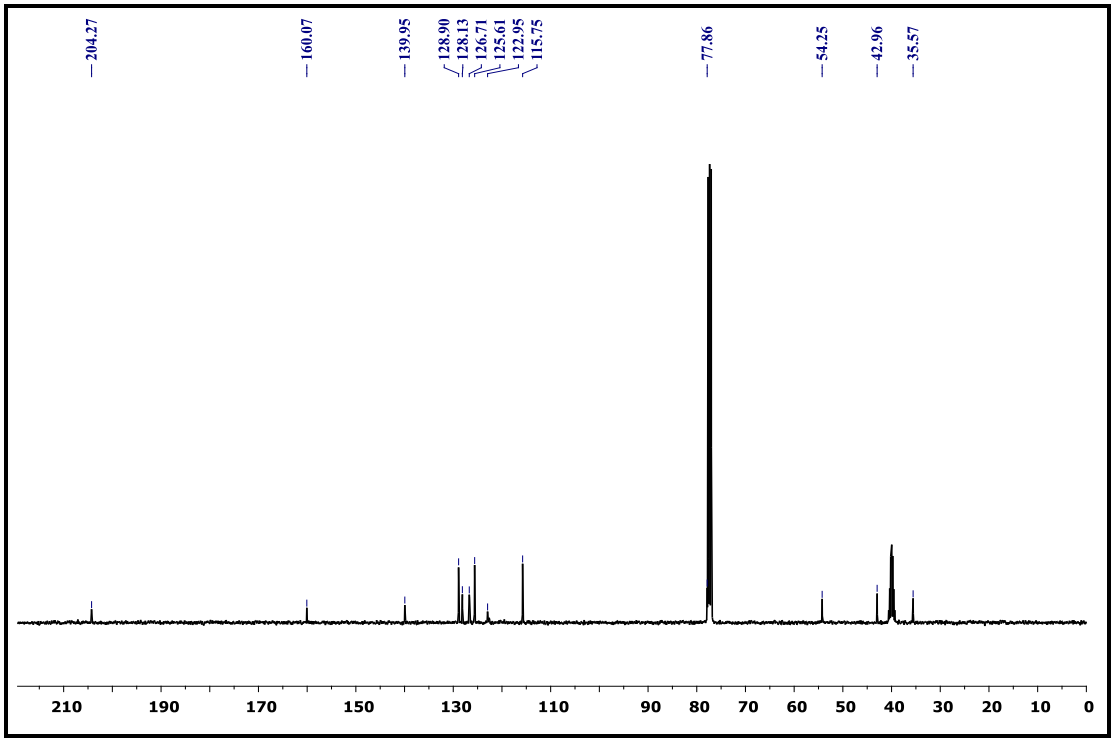

Figure 3A.18: *^{13}C-NMR Spectrum of **Zn(FLXDTC)$_2$** in $CDCl_3$ and DMSO mixture*

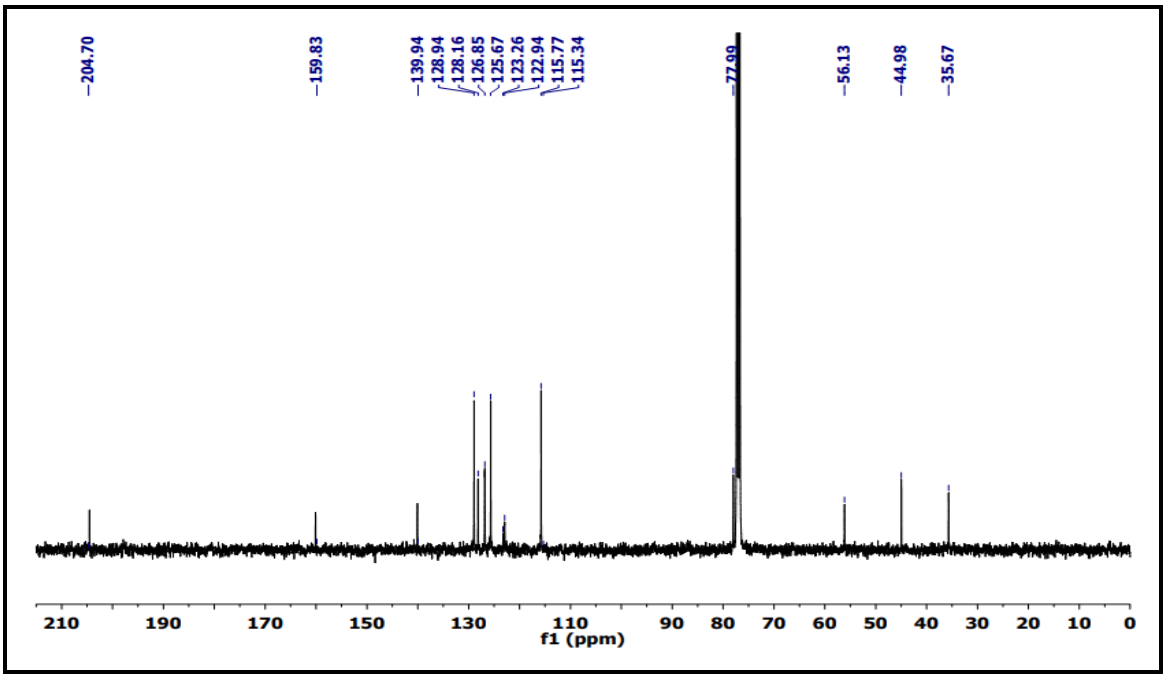

Figure 3A.19: *^{13}C-NMR Spectrum of* ***Cd(FLXDTC)$_2$*** *in $CDCl_3$*

3A.5 Metal to Ligand Ratio; Job's Monovariation Spectrophotometric Titration:

In order to arrive at the metal to ligand ratio (coordination number) a spectrophotometric titration has been carried out for a fixed amount of **FLXDTC** (titrand) and varied metal ion content (titrant) in a monovariation Job's method. In **Figure 3A.20** is shown the Job's plots obtained for **Ni(FLXDTC)$_2$** at the respective λ_{max} in the visible region. The Job's plots indicate the metal to ligand stoichiometry matching to the formulae, **M(FLXDTC)$_2$.**

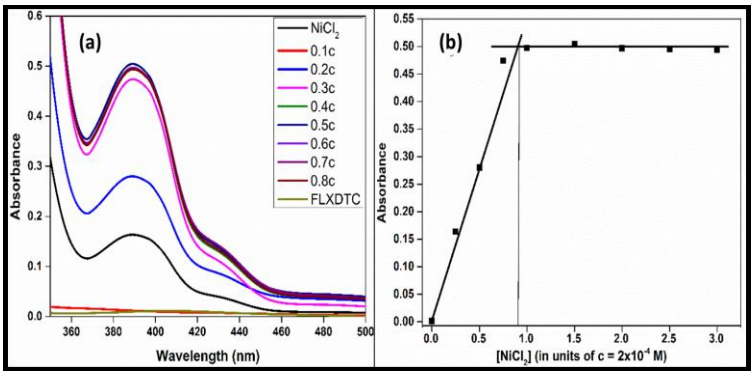

Figure 3A.20: (a) *Monovariation Job's plot for the spectrophotometric titration of* ***FLXDTC*** *(c = 4x10^{-4} M) against $NiCl_2$* ***(b)*** *Monovariation Job's plot for the spectrophotometric titration*

However, in the case of spectrophotometric titration by monovariation Job's method for a fixed amount of **FLXDTC** (titrand) and varied Cu^{2+} ion (titrant) content, an interesting observation is found. In **Figure 3A.22** are shown a set of overlapped spectra obtained for solutions of varied amounts of copper (II) ion for a fixed amount of **FLXDTC**. While the metal amount continues to increase, a new band at ~440 nm appears with an increasing absorbance reaching to a maximum at 0.5 c of the concentration of Cu(II) ion where c has been the amount of the titrand, **FLXDTC**, taken. This fact is indicative of the formation of **$Cu(FLXDTC)_2$**, as expected.

However, on further addition of Cu(II) ion, the absorbance ~440 nm gradually falls down, instead of staying constant (unlike in the cases of nickel and cobalt), and with a new band commencing at ~390 nm with absorbance increasing with Cu(II). A Job's plot is shown in **Figure 3A.23** for these two wavelengths.

This trend is suggestive of a consecutive metal–ligand complexation as shown below:

$$\mathbf{Cu^{2+} + 2\ FLXDTC \rightarrow [Cu(FLXDTC)_2]} \qquad (3.1)$$

$$\mathbf{[Cu(FLXDTC)_2] + CuCl_2 \rightarrow [Cu_2(FLXDTC)_2Cl_2]} \qquad (3.2)$$

The plausible structure for the binuclear[8] complex is tentatively shown below

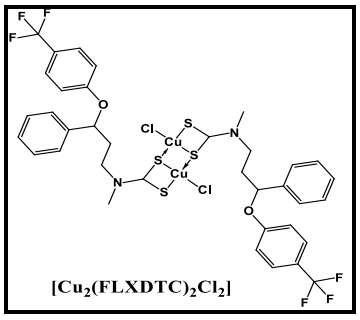

Figure 3A.21: *Sulfur bridged binuclear* ***[$Cu_2(FLXDTC)_2Cl_2$]***

That this is the most acceptable structure is deduced from the facts that (i) new band ~390 nm with an isosbestic point at ~400 nm appears only after the added metal ion content is above 0.5c with absorbance at ~390 nm reaching maximum and not in the range of 0.0c – 0.5c where c is the fixed concentration of the ligand, **FLXDTC** and (ii) addition of $CuCl_2$ in DMSO to a molar equivalent solution of **[$Cu(FLXDTC)_2$]** in DMSO has resulted in the blue shift of the spectrum of

[Cu(FLXDTC)$_2$] with λ_{max} at ~ 440 nm to a band at ~390 nm while the ratio, $A_{max(440)}/ A_{max(390)}$ being same as observed in the cases shown in **Figure 3A.22** and **Figure 3A.23**.

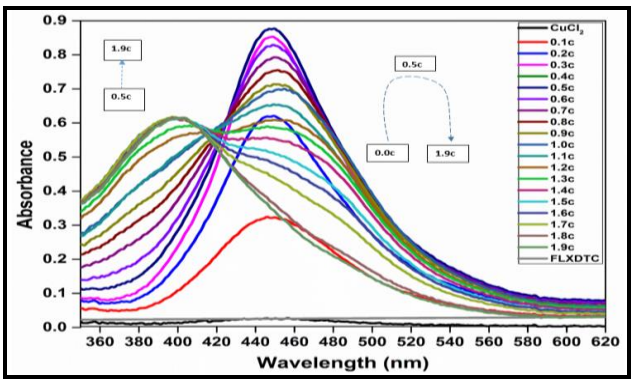

Figure 3A.22: *Spectrophotometric titration of* ***FLXDTC*** *(c = 1x10^{-4} M) against $CuCl_2$ (in jc concentrations where 0 ≤j ≤ 1.9); (—) $CuCl_2$ (0.5x 10^{-4} M) alone; (—)* ***FLXDTC*** *(0.5x10^{-4} M) alone*

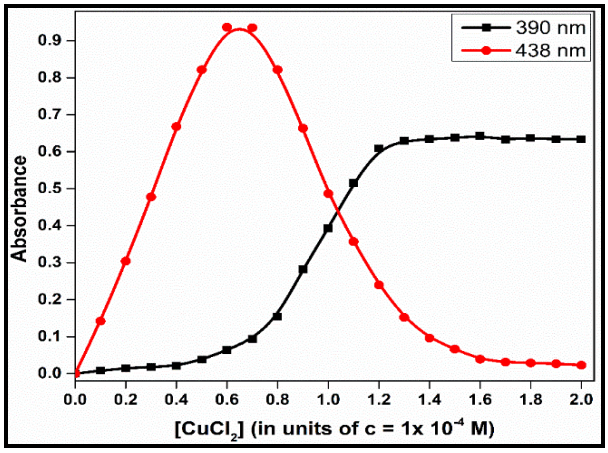

Figure 3A.23: *Monovariation Job's plot for the spectrophotometric titration of* ***FLXDTC*** *(c = 1x10^{-4} M) against $CuCl_2$*

3A.6 Electron Spin Resonance Spectroscopy of Cu(FLXDTC)$_2$:

The ESR spectra of **Cu(FLXDTC)$_2$** in both solid (polycrystalline) and liquid (as a solution in toluene) states are shown in **Figure 3A.24** and **Figure 3A.25** respectively. In solid state, a single broad peak centered at g = 2.045 is observed whereas a well resolved four-line fine spectrum in the solution. From this solution spectrum the g_{avg} and A_{avg} are evaluated as 2.042 and 80.126 G respectively. The instrument-embedded JEOL Software has been used to simulate and curve-fit

the spectrum to resolve the parallel and perpendicular parts of the ESR spectrum. From this simulation with a regression coefficient of 0.98, the tensor values, $g_{\parallel}$ and $g_{\perp}$, are evaluated as 2.056 and 2.012, respectively. The presence of unpaired electron in the $d_{x^2-y^2}$ (ground state) orbital is discerned from the fact that $g_{\parallel} > g_{\perp} > 2.0023$ which also infers a square planar geometry to the Cu(II) center[9]. The fact that the g_{avg} value is lower than 2.3 means a covalent character between the metal and the ligand.

The geometric parameter, G, also known as magnetic exchange interaction parameter, and calculated by the following formula,

$$G = \frac{g_{\parallel} - 2.0023}{g_{\perp} - 2.0023} \qquad \textbf{(3.3)}$$

is found out to be ~ 1.40. However, it is well known, as reported by Hathaway and Billing, that a value of G < 4 infers an appreciable magnetic interaction between adjacent metal centers in solid state whereas that of G > 4 a negligible one[10].

The exchange interaction parameter value of complex **Cu(FLXDTC)$_2$** being less than 4 suggests that copper centers have spin-exchange interaction between them as in certain Schiff base square planar complexes and copper[11].

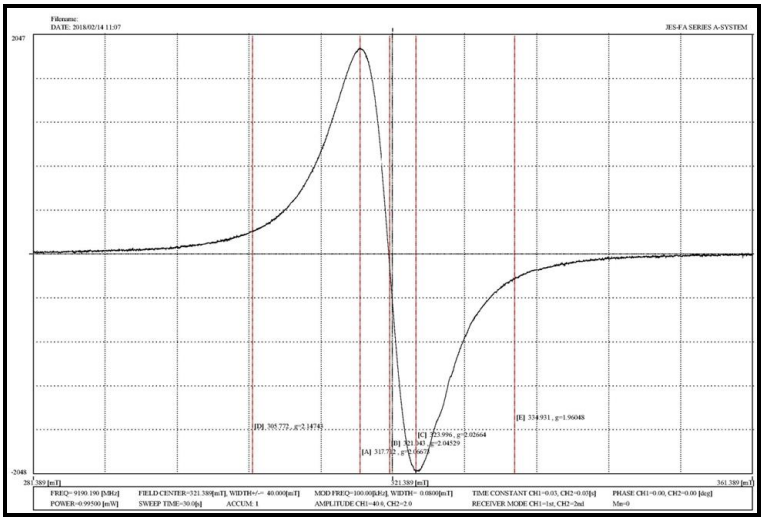

Figure 3A.24: *X-band electron spin resonance spectrum of* ***Cu(FLXDTC)$_2$*** *in solid state*

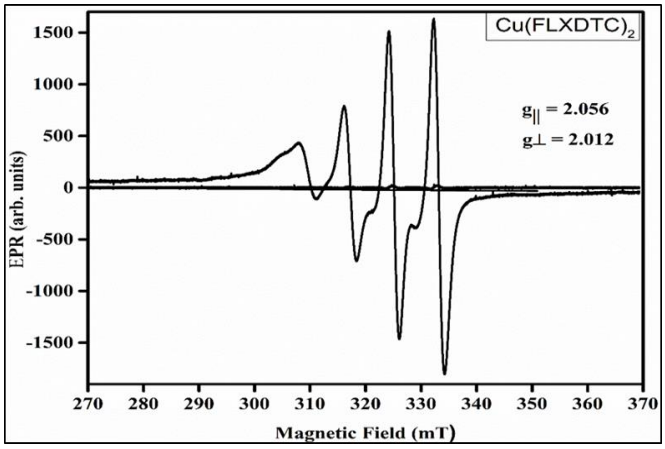

Figure 3A.25: *X-band electron spin resonance spectrum of* ***Cu(FLXDTC)₂*** *in toluene (ν = 9.191GHz)*

3A.7 Cyclic Voltammetric Studies of M(FLXDTC)₂:

An excellent monograph on the electrochemical redox behavior of transitional metal dithiocarbamate is available[12]. Many of the dithiocarbamates stabilize the metal centers for reduction while undergoing the following reversible oxidation process in non-aqueous media on solid electrode surfaces.

$$M(R_2DTC)_2 \rightleftharpoons M(R_2DTC)_2^{+\cdot} + e \qquad \textbf{(3.4)}$$

Copper dithiocarbamate complexes are known as excellent candidates for reversible cyclic voltammetry in non-aqueous media and some of them are used in academic jargon[13]. Depending upon the organic skeleton connected to the nitrogen atom of the dithiocarbamate, the degree of reversibility in the anodic sweep cyclic voltammetry varies. Copper dithiocarbamate are reported to undergo Cu(II) ⇌ Cu(III) anodic response and Cu(II) ⇌ Cu(I) reductive response. The strained four-membered chelation loop in the CuS_4 square planar coordination sphere is shown to be the cause for the stability of the unusual Cu(III) oxidation state[14]**.**

The cyclic voltammogram of **Cu(FLXDTC)₂** in acetone medium with tetraethyl ammonium perchlorate (TEAP) as supporting electrolyte is presented in **Figure 3A.26(a)**. This process has been found to be either quasi-reversible **[Cu(FLXDTC)₂]** or irreversible **[Co(FLXDTC)₂].**

The profile of the voltammogram besides the ratio of the peak currents (i_{pc}/i_{pa}), difference between the peak potentials ($\Delta E_p = |E_{pc}-E_{pa}|$) and effect of scan rate on the peak currents indicate that the electron transfer is quasi-reversible. The effect of concentration on the voltammetric behavior is presented in **Figure 3A.27.** The peak current is found to be linear to the concentration of the **Cu(FLXDTC)$_2$.** The effect of scan rate on the peak current is presented in **Figure 3A.28.** The linearity of both i_{pa} and i_{pc} independently to the square root of scan rate suggests that the electron transfer is a diffusion-controlled one. In the cathodic scan, no Cu(II) ⇌ Cu(I) reductive peak is observed even up to -1.0 V vs Ag | AgCl. The absence of the reductive peak of Cu(II) ⇌ Cu(I) though the standard reductive potential of Cu(II) | Cu(I) couple is + 0.34V, is attributed to the fact that higher oxidation states of metal centers are stabilized in dithiocarbamate complexes[15]. The dissimilar slopes of plots of anodic and cathodic potentials with concentrations (**Figure 3A.27**) further suggest the involvement of quasi reversible nature of electron transfer process in case of **Cu(FLXDTC)$_2$** (**Eqn 3.4**).

The cyclic voltammogram of **Co(FLXDTC)$_2$** is shown in **Figure 3A.26(b)**. Based on the fact that the peak currents of **Co(FLXDTC)$_2$** and **Cu(FLXDTC)$_2$** are linear independently to the concentrations of the respective metal complexes it is possible to assay **FLX**, **FLXDTC** and **M(FLXDTC)$_2$** by linear sweep voltammetry (LSV).

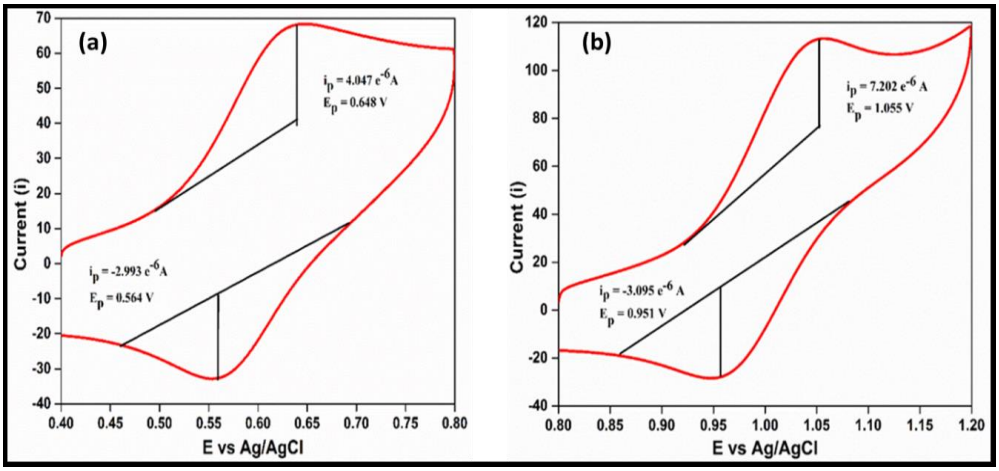

Figure 3A.26: *Cyclic voltammograms of 5x 10^{-4} M* ***(a) Cu(FLXDTC)$_2$ (b) Co(FLXDTC)$_2$*** *at 120 mVs^{-1} scan rate in acetone solvent*

From the studies of the effect of concentration and scan rate on peak potentials, the electron transfers coefficient (α_{na}) and heterogeneous electron transfer rate constant (k^o_h) have been evaluated. Relevant electrochemical data are presented in **Table 3A.4** along with the diffusion coefficients, D.

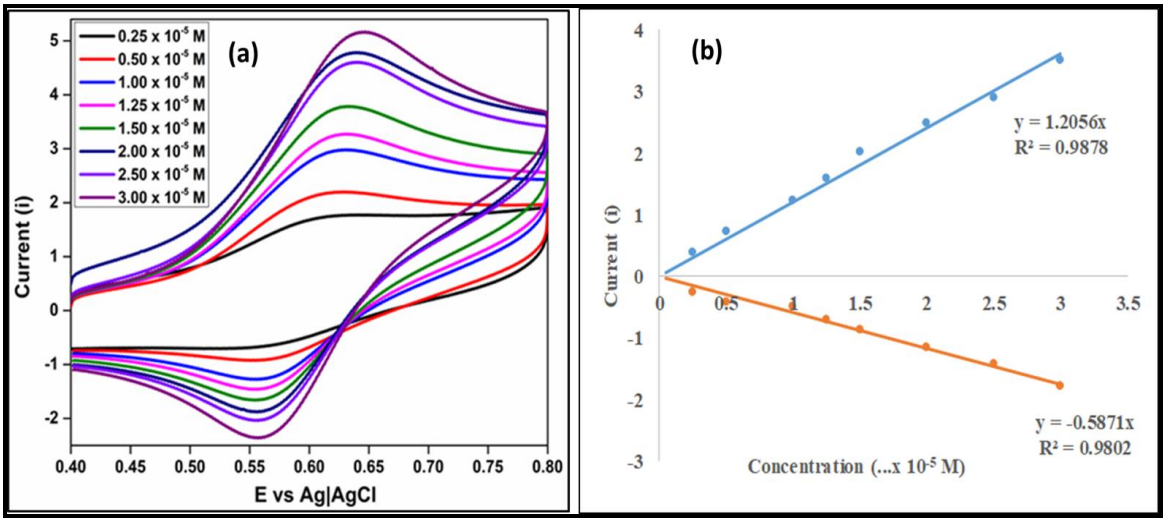

Figure 3A.27: (a) *Cyclic voltammograms of* ***Cu(FLXDTC)₂*** *in Acetone at different concentrations* ***(b)*** *Variation of anodic and cathodic currents of* ***Cu(FLXDTC)₂*** *with respect to various concentrations*

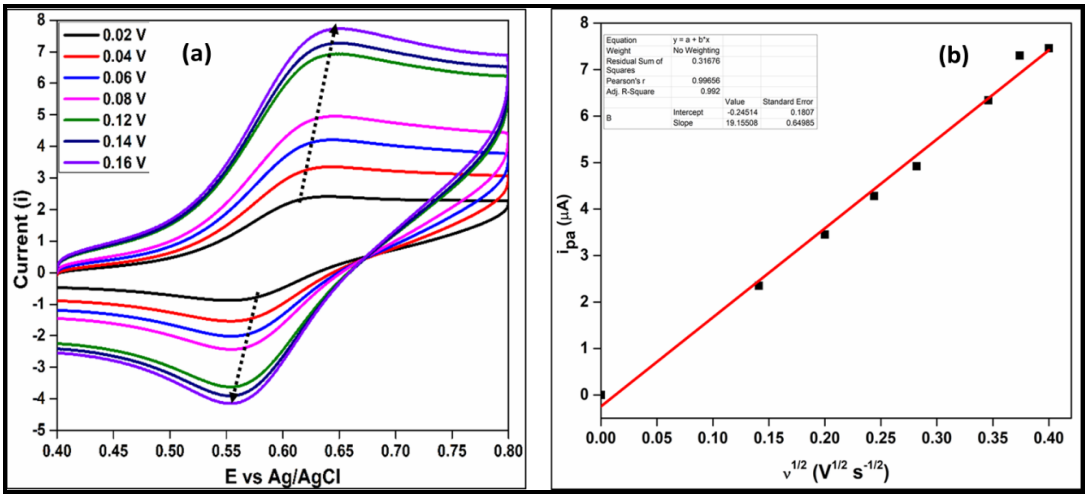

Figure 3A.28: (a) *Cyclic voltammogram of* ***Cu(FLXDTC)₂*** *(5x10^{-5} M) in acetone at different scan rates* ***(b)*** *Effect of scan rate on the anodic current of* ***Cu(FLXDTC)₂***

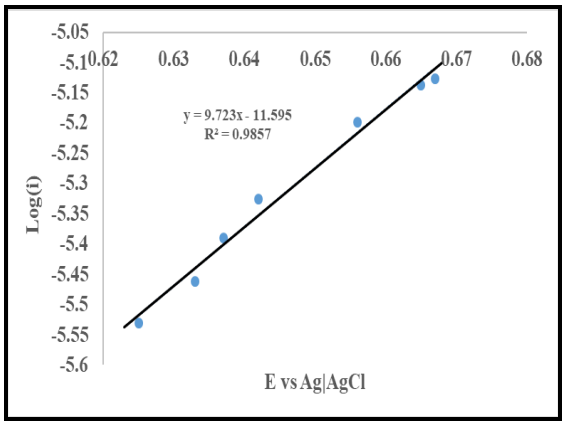

Figure 3A.29**: Plot of scan rate-dependent E_p vs log i for **Cu(FLXDTC)$_2$

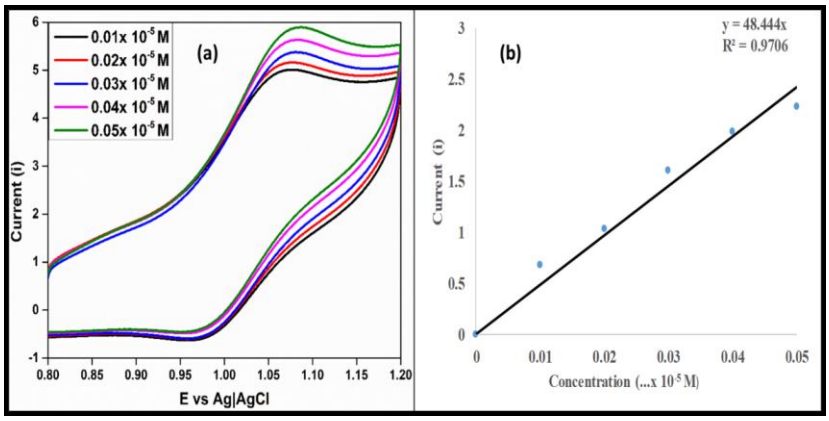

***Figure 3A.30: (a)** Cyclic voltammograms of **Co(FLXDTC)$_2$** in Acetone at different concentrations **(b)** Variation of anodic currents of **Co(FLXDTC)$_2$** with respect to concentration*

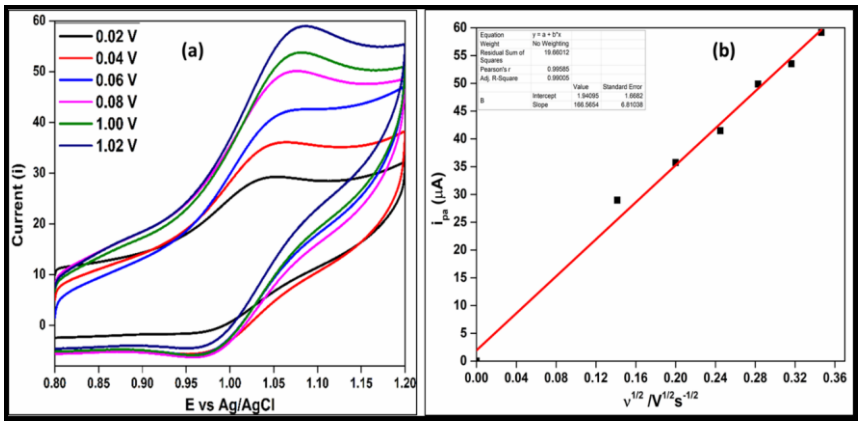

Figure 3A.31: (a)** Cyclic voltammogram of 5x10^{-4} M **Co(FLXDTC)$_2$** (5x10^{-5} M) in acetone at different scan rates **(b)** Effect of scan rate on the anodic current of **Co(FLXDTC)$_2$

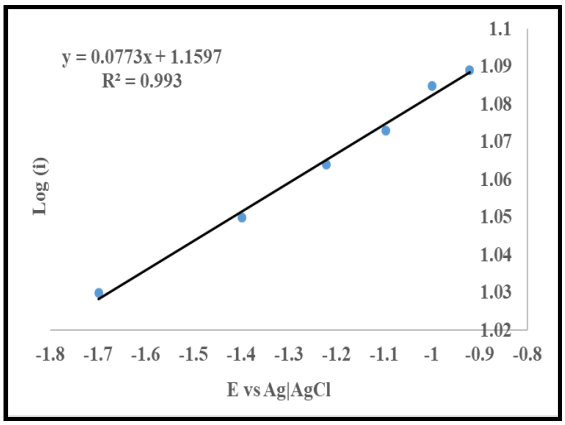

Figure 3A.32: *Plot of scan rate-dependent E_p vs log i for* ***Co(FLXDTC)$_2$***

Table 3A.4: *Electrochemical data of various metal complexes in acetone medium*

Compound	**Parameters**		
	(D) in cm^2 s^{-1}	**(α_{na}) in cm^2 s^{-1}**	**k^o_h in cm^2 s^{-1}**
Cu(FLXDTC)$_2$	9.75 x 10-5	0.57	8.78 x 10^{-6}
Co(FLXDTC)$_2$	1.64 x 10^{-5}	0.31	5.83 x 10^{-5}
Zn(FLXDTC)$_2$	4.25 x 10^{-5}	0.47	6.32 x 10^{-5}
Ni(FLXDTC)$_2$	3.46 x 10^{-5}	0.53	7.21 x 10^{-5}

PART B

COMPUTATIONAL MOLECULAR MODELLING AND MOLECULAR DOCKING STUDIES OF FLXDTC AND M(FLXDTC)$_2$

3B.1 Molecular Modelling Studies of FLXDTC and M(FLXDTC)$_2$ Complexes:

In order to address the stability aspects of the **FLXDTC** ligand and its metal complexes, we need to identify the conformational visualization of the molecules in various forms. For this purpose, molecular modelling studies were used. The MM2 force field method with an RMS gradient of 0.01 is used to calculate the global energy minimized structures. In any structural analysis the bond length, bond angles and torsional angles are some of the most essential structural factors. The ligand **FLXDTC**, as well as its complexes have been investigated using the change in these parameters. There is a great degree of consistency between the experimental and simulated data. Global minimized structures of **FLXDTC** ligand is depicted at **Figure 3B.1.** The numbering adaptation is shown in **Figure 3B.1** for subsequent reference in the discussion**.** To visualize the molecular disposition in space and to provide a 3D visual of it, the anaglyph picture and stereographic representation of the **FLXDTC** are given in **Figure 3B.2** and **Figure 3B.3**, respectively.

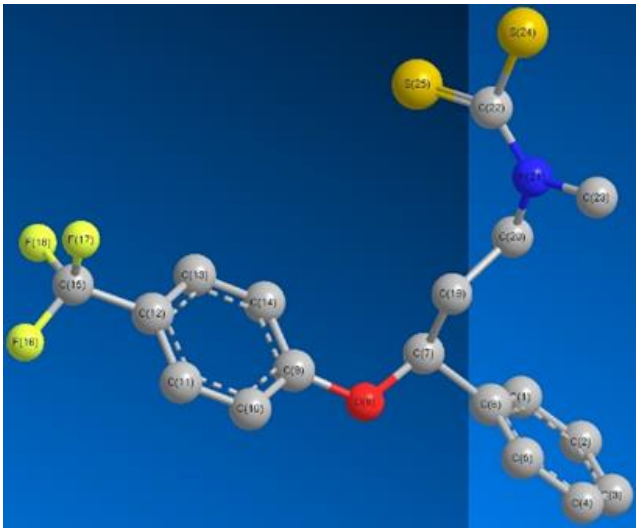

Figure 3B.1: *MM2-energy-minimized structure of* ***FLXDTC*** *with numbered atoms*

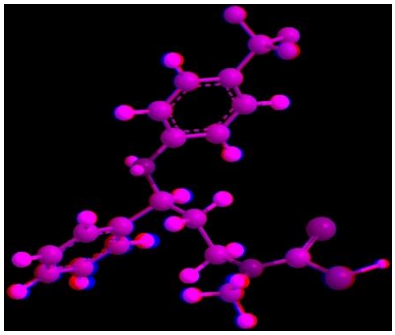

Figure 3B.2: *Anaglyph structure of* ***FLXDTC*** *obtained from ChemDrawPro*

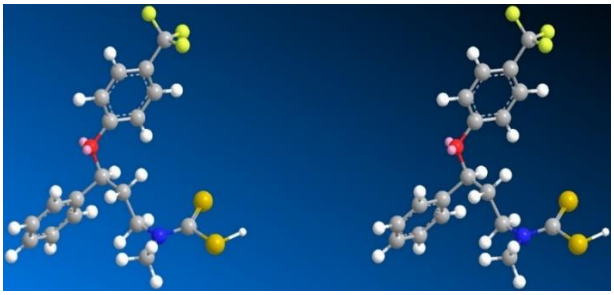

Figure 3B.3*: Stereographic projection of* ***FLXDTC*** *obtained from ChemDrawPro*

FLXDTC has a phenyl and benzyl bulky groups connected to the ethereal oxygen whereat the dithiocarbamate extension is also around. With the view to understand the best relative disposition of the bulky groups in space with the global minimum of the Eigen value, we have performed conformational analysis by torsioning over the selected single bonds in both dihedral driving and double dihedral driving computational methods. Conformational analysis plots of **FLXDTC** are shown in **Figure 3B.4** through **Figure 3B.19**.

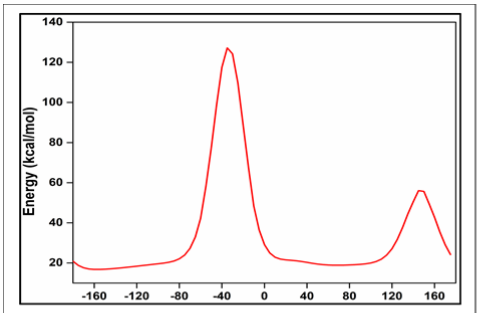

Figure 3B.4: *Conformational analysis over O8-C9*

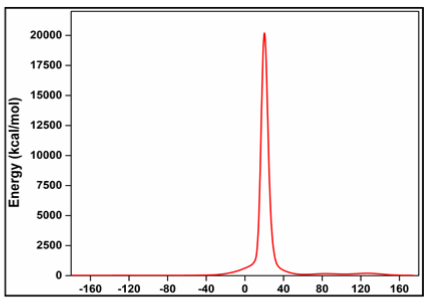

Figure 3B.5: *Conformational analysis over O8-C7*

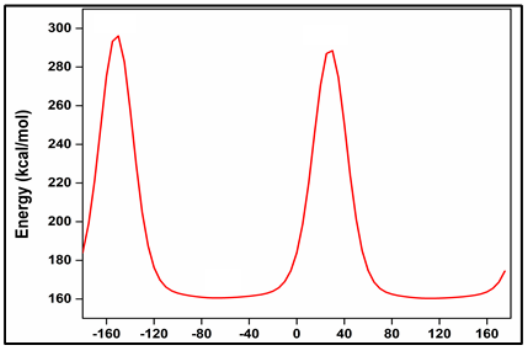

Figure 3B.6: *Conformational analysis over C6-C7*

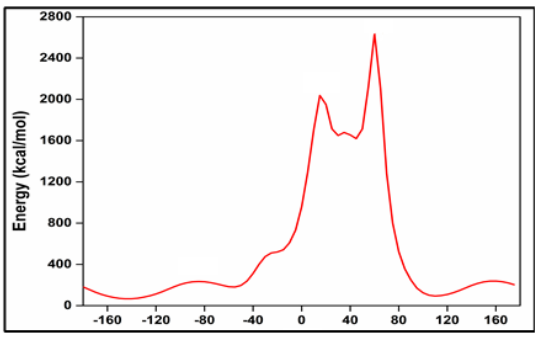

Figure 3B.7: *Conformational analysis over C7-C19*

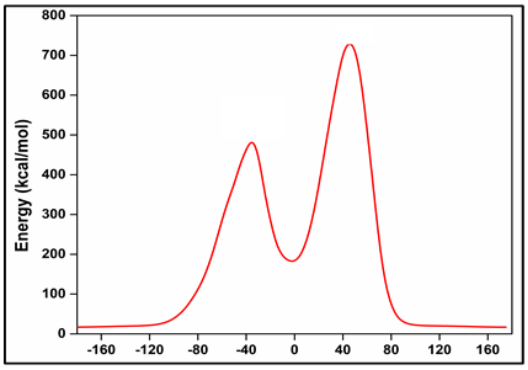

Figure 3B.8: *Conformational anaysis over C19-C20*

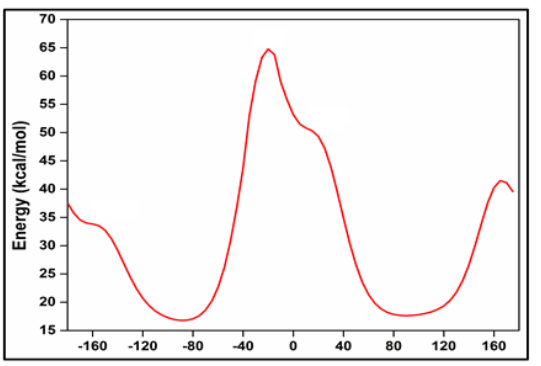

Figure 3B.9: *Conformational anaysis over C20-N21*

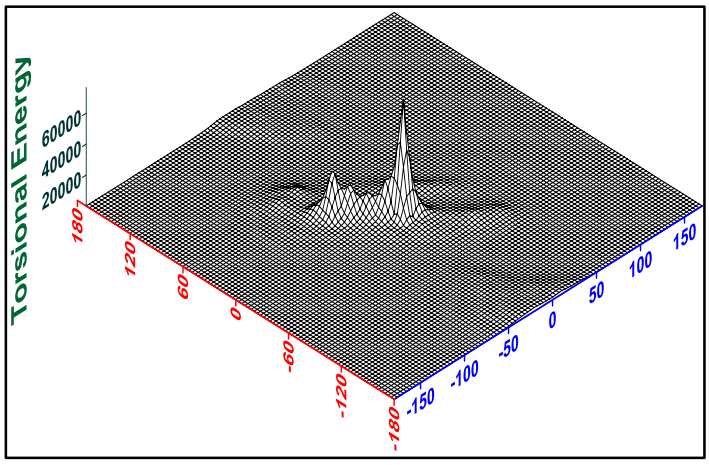

Figure 3B.10: *Double dihedral torsional energy Surfer plot of* ***FLXDTC*** *over C19-C20 (on axis shown in red) and C20-N21 (on axis shown in blue) bonds (Refer* ***Figure 3B.1*** *for numbering of the atoms)*

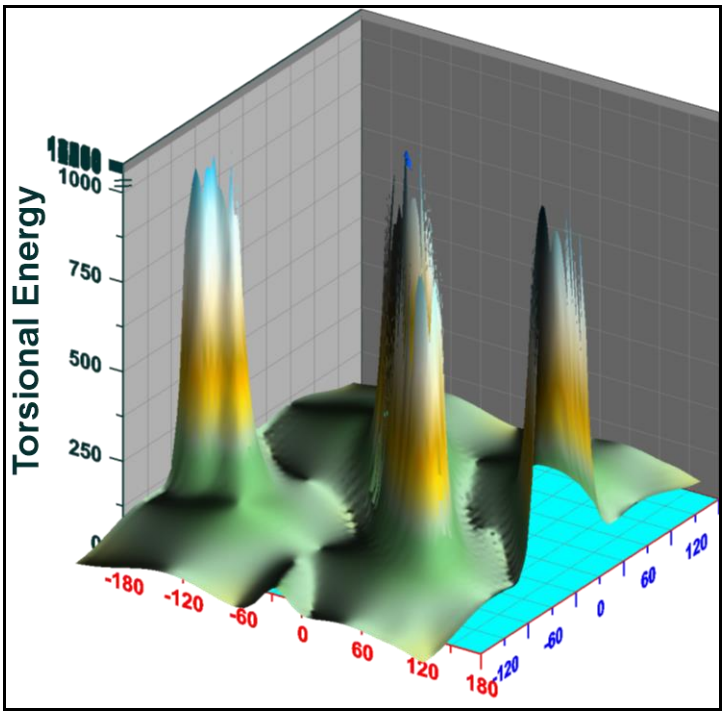

Figure 3B.11: *Double dihedral torsional energy Grapher plot of* ***FLXDTC*** *over C19-C20 (on axis shown in blue) and C20-N21 (on axis shown in red) bonds (Refer* ***Figure 3B.1*** *for numbering of the atoms)*

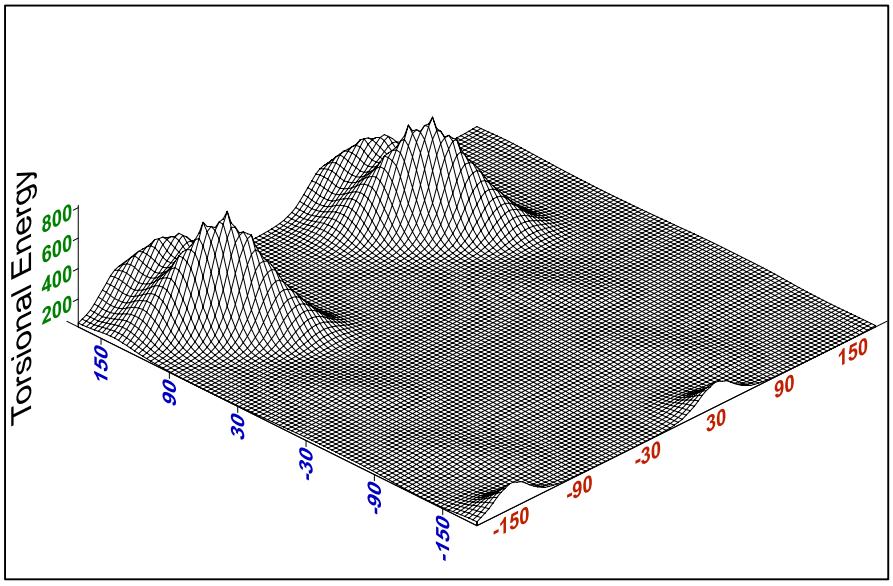

Figure 3B.12: *Double dihedral torsional energy Surfer plot of* ***FLXDTC*** *over C7-O8 (on axis shown in blue) and O8-C9 (on axis shown in red) bonds (Refer* ***Figure 3B.1*** *for numbering of the atoms)*

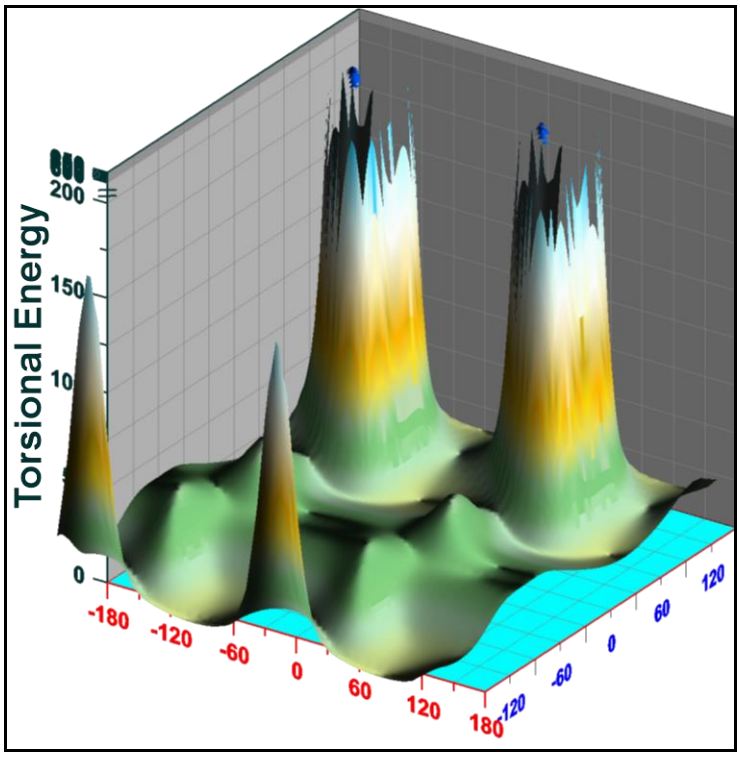

Figure 3B.13: *Double dihedral torsional energy Grapher plot of* ***FLXDTC*** *over C7-O8 (on axis shown in blue) and O8-C9 (on axis shown in red) bonds (Refer* ***Figure 3B.1*** *for numbering of the atoms)*

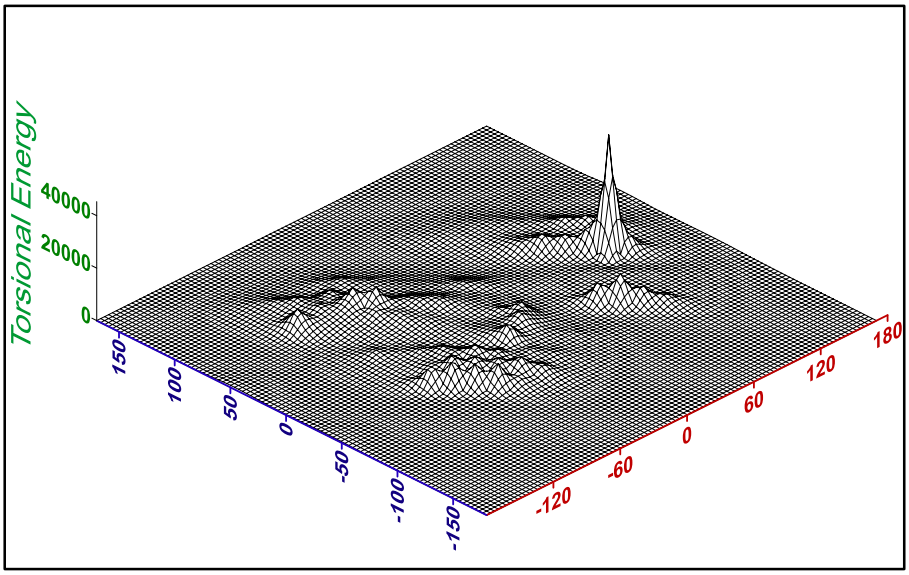

Figure 3B.14: *Double dihedral torsional energy Surfer plot of* ***FLXDTC*** *over C7-C9 (on axis shown in blue) and C9-C20 (on axis shown in red) bonds (Refer* ***Figure 3B.1*** *for numbering of the atoms)*

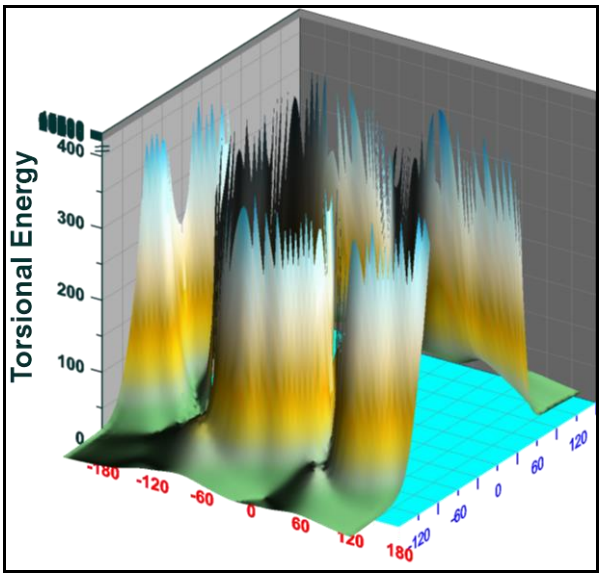

Figure 3B.15: *Double dihedral torsional energy Grapher plot of* ***FLXDTC*** *over C7-C9 (on axis shown in blue) and C9-C20 (on axis shown in red) bonds (Refer* ***Figure 3B.1*** *for numbering of the atoms)*

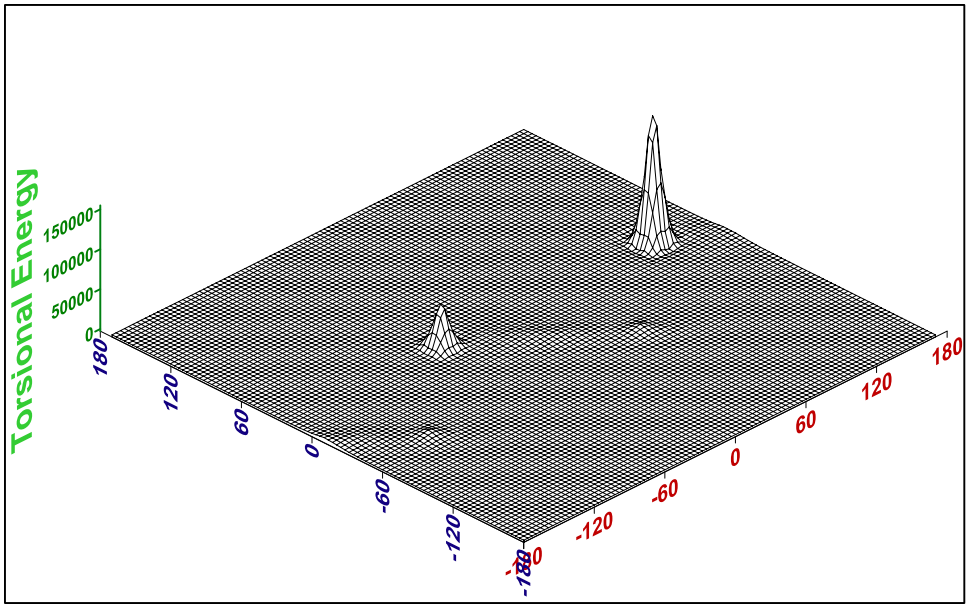

Figure 3B.16: *Double dihedral torsional energy Surfer plot of* ***FLXDTC*** *over C6-C7 (on axis shown in blue) and C7-O8 (on axis shown in red) bonds (Refer* ***Figure 3B.1*** *for numbering of the atoms)*

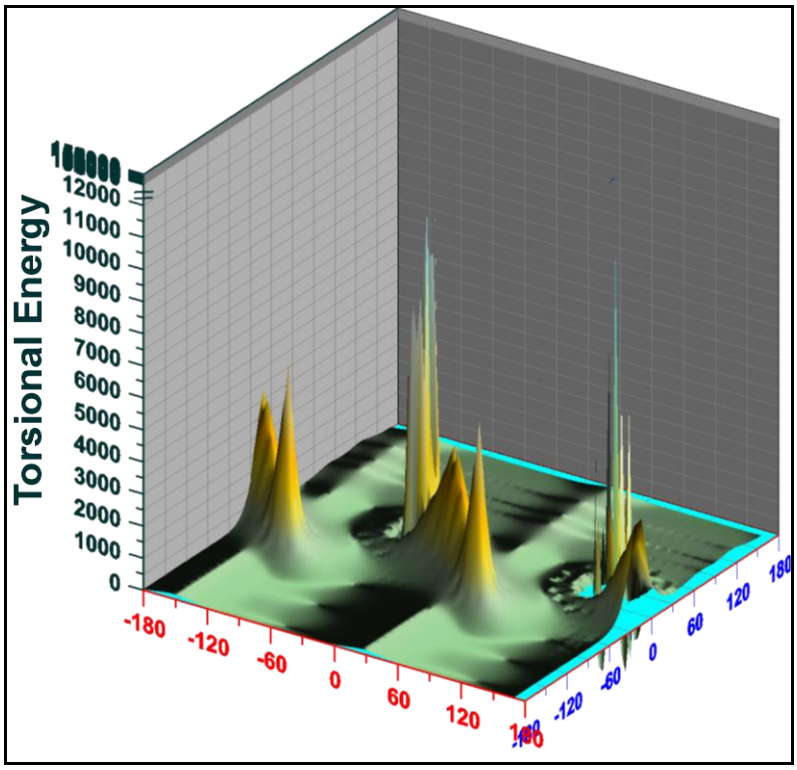

Figure 3B.17: *Double dihedral torsional energy Grapher plot of* ***FLXDTC*** *over C6-C7 (on axis shown in blue) and C7-O8 (on axis shown in red) bonds (Refer* ***Figure 3B.1*** *for numbering of the atoms)*

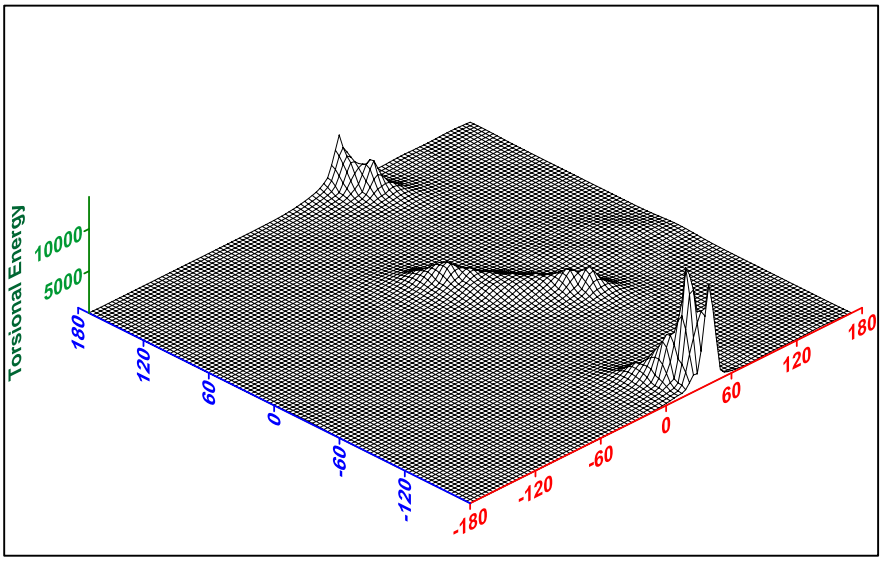

Figure 3B.18: *Double dihedral torsional energy Surfer plot of* ***FLXDTC*** *over C6-C7 (on axis shown in blue) and C7-C19 (on axis shown in red) bonds (Refer* ***Figure 3B.1*** *for numbering of the atoms)*

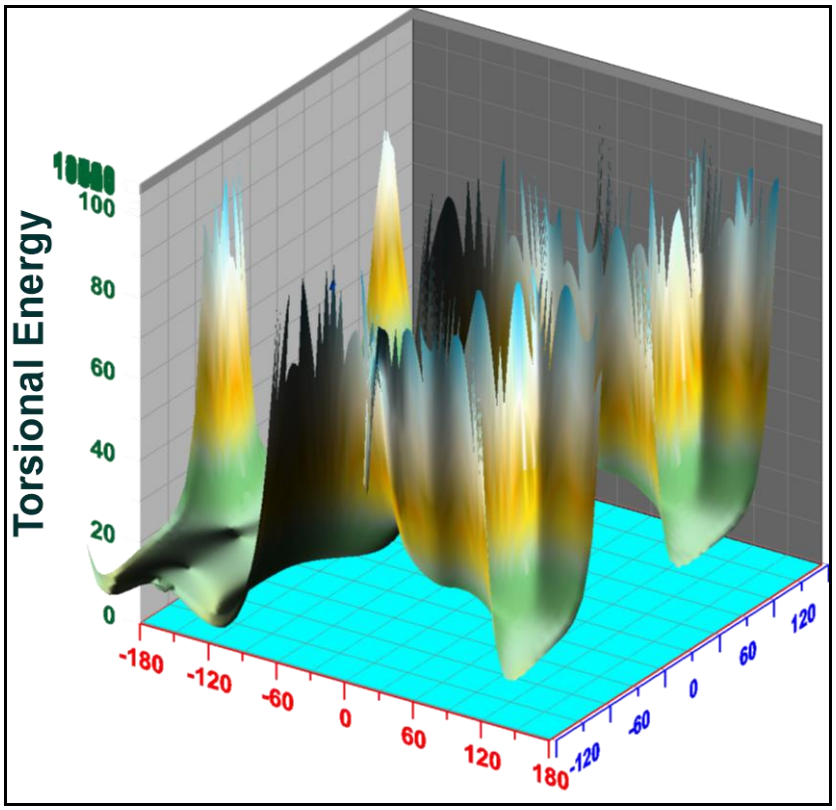

Figure 3B.19: *Double dihedral torsional energy Grapher plot of* ***FLXDTC*** *over C6-C7 (on axis shown in blue) and C7-C19 (on axis shown in red) bonds (Refer* ***Figure 3B.1*** *for numbering of the atoms)*

Quantum mechanical HOMO-LUMO orbital energy assessments were used to calculate the projected gas-phase electronic transitions. The HOMO-LUMO energy diagrams of **FLXDTC** ligand and corresponding metal complexes are depicted in **Figure 3B.21** through **Figure 3B.26.** Some of the data regarding bond length, bond angle and torsional angle for **M(FLXDTC)$_2$** complexes obtained from MM2 calculations are included in **Table 3B.1** and **Table 3B.2**.

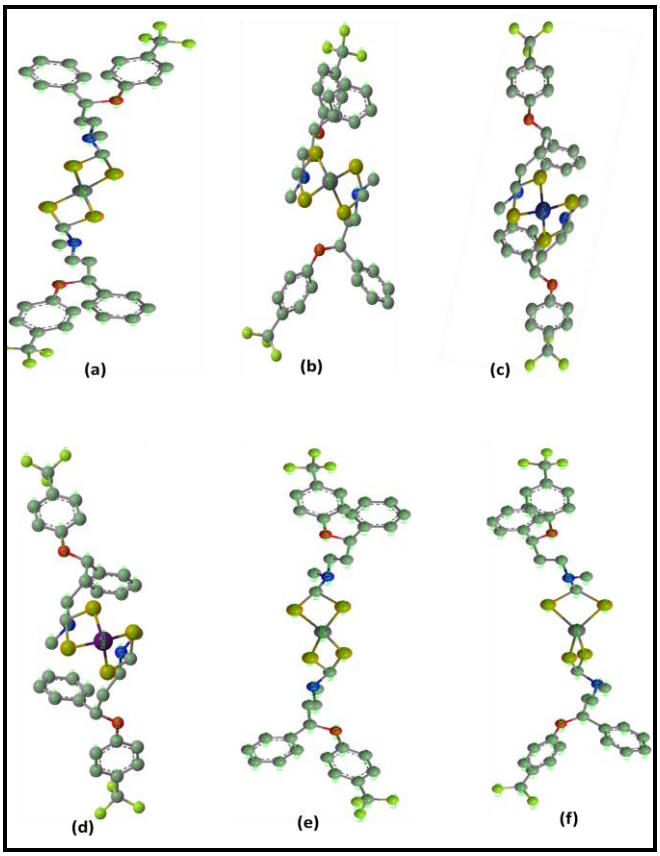

Figure 3B.20: *Global minimized ball-stick models of* ***(a) Cu(FLXDTC)$_2$ (b) Ni(FLXDTC)$_2$ (c) Co(FLXDTC)$_2$ (d) Mn(FLXDTC)$_2$ (e) Zn(FLXDTC)$_2$*** *and* ***(f) Cd(FLXDTC)$_2$*** *(The hydrogen atoms are hidden for clarity)*

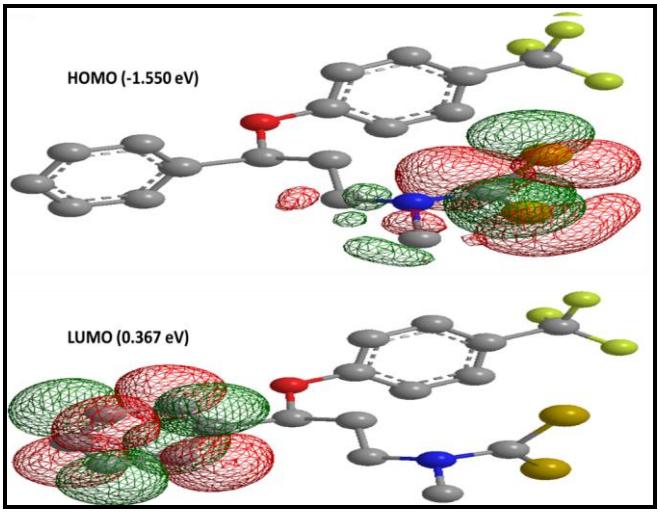

Figure 3B.21: *HOMO and LUMO molecular orbitals of* ***FLXDTC*** *in wire mesh format (H-atoms and lone pairs of electrons are excluded for clarity)*

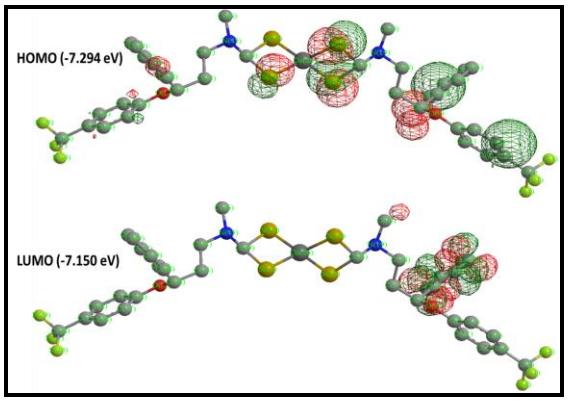

Figure 3B.22: *HOMO and LUMO molecular orbitals of* ***Cu(FLXDTC)$_2$*** *in wire mesh format (H-atoms and lone pairs of electrons are excluded for clarity)*

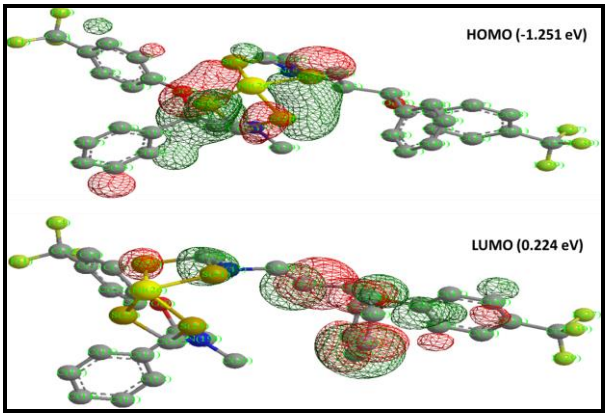

Figure 3B.23: *HOMO and LUMO molecular orbitals of* ***Ni(FLXDTC)$_2$*** *in wire mesh format (H-atoms and lone pairs of electrons are excluded for clarity)*

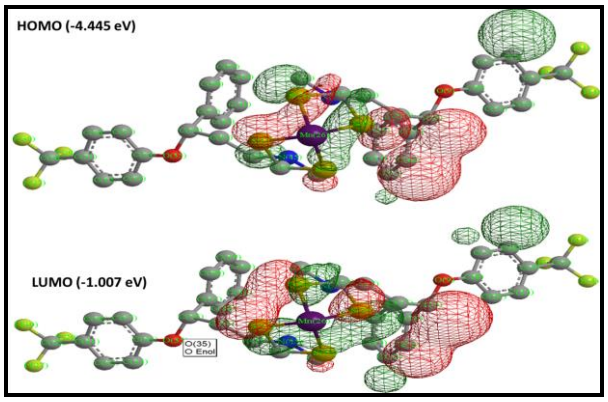

Figure 3B.24: *HOMO and LUMO molecular orbitals of* ***Mn(FLXDTC)$_2$*** *in wire mesh format (H-atoms and lone pairs of electrons are excluded for clarity)*

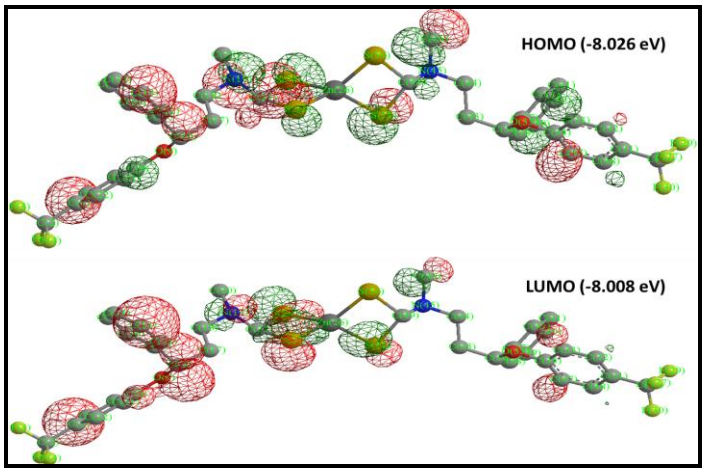

Figure 3B.25: *HOMO and LUMO molecular orbitals of* ***Zn(FLXDTC)$_2$*** *in wire mesh format (H-atoms and lone pairs of electrons are excluded for clarity)*

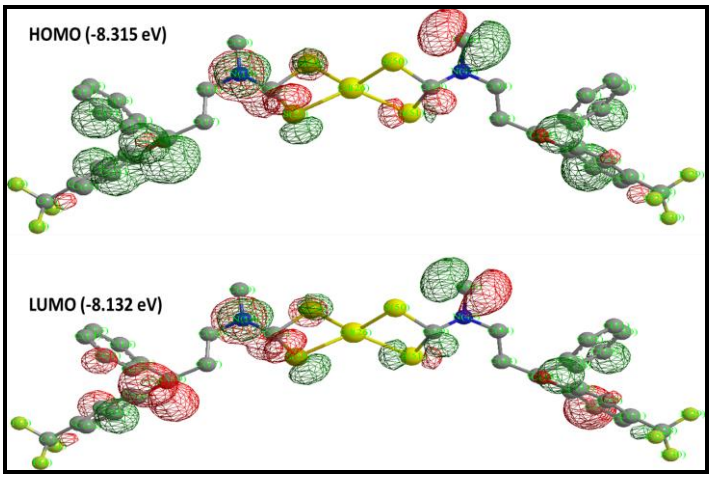

Figure 3B.26: *HOMO and LUMO molecular orbitals of* ***Cd(FLXDTC)$_2$*** *in wire mesh format (H-atoms and lone pairs of electrons are excluded for clarity)*

3B.2 Molecular Docking Studies of FLXDTC and M(FLXDTC)$_2$:

The cell-membrane receptor, EGFR-TK (pdb id: 4HJO), is in the family of epidermal growth factor tyrosine kinase receptors[16]. Anal cancer and epithelial tumors of the neck and head are caused by excess expression of EGFR[17]**.** On the basis of this feature, we have considered EGFR as a target protein receptor for molecular docking studies with **FLXDTC** and **M(FLXDTC)$_2$.** The binding energies resulted in after the docking studies are collected into **Table 3B.3**. The binding energies of the ligand and complexes with the protein receptor EGFR (as shown in **Table 3B.3**)

are suggestive of good binding to the EGFR protein receptor. The docking studies also reveal that the **Cd(FLXDTC)$_2$** and **Mn(FLXDTC)$_2$** exhibit least binding energies i.e., -9.0 kcal mol^{-1} and -8.6 kcal mol^{-1} respectively against EGFR. Molecular docking interactions are shown in **Figure 3B.9** through **Figure 3B.15**.

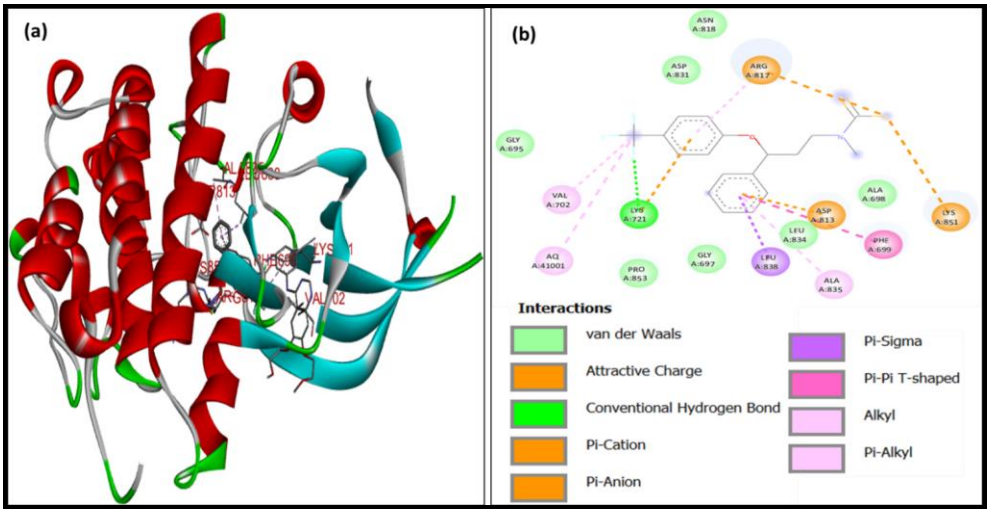

Figure 3B.27: *Molecular docking interactions of* ***FLXDTC*** *with EGFR protein; (a) 3D depiction of ligand-receptor binding interactions and (b) 2D representation of different forms of interactions with amino acid residues*

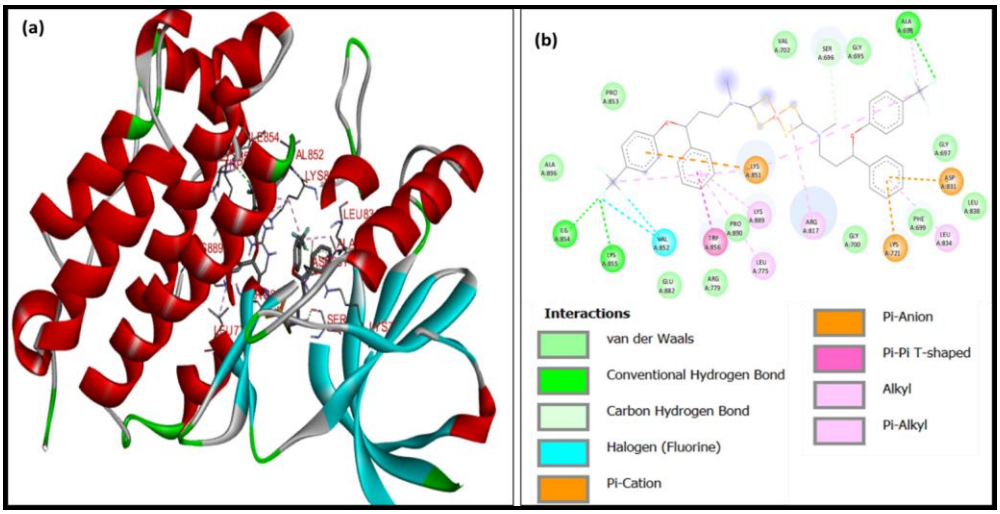

Figure 3B.28: *Molecular docking interactions of* ***Cu(FLXDTC)$_2$*** *with EGFR protein; (a) 3D depiction of ligand-receptor binding interactions and (b) 2D representation of different forms of interactions with amino acid residues*

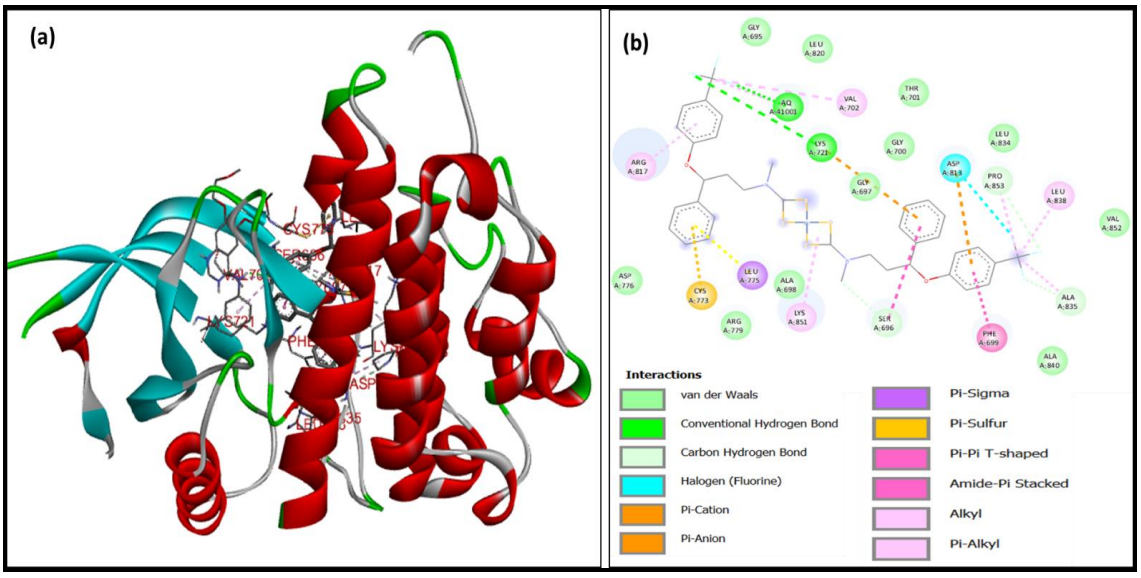

Figure 3B.29: *Molecular docking interactions of* ***Ni(FLXDTC)$_2$*** *with EGFR protein; (a) 3D depiction of ligand-receptor binding interactions and (b) 2D representation of different forms of interactions with amino acid residues*

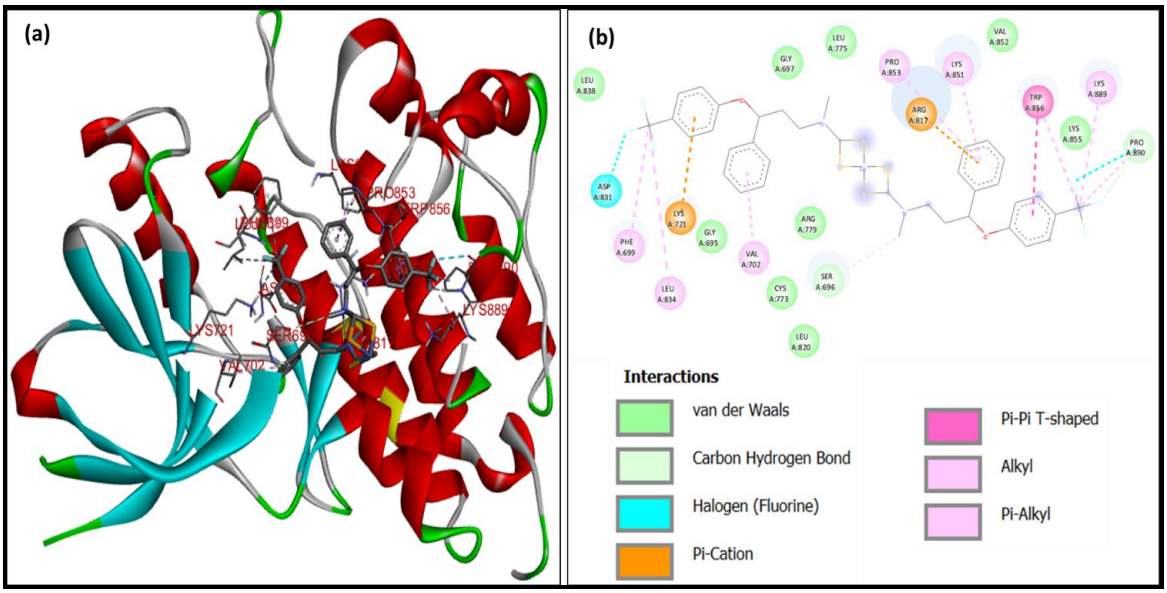

Figure 3B.30: *Molecular docking interactions of* ***Co(FLXDTC)$_2$*** *with EGFR protein; (a) 3D depiction of ligand-receptor binding interactions and (b) 2D representation of different forms of interactions with amino acid residues*

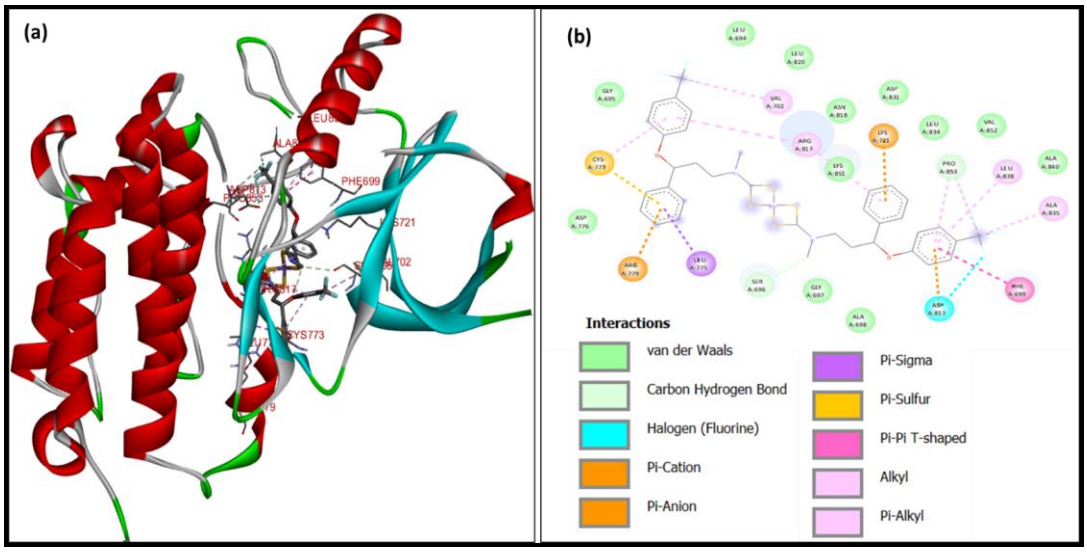

Figure 3B.31: *Molecular docking interactions of* ***Mn(FLXDTC)$_2$*** *with EGFR protein; (a) 3D depiction of ligand-receptor binding interactions and (b) 2D representation of different forms of interactions with amino acid residues*

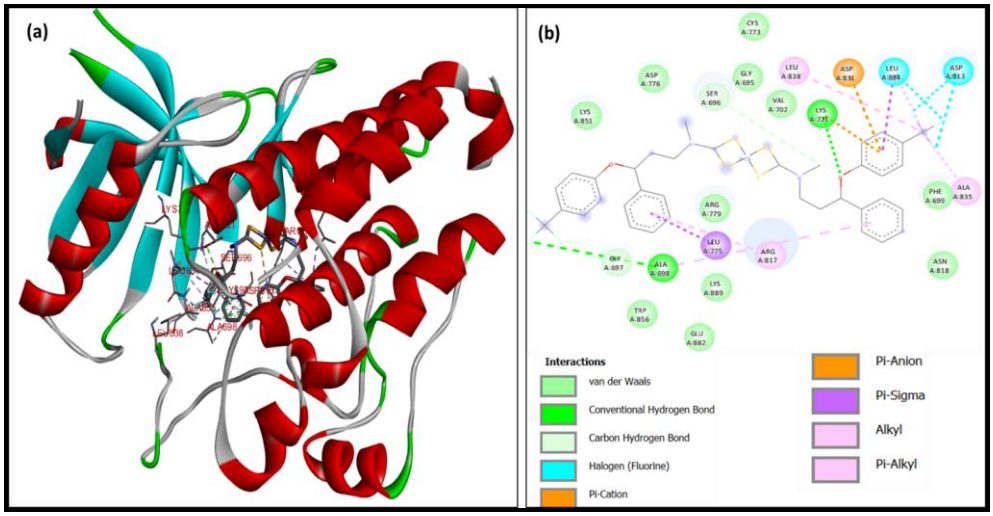

Figure 3B.32: *Molecular docking interactions of* ***Zn(FLXDTC)$_2$*** *with EGFR protein; (a) 3D depiction of ligand-receptor binding interactions and (b) 2D representation of different forms of interactions with amino acid residues*

The **Cu(FLXDTC)$_2$** complex docks to the EGFR protein via four hydrogen bond interactions, three of them are through fluorine atoms with the protein amino acid residues ALA698, ILE854 and LYS855 and one hydrogen bond interaction through the –NCH_3 group with the amino acid residue of SER696. Furthermore, this complex docks through two halogen

interactions with VAL852, three electrostatic interactions with ASP831, LYS721, LYS 851 and nine hydrophobic interactions with the amino residues of TRP856, ALA698, ARG817, LYS851, LEU834, LEU775 and LYS889.

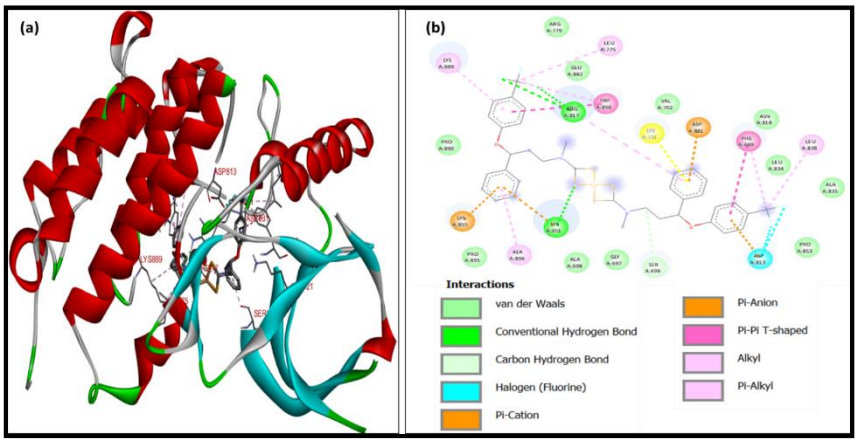

Figure 3B.33: *Molecular docking interactions of* ***Cd(FLXDTC)$_2$*** *with EGFR protein; (a) 3D depiction of ligand-receptor binding interactions and (b) 2D representation of different forms of interactions with amino acid residues*

The **Ni(FLXDTC)$_2$** complex docks to the EGFR through a total of five hydrogen bond interactions, three of them are through the fluorine atoms with protein amino acid residues of LYS721, ALA 835 and two are through –NCH_3 group with the amino acid residues of PRO853 and SER696. Furthermore, it docks through one hydrophobic interaction with ASP813, two electrostatic interactions with LYS721, ASP813 and nine hydrophobic interactions with the amino residues of PHE699, SER696, ALA835, LYS851, LEU838, PRO853, VAL702 and ARG817.

Table 3B.1: *Some of the important bond lengths and bond angles of* ***ML$_2$ (L=FLXDTC)*** *(Refer* ***Figure 3B.20*** *for numbering of the atoms)*

Bond lengths (Å)	**M = Cu**	**M = Ni**	**M = Co**	**M = Mn**	**M = Zn**	**M = Cd**
M-S_{50}	2.190	2.182	2.189	2.200	2.277	2.505
M-S_{51}	2.189	2.181	2.193	2.202	2.278	2.505
M-S_{24}	2.189	2.182	2.189	2.200	2.277	2.505
M-S_{25}	2.189	2.181	2.193	2.202	2.277	2.505
C_{49}-S_{50}	1.917	1.835	1.838	2.200	1.939	1.973

C_{49}-S_{51}	1.916	1.836	1.838	2.202	1.937	1.970
C_{23}-S_{24}	1.918	1.835	1.838	1.840	1.939	1.973
C_{23}-S_{24}	1.916	1.834	1.838	1.838	1.937	1.970
N_{19}-C_{23}	1.464	1.460	1.460	1.460	1.465	1.467
N_{19}-C_{20}	1.458	1.456	1.463	1.461	1.457	1.456
C_{18}-N_{19}	1.465	1.461	1.462	1.463	1.465	1.465
C_{49}-N_{45}	1.464	1.460	1.460	1.460	1.465	1.467
N_{45}-C_{46}	1.458	1.456	1.463	1.461	1.457	1.456
N_{45}-C_{44}	1.465	1.462	1.462	1.463	1.465	1.465
Bond angles (°)						
$C_{18}N_{19}C_{20}$	108.8	111.9	107.8	108.0	109.0	109.4
$C_{18}N_{19}C_{23}$	112.6	111.4	114.2	113.9	112.5	112.6
$C_{20}N_{19}C_{23}$	113.1	110.0	110.7	111.5	113.5	114.0
$N_{19}C_{23}S_{24}$	116.8	113.1	112.6	114.0	117.0	116.9
$N_{19}C_{23}S_{25}$	110.5	116.0	117.2	115.5	109.5	108.1
$C_{23}S_{24}M$	87.9	103.8	100.5	100.4	86.4	85.8
$C_{23}S_{25}M$	87.9	106.2	100.4	100.4	86.4	85.8
$S_{24}MS_{25}$	84.2	67.8	71.1	70.8	83.8	79.6
$S_{24}C_{23}S_{25}$	100.0	81.9	87.7	87.7	103.4	108.8
$S_{24}MS_{50}$	123.6	104.8	114.4	111.5	123.9	126.5
$S_{25}MS_{51}$	123.3	70.0	103.5	106.6	123.5	126.0
$S_{50}MS_{51}$	84.3	72.0	71.1	70.8	83.8	79.6
$S_{50}C_{49}S_{51}$	100.1	88.6	87.7	87.7	103.4	108.8
$N_{45}C_{49}S_{51}$	110.5	114.5	117.2	115.5	109.5	108.1
$N_{45}C_{49}S_{50}$	117.1	114.4	112.6	114.0	117.0	116.9
$C_{46}N_{45}C_{49}$	113.2	110.6	110.7	111.5	113.5	114.0
$C_{44}N_{45}C_{49}$	112.5	110.7	114.2	114.0	112.5	112.6

Table 3B.2: *Some of the important dihedral angles of* ***ML_2 (L=FLXDTC)*** *(Refer* ***Figure 3B.20*** *for numbering of the atoms)*

Dihedral angles (Å)	**M = Cu**	**M = Ni**	**M = Co**	**M = Mn**	**M = Zn**	**M = Cd**
$N_{19}C_{23}S_{25}M$	-123.2	-98.0	-109.3	-108.9	-125.3	-127.9
$N_{19}C_{23}S_{24}M$	+118.6	+95.5	+113.6	+110.3	+120.4	+122.7
$C_{23}S_{24}MS_{50}$	-125.9	-54.4	-51.6	-52.2	-126.6	-127.5
$C_{23}S_{24}MS_{51}$	+126.9	-118.5	-108.5	-110.8	+126.6	+127.3
$C_{23}S_{25}MS_{50}$	+126.3	+113.8	+121.9	+116.9	+126.8	+128.0

$C_{23}S_{25}MS_{51}$	-127.1	+53.7	+58.2	+55.2	-126.6	-127.4
$N_{45}C_{49}S_{50}M$	+119.5	+111.8	+113.6	-108.9	+120.4	+122.7
$N_{45}C_{49}S_{51}M$	-124.2	-111.7	-109.3	-108.9	-125.4	-127.9
$C_{49}S_{50}MS_{25}$	+126.3	-117.0	-108.5	-110.8	+126.6	+127.3
$C_{49}S_{50}MS_{24}$	-126.9	-58.7	-51.6	+127.6	-126.6	-127.5
$C_{49}S_{51}MS_{24}$	+127.0	+109.9	+121.9	+116.9	+126.8	+127.9
$C_{49}S_{51}MS_{25}$	-126.1	+54.0	+58.2	+55.2	-126.6	-127.4

Table 3B.3: *Docking data of* ***FLXDTC*** *and its metal complexes with the EGFR protein*

Compound	**Binding energy (kcal mol^{-1})**	**No. of H-bonds**	**Proteins residues involved in the interactions**
FLXDTC	-6.4	2	ASN818, ASP831, ARG817, GLY695, VAL702, LYS721, PRO853, GLY697, LEU838, LEU834, ASP813, ALA835, PHE699, LYS851
Cu(FLXDTC)$_2$	-8.3	4	ILE854, LYS855, VAL852, TRP856, LYS851, LYS889, LEU775, ARG817, SER696, ALA698, LYS721, ASP831, LEU834
Ni(FLXDTC)$_2$	-8.4	5	GLY695, LEU820, VAL702, LYS721, THR701, GLY700, GLY697, ASP813, LEU834, PRO853, LEU838, VAL852, ALA835, PHE699, ALA840, ARG817, ASP776, CYS773, LEU775, ALA698,
Co(FLXDTC)$_2$	-8.1	3	GLY697, LEU775, PRO853, ARG817, VAL852, TRP856, LYS855, LYS889, PRO890, LEU838, ASP831, LYS721, PHE699, GLY695, LEU834, VAL702, ARG779, SER696,CYS773, LEU820
Mn(FLXDTC)$_2$	-8.6	3	LEU694, LEU820, VAL702, ARG817, ASN818, ASP831, LYS851, LYS721, LEU834, PRO853, LEU838, ALA840, ALA835, ASP813, PHE699, GLY695, CYS773, ASP776, ARG779, LEU775, SER696, GLY697, ALA698
Zn(FLXDTC)$_2$	-7.8	5	LYS851, ASP776, SER696, GLY695, CYS773, VAL702, LEU838, LYS721, ASP831, LEU834, ASP813, PHE699, ALA835, ARG779, GLY697, ALA698, LEU775, ARG817, TRP856, LYS889
Cd(FLXDTC)$_2$	-9.0	5	GLY697, LEU775, PRO853, ARG817, LYS851, VAL852, TRP856, LYS855, LYS889, PRO890, LEU838, ASP831, PHE699, LYS721, LEU834, GLY695, VAL702, ARG779, SER696, CYS773

The **Co(FLXDTC)$_2$** complex docks to the EGFR via three hydrogen bond interactions, one through the fluorine atom with PRO890 protein amino acid residue and one through the -NCH3 group with SER696 amino acid residue. Two fluorine atoms interacts with the amino acid residues ASP831, PRO890 through halogen interactions. This complex also has two electrostatic interactions with LYS721, ARG817 along with nine hydrophobic interactions with TRP856, LYS889, PRO890, LEU834, PHE699, LYS851, PRO853, and VAL702.

The **Mn(FLXDTC)$_2$** complex docks to the EGFR via two hydrogen bond interactions, one through the aromatic carbon with amino acid residue PRO853, and another hydrogen bond interaction through the N-atom with SER696. Furthermore, this complex interacts with amino acid residues ASP813 via halogen interactions. This complex also interacts electrostatically with LYS721, ARG779, and ASP831, as well as hydrophobically with LEU775, PHE699, ALA835, PRO853, VAL702, LEU838, ARG817 and CYS773.

The **Zn(FLXDTC)$_2$** complex docks to the EGFR via five hydrogen bond interactions, two of them are through two fluorine atoms with the protein amino acid residues of ALA698, GLY697, one interaction is through –NCH_3 group with amino acid residue of SER696 and two more are formed with oxygen atom and EGFR's amino acid residue of LYS721. This complex has hydrophobic interactions with the amino acid residues of LEU775, LEU834, ALA835, LEU838, ALA698, ARG817. Moreover, it interacts with the amino acid residue of ASP831 through electrostatic interaction, in addition to the six hydrophobic interactions with LEU775, LEU834, ALA835, LEU838, ALA698 and ARG817.

The **Cd(FLXDTC)$_2$** complex has five hydrogen bonds, three of which are formed between fluorine atoms and amino acid residue of ARG817 and one is formed between the S-atom and LYS851 amino acid residue. Besides, this complex also interacts with amino acid residue ASP813 through halogen interactions, along with electrostatic interactions with amino acid residues LYS721, LYS851, LYS855, ASP813 and ASP831. This complex has nine hydrophobic interactions with the PHE699, TRP856, LEU838, LEU775, ARG817, LYS889 and ALA896.

PART C

BIOLOGICAL ACTIVITY STUDIES OF THE TITLE COMPOUNDS

3C.1 *In Vitro* Antimicrobial Activity:

The microbial activity of **FLXDTC** ligand and its various dithiocarbamate complexes were screened against two gram positive and two gram negative bacteria and with *streptomycin* as the standard[18]**.** The tested results are collected in **Table 3C.1.**

Table 3C.1*: Antibacterial MIC values of* ***FLXDTC*** *and* ***[M(FLXDTC)$_2$]*** *(μg/ml)*

Compound	*S. aureus*	*B. subtilis*	*K. pneumoniae*	*E. coli*
Cu(FLXDTC)$_2$	9.46	7.16	8.41	8.25
Zn(FLXDTC)$_2$	16.58	16.39	14.26	13.31
Cd(FLXDTC)$_2$	>100	21.22	18.25	26.45
Ni(FLXDTC)$_2$	15.25	22.36	14.52	12.95
Co(FLXDTC)$_2$	12.12	13.25	12.58	13.48
Mn(FLXDTC)$_2$	32.22	39.57	33.57	14.19
FLXDTC	>100	>100	40.12	30.14
Streptomycin	4.32	3.53	3.14	3.85

The results reveal that the ligand shows less activity against both gram negative and gram positive microorganisms. Complexes **Zn(FLXDTC)$_2$, Cd(FLXDTC)$_2$** and **Co(FLXDTC)$_2$** show moderate inhibitory activity whereas **Cu(FLXDTC)$_2$** shows good activity.

3C.2 *In Vitro* Antioxidant Property:

The scavenging activity has been studied on the free radical *DPPH* (2,2-Diphenyl-1-picrylhydrazyl). The results are collected in the **Table 3C.2.** The data suggest some reasonable antioxidant activity for **Cd(FLXDTC)$_2$**, **Mn(FLXDTC)$_2$**, and **Ni(FLXDTC)$_2$** in the same order. Further, the activity of some of the complexes, **Cd(FLXDTC)$_2$** and **Mn(FLXDTC)$_2$),** is lower than that of the standard to which **Cu(FLXDTC)$_2$** has a closer and some promising activity (**Figure 3C.1**).

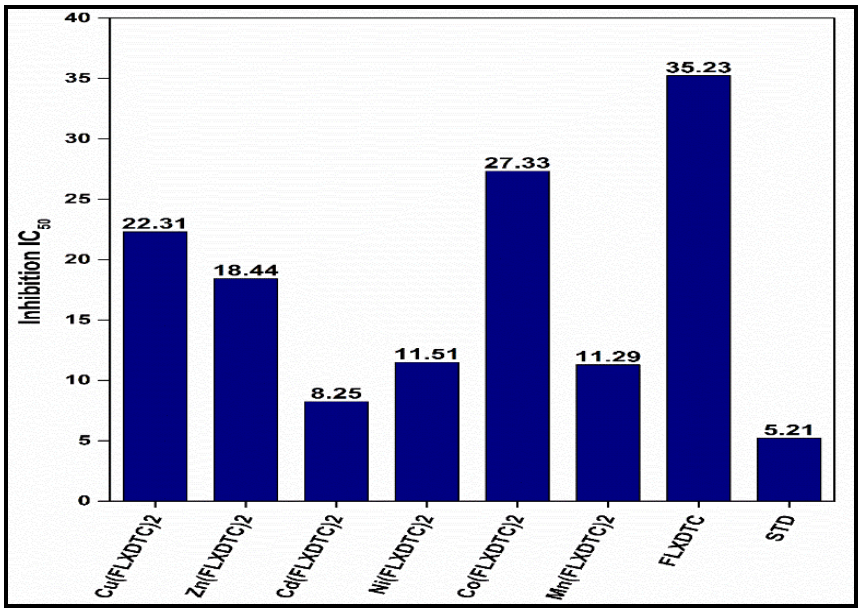

Figure 3C.1: *Histographical representation of the IC_{50} inhibition values of DPPH radical scavenging activity of* ***FLXDTC*** *and* ***M(FLXDTC)$_2$***

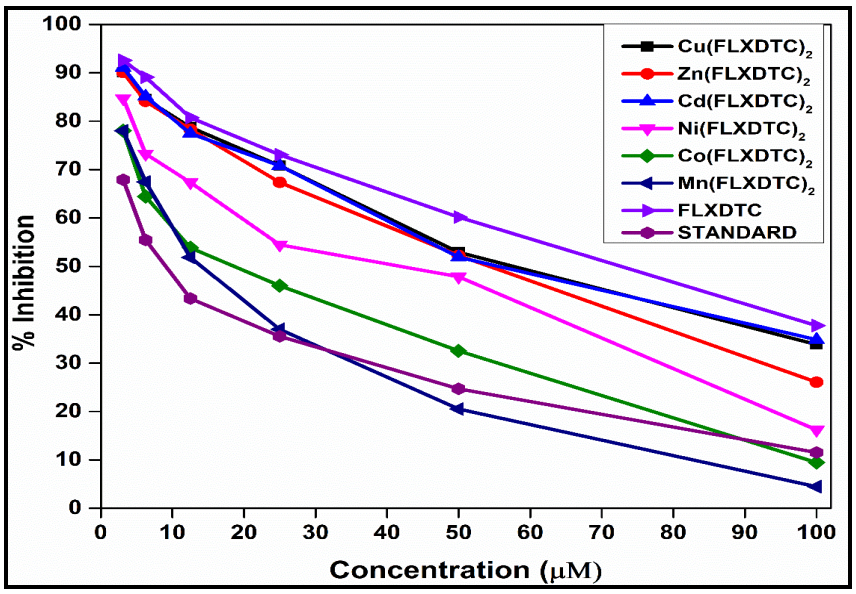

Figure 3C.2: *Cell viability assay; dose-response curves of* ***FLXDTC*** *and its metal complexes with different concentrations on MCF7 cells*

Table 3C.2: *Anti-scavenging activity MIC values of* ***FLXDTC*** *and* ***[M(FLXDTC)$_2$]*** *(µg/ml)*

Compound	IC_{50} (µM)
Cu(FLXDTC)$_2$	22.31 ± 1.25
Zn(FLXDTC)$_2$	18.44 ± 1.09
Cd(FLXDTC)$_2$	8.25 ± 1.13
Ni(FLXDTC)$_2$	11.51 ± 1.38
Co(FLXDTC)$_2$	27.33 ± 1.67
Mn(FLXDTC)$_2$	11.29 ± 1.85
FLXDTC	35.23 ± 1.41
Ascorbic acid	5.21 ± 0.12

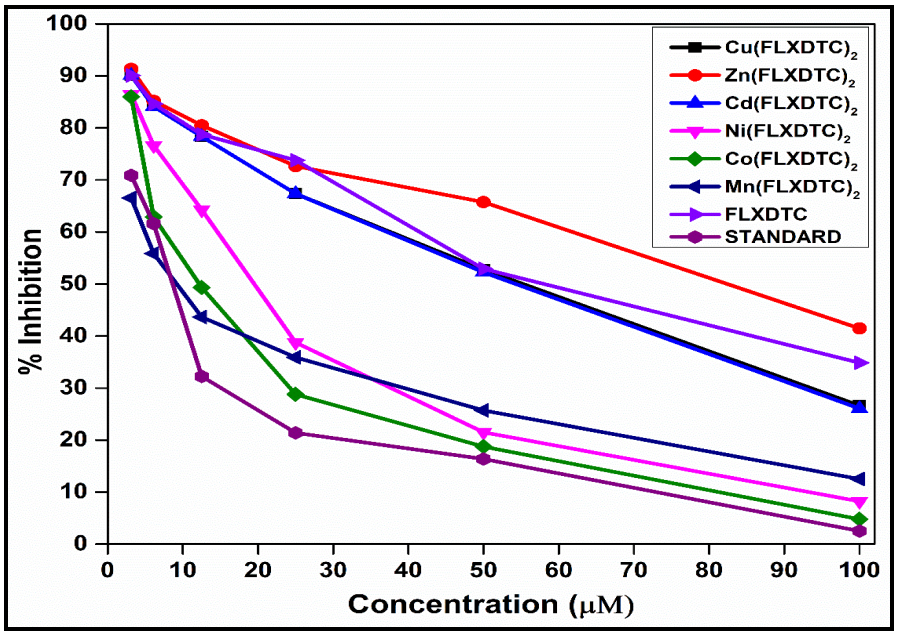

Figure 3C.3: *Cell viability assay; dose-response curves of* ***FLXDTC*** *and its metal complexes with different concentrations on HepG-2 cells*

3C.3 *In Vitro* Antifungal Activity:

In vitro antifungal activity studies of fluoxetine dithiocarbamate ligand **(FLXDTC)** and its complexes are investigated with help of the two fungal strains, *Asperegillusniger*, *pencilliumnotatum* with ketoconazole drug as standard. The results are furnished in the **Figure**

3C.3. The antifungal activity of **Cu(FLXDTC)$_2$**, **Co(FLXDTC)$_2$** are reasonably closer to the standard for both the fungal strains.

Table 3C.3: *Antifungal activity MIC values of* ***FLXDTC*** *and* ***[M(FLXDTC)$_2$]*** *(μg/ml)*

Compound	***Asperegillusniger***	***Pencilliumnotatum***
Cu(FLXDTC)$_2$	3.12	5.14
Zn(FLXDTC)$_2$	7.40	6.47
Cd(FLXDTC)$_2$	9.35	9.12
Ni(FLXDTC)$_2$	6.25	6.25
Co(FLXDTC)$_2$	4.12	5.73
Mn(FLXDTC)$_2$	8.12	7.17
FLXDTC	10.53	13.86
Ketoconazole	1.75	2.62

3C.4 *In Vitro* Anticancer Activity:

Anticancer activity of **FLXDTC** and its complexes was tested against three cancer cell lines, MCF-7, HepG-2 and HEK-293 by MTT assay method with cisplatin as standard. The results are put in the **Table 3C.4**. From the results only **Cd(FLXDTC)$_2$** and **Zn(FLXDTC)$_2$** exhibits some promising results.

Table 3C.4: *Anticancer activity MIC values of* ***FLXDTC*** *and* ***[M(FLXDTC)$_2$]*** *(μg/ml)*

Codes	**MCF-7**	**HepG-2**	**HEK 293**
Cu(FLXDTC)$_2$	63.49 ± 1.06	57.24 ± 1.14	ND
Zn(FLXDTC)$_2$	28.63 ± 1.36	19.24 ± 1.04	91.62 ± 1.121
Cd(FLXDTC)$_2$	23.08 ± 0.12	12.30 ± 0.25	85.58 ± 1.36
Ni(FLXDTC)$_2$	58.59 ± 0.382	80.97 ± 0.359	ND
Co(FLXDTC)$_2$	62.04 ± 1.219	58.12 ± 0.125	ND
Mn(FLXDTC)$_2$	49.04 ± 0.453	31.92 ± 1.28	ND
FLXDTC	74.15 ± 0.536	67.24 ± 1.39	ND
Cisplatin	11.60 ± 0.32	6.25 ± 0.17	ND

Note: A major part of the results and discussion presented in this Chapter have been published in a Springer journal (***Synthesis and Spectral, Electrochemical, Protein-Docking and Biological Studies of Fluoxetine Dithiocarbamate and Its Bivalent Metal Complexes***, Dhananjay Rao Thandra et al, *Chemistry Africa*, 2021, **4**, 777 – 789)

Springer Link

Original Article | Published: 29 September 2021

Synthesis and Spectral, Electrochemical, Protein-Docking and Biological Studies of Fluoxetine Dithiocarbamate and Its Bivalent Metal Complexes

Dhananjay Rao Thandra, Venkata Bharat Nishtala & Ramachandraiah Allikayala

Chemistry Africa **4**, 777–789 (2021) | Cite this article

28 Accesses | Metrics

Graphic Abstract

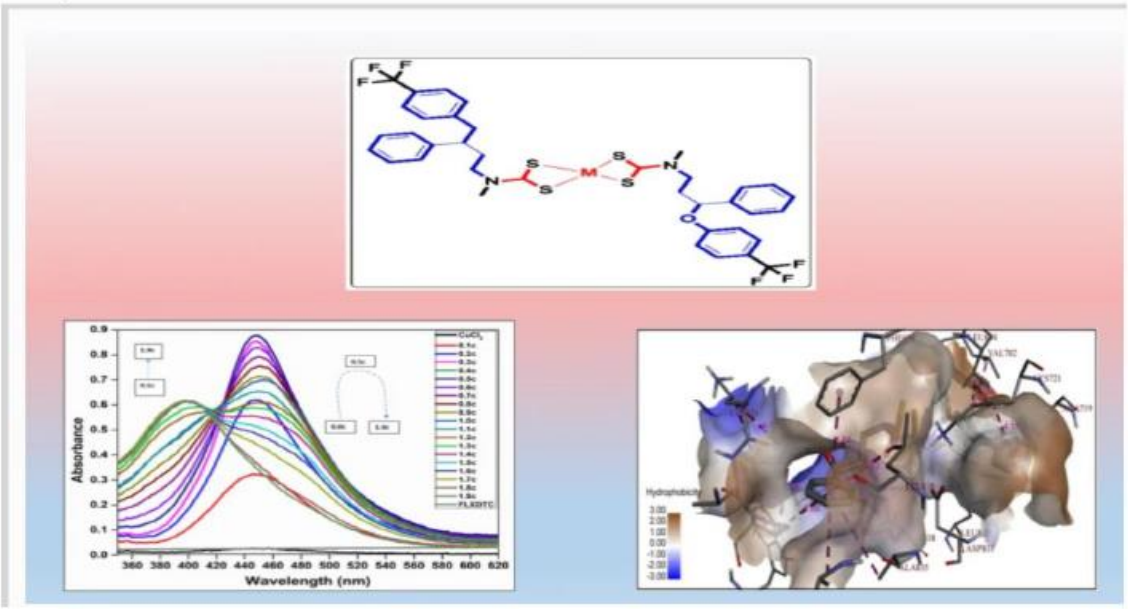

References

(1). (a) Gurumoorthy, G.; Thirumaran, S.; Ciattini, S. Synthesis and Characterization of Copper(II) Dithiocarbamate Complexes Involving Pyrrole and Ferrocenyl Moieties and Their Utility for Sensing Anions and Preparation of Copper Sulfide and Copper-Iron Sulfide Nanoparticles. Applied Organometallic Chemistry 2018, 32 (6), e4363. https://doi.org/10.1002/aoc.4363.

(b) Ekennia, A. C.; Onwudiwe, D. C.; Ume, C.; Ebenso, E. E. Mixed Ligand Complexes of N -Methyl- N -Phenyl Dithiocarbamate: Synthesis, Characterisation, Antifungal Activity, and Solvent Extraction Studies of the Ligand. Bioinorganic Chemistry and Applications 2015, 2015 (2), 1–10. https://doi.org/10.1155/2015/913424.

(c) Ajibade, P. A.; Andrew, F. P.; Fatokun, A. A.; Oluwalana, A. E. Synthesis, Characterization and in Vitro Screening for Anticancer Potential of Mn(II), Co(II), Cu(II), Zn(II), and Pt(II) Methoxyphenyl Dithiocarbamato Complexes. Journal of Molecular Structure 2021, 1230, 129894. https://doi.org/10.1016/j.molstruc.2021.129894.

(d) Boadi, N. O.; Degbevi, M.; Saah, S. A.; Badu, M.; Borquaye, L. S.; Kortei, N. K. Antimicrobial Properties of Metal Piperidine Dithiocarbamate Complexes against Staphylococcus Aureus and Candida Albicans. Scientific African 2021, 12, e00846. https://doi.org/10.1016/j.sciaf.2021.e00846.

(2). Kumar, A.; Jain, S. K. Development and Validation of UV-Spectroscopy Based Stability Indicating Method for the Determination of Fluoxetine Hydrochloride. Analytical Chemistry Letters 2016, 6 (6), 894–902. https://doi.org/10.1080/22297928.2016.1278180.

(3). (a) John, A.; Katiyar, V.; Pang, K.; Shaikh, M. M.; Nanavati, H.; Ghosh, P. Ni(II) and Cu(II) Complexes of Phenoxy-Ketimine Ligands: Synthesis, Structures and Their Utility in Bulk Ring-Opening Polymerization (ROP) of l-Lactide. Polyhedron 2007, 26 (15), 4033–4044. https://doi.org/10.1016/j.poly.2007.04.039.

(b) Takjoo, R.; Akbari, A.; Ahmadi, M.; Rudbari, H.; Bruno, G. New 5-Bromo-2-Hydroxybenzaldehyde S-Ethylisothiosemicarbazone and Its Mixed-Ligand Cu(II) Complex with Imidazole: Synthesis, Characterization and DFT Calculation. Open Chemistry 2013, 11 (11), 1844–1851. https://doi.org/10.2478/s11532-013-0313-5.

(c) Funkemeier, D.; Mattes, R. Synthesis and Structural Studies of Copper(II), Nickel(II) and Cobalt(II) Complexes of a 14-Membered Trans-N2S2 Dibenzo Macrocycle with Two Pendant Pyridylmethyl Groups. Journal of the Chemical Society, Dalton Transactions 1993, No. 8, 1313. https://doi.org/10.1039/dt9930001313.

(4). (a) Ünver, H.; Hayvali, Z. Synthesis, Spectroscopic Studies and Structures of Square-Planar Nickel(II) and Copper(II) Complexes Derived from 2-{(Z)-[Furan-2-Ylmethyl]Imino]Methyl}-6-Methoxyphenol. Spectrochimica Acta Part A: Molecular and Biomolecular Spectroscopy 2010, 75 (2), 782–788. https://doi.org/10.1016/j.saa.2009.11.055.

(b) Selvaganapathi, P.; Thirumaran, S.; Ciattini, S. Synthesis, Structural, DFT Calculations and Hirshfeld Surface Analysis of (N-Butyl-N-(4-Fluorobenzyl)Dithiocarbamato-S,S')-(Thiocyanato-N)(Triphenylphosphine)Nickel(II) and Preparation of Nickel Sulfide from

Nickel(II) Dithiocarbamate. Phosphorus, Sulfur, and Silicon and the Related Elements 2017, 192 (9), 1027–1033. https://doi.org/10.1080/10426507.2017.1317250.

(c) Nath, P.; Bharty, M. K.; Kushawaha, S. K.; Maiti, B. Synthesis, Spectral, Structural, Photoluminescence, Thermal and DFT Studies of Phenylmercury(II) and Ni(II) Complexes of 3-Methoxycarbonyl-Piperidine-1-Carbodithioate. Polyhedron 2018, 151, 503–509. https://doi.org/10.1016/j.poly.2018.06.010.

(5). Ekennia, A. C.; Onwudiwe, D. C.; Osowole, A. A. Spectral, Thermal Stability and Antibacterial Studies of Copper, Nickel and Cobalt Complexes of N -Methyl- N -Phenyl Dithiocarbamate. Journal of Sulfur Chemistry 2015, 36 (1), 96–104. https://doi.org/10.1080/17415993.2014.969731.94.

(6). Ajibade, P. A.; Andrew, F. P.; Botha, N. L.; Solomane, N. Synthesis, Crystal Structures and Anticancer Studies of Morpholinyldithiocarbamato Cu(II) and Zn(II) Complexes. Molecules 2020, 25 (16), 3584. https://doi.org/10.3390/molecules25163584.

(7). (a) Rani, P. J.; Thirumaran, S. Synthesis, Characterization, Cytotoxicity and Antimicrobial Studies on Bis(N -Furfuryl- N -(2-Phenylethyl)Dithiocarbamato- S , S ′)Zinc(II) and Its Nitrogen Donor Adducts. European Journal of Medicinal Chemistry 2013, 62, 139–147. https://doi.org/10.1016/j.ejmech.2012.12.047.

(b) Shaheen, F.; Badshah, A.; Gielen, M.; Dusek, M.; Fejfarova, K.; de Vos, D.; Mirza, B. Synthesis, Characterization, Antibacterial and Cytotoxic Activity of New Palladium(II) Complexes with Dithiocarbamate Ligands: X-Ray Structure of Bis(Dibenzyl-1-S:S′-Dithiocarbamato)Pd(II). Journal of Organometallic Chemistry 2007, 692 (14), 3019–3026. https://doi.org/10.1016/j.jorganchem.2007.03.019.

(c) Lakshmanan, P.; Sathiyaraj, E.; Thirumaran, S.; Ciattini, S. Unusual Intra- and Intermolecular Ni···H-C Anagostic Interactions in (N-(Pyrrol-2-Ylmethyl)-N-(2-Phenylethyl)Dithiocarbamato-S,S')- (Thiocyanato-KN)(Triphenylphosphine)Nickel(II): Synthesis, Spectral Properties, Crystal Structure, Hirshfeld Surface Analys. Phosphorus, Sulfur, and Silicon and the Related Elements 2021, 196 (7), 622–633. https://doi.org/10.1080/10426507.2021.1876059.

(8). (a) de Lima, G. M.; Menezes, D. C.; Cavalcanti, C. A.; dos Santos, J. A. F.; Ferreira, I. P.; Paniago, E. B.; Wardell, J. L.; Wardell, S. M. S. V.; Krambrock, K.; Mendes, I. C.; Beraldo, H. Synthesis, Characterisation and Biological Aspects of Copper(II) Dithiocarbamate Complexes, [Cu{S2CNR(CH2CH2OH)}2], (R=Me, Et, Pr and CH2CH2OH). Journal of Molecular Structure 2011, 988 (1–3), 1–8. https://doi.org/10.1016/j.molstruc.2010.11.048.

(b) Yamada, Y.; Uchida, M.; Fujita, M.; Miyashita, Y.; Okamoto, K. Optically Active Sulfur-Bridged Co(III)–M(II) (M=Pd, Pt) Dinuclear Complexes with Square-Planar [M(μ-S)2(Bpy)] (Bpy=2,2′-Bipyridine) Frameworks Derived from Octahedral Bidentate Sulfur-Donating Co(III) Metalloligands. Polyhedron 2003, 22 (12), 1507–1513. https://doi.org/10.1016/S0277-5387(03)00267-5.

(9). (a) Konakanchi, R.; Mallela, R.; Guda, R.; Kotha, L. R. Synthesis, Characterization, Biological Screening and Molecular Docking Studies of 2-Aminonicotinaldehyde (ANA) and Its Metal Complexes. Research on Chemical Intermediates 2018, 44 (1), 27–53.

https://doi.org/10.1007/s11164-017-3089-y.

(b) Abdi, Y.; Bensouilah, N.; Siziani, D.; Hamdi, M.; Silva, A. M. S.; Boutemeur-Kheddis, B. New Complexes of Manganese (II) and Copper (II) Derived from the Two New Furopyran-3, 4-Dione Ligands: Synthesis, Spectral Characterization, ESR, DFT Studies and Evaluation of Antimicrobial Activity. Journal of Molecular Structure 2020, 1202, 127307. https://doi.org/10.1016/j.molstruc.2019.127307.

(10). (a) Rabindra Reddy, P.; Shilpa, A. Synthesis, Characterization, and DNA-Binding and -Cleavage Properties of Dinuclear CuII□Salophen/Salen Complexes. Chemistry & Biodiversity 2011, 8 (7), 1245–1265. https://doi.org/10.1002/cbdv.201000153.

(b) Hathaway, B. J. A New Look at the Stereochemistry and Electronic Properties of Complexes of the Copper(II) Ion. In Complex Chemistry; Springer Berlin Heidelberg: Berlin, Heidelberg, 1984; pp 55–118. https://doi.org/10.1007/BFb0111454.

(11). Konakanchi, R.; Haribabu, J.; Prashanth, J.; Nishtala, V. B.; Mallela, R.; Manchala, S.; Gandamalla, D.; Karvembu, R.; Reddy, B. V.; Yellu, N. R.; Kotha, L. R. Synthesis, Structural, Biological Evaluation, Molecular Docking and DFT Studies of Co(II), Ni(II), Cu(II), Zn(II), Cd(II) and Hg(II) Complexes Bearing Heterocyclic Thiosemicarbazone Ligand. Applied Organometallic Chemistry 2018, 32 (8), e4415. https://doi.org/10.1002/aoc.4415.

(12). Bond, A. M.; Martin, R. L. Electrochemistry and Redox Behaviour of Transition Metal Dithiocarbamates. Coordination Chemistry Reviews 1984, 54 (C), 23–98. https://doi.org/10.1016/0010-8545(84)85017-1.

(13). (a) Petković, B.; Stevanović, S.; Budimir, M.; Sovilj, S. P.; Jovanović, V. M. Electrochemical Examination of Copper(II) Complexes with Octaazamacrocyclic Ligand and Heterocyclic Dithiocarbamate. Electroanalysis 2012, 24 (7), 1605–1612. https://doi.org/10.1002/elan.201200120.

(b) Ajmal, M. Review: Electrochemical Studies on Some Metal Complexes Having Anti-Cancer Activities. Journal of Coordination Chemistry 2017, 70 (15), 2551–2588. https://doi.org/10.1080/00958972.2017.1362559.

(14). Hogarth, G.; Onwudiwe, D. C. Copper Dithiocarbamates: Coordination Chemistry and Applications in Materials Science, Biosciences and Beyond. *Inorganics* **2021**, *9* (9), 70. https://doi.org/10.3390/inorganics9090070.

(15). Qiu, J.; Matyjaszewski, K.; Thouin, L.; Amatore, C. Cyclic Voltammetric Studies of Copper Complexes Catalyzing Atom Transfer Radical Polymerization. Macromolecular Chemistry and Physics 2000, 201 (14), 1625–1631. https://doi.org/10.1002/1521-3935(20000901)201:14<1625::AID-MACP1625>3.0.CO;2-9.

(16). Theocharis, A. D.; Karamanos, N. K. Proteoglycans Remodeling in Cancer: Underlying Molecular Mechanisms. Matrix Biology 2019, 75–76, 220–259. https://doi.org/10.1016/j.matbio.2017.10.008.

(17). (a) Foloppe, N.; MacKerell, Jr., A. D. All-Atom Empirical Force Field for Nucleic Acids: I. Parameter Optimization Based on Small Molecule and Condensed Phase Macromolecular

Target Data. Journal of Computational Chemistry 2000, 21 (2), 86–104. https://doi.org/10.1002/(SICI)1096-987X(20000130)21:2<86::AID-JCC2>3.0.CO;2-G.

(b) Breneman, C. M.; Wiberg, K. B. Determining Atom-Centered Monopoles from Molecular Electrostatic Potentials. The Need for High Sampling Density in Formamide Conformational Analysis. Journal of Computational Chemistry 1990, 11 (3), 361–373. https://doi.org/10.1002/jcc.540110311.

(c) Walker, F.; Abramowitz, L.; Benabderrahmane, D.; Duval, X.; Descatoire, V.; Hénin, D.; Lehy, T.; Aparicio, T. Growth Factor Receptor Expression in Anal Squamous Lesions: Modifications Associated with Oncogenic Human Papillomavirus and Human Immunodeficiency Virus. Human Pathology 2009, 40 (11), 1517–1527. https://doi.org/10.1016/j.humpath.2009.05.010.

(d) Lynch, T. J.; Bell, D. W.; Sordella, R.; Gurubhagavatula, S.; Okimoto, R. A.; Brannigan, B. W.; Harris, P. L.; Haserlat, S. M.; Supko, J. G.; Haluska, F. G.; Louis, D. N.; Christiani, D. C.; Settleman, J.; Haber, D. A. Activating Mutations in the Epidermal Growth Factor Receptor Underlying Responsiveness of Non–Small-Cell Lung Cancer to Gefitinib. New England Journal of Medicine 2004, 350 (21), 2129–2139. https://doi.org/10.1056/NEJMoa040938.

(18). Adeyemi, J.; Onwudiwe, D. Antimicrobial and Cytotoxicity Studies of Some Organotin(IV) N-Ethyl-N-Phenyl Dithiocarbamate Complexes. Polish Journal of Environmental Studies 2020, 29 (4), 2525–2532. https://doi.org/10.15244/pjoes/111231.

CHAPTER IV

SYNTHESIS AND SPECTRAL, ELECTROCHEMICAL, SINGLE CRYSTAL X-RAY DIFFRACTOMETRIC, COMPUTTIONAL CHEMISTRY AND BIOLOGICAL STUDIES OF 1-(((3-FLUORO-4-MORPHOLINOPHENYL)IMINO)METHYL)-NAPTHALEN-2-OL (FMIMN) AND ITS BIVALENT METAL COMPLEXES

The Schiff base compound (E)-1-((3-fluoro-4-morpholinophenyl)imino)methyl)-naphthalene-2-ol (**FMIMN**) and its metal complexes are discussed in this Chapter. The spectral (IR, UV-Visible absorption, mass, ^{1}H & ^{13}C NMR, fluorescence emission) properties, electrochemical properties, single crystal X-ray diffraction, molecular modelling, molecular docking and bio-activity studies have been extensively studied. The condensation of 2-hydroxy-1-napthaldehyde with 3-fluoro-4-morpholinoaniline yields this Schiff base, **FMIMN.** The details of synthesis of **FMIMN** ligand and its metal complexes is presented in **Chapter II**.

This Chapter is divided into 3 parts, **Part A**, **Part B** and **Part C.**

Part A discusses the results of the physical, analytical, spectroscopic, electrochemical, and coordination chemistry studies of the **FMIMN** and its metal complexes, **$M(FMIMN)_2$.**

In **Part B** are placed the results of conformational analysis, evaluation of structural parameters such as bond length, bond angles, torsional angles, HOMO-LUMO orbital energies, molecular docking studies, single and double dihedral conformational analysis of **FMIMN** ligand and its metal complexes.

Part C contains some biological activity studies of the **FMIMN** ligand and its metal complexes.

PART A

SPECTRAL, ELECTROCHEMICAL CRYSTALLOGRAPHIC STUDIES OF FMIMN AND [M(FMIMN)$_2$]

4A.1 Elemental Analysis:

Table 4A.1 incorporates the physical and analytical properties of the **FMIMN** ligand and its metal complexes. The chemical structures shown in **Figure 4A.1** are closely related to the results of the elemental analysis. These are briefly described in terms of their spectral properties.

Table 4A.1: *Analytical data[#] of* ***FMIMN*** *and* ***[M(FMIMN)$_2$]***

Compound	M.P (°C)	Molecular formula	Molecular Weight[*]	%C	%H	%N	%O
FMIMN	178-180	$C_{21}H_{19}FN_2O_2$	350	72.10 (71.98)	5.38 (5.47)	7.88 (8.00)	9.34 (9.13)
Cu(FMIMN)$_2$	342-344	$C_{42}H_{36}CuF_2N_4O_4$	762	66.28 (66.17)	4.84 (4.76)	7.47 (7.35)	8.49 (8.39)
Ni(FMIMN)$_2$	323-325	$C_{42}H_{36}NiF_2N_4O_4$	757	66.71 (66.60)	4.82 (4.79)	7.53 (7.40)	8.56 (8.45)
Co(FMIMN)$_2$	365-367	$C_{42}H_{36}CoF_2N_4O_4$	757	66.65 (66.58)	4.14 (4.79)	7.48 (7.39)	8.57 (8.45)
Mn(FMIMN)$_2$	328-330	$C_{42}H_{36}MnF_2N_4O_4$	754	67.08 (66.93)	4.92 (4.81)	7.54 (7.43)	8.62 (8.49)
Zn(FMIMN)$_2$	356-358	$C_{42}H_{36}ZnF_2N_4O_4$	764	66.03 (66.02)	4.85 (4.75)	7.42 (7.33)	8.41 (8.37)

[#] data in parenthesis are calculated ones; [*] data limited to integral values

4A.2 Mass Spectrum of FMIMN:

Figure 4A.2 shows the mass spectrum of the **FMIMN** ligand. M+1 is the highest intensity peak, which matches the molecular formula of **FMIMN, (Figure 4A.1).**

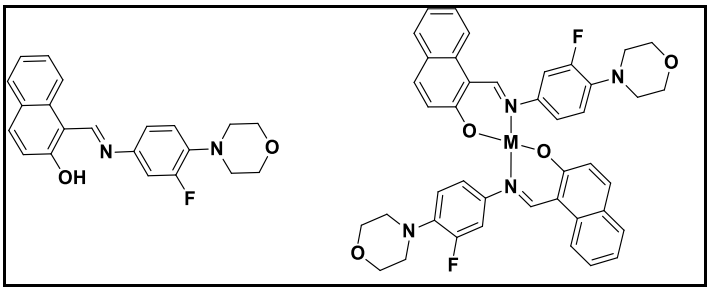

Figure 4A.1: *The chemical structure of* ***FMIMN*** *and* ***M(FMIMN)$_2$***

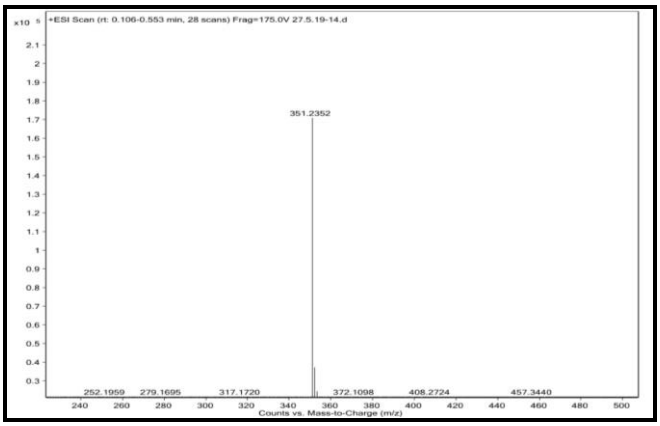

Figure 4A.2: *Mass spectrum of* ***FMIMN***

4A.3 IR Spectral Studies:

The infrared spectra of the **FMIMN** ligand and its metal complexes **[M(FMIMN)$_2$]** are shown in **Figures 4A.3–4A.6**. **Table 4A.2** holds some important IR data of the prepared compounds. As we can see, the most noticeable band in all Schiff base ligands is in the range of 1520–1622 cm^{-1} (1558 cm^{-1} for **FMIMN**).

Table 4A.2: *IR data$^{\#}$ of the* ***FMIMN*** *and* ***[M(FMIMN)$_2$]***

Compound	νC=N	νC-H$_{arom.}$	νC-H$_{aliph.}$	νC-OH	νM-O	νM-N
FMIMN	1558	3060	2885	1320	-	-
Cu(FMIMN)$_2$	1536	3053	2849	1361	519	463
Ni(FMIMN)$_2$	1536	3051	2854	1357	524	460
Co(FMIMN)$_2$	1534	3052	2853	1362	508	453
Zn(FMIMN)$_2$	1537	3058	2856	1340	511	448
Mn(FMIMN)$_2$	1533	3051	2853	1354	507	427

#, in KBr pellet

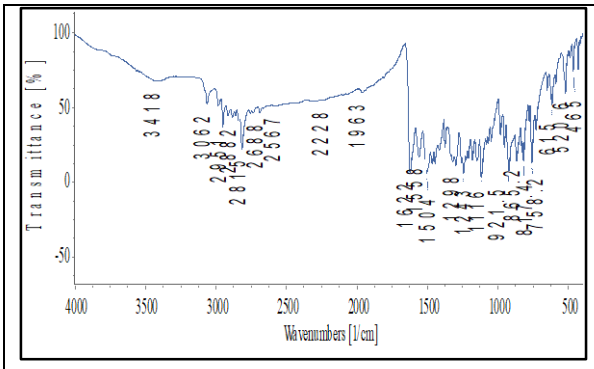

Figure 4A.3: *FTIR Spectrum of* ***FMIMN***

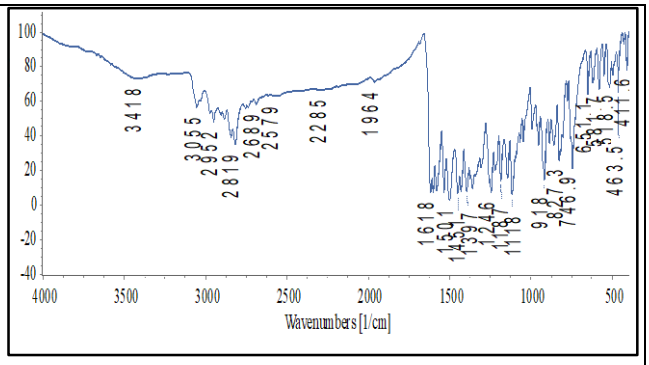

Figure 4A.4: *FTIR Spectrum of* ***Cu(FMIMN)$_2$***

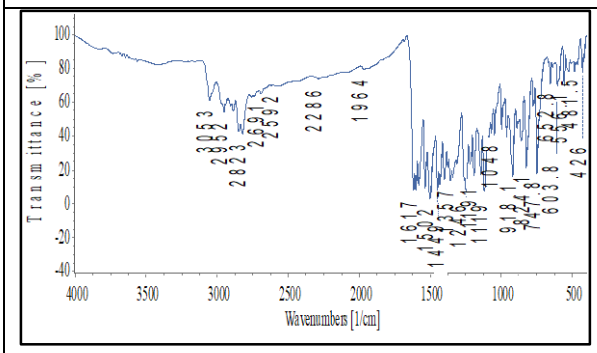

Figure 4A.5: *FTIR Spectrum of* ***Ni(FMIMN)$_2$***

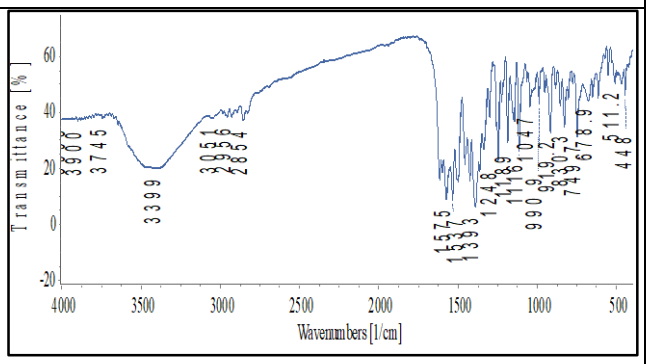

Figure 4A.6: *FTIR Spectrum of* ***Zn(FMIMN)$_2$***

The shift of this particular band towards lower wave number values by approximately 20-25 cm^{-1} in their metal complexes[1] indicates the participation of nitrogen atoms of the azomethine group in coordination with the metal ions. In the region of 1310–1335 cm^{-1}, a prominent band is observed, which is due to the naphthalic oxygen of the **FMIMN**. This band is observed in the region of 1354–1371 cm^{-1} in their metal complexes, which could be attributed to skeletal vibrations connected to the ligand's naphthalic oxygen. These bands are known to shift to higher frequencies when the naphthalic oxygen coordinates with metal ions[2]. Far infrared spectral bands in the 600–400 cm^{-1} range confirm the presence of oxygen and nitrogen atoms in coordination with metal ions (i.e., v(M-N) and (M-O). According to IR spectral data, the **FMIMN** works as a neutral bidentate ligand with O and N as donor atoms.

4A.4 Electronic Spectral Studies:

The uv-visible spectra of **FMIMN** and its copper complex are shown overlapped in **Figure 4A.7.** The ligand shown two bands one in the range of 220-250 nm that corresponds to the n-π^* transition and another in the range of 400-450 nm that corresponds to the π-π^* transition. The weak and broad band observed for **Cu(FMIMN)$_2$** at 576 nm corresponds to the $^2B_{1g} \rightarrow {}^2E_g$ d-d transition. The band at 410 nm corresponds to metal to ligand charge transfer. These findings point to the **Cu(FMIMN)$_2$** complex having a square planar structure[3]**.** The band, found for **Ni(FMIMN)$_2$** at ~462 nm, is assigned to the $^3A_{1g} \rightarrow {}^3B_{1g}$ transition. This indicates a square planar structure for the **Ni(FMIMN)$_2$** complex[4]**. Co(FMIMN)$_2$** has a single band at 451 nm that is attributed to the $^3A_g(F) \rightarrow {}^4T_1(F)$ d-d transition. These findings suggest that the **Co(FMIMN)$_2$** complex has a tetrahedral geometry[5]**.** The **Mn(FMIMN)$_2$** is a d^5 high spin system with d-d transitions that are Laporte- and spin-forbidden. At 462 nm, **Zn(FMIMN)$_2$** exhibits a Ligand to Metal Charge Transition (LMCT) band. **Table 4A.3** describes the relevant electronic spectral data of **M(FMIMN)$_2$**.

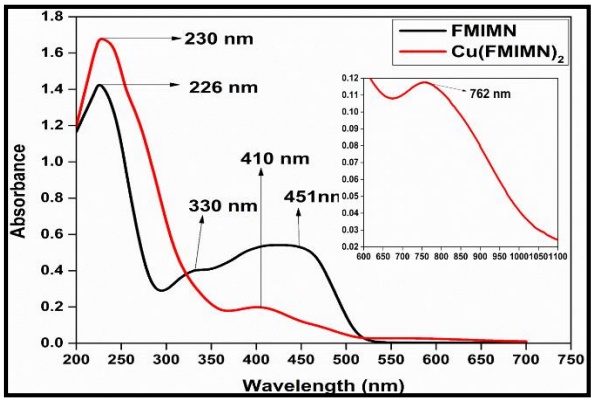

Figure 4A.7: *Electronic Spectra of* ***FMIMN*** *(—) and* ***Cu(FMIMN)$_2$*** *(—) in DMSO (5x 10^{-5} M); inset* (2x 10^{-2} M)

Table 4A.3: *Physical, spectral and magnetic data of* ***FMIMN*** *and* ***[M(FMIMN)$_2$]***

Compound	Color	Electronic spectral data λ (ε)*	μ_{eff} (BM)
FMIMN	Orange	226 (14500); 330 (4350); 451 (5820)	-
Cu(FMIMN)$_2$	Yellow	230 (16420); 410 (4130); 576 (450)	1.63
Ni(FMIMN)$_2$	Brown	337 (12400); 462 (8220)	2.82

Co(FMIMN)$_2$	Brown	226 (13400); 451(8450)	4.17
Mn(FMIMN)$_2$	Brown	230 (4125); 466 (8140)	5.24
Zn(FMIMN)$_2$	White	232 (14210); 462 (7980)	-

* λ in nm, ε in lt mol^{-1}cm^{-1}

4A.5 NMR Spectral Studies of FMIMN:

The ^{1}H NMR spectra of **FMIMN** and **Zn(FMIMN)$_2$** are shown in **Figure 4A.8** and **4A.10** respectively.

Table 4A.4: *^{1}H NMR data of **FMIMN** and **Zn(FMIMN)$_2$***

Moiety	**^{1}H NMR (FMIMN)**	**^{1}H NMR Zn(FMIMN)$_2$**
-HC=N-	15.37 (s, 1H)	9.29 (s, 1H)
-C-OH	9.34 (s, 1H)	-
Aromatic	8.12 (d, J = 8.4 Hz, 1H), 7.81 (d, J = 8.8 Hz, 1H), 7.74 (d, J = 8.0 Hz, 1H), 7.53 (t, J = 8.0 Hz, 1H), 7.35 (t, J = 7.2 Hz, 1H), 7.16–7.11 (m, 3H), 6.99 (t, J = 9.2 Hz, 1H),	8.24 (s, 1H), 7.08-7.87 (m, 6H), 6.94 (m, 1H), 6.92 (s, 1H)
Aliphatic	3.89 (t, J = 4.8 Hz, 4H), 3.13 (t, J = 4.8 Hz, 4H)	3.75 (m, 4H), 3.01 (m, 4H), 1.85 (m, 3H)

The imine (-HC=N-) proton, which is engaged in an intramolecular H-bonding, gives its ^{1}H-NMR chemical shift value at 15.37 ppm (a singlet), which is slightly higher than that of a non-H-bonded imine proton. This down field shift is due to its H-bonding to the phenolic electronegative oxygen. Conversely, the δ value of phenolic hydrogen (H-O-Ar) appears at 9.34 ppm (a singlet), which is slightly lower than that expected for free phenolic hydrogen due to partial syphoning of the electron cloud on oxygen towards the imine proton through the intramolecular H-bonding[6]**.** The two chemically distinguishable sets of the eight morpholine ring protons give their two triplets at 3.89 ppm (-CH_2-O-) and 3.13 ppm (CH_2-N-) as expected. The δ values of the aromatic protons appear in the usual range of 6.99–8.12 ppm.

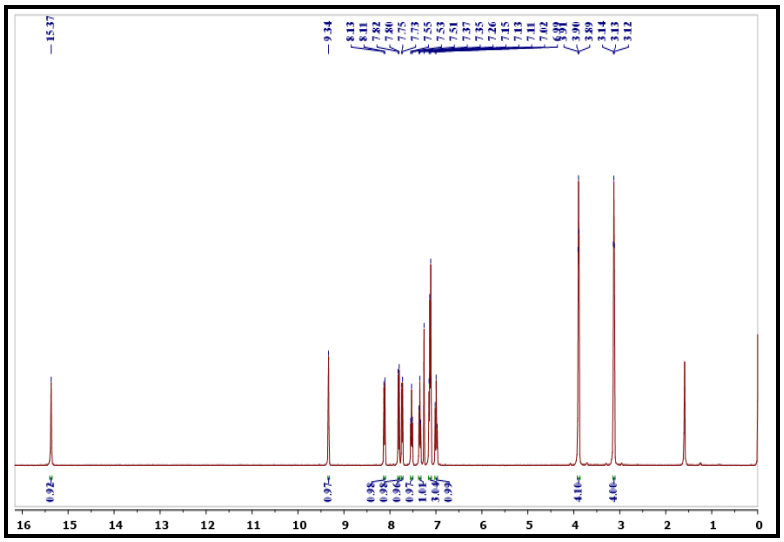

Figure 4A.8: *^{1}H-NMR spectrum of* ***FMIMN*** *in $CDCl_3$*

The δ values of the aromatic protons appear in the usual range of 6.99 - 8.12 ppm. The -CH=N and -OH functional group protons are shielded in **Zn(FMIMN)$_2$**. This enhanced shielding is attributed to the diffusion of the ligand's electron cloud to metal upon complexation with the zinc metal atom[7]**.**

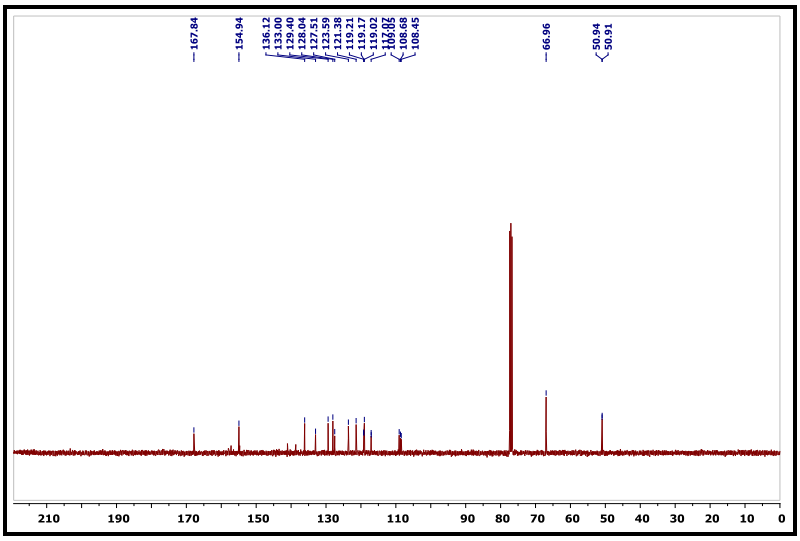

Figure 4A.9: *^{13}C-NMR spectrum of* ***FMIMN*** *in $CDCl_3$*

The spin-decoupled ^{13}C-NMR spectrum of **FMIMN** is shown in **Figure 4A.9**. The phenolic carbon (-C-OH) appears at 167.84 ppm whereas the fluorine atom-connected carbon

gives its peak at 141.04 ppm. All the other remaining aromatic carbon atoms appear in the range of 108.45–136.12 ppm. The imine carbon's (-CH=N-) peak appears at 154.94 ppm, while the carbon atoms of the morpholine ring show two peaks in the aliphatic region, at 50.92 ppm (-CH_2-N-) and at 66.96 ppm (-CH_2-O-).

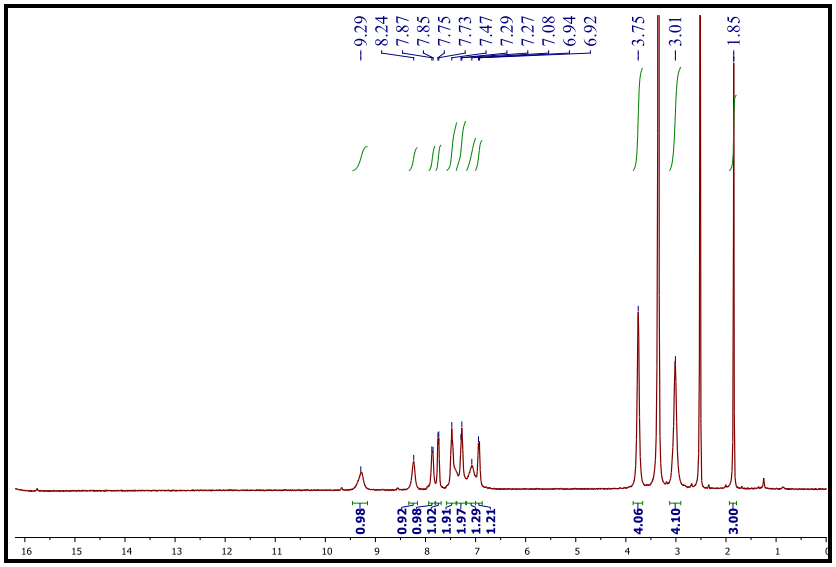

Figure 4A.10: *^{1}H-NMR spectrum of* ***Zn(FMIMN)$_2$*** *in DMSO-d6*

4A.6 Electron Spin Resonance Spectroscopy of Cu(FMIMN)$_2$:

The room temperature poly crystalline state ESR spectrum of **Cu(FMIMN)$_2$** is shown in **Figure 4A.11.** The two g-values detected in its ESR spectra are $g_{||}$ = 2.1476 and $g_{\perp}$ = 2.0508. The spectrum also reveals that these values are much greater than that of g_e (2.0023), indicating that the unpaired electron is mostly present in the ground state of Cu (II) $d_{x^2-y^2}$ orbital[8]**.** This suggests a typical square-planar geometry around Cu(II) ions. According to Hathway, if the axial symmetry parameter G > 4, the exchange interaction is said to be minor and if G = 4, the exchange interaction is reasonable in the solid state. The exchange interaction parameter term G was calculated using the formula G = ($g_{||}$-2.0023)/($g_{\perp}$-2.0023) = 2.99, which is less than 4, indicating that the copper center has significant exchange interaction[9]**.**

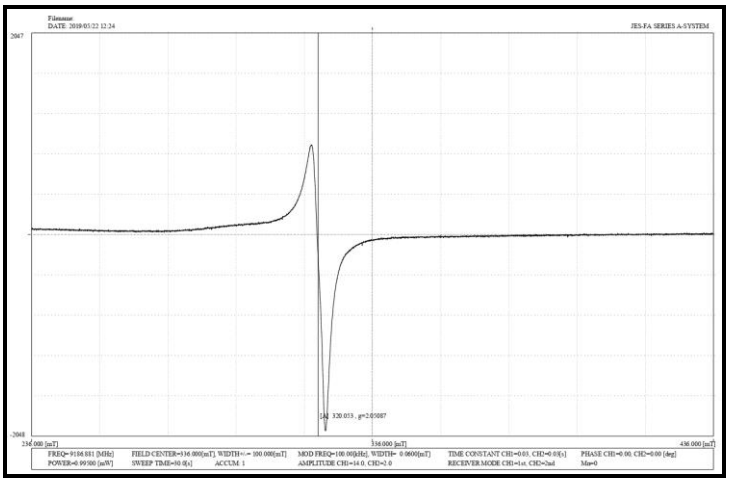

Figure 4A.11: *ESR spectrum of* ***Cu(FMIMN)$_2$***

4A.7 X-Ray Crystal Structure of FMIMN:

The ORTEP diagram of **FMIMN** is shown in **Figure 4A.12.** Single crystal X-Ray crystallographic studies of **FMIMN** relevant XRD data are given in **Table 4A.5.** The reflection angle vs intensity graph is presented in **Figure 4A.14.** It is found that **FMIMN** crystallizes in the $P_{21/n}$ space group. In **Figure 4A.16,** is shown the unit cell obtained from the single crystal X-ray diffraction studies. A close observation of the intermolecular arrangement of the 4 molecules reveals that the molecules are stacked in layers constituted by a number of possible intermolecular interactions[10].

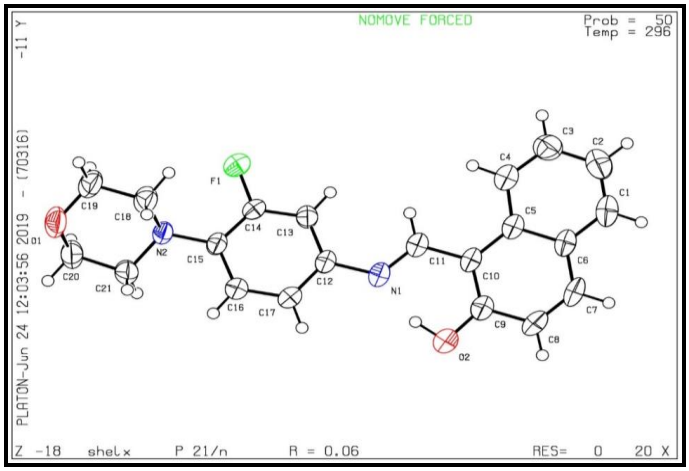

Figure 4A.12: *XRD- Platon diagram of* ***FMIMN*** *with atom-numbering*

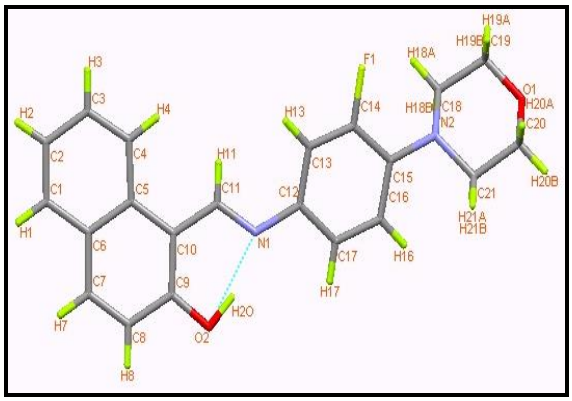

Figure 4A.13: *X-Ray crystallographic stick diagram of* ***FMIMN*** *showing intramolecular hydrogen bonding*

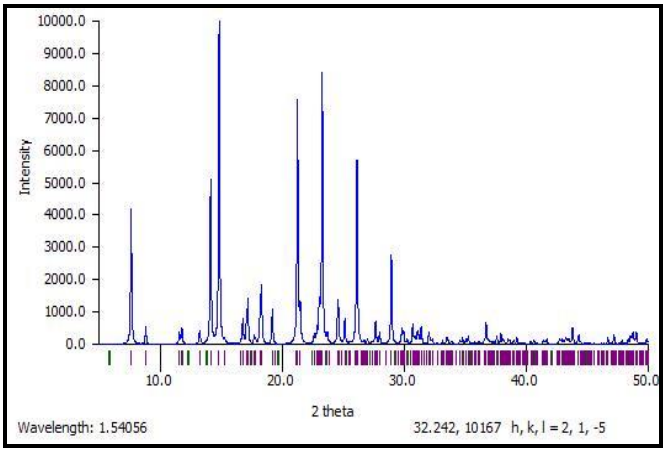

Figure 4A.14: *X-Ray diffraction intensity as a function of angle (^{o}) of reflection*

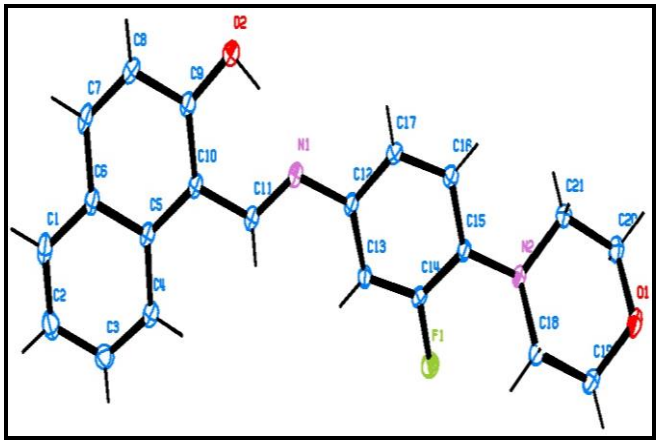

Figure 4A.15: *ORTEP diagram of the XRD structure of* ***FMIMN*** *molecule*

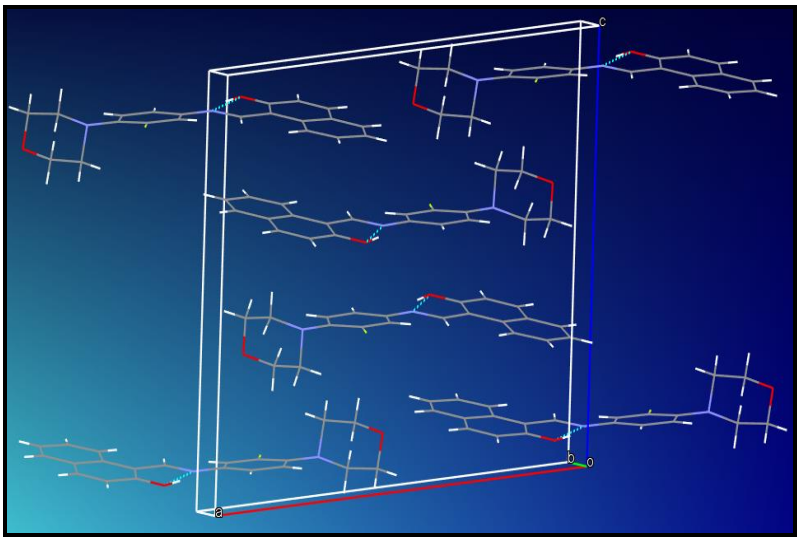

Figure 4A.16: *Unit cell crystal packing diagram of* ***FMIMN*** *showing the two dimesitional layer structure with O-H…N intramolecular hydrogen bonding*

The primary interactions seem to be weak π-π interactions between any pair of adjacent molecules, with one pair in a naphthalene-naphthalene stacking and another pair in a naphthalene-benzene stacking while any adjacent pair, *inter alia,* being in an inverse disposition. Most of the single crystal XRD structural data are presented in the next part juxtapositioned with the molecular modeled computational data.

Table 4A.5: *Crystallographic data of* ***FMIMN***

CCDC	2001213
Empirical formula	$C_{21}H_{19}FN_2O_2$
Formula weight	350.38
Color/shape	Yellow/needle
Crystal size, mm^3	0.6 x 0.3 x 0.3
Temperature, K	296(2)
Crystal system	P21/n
Space group	Monoclinic
Unit cell dimensions, Å	a = 15.1589(12)
	b = 7.4349(5)
	c = 15.4287(13)
Deg	β = 98.340(4)
Volume, $Å^3$	1720.5(2)

Z	4
Density, mg/m^3	1.353
Absorption coefficient, mm^{-1}	0.095
Reflections collected/unique	13631/ 4112
θ range for data collections	1.760 – 28.340°
F (000)	736
Limiting indices	-19 ≤ h ≤ 20
	-9 ≤ k ≤ 9
	-20 ≤ l ≤ 20
Completeness	100.0 %
Goodness-of-fit on F^2	1.008
Final R indices [I>2σ (1)]	R_1 = 0.0564, wR_2 = 0.1601
R indices (all data)	R_1 = 0.1170, wR_2 = 0.2123
Largest diff. peak and hole (eÅ^{-3})	0.525 and -0.229

Table 4A.6: *Data of hydrogen bonding of* ***FMIMN***$^{\#}$

D-H…A (Å)	d(D-H)	d(H…A)	d(D…A)	<(DHA) (°)
O(2)-H(2A)…N(1)	0.82	1.82	2.542 (2)	146.2
C(17)-H(17)…F(1)#1	0.93	2.62	3.471 (3)	152.7
C(18)-H(18A)…F(1)	0.97	2.32	2.948 (3)	121.4

Symmetry transformations used to generate equivalent atoms: # 1 x, y-1,

4A.8 Cyclic Voltammetric Studies of FMIMN and Cu(FMIMN)$_2$:

Figures 4A.17 and **4A.18** show the cyclic voltammograms (CV) and linear sweep voltammogram (LSV) of **FMIMN** ligand as a function of scan rate and concentration respectively. The ratio of peak currents (i_{pc}/i_{pa}), the gap between peak potentials ($\Delta E_p = |E_{pc}-E_{pa}|$) and the effect of scan rate on peak current values indicate that the electron transfer is irreversible in both cases. In the case of **FMIMN**, two irreversible oxidation peaks are detected in the cyclic voltammogram at 1.05 V and 1.20 V. The square root of the scan rate versus peak current values plot is presented in **Figure 4A.19**. Moreover, the anodic peak current is found to be linear with the concentration of the **FMIMN (Figure 4A.20)**. The relationship between the square root of the scan rate and peak current shows that electron transfer is diffusion-controlled.

The cyclic voltammogram of **[Cu(FMIMN)$_2$]** on a glassy carbon electrode revealed an anodic peak at 1.02 V, this may be attributed to ligand oxidation and possibly related to the

presence of an azomethine group, which facilitates electron transfer to the metal **[Figure 4A.21–4A.26].** Because of the ligand's coordination to the Cu(II) ion center, the oxidation peak potentials are slightly negative than those of the free ligand. The electron transfers coefficient (α_{na}) and heterogeneous electron transfer rate constant (k^o_h) have been evaluated from studies of the influence of concentration and scan rate on peak potentials. The respective electrochemical data of **FMIMN** ligand and **Cu(FMIMN)$_2$** along with the diffusion coefficients (D) are shown in **Table 4A.7.**

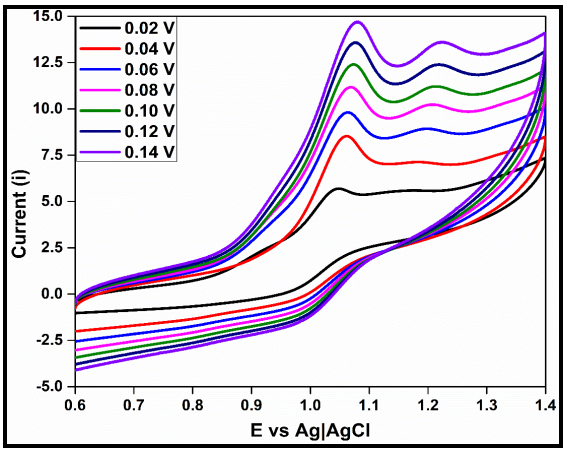

Figure 4A.17: *Cyclic Voltammogram of* ***FMIMN*** *(5x10^{-4} M) in DMSO at different scan rates*

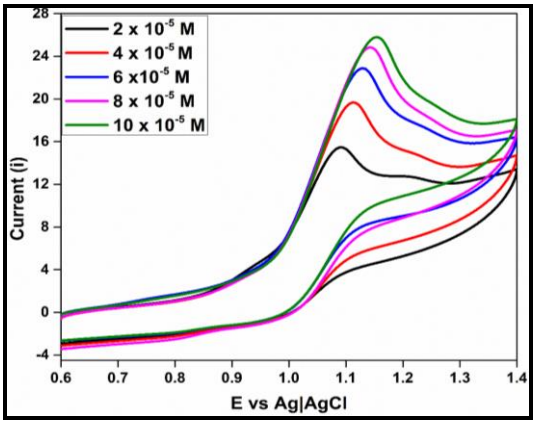

Figure 4A.18: *Cyclic Voltammogram of* ***FMIMN*** *(5x10^{-4} M) in DMSO at different concentration*

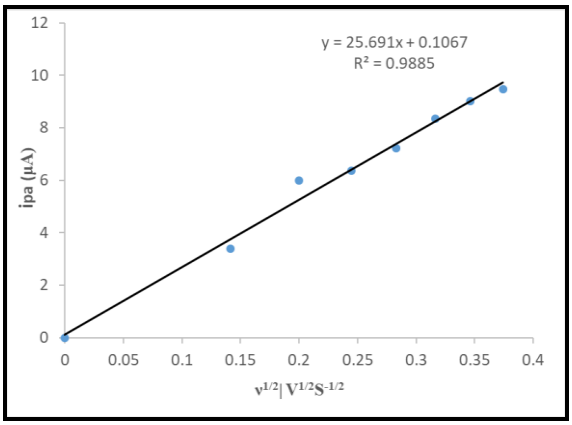

Figure 4A.19: *Effect of scan rate on the anodic current of* ***FMIMN*** *in cyclic voltammogram*

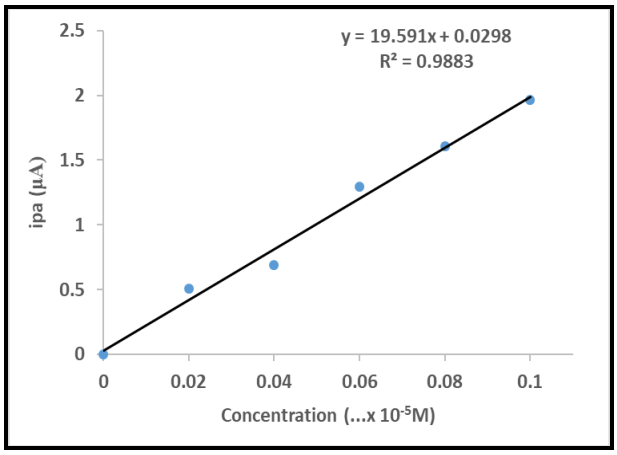

Figure 4A.20: *Variation of anodic currents of* ***FMIMN*** *with respect to various concentrations*

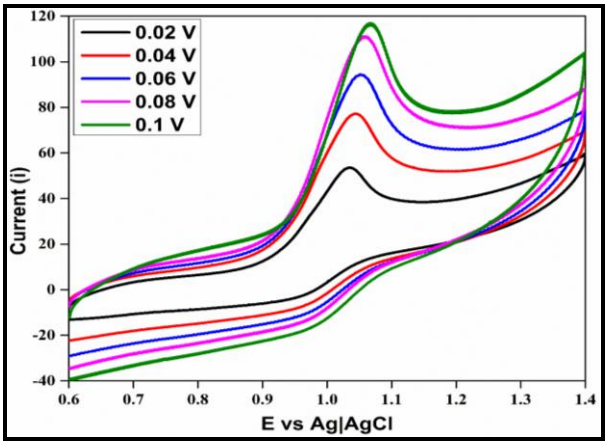

Figure 4A.21: *Cyclic Voltammogram of* ***Cu(FMIMN)$_2$*** *in DMSO at different scan rates*

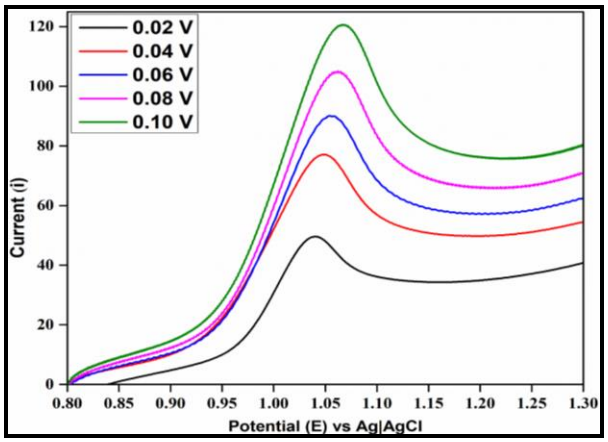

Figure 4A.22: *Linear Sweep Voltammogram of* ***Cu(FMIMN)$_2$*** *in DMSO at different scan rates*

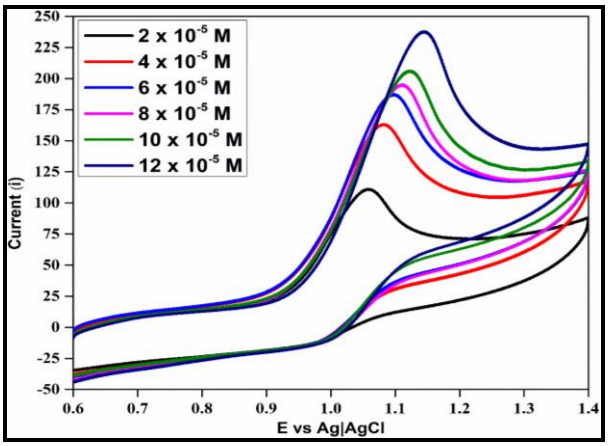

Figure 4A.23: *Cyclic Voltammogram of* ***Cu(FMIMN)$_2$*** *in DMSO at different concentrations*

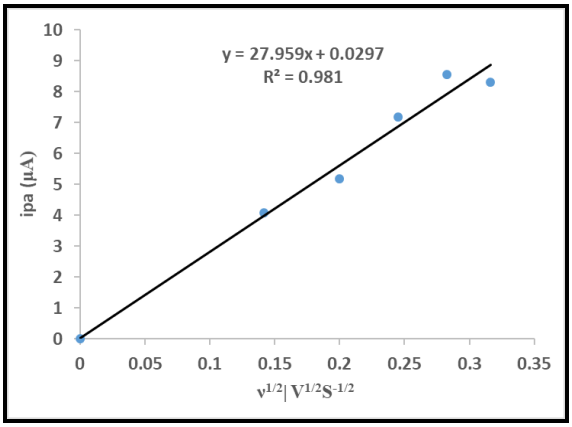

Figure 4A.24: *Effect of scan rate on the anodic current of* ***Cu(FMIMN)$_2$*** *in cyclic voltammogram*

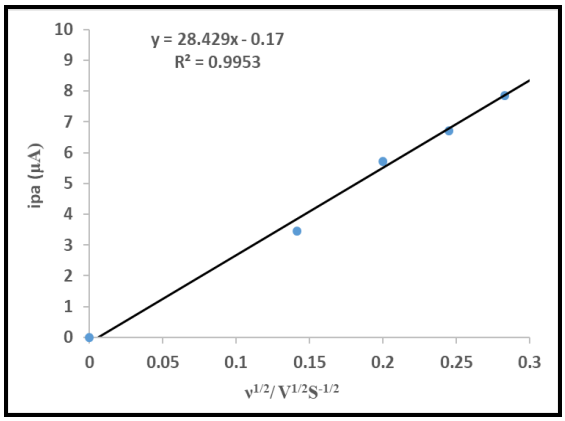

Figure 4A.25: *Effect of scan rate on the anodic current of* ***Cu(FMIMN)$_2$*** *in linear sweep voltammetry*

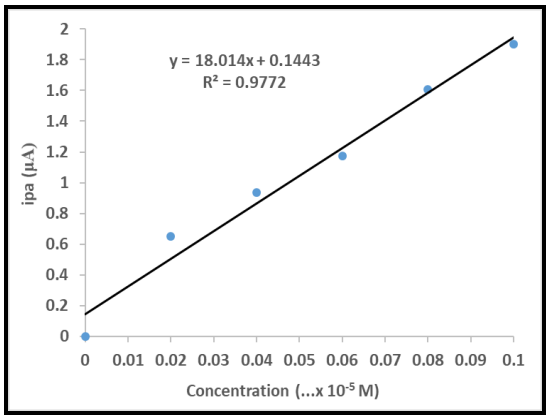

Figure 4A.26: *Variation of anodic currents of* ***Cu(FMIMN)$_2$*** *with respect to concentration*

Table 4A.7: *Electrochemical data of* ***FMIMN*** *and* ***Cu(FMIMN)$_2$*** *in DMSO medium*

Compound	**Parameters**		
	(D) **in $cm^2\ s^{-1}$**	**(α_{na})** **in $cm^2\ s^{-1}$**	**k^o_h** **in $cm^2\ s^{-1}$**
FMIMN	17.43×10^{-5}	0.84	13.00×10^{-5}
Cu(FMIMN)$_2$	18.18×10^{-5}	0.95	14.59×10^{-5}

PART B

COMPUTATIONAL AND DOCKING STUDIES OF FMIMN AND [M(FMIMN)$_2$] AND CORRELATION WITH CRYSTALLOGRAPHIC DATA

4B.1 Computational Methods:

The structures of multi-atom, multi-ring organic molecules in the solid state and gaseous state differ mostly in the bond angles and dihedral angles close to the locations of the intermolecular packing interactions[11]**.** To understand these aspects, semi-empirical molecular orbital calculations were performed using the Austin Model-1 (AM1) and density functional theory (DFT) methods on B3LYP platform.

The initial molecular geometry was adopted as Pople's standard data[12]**,** and subsequently optimized using a fully optimized energy gradient method. The conformations were designated by Klyne-Prelog terms[13] using s = syn, a = anti, c = clinal (0±300& 180±300) and all other angles p = peri-planar. Conformational analysis of isolated molecules was done in the form of conformational flexible compounds[14]**.** Initial X-ray structure of the molecule were used for conformational analysis and then using semi-empirical AM1 and B3LYP calculations, the energy minimized stable conformer was generated. Geometry optimizations of the crystal structure of the title compound were carried out using the Fletcher-Powell-Davidson algorithm implemented in the package and the PRECISE option to improve the convergence criteria[15]**.** The correlation data of various molecular parameters obtained by empirical XRD and semi-empirical AM1 and DFT method B3LYP calculations are collected in **Table 4B.1** through **Table 4B.4.** The DFT/B3LYP with the 6-31G* basis set calculations were obtained from Gaussian 16 platform[16], whereas molecular mechanics (MM2)[17] were done by ChemSoft's ChemOffice Pro (version 12). The stereographic projection of the molecule after energy-minimization through MM2 on the Chem3D Pro platform is shown in **Figure 4B.1(a).** The corresponding anaglyph picture is presented in **Figure 4B.1(b).**

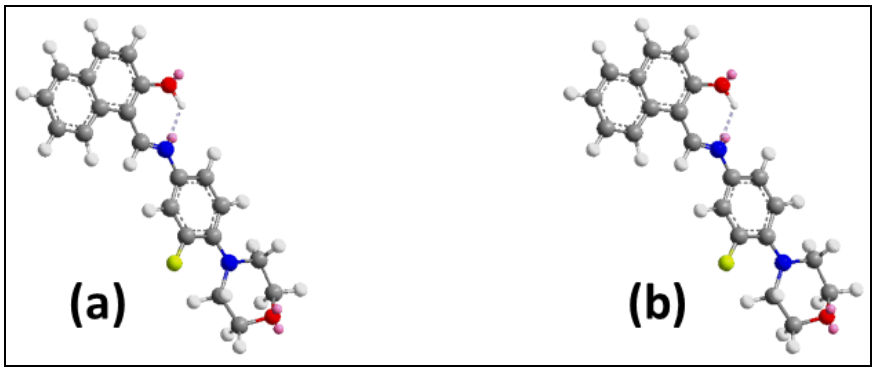

Figure 4B.1: *Stereographic projections of MM2-energy-minimised* ***FMIMN*** *obtained from ChemDraw Pro*

An interesting aspect is found here. In order to avoid steric hindrance and presumably to retain the aromaticity of each of the two aromatic rings, viz., naphthalene and benzene, the molecule is expected to have a finite dihedral angle (close to 90^o) over the =N-C- bond location, if not over C-C-N (to facilitate hydrogen bond, N$^{\cdots}$H-O-). However, the modelling by AM1, DFT/B3LYP and ChemDraw Pro (MM2) on **FMIMN** shows near planarity of the molecule from the naphthalene ring till the nitrogen of the morpholine. Relevant dihedral angles over some pertinent moieties are shown in **Figure 4B.2,** from which it is clear that the stable gas phase molecule is planar till the morpholine nitrogen. Conformational torsional energy analysis over the C(Naphthyl)-CH(azomethine) and N(azomethine)-C(benzene) are done by ChemDraw and are shown in **Figures 4B.3** and **4B.4** respectively. The global minima represent the energy-minimized molecule (**Figure 4B.1)** with dihedral angles as mentioned in **Figure 4B.2.** The local minima and global maxima related to the dihedral angles are shown in **Figure 4B.3** and **Figure 4B.4**. Since MM2 calculations take Huckel's aromaticity into account, the additional stability, despite planarity, is understood on the basis of the number of π-bonds in conjugation, viz., 5 (naphthalene) +1 (azomethine) +3 (benzene) = 9. The number of π electrons in conjugation becomes 18, which follows Huckel's 4n+2 rule with n=4. As shown in **Figure 4B.3,** the local minimum with naphtholic oxygen and azomethine's nitrogen is in an anti-geometric posture with no possibility of hydrogen bond and with a dihedral angle of about 9.5^o (due to steric hindrance from the oxygen's lone pair of electrons or the naptholic proton and the hydrogen of the azomethine moiety, -CH=N-). From this diagram, one can evaluate the hydrogen bond energy to be about 10 kcal mol^{-1} (the difference between the Global Minimum and the Local Minimum). The Double Dihedral

Torsional Energy Conformational Analysis over the C(Naphth)-CH=N-C performed by GoldenSoft's Surfer mathematical gridding on the double-dihedral torsion derived from the Chem3D is shown in **Figure 4B.5**, which indicates higher energies when rings cross and when the system has dihedral angles close to 90^{o} and minima with planarity with rings not crossing.

Although the preferred conformation in the solid phase may differ from that in the dilute solution and the gas phase, X-ray diffraction data is used for comparison. As a whole, it can help us understand the physical and chemical properties of this molecule when it is both condensed and gaseous.

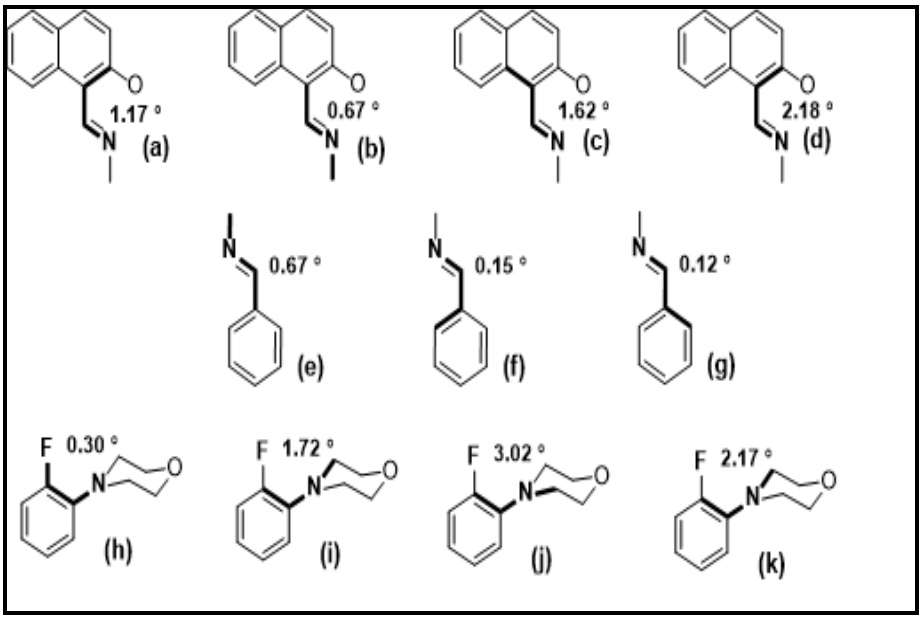

Figure 4B.2: *Dihedral angles over various locations of energy-minimized structure of* ***FMIMN***

Some small deviations are observed between the X-ray diffraction data in the solid state and the computational data in the gaseous state under vacuum. The geometrical parameters are incorporated in **Table 4B.2** (bond lengths), **Table 4B.3** (bond angles), and the dihedral angles or torsion angles in **Table 4B.4**. These results can be applied as groundwork for prediction and exploring the other properties of the molecule (**FMIMN**). The numbering system of the AM1 method is indicated in **Figure 4B.6.**

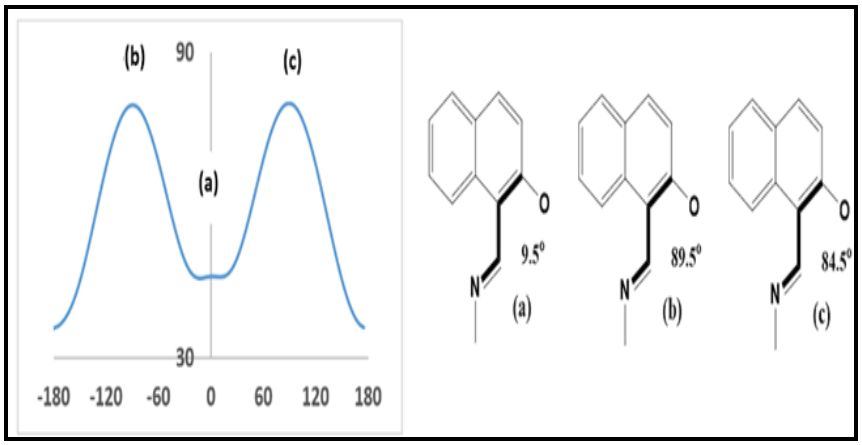

Figure 4B.3: *Conformational Analysis over C-C Bond, shown*

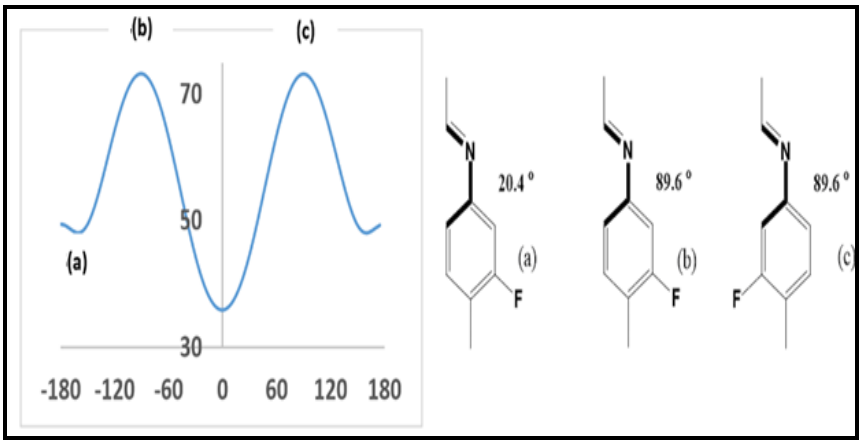

Figure 4B.4: *Conformational Analysis over N-C Bond, shown*

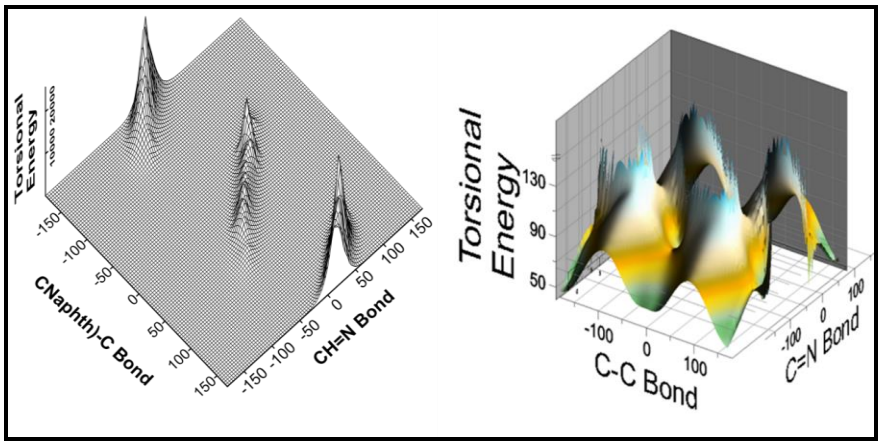

Figure 4B.5: *Double Angle Torsional Energy Plot Over –C(Naphth)-C=N- Moiety of* ***FMIMN****. Full z-scale (left, wireframe) and truncated z-scale (right, surface)*

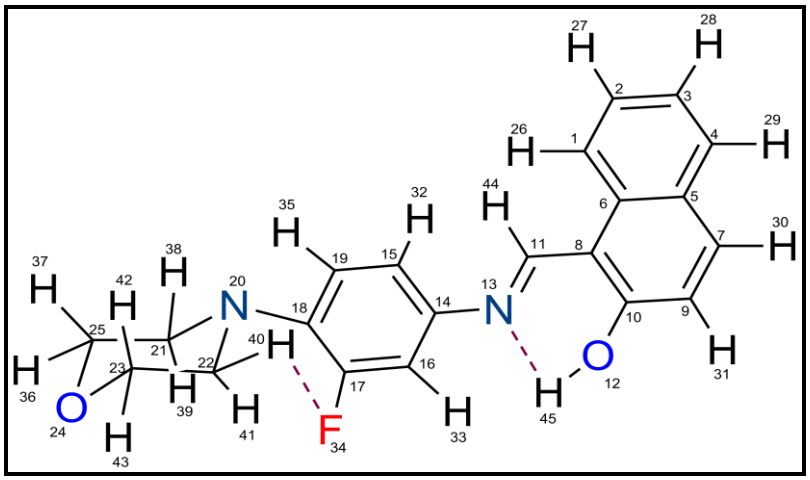

Figure 4B.6: *AM1- Structure along with atom-numbering*

4B.2 Comparison of the X-Ray Data with Computational Data:

The Schiff base, **FMIMN**, is the combination of naphthalene, benzene, and morpholin moieties. Ionization potential (I), electron affinity (A), chemical potential (μ), chemical hardness (η), global softness (S) and electronegativity (χ) of the Schiff base, **FMIMN**, are calculated from the AM1 and DFT/B3LYP methods and the same are incorporated in **Table 4B.1**. It is found that N_{20} of morpholine has more electron density than the N_{13} atom of the imine, as O_{24} of morpholine has more than the naphthenic O_{12} atom.

Table 4B.1: *Important molecular energy data evaluated by AM1 and B3LYP calculations on* ***FMIMN***

Parameter	AM1 value	B3LYP
E_{HOMO} (eV)	-8.3483	-7.8665
E_{LUMO} (eV)	-0.7490	-1.8005
I (eV)	8.3483	7.8665
A (eV)	0.7490	1.8005
η (eV)	3.7996	3.0031
μ (eV)	4.5486	4.8335
χ (eV)	- 4.5486	-4.8335
S (eV^{-1})	0.1315	0.1665

Table 4B.2: *Comparative list of selected bond lengths (A^o) between experimental XRD and AM1, MM2 and B3LYP Calculations of* ***FMIMN***

Bond type	**Bond location**	**Bond (Figure-4A.14)**	**Bond lengths (Å)**				**Variation, δ, (Å)***		
			XRD	**B3LYP**	**AM1**	**MM2**	**Δ(XRD-B3LYP)**	**Δ(XRD-AM1)**	**Δ(XRD-MM2)**
σH-C(***sp2***)	Aromatic	$H_{26} - C_1$	**0.930**	**1.084**	**1.099**	**1.099**	**-0.154**	**-0.169**	**-0.169**
		$H_{27} - C_2$	**0.930**	**1.086**	**1.100**	**1.104**	**-0.156**	**-0.170**	**-0.174**
		$H_{28} - C_3$	**0.930**	**1.086**	**1.099**	**1.103**	**-0.156**	**-0.169**	**-0.173**
		$H_{29} - C_4$	**0.930**	**1.087**	**1.101**	**1.104**	**-0.157**	**-0.171**	**-0.174**
		$H_{30} - C_7$	**0.930**	**1.087**	**1.101**	**1.104**	**-0.157**	**-0.171**	**-0.174**
		$H_{31} - C_9$	**0.930**	**1.085**	**1.099**	**1.104**	**-0.155**	**-0.169**	**-0.174**
		$H_{32} - C_{15}$	**0.930**	**1.085**	**1.102**	**1.106**	**-0.155**	**-0.172**	**-0.176**
		$H_{33} - C_{16}$	**0.930**	**1.084**	**1.102**	**1.102**	**-0.154**	**-0.172**	**-0.172**
		$H_{35} - C_{19}$	**0.930**	**1.083**	**1.102**	**1.101**	**-0.153**	**-0.172**	**-0.171**
		$H_{44} - C_{11}$	**0.930**	**1.092**	**1.116**	**1.093**	**-0.162**	**-0.186**	**-0.163**
σH-C(***sp3***)	Alkenyl	$H_{36} - C_{25}$	**0.970**	**1.102**	**1.121**	**1.115**	**-0.132**	**-0.151**	**-0.145**
		$H_{37} - C_{25}$	**0.970**	**1.093**	**1.122**	**1.115**	**-0.123**	**-0.152**	**-0.145**
		$H_{38} - C_{21}$	**0.970**	**1.100**	**1.129**	**1.118**	**-0.130**	**-0.159**	**-0.148**
		$H_{39} - C_{21}$	**0.970**	**1.091**	**1.123**	**1.117**	**-0.121**	**-0.153**	**-0.147**
		$H_{40} - C_{22}$	**0.970**	**1.090**	**1.124**	**1.116**	**-0.120**	**-0.154**	**-0.146**
		$H_{41} - C_{22}$	**0.970**	**1.097**	**1.127**	**1.118**	**-0.127**	**-0.157**	**-0.148**
		$H_{42} - C_{23}$	**0.970**	**1.103**	**1.121**	**1.115**	**-0.133**	**-0.151**	**-0.145**
		$H_{43} - C_{23}$	**0.970**	**1.093**	**1.122**	**1.115**	**-0.123**	**-0.152**	**-0.145**
σH-O(***sp3***)		$H_{45} - O_{12}$	**0.820**	**1.007**	**0.968**	**0.966**	**-0.187**	**-0.148**	**-0.146**

σF-C(***sp2***)		$F_{34} - C_{17}$	**1.360**	**1.356**	**1.357**	**1.325**	**+0.004**	**+0.003**	**+0.035**
N(***sp2***)-C(***sp2***)	Imine	$N_{13} - C_{11}$	**1.285**	**1.298**	**1.290**	**1.266**	**-0.013**	**-0.005**	**+0.019**
		$C_{14} - N_{13}$	**1.417**	**1.403**	**1.412**	**1.269**	**+0.014**	**+0.005**	**+0.148**
σN(***sp3***)-C(***sp2***)		$N_{20} - C_{18}$	**1.412**	**1.411**	**1.419**	**1.286**	**+0.001**	**-0.007**	**+0.126**
σC(***sp3***)-N(***sp3***)	Aliphatic	$C_{21} - N_{20}$	**1.458**	**1.463**	**1.454**	**1.490**	**-0.005**	**+0.004**	**-0.032**
		$C_{22} - N_{20}$	**1.453**	**1.464**	**1.458**	**1.486**	**-0.011**	**-0.005**	**-0.033**
σC(***sp2***)-O(***sp3***)		$O_{12} - C_{10}$	**1.317**	**1.335**	**1.377**	**1.365**	**-0.018**	**-0.060**	**-0.048**
σC(***sp3***)-O(***sp3***)		$O_{24} - C_{23}$	**1.409**	**1.426**	**1.424**	**1.402**	**-0.017**	**-0.015**	**+0.007**
		$C_{25} - O_{24}$	**1.403**	**1.417**	**1.423**	**1.402**	**-0.014**	**-0.020**	**+0.001**
σC(***sp3***)-C(***sp3***)		$C_{22} - C_{23}$	**1.496**	**1.551**	**1.533**	**1.529**	**-0.055**	**-0.037**	**-0.033**
σC(***sp2***)-C(***sp2***)		$C_{11} - C_{8}$	**1.437**	**1.446**	**1.471**	**1.356**	**-0.009**	**-0.034**	**+0.081**
C(***sp2***)-C(***sp2***)	Aromatic	$C_{2} - C_{1}$	**1.360**	**1.380**	**1.374**	**1.342**	**-0.02**	**-0.014**	**+0.018**
		$C_{3} - C_{2}$	**1.394**	**1.410**	**1.414**	**1.337**	**-0.016**	**-0.020**	**+0.057**
		$C_{4} - C_{3}$	**1.355**	**1.377**	**1.372**	**1.338**	**-0.022**	**-0.017**	**+0.017**
		$C_{5} - C_{4}$	**1.399**	**1.416**	**1.422**	**1.347**	**-0.017**	**-0.023**	**+0.052**
		$C_{6} - C_{5}$	**1.421**	**1.432**	**1.422**	**1.354**	**-0.011**	**-0.001**	**+0.067**
		$C_{7} - C_{5}$	**1.414**	**1.424**	**1.421**	**1.341**	**-0.01**	**-0.007**	**+0.073**
		$C_{8} - C_{6}$	**1.427**	**1.448**	**1.426**	**1.364**	**-0.021**	**+0.001**	**+0.063**
		$C_{9} - C_{7}$	**1.342**	**1.367**	**1.369**	**1.335**	**-0.025**	**-0.027**	**+0.007**
		$C_{10} - C_{8}$	**1.401**	**1.413**	**1.393**	**1.358**	**-0.012**	**+0.008**	**+0.043**
		$C_{15} - C_{14}$	**1.379**	**1.402**	**1.412**	**1.344**	**-0.023**	**-0.033**	**+0.035**

		$C_{16} - C_{14}$	**1.388**	**1.406**	**1.406**	**1.343**	**-0.018**	**-0.018**	**+0.045**
		$C_{17} - C_{16}$	**1.365**	**1.382**	**1.403**	**1.346**	**-0.017**	**-0.038**	**+0.019**
		$C_{18} - C_{17}$	**1.385**	**1.408**	**1.427**	**1.357**	**-0.023**	**-0.042**	**+0.028**
		$C_{19} - C_{18}$	**1.392**	**1.405**	**1.410**	**1.353**	**-0.013**	**-0.018**	**+0.039**
*__Red color__ indicates difference of variation competed between AM1, MM2 and B3LYP Calculations									

Table 4B.3: *Comparative list of selected bond angles (°) between experimental XRD and calculated AM1, MM2 and B3LYP studies of* ***FMIMN***

Central atom	**Atomic string**						**Variation, δ, (°)***	
		XRD	**B3LYP**	**AM1**	**MM2**	**Δ(XRD-B3LYP)**	**Δ(XRD-AM1)**	**Δ(XRD-MM2)**
Csp^2	$C_3\ C_2\ C_1$	**120.80**	**120.92**	**120.70**	**120.11**	**-0.12**	**+0.10**	**+0.69**
	$C_4\ C_3\ C_2$	**119.30**	**119.16**	**119.82**	**118.34**	**+0.14**	**-0.52**	**+0.96**
	$C_5\ C_4\ C_3$	**121.30**	**121.15**	**120.68**	**120.94**	**+0.15**	**+0.62**	**+0.36**
	$C_6\ C_5\ C_4$	**120.30**	**120.08**	**119.74**	**122.23**	**+0.22**	**+0.56**	**-1.93**
	$C_7\ C_5\ C_4$	**121.00**	**120.69**	**120.31**	**117.65**	**+0.31**	**+0.69**	**+3.35**
	$C_8\ C_6\ C_5$	**119.30**	**119.13**	**119.05**	**120.25**	**+0.17**	**+0.25**	**-0.95**
	$C_9\ C_7\ C_5$	**122.00**	**121.59**	**120.82**	**119.47**	**+1.41**	**+1.18**	**+2.53**
	$C_{10}\ C_8\ C_6$	**119.54**	**118.97**	**119.12**	**118.90**	**+0.57**	**+0.42**	**+0.64**
	$C_{11}\ C_8\ C_6$	**121.30**	**121.58**	**123.77**	**121.78**	**-0.28**	**-2.47**	**-0.48**
	$O_{12}\ C_{10}\ C_8$	**123.50**	**122.76**	**117.43**	**124.75**	**+0.74**	**+6.07**	**-1.25**
	$C_{15}\ C_{14}\ N_{13}$	**116.20**	**118.00**	**118.02**	**116.01**	**-1.80**	**-1.82**	**+0.19**
	$C_{16}\ C_{14}\ N_{13}$	**125.10**	**123.91**	**123.79**	**128.88**	**+1.19**	**+1.31**	**-3.78**
	$C_{17}\ C_{16}\ C_{14}$	**118.80**	**119.66**	**121.02**	**122.98**	**-0.86**	**-2.22**	**-4.18**
	$C_{18}\ C_{17}\ C_{16}$	**124.50**	**123.58**	**121.02**	**122.57**	**+0.92**	**+3.48**	**+1.93**
	$C_{19}\ C_{18}\ C_{17}$	**115.50**	**115.66**	**116.72**	**113.44**	**-0.16**	**-1.22**	**+2.06**
	$N_{20}\ C_{18}\ C_{17}$	**120.70**	**119.33**	**119.66**	**125.00**	**+1.37**	**+1.04**	**-4.30**
	$H_{26}\ C_1\ C_2$	**119.00**	**118.11**	**119.38**	**112.86**	**-0.89**	**-0.38**	**+6.14**
	$H_{27}\ C_2\ C_3$	**119.60**	**119.72**	**119.03**	**119.39**	**-0.12**	**+0.57**	**+0.21**
	$H_{28}\ C_3\ C_2$	**120.40**	**120.22**	**119.31**	**120.72**	**0.18**	**+1.09**	**-0.32**
	$H_{29}\ C_4\ C_3$	**119.30**	**120.49**	**120.82**	**117.64**	**-1.19**	**-1.52**	**+1.66**
	$H_{30}\ C_7\ C_5$	**119.00**	**118.43**	**118.68**	**121.98**	**+0.57**	**+0.32**	**-2.98**
	$H_{31}\ C_9\ C_7$	**119.70**	**122.08**	**121.29**	**118.74**	**-2.38**	**-1.59**	**+0.96**
	$H_{32}\ C_{15}\ C_{14}$	**119.50**	**118.67**	**119.88**	**119.86**	**+0.83**	**-0.38**	**-0.36**
	$H_{33}\ C_{16}\ C_{14}$	**120.60**	**122.07**	**120.85**	**121.12**	**-1.47**	**-0.25**	**-0.52**

	F_{34} C_{17} C_{16}	**117.40**	**117.82**	**117.90**	**113.92**	**-0.42**	**-0.50**	**+3.48**
	H_{35} C_{19} C_{18}	**119.30**	**119.16**	**119.76**	**122.86**	**+0.14**	**-0.46**	**-3.56**
	H_{44} C_{11} C_{8}	**119.20**	**117.84**	**112.49**	**119.04**	**+1.36**	**+6.71**	**+0.16**
	N_{13} C_{11} C_{8}	**121.50**	**122.52**	**123.39**	**127.61**	**-1.02**	**-1.89**	**-6.11**
Csp^3	C_{23} C_{22} N_{20}	**109.50**	**111.40**	**114.53**	**114.83**	**-1.9**	**-5.03**	**-5.33**
	O_{24} C_{23} C_{22}	**111.70**	**110.23**	**111.52**	**111.15**	**+1.47**	**+0.18**	**+0.55**
	H_{36} C_{25} O_{24}	**109.20**	**110.38**	**104.26**	**107.84**	**-1.18**	**+4.94**	**+1.36**
	H_{37} C_{25} O_{24}	**109.20**	**105.24**	**109.31**	**109.32**	**+3.96**	**-0.11**	**-0.12**
	H_{38} C_{21} N_{20}	**109.70**	**107.28**	**105.43**	**108.33**	**+2.42**	**+4.27**	**+1.37**
	H_{39} C_{21} N_{20}	**109.70**	**108.95**	**110.31**	**111.45**	**+0.75**	**-0.61**	**-1.75**
	H_{40} C_{22} N_{20}	**109.80**	**110.26**	**109.97**	**110.99**	**-0.46**	**-0.17**	**-1.19**
	H_{41} C_{22} N_{20}	**109.80**	**107.28**	**106.01**	**108.36**	**+2.52**	**+3.79**	**+1.44**
	H_{42} $C_{23}C_{22}$	**109.80**	**108.23**	**110.30**	**111.59**	**+1.57**	**-0.50**	**-1.79**
	H_{43} C_{23} C_{22}	**109.80**	**111.09**	**111.09**	**110.55**	**-1.29**	**-1.29**	**-0.75**
Nsp^2	C_{14} N_{13} C_{11}	**123.80**	**121.86**	**121.14**	**128.77**	**+1.94**	**+2.66**	**-4.97**
Nsp^3	C_{21} N_{20} C_{18}	**117.16**	**119.35**	**117.39**	**119.75**	**-2.19**	**-0.23**	**-2.59**
	C_{22} N_{20} C_{18}	**114.71**	**117.11**	**115.74**	**120.57**	**-2.40**	**-1.03**	**-5.86**
Osp^3	C_{25} O_{24} C_{23}	**110.40**	**111.97**	**112.70**	**110.21**	**-1.57**	**-2.30**	**+0.19**
	H_{45} O_{12} C_{10}	**109.50**	**107.11**	**108.02**	**112.39**	**+2.39**	**+1.48**	**-2.89**
*__Red color__ indicates difference of variation competed between AM1, MM2 and B3LYP Calculations								

Table 4B.4: *Comparative list of selected Dihedral angle (°) of Schiff base, from experimental XRD and AM1, MM2, B3LYP calculations of* ***FMIMN***

Dihedral angle (°)	**XRD**		**B3LYP**		**AM_1**		**MM2**	
	Angle	**(*)**	**Angle**	**(*)**	**Angle**	**(*)**	**Angle**	**(*)**
C_4 C_3 C_2 C_1	**+ 1.1**	***+sc***	**+ 0.08**	***+sc***	**- 0.48**	***- sc***	**- 0.006**	***-sc***
C_5 C_4 C_3 C_2	**- 0.2**	***-sc***	**- 0.05**	***-sc***	**+ 0.36**	***+sc***	**- 0.005**	***-sc***
C_6 C_5 C_4 C_3	**- 0.7**	***-sc***	**- 0.08**	***-sc***	**+ 0.67**	***-sc***	**+ 0.04**	***+sc***
C_7 C_5 C_4 C_3	**+ 178.8**	***+ac***	**+ 179.81**	***+ac***	**- 179.12**	***+ac***	**+ 179.95**	***+ac***
C_8 C_6 C_5 C_4	**- 179.5**	***-ac***	**- 179.81**	***-ac***	**+ 179.53**	***+ac***	**- 179.90**	***-ac***
C_9 C_7 C_5 C_4	**+ 180.0**	***+ac***	**- 179.78**	***-ac***	**+ 179.20**	***+ac***	**- 179.79**	***-ac***
C_{10} C_8 C_6 C_5	**- 0.6**	***-sc***	**- 0.57**	***-sc***	**+ 1.79**	***+sc***	**- 0.05**	***-sc***
C_{11} C_8 C_6 C_5	**+ 177.4**	***+ac***	**+ 179.26**	***+ac***	**- 179.04**	***-ac***	**+ 179.50**	***+ac***
O_{12} C_{10} C_8 C_6	**+ 178.8**	***+ac***	**- 179.43**	***-ac***	**+ 178.45**	***+ac***	**- 178.26**	***-ac***
O_{12} C_{10} C_8 C_{11}	**- -**	**- -**	**+ 0.72**	***+sc***	**- -**	**- -**	**+2.18**	***+sc***
C_8 C_7 C_{11} N_{13}	**- -**	**- -**	**+ 1.14**	***+sc***	**- -**	**- -**	**+1.17**	***+sc***
N_{13} C_{11} C_8 C_6	**- 178.4**	***-ac***	**+ 179.02**	***+ac***	**+ 49.29**	***+sp***	**- 178.38**	***-ac***
C_{14} N_{13} C_{11} C_8	**+ 178.9**	***+ac***	**+177.20**	***+ac***	**+ 179.02**	***+ac***	**- 179.73**	***-ac***

C_{15} C_{14} N_{13} C_{11}	**- 171.5**	***-ac***	**+153.46**	***+ac***	**- 150.99**	***-ac***	**- 179.88**	***-ac***
C_{16} C_{14} N_{13} C_{11}	**+ 9.6**	***+sc***	**-28.58**	***-sc***	**+ 32.06**	***+sp***	**- 0.15**	***-sc***
C_{17} C_{16} C_{14} N_{13}	**- 179.3**	***-ac***	**179.63**	***+ac***	**+ 176.37**	***+ac***	**+ 179.99**	***+ac***
C_{18} C_{17} C_{16} C_{14}	**+0.0**	***+sc***	**+1.51**	***+sc***	**+ 0.76**	***+sc***	**- 0.15**	***-sc***
F_{34} C_{17} C_{16} C_{14}	**-179.3**	***-ac***	**-179.51**	***-ac***	**-179.44**	***-ac***	**+ 179.45**	***+ac***
F_{34} C_{17} C_{18} N_{20}	**- -**	**- -**	**+ 3.12**	***+sc***	**- -**	**- -**	**+ 0.30**	***+sc***
C_{19} C_{18} C_{17} C_{16}	**- 1.9**	***-sc***	**+ 0.27**	***+sc***	**-0.01**	***-sc***	**+ 0.74**	***+sc***
N_{20} C_{18} C_{17} C_{16}	**- 179.4**	***-ac***	**-177. 91**	***-ac***	**- 175.9**	***-ac***	**+ 180.00**	***+ac***
C_{17} C_{18} N_{20} C_{21}	**- -**	**- -**	**+1.86**	***+sc***	**- -**	**- -**	**+2.17**	***+sc***
C_{21} N_{20} C_{18} C_{17}	**+ 164.3**	***+ac***	**+ 158.90**	***+ac***	**+ 159.81**	***+ac***	**- 176.98**	***-ac***
C_{22} N_{20} C_{18} C_{17}	**- 64.3**	***-sp***	**-64.65**	***-sp***	**- 65.35**	***-sp***	**- 1.72**	***-ac***
C_{23} C_{22} N_{20} C_{18}	**+ 169.2**	***+ac***	**-76.35**	***-sp***	**- 91.61**	***-ap***	**+ 174.25**	***+ac***
O_{24} C_{23} C_{22} N_{20}	**+ 57.9**	***+sp***	**-23.50**	***-sc***	**- 51.53**	***-sp***	**+ 36.74**	***+sp***
C_{25} O_{24} C_{23} C_{22}	**- 58.2**	***-sp***	**-40.65**	***-sp***	**+ 55.56**	***+sp***	**- 66.91**	***-sp***
* Conformational analyses using prefixes a = anti, s = syn, p = peri-planar, c = clinal (0 ± 30^0& 180 ± 30^0) and + & - signs.								

The bond lengths (in Å) are found to vary slightly in the gaseous state. It is observed that σH-C(***sp²***) of aromatic rings is increased by about 0.170 Å in the gaseous state. σH-C(***sp²***) of alkenyl is increased by about 0.185 Å. The aliphatic σH-C(***sp3***) is also increased by ~0.15 Å. The lengths of the other bonds, such as, σH-O(***sp3***), σN(***sp3***)-C(***sp2***) and σC(***sp2***)-O(***sp3***) are noted to have increased their lengths by ~0.148 Å, ~0.007, ~0.060 and ~0.017 Å, respectively whereas σF-C(***sp²***) is decreased by ~0.003 Å. The variation of bond lengths as evaluated by computational methods on a gaseous molecule of **FMIMN** Vis a Vis the corresponding values for various bonds obtained from the XRD for **FMIMN** in its solid state is presented in **Table 4B.2.** The increase in bond length in gaseous state suggests a possible zone of steric strain in the solid state and a decrease in any bond length, a location of intermolecular interaction in the solid state.

The difference in bond angles between XRD and computational data over several atomic strings is shown in **Table 4B.3**. The closer are the two angles, the less is the strain experienced by the respective atomic string.

Bond angle (^{o}) at C-sp^2 is observed to vary from -6.7 ^{o} to +2.47 ^{o} due to angle strain or aromatic strain in the gaseous state. Bond angle (^{o}) at C-sp^3 is found to vary from -4.94 ^{o} to +5.03 ^{o}. The bond angle at N-sp^2 is decreased (by ~ 2.66 ^{o}) and that at N-sp^3 is increased (by ~ 2.25^o), whereas the bond angle at O-sp^3 is increased by +2.30 ^{o} in the case of morpholin and decreased by -1.48 ^{o} in the case of aromatic H-O-C.

The conformational changes as seen from the variation through several dihedral angles over some selected atomic strings are shown in **Table 4B.4.** For example, the dihedral angles of C_5-C_4-C_3-C_2 and C_{10}-C_8-C_6-C_5 are changed from –sc to +sc conformation under the AM1 method. The +ac of C_9-C_7-C_5-C_4 and O_{12}-C_{10}-C_8-C_6 change to –ac under DFT. Similarly, the +sc of C_{18}-C_{17}-C_{16}-C_{14} changes to –sc under MM2 method. The –ac of C_{17}-C_{16}-C_{14}-N_{13} change to +ac under all the three computational platforms. The trends of other methods with respect to the empirical data can be seen in **Table 4B.4.** In near all cases of molecular structural parameters, it is evident from **Table 4B.2** through **Table 4B.4.** That the values obtained from the DFT/B3LYP method appear to be in better agreement with the experimental data than those from the other two platforms, viz., AM1 and MM2.

4B.3 Hirshfeld Surface Analysis:

Hirshfeld surface analysis is a tool for analyzing molecular interactions and arrangements in a crystal[18]. CrystalExplorer 17.5 software has been used to generate Hirshfeld surfaces[19]**.** Hirshfeld analysis was performed on **FMIMN** in order to examine the strength and role of hydrogen bonds and other intermolecular contacts, Hirshfeld surfaces and the corresponding fingerprint plots and to assess their importance in the stability of the crystal lattice. **Figure 4B.7** shows the molecule's Hirshfeld surface mapped over the d_{norm} range of -0.0441 to 1.4288 a.u. **Figure 4B.8** shows intermolecular hydrogen bonding interactions of **FMIMN**.

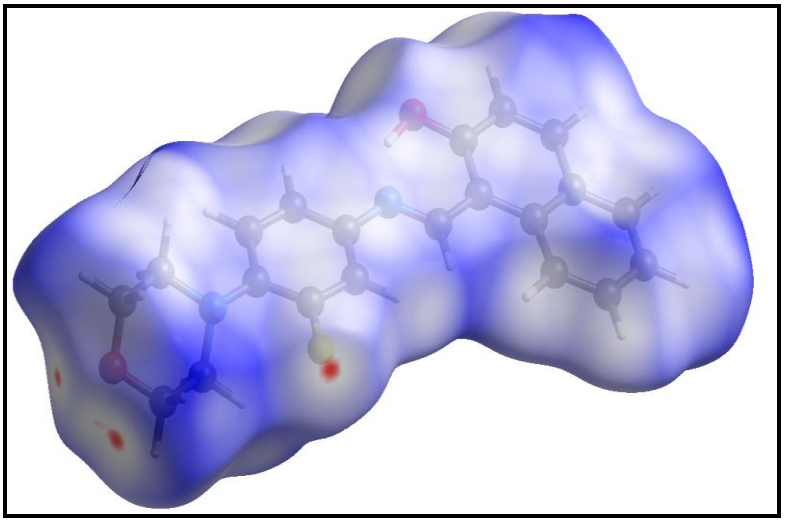

Figure 4B.7: *Hirshfeld d_{norm} surface of* ***FMIMN***

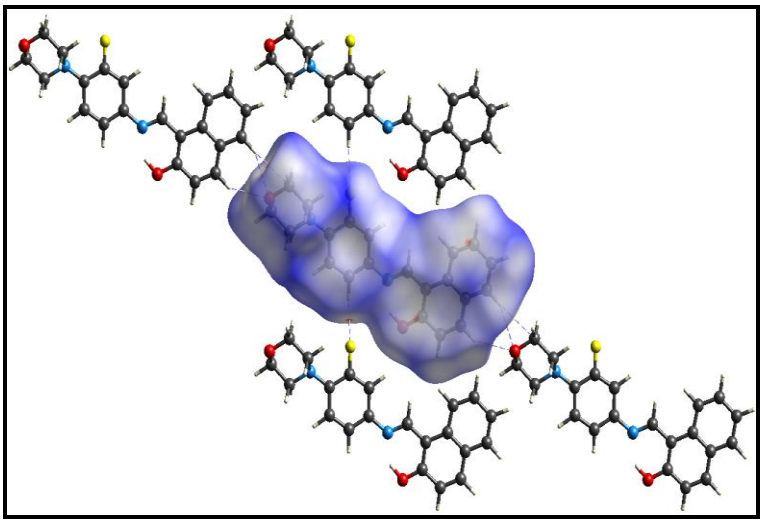

Figure 4B.8: *Hirshfeld d_{norm} surface of* ***FMIMN*** *showing intermolecular hydrogen bonding interactions*

4B.3.1 ***Hirshfeld Fingerprint Plots:***

In a crystal, fingerprint plots show the specific atom pair interactions**.** They are a graphic representation of the intermolecular interactions in a crystalline structure[20]. The intermolecular interactions of molecules appear as sharp spikes and wings[21]. Complementary regions in the fingerprint plot indicate one molecule as a donor ($d_e > d_i$) and another molecule as an acceptor ($d_e < d_i$)[22]. The shortest H...H contact has a minimal value of (de + di) about 2 Å. The H...H contact accounts for the majority of the overall Hirshfeld surface area (48%). **Figure 4B.10** shows the contributions of several interactions to the total Hirshfeld surface area. **Figure 4B.9** shows two-dimensional fingerprint plots of various intermolecular interactions on the Hirshfeld surface area. The strong acceptor-donor intermolecular hydrogen bond interactions that appear at C_4-H_{29}···O_{24}, C_4-H_{29}-···C_{23}, C_7-H_{30}···O_{24}, C_{17}-F_{34}···H_{32} are indicated as bright red color spots. **Figure 4B.9** indicates H···H interactions as the largest, which is about 48% of the surface concentration. The C···H/ H···C contact accounts for approximately 24.1% of the total, with two spikes at de + di values of 1.6 Å. The F···H/ H···F contact contributes around 6.8% with a $d_e + d_i$ value of ~1.3 Å. The O···H/ H···O contact contributes nearly 9.9%, with a $d_e + d_i$ value of ~1.4 Å. All other intermolecular interatomic contacts and the corresponding interactions are found to contribute less than 7.0%.

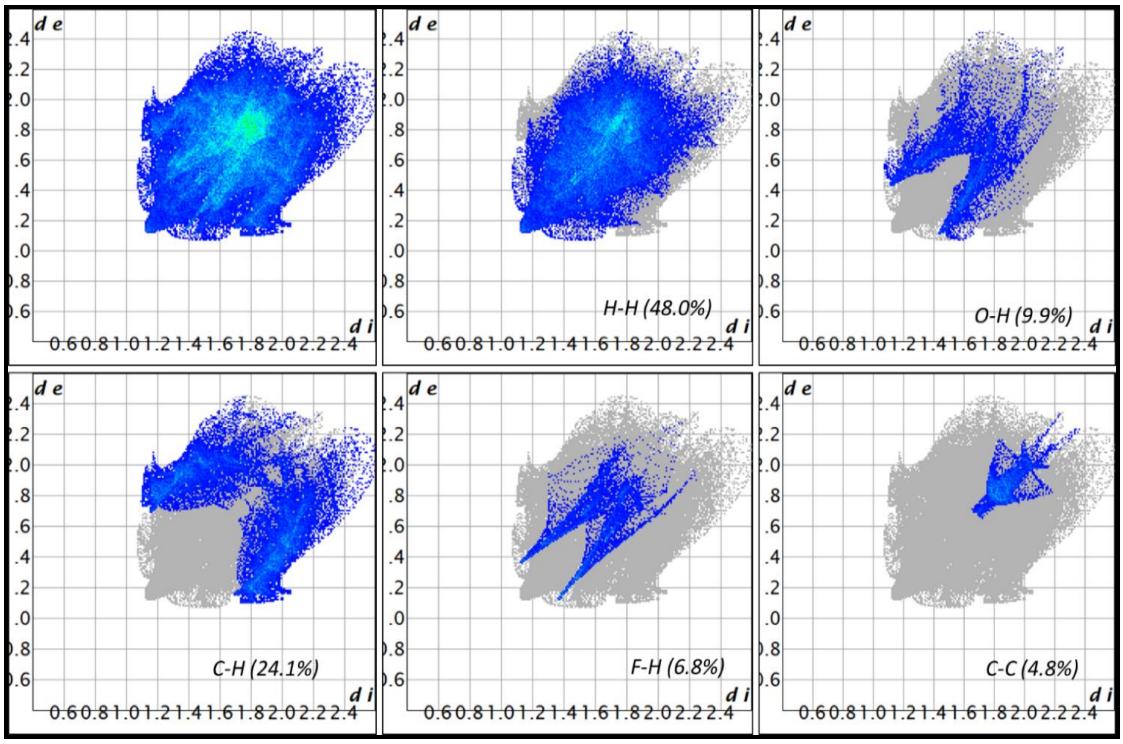

Figure 4B.9: *Hirshfeld finger print plots of* ***FMIMN***

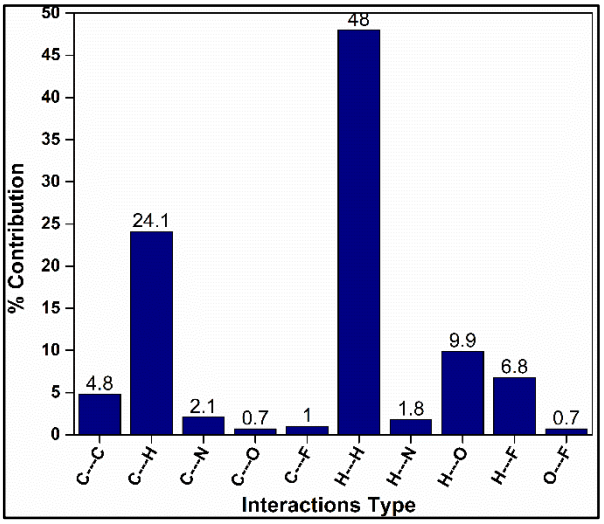

Figure 4B.10: *Intermolecular Hirshfeld inter-atomic interaction percentages*

4B.3.2 *Shape Index, Curvedness, Electrostatic Potential and Fragment Patches:*

The surface parameters of shape index and curvedness are used to determine the molecular arrangements in the crystal[23,24]**.** The flat regions on the curvedness plot reflect planar molecule

stacking. The arrangement of red and blue triangles on the contour index map exemplifies a common property of π- π interactions. The molecule is clearly stacked in a planar way since it has flat portions on the curvedness map. **Figure 4B.13** represents the surfaces of shape-index **(a)**, curve index **(b),** fragment patches **(c)**, diffuse graphical portrayal (positive electrostatic potential is shown in blue shade and negative in red) color coded interactions with in 3.8 Å **(d)**.

Small blue regions around the bright-red spots in the shape index plot indicate π- π stacking between the benzene and quinoline rings. The green shade in the flat region of the curve index plot represents the π- π stacking around the benzene and quinoline rings. **Figure 4B.13(d)** depicts the electrostatic potential map generated by the HF/3-21G basis set, with a red region indicating negative electrostatic potential (hydrogen acceptors) and a blue region indicating positive electrostatic potential (hydrogen donor)[25].

4B.3.3 *Hirshfeld Interaction Energies and Energy Frameworks:*

The HF/3-21G quantum theory, which is available in CrystalExplorer software, was used to compute the interaction energies in **FMIMN**[26]**. Figure 4B.12** shows molecular packing corresponding to dispersion energy, coulomb energy and total energy along a, b, and c axes, respectively. It exhibits individual energy components as cylinders between the centroids of interacting molecular pairs with the corresponding energies. **Figure 4B.11** depicts a graphical representation of the interaction energy calculations performed for the molecule clusters. The cylindrical radii in the laddered bars are represented as a function of the strength of the interaction energies[27]**,** normalized to 100 with a minimum value of 5 kJ mol^{-1}.

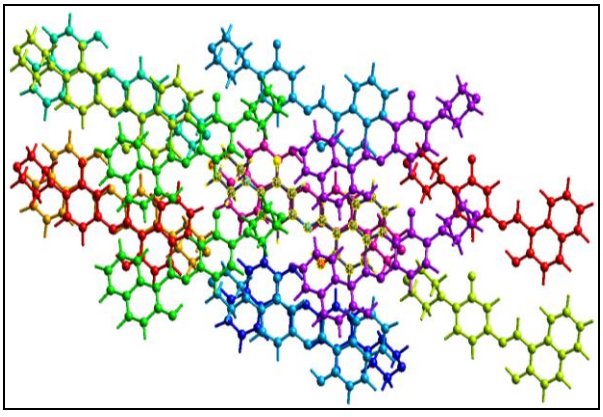

Figure 4B.11: *Pair-wise intermolecular interactions in* ***FMIMN*** *(viewed along the c axis)*

Table 4B.5: *Pair-wise intermolecular interaction energies of* ***FMIMN***

N	Symop	R	E_{ele}	E_{pol}	E_{dis}	E_{rep}	E_{tot}
2	x, y, z	15.16	3.4	-1.4	-11.2	0.0	-7.5
1	-x, -y, -z	14.95	1.9	-0.8	-8.5	0.0	-6.3
2	x, y, z	16.88	-12.9	-3.0	-12.6	0.0	-26.5
2	-x+1/2, y+1/2, -z+1/2	9.66	-3.1	-1.1	-24.6	8.9	-18.8
1	-x, -y, -z	16.93	1.2	-0.3	-6.0	0.0	-4.3
2	x, y, z	7.43	-10.3	-3.1	-26.7	12.6	-26.4
1	-x, -y, -z	7.88	-4.6	-4.0	-29.3	13.6	-22.6
2	-x+1/2, y+1/2, -z+1/2	8.96	-7.5	-2.6	-43.9	19.3	-33.2
1	-x, -y, -z	3.82	-7.5	-6.2	-107.6	43.1	-73.7

Energy Model	k_{ele}	k_{pol}	k_{disp}	k_{rep}
CE-HF ... HF/3-21G electron densities	1.019	0.651	0.901	0.811
CE-B3LYP ... B3LYP/6-31G(d,p) electron densities	1.057	0.740	0.871	0.618

The scaling parameters for the evaluated energies for the HF/3-21G are k_{ele} = 1.019 kJ mol^{-1}, k_{pol} = 0.651 kJ mol^{-1}, k_{disp} = 0.901 kJ mol^{-1}, and k_{rep} = 0.811 kJ mol^{-1} and the energy framework values for the above evaluated energies are -39.4 kJ mol^{-1}, -270.4 kJ mol^{-1}, -22.5 kJ mol^{-1}, and 97.5 kJ mol^{-1}, respectively. From these values, it can be observed that the dispersion energy dominates the electrostatic energy. The total energy is found to be 219.3 kJ mol^{-1}. The chemical pair-wise interaction energies are listed in **Table 4B.5**. In the table, R stands for the distance between the mean atomic locations. The molecular packing interactions are illustrated along the a, b, and c axes in **Figure 4B.10**, which correspond to coulomb energy (red), dispersion energy (green), and total energy (blue). The size of the cylinders in the energy frameworks represents molecular packing and the strength of the interaction energy[28]**.**

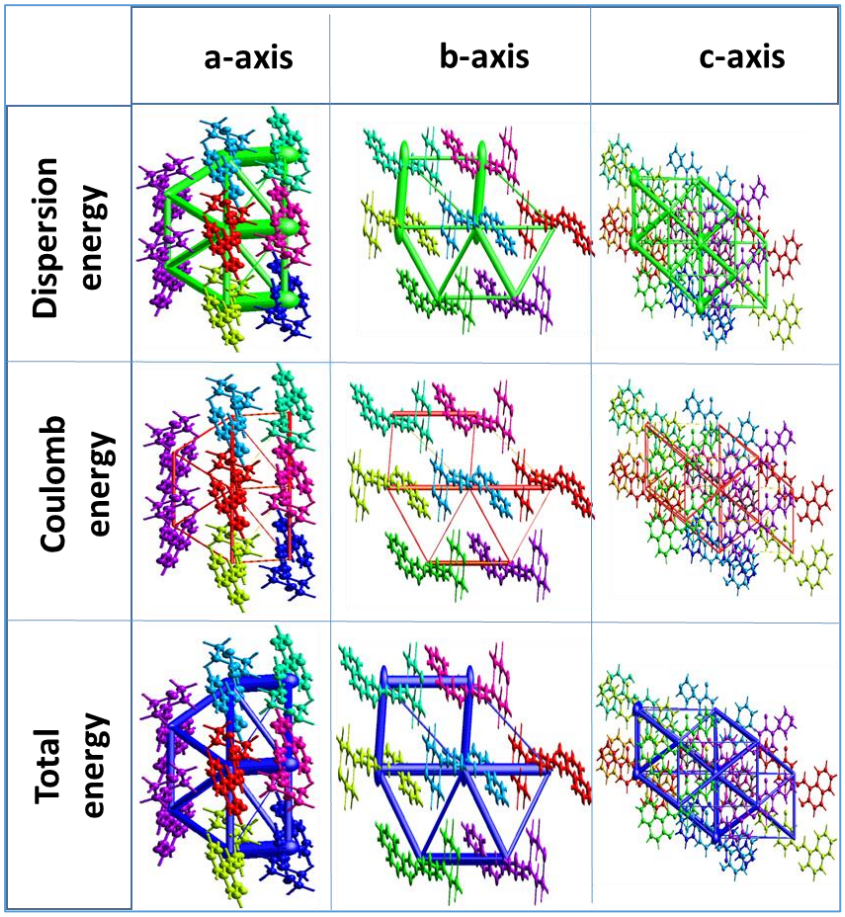

Figure 4B.12: *Crystallographic axis-wise modes of intermolecular energies in* ***FMIMN***

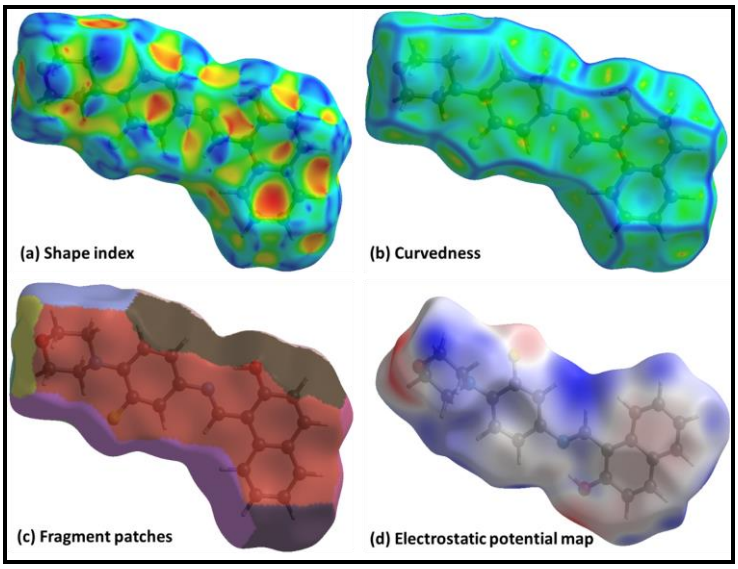

Figure 4B.13: *Hirshfeld surface maps of* ***FMIMN*** *represented by modes*

4B.4 Molecular Modelling and Docking Studies of FMIMN and M(FMIMN)$_2$:

Molecular modelling studies were used to determine the conformational visualization of the molecules in various forms in order to address the stability aspects of the **FMIMN** ligand and its metal complexes. The global energy minimized structures are calculated using the MM2 force field method with a RMS gradient of 0.01. In any structural analysis, the bond length, bond angles and torsional angles are some of the most essential structural factors. The ligand **FMIMN** as well as its complexes are being investigated. There is a great degree of consistency between the experimental and simulated results. **Figure 4B.14** shows the globally minimized structures of the **FMIMN** ligand and associated metal complexes. Quantum mechanical HOMO-LUMO orbital energy estimates were used to compute the expected gas-phase electronic transitions. **Figures 4B.15** and **4B.16** show the HOMO-LUMO structures of **FMIMN** and **M(FMIMN)$_2$**. Some of the important bond lengths, bond angles, and torsional angles data of **M(FMIMN)$_2$** obtained from MM2 calculations are shown in **Tables 4B.6** and **4B.7.**

The cell-membrane receptor EGFR-TK (pdb id: 4HJO) belongs to the tyrosine kinase family of epidermal growth factor receptors[29]. Excess EGFR expression causes anal cancer and epithelial tumors of the neck and head[30]**.** We chose EGFR as a target protein receptor for molecular docking studies with **FMIMN** and **[M(FMIMN)$_2$** because of this feature. **Figures 4B.17–4B.22** show molecular docking interactions of **FMIMN** and its complexes. **Table 4B.8** comprises the binding energies obtained from the docking investigations. The binding energies of the ligand and complexes with the protein receptor EGFR (as shown in **Table 4B.8**) indicate that the ligand and complexes have a good affinity for the EGFR protein receptor. Docking experiments also show that **[Co(FMIMN)$_2$]** and **[Cu(FMIMN)$_2$]** have the lowest EGFR binding energies, with values of -11.4 and -9.8 kcal mol^{-1}, respectively.

The **[Co(FMIMN)$_2$]** complex interacts with the EGFR via three carbon hydrogen bond interactions with ARG817, LYS851, and LYS852 protein amino acid residues. It also docks via one halogen interaction with SER696, four electrostatic interactions with LYS721, ARG817, and ASP813, and ten hydrophobic interactions with PHE699, ASP813, LYS721, PHE699, ALA698, and ARG817 amino acids.

The **[Ni(FMIMN)$_2$]** complex docks to the EGFR through a total of four hydrogen bond interactions with the protein amino acid residues of LYS836, ASP737, GLU734, and VAL741.

Further, it docks through five hydrophobic interactions with VAL741, LEU809, and LYS836. Moreover, it docks through GLU738, ASP737, and LYS836 with three electrostatic interactions.

The **[Cu(FMIMN)$_2$]** complex docks to the EGFR via four hydrogen bond interactions with ALA698, ARG817, and ASN818 protein amino acid residues. There are two halogen interactions with ASP813 and ASN818, as well as ten hydrophobic interactions with ALA698, LEU694, GLY695, LEU838, PHE699, LYS851, VAL702, and ARG817.

The **[Mn(FMIMN)$_2$]** complex has three hydrogen bond interactions with ARG817, and GLY697. Moreover, it has two halogen interactions with GLY697 and ARG817 amino acid residues and six hydrophobic interactions with PHE699, LYS855, TRP856, ARG817 and LYS851.

The **[Zn(FMIMN)$_2$]** complex docks to the EGFR via three hydrogen bond interactions with LYS836 and ALA698 protein amino acid residues. The amino acid residues of LEU809, PHE832, HIS869, VAL741, LEU809, LYS836, and ARG808 interact with this complex through hydrophobic interactions. Furthermore, it also interacts with the amino acid residue of ARG808 through halogen interaction.

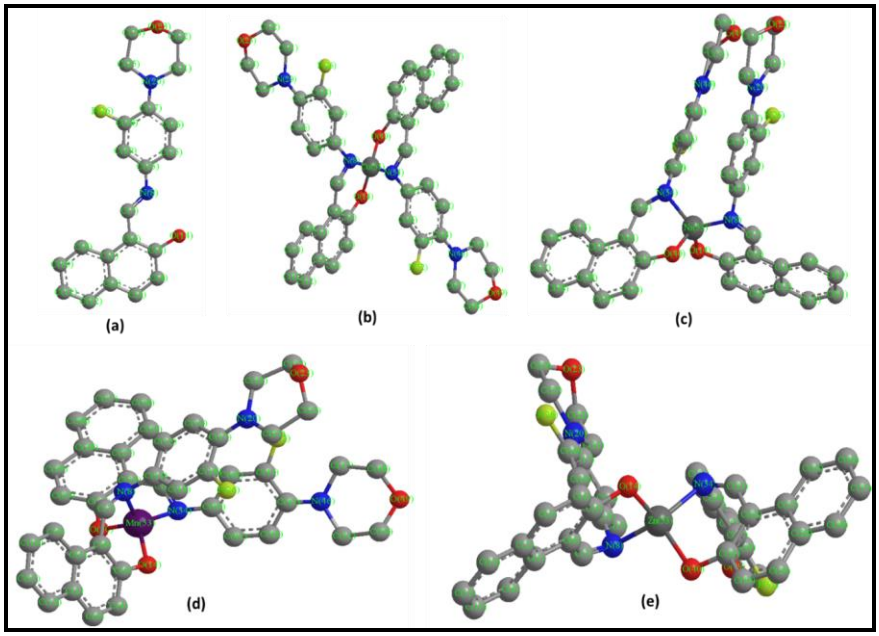

Figure 4B.14: *Global minimized ball-stick models of (a)* ***FMIMN*** *(b)* ***Cu(FMIMN)$_2$*** *(c)* ***Ni(FMIMN)$_2$*** *(d)* ***Mn(FMIMN)$_2$*** *and (e)* ***Zn(FMIMN)$_2$*** *(The hydrogen atoms are hidden for clarity)*

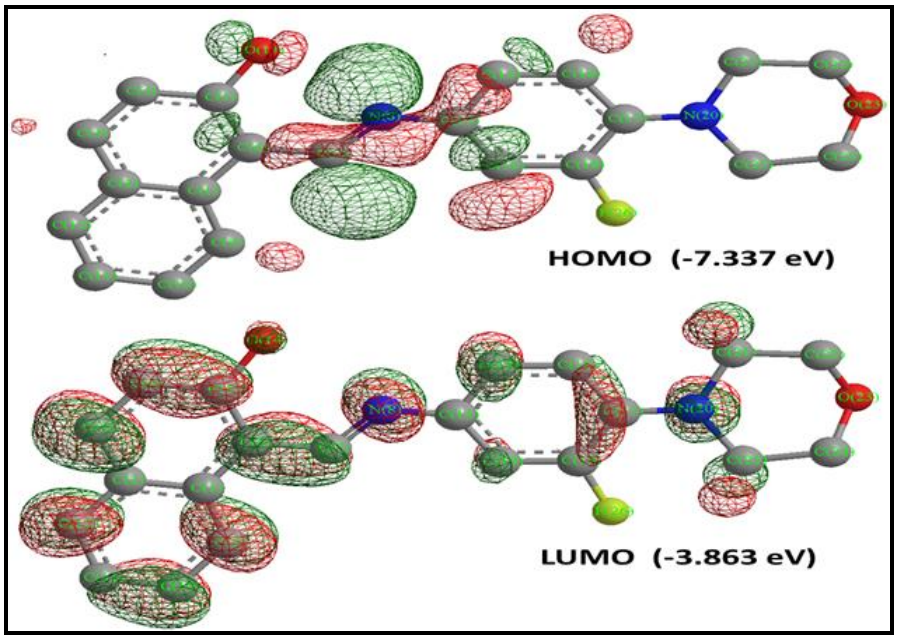

Figure 4B.15: *HOMO and LUMO molecular orbitals of* ***FMIMN*** *in wire mesh format (H-atoms and lone pairs of electrons are excluded for clarity)*

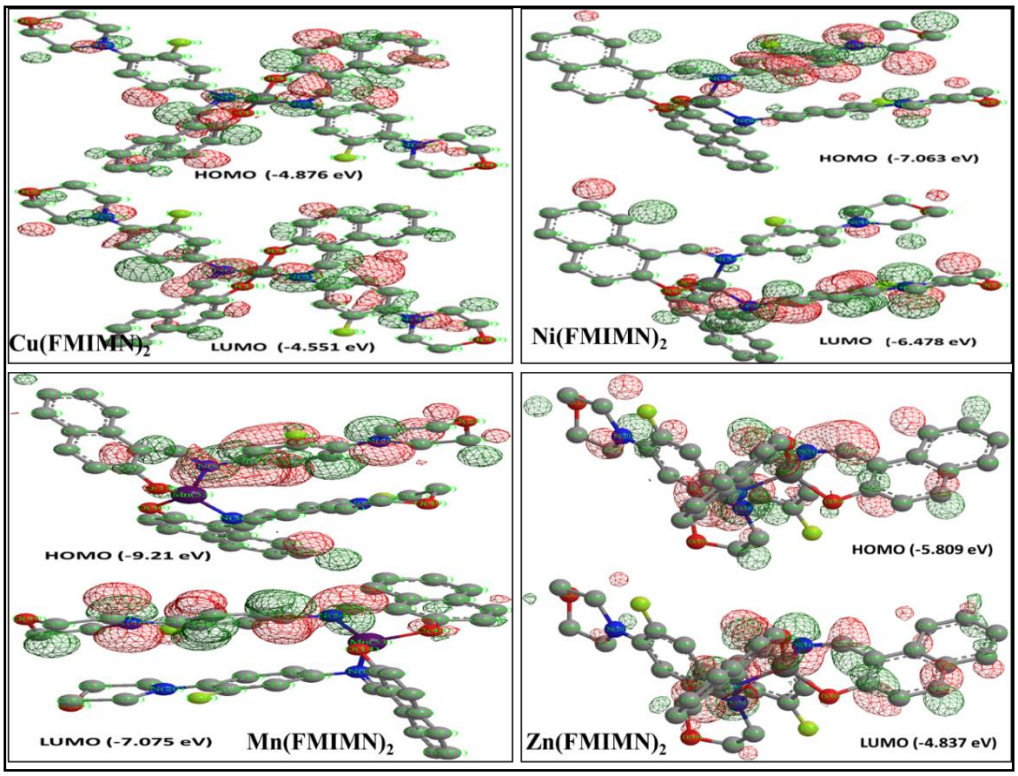

Figure 4B.16: *HOMO and LUMO molecular orbitals of* ***M(FMIMN)$_2$*** *in wire mesh format (H-atoms and lone pairs of electrons are excluded for clarity)*

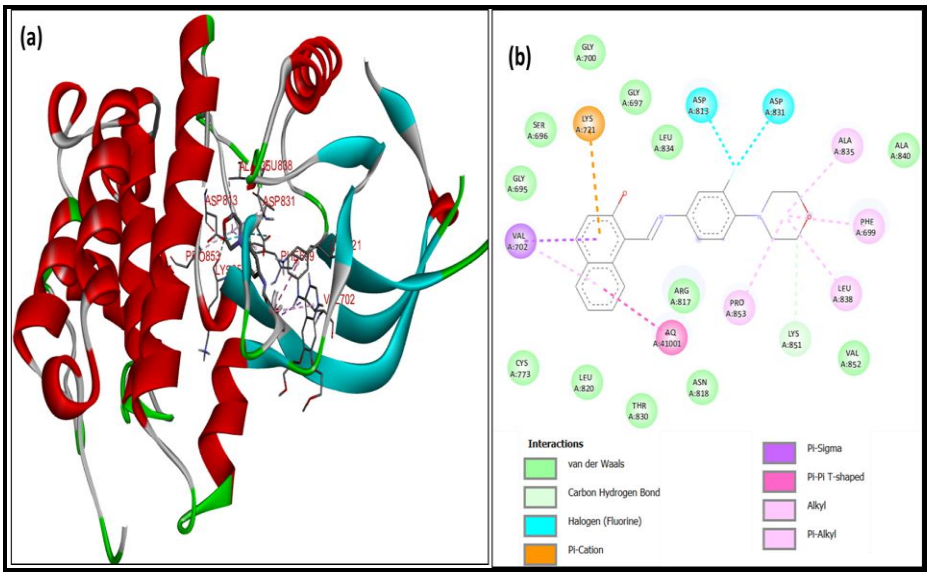

Figure 4B.17: *Molecular docking interactions of* ***FMIMN*** *with EGFR protein; (a) 3D depiction of ligand-receptor binding interactions and (b) 2D representation of different forms of interactions with amino acid residues*

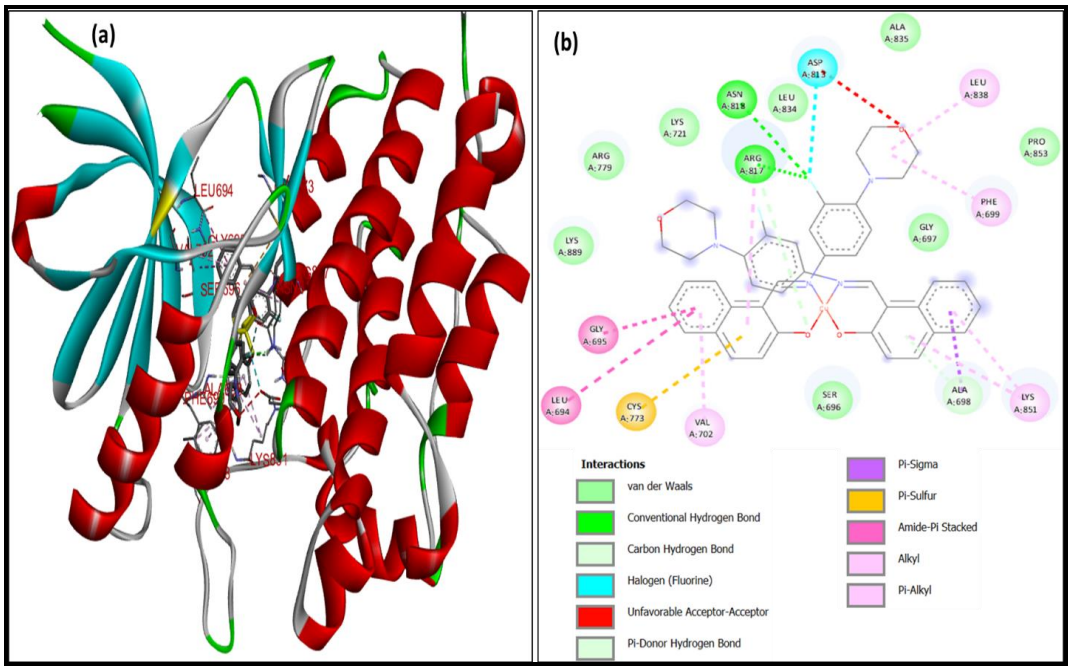

Figure 4B.18: *Molecular docking interactions of* ***Cu(FMIMN)$_2$*** *with EGFR protein; (a) 3D depiction of ligand-receptor binding interactions and (b) 2D representation of different forms of interactions with amino acid residues*

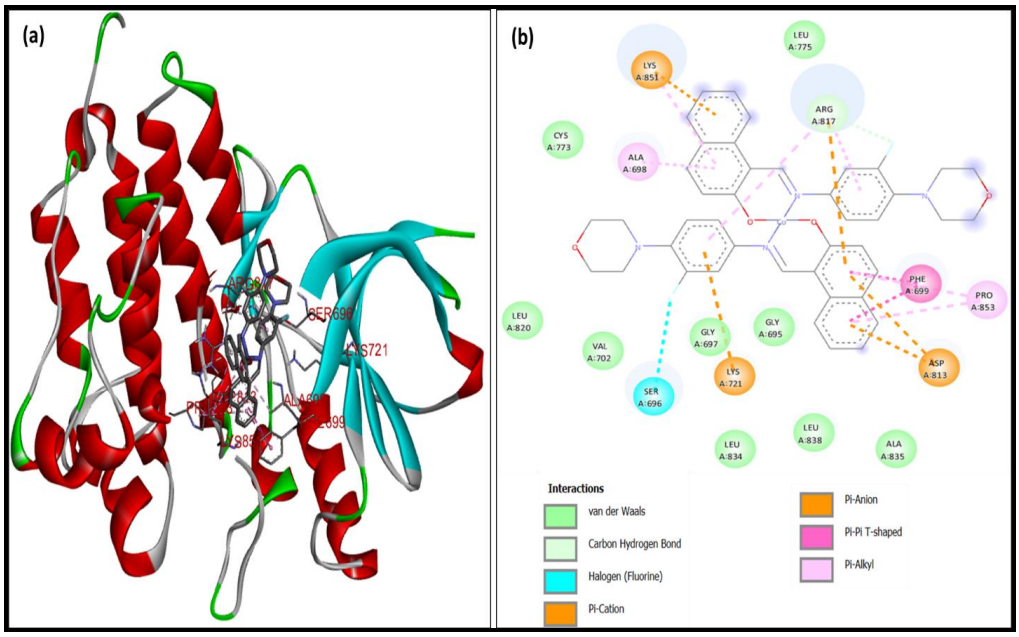

Figure 4B.19: *Molecular docking interactions of* ***Co(FMIMN)$_2$*** *with EGFR protein; (a) 3D depiction of ligand-receptor binding interactions and (b) 2D representation of different forms of interactions with amino acid residues*

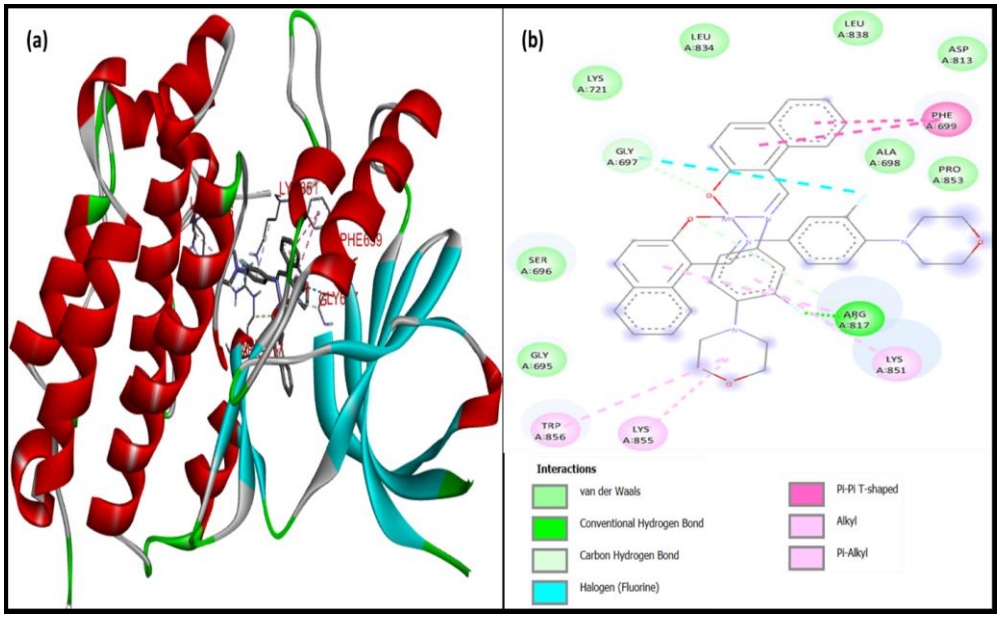

Figure 4B.20: *Molecular docking interactions of* ***Mn(FMIMN)$_2$*** *with EGFR protein; (a) 3D depiction of ligand-receptor binding interactions and (b) 2D representation of different forms of interactions with amino acid residues*

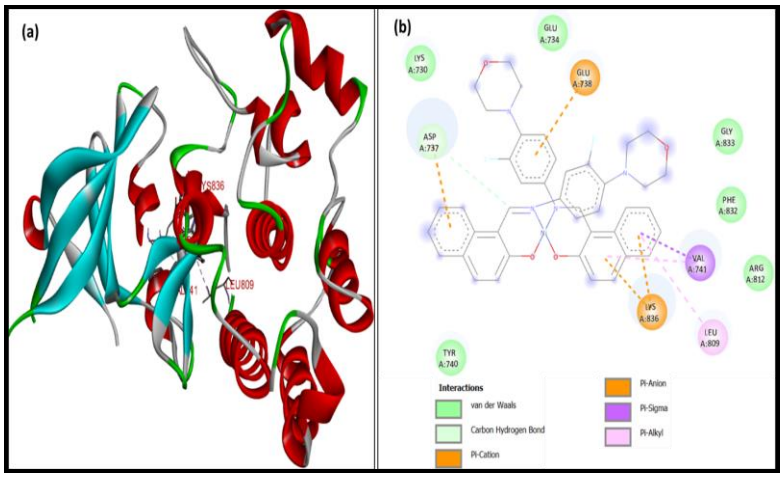

Figure 4B.21: *Molecular docking interactions of* ***Ni(FMIMN)$_2$*** *with EGFR protein; (a) 3D depiction of ligand-receptor binding interactions and (b) 2D representation of different forms of interactions with amino acid residues*

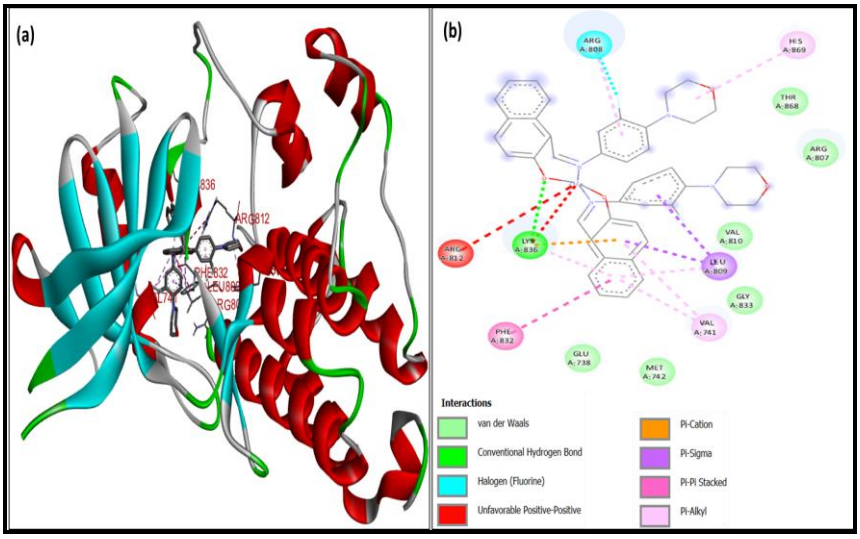

Figure 4B.22: *Molecular docking interactions of* ***Zn(FMIMN)$_2$*** *with EGFR protein; (a) 3D depiction of ligand-receptor binding interactions and (b) 2D representation of different forms of interactions with amino acid residues*

Table 4B.6: *Some of the important bond lengths and bond angles of* ***ML$_2$ (L=FMIMN)*** *(Refer* ***Figure 4B.13*** *for numbering of the atoms)*

Bond lengths (Å)	**Cu(FMIMN)$_2$**	**Ni(FMIMN)$_2$**	**Co(FMIMN)$_2$**	**Mn(FMIMN)$_2$**	**Zn(FMIMN)$_2$**

M-O_{52}	1.811	1.773	0.731	1.792	1.892
M-O_{26}	1.811	1.771	0.731	1.792	1.893
M-N_{12}	1.334	1.811	1.839	1.832	1.936
M-N_{38}	1.335	1.811	1.839	1.833	1.937
N_{12}-C_{13}	1.290	1.282	1.278	1.279	1.281
N_{12}-C_7	1.285	1.279	1.278	1.283	1.276
O_{26}-C_5	1.364	1.373	1.425	1.376	1.372
N_{38}-C_{33}	1.285	1.277	1.279	1.282	1.276
N_{38}-C_{39}	1.290	1.278	1.278	1.279	1.280
O_{52}-C_{31}	1.364	1.372	1.425	1.376	1.373
C_{32}-C_{33}	1.357	1.361	1.346	1.364	1.361
C_7-C_6	1.358	1.360	1.347	1.352	1.361
Bond angles (°)					
$C_{14}C_{13}N_{12}$	119.5	118.6	125.1	125.5	127.2
$C_{18}C_{13}N_{12}$	126.9	127.0	119.4	119.6	118.0
$C_6C_7N_{12}$	134.3	135.1	123.7	133.2	136.2
$C_1C_6C_7$	124.8	121.6	126.8	122.3	120.2
$N_{12}MO_{26}$	107.6	103.1	107.2	98.7	99.7
$N_{12}MO_{52}$	104.9	110.7	101.3	113.7	115.2
$O_{26}MN_{38}$	112.9	115.0	100.9	113.8	113.8
$N_{38}MO_{52}$	107.5	98.7	107.2	98.7	99.1
$C_{13}N_{12}M$	113.7	108.8	120.6	114.9	101.7
$C_{13}N_{12}C_{17}$	107.6	111.4	110.8	119.3	115.0
$C_{33}N_{38}C_{39}$	107.6	123.3	110.4	119.1	115.2
$O_{52}C_{31}C_{32}$	122.3	125.5	123.7	126.1	126.7
$MN_{38}C_{39}$	113.7	112.5	121.1	115.0	102.7
$MN_{38}C_{33}$	115.4	107.1	110.7	106.6	107.2
$MO_{26}C_5$	111.3	111.2	126.6	113.3	112.1

Table 4B.7: *Some of the important dihedral angles of* ***ML_2 (L=FMIMN)*** *(Refer* ***Figure 4B.13*** *for numbering of the atoms)*

Torsional angles (Å)	**$Cu(FMIMN)_2$**	**$Ni(FMIMN)_2$**	**$Co(FMIMN)_2$**	**$Mn(FMIMN)_2$**	**$Zn(FMIMN)_2$**
$C_{14}C_{13}N_{12}M$	-96.1	+100.9	-85.2	+85.7	+88.2
$C_{14}C_{13}N_{12}C_7$	+134.7	-140.9	+46.9	-42.6	-28.1
$C_{18}C_{13}N_{12}C_7$	+18.2	+37.2	+30.2	-32.8	+151.3
$C_{18}C_{13}N_{12}M$	+104.7	-81.0	+100.7	-97.6	-92.5
$C_{13}N_{12}MO_{52}$	+27.8	-164.4	-126.6	-67.9	+151.6
$C_{13}N_{12}MO_{26}$	-87.4	+79.7	++99.7	+175.1	-83.6

$C_{13}N_{12}MN_{38}$	+148.6	-50.1	-11.5	+49.9	+38.1
$N_{12}C_7C_6C_5$	-3.4	+0.6	+6.1	-5.8	+0.9
$MO_{26}C_5C_6$	+20.9	-27.3	-47.0	-26.8	+26.0
$N_{38}MO_{26}C_5$	+82.7	+177.0	+172.0	+178.6	-161.5
$N_{38}MO_{52}C_{31}$	-40.2	-49.5	+51.8	+48.0	+43.4
$N_{38}C_{33}C_{32}C_{31}$	-3.5	+4.3	-174.4	-5.8	0.0
$C_{32}C_{33}N_{38}C_{39}$	+107.1	-167.3	-135.0	+168.0	-88.6
$C_{39}N_{38}MN_{12}$	+148.6	-119.1	-13.6	+50.3	-156.0
$C_{39}N_{38}MO_{52}$	-87.5	-170.8	+98.1	+175.3	+81.1
$C_{39}N_{38}MO_{26}$	+27.7	-55.5	-128.5	-67.7	-42.6

Table 4B.8: *Docking data of* ***FMIMN*** *and its metal complexes with the EGFR protein*

Compound	Binding energy (kcal mol^{-1})	No. of H-bonds	Proteins residues involved in the interactions
FMIMN	-9.1	1	VAL702, GLY695, SER696, GLY700, LYS721, GLY697, LEU834, ASP831, ALA835, ALA840, PHE699, CYS773, LEU820, THR830, ARG817, PRO853, LYS851, LEU838, VAL852
Cu(FMIMN)$_2$	-9.8	4	LYS889, ARG779, LYS721, ARG817, ASN818, LEU834, ASP813, ALA835, LEU838, PRO853, PHE699, GLY697, GLY695, LEU694, CYS773, VAL702, SER696, ALA698, LYS851
Ni(FMIMN)$_2$	-9.4	4	LYS730, ASP737, TYR740, GLU734, GLU738, GLY833, PHE832, VAL741, ARG812, LYS836, LEU809
Co(FMIMN)$_2$	-11.4	3	CYS773, ALA698, LYS851, LEU775, ARG817, LEU820, VAL702, SER696, GLY697, LYS721, GLY695, PHE699, PRO853, ASP813, LEU834, LEU838, ALA835
Mn(FMIMN)$_2$	-9.4	3	LYS721, GLY697, LEU834, LEU838, ASP813, PHE699, ALA698, PRO853, SER696,GLY695, TRP856, LYS855, ARG817, LYS851
Zn(FMIMN)$_2$	-9.4	3	ARG808, HIS869, THR868, ARG807, VAL810, LEU809, GLY833, VAL741, MET742, GLU738, PHE832, LYS836, ARG812

PART C

BIOLOGICAL ACTIVITY STUDIES OF FMIMN AND [M(FMIMN)$_2$]

4C.1 *In vitro* Antimicrobial Activity:

The **FMIMN** ligand and its various Schiff base complexes were tested for microbiological activity against two gram-positive and two gram-negative bacteria, along with streptomycin as a standard[31]. **Table 4C.1** lists the results of the studies.

Table 4C.1: *Antibacterial MIC values of* ***FMIMN*** *and* ***[M(FMIMN)$_2$]*** *(µg/ml)*

Compound	*S. aureus*	*B. subtilis*	*K. pneumoniae*	*E. coli*
Cu(FMIMN)$_2$	8.36	9.15	11.31	8.73
Zn(FMIMN)$_2$	9.12	13.39	10.76	11.31
Ni(FMIMN)$_2$	13.14	14.26	11.58	14.58
Co(FMIMN)$_2$	34.21	42.36	24.12	42.75
Mn(FMIMN)$_2$	42.23	49.67	36.57	24.19
FMIMN	80.14	73.24	>100	>100
Streptomycin	5.62	7.26	7.15	5.80

The results reveal that the ligand shows less activity against both gram negative and gram positive microorganisms. The activity of **Zn(FMIMN)$_2$**, **Cu(FMIMN)$_2$**, and **Ni(FMIMN)$_2$** complexes have moderate to good activity.

4C.2 *In vitro* Antioxidant Property:

The scavenging activity has been studied for the free radical *DPPH* (2,2-Diphenyl-1-picrylhydrazyl)[32]**.** The results are presented in **Table 4C.2.** According to the findings, the complexes **[Zn(FMIMN)$_2$]**, [**Ni(FMIMN)$_2$]**, and **[Co(FMIMN)$_2$]** have significant antioxidant activity in that order. However, the activity of some of the complexes **[Cu(FMIMN)$_2$]** and **[Mn(FMIMN)$_2$])** is lower than the standard **(Figure 4C.1).**

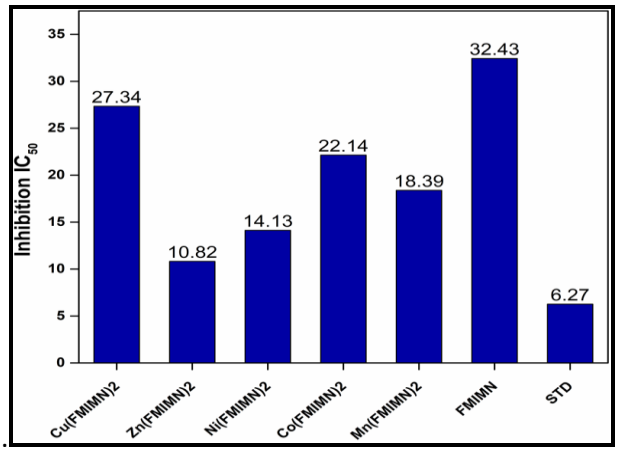

Figure 4C.1: *Histographical representation of the IC_{50} inhibition values of DPPH radical scavenging activity of* ***FMIMN*** *and* ***M(FMIMN)$_2$***

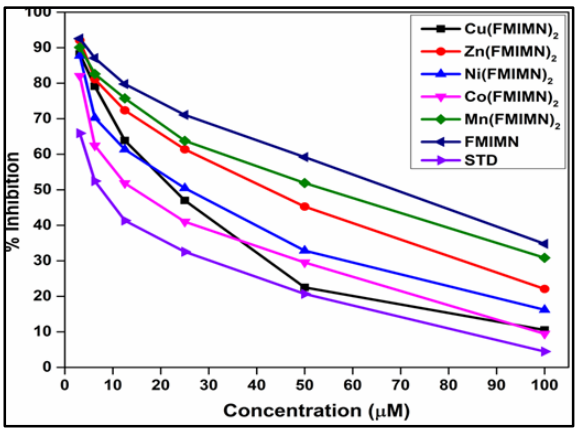

Figure 4C.2: *Cell viability assay; dose-response curves of* ***FMIMN*** *and its metal complexes with different concentrations on MCF7 cells*

Table 4C.2: *Anti-scavenging activity MIC values of* ***FMIMN*** *and* ***[M(FMIMN)$_2$]*** *(μg/ml)*

Compound	**IC_{50} (μM)**
Cu(FMIMN)$_2$	27.34 ± 1.37
Zn(FMIMN)$_2$	10.82 ± 2.12
Ni(FMIMN)$_2$	14.13 ± 1.15
Co(FMIMN)$_2$	22.14 ± 1.23
Mn(FMIMN)$_2$	18.39 ± 2.52
FMIMN	32.43 ± 1.03
Ascorbic acid	6.27 ± 0.24

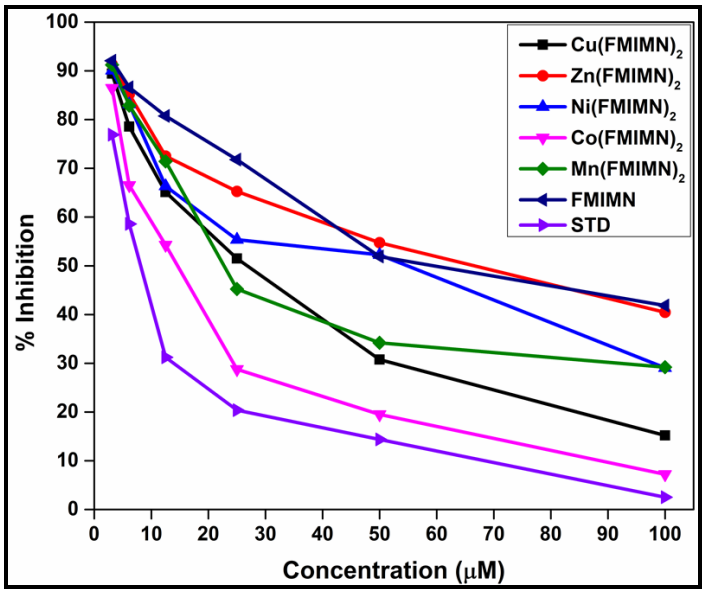

Figure 4C.3: *Cell viability assay; dose-response curves of* ***FMIMN*** *and its metal complexes with different concentrations on HepG-2 cells*

4C.3 *In vitro* Antifungal Activity:

In vitro antifungal activity studies of Schiff base ligand **(FMIMN)** and its complexes are investigated with the help of two fungal strains, *Asperegillusniger and pencilliumnotatum*, with ketoconazole drug as a standard. The results are furnished in **Table 4C.3.**

The anti-fungal activities of **Cu(FMIMN)$_2$** and **Ni(FMIMN)$_2$** complexes are comparable to those of standard for both the fungal strains.

Table 4C.3: *Antifungal activity MIC values of* ***FMIMN*** *and* ***[M(FMIMN)$_2$]*** *(μg/mL)*

Compound	*Asperegillusniger*	*Pencilliumnotatum*
Cu(FMIMN)$_2$	5.32	7.28
Zn(FMIMN)$_2$	18.67	16.93
Ni(FMIMN)$_2$	7.86	9.35
Co(FMIMN)$_2$	55.73	42.12
Mn(FMIMN)$_2$	26.67	38.17
FMIMN	57.13	62.38
Ketoconazole	3.64	3.49

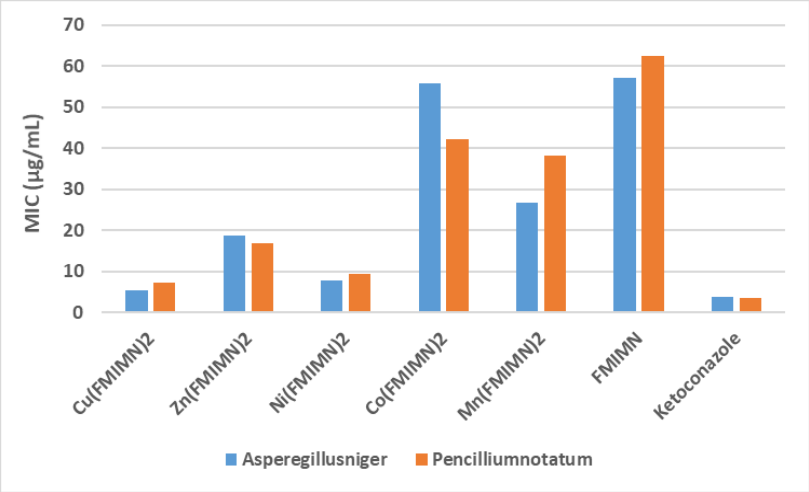

Figure 4C.4: *Graphical representation MIC values of antifungal activity of* ***FMIMN*** *and its metal complexes*

4C.4 *In vitro* Anticancer Activity:

The anticancer activity of **FMIMN** and its complexes was tested against two cancer cell lines, MCF-7 and HepG-2, by the MTT assay method with cisplatin as standard[33]. **Table 4C.4** shows the results. Out of all the complexes tested, only **Cd(FMIMN)$_2$** and **Zn(FMIMN)$_2$** showed some promising results.

Table 4C.4: *MIC values of anticancer activity of* ***FMIMN*** *and* ***[M(FMIMN)$_2$]*** *(µg/ml)*

Codes	MCF-7	HepG-2	HEK 293
Cu(FMIMN)$_2$	28.65 ± 0.56	37.24 ± 1.23	63.12 ± 1.02
Zn(FMIMN)$_2$	47.58 ± 1.63	52.89 ± 1.16	83.62 ± 1.13
Ni(FMIMN)$_2$	58.59 ± 0.382	72.97 ± 0.359	ND
Co(FMIMN)$_2$	21.04 ± 1.321	16.43 ± 0.327	58.48 ± 1.28
Mn(FMIMN)$_2$	49.04 ± 0.453	39.72 ± 1.28	ND
FMIMN	74.15 ± 0.536	67.24 ± 1.39	ND
Cisplatin	10.58 ± 0.32	5.25 ± 0.27	41.86 ± 0.43

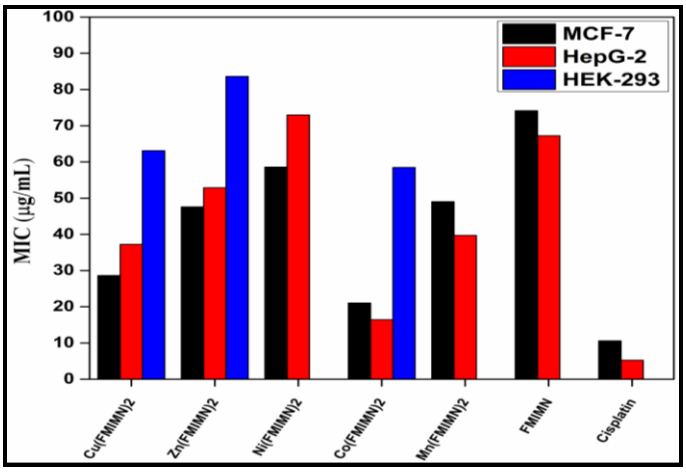

Figure 4C.5: *Graphical representation MIC values of anti-cancer activity of* ***FMIMN*** *and* ***M(FMIMN)$_2$***

Note: The ligand part of this Chapter has been published in a Springer journal (***Synthesis, spectral studies, molecular structure determination by single crystal X-ray diffraction of (E)-1-(((3-fuoro-4-morpholinophenyl)imino)methyl)napthalen-2-ol and computational studies by Austin model-1(AM1), MM2 and DFT/ B3LYP),*** Dhananjay Rao Thandra et al, *SN Applied Sciences*, 2021, **2**, 1765)

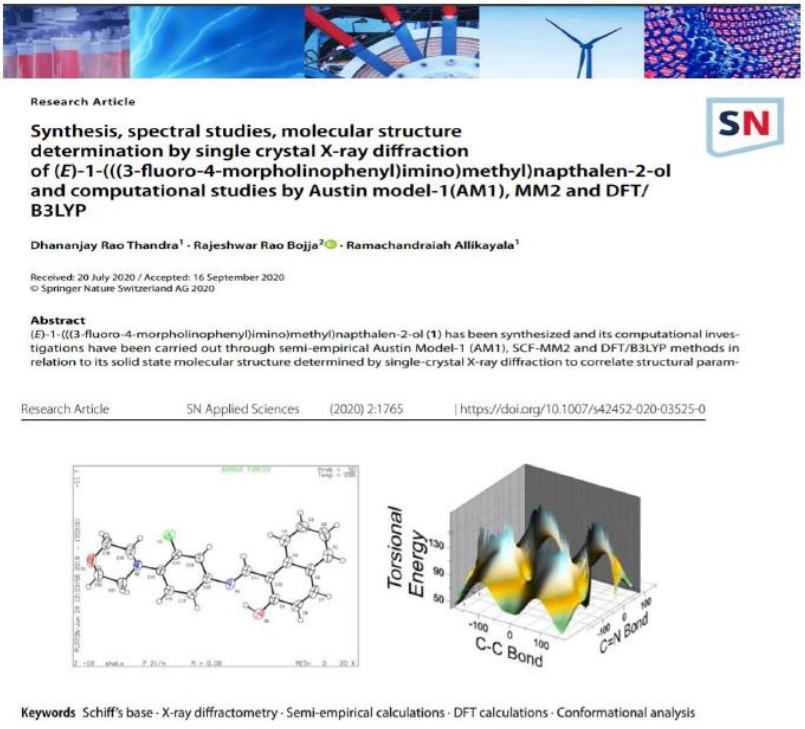

Research Article

Synthesis, spectral studies, molecular structure determination by single crystal X-ray diffraction of (*E*)-1-(((3-fluoro-4-morpholinophenyl)imino)methyl)napthalen-2-ol and computational studies by Austin model-1(AM1), MM2 and DFT/ B3LYP

Dhananjay Rao Thandra[1] · Rajeshwar Rao Bojja[2] · Ramachandraiah Allikayala[1]

Received: 20 July 2020 / Accepted: 16 September 2020
© Springer Nature Switzerland AG 2020

Abstract
(*E*)-1-(((3-fluoro-4-morpholinophenyl)imino)methyl)napthalen-2-ol (**1**) has been synthesized and its computational investigations have been carried out through semi-empirical Austin Model-1 (AM1), SCF-MM2 and DFT/B3LYP methods in relation to its solid state molecular structure determined by single-crystal X-ray diffraction to correlate structural param-

Research Article SN Applied Sciences (2020) 2:1765 | https://doi.org/10.1007/s42452-020-03525-0

Keywords Schiff's base · X-ray diffractometry · Semi-empirical calculations · DFT calculations · Conformational analysis

References

(1). (a) Parashar, R. K.; Sharma, R. C.; Kumar, A.; Mohan, G. Stability Studies in Relation to IR Data of Some Schiff Base Complexes of Transition Metals and Their Biological and Pharmacological Studies. Inorganica Chimica Acta 1988, 151 (3), 201–208. https://doi.org/10.1016/S0020-1693(00)83468-4.

(b) Bartyzel, A. Synthesis, Thermal Study and Some Properties of N2O4—Donor Schiff Base and Its Mn(III), Co(II), Ni(II), Cu(II) and Zn(II) Complexes. Journal of Thermal Analysis and Calorimetry 2017, 127 (3), 2133–2147. https://doi.org/10.1007/s10973-016-5804-0.

(2). Aryaeifar, M.; Amiri Rudbari, H.; Blacque, O.; Islam, M. K.; Scopelliti, R.; Braun, J. D.; Herbert, D. E.; Bruno, G.; Janiak, C.; Enamullah, M. Schiff Base Ligands Derived from 1,2-Bis(2′-Nitro-/Amino-Phenoxy)-3-R-Benzene and 2-Hydroxy-1-Naphthaldehyde and Their Cu/Zn(<scp>ii</Scp>) Complexes: Synthesis, Characterization, X-Ray Structures and Computational Studies. CrystEngComm 2021, 23 (36), 6322–6339. https://doi.org/10.1039/D1CE00829C.

(3). (a) D, M.; S, A. Synthesis, Spectral Characterization of Schiff base Complexes Based on Pyrimidine Moiety with Molecular Docking with Biomolecules. Asian Journal of Pharmaceutical and Clinical Research 2018, 11 (10), 93. https://doi.org/10.22159/ajpcr.2018.v11i10.26823.

(b) Anitha, C.; Sumathi, S.; Tharmaraj, P.; Sheela, C. D. Synthesis, Characterization, and Biological Activity of Some Transition Metal Complexes Derived from Novel Hydrazone Azo Schiff Base Ligand. International Journal of Inorganic Chemistry 2011, 2011, 1–8. https://doi.org/10.1155/2011/493942.

(4). Chellaian, J. D.; S.S, S. R. Co(II), Ni(II), Cu(II) and Zn(II) complexes of 4-aminoantipyrine derived Schiff base. Synthesis, structural elucidation, thermal, biological studies. photo catalytic activity. Synthesis, Structural Elucidation, Thermal, Biological Studies, and Photocatalytic Activity. Journal of Heterocyclic Chemistry 2021, 58 (4), 928–941. https://doi.org/10.1002/jhet.4209.

(5). Keypour, H.; Shayesteh, M.; Rezaeivala, M.; Chalabian, F.; Elerman, Y.; Buyukgungor, O. Synthesis, Spectral Characterization, Structural Investigation and Antimicrobial Studies of Mononuclear Cu(II), Ni(II), Co(II), Zn(II) and Cd(II) Complexes of a New Potentially Hexadentate N2O4 Schiff Base Ligand Derived from Salicylaldehyde. Journal of Molecular Structure 2013, 1032, 62–68. https://doi.org/10.1016/j.molstruc.2012.07.056.

(6). Bilge, S.; Kiliç, Z.; Hayvali, Z.; Hökelek, T.; Safran, S. Intramolecular Hydrogen Bonding and Tautomerism in Schiff Bases: Part VI. Syntheses and Structural Investigation of Salicylaldimine and Naphthaldimine Derivatives. Journal of Chemical Sciences 2009, 121 (6), 989–1001. https://doi.org/10.1007/s12039-009-0128-2.

(7). Mbugua, S. N.; Njenga, L. W.; Odhiambo, R. A.; Wandiga, S. O.; Meyer, M.; Sibuyi, N.; Lalancette, R. A.; Onani, M. O. Synthesis, Characterization, and DNA-Binding Kinetics of New Pd(II) and Pt(II) Thiosemicarbazone Complexes: Spectral, Structural, and Anticancer Evaluation. Journal of Chemistry 2020, 2020, 1–17. https://doi.org/10.1155/2020/3863269.

(8). Veith, M.; Müller, A.; Stahl, L.; Nötzel, M.; Jarczyk, M.; Huch, V. Formation of Metal Clusters or Nitrogen-Bridged Adducts by Reaction of a Bis(Amino)Stannylene with Halides of Two-Valent Transition Metals. Inorganic Chemistry 1996, 35 (13), 3848–3855. https://doi.org/10.1021/ic960007a.

(9). Selwin Joseyphus, R.; Sivasankaran Nair, M. Synthesis, Characterization and Biological Studies of Some Co(II), Ni(II) and Cu(II) Complexes Derived from Indole-3-Carboxaldehyde and Glycylglycine as Schiff Base Ligand. Arabian Journal of Chemistry 2010, 3 (4), 195–204. https://doi.org/10.1016/j.arabjc.2010.05.001.

(10). (a) Umezawa, Y.; Tsuboyama, S.; Takahashi, H.; Uzawa, J.; Nishio, M. Interaction in the Conformation of Organic Compounds. A Database Study. Tetrahedron 1999, 55 (33), 10047–10056. https://doi.org/10.1016/S0040-4020(99)00539-6.

(b) Ueda, H.; Onishi, H.; Nagai, T. Structure of P-Aminobenzoic Acidi–1,3-Dimethyl-2-Imidazolidinone (1/1). Acta Crystallographica Section C Crystal Structure Communications 1986, 42 (4), 462–464. https://doi.org/10.1107/S0108270186095793.

(11). (a) Kapon, M.; Reisner, G. M. Structure of 2-Imidazolidinone Hemihydrate. Acta Crystallographica Section C Crystal Structure Communications 1989, 45 (5), 780–782. https://doi.org/10.1107/S010827018801368X.

(b) Peeters, O. M.; Blaton, N. M.; De Ranter, C. J. Structure of 1-(5-Nitro-1,3-Thiazol-2-Yl)-2-Imidazolidinone (Niridazole), C6H6N4O3S. Acta Crystallographica Section C Crystal Structure Communications 1984, 40 (10), 1748–1750. https://doi.org/10.1107/S0108270184009392.

(12). El-Kareem, M. S. M. A.; Rabbih, M. A. E. F.; Selim, E. T. M.; Elsherbiny, E. A. E.; El-Khateeb, A. Y. Application of GC/EIMS in Combination with Semi-Empirical Calculations for Identification and Investigation of Some Volatile Components in Basil Essential Oil. International Journal of Analytical Mass Spectrometry and Chromatography 2016, 04 (01), 14–25. https://doi.org/10.4236/ijamsc.2016.41002.

(13). (a) Olalekan, T. E.; Adejoro, I. A.; VanBrecht, B.; Watkins, G. M. Crystal Structures, Spectroscopic and Theoretical Study of Novel Schiff Bases of 2-(Methylthiomethyl)Anilines. Spectrochimica Acta Part A: Molecular and Biomolecular Spectroscopy 2015, 139, 385–395. https://doi.org/10.1016/j.saa.2014.12.018.

(b) Klyne, W.; Prelog, V. Description of Steric Relationships across Single Bonds. Experientia 1960, 16 (12), 521–523. https://doi.org/10.1007/BF02158433.

(14). Stewart, J. J. P. Optimization of Parameters for Semiempirical Methods II. Applications. Journal of Computational Chemistry 1989, 10 (2), 221–264. https://doi.org/10.1002/jcc.540100209.

(15). (a) Fletcher, R.; Powell, M. J. D. A Rapidly Convergent Descent Method for Minimization. The Computer Journal 1963, 6 (2), 163–168. https://doi.org/10.1093/comjnl/6.2.163.

(b) Davidon, W. C. Variance Algorithm for Minimization. The Computer Journal 1968, 10 (4), 406–410. https://doi.org/10.1093/comjnl/10.4.406.

(16). Wałęsa, R.; Kupka, T.; Broda, M. A. Density Functional Theory (DFT) Prediction of

Structural and Spectroscopic Parameters of Cytosine Using Harmonic and Anharmonic Approximations. Structural Chemistry 2015, 26 (4), 1083–1093. https://doi.org/10.1007/s11224-015-0573-0.

(17). Fernández, B.; Ríos, M. A.; Carballeira, L. Molecular Mechanics (MM2) and Conformational Analysis of Compounds with N-C-O Units. Parametrization of the Force Field and Anomeric Effect. Journal of Computational Chemistry 1991, 12 (1), 78–90. https://doi.org/10.1002/jcc.540120109.

(18). (a) Tan, S. L.; Jotani, M. M.; Tiekink, E. R. T. Utilizing Hirshfeld Surface Calculations, Non-Covalent Interaction (NCI) Plots and the Calculation of Interaction Energies in the Analysis of Molecular Packing. Acta Crystallographica Section E Crystallographic Communications 2019, 75 (3), 308–318. https://doi.org/10.1107/S2056989019001129.

(b) Jayatilaka, D.; Wolff, S. K.; Grimwood, D. J.; McKinnon, J. J.; Spackman, M. A. CrystalExplorer: A Tool for Displaying Hirshfeld Surfaces and Visualising Intermolecular Interactions in Molecular Crystals. Acta Crystallographica Section A Foundations of Crystallography 2006, 62 (a1), s90–s90. https://doi.org/10.1107/S0108767306098199.

(19). Spackman, M. A.; Mckinnon, J. J.; April, R.; May, A. Fingerprinting Intermolecular Interactions in Molecular Crystals 2002, 4 (66), 378–392. https://doi.org/10.1039/b203191b.

(20). Al-Wahaibi, L. H.; Joubert, J.; Blacque, O.; Al-Shaalan, N. H.; El-Emam, A. A. Crystal Structure, Hirshfeld Surface Analysis and DFT Studies of 5-(Adamantan-1-Yl)-3-[(4-Chlorobenzyl)Sulfanyl]-4-Methyl-4H-1,2,4-Triazole, a Potential 11β-HSD1 Inhibitor. Scientific Reports 2019, 9 (1), 19745. https://doi.org/10.1038/s41598-019-56331-z.

(21). Baydere, C.; Taşçı, M.; Dege, N.; Arslan, M.; Atalay, Y.; Golenya, I. A. Crystal Structure and Hirshfeld Surface Analysis of (E)-2-(2,4,6-Trimethylbenzylidene)-3,4-Dihydronaphthalen-1(2 H)-One. Acta Crystallographica Section E Crystallographic Communications 2019, 75 (6), 746–750. https://doi.org/10.1107/S2056989019006182.

(22). Dutta, B.; Purkait, R.; Bhunia, S.; Khan, S.; Sinha, C.; Mir, M. H. Selective Detection of Trinitrophenol by a Cd(Ii)-Based Coordination Compound. RSC Advances 2019, 9 (66), 38718–38723. https://doi.org/10.1039/c9ra08614e.

(23). Sanjeeva Murthy, T. N.; Chidan Kumar, C. S.; Naveen, S.; Veeraiah, M. K.; Raghava Reddy, K.; Warad, I. Crystal Structure and Hirshfeld Surface Analysis of 2-(4-Nitrophenyl)-2-Oxoethyl Picolinate. Acta Crystallographica Section E Crystallographic Communications 2019, 75 (11), 1763–1767. https://doi.org/10.1107/S2056989019014105.

(24). Hu, H.-H.; Chen, H.-Y.; Hung, C.-I.; Guo, W.-Y.; Wu, Y.-T. Shape and Curvedness Analysis of Brain Morphology Using Human Fetal Magnetic Resonance Images in Utero. Brain Structure and Function 2013, 218 (6), 1451–1462. https://doi.org/10.1007/s00429-012-0469-3.

(25). Hu, H.-H.; Chen, H.-Y.; Hung, C.-I.; Guo, W.-Y.; Wu, Y.-T. Shape and Curvedness Analysis of Brain Morphology Using Human Fetal Magnetic Resonance Images in Utero. Brain Structure and Function 2013, 218 (6), 1451–1462. https://doi.org/10.1007/s00429-012-0469-3.

(26). Tojiboev, A.; Zhurakulov, S.; Englert, U.; Wang, R.; Kalf, I.; Vinogradova, V.; Turgunov, K.; Tashkhodjaev, B. Hirshfeld Surface Analysis and Energy Framework for Crystals of Quinazoline Methylidene Bridged Compounds. Proceedings 2020, 62 (1), 1. https://doi.org/10.3390/proceedings2020062001.

(27). Tojiboev, A.; Zhurakulov, S.; Englert, U.; Wang, R.; Kalf, I.; Vinogradova, V.; Turgunov, K.; Tashkhodjaev, B. Hirshfeld Surface Analysis and Energy Framework for Crystals of Quinazoline Methylidene Bridged Compounds. Proceedings 2020, 62 (1), 1. https://doi.org/10.3390/proceedings2020062001.

(28). Turner, M. J.; Thomas, S. P.; Shi, M. W.; Jayatilaka, D.; Spackman, M. A. Energy Frameworks: Insights into Interaction Anisotropy and the Mechanical Properties of Molecular Crystals. Chemical Communications 2015, 51 (18), 3735–3738. https://doi.org/10.1039/C4CC09074H.

(29). (a) Wang, S.-C.; Hung, M.-C. Nuclear Translocation of the Epidermal Growth Factor Receptor Family Membrane Tyrosine Kinase Receptors. Clinical Cancer Research 2009, 15 (21), 6484–6489. https://doi.org/10.1158/1078-0432.CCR-08-2813.

(b) Prenzel, N.; Zwick, E.; Leserer, M.; Ullrich, A. Tyrosine Kinase Signalling in Breast Cancer: Epidermal Growth Factor Receptor - Convergence Point for Signal Integration and Diversification. Breast Cancer Research 2000, 2 (3), 184. https://doi.org/10.1186/bcr52.

(c) Du, Z.; Lovly, C. M. Mechanisms of Receptor Tyrosine Kinase Activation in Cancer. Molecular Cancer 2018, 17 (1), 58. https://doi.org/10.1186/s12943-018-0782-4.

(30). (a) O-Charoenrat, P.; Rhys-Evans, P.; Modjtahedi, H.; Court, W.; Box, G.; Eccles, S. Overexpression of Epidermal Growth Factor Receptor in Human Head and Neck Squamous Carcinoma Cell Lines Correlates with Matrix Metalloproteinase-9 Expression Andin Vitro Invasion. International Journal of Cancer 2000, 86 (3), 307–317. https://doi.org/10.1002/(SICI)1097-0215(20000501)86:3<307::AID-IJC2>3.0.CO;2-I.

(b) Salem, H. Spectrofluorimetric, Atomic Absorption Spectrometric and Spectrophotometric Determination of Some Fluoroquinolones. American Journal of Applied Sciences 2005, 2 (3), 719–729. https://doi.org/10.3844/ajassp.2005.719.729.

(31). Nasiri Sovari, S.; Zobi, F. Recent Studies on the Antimicrobial Activity of Transition Metal Complexes of Groups 6–12. Chemistry 2020, 2 (2), 418–452. https://doi.org/10.3390/chemistry2020026.

(32). Hazra, B.; Biswas, S.; Mandal, N. Antioxidant and Free Radical Scavenging Activity of Spondias Pinnata. BMC Complementary and Alternative Medicine 2008, 8 (1), 63. https://doi.org/10.1186/1472-6882-8-63.

(33). (a) Tanaka, N.; Kimura, H.; Faried, A.; Sakai, M.; Sano, A.; Inose, T.; Sohda, M.; Okada, K.; Nakajima, M.; Miyazaki, T.; Fukuchi, M.; Kato, H.; Asao, T.; Kuwano, H.; Satoh, T.; Oikawa, M.; Kamiya, T.; Arakawa, K. Quantitative Analysis of Cisplatin Sensitivity of Human Esophageal Squamous Cancer Cell Lines Using In-Air Micro-PIXE. Cancer Science 2010, 101 (6), 1487–1492. https://doi.org/10.1111/j.1349-7006.2010.01542.x.

CHAPTER V

SYNTHESIS, CHARACTERIZATION AND SINGLE CRYSTAL X-RAY DIFFRACTOMETRIC, COMPUTATIONAL CHEMISTRY AND BIOLOGICAL STUDIES OF A PAIR OF PHENYL QUINOLINIUM SALTS

A pair of novel organic molecules, 7-fluoro-6-morpholino-3-phenylquinolin-1-ium **(FMPC)** and 7-fluoro-3-(4-methoxyphenyl)-6-morpholinoquinolin-1-ium chloride **(FMMC)** salts, have been synthesized and characterized by various spectroscopic techniques and by single crystal XRD studies. The detailed synthesis is presented in **Chapter II.** Computational molecular modelling studies were also performed on its cationic skeleton on the platforms of AM1, MM2 and B3LYP calculations and the data has been correlated with the XRD data.

This Chapter is divided into two parts, **Part A** and **Part B.** From these parts, **Part A** focuses on the characterization and electrochemical, fluorescent and single crystal XRD studies of the 7-fluoro-6-morpholino-3-phenylquinolin-1-ium chloride salt **(FMPC)** and the 7-fluoro-3-(4-methoxyphenyl)-6-morpholinoquinolin-1-ium chloride salt **(FMMC)** and in **Part B,** we discuss the computational analysis and molecular modeling studies of **FMPC** and **FMMC** from their fully optimized semi empirical AM1 calculations by MOPAC, MM2 and DFT/B3LYP calculations. The comparison of experimental XRD crystal data of **FMPC** and **FMMC** with those evaluated by these molecular modelling studies is also presented.

PART A

CHARACTERIZATION AND SINGLE CRYSTAL X-RAY DIFFRACTOMETRIC STUDIES OF FMPC AND FMMC

5A.1 Analytical Characteristics of FMPC and FMMC:

The physical and analytical characteristics of the **FMPC** and **FMMC** are shown in **Table 5A.1**.

Table 5A.1: *Analytical data[#] of* ***FMPC*** *and* ***FMMC***

Compound	M.P (°C)	Molecular formula	Molecular weight	Elemental analysis*			
				%C	%H	%N	%O
FMPC	174-175	$C_{19}H_{18}ClFN_2O^+$	344.8	66.02 (66.18)	5.11 (5.26)	8.02 (8.12)	4.51 (4.64)
FMMC	191193	$C_{20}H_{22}ClFN_2O_3^+$	392.8	60.96 (61.15)	5.51 (5.64)	7.02 (7.13)	12.14 (12.22)

[#] data in parenthesis are calculated ones; [*] data limited to integral values

Figure 5A.2 shows the mass spectra of the **FMPC** and **FMMC**. The M+1 is the base peak, which matches the molecular cationic formula of both **FMPC** and **FMMC,** viz., 308.34 and 338.37, respectively.

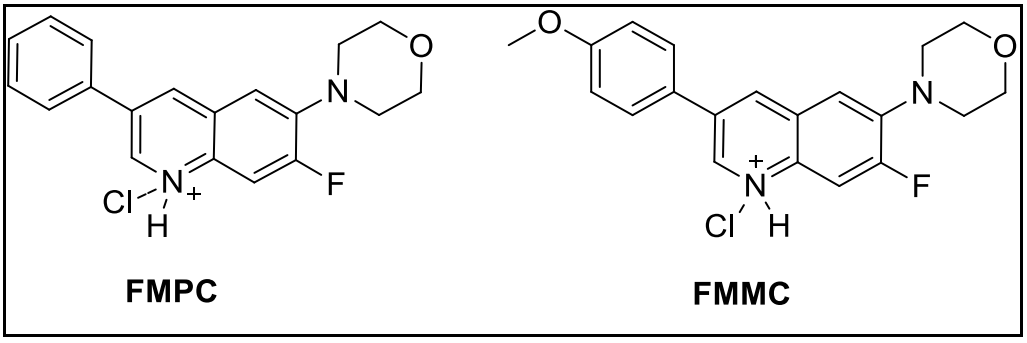

Figure 5A.1: *Structure of* ***FMPC*** *and* ***FMMC***

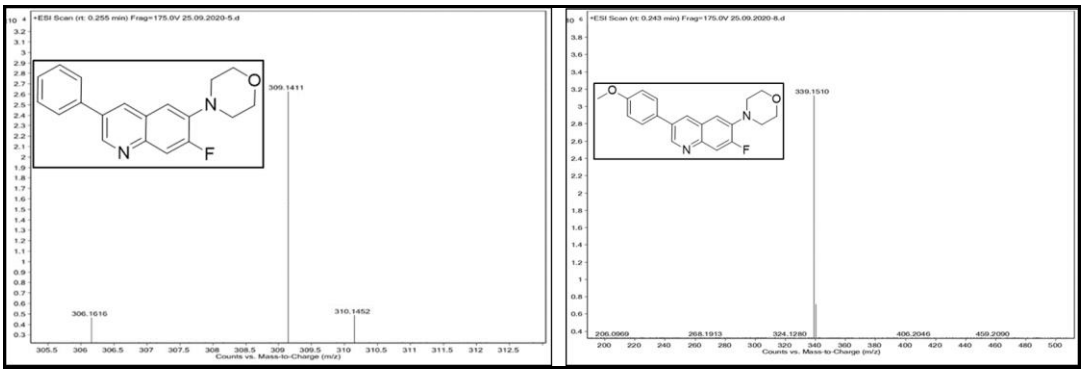

Figure 5A.2: *MASS Spectra of* ***FMPC*** *and* ***FMMC***

5A.2 Electronic Spectral Studies of FMPC and FMMC:

Figure 5A.3 shows the UV–Visible spectra of **FMPC** and **FMMC** in DMSO solvent. Two bands are found for **FMPC** at 301 and 348 nm, which are attributable to the aromatic $\pi \rightarrow \pi^*$ transition and then the $n \rightarrow \pi^*$ transition of the quinoline nitrogen of the ligand, respectively. The respective bands for **FMMC** compound are found at 260, 308 and 423nm. The red shift of both the peaks is attributed to the excess electron density pumped into the aromatic skeleton by the methoxy group. **Figure 5A.4** shows the UV-Visible spectra of **FMPC** and its metal complexes. As a result of coordination with the central metal atoms, the $\pi \rightarrow \pi^*$ and $n \rightarrow \pi^*$ transitions of metal complexes are pushed to lower wavelengths. That the ligand peaks are not varied considerably is due to the fact that the coordination is through the quinoline nitrogen lone pair which is orthogonal to the aromatic π bond.

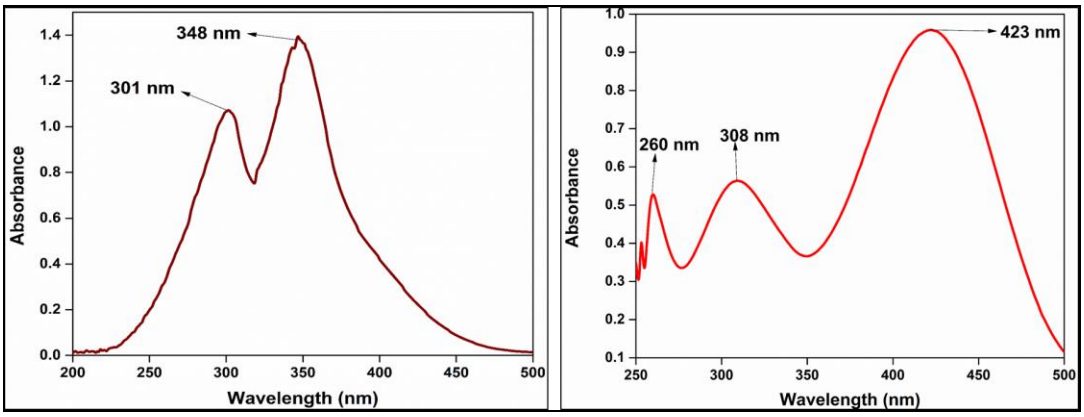

Figure 5A.3: *Electronic Spectra of* ***FMPC*** *and* ***FMMC***

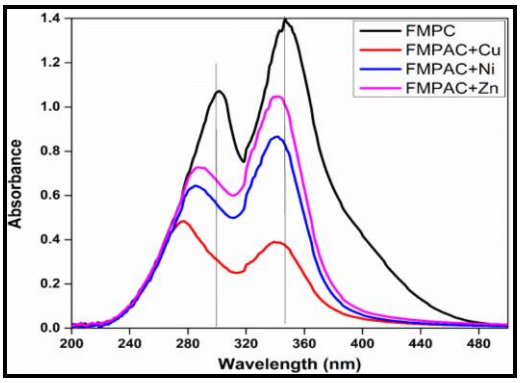

Figure 5A.4: *UV-Visible spectra of* ***FMPC*** *and its complexes in DMSO*

5A.3 FTIR Spectral Studies of FMPC and FMMC:

Figure 5A.5 shows the infrared spectra of **FMPC** and **FMMC**. FT-IR (KBr) ν (cm^{-1}); **FMPC**: 3445 br (N–H); 3000-3060 s (=N–H in aromatic); 2860-2980 s (aliphatic C–H); 1568, (C=N); 1500 (=C-H in aromatic); 1108 (C-O in morpholine). **FMMC:** 3445 br (N–H); 3000-3060 s (=N–H in aromatic); 2860-2980 s (aliphatic C–H); 1561 s (C=N); 1516 s (=C-H in aromatic); 1112 (C-O in morpholine).

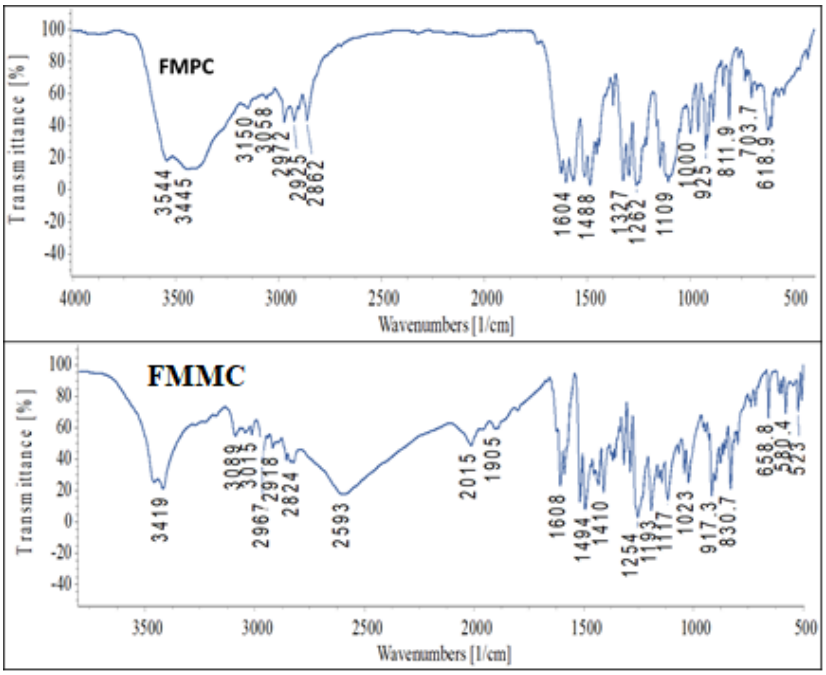

Figure 5A.5: *FT-IR spectra of* ***FMPC*** *and* ***FMMC***

5A.4 NMR Spectral Analysis of FMPC and FMMC:

The ^{1}H NMR spectrum of **FMPC** is shown in **Figure 5A.6.** In the **FMPC** ^{1}H NMR spectrum, the imine proton (C<u>H</u>=N-) gives its ^{1}H-NMR chemical shift value at 10.81 ppm as a doublet. All the remaining aromatic hydrogens appear at chemical shift values in the range of δ 7.09-9.07 ppm. The hydrogen attached to the quinolinium nitrogen atom appears at δ 4.59 ppm. The two ^{1}H NMR triplets at 3.74 ppm (-C<u>H</u>$_2$-O-) and 3.01 ppm (C<u>H</u>$_2$-N-) are due to morpholine protons.

The ^{1}H NMR spectrum of **FMMC** is shown in **Figure 5A.7.** The imine proton (C<u>H</u>=N-) gives its ^{1}H-NMR chemical shift value of 10.03 ppm as a singlet. Methoxy protons appear at 3.84 ppm with three protons integration. All the remaining aromatic hydrogens appear at chemical shift values in the range of δ 7.13-9.35 ppm. The hydrogen attached to the quinolinium nitrogen atom appears at δ 4.5 ppm. The two ^{1}H NMR triplets at 3.83 ppm (-C<u>H</u>$_2$-O-) and 3.21 ppm (C<u>H</u>$_2$-N-) are due to morpholine protons.

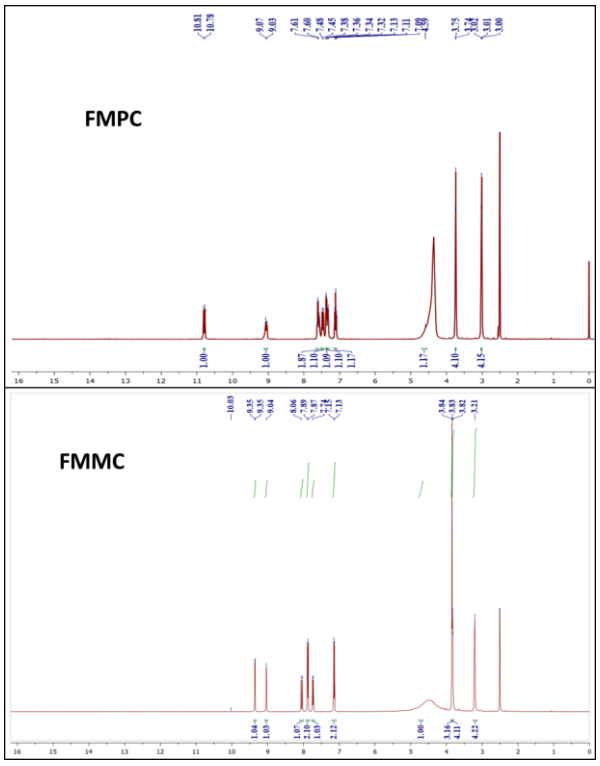

Figure 5A.6: *^{1}H and spectra of **FMPC** and **FMMC** in DMSO-d6*

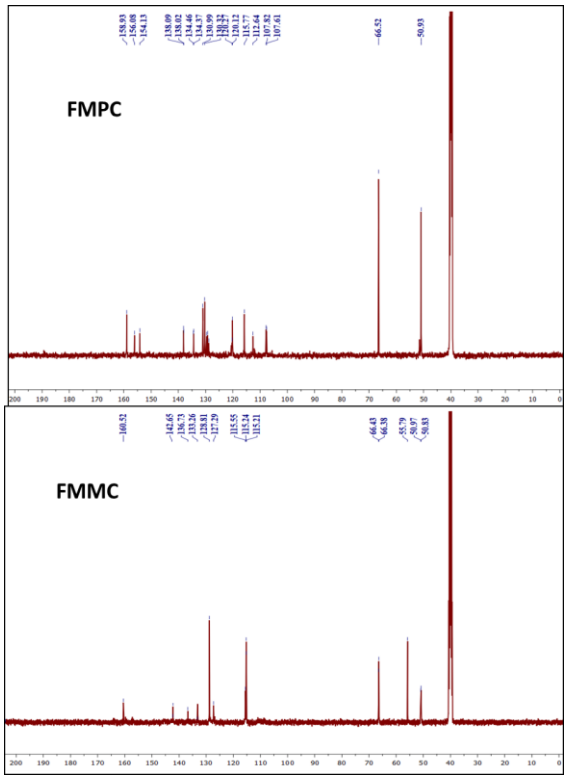

Figure 5A.7: *^{13}C NMR spectra of **FPMC** and **FMMC** in DMSO-d6*

Figure 5A.6 shows the ^{13}C NMR spectrum of **FMPC.** The spin-decoupled ^{13}C-NMR spectral line of the imine C=N- carbon appears at 158.93 ppm. The ring carbon connected to the fluorine gives its peak at 155 ppm with $^{1}J(^{19}F,^{13}C)$ = 243.75 Hz, $^{2}J(^{19}F,^{13}C)$ = 26.25 Hz; $^{3}J(^{19}F,^{13}C)$ = 11.25 Hz and $^{4}J(^{19}F,^{13}C)$ = 8.75 Hz, remaining aromatic carbon atoms are found in the range of 107.61–138.09 ppm while the morpholine aliphatic carbon atoms show four peaks in the range of 50.93, 51.50 ppm (-$\underline{C}H_2$-N-) and at 66.44, 66.52 ppm (-$\underline{C}H_2$-O-).

The ^{13}C NMR spectrum of **FMMC** is shown in **Figure 5A.7.** The spin-decoupled ^{13}C-NMR spectral line of the imine C=N- carbon appears at 160.52 ppm. The peak of the ring carbon connected to fluorine is 142.65 ppm. The remaining aromatic carbon atoms are found in the range of 115.21-136.73 ppm, while the morpholine aliphatic carbon atoms show five peaks in the range of 50.83, 50.97 ppm (-$\underline{C}H_2$-N-), at 66.38, 66.43 ppm (-$\underline{C}H_2$-O-) and at 55.79 (-O-CH_3).

5A.5 Fluorescence Spectral Studies of FMPC and FMPC:

The luminisence spectra of **FMPC** and **FMMC** in DMSO are shown in **Figure 5A.8.** The broad emission peaks are observed at 497 and 458 nm, respectively, owing to the emission of green light, which corresponds to the flow of electrons from the benzene ring to the quinolinium cation through the single bond. The band gap energies were calculated to be about 2.38 and 2.71 eV. The close proximity of the λ_{max} at ~500 nm of absorption (excitation) and fluorescence (emission) in the visible region indicates negligible inter-system crossing or molecular vibrational relaxation mechanism[1]**.**

The luminous behavior of Copper(II), Nickel(II), Zinc(II) and **FMPC** ligand was examined in the solid state. **Figure 5A.9** depicts the emission spectra of a few metal complexes containing the ligand **FMPC**. At 270 nm, the ligand **FMPC** was excited, resulting in a 520 nm emission band. Excitation of metal complexes of Copper(II), Nickel(II), and Zinc(II) at 270 nm caused emission bands to move to longer wavelengths[2]. The luminescence intensity of the complexes was lowered due to ligand metal charge transfer transitions (LMCT)[3]. The relatively large wavelength shifts show that the energy taken in by the organic ligand was transferred to the metal ions in an effective way.

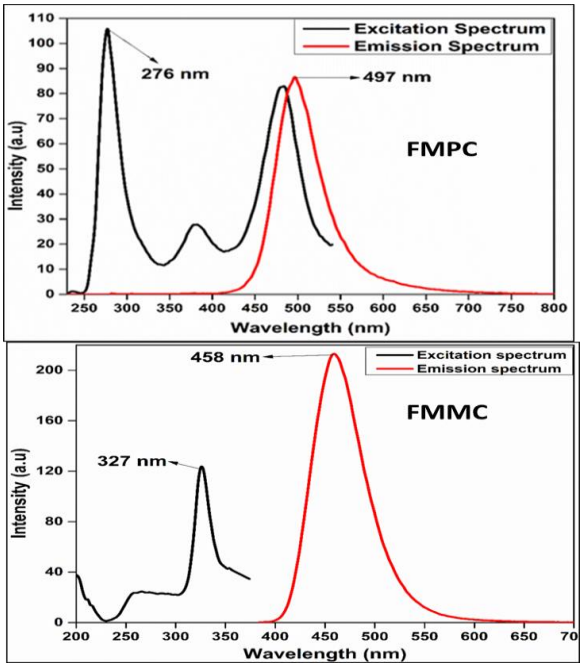

Figure 5A.8: *Absorption (black) and emission (red) spectra of* ***FMPC*** *and* ***FMMC*** *in DMSO*

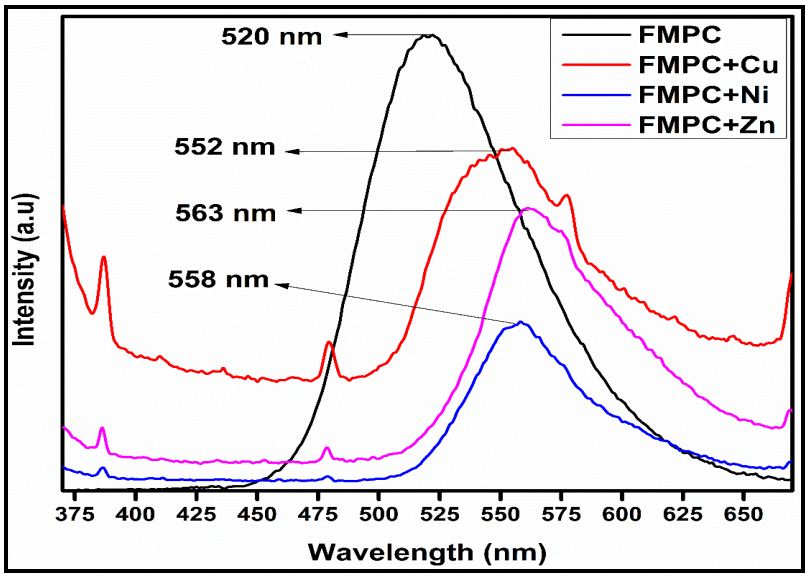

Figure 5A.9: *Fluorosence emission spectra of* ***FMPC*** *and its complexes (in their powder form)*

5A.6 Electrochemical Studies of FMPC:

The cyclic voltammogram of **FMPC** on a glassy carbon electrode in DMSO acetate buffer medium (pH = 4) is shown in **Figure 5A.10,** which exhibits an irreversible anodic electron transfer at ~0.50 V vs Ag|AgCl. The compound **FMPC** is expected to be electrochemically inert, with the overall molecular skeletal frame having been stabilised by conjugated and hence delocalised π - electron aromaticity. There is hardly any reducible electrophore on the molecule. In the DMSO, no cathodic response was observed up to a potential of -1.2 V vs Ag|AgCl. On the anodic side too, morpholine's sp^3 nitrogen alone is oxidizable as the quinoline's sp^2 nitrogen is already protonated in acid media. The effect of scan rate on the peak potential, E_{pa} and the anodic peak current, $i_{pa,}$ is also shown in **Figure 5A.10 (b)**. Though the irreversible electron process appears to be diffusion controlled, as evidenced by the linearity of i_{pa} vs square root of scan rate ($\nu^{1/2}$) **(Figure 5A.10 (c))**[4], the process appears to involve an E-C mechanism, as evidenced by the anodic drift of E_{pa} **(Figure 5A.10 (b))** with increased scan rate[5]. Tentatively, the cyclic voltammetric response may be considered as shown in **Scheme 5A.1**.

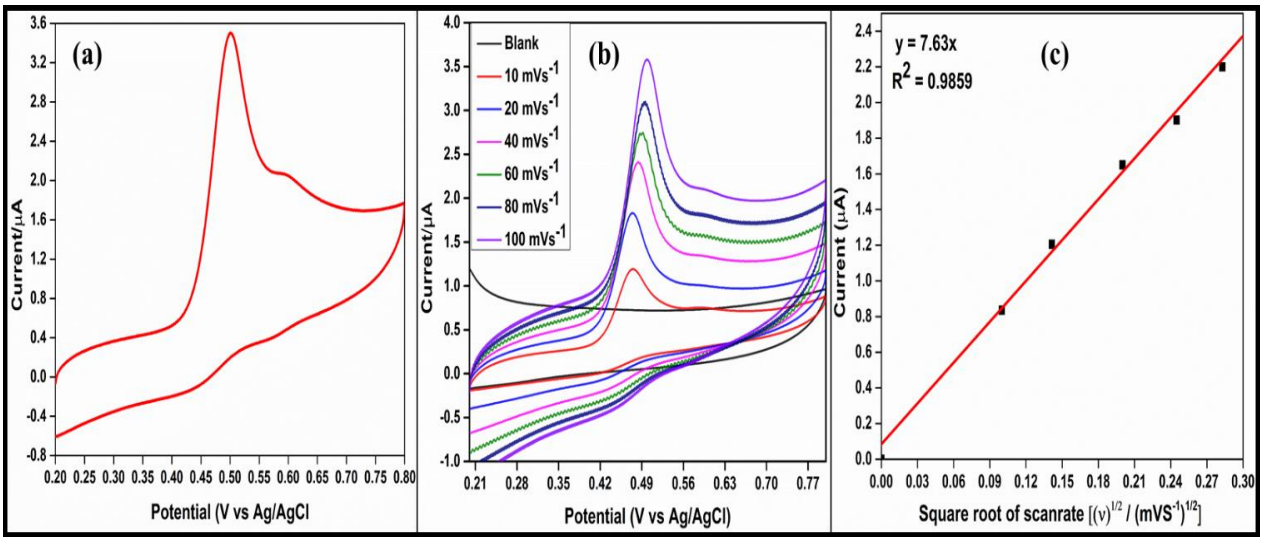

Figure 5A.10: *Cyclic voltammograms of* ***FMPC*** *(3.5 x 10^{-4} mM**)** on glassy carbon electrode at scan rates of **(a)** 40 mVs^{-1} and **(b)** at different scanrates and **(c)** the plot of the effect of the scan rate on the anodic peak current (in DMSO; pH= 4 buffer as the supporting electrolyte)*

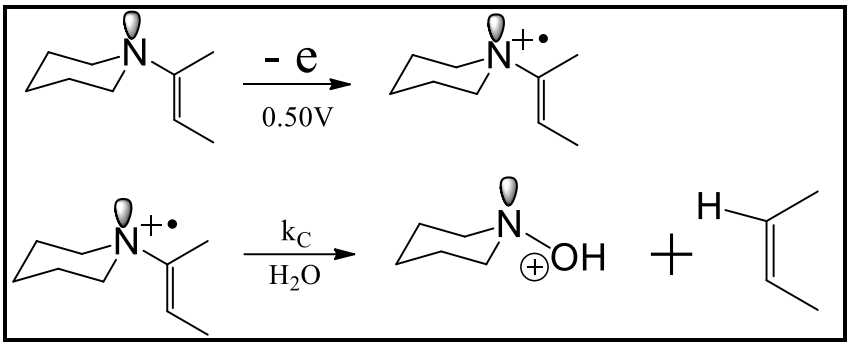

Scheme 5A.1: *Oxidative electron transfer by E-C mechanism of* ***FMPC***

Using the Randles-Sevcick Equation[6] for a temperature of 25 °C,

$$i_p = 8.51 n^{\frac{3}{2}} A D^{\frac{1}{2}} c \nu^{\frac{1}{2}} \quad \textbf{(5.1)}$$

where i_p = current in amps, n, the number of electrons transferred in the redox event (usually 1), A is electrode area in cm^2, D is the diffusion coefficient in cm^2s^{-1}, c, the concentration in mol lt^{-1} and ν is the scan rate in mVs^{-1}, the diffusion coefficient has been evaluated as 1.612 cm^2s^{-1} for **FMPC**.

5A.7 Crystal Structure Analysis of FMPC and FMMC:

Figure 5A.11 shows the crystal structures of **FMPC** and **FMMC** in there ORTEP mode**.** The **FMPC** crystallizes in a centrosymmetric monoclinic P21/c space group whereas the compound **FMMC** crystallizes in a centrosymmetric monoclinic $P2_1$ (4) space group. **Table 5A.2** contains the relevant XRD data for **FMPC** and **FMMC**. In **Figure 5A.13,** the unit cells are shown in three different dispositions, one seen along each of the three crystallographic axes. Careful observation of **FMPC** reveals that the molecules are stacked in pairs. Each pair assumes an inversion symmetry with the two molecules slightly staggered as viewed from the ab or ac planes. A close observation of the unit cell also discloses that adjacent pairs of **FMPC** are oriented in a crisscross manner as seen over the crystallographic c-axis. The crystal structure analysis further reveals that the molecules form a parquet floor structure in the crystal[7]. The molecules form right-handed and left-handed helices on the 2_1 screw axis with C–H···Cl, N–H···Cl and C–H···O hydrogen bonds along the crystallographic *a*-axis. The right-handed helices are interconnected with other inversion related right-handed helices via C–H···Cl, N–H···Cl and C–H···O hydrogen bonds along the crystallographic *c*-axis. Both these helices combine and give a parquet floor structure along the crystallographic *a*-axis (**Figure 5A.14**). These parquet floor structures are stabilized by C–H···π weak interactions.

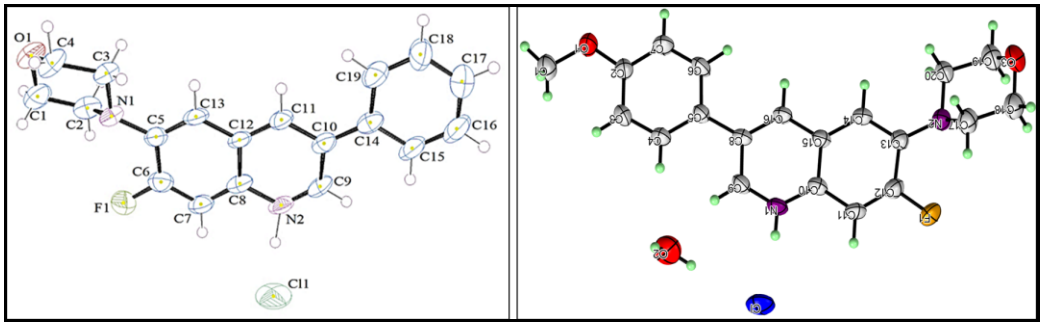

Figure 5A.11: *XRD-Platon diagrams of* ***FMPC*** *and* ***FMMC*** *with atom numbering*

A close observation of the unit cell also discloses that adjacent pairs of **FMMC** are oriented in a parallel manner with structural inversion as seen over the crystallographic c-axis. The crystal structure analysis further reveals that the molecules form a parquet floor structure in the crystal with N–H···Cl and H_2O···Cl hydrogen bond intermolecular interactions[8] **(Figure 5A.15).** The reflection angle vs intensity graphs are presented in **Figure 5A.16**.

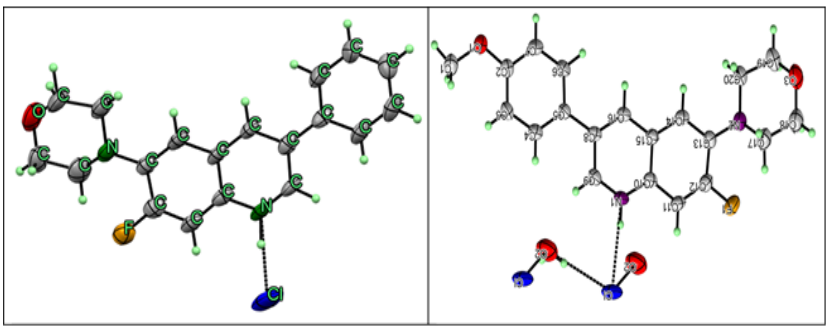

Figure 5A.12: *X-Ray crystallographic stick diagrams of* ***FMPC*** *and* ***FMMC*** *showing intramolecular hydrogen bonding (The atom numbering here is different from that in the manuscript)*

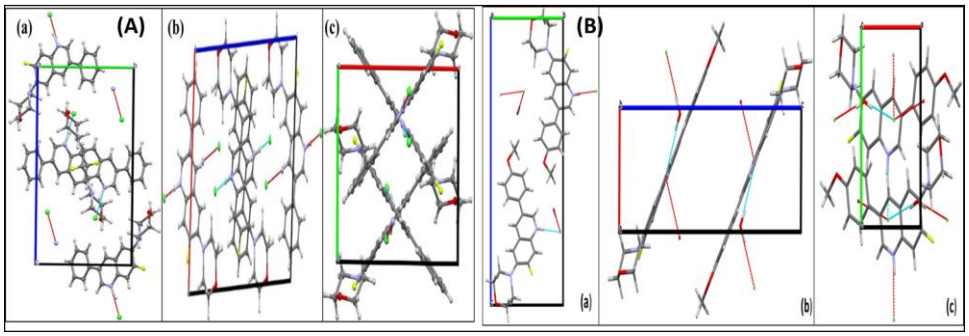

Figure 5A.13: *Unit cells of* ***FMPC (A)*** *and* ***FMMC (B)*** *seen along crystallographic* ***(a)*** *a-axis* ***(b)*** *b-axis* ***(c)*** *c-axis*

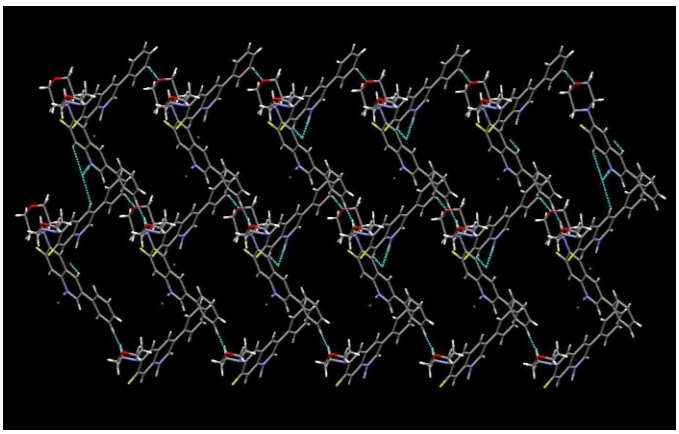

Figure 5A.14: *Parquet floor structure of* ***FMPC*** *with C–H···Cl, N–H···Cl and C–H···O hydrogen bond intermolecular interactions (shown in blue dotted lines)*

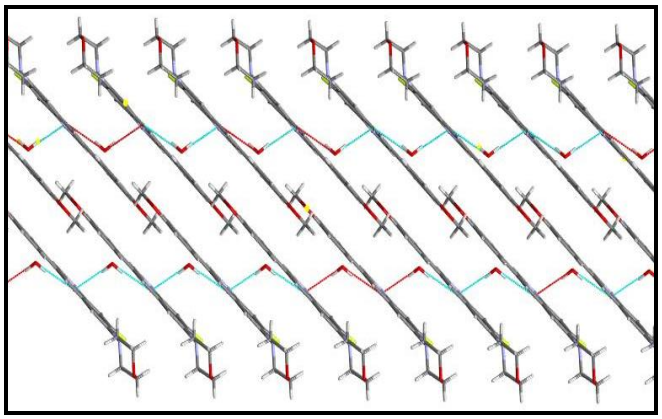

Figure 5A.15: *Parquet floor structure of* ***FMMC*** *with N–H···Cl and H_2O···Cl hydrogen bond intermolecular interactions (shown in blue and red dotted lines)*

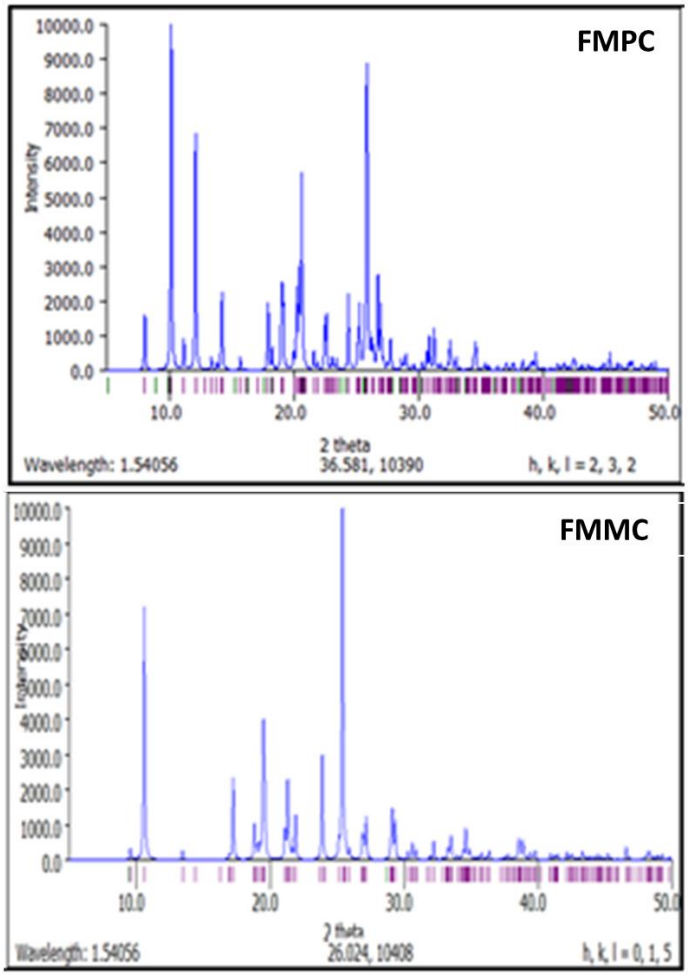

Figure 5A.16: *X-Ray diffraction intensity as a function of angle (^{o}) of reflection of* ***FMPC*** *and* ***FMMC***

Table 5A.2: *X-ray crystallographic data for* ***FMPC*** *and* ***FMMC***

	FMPC	**FMMC**
CCDC	2036305	2181246
Empirical formula	$C_{19}H_{18}ClFN_2O^+$	$C_{20}H_{22}ClFN_2O_3^+$
Formula weight	344.11	392.13
Color/shape	Orange/needle	Orange red/needle
Temperature, K	293	293 (2)
Crystal system	P21/c	P 2_1(4)
Space group	Monoclinic	Monoclinic
Unit cell dimensions, Å	a = 11.050 (4); b = 8.871 (3); c = 17.510 (5)	a = 5.4436 (18); b = 9.337 (3); c = 18.471 (7)
Deg	$\alpha = \gamma = 90$; $\beta = 97.605$ (17)	$\alpha = \gamma = 90$; $\beta = 90.600$ (13)
Z	4	2
Density, Mg/m^3	1.346	1.008
Absorption coefficient, mm^{-1}	0.242	0.141
Reflections collected/unique	18681/ 2981	4281/ 3061
θ range for data collections	2.347 – 25.000°	2.444 – 27.551°
F (000)	720	299
Limiting Indices	$-13 \leq h \leq 13$; $-10 \leq k \leq 10$; $-20 \leq l \leq 20$	$-7 \leq h \leq 7$; $-12 \leq k \leq 12$; $-23 \leq l \leq 24$
Goodness-of-fit on F^2	1.126	1.004
Final R indices [$I > 2\sigma$ (1)]	$R_1 = 0.1152$, $wR_2 = 0.3859$	$R_1 = 0.0717$, $wR_2 = 0.0933$
R indices (all data)	$R_1 = 0.2241$, $wR_2 = 0.3076$	$R_1 = 0.0399$, $wR_2 = 0.0848$
Largest diff. peak and hole ($eÅ^{-3}$)	0.542 and -0.470	0.164 and -0.198

PART B

Molecular Modelling and Biological Docking Studies of FMPC and FMMC and Correlation of the Computational Data with the X-Ray Diffraction Data

5B.1 Correlation of the X-Ray Crystallographic and Molecular Modelled Data of FMPC and FMMC Cations:

The title compounds, **FMPC** and **FMMC,** have quinoline, benzene, and morpholine moieties connected. In order to understand the quantum mechanical aspects and structural parameters of both the molecules in their free molecular entity form (gaseous state), we have run computational studies for them on a few modelling platforms, viz., MM2 (ChemSoft), AM1 (Austin Model-1) and DFT (B3LYP/6-31G*). Here, we present molecular structural data of **FMPC** and **FMMC** obtained from these competing and progressive platforms in comparison with the experimental single crystal XRD data to correlate the geometry of both the compounds in free and solid state forms. This exercise would also serve as an example of the reliability and usability of the three computational methods mentioned above.

The AM1, MM2, and DFT/B3LYP platforms were used independently to obtain quantum mechanical molecular energy data such as ionization potential (I), electron affinity (A), chemical potential (μ), chemical hardness (η), global softness (S), and electronegativity (χ) of the **FMPC** and **FMMC** cations, which are included in **Table 5B.1**. The geometrical parameters are incorporated in **Table 5B.2** (bond lengths), **Table 5B.3** (bond angles) and **Table 5B.4** (dihedral angles or torsional angles) along with those obtained from the single crystal XRD measurements. The experimental XRD data and the computationally evaluated values are in reasonably good agreement. The larger deviations, wherever observed, would have to be attributed to the fact that XRD studies are for a multi-molecular solid state material with molecular geometric parameters affected by possible intermolecular and inter-ionic interactions, whereas the computational results are for isolated cations of **FMPC** and **FMMC**. The conformational labels, abbreviated as **s = syn, a = anti**, **p = peri-planar** (0+300, 180+300), and all other angles **c = clinal,** are designated as per Klyne-Prelog terms. The charge of N_5-(-0.30) of morpholine has more electron density than the charge of N9-atom (-0.07) of quinoline, whereas O_{21} of morpholine has -0.25. Some minor changes are observed in the bond lengths also. It is observed that σH-C (sp^2) of aromatic rings is higher by

about ~0.17Å as obtained by AM1 and MM2, whereas the DFT/B3LYP gave very close to the experimental data. The σF-C (sp^2) is shown to be lower by 0.01Å (AM1), 0.04 Å (MM2) and 0.03 Å (DFT/B3LYP) from the XRD data. The quinoline ring's amine bond, H-N(sp2), is reduced by 0.144 (AM1), 0.121 (MM2), and 0.134 (DFT/B3LYP). The trends of the remaining and pertinent bond lengths follow a similar pattern. A keen look at **Table 5B.2** leads us to conclude that the empirical bond length data has negligibly fewer deviations from the ones theoretically computed by B3LYP than those by MM2 and AM1platforms, as expected. Similar kinds of correlations were observed with other structural data such as bond angles, dihedral angles, etc.

Important selective bond angles at various parts of the molecule of the cations of **FMPC** and **FMMC** are presented in **Table 5B.3**. The bond angles at C-sp^2 obtained by the three computational platforms are observed to vary from ~−2.5º to ~+2.5º from the XRD counterparts. But the bond angles at C-sp^3 are found to differ by a higher range due to the 3-dimensional and all-single-bonded torsional and spanning nature. However, the bond angles at both N-sp^2 and N-sp^3 are found to differ to a greater extent than at the C-sp^2 and C-sp^3 respectively due to nitrogen's higher capability of engaging in interatomic interaction than organic carbon atoms. Inspection of **Table 5B.3** also reveals higher deviations for bond angle at O-sp^3 than that at C-sp^3 for the computational data from the bond angle at O-sp^3 evaluated from the XRD measurements.

Various dihedral angles are presented in **Table 5B.4**. These values engaged with the atoms of the aromatic rings infer the near planarity of the whole molecule beyond the morpholine ring, as seen for both computational and experimental data. Both XRD and computations show quinoline, benzene and morpholine rings near coplanar despite Baeyer's strain[9]. Many of the dihedral angles obtained from XRD are in reasonable agreement with those computed. The total number of π-electrons spread over the quinoline and the phenyl rings turns out to be 16 which does not fall under the Huckel's rule of 4n+2 many delocalizable π-electrons. However, with the indulgence of the nitrogen loan pair electrons of the morpholine ring, the total number of delocalizable π-electrons becomes 18 by way of which the molecule acquires aromatic stability by Huckel's rule of 4n+2 many delocalizable π-electrons. This necessitates that not only the dihedral angle between the quinoline and benzene rings but also that between the quinoline and the morpholine's atomic moiety connected to the quinoline be close to zero. In **Figure 5B.1(b),** is shown the molecular skeleton of **FMPC**, from which one can clearly see a near total planarity over

the whole molecular skeleton of sp^2-hybrid atoms till the nitrogen of the morpholine heterocycle. Conformational analysis plots over the inter-cyclic C-C bond and the C-N bond of cations **FMPC** and **FMMC** are shown in **Figures 5B.2** and **5B.3** respectively. It is clear from these plots that the conformers expected with near -90^o dihedral angles are more energetic (about 30 at C-C and about 60 kcal mol^{-1} at C-N bonds) than the ones with co-planarity. The co-planarity of the quinoline ring with the connected NCC atomic skeleton of the morpholine seems to be further favored by possible H···F hydrogen bond.

In **FMPC**, the dihedral angle is changed from +*ap* of H_1-N_1-C_{10}-C_{15} and N_1-C_{10}-C_{15}-C_{14} to -*ap* whereas the –*ap* of H_1-N_1-C_9-C_8 is changed to +*ap* conformation under AM1, MM2 and B3LYP methods. It is also observed that the conformation +*sp* of C_8-C_5-C_4-C_3, H_{16}-C_{16}-C_{15}-C_{10} and H_{16}-C_{16}-C_{15}-C_{14} changed to –*sp* conformation in all methods (AM1, MM2 and B3LYP). The conformation –*sc* of H_{19A}-C_{19}-O_5-C_{18} is found to become +*sc* (B3LYP and AM1). The +*sc* of O_3-C_{18}-C_{17}-N_2 alters to -*sc* (B3LYP), +*ac* (AM1) and +*sp* (MM2) conformations.

In **FMMC**, the dihedral angle is changed from +*ap* of F-C_{12}-C_{13}-C_{14} to –*ap* whereas –*ap* of H_1-N_1-C_9-C_8, H_{16}-C_{16}-C_8-C_9, C_5-C_8-C_{16}-C_{15}, C_1-O_1-C_2-C_7 is changed to +*ap* conformation under AM1, MM2 and B3LYP methods. It is also observed that conformation +*sp* of C_8-C_5-C_4-H_4, C_{14}-C_{15}-C_{16}-H_{16} and C_{12}-C_{13}-C_{14}-C_{15} changed to –*sp* conformation in all methods (AM1, MM2 and B3LYP). The conformation –*sc* of H_{18B}-C_{18}-C_{17}-N_2 and C_{13}-N_2-C_{17}-C_{18} is found to become -*ap* (B3LYP and AM1) and +*ap* (MM2) whereas the +*ap* of O_3-C_{18}-C_{17}-H_{17A} to –*ap* (B3LYP and AM1) and -*sc* (MM2). Under AM1, MM2, and B3LYP methods, the -sp of C_{11}-C_{12}-C_{13}-C_{14}, C_7-C_2-C_3-C_4, C_{14}-C_{13}-N_2-C_{20} and C_9-C_8-C_{16}-H_{16} is a +sp conformation.

The HOMO and LUMO molecular orbitals and their corresponding energies of the cations of **FMPC** and **FMMC** are shown in **Figures 5B.4** and **5B.5** respectively.

Table 5B.1: *Important molecular energy data evaluated by AM1, B3LYP and MM2 calculations on the cation of **FMPC** and **FMMC***

Parameter	**FMPC**			**FMMC**		
	AM1	**B3LYP**	**MM2**	**AM1**	**B3LYP**	**MM2**
E_{HOMO} (eV)	-11.673	-9.006	-3.060	-0.4290	-0.3180	-2.722

E_{LUMO} (eV)	-5.307	-6.097	-0.182	-0.1949	-0.2187	+0.149
I (eV) Ionization Potential	11.673	9.006	3.060	0.4290	0.3180	2.722
A (eV) Electron affinity	5.307	6.097	0.182	0.1949	0.2187	-0.149
η (eV) Chemical hardness	3.183	1.454	1.439	0.1170	0.0496	1.4355
μ (eV) Chemical potential	8.490	7.551	1.621	0.3119	0.2683	1.2865
χ (eV) Electro negativity	-8.490	-7.551	-1.621	-0.3119	-0.2683	-1.2865
S (eV^{-1}) Global softness	0.157	0.343	0.347	4.2735	10.0806	0.3483

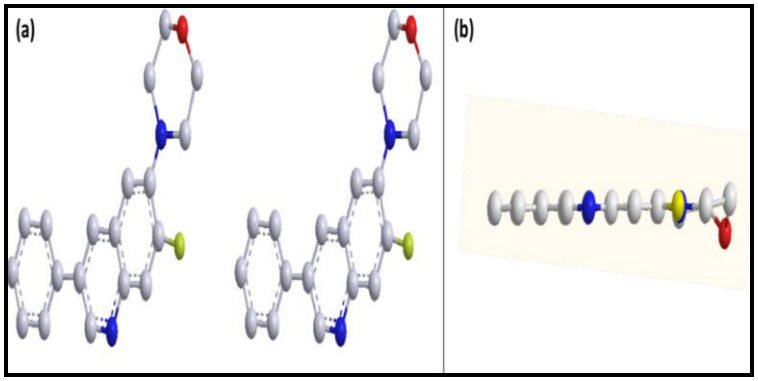

Figure 5B.1: *Energy-minimized (38.07 kcal mol^{-1}) cationic form of **FMPC** (by MM2) in **(a)** stereo view and **(b)** its lateral view with the line joining N9 and C8 atoms perpendicular to the plane of the page (H-atoms are hidden for clarity)*

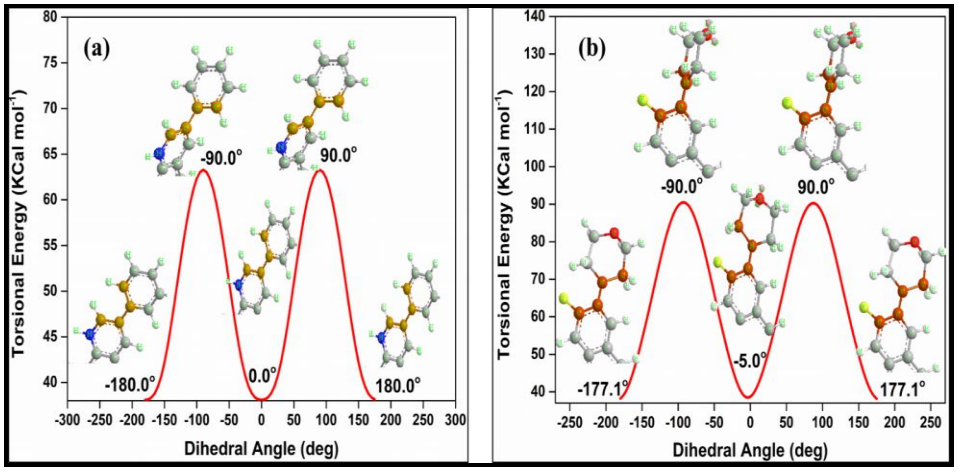

Figure 5B.2: *Torsional energy plots of **FMPC** over (a) **C-C** and (b) **C-N** bonds*

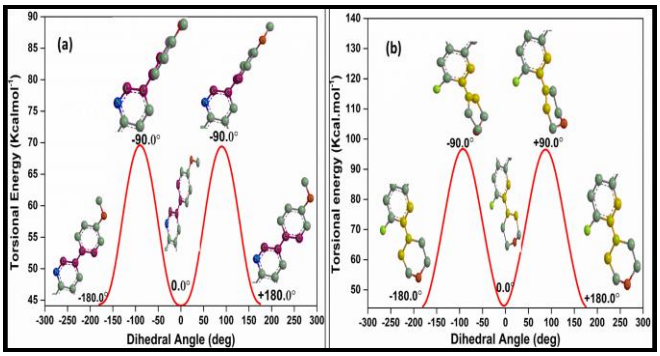

Figure 5B.3: *Torsional energy plots of* ***FMMC*** *over (a)* ***C-C*** *and (b)* ***C-N*** *bonds*

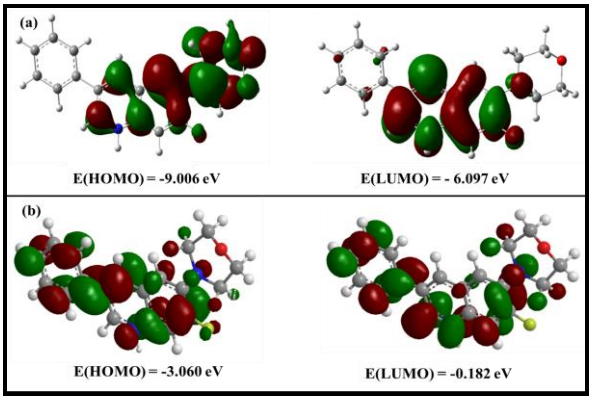

Figure 5B.4: *HOMO-LUMO orbitals of* ***FMPC*** *obtained from (a) B3LYP and (b) MM2*

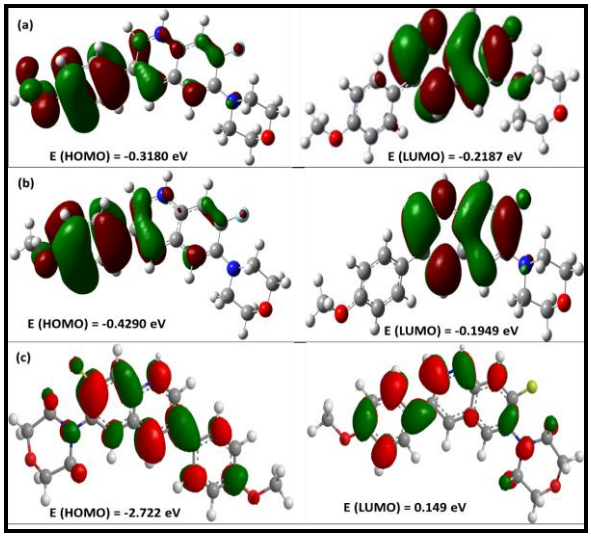

Figure 5B.5: *HOMO-LUMO orbitals of* ***FMMC*** *obtained from (a) B3LYP and (b) AM1 (c) MM2*

Table 5B.2: *Comparative list of selected bond lengths of* ***FMPC*** *(block),* ***FMMC*** *(RED) in (Å)*

Bond	Bond type	Bond lengths (Å)				Fractional variation (Δ/XRD)		
		XRD	AM1	MM2	B3LYP	AM1	MM2	B3LYP
$H_{19A} - C_{19}$	$H–Csp^3$	0.970 0.970	1.125 1.121	1.116 1.115	1.087 1.101	0.160 -0.156	0.151 -0.149	0.121 -0.135
$H_6 - C_6$	$H–Csp^2$	0.930 0.930	1.100 1.101	1.009 1.100	1.086 1.086	0.183 -0.184	0.182 -0.183	0.168 -0.168
$H_7 - C_7$	$H–Csp^2$	0.930 0.931	1.101 1.100	1.104 1.102	1.085 1.084	0.184 -0.182	0.187 -0.184	0.167 -0.164
$H_{20A} - C_{20}$	$H–Csp^3$	0.970 0.970	1.129 1.125	1.118 1.117	1.100 1.094	0.164 -0.160	0.153 -0.152	0.134 -0.128
$C_6 - C_7$	$Csp^2–Csp^2$	1.371 1.370	1.382 1.384	1.346 1.344	1.382 1.380	0.011 -0.010	0.003 0.019	0.006 -0.007
$C_6 - C_5$	$Csp^2–Csp^2$	1.400 1.398	1.403 1.407	1.353 1.351	1.404 1.410	0.002 -0.006	-0.034 0.034	0.003 -0.009
$H_{19B} - C_{19}$	$H– Csp^3$	0.970 0.930	1.122 1.122	1.115 1.144	1.093 1.093	-0.157 0.206	0.198 -0.149	0.175 -0.127
$C_7 - C_2$	$Csp^2–Csp^2$	1.383 1.360	1.412 1.396	1.345 1.338	1.407 1.396	0.026 -0.021	-0.016 0.027	0.026 -0.017
$H_{20B} - C_{20}$	$H– Csp^3$	0.970 0.930	1.537 1.122	1.528 1.144	1.532 1.093	0.206 -0.585	0.198 -0.575	0.175 -0.579
$C_{19} - O_3$	$Csp^3–Osp^3$	1.420 1.390	1.420 1.420	1.402 1.402	1.415 1.414	0.000 0.022	0.009 0.013	0.017 0.004
$H_{18A} - C_{18}$	$H–Csp^3$	0.970 0.970	1.121 1.129	1.115 1.118	1.101 1.100	0.164 -0.156	0.153 -0.149	0.134 -0.135

$H_1 – N_1$	H–Nsp^2	0.860 1.150	1.005 1.006	1.030 1.029	1.016 1.016	-0.125 -0.169	-0.105 -0.198	-0.117 -0.181
$H_9 – C_9$	H–Csp^2	0.930 0.930	1.111 1.111	1.100 1.100	1.082 1.082	0.195 -0.195	0.183 -0.183	0.163 -0.163
$H_{11} – C_{11}$	H–Csp^2	0.930 0.930	1.103 1.103	1.104 1.104	1.085 1.085	0.186 -0.186	0.187 -0.187	0.167 -0.167
$N_1 – C_9$	Nsp^2–Csp^2	1.325 1.310	1.347 1.345	1.306 1.306	1.342 1.342	0.027 -0.017	-0.003 0.014	0.024 -0.013
$N_1 – C_{10}$	Nsp^2–Csp^2	1.357 1.389	1.389 1.390	1.306 1.306	1.368 1.369	-0.024 0.001	0.038 -0.060	-0.008 -0.014
$C_9 – C_8$	Csp^2 – Csp^2	1.402 1.400	1.420 1.389	1.351 1.352	1.404 1.397	-0.008 -0.013	-0.034 0.036	-0.002 -0.001
$F_1 – C_{12}$	Fsp^3 – Csp^2	1.356 1.361	1.348 1.350	1.325 1.325	1.337 1.336	-0.008 0.006	-0.026 0.023	-0.018 0.014
$C_{11} – C_{10}$	Csp^2 – Csp^2	1.403 1.437	1.419 1.463	1.341 1.356	1.406 1.443	0.018 -0.011	-0.056 0.044	0.004 -0.002
$C_{11} – C_{12}$	Csp^2 – Csp^2	1.345 1.359	1.386 1.385	1.345 1.344	1.370 1.370	0.019 -0.030	-0.011 0.000	0.008 -0.019
$C_{10} – C_{15}$	Csp^2 – Csp^2	1.411 1.407	1.428 1.428	1.340 1.340	1.426 1.427	0.015 -0.012	-0.048 0.050	0.014 -0.011
$C_{20} – N_2$	Csp^3 – Nsp^3	1.464 1.455	1.457 1.449	1.491 1.490	1.469 1.469	-0.004 0.005	0.024 -0.018	0.010 -0.003
$C_{20} – H_{20B}$	Csp^3 – H	0.970 0.970	1.289 1.123	1.118 1.118	1.102 1.094	0.158 -0.329	0.153 -0.153	0.128 -0.136
$C_{12} – C_{13}$	Csp^2 – Csp^2	1.429 1.437	1.460 1.463	1.356 1.356	1.443 1.443	0.018 -0.022	-0.056 0.051	0.004 -0.010
$C_8 – C_5$	Csp^2 – Csp^2	1.483	1.454	1.362	1.474	-0.003	-0.067	0.013

		1.461	1.457	1.363	1.480	0.020	0.082	0.006
$C_8 - C_{16}$	$Csp^2 - Csp^2$	1.381 1.380	1.391 1.420	1.352 1.348	1.399 1.412	0.029 -0.007	-0.023 0.021	0.023 -0.013
$C_5 - C_4$	$Csp^2 - Csp^2$	1.390 1.389	1.401 1.402	1.351 1.353	1.401 1.405	0.009 -0.008	-0.026 0.028	0.012 -0.008
$C_{15} - C_{16}$	$Csp^2 - Csp^2$	1.415 1.416	1.417 1.408	1.348 1.348	1.417 1.414	-0.006 -0.001	-0.048 0.047	-0.001 -0.001
$C_{15} - C_{14}$	$Csp^2 - Csp^2$	1.402 1.416	1.412 1.408	1.348 1.348	1.412 1.414	-0.006 -0.007	-0.048 0.039	-0.001 -0.007
$O_1 - C_2$	$Osp^3 - Csp^2$	1.369	1.370	1.374	1.370	-0.001	-0.004	-0.001
$O_1 - C_1$	$Osp^3 - Csp^3$	1.419	1.427	1.409	1.427	-0.006	0.007	-0.006
$C_{16} - H_{16}$	$Csp^2 - H$	0.930 0.930	1.105 1.105	1.099 1.098	1.105 1.086	0.188 -0.188	0.181 -0.182	0.168 -0.188
$C_2 - C_3$	$Csp^2 - Csp^2$	1.383 1.380	1.403 1.395	1.344 1.338	1.403 1.396	0.011 -0.014	-0.030 0.028	0.012 -0.014
$C_{13} - C_{14}$	$Csp^2 - Csp^2$	1.379 1.370	1.397 1.392	1.355 1.343	1.397 1.393	0.016 -0.013	-0.020 0.017	0.017 -0.013
$C_{13} - N_2$	$Csp^2 - Nsp^3$	1.401 1.408	1.393 1.374	1.287 1.287	1.393 1.376	-0.024 0.006	-0.086 0.081	-0.023 0.006
$C_{14} - H_{14}$	$Csp^2 - H$	0.930 0.931	1.104 1.104	1.100 1.099	1.104 1.082	0.186 -0.187	0.180 -0.183	0.162 -0.187
$N_2 - C_{17}$	$Nsp^3 - Csp^3$	1.475 1.470	1.458 1.450	1.487 1.487	1.458 1.483	-0.014 0.012	0.012 -0.008	0.009 0.012
$H_{1A} - C_1$	$H - Csp^3$	0.960	1.116	1.113	1.116	-0.163	-0.159	-0.163
$O_3 - C_{18}$	$Osp^3 - Csp^2$	1.428 1.401	1.421 1.420	1.402 1.402	1.421 1.418	0.014 0.005	0.001 0.018	0.012 0.005
$H_{1B} - C_1$	$H - Csp^2$	0.960	1.120	1.113	1.120	-0.167	-0.159	-0.167

$C_{18} - C_{17}$	$Csp^3 - Csp^3$	1.510 1.510	1.536 1.535	1.529 1.529	1.536 1.505	0.017 -0.017	0.013 -0.013	-0.013 -0.017
$C_{18} - H_{18A}$	$Csp^3 - H$	0.970 0.970	1.122 1.123	1.115 1.115	1.122 1.101	0.158 -0.157	0.149 -0.149	0.135 -0.157
$C_4 - C_3$	$Csp^2 - Csp^2$	1.380 1.370	1.390 1.392	1.342 1.343	1.390 1.393	0.016 -0.007	-0.020 0.028	0.017 -0.007
$C_4 - H_4$	$Csp^2 - H$	0.930 0.930	1.101 1.100	1.100 1.099	1.101 1.087	0.183 -0.184	0.182 -0.183	0.169 -0.184
$C_1 - H_{1C}$	$Csp^3 - H$	0.960	1.116	1.113	1.116	-0.163	-0.159	-0.163
$C_3 - H_3$	$Csp^2 - H$	0.930 0.930	1.099 1.102	1.105 1.104	1.099 1.085	0.185 -0.182	0.187 -0.188	0.167 -0.182
$C_{17} - H_{17A}$	$Csp^3 - H$	0.970 0.970	1.124 1.122	1.118 1.115	1.124 1.101	0.158 -0.159	0.149 -0.153	0.135 -0.159
$C_{17} - H_{17B}$	$Csp^3 - H$	0.970 0.970	1.129 1.123	1.116 1.115	1.129 1.093	0.157 -0.164	0.149 -0.151	0.127 -0.164

Table 5B.3: *Comparative list of selected bond angles of* ***FMPC*** *(block),* ***FMMC*** *(RED) in (°)*

Atomic string	**Central atom**	**XRD**	**B3LYP**	**AM1**	**MM2**	**Variation from XRD data (%)**		
						B3LYP	**AM1**	**MM2**
C_1-O_1-C_2	Osp^3	117.2	119.1	116.8	118.7	1.62	0.34	1.28
C_{18}-O_3-C_{19}	Osp^3	108.7 109.0	110.6 110.6	111.8 112.1	110.1 110.1	1.75 1.47	2.85 2.84	1.29 1.01
C_9-N_1-H_1	Nsp^2	118.2 109.0	118.0 117.6	120.4 118.3	120.2 120.7	0.17 7.89	1.86 8.53	1.69 1.73
C_{10}-N_1-H_1	Nsp^2	118.2 109.2	117.6 117.7	118.2 118.3	120.7 120.8	0.51 7.86	0.00 8.42	2.03 1.69

C_9-N_1-C_{10}	Nsp^2	123.7 122.6	124.2 124.2	121.3 121.2	119.2 119.1	0.40 1.31	1.94 1.14	3.64 2.85
C_{13}-N_2-C_{20}	Nsp^3	115.4 116.0	118.6 118.7	117.3 122.3	119.9 120.2	2.77 2.33	1.65 5.43	3.90 3.62
C_{17}-N_2-C_{20}	Nsp^3	110.4 118.1	112.0 120.8	113.4 122.2	120.4 119.3	1.45 2.41	2.72 2.68	8.06 6.32
C_{13}-N_2-C_{17}	Nsp^3	118.1 117.0	120.8 120.7	122.2 118.9	120.4 120.7	2.29 3.16	3.47 1.62	1.95 3.16
O_1-C_1-H_{1C}	Csp^3	109.5	111.1	110.5	110.4	1.46	0.91	0.82
O_1-C_1-H_{1B}	Csp^3	109.5	105.5	103.0	110.3	3.65	5.94	0.73
O_1-C_1-H_{1A}	Csp^3	109.5	111.1	110.5	107.8	1.46	0.91	1.55
H_{1B}-C_1-H_{1C}	Csp^3	109.5	109.5	110.8	111.8	0.00	1.19	2.10
H_{1A}-C_1-H_{1C}	Csp^3	109.4	109.8	110.9	108.2	0.37	1.37	1.10
H_{1A}-C_1-H_{1B}	Csp^3	109.5	109.5	110.8	108.2	0.00	1.19	1.19
O_1-C_2-C_7	Csp^2	116.1	115.6	114.8	119.3	0.43	1.12	2.76
C_3-C_2-C_7	Csp^2	119.2 118.3	119.9 119.3	119.7 120.3	118.1 114.5	1.35 0.08	0.18 0.92	0.17 3.94
O_1-C_2-C_3	Csp^2	124.7	124.9	124.7	126.2	0.16	0.00	1.20
C_2-C_3-C_4	Csp^2	119.7 120.2	120.1 119.6	120.3 119.4	120.4 122.3	0.08 0.08	0.08 0.25	0.17 2.17
H_3-C_3-C_4	Csp^2	119.9 120.1	119.7 119.3	119.7 119.7	120.3 117.4	0.17 0.67	0.17 0.33	0.33 2.25
C_3-C_4-C_5	Csp^2	122.7 122.31	120.4 121.5	120.0 120.7	123.5 123.8	1.87 0.66	2.20 1.32	0.65 1.22
H_4-C_4-C_5	Csp^2	118.6 118.8	120.2 120.1	120.2 120.1	123.2 122.6	1.35 1.09	1.35 1.09	3.88 3.20
C_3-C_4-H_4	Csp^2	119.9	119.7	119.7	120.3	0.17	0.17	0.33

		118.8	118.2	120.7	113.6	0.51	1.60	4.38
C_6-C_5-C_8	Csp^2	121.9 121.3	120.3 120.7	120.0 119.9	123.1 123.4	1.31 0.49	1.56 1.15	0.98 1.73
C_4-C_5-C_6	Csp^2	122.8 116.5	120.6 118.0	120.5 119.3	123.0 115.7	1.79 1.29	1.87 2.40	2.20 0.69
C_4-C_5-C_8	Csp^2	122.8 122.1	120.6 121.2	120.5 120.7	123.0 120.9	1.79 0.74	1.87 1.15	0.16 0.98
H_6-C_6-C_7	Csp^2	119.2 119.1	120.0 118.8	120.1 119.4	123.2 113.6	0.67 0.25	0.76 0.25	3.36 4.62
C_5-C_6-C_7	Csp^2	119.2 121.8	120.0 121.0	120.1 120.7	123.2 123.3	0.67 0.66	0.76 0.90	3.36 1.23
C_6-C_7-H_7	Csp^2	119.2 119.8	120.1 121.2	120.0 121.3	119.3 119.0	0.76 1.17	0.67 1.25	0.08 0.67
C_2-C_7-H_7	Csp^2	119.2 119.7	120.1 118.4	120.0 119.2	119.3 118.1	0.76 1.09	0.67 0.42	0.08 1.34
N_1-C_9-H_9	Csp^2	118.3 119.3	119.9 116.2	119.7 117.6	118.1 111.6	1.35 2.60	0.18 1.42	0.17 6.45
C_8-C_9-H_9	Csp^2	120.5 119.2	119.2 122.7	118.8 120.6	118.3 122.5	1.08 2.94	1.41 1.17	1.83 2.77
N_1-C_9-C_8	Csp^2	109.7 121.5	109.9 121.0	113.1 121.6	114.9 125.9	0.18 0.41	3.10 0.08	4.74 3.62
N_1-C_{10}-C_{11}	Csp^2	117.0 122.0	117.6 121.8	119.4 121.4	120.4 122.3	0.51 0.16	2.05 0.49	2.91 0.25
N_1-C_{10}-C_{15}	Csp^2	119.4 118.2	120.5 117.5	121.5 119.2	124.4 120.3	0.92 0.59	1.76 0.85	4.19 1.78
C_{11}-C_{10}-C_{15}	Csp^2	122.9 119.8	124.1 120.5	121.9 119.3	121.9 117.5	0.98 0.58	0.81 0.42	0.81 1.92

C_{10}-C_{11}-H_{11}	Csp^2	120.5 120.8	119.2 122.3	118.8 120.7	118.3 119.2	1.08 1.24	1.41 0.08	1.83 1.32
H_{11}-C_{11}-C_{12}	Csp^2	119.2 120.8	120.0 119.1	120.1 118.9	123.2 118.2	0.67 1.41	0.76 1.57	3.36 2.15
C_{10}-C_{11}-C_{12}	Csp^2	122.9 118.4	124.1 118.4	121.9 120.3	121.9 122.6	0.98 0.00	0.81 1.60	0.81 3.55
F_1-C_{12}-C_{11}	Csp^2	118.1 117.5	118.5 117.3	120.1 117.9	124.5 113.8	0.34 0.17	1.69 0.34	2.03 3.15
F_1-C_{12}-C_{13}	Csp^2	118.1 117.9	118.5 118.5	120.1 120.4	124.5 124.4	0.34 0.51	1.69 2.12	2.03 5.51
C_{11}-C_{12}-C_{13}	Csp^2	122.9 124.6	124.1 124.0	121.9 121.5	121.9 121.8	0.98 0.48	0.81 2.49	0.81 2.25
C_{12}-C_{13}-C_{14}	Csp^2	115.8 115.8	115.6 115.7	116.2 116.6	113.8 113.8	0.17 0.09	0.35 0.69	1.73 1.73
N_2-C_{13}-C_{12}	Csp^2	119.4 120.4	120.5 120.4	121.5 120.6	124.4 124.5	0.92 0.00	1.76 0.17	4.19 3.41
N_2-C_{13}-C_{14}	Csp^2	119.4 123.7	120.5 123.6	121.5 122.4	124.4 121.7	0.92 0.08	1.76 1.05	4.19 1.62
C_{13}-C_{14}-C_{15}	Csp^2	123.6 122.0	122.5 122.5	122.9 122.8	125.2 125.3	0.89 0.41	0.57 0.66	1.29 2.70
H_{14}-C_{14}-C_{15}	Csp^2	118.2 119.0	119.7 117.6	120.2 116.7	120.6 114.0	1.27 1.18	1.69 1.93	2.03 4.20
C_{13}-C_{14}-H_{14}	Csp^2	118.2 119.0	119.7 119.7	120.2 120.3	120.6 120.7	1.27 0.59	1.69 1.09	2.03 1.43
C_{10}-C_{15}-C_{16}	Csp^2	116.6 118.0	118.7 117.9	119.4 118.9	119.1 118.6	1.80 0.08	2.40 0.76	2.14 0.51
C_{10}-C_{15}-C_{14}	Csp^2	123.7	123.3	121.7	122.4	0.32	1.62	1.05

		119.3	118.6	119.1	119.1	0.59	0.17	0.17
C_{14}-C_{15}-C_{16}	Csp^2	123.6 122.7	122.5 123.3	122.9 121.8	125.2 122.3	0.89 0.49	0.57 0.73	1.29 0.33
C_8-C_{16}-C_{15}	Csp^2	122.8 122.1	122.5 122.6	120.2 120.4	123.5 123.4	0.24 0.41	2.12 1.39	0.57 1.06
C_8-C_{16}-H_{16}	Csp^2	118.6 118.9	118.5 118.9	119.4 120.1	115.3 121.2	0.08 0.00	0.67 1.01	2.78 1.93
C_{15}-C_{16}-H_{16}	Csp^2	118.2 119.0	119.7 118.3	120.2 119.4	120.6 115.4	1.27 0.59	1.69 0.34	2.03 3.03
N_2-C_{17}-C_{18}	Csp^3	109.7 109.7	109.9 109.8	113.1 112.0	114.9 115.1	0.18 0.09	3.10 2.10	4.74 4.92
N_2-C_{17}-H_{17A}	Csp^3	109.7 109.7	108.7 110.2	109.2 109.9	110.9 110.9	0.91 0.46	0.46 0.18	1.09 1.09
N_2-C_{17}-H_{17B}	Csp^3	109.7 109.7	110.3 108.7	108.3 109.5	108.4 108.3	0.55 0.91	1.28 0.18	1.19 1.28
H_{17A}-C_{17}-C_{18}	Csp^3	109.7 109.8	109.8 110.1	110.6 108.1	111.6 107.0	0.09 0.27	0.82 1.55	1.73 2.55
H_{17B}-C_{17}-C_{18}	Csp^3	109.7 109.7	109.8 109.2	110.6 108.5	111.6 104.9	0.09 0.46	0.82 1.09	1.73 4.38
H_{17B}-C_{17}-H_{17A}	Csp^3	108.0 108.2	108.8 108.4	110.3 108.4	106.4 110.6	0.74 0.18	2.13 0.18	1.48 2.22
O_3-C_{18}-H_{18A}	Csp^3	111.3 109.4	110.9 110.4	112.2 110.0	111.0 107.9	0.36 0.91	0.81 0.55	0.27 1.37
C_{17}-C_{18}-H_{18A}	Csp^3	107.7 109.4	109.8 109.8	110.6 110.7	111.6 110.6	0.09 0.37	0.82 1.19	1.73 1.10
H_{18A}-C_{18}-H_{18B}	Csp^3	108.2 108.0	108.4 108.8	108.4 110.3	110.6 106.4	0.18 0.74	0.18 2.13	2.22 1.48

O_3-C_{18}-C_{17}	Csp^3	111.3 111.3	110.9 110.9	112.2 111.2	111.0 111.0	0.36 0.36	0.81 0.09	0.27 0.27
O_3-C_{18}-H_{18B}	Csp^3	109.7 109.4	109.8 106.7	109.4 104.6	107.8 109.2	0.09 2.47	0.27 4.39	1.73 0.18
C_{17}-C_{18}-H_{18B}	Csp^3	109.7 109.4	109.8 109.8	110.6 109.6	111.6 111.6	0.09 0.37	0.82 0.18	1.73 2.01
H_{19A}-C_{19}-H_{19B}	Csp^3	108.1 107.9	108.6 108.7	108.8 110.3	110.1 106.4	0.46 0.74	0.65 2.22	1.85 1.39
H_{19A}-C_{19}-C_{20}	Csp^3	109.7 109.2	109.8 109.3	110.6 110.6	111.6 111.6	0.09 0.09	0.82 1.28	1.73 2.20
O_3-C_{19}-H_{19A}	Csp^3	111.3 109.2	110.9 110.4	112.2 110.0	111.0 109.4	0.36 1.10	0.81 0.73	0.27 0.18
H_{19B}-C_{19}-C_{20}	Csp^3	109.7 109.2	109.8 109.7	110.6 109.6	111.6 110.5	0.09 0.46	0.82 0.37	1.73 1.19
O_3-C_{19}-H_{19B}	Csp^3	111.3 109.2	110.9 106.9	112.2 104.6	111.0 107.8	0.36 2.11	0.81 4.21	0.27 1.28
O_3-C_{19}-C_{20}	Csp^3	123.6 112.2	110.5 111.5	110.3 111.2	107.8 110.9	10.60 0.62	10.76 0.89	12.78 1.16
C_{19}-C_{20}-H_{20A}	Csp^3	109.7 109.6	109.8 108.9	109.4 108.2	107.8 107.2	0.09 0.64	0.27 1.28	1.73 2.19
N_2-C_{20}-H_{20A}	Csp^3	110.2 109.6	109.0 109.0	107.3 108.7	111.3 108.4	1.09 0.55	2.63 0.82	1.00 1.09
H_{20A}-C_{20}-H_{20B}	Csp^3	107.9 108.1	108.7 108.6	110.3 108.8	106.4 110.1	0.74 0.46	2.22 0.65	1.39 1.85
N_2-C_{20}-C_{19}	Csp^3	109.7 110.2	109.9 109.5	113.1 112.0	114.9 114.7	0.18 0.64	3.10 1.63	4.74 4.08

Table 5B.4: *Comparative list of selected torsional angles of* ***FMPC*** *(block),* ***FMMC*** *(RED) in (°)*

Atomic string	**XRD**		**B3LYP**		**AM1**		**MM2**	
	Angle	(*)	Angle	(*)	Angle	(*)	Angle	(*)
H_6-C_6-C_7-H_7	+0.8 +0.1	+*sp* +*sp*	+10.2 +1.1	+*sp* +*sp*	+7.6 +0.3	+*sp* +*sp*	-	-
H_6-C_6-C_7-C_2	+82.3 +79.8	+*sc* +*sc*	-164.3 -178.0	-*ap* -*ap*	-179.2 -179.5	-*ap* -*ap*	+7.8 +0.1	+*sp* +*sp*
C_5-C_6-C_7-H_7	-159.7 -179.8	-*ap* -*ap*	+163.2 +179.0	+*ap* +*ap*	+143.5 +179.6	+*ac* +*ap*	-10.4 -0.1	-*sp* -*sp*
H_6-C_6-C_5-C_8	-1.0 -0.6	-*sp* -*sp*	-2.0 -2.2	-*sp* -*sp*	-0.67 -0.8	-*sp* -*sp*	-0.08 -0.1	-*sp* -*sp*
H_6-C_6-C_5-C_4	+172.1 +179.3	+*ap* +*ap*	+175.3 +177.9	+*ap* +*ap*	+165.6 +179.4	+*ap* +*ap*	+175.6 +180.0	+*ap* +*ap*
C_7-C_6-C_5-C_8	+169.6 +179.4	+*ap* +*ap*	+177.4 +179.8	+*ap* +*ap*	+176.8 +179.8	+*ap* +*ap*	+0.6 +0.2	+*sp* +*sp*
C_7-C_6-C_5-C_4	-0.6 -0.7	-*sp* -*sp*	+0.2 +0.1	+*sp* +*sp*	+0.6 +0.2	+*sp* +*sp*	+175.7 +178.3	+*ap* +*ap*
H_7-C_7-C_2-C_3	-176.8 -179.5	-*ap* -*ap*	-179.4 -179.1	-*ap* -*ap*	-179.8 -179.8	-*ap* -*ap*	-179.8 -179.5	-*ap* -*ap*
C_6-C_7-C_2-O_1	-178.3 -179.0	-*ap* -*ap*	-176.8 -179.9	-*ap* -*ap*	-176.5 -179.8	-*ap* -*ap*	-1.8 -2.0	-*sp* -*sp*
C_6-C_7-C_2-C_3	+0.4 +0.5	+*sp* +*sp*	+0.6 +0.1	+*sp* +*sp*	+0.7 +0.1	+*sp* +*sp*	-1.8 -1.6	-*sp* -*sp*
H_{19A}-C_{19}-C_{20}-N_2	+66.1 +64.1	+*sc* +*sc*	-64.3 -66.4	-*sc* -*sc*	-71.6 -70.0	-*sc* -*sc*	+79.8 +84.2	+*sc* +*sc*
H_{19A}-C_{19}-C_{20}-H_{20B}	-55.5 -56.6	-*sc* -*sc*	+174.8 +171.5	+*ap* +*ap*	+176.8 +167.6	+*ap* +*ap*	-167.9 -155.4	-ap -*ap*
H_{19B}-C_{19}-C_{20}-H_{20A}	-73.4 -57.4	-*sc* -*sc*	+65.2 -66.3	+*sc* -*sc*	-71.3 -72.2	-*sc* -*sc*	+170.9 +145.5	+*ac* +*ac*
H_{19B}-C_{19}-C_{20}-N_2	-169.8 -178.2	-*ap* -*ap*	+174.3 +173.2	+*ap* +*ap*	+167.9 -167.4	+*ap* -*ap*	-157.5 -179.3	-*ap* -*ap*
H_{19B}-C_{19}-C_{20}-H_{20B}	+79.3 +61.1	+*sc* +*sc*	+52.4 +11.6	+*sc* +*sp*	+45.6 +79.6	+*sc* +*sc*	-37.2 -59.6	-*sc* -*sc*
O_3-C_{19}-C_{20}-H_{20A}	+63.7 +52.8	+*sc* +*sc*	+175.3 +168.7	+*ap* +*ap*	+172.4 +171.6	+*ap* +*ap*	-33.1 -43.9	-*sc* -*sc*
O_3-C_{19}-C_{20}-N_2	-57.0 -11.6	-*sc* -*sp*	+56.0 +59.3	+*sc* +*sc*	+52.6 -0.9	+*sc* -*sp*	-146.0 -176.2	-*ac* -*ap*
O_3-C_{19}-C_{20}-H_{20B}	-177.8 -165.2	-*ap* -*ap*	-65.9 -60.5	-*sc* -*sc*	-69.6 -72.6	-*sc* -*sc*	-27.2 -31.9	-*sp* +*sc*

H_{19A}-C_{19}-O_3-C_{18}	-61.4 -7.9	*-sc* *-sp*	+61.2 +72.3	*+sc* *+sc*	+64.5 +63.7	*+sc* *+sc*	+24.9 +15.2	*+sp* *+sp*
H_{19B}-C_{19}-O_3-C_{18}	-179.0 -158.9	*-ap* *-ap*	+179.3 -179.4	*+ap* *-ap*	-176.9 -176.6	*-ap* *-ap*	-170.9 -53.3	*-ap* *-sc*
C_{20}-C_{19}-O_3-C_{18}	+59.8 +61.2	*+sc* *+sc*	-60.6 -71.3	*-sc* *-sc*	-58.5 -52.5	*-sc* *-sc*	-33.3 -176.1	*-sc* *-sc*
H_1-N_1-C_9-C_8	-179.9 -177.5	*-ap* *-ap*	+179.7 +177.8	*+ap* *+ap*	+179.7 +179.8	*+ap* *+ap*	+179.8 +179.7	*+ap* *+ap*
C_{10}-N_1-C_9-H_9	-179.9 -179.4	*-ap* *+ap*	-177.8 -178.6	*-ap* *-ap*	-179.4 +179.5	*-ap* *+ap*	-0.1 +179.9	*-sp* *+ap*
C_{10}-N_1-C_9-C_8	+0.1 +2.0	*+sp* *+sp*	+0.8 +0.4	*+sp* *+sp*	+0.2 +0.09	*+sp* *-sp*	-180.0 -0.03	*-ap* *-sp*
H_1-N_1-C_{10}-C_{11}	+1.6 +2.0	*+sp* *+sp*	+0.9 +37.6	*+sp* *+sc*	+0.3 +41.9	*+sp* *+sc*	-179.8 -0.4	*-ap* *-sp*
H_1-N_1-C_{10}-C_{15}	+168.0 -179.5	*+ap* *-ap*	-178.7 -178.6	*-ap* *-ap*	-179.7 -179.4	*-ap* *-ap*	-179.9 +0.1	*-ap* *+sp*
C_9-N_1-C_{10}-C_{11}	-178.4 -176.1	*-ap* *-ap*	+179.8 +178.2	*+ap* *+ap*	+179.8 +179.5	*+ap* *+ap*	-0.4 -1.0	*-sp* *-sp*
C_9-N_1-C_{10}-C_{15}	+0.5 +4.0	*+sp* *+sp*	+0.2 +0.1	*+sp* *+sp*	+0.1 0.01	*+sp* *+sp*	-179.9 -178.9	*-ap* *-ap*
H_9-C_9-C_8-C_5	-1.2 -2.0	*-sp* *-sp*	-1.6 -0.1	*-sp* *-sp*	-0.2 +0.2	*-sp* *+sp*	+179.9 +179.9	*+ap* *+ap*
N_1-C_{10}-C_{15}-C_{14}	+178.6 +178.0	*+ap* *+ap*	-178.9 -179.0	*-ap* *-ap*	-179.5 -179.3	*-ap* *-ap*	-179.9 +0.1	*-ap* *+sp*
C_{11}-C_{10}-C_{15}-C_{16}	+178.4 +178.9	*+ap* *+ap*	+179.2 +142.3	*+ap* *+ac*	+179.8 +179.6	*+ap* *+ap*	-179.7 -179.8	*-ap* *-ap*
C_{11}-C_{10}-C_{15}-C_{14}	-3.0 -2.0	*-sp* *-sp*	+1.4 +0.4	*+sp* *+sp*	+0.8 +0.1	*+sp* *+sp*	+0.2 +0.4	*+sp* *+sp*
H_{20A}-C_{20}-N_2-C_{13}	+68.5 +79.3	*+sc* *+sc*	+40.1 +60.7	*+sc* *+sc*	+47.6 +57.8	*+sc* *+sc*	+66.2 +67.3	*+sc* *+sc*
H_{20A}-C_{20}-N_2-C_{17}	-67.0 -46.5	*-sc* *-sc*	-171.6 -102.04	*-ap* *-ac*	-167.4 -179.8	*-ap* *-ap*	-109.1 -56.3	*-ac* *-sc*
C_{19}-C_{20}-N_2-C_{13}	-170.8 -177.8	*-ap* *-ap*	+159.4 +179.2	*+ap* *+ap*	+167.1 +178.8	*+ap* *+ap*	-111.2 -178.9	*-ac* *-ap*
C_{19}-C_{20}-N_2-C_{17}	+53.7 +73.2	*+sc* *+sc*	-52.4 -79.6	*-sc* *-sc*	-47.8 -102.2	*-sc* *-ac*	+170.8 +163.0	*+ap* *+ap*
H_{20B}-C_{20}-N_2-C_{13}	-50.1 -72.4	*-sc* *-sc*	-79.3 -37.8	*-sc* *-sc*	-71.7 -98.1	*-sc* *-ac*	-55.0 -65.6	*-sc* *-sc*
H_{20B}-C_{20}-N_2-C_{17}	+174.4 +178.2	*+ap* *+ap*	+68.7 +66.1	*+sc* *+sc*	+73.2 +68.1	*+sc* *+sc*	+129.6 +106.5	*+ac* *+ac*
F-C_{12}-C_{13}-C_{14}	+174.0	*+ap*	-176.0	*-ap*	-178.5	*-ap*	-178.9	*-ap*

	+178.2	+*ap*	-179.3	-*ap*	-179.8	-*ap*	-179.7	-*ap*
F-C_{12}-C_{13}-N_2	-1.5 -2.3	-*sp* -*sp*	-0.3 -0.1	-*sp* -*sp*	-3.7 -2.2	-*sp* -*sp*	+0.4 +6.2	+*sp* +*sp*
C_{11}-C_{12}-C_{13}-C_{14}	-3.4 -7.2	-*sp* -*sp*	+2.0 +9.8	+*sp* +*sp*	+0.5 +23.3	+*sp* +*sp*	+0.7 +1.7	+*sp* +*sp*
C_{11}-C_{12}-C_{13}-N_2	-178.9 +178.8	-*ap* +*ap*	+177.7 +66.1	+*ap* +*sc*	+175.3 +163.8	+*ap* +*ap*	+179.9 +175.3	+*ap* +*ap*
C_9-C_8-C_5-C_4	+0.5 +4.3	+*sp* +*sp*	-35.1 -59.7	-*sc* -*sc*	-40.7 -59.7	-*sc* -*sc*	-2.2 -4.8	-*sp* -*sp*
C_{16}-C_8-C_5-C_6	-0.2 -2.1	-*sp* -*sp*	-34.1 -37.6	-*sc* -*sc*	-39.9 -41.9	-*sc* -*sc*	-0.5 -0.4	-*sp* -*sp*
C_{16}-C_8-C_5-C_4	+179.9 +174.5	+*ap* +*ap*	+145.6 142.3	+*ac* +*ac*	+139.6 137.8	+*ac* +*ac*	+177.8 179.5	+*ap* +*ap*
C_9-C_8-C_{16}-H_{16}	-179.6 -178.6	-*ap* -*ap*	+178.9 +178.9	+*ap* +*ap*	+179.7 +179.5	+*ap* +*ap*	+179.8 +179.9	+*ap* +*ap*
C_5-C_8-C_{16}-C_{15}	-179.0 -178.5	-*ap* -*ap*	+179.3 +179.9	+*ap* +*ap*	+179.6 +179.8	+*ap* +*ap*	-179.1 +179.9	-*ap* +*ap*
C_8-C_5-C_4-C_3	+179.5 -179.5	+*ap* -*ap*	-179.9 -179.6	-*ap* -*ap*	-179.8 -179.5	-*ap* -*ap*	-179.9 +0.4	-*ap* +*sp*
C_8-C_5-C_4-H_4	+0.0 +0.5	+*sp* +*sp*	-2.2 -2.1	-*sp* -*sp*	-0.8 -0.7	-*sp* -*sp*	-0.1 -10.1	-*sp* -*sp*
C_{10}-C_{15}-C_{16}-C_8	+0.1 +3.8	+*sp* +*sp*	+0.9 +0.4	+*sp* +*sp*	+0.2 0.7	+*sp* +*sp*	-0.1 -0.0	-*sp* -*sp*
C_{10}-C_{15}-C_{16}-H_{16}	+0.0 -179.9	+*sp* -*ap*	-0.3 -177.8	-*sp* -*ap*	-0.2 -179.4	-*sp* -*ap*	-0.1 -179.2	-*sp* -*ap*
C_{14}-C_{15}-C_{16}-C_8	-178.4 +176.1	-*ap* +*ap*	+178.7 +179.9	+*ap* +*ap*	+179.2 +179.9	+*ap* +*ap*	-179.2 -179.5	-*ap* -*ap*
C_{14}-C_{15}-C_{16}-H_{16}	+1.6 +0.1	+*sp* +*sp*	-0.1 -2.1	-*sp* -*sp*	-0.4 -0.8	-*sp* -*sp*	-0.1 -0.2	-*sp* -*sp*
C_{10}-C_{15}-C_{14}-C_{13}	+3.0 +1.1	+*sp* +*sp*	-1.0 -1.0	-*sp* -*sp*	-0.7 -1.2	-*sp* -*sp*	-0.3 +0.3	-*sp* +*sp*
C_{16}-C_{15}-C_{14}-C_{13}	+179.6 +176.2	+*ap* +*ap*	-178.8 -178.2	-*ap* -*ap*	+179.7 +179.7	+*ap* +*ap*	-179.8 -179.9	-*ap* -*ap*
C_1-O_1-C_2-C_7	-177.9	-*ap*	+179.5	+*ap*	+179.7	+*ap*	+178.8	+*ap*
C_1-O_1-C_2-C_3	+2.6	+*sp*	+0.3	+*sp*	-0.2	-*sp*	+0.7	+*sp*
C_1-O_1-C_1-H_{1C}	+58.0	+*sc*	+60.9	+*sc*	+61.6	+*sc*	+62.5	+*sc*
C_2-O_1-C_1-H_{1B}	+178.0	+*ap*	+179.6	+*ap*	-179.9	-*ap*	-179.6	-*ap*
C_2-O_1-C_1-C_{1A}	-62.0	-*sc*	-61.7	-*sc*	-61.5	-*sc*	-61.6	-*sc*
O_1-C_2-C_3-H_3	-1.1	-*sp*	+0.9	+*sp*	+0.3	+*sp*	-1.8	-*sp*
C_{12}-C_{13}-C_{14}-C_{15}	+1.9	+*sp*	-0.5	-*sp*	+0.5	+*sp*	-0.7	-*sp*

	+4.3	*+sp*	-0.1	*-sp*	-8.4	*-sp*	-10.3	*-sp*
C_{12}-C_{13}-C_{14}-H_{14}	+177.8 -178.0	*+ap* *-ap*	-179.2 -179.2	*-ap* *-ap*	-178.8 -179.0	*-ap* *-ap*	-178.2 +178.9	*-ap* *+ap*
N_2-C_{13}-C_{14}-C_{15}	+177.3 +178.2	*+ap* *+ap*	-176.0 -79.5	*-ap* *-sc*	-176.1 -156.4	*-ap* *-ap*	+179.8 +177.3	*+ap* *+ap*
C_{12}-C_{13}-N_2-C_{20}	+170.9 +176.1	*+ap* *+ap*	-163.8 -179.9	*-ap* *-ap*	-162.3 -179.9	*-ap* *-ap*	+177.1 +179.8	*+ap* *+ap*
C_{12}-C_{13}-N_2-C_{17}	-58.1 -56.6	*-sc* *-sc*	+50.3 +50.8	*+sc* *+sc*	+31.5 +54.6	*+sc* *+sc*	1.76 -1.8	*+sp* *-sp*
C_{14}-C_{13}-N_2-C_{20}	-4.3 -4.3	*-sp* *-sp*	+11.5 +0.1	*+sp* *+sp*	+12.1 +10.8	*+sp* *+sp*	+2.1 +0.3	*+sp* *+sp*
C_{14}-C_{13}-N_2-C_{17}	+128.2 +145.6	*+ac* *+ac*	-133.8 -137.8	*-ac* *-ac*	-130.8 -171.5	*-ac* *-ap*	+177.4 +179.5	*+ap* *+ap*
C_{20}-N_2-C_{17}-C_{18}	-54.9 -58.2	*-sc* *-sc*	+52.9 +50.3	*+sc* *+sc*	+47.8 +31.4	*+sc* *+sc*	-9.8 -1.2	*-sp* *-sp*
C_{13}-N_2-C_{17}-C_{18}	+167.0 -54.9	*+ap* *-sc*	-159.3 -159.5	*-ap* *-ap*	+140.8 -167.7	*+ac* *-ap*	-174.8 +174.9	*-ap* *+ap*
C_{19}-O_3-C_{18}-C_{17}	-119.0 -60.9	*-ac* *-sc*	+61.1 -67.1	*+sc* *-sc*	-64.1 +58.4	*-sc* *+sc*	+171.1 -67.1	*+ap* *-sc*
H_{18A}-C_{18}-C_{17}-H_{17A}	-68.1 -59.4	*-sc* *-sc*	-26.1 -55.5	*-sp* *-sc*	+79.3 -51.1	*+sc* *-sc*	-0.9 -17.0	*-sp* *-sp*
H_{18A}-C_{18}-C_{17}-H_{17B}	+11.4 +59.4	*+sp* *+sc*	-165.3 -174.6	*-ap* *-ap*	-179.4 -168.6	*-ap* *-ap*	+49.6 +31.3	*+sc* *+sc*
O_3-C_{18}-C_{17}-N_2	+63.4 +59.1	*+sc* *+sc*	+146.8 -56.3	*+ac* *-sc*	-78.5 -52.5	*-sc* *-sc*	+10.5 +36.5	*+sp* *+sc*
O_3-C_{18}-C_{17}-H_{17A}	+163.8 +179.7	*+ap* *+ap*	-179.3 -177.9	*-ap* *-ap*	-156.9 -173.8	*-ap* *-ap*	+69.0 -83.9	*+sc* *-sc*
O_3-C_{18}-C_{17}-H_{17B}	-36.2 -61.6	*-sc* *-sc*	+179.2 +62.9	*+ap* *+sc*	-70.2 +68.6	*-sc* *+sc*	+156.5 +158.6	*+ap* *+ap*
H_{18B}-C_{18}-C_{17}-N_2	-11.3 -61.9	*-sp* *-sc*	+178.1 -174.2	*+ap* *-ap*	-2.6 -167.7	*-sp* *-ap*	+161.4 +59.2	*+ap* *+ap*
H_{18B}-C_{18}-C_{17}-H_{17A}	+71.3 +58.7	*+sc* *+sc*	-179.5 +64.1	*-ap* *+sc*	+56.9 +70.9	*+sc* *+sc*	-176.1 +35.8	*-ap* *+sc*
H_{18B}-C_{18}-C_{17}-H_{17B}	+159.2 +177.5	*+ap* *+ap*	+67.1 -54.9	*+sc* *-sc*	-51.9 -46.6	*-sc* *-sc*	+45.3 -81.7	*+sc* *-sc*
C_5-C_4-C_3-C_2	-	-	-6.4 -0.2	*-sp* *-sp*	-11.7 -0.2	*-sp* *-sp*	+165.7 -0.1	*+ac* *-sp*
H_4-C_4-C_3-C_2	-176.3 -180.0	*-ap* *-ap*	+179.3 -177.7	*+ap* *-ap*	+179.8 -179.1	*+ap* *-ap*	+179.9 +178.2	*+ap* *+ap*

* The conformations were designated by Klyne-Prelog terms using *s* = syn, *a* = anti, *p* = peri-planar (0 ± 30^0& 180 ± 30^0) and all other angles *c* = clinal, and + & - signs.

5B.2 Hirshfeld Surface Analysis of FMPC and FMMC:

A Hirshfeld analysis was performed on **FMPC** and **FMMC** to investigate the strength and role of hydrogen bonds and other intermolecular contacts, Hirshfeld surfaces, and the corresponding fingerprint plots, and to assess their importance in the crystal lattice's stability.

Figure 5B.6 shows the Hirshfeld surface interaction diagram and fingerprint plots of **FMPC.** The surfaces show the d_{norm} in the range of -0.23 to 1.42 Å. Strong acceptor-donor intermolecular hydrogen bond interactions appear at N_2-H_2···Cl_1, C_{16}-H_{16}-···O_1, C_7-H_7···Cl_1, C_{11}-H_{11}···Cl_1 and O_1···C_{16}-H_{16} and are indicated as bright red color spots. **Table 5B.5** indicates H···H interactions as the largest, with about 47% surface concentration. The Cl···H/ H···Cl contacts contribute to about 16% with two spikes at $d_e + d_i$ value of ~2.8 Å, F···H/ H···F to 7.0% with $d_e + d_i$ value of ~2.3 Å and O···H/ H···O to about 5% with $d_e + d_i$ value of ~2.3 Å. The C···H/ H···C interactions due to π···π stacking and shown in green patch contribute to about 8% with $d_e + d_i$ value of ~1.8 Å. All other intermolecular interatomic contacts and the corresponding interactions are found to contribute less than 3.0%.

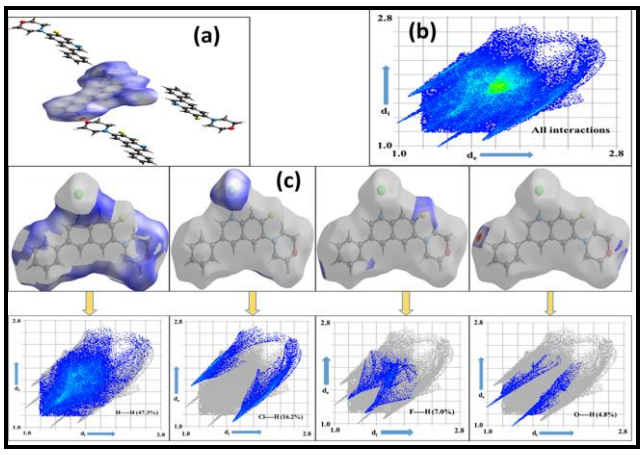

Figure 5B.6: *Hirshfeld surface maps (a) with d_{norm} neighboring molecules associated with close contacts among **FMPC**, (b) two-dimensional fingerprint plot and (c) deconvolution of two-dimensional fingerprint plot illustrating percent interactions*

In **Figure 5B.7,** the small blue regions around the bright-red spots indicate π- π stacking between the benzene and quinoline rings whereas the green shade in the flat region indicates the π- π stacking around the benzene and quinoline rings in **FMPC**. The electrostatic potential generated by using the HF/3-21G basis set is shown in **Figure 5B.7(c)** with red region indicating

negative electrostatic potential (hydrogen acceptors) and blue region, positive electrostatic potential (hydrogen donor).

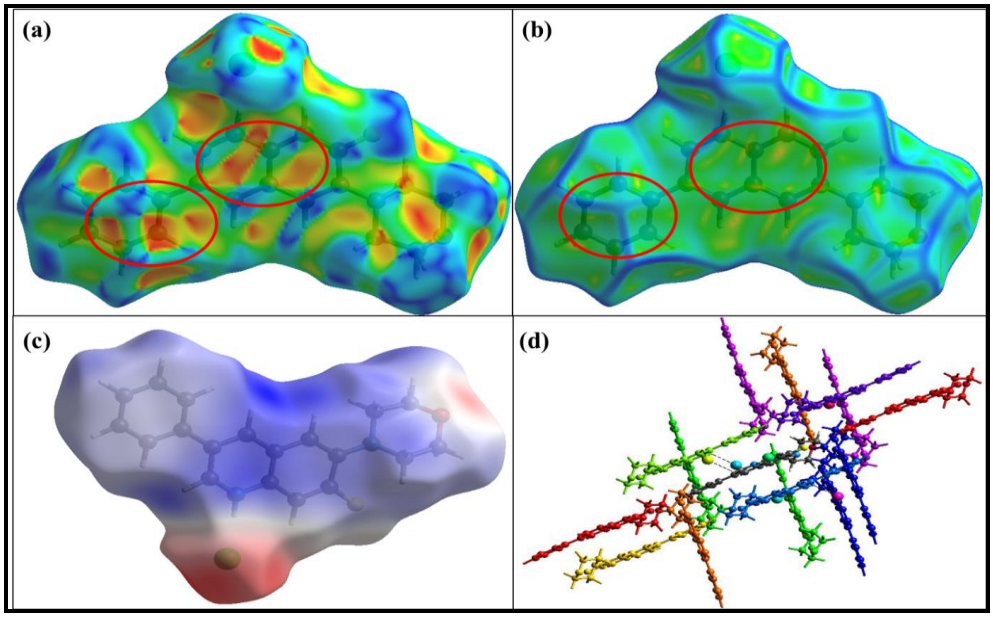

Figure 5B.7: *Graphical visuals of the Hirshfeld surface for* ***FMPC*** *mapped over as (a) shape index property (b) curve index flat region (rings, referred to, are marked in red) (c) diffuse color graphical portrayal (positive electrostatic potential is shown in blue shade and negative in red) (d) color coded interactions with in 3.8 Å*

In the **FMMC**, the surfaces show the d_{norm} in the range of -0.4657 to 1.2780 Å. The intermolecular hydrogen bond interactions appear at C_{16}-H_{16}···Cl, Cl-···H_2O, C_{14}-H_{14}···Cl_1, H_1-N_1···Cl, C_3-H_3···O_1, C_9-H_9···O_2 is indicated as bright red color spots (**Figure 5B.8)**. **Figure 5B.9** shows the finger print plots for **FMMC. Figure 5B.11** and **Table 5B.5** collectively indicate H···H interactions as the largest, with about 47.2% surface concentration. The C···H/ H···C contacts contribute to about 11.2% with two spikes at $d_e + d_i$ value of ~1.6 Å, O···H/ H···O to 11.6% with $d_e + d_i$ value of ~1.42 Å and Cl···H/ H···Cl to about 11.0% with $d_e + d_i$ value of ~1.4 Å. The C···C/ C···C interactions due to π···π stacking and shown in the green patch contribute to about 7.4% with a $d_e + d_i$ value of ~1.7 Å. All other intermolecular interatomic contacts and the corresponding interactions are found to contribute to less than 1%. **Figure 5B.10** show the Hirshfeld surface of molecule **FMMC** mapped with shape index map, curvedness map, electrostatic potential map, and fragment patches.

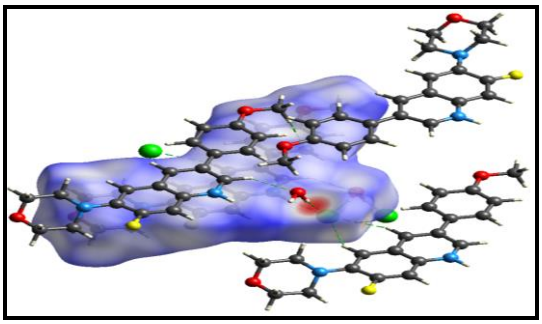

Figure 5B.8: *Hirshfeld d_{norm} surface of* ***FMMC*** *showing intermolecular hydrogen bonding interactions*

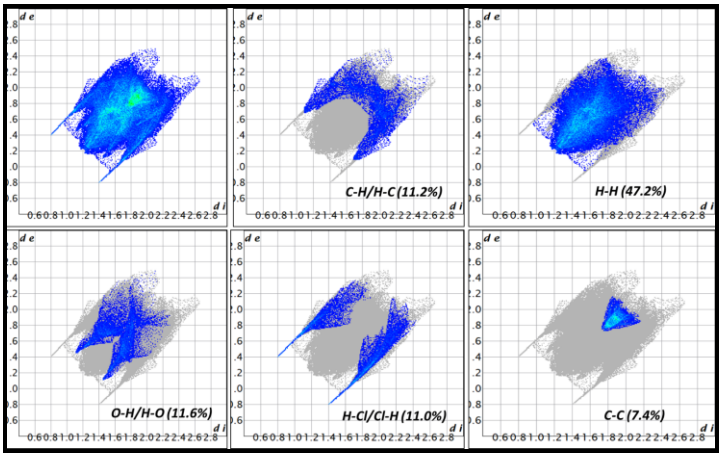

Figure 5B.9: *Hirshfeld finger print plots of* ***FMMC***

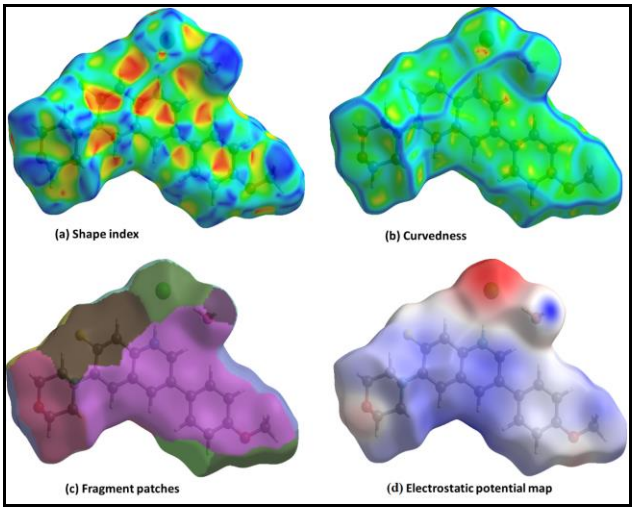

Figure 5B.10: *Hirshfeld surface maps of* ***FMMC*** *represented by modes*

Table 5B.5: *Intermolecular Hirshfeld inter-atomic interaction percentages*

Interaction	Contribution (%)	
	FMPC	FMMC
C-C	11.1	7.4
C-H/H-C	7.9	11.2
C-N/N-C	1.8	1.1
C-O/O-C	-	1.6
C-F/F-C	2.2	1.8
H-H	47.2	47.2
H-N/N-H	1.8	1.1
H-O/O-H	4.8	11.6
H-F/F-H	7.0	4.3
O-F/F-O	0.6	0.8
H-Cl/Cl-H	16.1	11.0

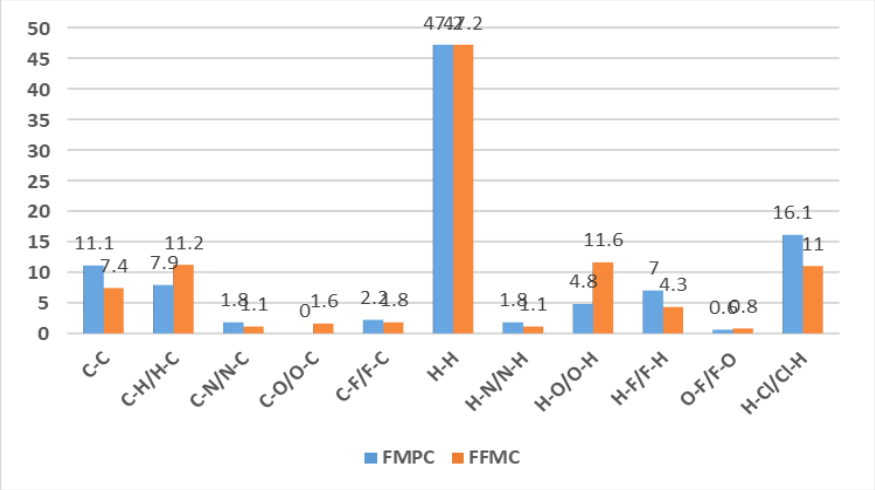

Figure 5B.11: *Histogram of percentage contributions of various intermolecular interactions* ***FMPC*** *and* ***FMMC***

Users usually correlate the results of the Hirshfeld surface analysis with the strength of the electronic contacts and their corresponding interaction energies[10]. The scale factors used for the construction of energy frame works for **FMPC** are E_ele = 34.0, E_pol = -43.8, E_dis = -450.3, E_rep = 201.0, E_tot = 236.9, whereas E_ele = 32.0, E_pol = -32.6, E_dis = -296.4, E_rep = 106.9, E_tot = -168.9 kJ mol^{-1} for **FMMC**. These model energies reveal that dispersion energy contributes significantly to the interactions in the crystal.

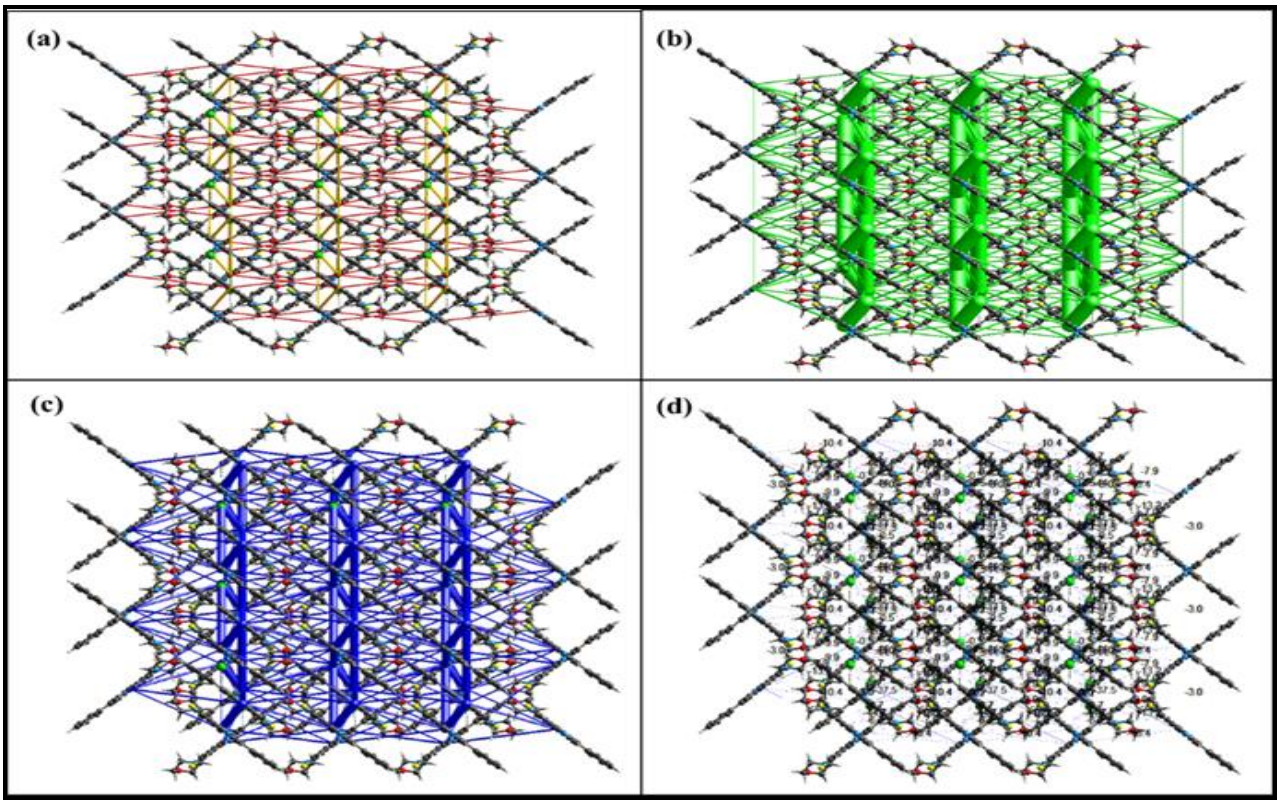

Figure 5B.12: *Hirshfeld energy frameworks calculated for* ***FMPC*** *and as viewed along the c-axis showing the* ***(a)*** *electrostatic potential force,* ***(b)*** *dispersion force and* ***(c)*** *total energy diagram and (d) its annotated total energy diagram*

Individual energy components are shown as cylinders between the centroids of interacting molecular pairs in **Figure 5B.12** and **5B.13,** corresponding to dispersion energy, coulomb energy, and total energy along the a, b, and c axes, respectively. The cylindrical radii are represented as a proportionate measure of the strength of the interaction energies in the laddered bars, normalized to 100 with a minimum value of 5 kJ mol^{-1}. **Figure 5B.14** represents the molecular pairs that participate in the interaction of **FMMC** when viewed along the c axis.

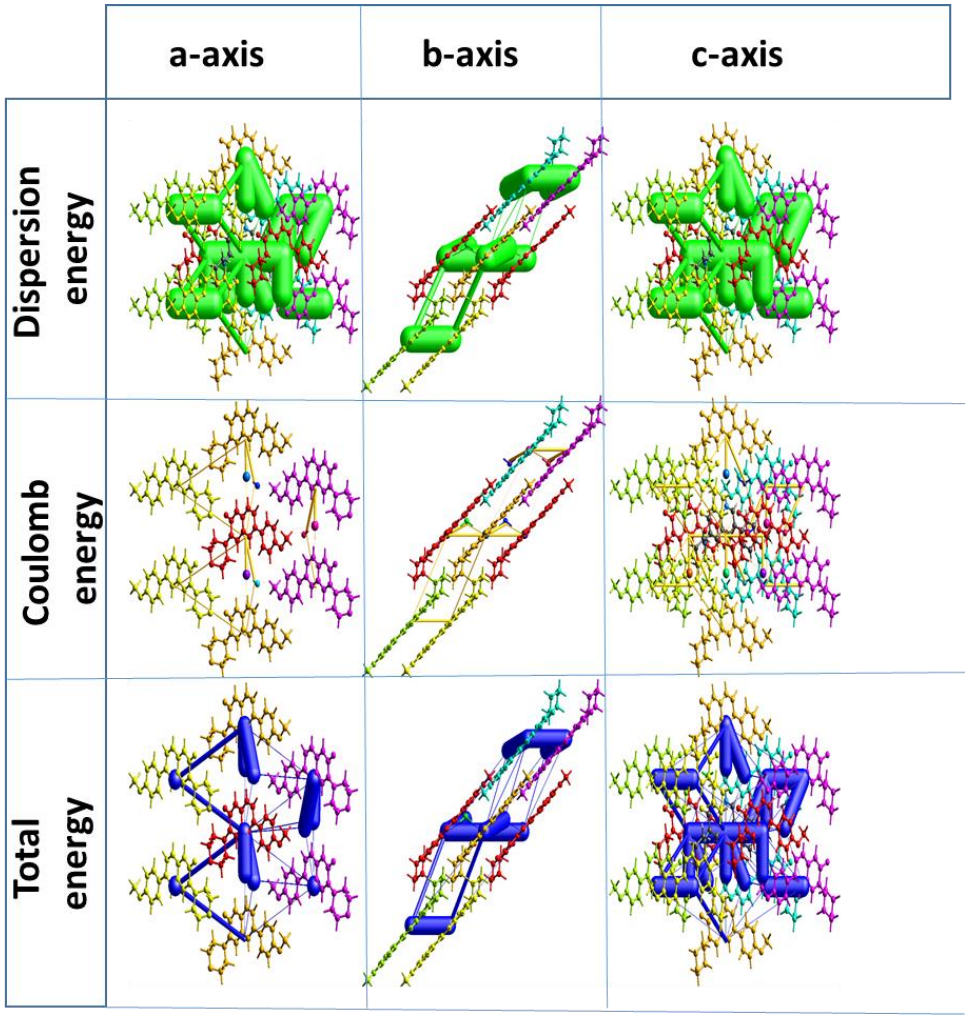

Figure 5B.13: *Crystallographic axis-wise modes of intermolecular energies in* ***FMMC***

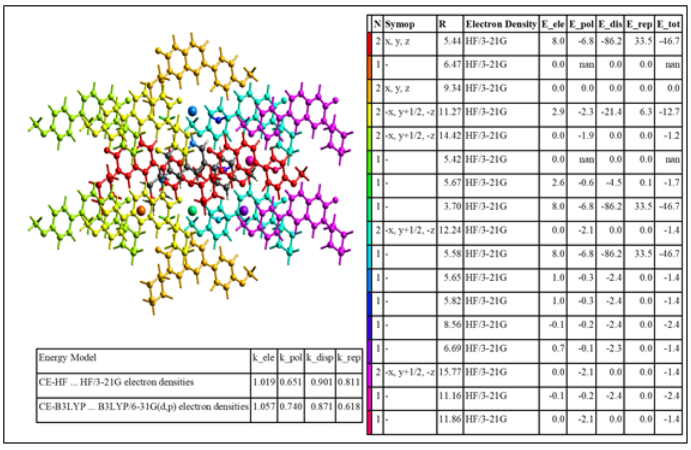

N	Symop	R	Electron Density	E_ele	E_pol	E_dis	E_rep	E_tot
2	x, y, z	5.44	HF/3-21G	8.0	-6.8	-86.2	33.5	-46.7
1	-	6.47	HF/3-21G	0.0	nan	0.0	0.0	nan
2	x, y, z	9.34	HF/3-21G	0.0	0.0	0.0	0.0	0.0
2	-x, y+1/2, -z	11.27	HF/3-21G	2.9	-2.3	-21.4	6.3	-12.7
2	-x, y+1/2, -z	14.42	HF/3-21G	0.0	-1.9	0.0	0.0	-1.2
1	-	5.42	HF/3-21G	0.0	nan	0.0	0.0	nan
1	-	5.67	HF/3-21G	2.6	-0.6	-4.5	0.1	-1.7
1	-	3.70	HF/3-21G	8.0	-6.8	-86.2	33.5	-46.7
2	-x, y+1/2, -z	12.24	HF/3-21G	0.0	-2.1	0.0	0.0	-1.4
1	-	5.58	HF/3-21G	8.0	-6.8	-86.2	33.5	-46.7
1	-	5.65	HF/3-21G	1.0	-0.3	-2.4	0.0	-1.4
1	-	5.82	HF/3-21G	1.0	-0.3	-2.4	0.0	-1.4
1	-	8.56	HF/3-21G	-0.1	-0.2	-2.4	0.0	-2.4
1	-	6.69	HF/3-21G	0.7	-0.1	-2.3	0.0	-1.4
2	-x, y+1/2, -z	15.77	HF/3-21G	0.0	-2.1	0.0	0.0	-1.4
1	-	11.16	HF/3-21G	-0.1	-0.2	-2.4	0.0	-2.4
1	-	11.86	HF/3-21G	0.0	-2.1	0.0	0.0	-1.4

Energy Model	k_ele	k_pol	k_disp	k_rep
CE-HF ... HF/3-21G electron densities	1.019	0.651	0.901	0.811
CE-B3LYP ... B3LYP/6-31G(d,p) electron densities	1.057	0.740	0.871	0.618

Figure 5B.14: *Pair-wise intermolecular interactions in* ***FMMC*** *(viewed along the c axis)*

5B.3 Biological Studies of FMPC and FMMC:

5B.3.1 *Cell Viability (MTT Assay) of FMPC and FMMC:*

The MTT (3-(4,5-dimethylthiazolyl-2)-2,5-diphenyltetrazolium bromide) assay is used to investigate the drug resistant sensitivities of the hypopharyngeal cancer cell line FaDu, as described by Mossman[11]. FaDu cancer line cells are seeded in a 96-well cluster with a cell population density of 10^4 per well. The nourishing medium (RPMI + 10% FBS) is administered to each well and incubated for 24 hours. A series of specified concentrations of **FMPC** and **FMMC** (in 5, 10, 15, 20, 25, 30, 35, and 40 µg/mL) are added to cells and incubated (37 °C, 5% CO_2) for about 4 hrs. Once incubation period was completed, the left-over nourishing medium was removed by decanting and each well was administered with the fresh nourishing (RPMI + 10% FBS) medium. The incubation was continued for an additional 24 hrs before adding 10 µL of the MTT reagent prepared in PBS (5 mg mL^{-1}), followed by further incubation for 4 hours at 37°C. The purple-colored formazan crystals were extracted by adding 100 µL of DMSO (dimethyl sulfoxide) to each well for which the absorbance was measured at 570 nm. In a blank (control) experiment, the above procedure was repeated with no addition of **FMPC** and **FMMC**. The following equation has been used to compute the relative cell viability.

$$\frac{A_{sample}}{A_{control}} x100 = RCVP$$

where RCVP is the relative cell viability percentage. It is established that **FMPC** and **FMMC** have a reasonably promising RCVP as depicted in **Figures 5B.15** and **5B.16,** respectively.

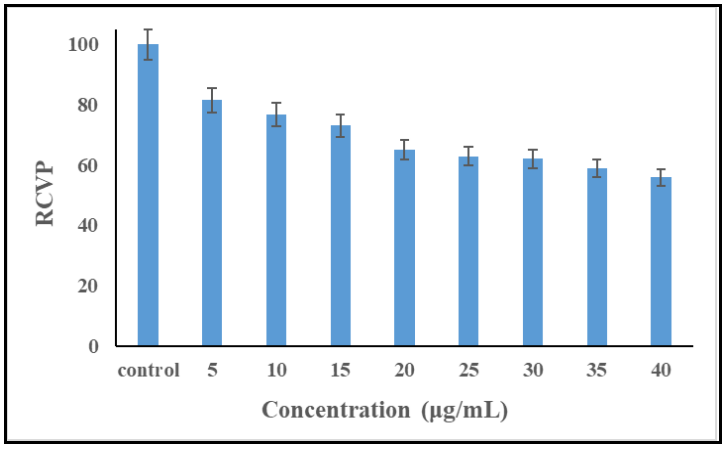

Figure 5B.15: *Cell viability graph of **FMPC** using FaDu cells by MTT assay*

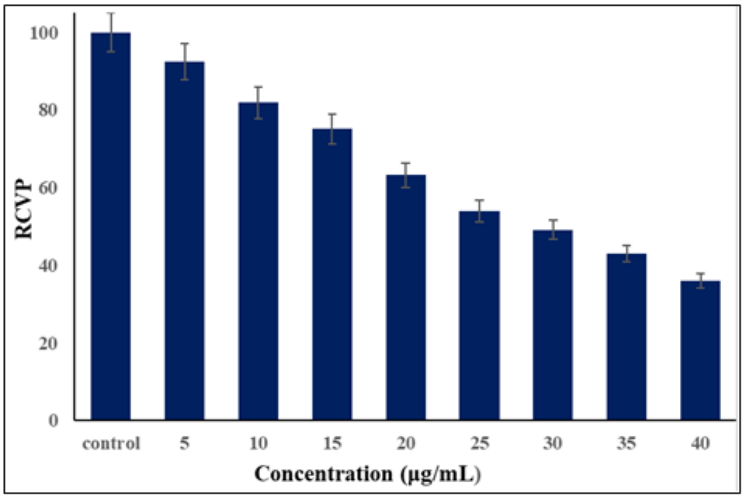

Figure 5B.16: *Cell viability graph of* ***FMMC*** *using FaDu cells by MTT assay*

5B.4 Molecular Docking Studies of FMPC and FMMC:

EGFR-TK (pdb id: 1m17) belongs to the epidermal growth factor receptor family[12]. Excess EGFR expression results in anal cancer and epithelial malignancies of the neck and head[13]. We chose EGFR as a target protein receptor for molecular docking by the cation of **FMPC**.

The DockVina software[14] was used to perform docking calculations. Using AutoDockTools-1.5.6, the ligand is prepared by eliminating water molecules and adding polar hydrogens, as well as ascribing Kollman and Gasteiger partial charges[15]**.** The AutoGrid application was used to create affinity maps with 60 x 60 x 60 grid points and with 0.575 spacing. The discovery studio visualizer software was used to understand the 2D structure and to explore the mode of binding interactions. The cationic form of **FMPC** has a binding energy of -9.1 kcal mole^{-1} and docks to the EGFR through three hydrogen bonds, seven electrostatic interactions and one hydrophobic interaction; one hydrogen bond is through the fluorine atom with the protein amino acid residue of GLY-833, as well as the other two hydrogen bonds are through the morpholine ring carbons with amino acid residues of GLU-734, GLU-738. There is one hydrophobic interaction in the ALA-731 and seven electrostatic interactions in the ASP-831, ASP-813, and LYS-721 amino acid residues are shown in **Figure 5B.17.**

The cationic form of **FMMC** has a binding energy of -9.3 kcal mole^{-1} and docks to the EGFR through, two halogen interactions with the protein amino acid residue of GLY-695, SER-696 and three electrostatic interactions with amino acid residues of LYS-721, ASP-813. There are

eight hydrophobic interactions in the ALA-835 LEU-838, ALA-840, ARG-817, CYS-773, and PHE-699 amino acid residues are shown in **Figure 5B.18.**

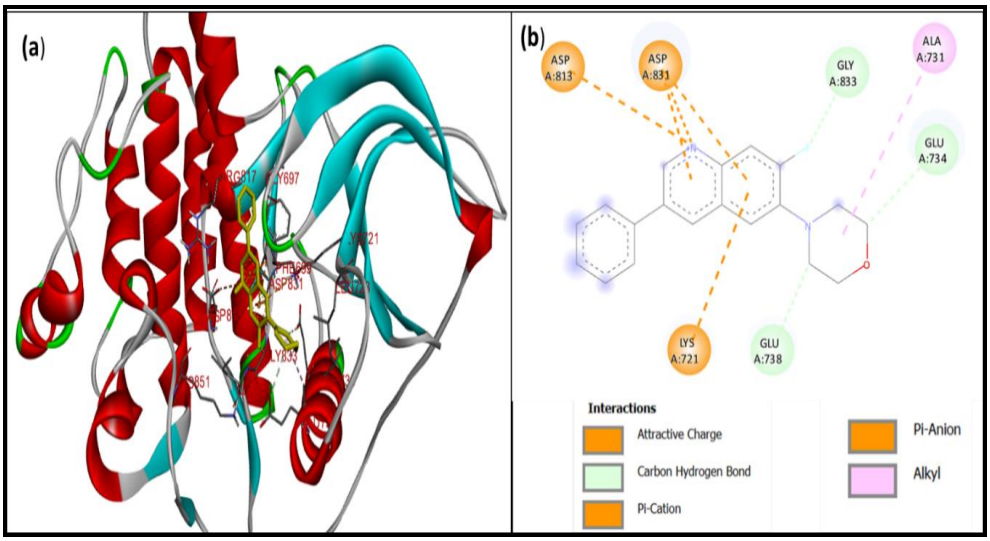

Figure 5B.17: *Molecular docking interactions of* ***FMPC*** *with EGFR-TK protein; (a) 3D depiction of ligand-receptor binding interactions and (b) 2D representation of different forms of interactions with amino acid residues*

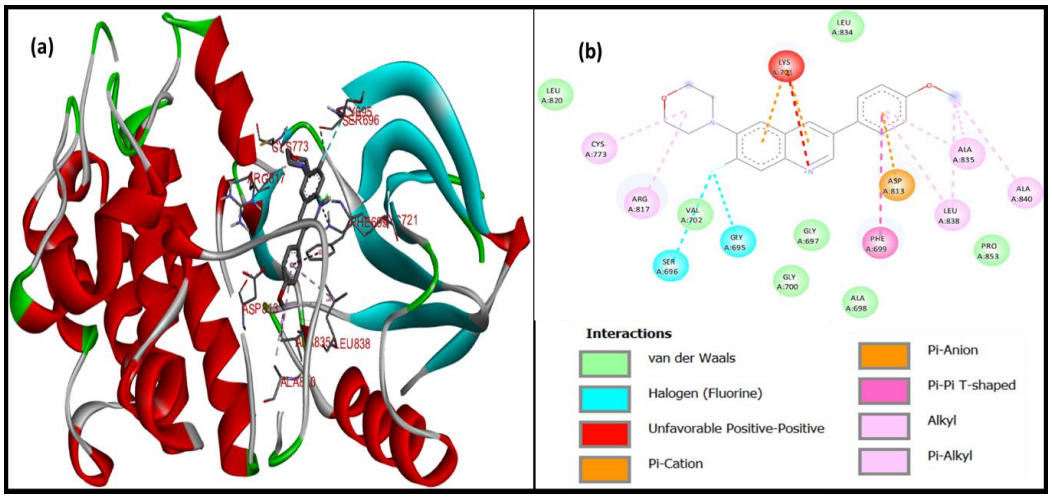

Figure 5B.18: *Molecular docking interactions of* ***FMMC*** *with EGFR-TK protein; (a) 3D depiction of ligand-receptor binding interactions and (b) 2D representation of different forms of interactions with amino acid residues*

Note: The **FMPC** crystal part of this Chapter has been published in a Elsevier journal (***Synthesis, characterization, molecular structure determination by single crystal X-ray diffraction, and Hirshfeld surface analysis of 7-fluoro-6-morpholino-3-phenylquinolin-1-ium chloride salt and computational studies of its cation),*** Dhananjay Rao Thandra et al, *Journal of Molecular Structure*, 2022, **1250**, 131701)

Contents lists available at ScienceDirect

Journal of Molecular Structure

journal homepage: www.elsevier.com/locate/molstr

Synthesis, characterization, molecular structure determination by single crystal X-ray diffraction, and Hirshfeld surface analysis of 7-fluoro-6-morpholino-3-phenylquinolin-1-ium chloride salt and computational studies of its cation

Dhananjay Rao Thandra, Ramachandraiah Allikayala*

Department of Chemistry, National Institute of Technology Warangal, Telangana 506004, India

ARTICLE INFO

Article history:
Received 3 August 2021
Revised 1 October 2021
Accepted 10 October 2021
Available online 13 October 2021

ABSTRACT

7-fluoro-6-morpholino-3-phenylquinolin-1-ium chloride **2** has been synthesized and characterised by various spectral and electrochemical studies besides its molecular structure determination by a single-crystal X-ray diffraction investigation. Computational studies by Austin Model-1 (AM1), SCF-MM2 and DFT/B3LYP to compare the structural data with the single crystal XRD data have been performed on the cation of **2**. The compound is found to crystallize in a monoclinic system in space group P21/c with crystal data as

Graphical abstract

7-fluoro-6-morpholino-3-phenylquinolin-1-ium, has been synthesized and characterised before single crystal X-ray diffraction and Hirshfeld surface analysis studies have been carried out on it.

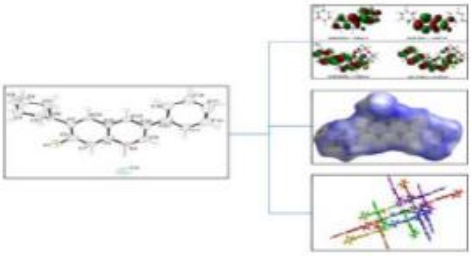

A novel organic molecule 7-fluoro-6-morpholino-3-phenylquinolin-1-ium chloride salt, (**2**), was synthesized and characterized by various spectroscopic techniques and by single crystal XRD studies. Computational molecular modelling studies were also performed on its cationic skeleton on the platforms of AM1, MM2 and B3LYP calculations and the data are correlated with the XRD data. The computationally evaluated data are in excellent agreement with the empirical single crystal XRD data. Some negligibly small deviations are observed in the locations at –C═NH, F-C- and H┅O-C- moieties. These minor deviations are obviously due to the fact that XRD studies are for molecules in crystalline solid state which engage a variety interaction amongst the neighbouring molecules whereas the computational data are on the isolated gas phase molecule.

References

(1). van der Veen, R. M.; Cannizzo, A.; van Mourik, F.; Vlček, A.; Chergui, M. Vibrational Relaxation and Intersystem Crossing of Binuclear Metal Complexes in Solution. Journal of the American Chemical Society 2011, 133 (2), 305–315. https://doi.org/10.1021/ja106769w.

(2). Mendes, R. A.; Germino, J. C.; Fazolo, B. R.; Thaines, E. H. N. S.; Ferraro, F.; Santana, A. M.; Ramos, R. J.; de Souza, G. L. C.; Freitas, R. G.; Vazquez, P. A. M.; Barboza, C. A. Electronic and Magnetic Properties of the [Ni(Salophen)]: An Experimental and DFT Study. Journal of Advanced Research 2018, 9, 27–33. https://doi.org/10.1016/j.jare.2017.10.004.

(3). (a) Liu, J.; Mei, S.; Chen, X.; Yao, C. Recent Advances of Near-Infrared (NIR) Emissive Metal Complexes Bridged by Ligands with N- and/or O-Donor Sites. Crystals 2021, 11 (2), 155. https://doi.org/10.3390/cryst11020155.

(b) Pamei, M.; Puzari, A. Luminescent Transition Metal–Organic Frameworks: An Emerging Sensor for Detecting Biologically Essential Metal Ions. Nano-Structures & Nano-Objects 2019, 19, 100364. https://doi.org/10.1016/j.nanoso.2019.100364.

(4). Belbacha, W.; Naamoune, F.; Bezzi, H.; Hellal, N.; Zerroual, L.; Abdelkarim, K.; Brahim, B.; Fernandez Garcia, M.; López, D. Elaboration of Carbon Paste Electrode Containing Pentadentate Nickel-(II) Schiff Base Complex: Application to Electrochemical Oxidation of Thiosulfate in Alkaline Medium. Arabian Journal of Chemistry 2020, 13 (7), 6072–6083. https://doi.org/10.1016/j.arabjc.2020.05.007.

(5). Song, P.; Fisher, A. C.; Wadhawan, J. D.; Cooper, J. J.; Ward, H. J.; Lawrence, N. S. A Mechanistic Study of the EC′ Mechanism – the Split Wave in Cyclic Voltammetry and Square Wave Voltammetry. RSC Advances 2016, 6 (74), 70237–70242. https://doi.org/10.1039/C6RA08723J.

(6). Leftheriotis, G.; Papaefthimiou, S.; Yianoulis, P. Dependence of the Estimated Diffusion Coefficient of LixWO3 Films on the Scan Rate of Cyclic Voltammetry Experiments. Solid State Ionics 2007, 178 (3–4), 259–263. https://doi.org/10.1016/j.ssi.2006.12.019.

(7). (a) Samanta, R.; Kanaujia, S.; Reddy, C. M. New Co-Crystal and Salt Form of Sulfathiazole with Carboxylic Acid and Amide. Journal of Chemical Sciences 2014, 126 (5), 1363–1367. https://doi.org/10.1007/s12039-014-0698-5.

(b) Shtukenberg, A. G.; Zhu, Q.; Carter, D. J.; Vogt, L.; Hoja, J.; Schneider, E.; Song, H.; Pokroy, B.; Polishchuk, I.; Tkatchenko, A.; Oganov, A. R.; Rohl, A. L.; Tuckerman, M. E.; Kahr, B. Powder Diffraction and Crystal Structure Prediction Identify Four New Coumarin Polymorphs. Chemical Science 2017, 8 (7), 4926–4940. https://doi.org/10.1039/C7SC00168A.

(8). Aitipamula, S.; Desiraju, G. R.; Jaskólski, M.; Nangia, A.; Thaimattam, R. Multiple Molecules in the Crystallographic Asymmetric Unit. Self Host–Guest and Doubly Interpenetrated Hydrogen Bond Networks in a Pair of Keto-Bisphenols. *CrystEngComm* **2003**, *5* (78), 447. https://doi.org/10.1039/b312085f.

(9). Goodwin, W. M. Structural Formulas and Explanation in Organic Chemistry. Foundations of Chemistry 2008, 10 (2), 117–127. https://doi.org/10.1007/s10698-007-9033-2.

(10). McKinnon, J. J.; Spackman, M. A.; Mitchell, A. S. Novel Tools for Visualizing and Exploring Intermolecular Interactions in Molecular Crystals. Acta Crystallographica Section B Structural Science 2004, 60 (6), 627–668. https://doi.org/10.1107/S0108768104020300.

(11). Mosmann, T. Rapid Colorimetric Assay for Cellular Growth and Survival: Application to Proliferation and Cytotoxicity Assays. *Journal of Immunological Methods* **1983**, *65* (1–2), 55–63. https://doi.org/10.1016/0022-1759(83)90303-4.

(12). Fayed, E. A.; Eldin, R. R. E.; Mehany, A. B. M.; Bayoumi, A. H.; Ammar, Y. A. Isatin-Schiff's Base and Chalcone Hybrids as Chemically Apoptotic Inducers and EGFR Inhibitors; Design, Synthesis, Anti-Proliferative Activities and in Silico Evaluation. *Journal of Molecular Structure* **2021**, *1234*, 130159. https://doi.org/10.1016/j.molstruc.2021.130159.

(13). Soonthornthum, T.; Arias-Pulido, H.; Joste, N.; Lomo, L.; Muller, C.; Rutledge, T.; Verschraegen, C. Epidermal Growth Factor Receptor as a Biomarker for Cervical Cancer. *Annals of Oncology* **2011**, *22* (10), 2166–2178. https://doi.org/10.1093/annonc/mdq723.

(14). Trott, O.; Olson, A. J. AutoDock Vina: Improving the Speed and Accuracy of Docking with a New Scoring Function, Efficient Optimization, and Multithreading. *Journal of Computational Chemistry* **2009**, *32*, NA-NA. https://doi.org/10.1002/jcc.21334.

(15). Kim, J.; Kwon, J.; Kim, M.; Do, J.; Lee, D.; Han, H. Low-Dielectric-Constant Polyimide Aerogel Composite Films with Low Water Uptake. *Polymer Journal* **2016**, *48* (7), 829–834. https://doi.org/10.1038/pj.2016.37.

CHAPTER VI

SPECTRAL CHARACTERIZATION, AND SINGLE CRYSTAL X-RAY DIFFRACTOMETRIC, COMPUTATIONAL AND BIOLOGICAL STUDIES OF MONO- AND DI-AZA DERIVATIVES OF A PAIR OF MALONALDEHYDES

A pair of malonaldehydes, viz., 2-phenylmalonaldehyde and 2-(4-methoxyphenyl)-malonaldehyde, each possessing two terminal aldehyde groups and potential candidates of tautomerism has been chosen to synthesize their corresponding mono- and di-azomethine derivatives of 3-fluoro-4-morpholinoaniline. The results and discussions of these four Schiff bases have been presented in this Chapter.

Single crystals could be generated only for (Z)-3-((3-fluoro-4-morpholinophenyl)amino)-2-phenylacrylaldehyde **(FMAPA),** with one of the carbonyl groups converted to azomethine, and 3-fluoro-N-((1E,2Z)-3-((3-fluoro-4-morpholinophenyl)amino)-2-(4-methoxyphenyl)allylidene)-4-morpholinobenzenaminium **(FFMMMC)**, with both the carbonyl groups converted to azomethines, whereas we could not obtain single crystals of 3-fluoro-N-((1Z,3E)-3-((3-fluoro-4-morpholinophenyl)imino)-2-phenylprop-1-en-1-yl)-4-morpholinobenzenaminium (**FFMPMC)** and (Z)-3-((3-fluoro-4-morpholinophenyl)amino)-2-(4-methoxyphenyl)acrylaldehyde (**FMAMA)**. The **FMAPA** crystallizes in a centrosymmetric monoclinic $P2_1/c$ space group but with four molecules in a one-unit cell, whereas **FFMMMC** crystallizes in a centrosymmetric triclinic P_{-1} space group with only two molecules in a one-unit cell.

This Chapter is also divided into two parts, **Part A** and **Part B**. Each of these two parts has been sub-divided into two sections, **Section 1** and **Section 2**.

Section 1 of **Part A** (**Section A1**) deals with the spectral studies of **FMAPA** and **FMAMA (Figure 6A.1)** and single crystal XRD studies besides molecular structural determination of **FMAPA**. **FMAMA,** while **Section 2** of this Part (**Section A2**) discusses the computational chemistry of **FMAPA** and **FMAMA** along with their protein docking studies. Similarly, **Section 1** of **Part B** (**Section B1**) and **Section 2** of **Part B** (**Section B2**) covers the corresponding bis-derivatives of dialdehyde, viz. **FFMPMC** and **FFMMMC (Figure 6B.1).**

PART A

SPECTRAL, SINGLE CRYSTAL X-RAY DIFFRACTOMETRIC AND COMPUTATIONAL CHEMISTRY STUDIES OF FMAPA AND FMAMA

SECTION-A1

6A.1 Physical and Analytical Characterization of FMAPA and FMAMA:

Table 6A.1 shows the physical and analytical characteristics of the **FMAPA** and **FMAMA**.

Table 6A.1: *Physical data[#] of* ***FMAPA*** and ***FMAMA***

Compound	Color	M.P (°C)	Molecular formula	Molecular weight	Elemental analysis*			
					%C	%H	%N	%O
FMAPA	Yellow	210-212	$C_{19}H_{19}FN_2O_2$	326.3	66.92 (67.05)	5.87 (5.95)	8.58 (8.72)	9.80 (9.87)
FMAMA	Orange	217-219	$C_{20}H_{21}FN_2O_3$	356.4	67.40 (67.51)	5.94 (6.14)	7.86 (7.93)	13.47 (13.58)

[#] data in parenthesis are calculated ones; [*] data limited to integral values

The mass spectra of the **FMAPA** and **FMAMA** are shown in **Figure 6A.2.** The molecular formulae of both **FMAPA** and **FMAMA,** which are 327.15 and 357.16, match with the M+1 molecular ion peak.

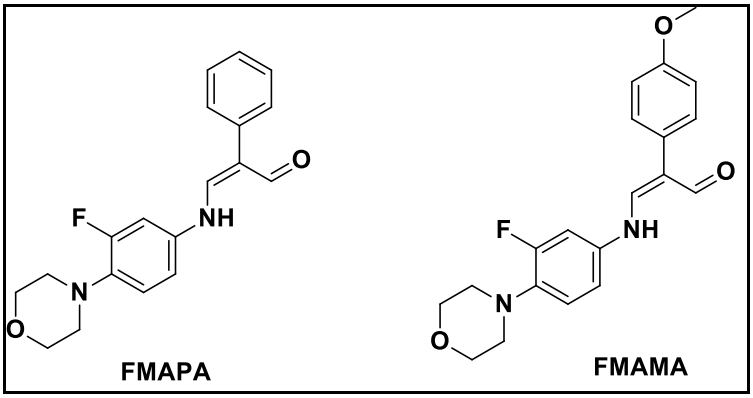

Figure 6A.1: *Structures of* ***FMAPA*** *and* ***FMAMA***

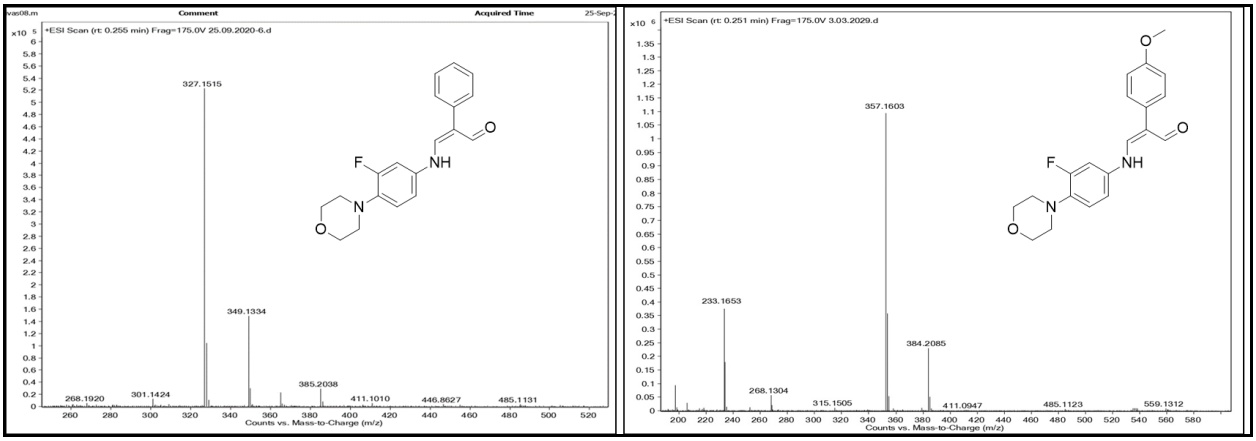

Figure 6A.2: *Mass Spectra of* ***FMAPA*** *and* ***FMAMA***

6A.2 IR Spectral Studies of FMAPA and FMAMA:

Table 6A.2: *IR data# of* ***FMAPA*** *and* ***FMAMA*** *(in cm^{-1})*

Compound	ν (N-H)	ν (=N–H)	ν (C–H)	ν (C=N)	ν (C=O)	ν (=C-H)	ν (C-O)
FMAPA	3435	3000-3060	2821-2980	1520	1617	1500	1118
FMAMA	3411	3000-3080	2860-2980	1605	1617	1515	1110

#, in KBr pellet

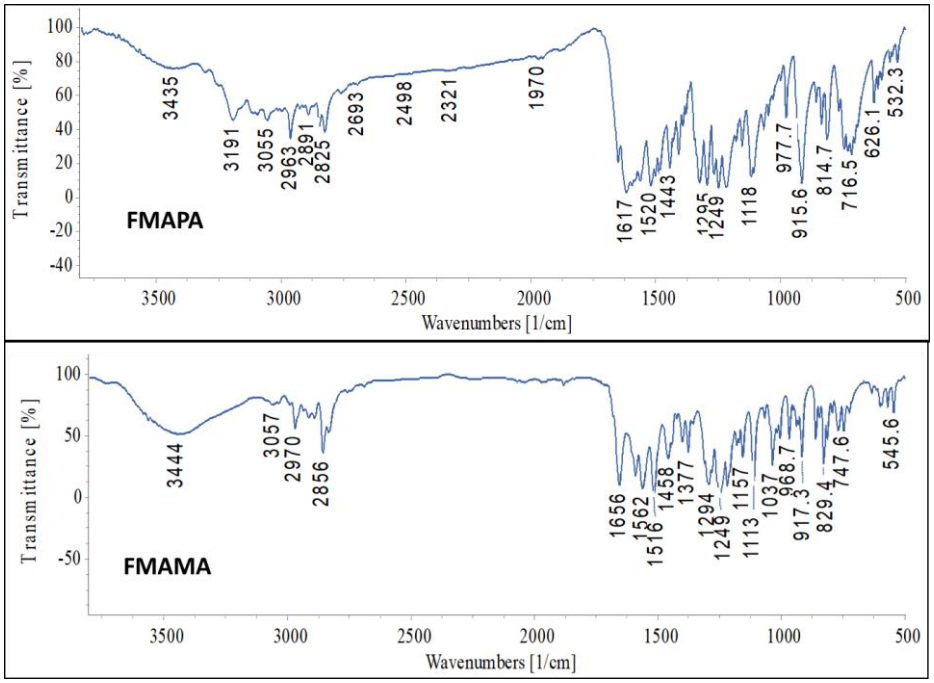

Figure 6A.3: *FT-IR Spectra of* ***FMAPA*** *and* ***FMAMA***

6A.3 NMR Spectral Analysis of FMAPA and FMAMA:

The overlay ^{1}H NMR spectra of **FMAPA** and **FMAMA** are shown in **Figure 6A.4.** In the **FMAPA** ^{1}H NMR spectrum, the imine proton (C<u>H</u>=N-) gives its ^{1}H-NMR chemical shift value at 10.81 ppm as a doublet. All the remaining aromatic hydrogens appear at chemical shift values in the range of δ 7.09-9.07 ppm. The hydrogen attached to the quinolinium nitrogen atom appears at δ 4.59 ppm. The two ^{1}H NMR triplets at 3.74 ppm (-C<u>H$_2$</u>-O-) and 3.01 ppm (C<u>H$_2$</u>-N-) are due to morpholine protons.

In the **FMAMA** ^{1}H-NMR spectrum, the (=C-NH-) proton gives its ^{1}H-NMR chemical shift value at 9.35 ppm as a doublet and the aledhydic proton gives as a singlet at a chemical shift value of 9.02 ppm. All of the remaining aromatic hydrogens appear as multiplets with chemical shift values ranging from 6.86 to 7.54 ppm, and the morpholine protons appear as multiplets with chemical shift values ranging from 2.51-3.83 ppm. Methoxy protons appeared at 3.85 ppm as singlets.

Figure 6A.5 shows the **FMAPA** and **FMAMA** ^{13}C-NMR spectra overlayed. In the **FMAPA** ^{13}C-NMR spectrum, the aldehyde carbon spectral line (C=O) appears at 190.88 ppm. The ring carbon connected to the fluorine gives its peak at 156 ppm with $^{1}J(^{19}\mathrm{F},^{13}\mathrm{C})$ = 246.12 Hz, remaining aromatic carbon atoms are found in the range of 105.20 -143.32 ppm while the morpholine aliphatic carbon atoms show peaks at 66.88 ppm (-<u>C</u>H$_2$-N-) and at 51.13, (-<u>C</u>H$_2$-O-).

In the **FMAMA** ^{13}C-NMR spectrum, the spin-decoupled ^{13}C-NMR spectral line of the imine C=N- carbon appears at 189.94 ppm. The peak of the ring carbon connected to fluorine is 147.49 ppm. The remaining aromatic carbon atoms are found in the range of 114.46-143.13 ppm, while the morpholine aliphatic carbon atoms show two peaks at a range of 46.96 (-<u>C</u>H$_2$-N-), 55.59 ppm (-<u>C</u>H$_2$-O-) and methoxy protons appear at 55.77 ppm.

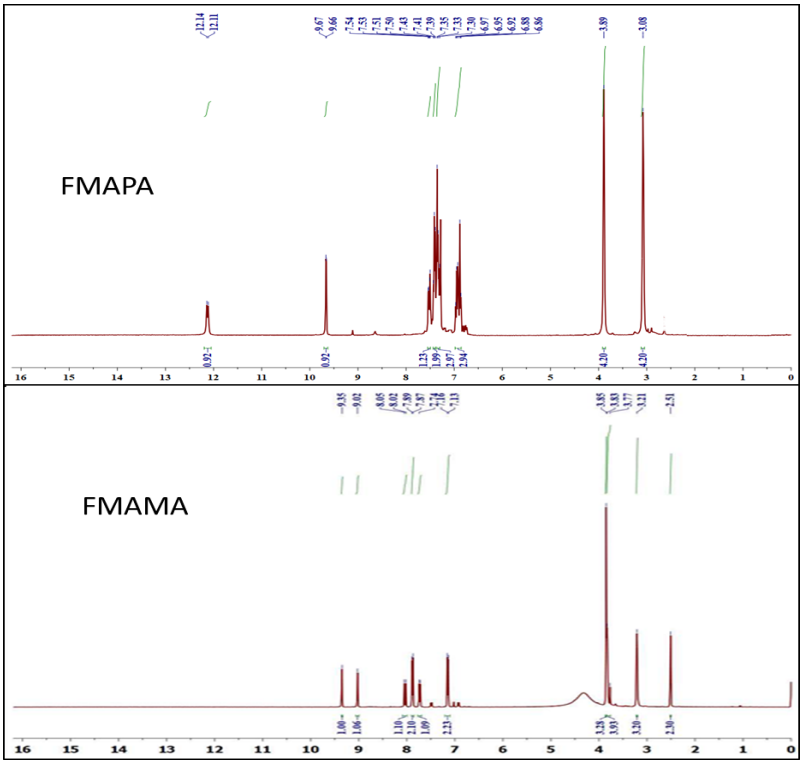

Figure 6A.4: *Overlay ^{1}H-NMR spectra of* ***FMAPA*** *and* ***FMAMA***

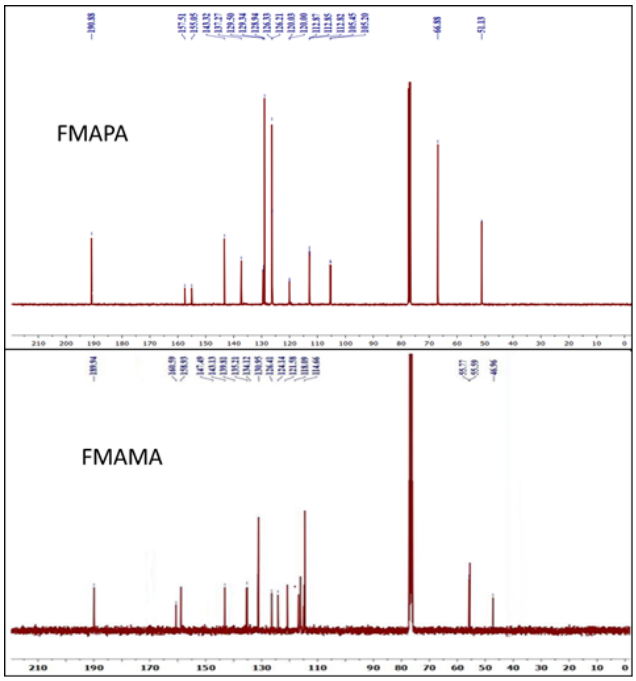

Figure 6A.5: *Overlay ^{13}C-NMR spectra of* ***FMAPA*** *and* ***FMAMA***

6A.4 Fluorescence Studies of FMAPA and FMAMA:

The luminisence spectra of **FMAPA** and **FMAMA** in DMSO are shown in **Figure 6A.6.** The broad emission peaks are observed at 525 nm. The broad emission peak is observed at 525 nm, owing to the emission of green light, which corresponds to the flow of electrons from aldehyde to benzene rings[1,2]. The band gap energy was calculated to be about 2.37 eV. The close proximity of the λ_{max} at ~ 455 nm of absorption (excitation) and fluorescence (emission) in the visible region indicates negligible inter-system crossing or molecular vibrational relaxation mechanism.

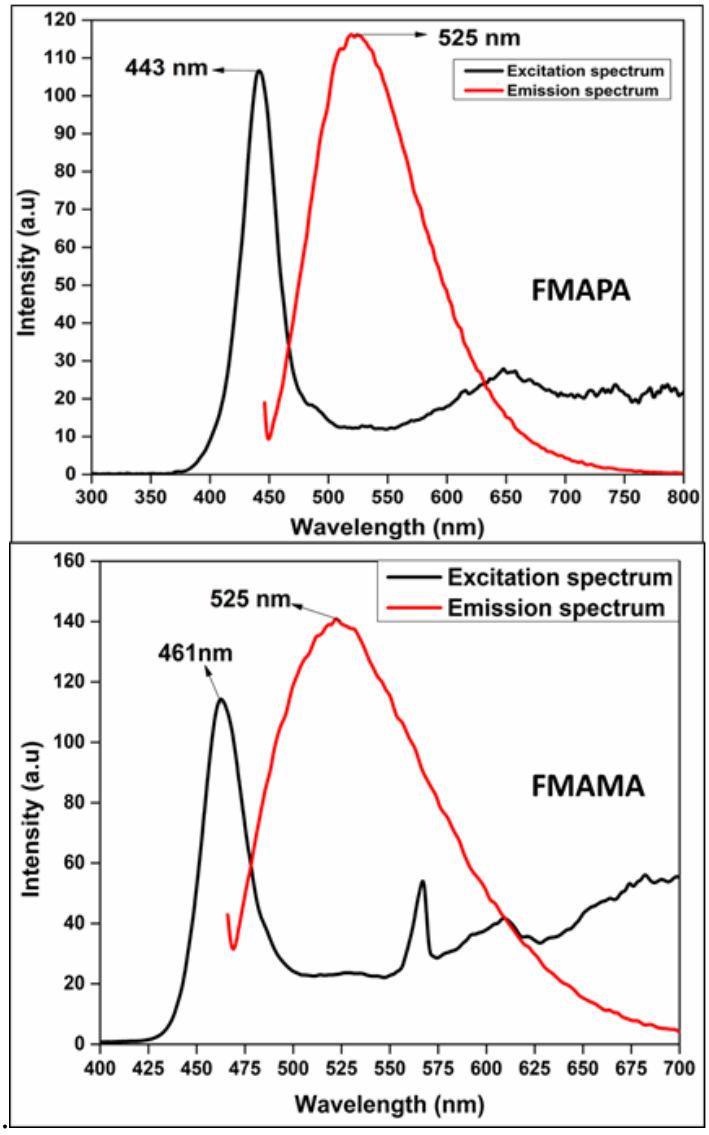

Figure 6A.6: *The absorptive (black) and emission (red) spectra of* ***FMAPA*** *and* ***FMAMA***

6A.5 Crystal Structure Analysis of FMAPA:

The compound **FMAPA** crystallizes in a centrosymmetric monoclinic $P2_1/c$ space group[3] with four molecules in a one-unit cell (**Figure 6A.7**) and relevant XRD data is shown in **Table 6A.2**. The reflection angle vs intensity graph is in **Figure 6A.8**. **Figure 6A.9** shows intermolecular hydrogen bonding present in the crystal. In **Figure 6A.10,** the unit cell is shown in three different dispositions seen along each of the three crystallographic axes.

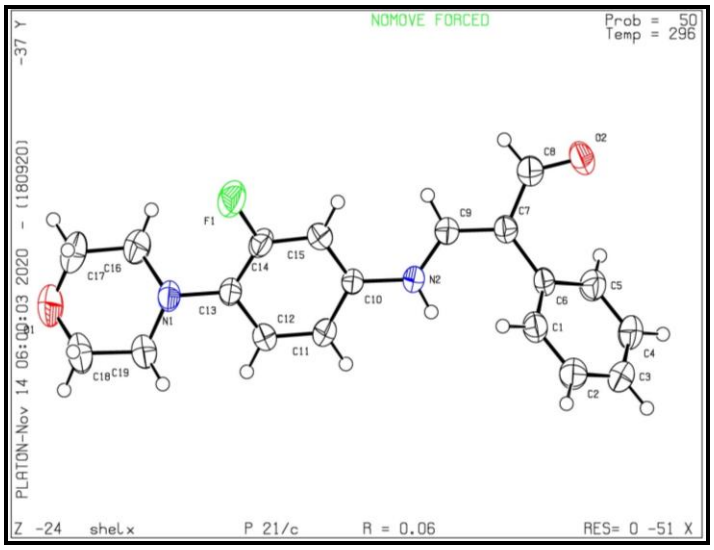

Figure 6A.7: *XRD- Platon diagram of* ***FMAPA*** *with atom-numbering*

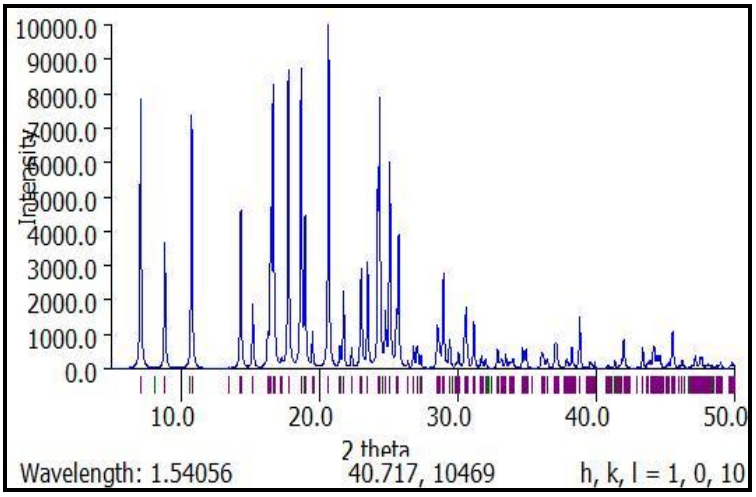

Figure 6A.8: *X-Ray diffraction intensity as a function of angle (^{o}) of reflection*

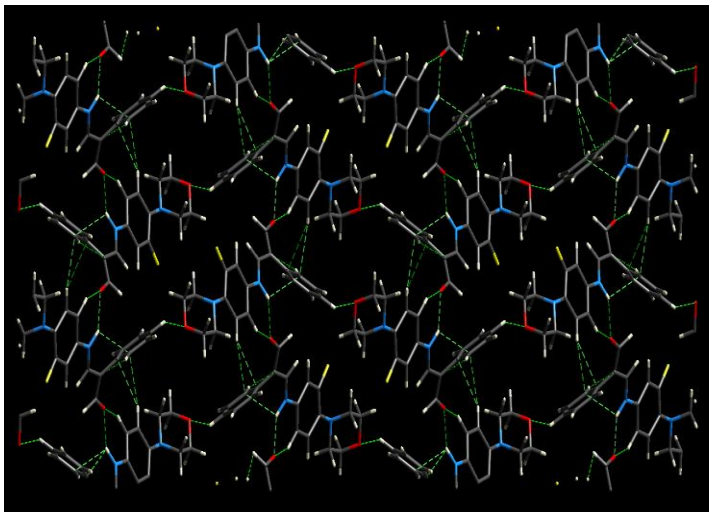

Figure 6A.9: *Crystal packing diagram of* ***FMAPA*** *showing the two dimesitional layer structure with O-H…N intramolecular hydrogen bonding*

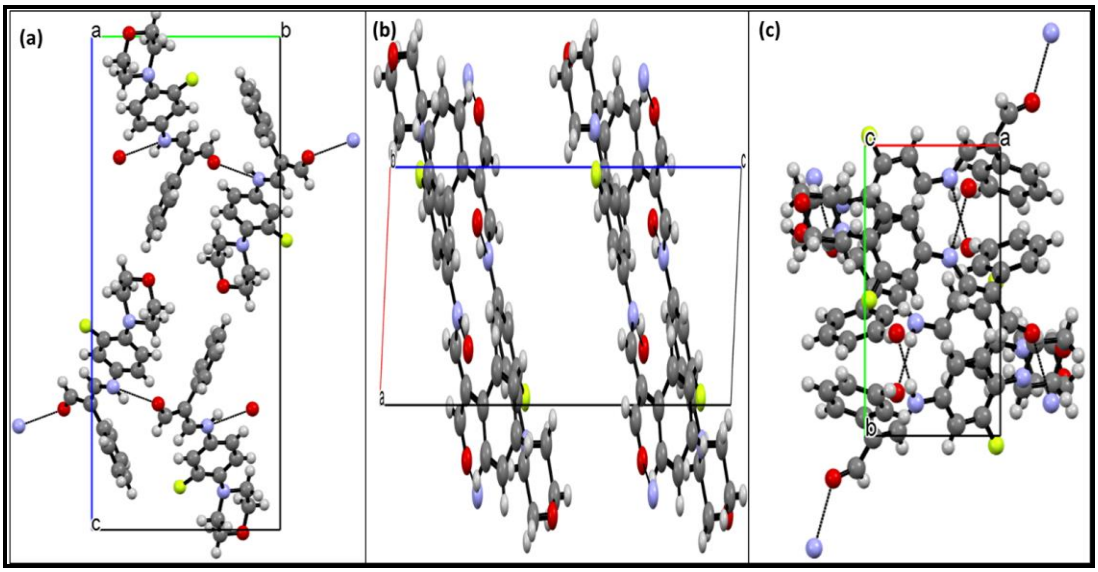

Figure 6A.10: *Unit cell of* ***FMAPA*** *seen along crystallographic* ***(a)*** *a-axis* ***(b)*** *b-axis* ***(c)*** *c-axis*

Table 6A.3: *X-ray crystallographic data for* ***FMAPA***

CCDC	2181229
Empirical formula	$C_{19}H_{19}N_2O_2F$
Formula weight	326.36
Color/shape	Greenish yellow/needle
Temperature, K	293
Crystal system	P21/c
Space group	Monoclinic
Unit cell dimensions, Å	a = 6.2176 (14); b = 10.8756 (4); c = 25.0144 (7) $\alpha = \gamma = 90$; $\beta = 96.990$ (9)
Z	4
Density, Mg/m^3	1.291
Absorption coefficient, mm^{-1}	0.092
Reflections collected/unique	4031/ 1994
θ range for data collections	1.640 – 28.222°
F (000)	688
Limiting Indices	$-7 \leq h \leq 8$; $-12 \leq k \leq 14$; $-33 \leq l \leq 33$
Goodness-of-fit on F^2	0.985
Final R indices [$I > 2\sigma$ (1)]	$R_1 = 0.0643$, $wR_2 = 0.1525$
R indices (all data)	$R_1 = 0.1371$, $wR_2 = 0.1986$
Largest diff. peak and hole ($eÅ^{-3}$)	0.322 and -0.325

SECTION-A2

6A.6 Correlation of the X-Ray Crystallographic Data with the Molecular Modelled Data of FMAPA:

In order to understand the quantum mechanical aspects and structural parameters of the molecule **FMAPA** in its free form (gaseous state), we have run computational studies on it under a few modeling platforms, viz., MM2 (ChemSoft), AM1 (Austin Model-1) and DFT (B3LYP/6-31G*). The Austin Model-1 (AM1) produces energy-minimized molecules using a force field and a self-consistent field (SCF) approach[4], whereas the MM2[5] uses a semi-empirical approach. The Becke-3-Parameter-Lee–Yang–Parr (B3LYP) hybrid functional (DFT/B3LYP/6-31G*)[6] operates on the nature and extent of inter-electronic interactions rather than simple electronic wave functions. Here, we present molecular structural data of **FMAPA** obtained from these competing and progressive platforms in comparison with the experimental single crystal XRD data to correlate the geometry of **FMAPA** in free and solid state forms. This exercise would also serve as an example of the reliability and usability of the above-mentioned three computational methods.

The AM1, MM2, and DFT/B3LYP platforms were used independently to obtain quantum mechanical molecular energy data for **FMAPA** such as ionization potential (I), electron affinity (A), chemical potential (μ), chemical hardness (η), global softness (S), and electronegativity (χ), which are included in **Table 6A.4.** The geometrical parameters are incorporated in **Table 6A.5** (bond lengths), **Table 6A.6** (bond angles) and **Table 6A.7** (dihedral angles or torsional angles) along with those obtained from the single crystal XRD measurements. The experimental XRD data and the computationally evaluated values are in reasonably good agreement. The larger deviations, wherever observed, would have to be attributed to the fact that XRD studies are for a multi-molecular solid state material with molecular geometric parameters affected by possible intermolecular and inter-ionic interactions. The conformational labels, abbreviated as **s = syn, a = anti**, **p = peri-planar** (0 ± 30^0 and 180 ± 30^0) and all other angles **c = clinal,** are designated as per Klyne-Prelog terms. Some minor changes are observed in the bond lengths also. The H-C(sp^2) of aromatic rings is found to be higher by about 0.15-0.35 as determined by DFT/B3LYP and MM2, whereas AM1 produced results that were very close to the experimental data. The σF-C(sp^2) is shown to be lower by 0.017Å (AM1), 0.018Å (MM2) and 0.011Å (DFT/B3LYP) from the XRD data. The trends of the remaining and pertinent bond lengths follow a similar pattern. A keen look

at **Table 6A.5** leads us to conclude that the empirical bond length data has negligibly fewer deviations from the ones theoretically computed by B3LYP than those by MM2 and AM1 platforms, as expected. Other structural data, like bond angles, dihedral angles, etc., showed the same kinds of correlations.

Important selective bond angles at various parts of the molecule **FMAPA** are presented in **Table 6A.6**. The bond angles at C-sp^2 obtained by the three computational platforms are observed to vary from ~ -10^o to ~ $+10^o$ from the XRD counterparts. But the bond angles at C-sp^3 are found to differ by a higher range due to the 3-dimensional and all-single-bonded torsional and spanning nature. However, the bond angle at N-sp^3 is found to differ to a greater extent than at the C-sp^2 and C-sp^3 due to nitrogen's higher capability of engaging in interatomic interaction than organic carbon atoms. Inspection of **Table 6A.5** also reveals higher deviations for bond angle at O-sp^3 than that at C-sp^3 for the computational data from the bond angle at O-sp^3 evaluated from the XRD measurements.

Various dihedral angles are presented in **Table 6A.6**. These values engaged with the atoms of the aromatic rings infer the near planarity of the whole molecule beyond the morpholine ring, as seen for both computational and experimental data. Both XRD and computations show benzene and morpholine rings near coplanar despite Baeyer's strain. Many of the dihedral angles obtained from XRD are in reasonable agreement with those computed.

The dihedral angle is changed from +*ap* of O_1-C_{18}-C_{19}-C_{19A} and O_1-C_{18}-C_{19}-C_{19A} to –*sc* whereas –*ap* of C_{16}-N_1-C_{19}-H_{19A} and H_{17B}-C_{17}-O_1-C_{18} is changed to +*sc* conformation under AM1, MM2 and B3LYP methods. It is also observed that conformation +*sc* of C_{16}-N_1-C_{19}-H_{19B} to –*ap* conformation in all methods (AM1, MM2 and B3LYP), while the dihedral angles of N_1-C_{13}-C_{12}-C_{11} +*ap* to –*ap* conformation in the case of methods (B3LYP, MM2 and AM1). The conformation -*ap* of H_{17B}-C_{17}-C_{16}-N_1 is found to become +*sc* (B3LYP and MM2) and -*sc* of H_{16A}-C_{16}-N_1-$C_{19}$to +*ap* (B3LYP and MM2) and +*sc* (AM1). The +*ap* of C_{13}-N_1-C_{19}-C_{18} alters to +*ac* (B3LYP), +*sc* (AM1) and -*ap* (MM2) conformations.

Table 6A.4: *Important molecular energy data evaluated by AM1, B3LYP and MM2 calculations on the cation of* ***FMAPA***

Parameter	**AM1**	**B3LYP**	**MM2**
E_{HOMO} (eV)	-0.3045	-0.1851	-7.469
E_{LUMO} (eV)	-0.0230	-0.0550	-1.803
I (eV) Ionisation Potential	0.3045	0.1851	7.469
A (eV) Electron affinity	0.0230	0.0550	1.803
η (eV) Chemical hardness	0.1407	0.0650	2.833
μ (eV) Chemical potential	0.1637	0.1200	4.636
χ (eV) Electro negativity	-0.1637	-0.1200	-4.636
S (eV^{-1}) Global softness	3.553	7.6923	0.1765

There is a great degree of consistency between the experimental and simulated data. Global minimized structures of **FMAPA** ligand is depicted at **Figure 6A.11.** The numbering adaptation is shown in **Figure 6A.11** for subsequent reference in the discussion**.** To visualize the molecular disposition in space and to provide a 3D visual of it, the anaglyph picture and stereographic representation of the **FMAPA** are given in **Figure 6A.12** and **Figure 6A.13**, respectively.

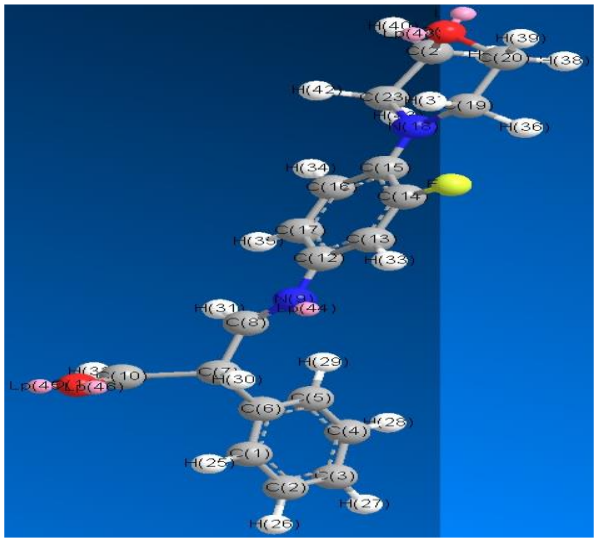

Figure 6A.11: *MM2-energy-minimized structure of* ***FMAPA*** *(keto form) with numbered atoms*

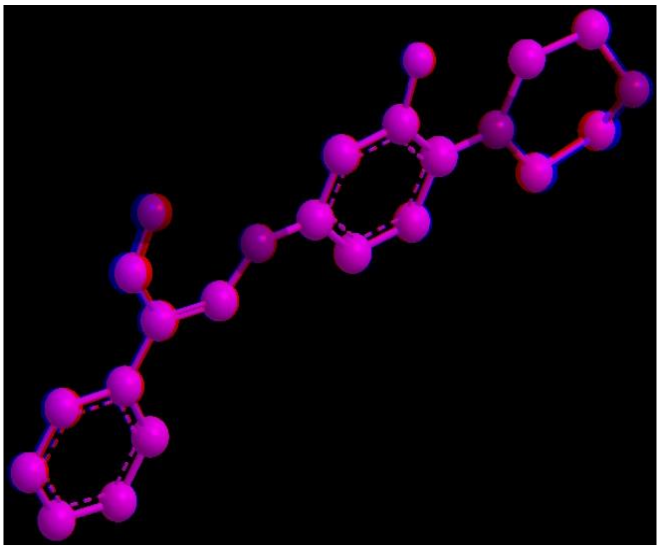

Figure 6A.12: *Anaglyph structure of* ***FMAPA*** *(enamine form) obtained from ChemDrawPro*

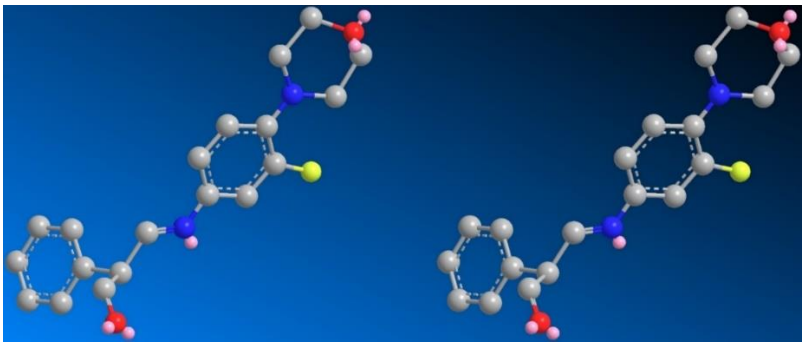

Figure 6A.13*: Anaglyph structure of* ***FMAPA*** *(keto form) obtained from ChemDrawPro*

FMAPA has a phenyl and benzyl bulky groups connected to the imine bond whereat the Schiff base extension is also around. With the view to understand the best relative disposition of the bulky groups in space with the global minimum of the Eigen value, we have performed conformational analysis by torsioning over the selected single bonds in both dihedral driving and double dihedral driving computational methods. Conformational analysis plots of **FMAPA** are shown in **Figure 6A.14** through **Figure 6A.28**.

The HOMO and LUMO molecular orbitals and their corresponding energies of **FMAPA** are shown in **Figure 6A.29**.

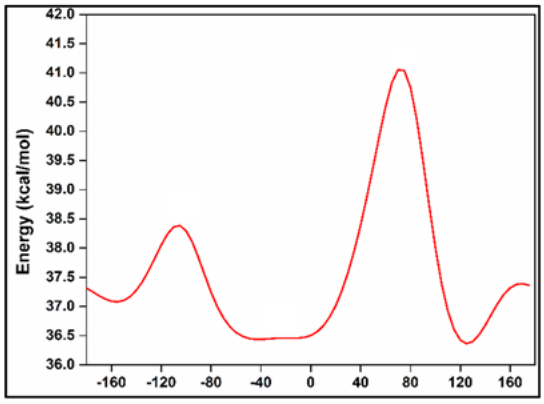

Figure 6A.14: *Conformational analysis over C6-C7*

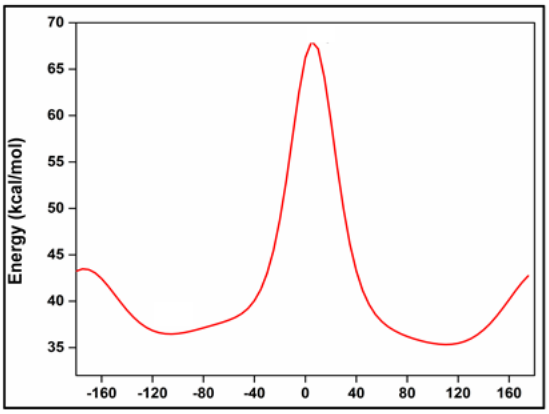

Figure 6A.15: *Conformational analysis over C7-C8*

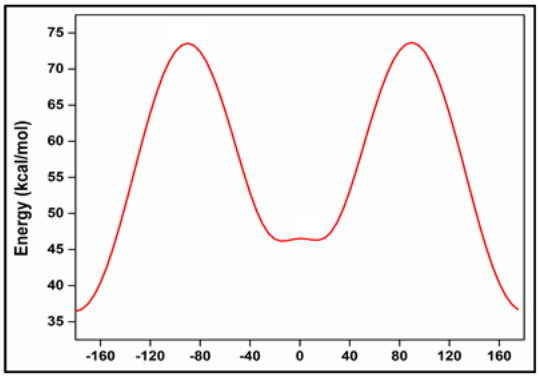

Figure 6A.16: *Conformational analysis over N9-C12*

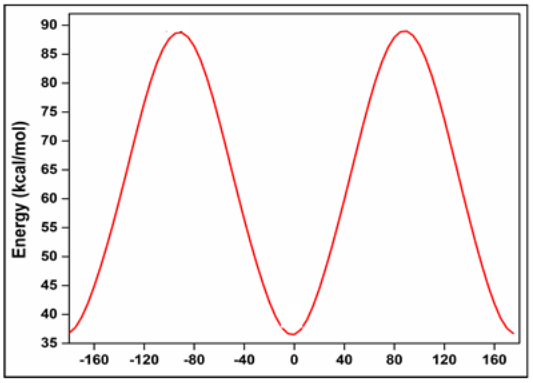

Figure 6A.17: *Conformational analysis over C15-N18*

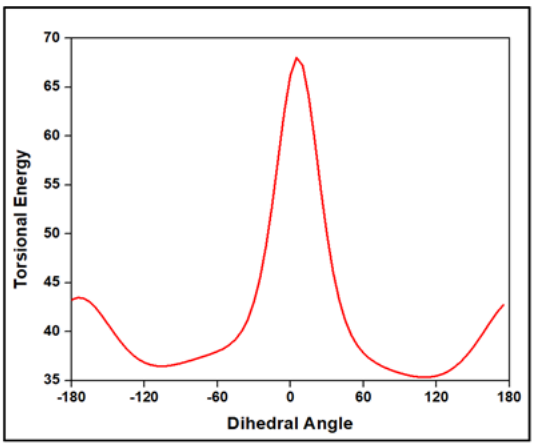

Figure 6A.18: *Conformational analysis over C6-C7-C8-N9*

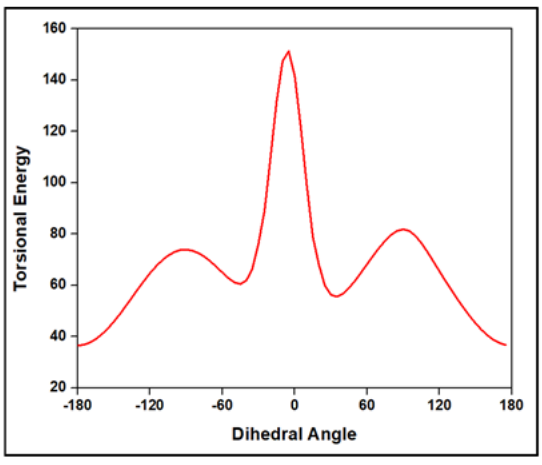

Figure 6A.19: *Conformational analysis over C7-C8-N9-C12*

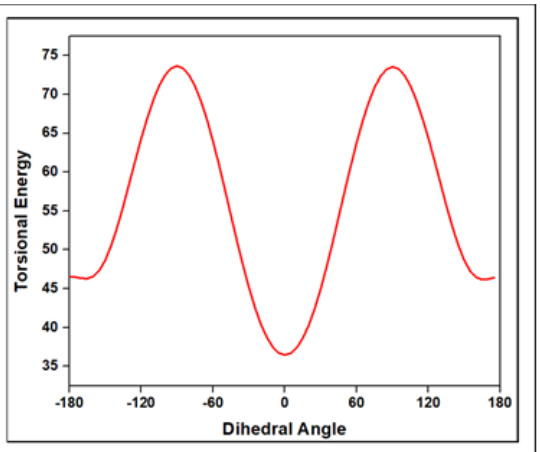

Figure 6A.20: *Conformational analysis over C8-N9-C12-C17*

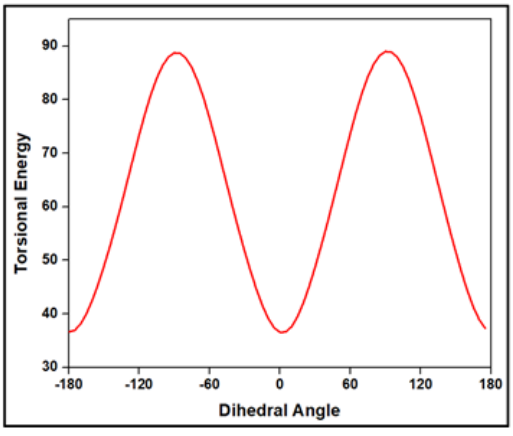

Figure 6A.21: *Conformational analysis over C5-C6-C7-C8*

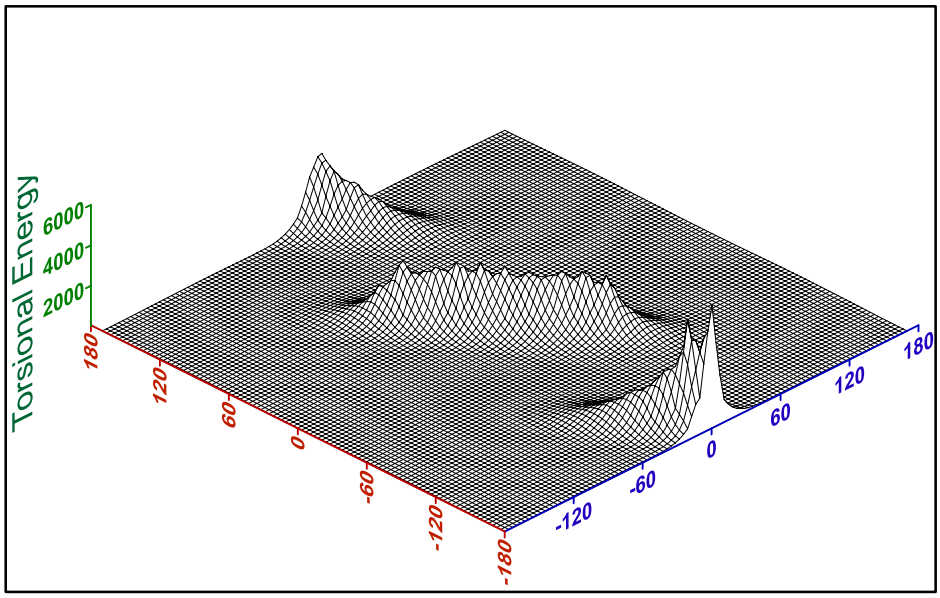

Figure 6A.22: *Double dihedral torsional energy Surfer plot of* ***FMAPA*** *(enamine form) over C19-C20 (on axis shown in red) and C20-N21 (on axis shown in blue) bonds (Refer* ***Figure 6A.11*** *for numbering of the atoms)*

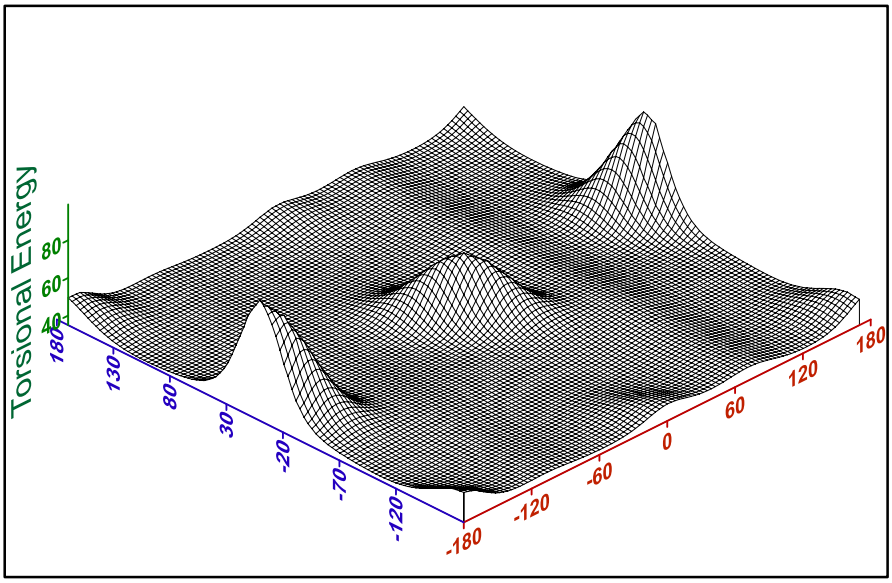

Figure 6A.23: *Double dihedral torsional energy Surfer plot of* ***FMAPA*** *(keto form) over C6-C7 (on axis shown in blue) and C7-C8 (on axis shown in red) bonds (Refer* ***Figure 6A.11*** *for numbering of the atoms)*

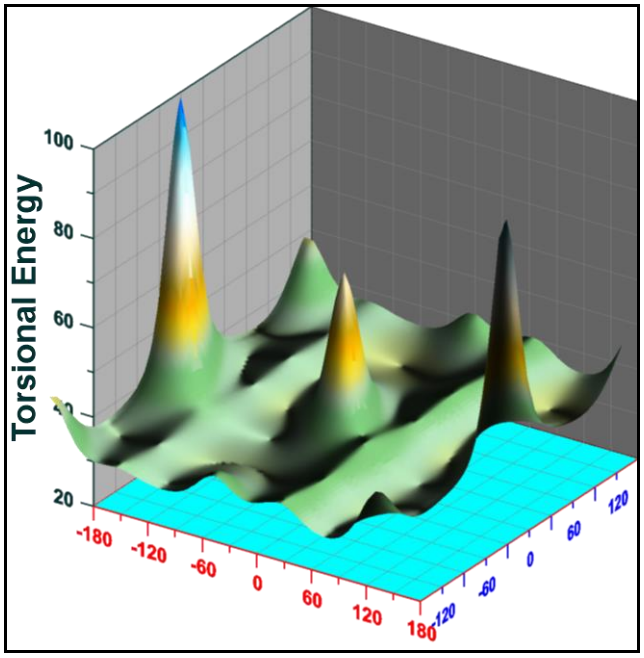

Figure 6A.24: *Double dihedral torsional energy Grapher plot of* ***FMAPA*** *(keto form) over C6-C7 (on axis shown in blue) and C7-C8 (on axis shown in red) bonds (Refer* ***Figure 6A.11*** *for numbering of the atoms)*

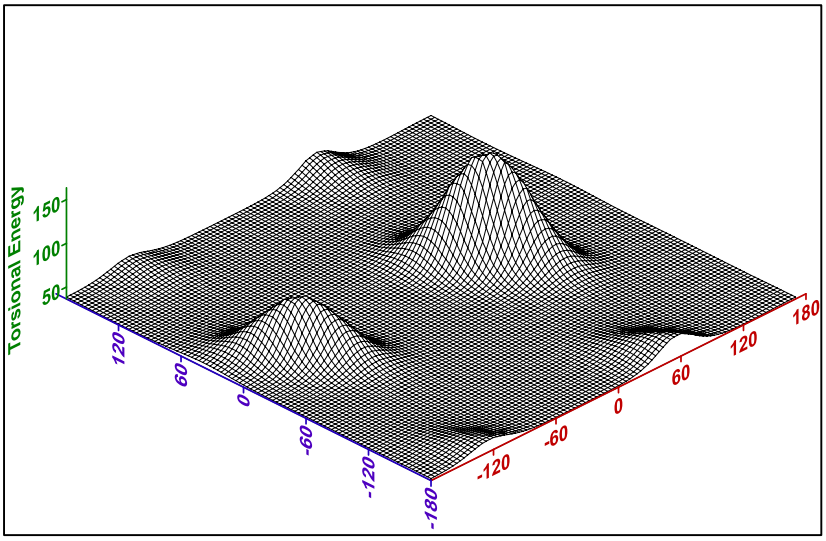

Figure 6A.25: *Double dihedral torsional energy Surfer plot of* ***FMAPA*** *(keto form) over C6-C7 (on axis shown in blue) and C7-C10 (on axis shown in red) bonds (Refer* ***Figure 6A.11*** *for numbering of the atoms)*

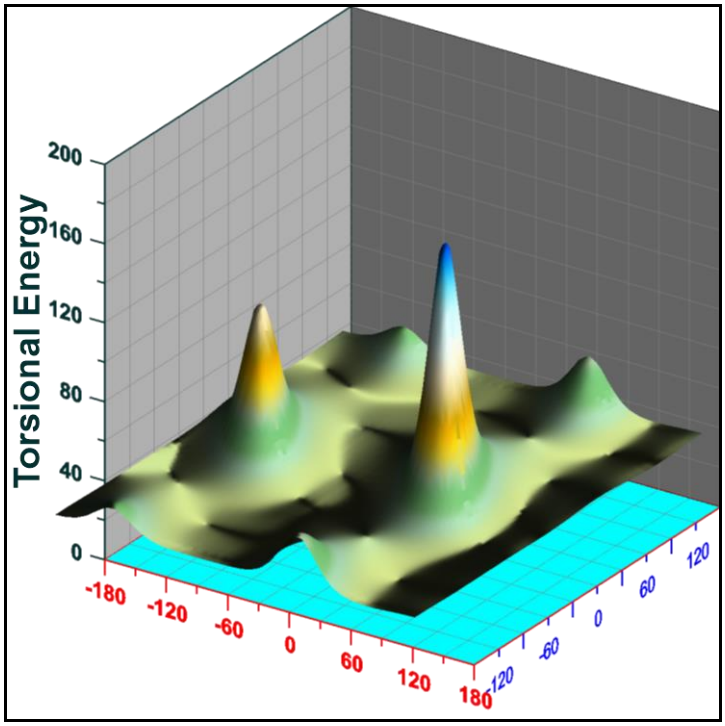

Figure 6A.26: *Double dihedral torsional energy Grapher plot of* ***FMAPA*** *(keto form) over C6-C7 (on axis shown in blue) and C7-C10 (on axis shown in red) bonds (Refer* ***Figure 6A.11*** *for numbering of the atoms)*

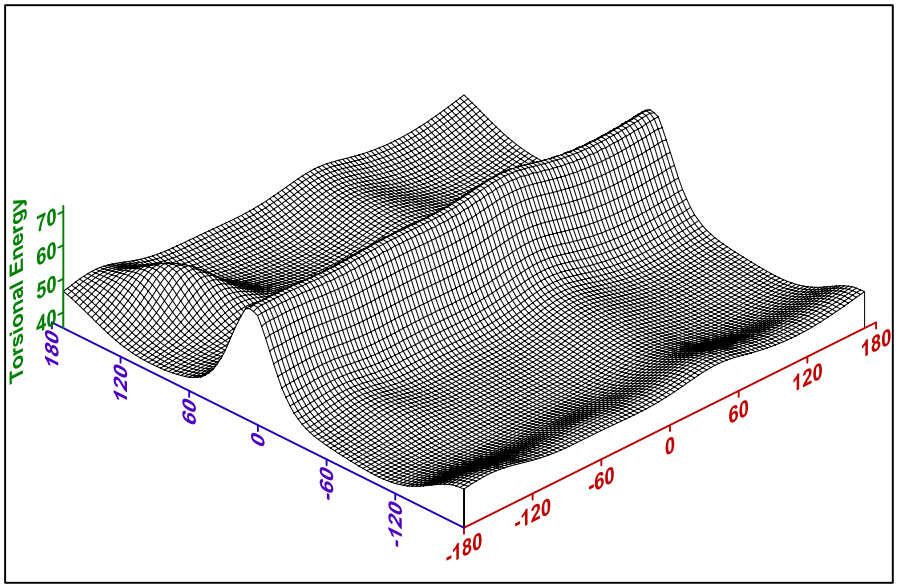

Figure 6A.27: *Double dihedral torsional energy Surfer plot of* ***FMAPA*** *(keto form) over C8-C7 (on axis shown in blue) and C7-C10 (on axis shown in red) bonds (Refer* ***Figure 6A.11*** *for numbering of the atoms)*

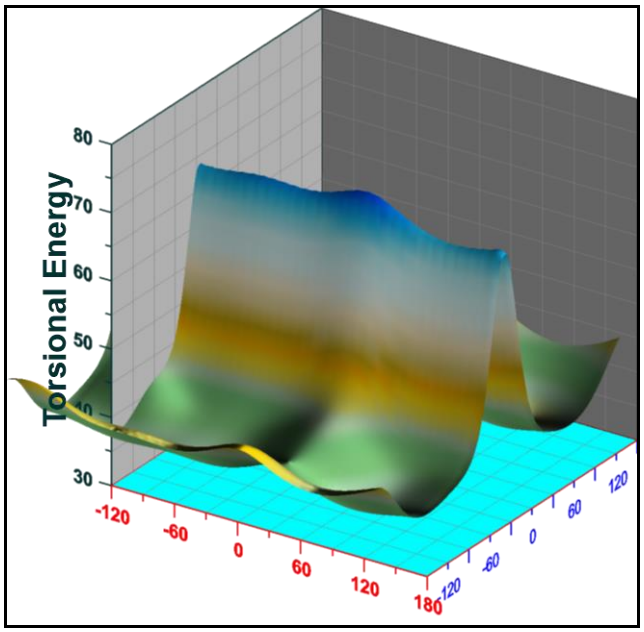

Figure 6A.28: *Double dihedral torsional energy Grapher plot of* ***FMAPA*** *(keto form) over C8-C7 (on axis shown in blue) and C7-C10 (on axis shown in red) bonds (Refer* ***Figure 6A.11*** *for numbering of the atoms))*

Table 6A.5: *Comparative list of selected bond lengths (Å) of* ***FMAPA***

Bond	Bond type	Bond lengths (Å)				Fractional variation (Δ/XRD)		
		XRD	**AM1**	**MM2**	**B3LYP**	**AM1**	**MM2**	**B3LYP**
$H_{17A} – C_{17}$	$H – Csp^3$	0.970	1.070	1.114	1.094	0.103	0.148	0.128
$H_{16A} – C_{16}$	$H – Csp^2$	0.969	1.070	1.113	1.098	0.104	0.149	0.133
$C_{17} – O_1$	$H – Osp^3$	1.404	1.433	1.403	1.424	0.021	-0	0.014
$C_{17} – C_{16}$	$Csp^3 – Csp^3$	1.492	1.507	1.528	1.530	0.01	0.024	0.025
$C_{17} – H_{17B}$	$Csp^3 – H$	0.971	1.070	1.115	1.103	0.102	0.148	0.136
$O_1 – C_{18}$	$Osp^3 – Csp^3$	1.412	1.463	1.403	1.422	0.036	-0.01	0.007
$C_{16} – H_{16B}$	$Csp^3 – H$	0.969	1.070	1.117	1.089	0.104	0.153	0.124
$C_{16} – N_1$	$Csp^3 – Nsp^3$	1.465	1.434	1.457	1.471	-0.02	-0.01	0.004
$H_{19A} – C_{19}$	$H – Csp^3$	0.971	1.071	1.117	1.098	0.103	0.15	0.131
$H_{18A} – C_{18}$	$H – Csp^3$	0.969	1.070	1.114	1.094	0.104	0.15	0.129
$C_{18} – C_{19}$	$Csp^3 – Csp^3$	1.503	1.566	1.528	1.533	0.042	0.017	0.02
$C_{18} – H_{18B}$	$Csp^3 – H$	0.970	1.069	1.115	1.103	0.102	0.149	0.137
$N_1 – C_{19}$	$Nsp^3 – Csp^3$	1.452	1.472	1.455	1.462	0.014	0.002	0.007
$N_1 – C_{13}$	$Nsp^3 – Csp^3$	1.420	1.469	1.461	1.402	0.035	0.029	-0.01
$C_{19} – H_{19B}$	$Csp^3 – H$	0.970	1.069	1.117	1.093	0.102	0.152	0.127
$F – C_{14}$	$F – Csp^2$	1.366	1.349	1.348	1.355	-0.01	-0.01	-0.01
$C_{13} – C_{14}$	$Csp^2 – Csp^2$	1.383	1.353	1.516	1.411	-0.02	0.096	0.02
$C_{13} – C_{12}$	$Csp^2 – Csp^2$	1.390	1.398	1.533	1.407	0.006	0.103	0.012
$C_{14} – C_{15}$	$Csp^2 – Csp^2$	1.367	1.356	1.504	1.380	-0.01	0.1	0.01
$H_{15} – C_{15}$	$H – Csp^2$	0.930	1.070	1.114	1.085	0.151	0.198	0.167
$C_{15} – C_{10}$	$Csp^2 – Csp^2$	1.385	1.358	1.526	1.403	-0.02	0.102	0.013

C_{12}– H_{12}	Csp^2 – H	0.930	1.069	1.115	1.083	0.149	0.199	0.165
C_{12} – C_{11}	Csp^2 – Csp^2	1.385	1.353	1.525	1.394	-0.02	0.101	0.006
C_{11} – C_{10}	Csp^2 – Csp^2	1.377	1.357	1.525	1.394	-0.01	0.107	0.012
C_{11} – H_{11}	Csp^2 – H	0.930	1.069	1.115	1.084	0.149	0.199	0.166
C_{10} – N_2	Csp^2 – N	1.415	1.469	1.461	1.403	0.038	0.033	-0.01
N_2 – H_{2N}	Nsp^2 – H	0.861	1.001	1.050	1.026	0.163	0.22	0.192
N_2 – C_9	Nsp^2 – Csp^2	1.342	1.337	1.459	1.347	-0	0.087	0.004
O_2 – C_8	Osp^2 – Csp^2	1.226	1.258	1.395	1.240	0.026	0.138	0.011
C_9 – H_9	Csp^2 – H	0.931	1.070	1.114	1.086	0.149	0.197	0.166
C_9 – C_7	Csp^2– Csp^2	1.360	1.539	1.530	1.384	0.132	0.125	0.018
C_8 – C_7	Csp^2– Csp^2	1.433	1.539	1.522	1.448	0.074	0.062	0.01
C_8 – H_8	Csp^2 – H	0.930	1.070	1.112	1.106	0.151	0.196	0.189
C_7– C_6	Csp^2 – Csp^2	1.481	1.539	1.529	1.482	0.039	0.032	7E-04
H_1 – C_1	H – Csp^2	0.930	1.070	1.114	1.087	0.151	0.198	0.169
C_6 – C_1	Csp^2– Csp^2	1.388	1.534	1.526	1.406	0.105	0.099	0.013
C_6 – C_5	Csp^2– Csp^2	1.382	1.361	1.525	1.407	-0.02	0.103	0.018
C_1 – C_2	Csp^2– Csp^2	1.378	1.343	1.526	1.393	-0.03	0.107	0.011
H_5 – C_5	H – Csp^2	0.929	1.070	1.114	1.086	0.152	0.199	0.169
C_5 – C_4	Csp^2– Csp^2	1.382	1.366	1.526	1.394	-0.01	0.104	0.009
C_2 – H_2	Csp^2 – H	0.930	1.070	1.115	1.087	0.151	0.199	0.169
C_2 – C_3	Csp^2– Csp^2	1.369	1.534	1.526	1.396	0.121	0.115	0.02
C_4 – C_3	Csp^2 – Csp^2	1.369	1.361	1.526	1.395	-0.01	0.115	0.019
C_4 – H_4	Csp^2 – H	0.930	1.070	1.115	1.086	0.151	0.199	0.168
C_3 – H_3	Csp^2 – H	0.930	1.069	1.115	1.086	0.149	0.199	0.168

Table 6A.6: *Comparative list of selected bond angles (°) of* ***FMAPA***

Atomic string	Central atom	XRD	B3LYP	AM1	MM2	Variation from XRD data (%)		
						B3LYP	AM1	MM2
H_1-C_1-C_6	Csp^2	119.5	119.3	120.8	109.5	-0.168	1.076	-9.132
H_1-C_1-C_2	Csp^2	119.4	119.5	120.8	109.5	0.084	1.159	-9.041
C_2-C_1-C_6	Csp^2	121.2	121.1	118.2	110.9	-0.083	-2.538	-9.288
C_1-C_2-H_2	Csp^2	119.7	119.6	120.8	109.6	-0.084	0.911	-9.215
C_1-C_2-C_3	Csp^2	120.6	120.2	118.2	110.6	-0.333	-2.030	-9.042
H_2-C_2-C_3	Csp^2	119.7	120.1	120.8	109.7	0.333	0.911	-9.116
C_2-C_3-C_4	Csp^2	119.0	119.3	120.1	110.4	0.251	0.916	-7.790
C_2-C_3-H_3	Csp^2	120.5	120.3	119.9	109.6	-0.166	-0.500	-9.945
H_3-C_3-C_4	Csp^2	120.5	120.3	119.9	109.6	-0.166	-0.500	-9.945
C_3-C_4-C_5	Csp^2	120.9	120.3	121.6	110.6	-0.499	0.576	-9.313
H_4-C_4-C_5	Csp^2	119.6	119.5	119.1	109.6	-0.084	-0.420	-9.124
C_3-C_4-H_4	Csp^2	119.5	120.0	119.1	109.7	0.417	-0.336	-8.933
H_5-C_5-C_6	Csp^2	119.6	119.5	119.1	109.4	-0.084	-0.420	-9.324
C_4-C_5-C_6	Csp^2	120.8	121.0	121.6	110.9	0.165	0.658	-8.927
C_4-C_5-H_5	Csp^2	119.6	119.4	119.2	109.7	-0.168	-0.336	-9.025
C_1-C_6-C_7	Csp^2	120.4	121.3	120.0	112.7	0.742	-0.333	-6.832
C_5-C_6-C_7	Csp^2	121.8	120.9	119.8	111.0	-0.744	-1.669	-9.730
C_1-C_6-C_5	Csp^2	117.6	117.8	120.1	111.7	0.170	2.082	-5.282
C_8-C_7-C_9	Csp^2	114.8	119.7	119.9	111.3	4.094	4.254	-3.145
C_6-C_7-C_9	Csp^2	125.0	120.3	120.0	109.8	-3.907	-4.167	-13.843
C_6-C_7-C_8	Csp^2	120.1	119.9	119.9	112.3	-0.167	-0.167	-6.946
C_7-C_8-O_2	Csp^2	126.8	125.4	119.9	109.6	-1.116	-5.755	-15.693

H_8-C_8-O_2	Csp^2	116.6	118.8	120.0	106.3	1.852	2.833	-9.690
C_7-C_8-H_8	Csp^2	116.6	115.6	119.9	110.8	-0.865	2.752	-5.235
H_9-C_9-N_2	Csp^2	116.8	116.2	120.0	110.4	-0.516	2.667	-5.797
C_7-C_9-N_2	Csp^2	126.4	124.2	119.9	110.8	-1.771	-5.421	-14.079
C_7-C_9-H_9	Csp^2	116.8	119.5	120.0	109.0	2.259	2.667	-7.156
C_{11}-C_{10}-C_{15}	Csp^2	118.4	118.2	120.4	108.5	-0.169	1.661	-9.124
C_{15}-C_{10}-N_2	Csp^2	123.3	118.0	119.7	112.3	-4.492	-3.008	-9.795
C_{11}-C_{10}-N_2	Csp^2	118.3	123.7	119.8	108.5	4.365	1.252	-9.032
C_{10}-C_{11}-C_{12}	Csp^2	120.8	120.5	119.9	111.7	-0.249	-0.751	-8.147
H_{12}-C_{12}-C_{11}	Csp^2	119.6	118.6	120.0	109.4	-0.843	0.333	-9.324
C_{10}-C_{11}-H_{11}	Csp^2	119.6	120.8	119.9	109.6	0.993	0.250	-9.124
H_{12}-C_{12}-C_{13}	Csp^2	118.9	119.3	120.2	109.7	0.335	1.082	-8.387
C_{11}-C_{12}-C_{13}	Csp^2	122.2	122.6	119.5	112.8	0.326	-2.259	-8.333
C_{11}-C_{12}-H_{12}	Csp^2	119.0	117.9	120.2	105.7	-0.933	0.998	-12.583
C_{14}-C_{13}-N_1	Csp^2	122.6	120.6	120.1	109.8	-1.658	-2.082	-11.658
C_{12}-C_{13}-N_1	Csp^2	122.7	124.3	120.2	114.6	1.287	-2.080	-7.068
C_{12}-C_{13}-C_{14}	Csp^2	114.6	114.9	119.5	108.6	0.261	4.100	-5.525
C_{13}-C_{14}-F	Csp^2	118.8	118.9	119.9	110.5	0.084	0.917	-7.511
C_{15}-C_{14}-F	Csp^2	116.4	117.4	119.9	106.4	0.852	2.919	-9.398
C_{13}-C_{14}-C_{15}	Csp^2	124.8	123.6	120.0	113.9	-0.971	-4.000	-9.570
C_{14}-C_{15}-H_{15}	Csp^2	120.4	118.6	119.7	108.1	-1.518	-0.585	-11.378
C_{10}-C_{15}-C_{14}	Csp^2	119.1	119.9	120.4	111.2	0.667	1.080	-7.104
C_{10}-C_{15}-H_{15}	Csp^2	120.5	121.3	119.7	110.0	0.660	-0.668	-9.545
H_{16A}-C_{16}-C_{17}	Csp^3	109.6	108.9	86.9	109.5	-0.643	-26.122	-0.091
H_{16A}-C_{16}-H_{16B}	Csp^3	108.1	107.9	137.9	106.4	-0.185	21.610	-1.598
H_{16A}-C_{16}-N_1	Csp^3	109.6	108.0	87.1	111.7	-1.481	-25.832	1.880

C_{17}-C_{16}-H_{16B}	Csp^3	109.6	110.8	77.4	111.2	1.083	-41.602	1.439
C_{17}-C_{16}-N_1	Csp^3	110.4	110.8	133.8	111.3	0.361	17.489	0.809
N_1-C_{16}-H_{16B}	Csp^3	109.5	110.0	76.9	111.7	0.455	-42.393	1.970
H_{17A}-C_{17}-O_1	Csp^3	109.1	106.2	110.4	109.4	-2.731	1.178	0.274
C_{16}-C_{17}-H_{17A}	Csp^3	109.1	110.8	111.4	110.5	1.534	2.065	1.267
H_{17A}-C_{17}-H_{17B}	Csp^3	107.9	108.5	109.0	107.6	0.553	1.009	-0.279
C_{16}-C_{17}-O_1	Csp^3	112.3	111.1	106.1	110.4	-1.080	-5.844	-1.721
H_{17B}-C_{17}-O_1	Csp^3	109.1	110.1	110.3	107.4	0.908	1.088	-1.583
C_{16}-C_{17}-H_{17B}	Csp^3	109.1	109.8	109.3	107.5	0.638	0.183	-1.488
H_{18A}-C_{18}-O_1	Csp^3	109.2	106.3	108.3	107.4	-2.728	-0.831	-1.676
C_{19}-C_{18}-O_1	Csp^3	112.3	110.5	109.8	110.2	-1.629	-2.277	-1.906
H_{18B}-C_{18}-O_1	Csp^3	109.1	109.9	110.3	107.4	0.728	1.088	-1.583
H_{18A}-C_{18}-C_{19}	Csp^3	109.1	110.8	108.8	110.4	1.534	-0.276	1.178
H_{18A}-C_{18}-H_{18B}	Csp^3	107.9	108.4	109.5	107.6	0.461	1.461	-0.279
H_{18B}-C_{18}-C_{19}	Csp^3	109.1	110.6	109.8	111.4	1.356	0.638	2.065
C_{18}-C_{19}-H_{19A}	Csp^3	109.4	108.0	107.8	107.3	-1.296	-1.484	-1.957
H_{19A}-C_{19}-N_1	Csp^3	109.4	107.3	109.9	110.3	-1.957	0.455	0.816
H_{19A}-C_{19}-H_{19B}	Csp^3	108.0	107.4	109.5	108.5	-0.559	1.370	0.461
C_{18}-C_{19}-N_1	Csp^3	111.1	112.1	110.0	110.9	0.892	-1.000	-0.180
C_{18}-C_{19}-H_{19B}	Csp^3	109.4	111.7	110.8	108.6	2.059	1.264	-0.737
N_1-C_{19}-H_{19B}	Csp^3	109.5	109.9	108.6	111.0	0.364	-0.829	1.351
C_{16}-N_1-C_{19}	Nsp^3	109.6	110.7	105.3	108.2	0.994	-4.084	-1.294
C_{13}-N_1-C_{16}	Nsp^3	114.7	119.9	108.8	109.9	4.337	-5.423	-4.368
C_{13}-N_1-C_{19}	Nsp^3	115.7	120.1	111.3	114.9	3.664	-3.953	-0.696
C_{10}-N_2-H_{2N}	Nsp^3	117.0	119.2	119.9	108.5	1.846	2.419	-7.834
C_9-N_2-C_{10}	Nsp^3	126.0	127.6	120.1	112.7	1.254	-4.913	-11.801

C_9-N_2-H_{2N}	Nsp^3	117.0	113.0	119.9	109.0	-3.540	2.419	-7.339
C_{17}-O_1-C_{18}	Osp^3	108.8	111.5	112.4	110.8	2.422	3.203	1.805

Table 6A.7: *Comparative list of selected torsional angles (^{o}) of* ***FMAPA***

Atomic string	**XRD**		**B3LYP**		**AM1**		**MM2**	
	Angle	**(*)**	**Angle**	**(*)**	**Angle**	**(*)**	**Angle**	**(*)**
H_{17A}-C_{17}-O_1-C_{18}	-61.5	*-sc*	+179.7	*+ap*	+163.1	*+ap*	+179.5	*+ap*
C_{16}-C_{17}-O_1-C_{18}	+59.6	*+sc*	+59.0	*+sc*	+42.1	*+sc*	+58.9	*+sc*
H_{17B}-C_{17}-O_1-C_{18}	-179.2	*-ap*	-62.9	*-sc*	-76.2	*-sc*	-63.5	*-sc*
H_{17A}-C_{17}-C_{16}-H_{16B}	-58.2	*-sc*	-55.1	*-sc*	-66.0	*-sc*	-173.8	*-ap*
H_{17A}-C_{17}-C_{16}-H_{16A}	-176.7	*-ap*	+63.5	*+sc*	+153.2	*+ap*	+61.0	*+sc*
H_{17A}-C_{17}-C_{16}-N_1	+62.6	*+sc*	-173.9	*-ap*	-149.0	*-ac*	-176.2	*-ap*
O_1-C_{17}-C_{16}-H_{16B}	-179.3	*-ap*	+62.7	*+sc*	+54.3	*+sc*	+64.4	*+sc*
O_1-C_{17}-C_{16}-H_{16A}	+62.2	*+sc*	-178.5	*-ap*	-86.4	*-sc*	-176.2	*-ap*
O_1-C_{17}-C_{16}-N_1	-58.6	*-sc*	-56.0	*-sc*	-28.7	*-sp*	-57.5	*-sc*
H_{17B}-C_{17}-C_{16}-H_{16B}	+59.5	*+sc*	-175.1	*-ap*	+173.4	*+ap*	-58.5	*-sc*
H_{17B}-C_{17}-C_{16}-H_{16A}	-59.0	*-sc*	-56.4	*-sc*	+32.6	*+sc*	-72.0	*-sc*
H_{17B}-C_{17}-C_{16}-N_1	-179.7	*-ap*	+66.1	*+sc*	+90.3	*+ac*	+64.2	*+sc*
C_{17}-O_1-C_{18}-H_{18A}	-179.5	*-ap*	-178.3	*-ap*	+175.8	*+ap*	+179.9	*+ap*
C_{17}-O_1-C_{18}-C_{19}	-58.3	*-sc*	-57.9	*-sc*	-65.3	*-sc*	-59.6	*-sc*
C_{17}-O_1-C_{18}-H_{18B}	+62.8	*+sc*	+64.4	*+sc*	+55.9	*+sc*	+63.3	*+sc*
H_{16B}-C_{16}-N_1-C_{19}	+174.7	*+ap*	-66.7	*-sc*	-52.3	*-sc*	-66.1	*-sc*
H_{16B}-C_{16}-N_1-C_{13}	-53.3	*-sc*	+146.4	*+ac*	-171.7	*-ap*	+60.1	*+sc*
C_{17}-C_{16}-N_1-C_{19}	+53.9	*+sc*	+52.6	*+sc*	+30.6	*+sc*	+55.4	*+sc*
C_{17}-C_{16}-N_1-C_{13}	-174.0	*-ap*	-94.2	*-ac*	-88.8	*-sc*	-178.2	*-ap*
H_{16A}-C_{16}-N_1-C_{19}	-66.9	*-sc*	+175.6	*+ap*	+88.4	*+sc*	+175.7	*+ap*
H_{16A}-C_{16}-N_1-C_{13}	+65.2	*+sc*	+28.7	*+sp*	-30.9	*-sc*	-57.8	*-sc*
O_1-C_{18}-C_{19}-C_{19A}	177.5	*+ap*	-62.9	*-sc*	-53.6	*-sc*	-63.4	*-sc*
O_1-C_{18}-C_{19}-N_1	+56.6	*+sc*	+55.0	*+sc*	+66.3	*+sc*	+58.8	*+sc*
O_1-C_{18}-C_{19}-H_{19B}	-64.4	*-sc*	+179.0	*+ap*	-173.4	*-ap*	+179.4	*+ap*
H_{18A}-C_{18}-C_{19}-H_{19A}	-61.3	*-sc*	+54.7	*+sc*	+64.9	*+sc*	+57.6	*+sc*
H_{18A}-C_{18}-C_{19}-N_1	+177.8	*+ap*	+172.7	*+ap*	-175.1	*-ap*	+177.4	*+ap*
H_{18A}-C_{18}-C_{19}-H_{19B}	+56.8	*+sc*	-63.2	*-sc*	-54.9	*-sc*	-61.9	*-sc*
H_{18B}-C_{18}-C_{19}-H_{19A}	+56.4	*+sc*	+175.0	*+ap*	-175.1	*-ap*	-172.8	*-ap*
H_{18B}-C_{18}-C_{19}-N_1	-64.5	*-sc*	-66.9	*-sc*	-55.2	*-sc*	+174.7	*+ap*
H_{18B}-C_{18}-C_{19}-H_{19B}	+174.5	*+ap*	+57.0	*+sc*	+64.9	*+sc*	+57.6	*+sc*

C_{16}-N_1-C_{19}-H_{19A}	-174.0	*-ap*	+65.8	*+sc*	+74.9	*+sc*	+78.2	*+sc*
C_{16}-N_1-C_{19}-C_{18}	-53.1	*-sc*	-52.6	*-sc*	-43.6	*-sc*	-56.0	*-sc*
C_{16}-N_1-C_{19}-H_{19B}	+67.9	*+sc*	-177.5	*-ap*	-165.1	*-ap*	-174.8	*-ap*
C_{13}-N_1-C_{19}-H_{19A}	+54.4	*+sc*	-147.3	*-ac*	-167.2	*-ap*	+61.8	*+sc*
C_{13}-N_1-C_{19}-C_{18}	+175.4	*+ap*	+94.1	*+ac*	+74.1	*+sc*	-179.3	*-ap*
C_{13}-N_1-C_{19}-H_{19B}	-63.7	*-sc*	-30.7	*-sc*	-47.3	*-sc*	-58.4	*-sc*
C_{16}-N_1-C_{13}-C_{14}	+54.9	*+sc*	-53.6	*-sc*	-32.0	*-sc*	+92.1	*+ac*
C_{16}-N_1-C_{13}-C_{12}	-128.3	*-ac*	+130.4	*+ac*	+148.0	*+ac*	-145.1	*-ac*
C_{19}-N_1-C_{13}-C_{14}	-176.0	*-ap*	+162.5	*+ap*	-147.6	*-ac*	-145.1	*-ac*
C_{19}-N_1-C_{13}-C_{12}	+0.8	*+sp*	-13.2	*-sp*	+32.3	*+sc*	-22.7	*-sp*
N_1-C_{13}-C_{14}-F	+3.9	*+sp*	+2.0	*+sp*	+0.1	*+sp*	-60.5	*-sc*
N_1-C_{13}-C_{14}-C_{15}	-179.0	*-ap*	-177.2	*-ap*	-179.9	*-ap*	+179.6	*+ap*
C_{12}-C_{13}-C_{14}-F	-173.1	*-ap*	+178.2	*+ap*	-179.9	*-ap*	+173.4	*+ap*
C_{12}-C_{13}-C_{14}-C_{15}	+3.9	*+sp*	-1.0	*-sp*	+0.1	*+sp*	+53.6	*+sc*
N_1-C_{13}-C_{12}-H_{12}	+0.3	*+sp*	-5.3	*-sp*	-0.1	*-sp*	+66.8	*+sc*
N_1-C_{13}-C_{12}-C_{11}	-179.7	*-ap*	+176.0	*+ap*	+179.9	*+ap*	+175.5	*+ap*
C_{14}-C_{13}-C_{12}-H_{12}	+177.4	*+ap*	+178.6	*+ap*	+179.9	*+ap*	-169.9	*-ap*
C_{14}-C_{13}-C_{12}-C_{11}	-2.7	*-sp*	+0.1	*+sp*	-0.1	*-sp*	-52.2	*-sc*
F-C_{14}-C_{15}-H_{15}	-4.6	*-sp*	-0.1	*-sp*	-0.1	*-sp*	+59.2	*+sc*
F-C_{14}-C_{15}-C_{10}	+175.5	*+ap*	-177.7	*-ap*	+179.9	*+ap*	-179.8	*-ap*
C_{13}-C_{14}-C_{15}-H_{15}	+178.3	*+ap*	+179.2	*+ap*	+179.9	*+ap*	-178.7	*-ap*
C_{13}-C_{14}-C_{15}-C_{10}	-1.6	*-sp*	+1.5	*+sp*	-0.1	*-sp*	-57.8	*-sc*
C_{14}-C_{15}-C_{10}-C_{11}	-2.1	*-sp*	-0.9	*-sp*	-0.1	*-sp*	+56.9	*+sc*
C_{14}-C_{15}-C_{10}-N_2	-178.8	*-ap*	+179.5	*+ap*	+179.9	*+ap*	+177.0	*+ap*
H_{15}-C_{15}-C_{10}-C_{11}	+178.0	*+ap*	-178.6	*-ap*	+179.9	*+ap*	+176.3	*+ap*
H_{15}-C_{15}-C_{10}-N_2	+1.3	*+sp*	+1.9	*+sp*	-0.1	*-sp*	-63.2	*-sc*
C_{13}-C_{12}-C_{11}-C_{10}	-0.7	*-sp*	+0.4	*+sp*	+0.1	*+sp*	+56.1	*+sc*
C_{13}-C_{12}-C_{11}-H_{11}	+179.3	*+ap*	+178.2	*+ap*	-179.9	*-ap*	+177.7	*+ap*
H_{12}-C_{12}-C_{11}-C_{10}	+179.2	*+ap*	-178.1	*-ap*	-179.9	*-ap*	+176.1	*+ap*
H_{12}-C_{12}-C_{11}-H_{11}	-0.8	*-sp*	-0.4	*-sp*	+0.3	*+sp*	-62.2	*-sc*
C_{12}-C_{11}-C_{10}-C_{15}	+3.2	*+sp*	+0.2	*+sp*	-0.1	*-sp*	-56.5	*-sc*
C_{12}-C_{11}-C_{10}-N_2	-179.9	*-ap*	+179.4	*+ap*	+179.9	*+ap*	-178.9	*-ap*
H_{11}-C_{11}-C_{10}-C_{15}	-176.8	*-ap*	-177.7	*-ap*	+179.9	*+ap*	-178.0	*-ap*
H_{11}-C_{11}-C_{10}-N_2	+0.1	*+sp*	+1.7	*+sp*	+0.1	*+sp*	+59.5	*+sc*
C_{15}-C_{10}-N_2-H_{2N}	+166.2	*+ap*	+11.9	*+sp*	+0.1	*+sp*	-167.7	*-ap*
C_{15}-C_{10}-N_2-C_9	-13.8	*-sp*	-166.3	*-ap*	-179.9	*-ap*	+71.3	*+sc*
C_{11}-C_{10}-N_2-H_{2N}	-10.6	*-sp*	-167.4	*-ap*	-179.8	*-ap*	-47.7	*-sc*
C_{11}-C_{10}-N_2-C_9	+169.4	*+ap*	+14.2	*+sp*	+0.2	*+sp*	-168.6	*-ap*
C_{10}-N_2-C_9-H_9	-5.8	*-sp*	+1.9	*+sp*	+0.1	*+sp*	-73.6	*-sc*

C_{10}-N_2-C_9-C_7	+174.2	+*ap*	-179.6	-*ap*	-179.8	-*ap*	+165.3	+*ap*
H_{2N}-N_2-C_9-H_9	+174.2	+*ap*	-176.5	-*ap*	-179.8	-*ap*	+165.7	+*ap*
H_{2N}-N_2-C_9-C_7	-5.8	-*sp*	+1.9	+*sp*	+0.1	+*sp*	+44.7	+*sc*
N_2-C_9-C_7-C_8	+174.6	+*ap*	-0.3	-*sp*	+90.1	+*ac*	+177.1	+*ap*
N_2-C_9-C_7-C_6	-8.3	-*sp*	+179.2	+*ap*	-89.9	-*sc*	-57.7	-*sc*
H_9-C_9-C_7-C_8	-5.4	-*sp*	+178.0	+*ap*	-89.9	-*sc*	+55.3	+*sc*
H_9-C_9-C_7-C_6	+171.7	+*ap*	-2.3	-*sp*	+90.1	+*ac*	-179.5	-*ap*
O_2-C_8-C_7-C_9	-177.9	-*ap*	-1.3	-*sp*	-90.1	-*ac*	-172.4	-*ap*
O_2-C_8-C_7-C_6	+4.9	+*sp*	+179.0	+*ap*	+89.9	+*sc*	+63.8	+*sc*
H_8-C_8-C_7-C_9	+2.0	+*sp*	+177.7	+*ap*	+89.6	+*sc*	+55.3	+*sc*
H_8-C_8-C_7-C_6	-175.2	-*ap*	-1.9	-*sp*	-90.1	-*ac*	-179.0	-*ap*
C_9-C_7-C_6-C_1	-48.4	-*sc*	-41.25	-*sc*	-90.2	-*ac*	-82.4	-*ac*
C_9-C_7-C_6-C_5	+136.4	+*ac*	+138.8	+*ac*	+89.7	+*sc*	+151.1	+*ap*
C_8-C_7-C_6-C_1	128.6	+*ac*	+138.3	+*ac*	+89.7	+*sc*	+42.1	+*sc*
C_8-C_7-C_6-C_5	-46.7	-*sc*	-41.5	-*sc*	-90.2	-*ac*	-84.2	-*sc*
C_7-C_6-C_1-H_1	+5.4	+*sp*	-2.3	-*sp*	-0.1	-*sp*	+58.2	+*sc*
C_7-C_6-C_1-C_2	-174.5	-*ap*	+179.3	+*ap*	-179.9	-*ap*	+179.2	+*ap*
C_5-C_6-C_1-H_1	-179.2	-*ap*	+177.5	+*ap*	+179.9	+*ap*	-175.7	-*ap*
C_5-C_6-C_1-C_2	+0.9	+*sp*	-0.8	-*sp*	-0.2	-*sp*	-54.7	-*sc*
C_7-C_6-C_5-H_5	-5.1	-*sp*	-1.8	-*sp*	+0.1	+*sp*	-56.9	-*sc*
C_7-C_6-C_5-C_4	+174.8	+*ap*	+179.7	+*ap*	-179.9	-*ap*	-178.2	-*ap*
C_1-C_6-C_5-H_5	+179.5	+*ap*	+178.2	+*ap*	-179.9	-*ap*	+176.0	+*ap*
C_1-C_6-C_5-C_4	-0.6	-*sp*	-0.1	-*sp*	+0.1	+*sp*	+54.8	+*sc*
H_1-C_1-C_2-H_2	-0.5	-*sp*	+1.6	+*sp*	-0.1	-*sp*	-61.6	-*sc*
H_1-C_1-C_2-C_3	+179.5	+*ap*	-177.2	-*ap*	+179.9	+*ap*	+177.0	+*ap*
C_6-C_1-C_2-H_2	+179.3	+*ap*	+179.9	+*ap*	+179.9	+*ap*	+177.2	+*ap*
C_6-C_1-C_2-C_3	-0.6	-*sp*	+1.1	+*sp*	-0.1	-*sp*	+56.0	+*sc*
C_6-C_5-C_4-C_3	-0.1	-*sp*	+0.8	+*sp*	-0.1	-*sp*	-56.2	-*sc*
C_6-C_5-C_4-H_4	+179.9	+*ap*	+179.8	+*ap*	+179.9	+*ap*	-177.4	-*ap*
H_5-C_5-C_4-C_3	+179.9	+*ap*	-177.6	-*ap*	+179.9	+*ap*	-177.2	-*ap*
H_5-C_5-C_4-H_4	-0.1	-*sp*	+1.4	+*sp*	-0.1	-*sp*	+61.0	+*sc*
C_1-C_2-C_3-C_4	-0.6	-*sp*	-0.4	-*sp*	+0.1	+*sp*	-57.8	-*sc*
C_1-C_2-C_3-H_3	+180.0	+*ap*	+179.4	+*ap*	-179.9	-*ap*	-178.8	-*ap*
H_2-C_2-C_3-C_4	+180.0	+*ap*	-179.2	-*ap*	-179.9	-*ap*	-178.9	-*ap*
H_2-C_2-C_3-H_3	0.0	*sp*	+0.5	+*sp*	0.0	*sp*	+60.0	+*sc*
C_5-C_4-C_3-C_2	+0.9	+*sp*	-0.5	-*sp*	-0.1	-*sp*	+57.8	+*sc*
C_5-C_4-C_3-H_3	-179.6	-*ap*	+179.6	+*ap*	+179.9	+*ap*	+178.8	+*ap*
* The conformations were designated by Klyne-Prelog termsusing *s* = syn, *a* = anti, *p* = peri-planar (0 ± 30^0& 180 ± 30^0) and all other angles *c* = clinal, and + & - signs.								

Modelling platform	HOMO	LUMO
AM1	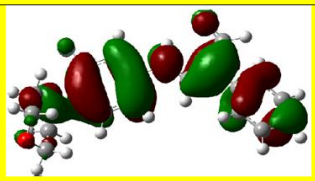 E = -0.3045 eV	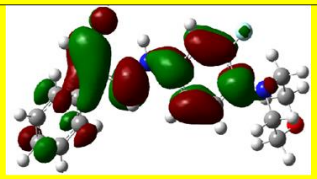 E = -0.0230 eV
B3LYP	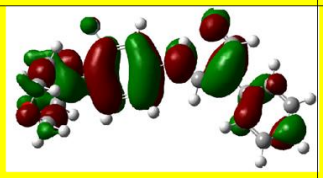 E = -0.1851 eV	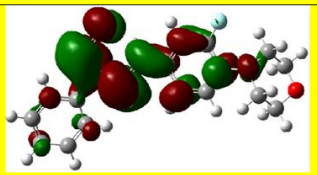 E = -0.0550 eV
MM2	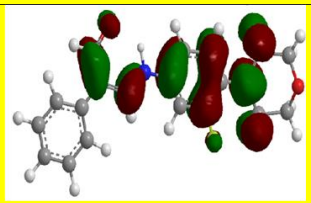 E = -7.469 eV	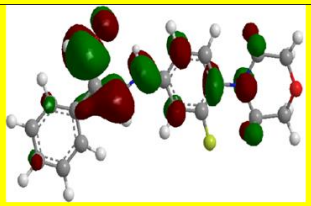 E = -1.803 eV

Figure 6A.29: *HOMO and LUMO orbitals of* ***FMAPA*** *obtained from different modelling platforms*

6A.7 Hirshfeld Surface Analysis:

Figure 6A.30 is obtained by mapping d_{norm} over the Hirshfeld surface[7] over a range of -0.4786 to 1.8997 Å. Strong acceptor-donor intermolecular hydrogen bond interactions appear at O_2----H_{11}-C_{11}, C_8-O_2----H_{2N}, C_{12}-H_{12}----C_1, and C_{12}-H_{12}----C_6 are indicated as bright red color spots. The relative percent Hirshfeld surface area contributions of various intermolecular interatomic interactions are shown in **Table 6A.8**. **Figure 6A.31** shows the finger print plots[8] of **FMAPA.** This and **Figure 6A.32** together suggest some H···H interactions as the strongest, with nearly 46.9% surface concentration. The O···H/ O···H contacts contribute approximately 14.9% with two spikes at a de + di value of ~1.18 Å, the F···H/ H···F contacts contribute approximately 8.5% with a de + di value of ~1.5 Å and the C···H/ H···C contacts contribute approximately 23.0% with a de + di value of ~1.58 Å. The contributions of all other intermolecular interatomic interactions are less than 8%.

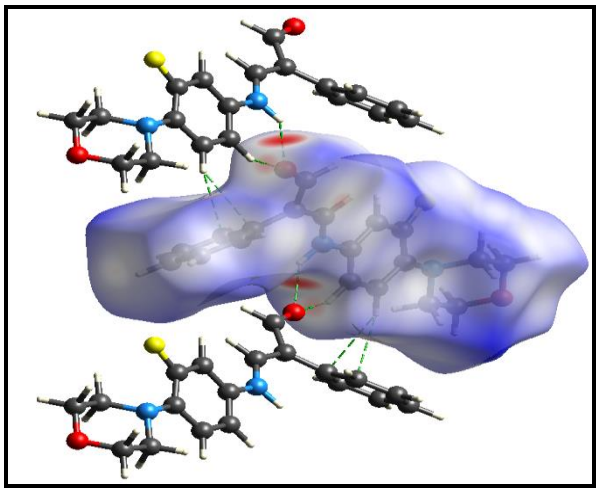

Figure 6A.30: *Hirshfeld d_{norm} surface of* ***FMAPA*** *showing intermolecular hydrogen bonding interactions*

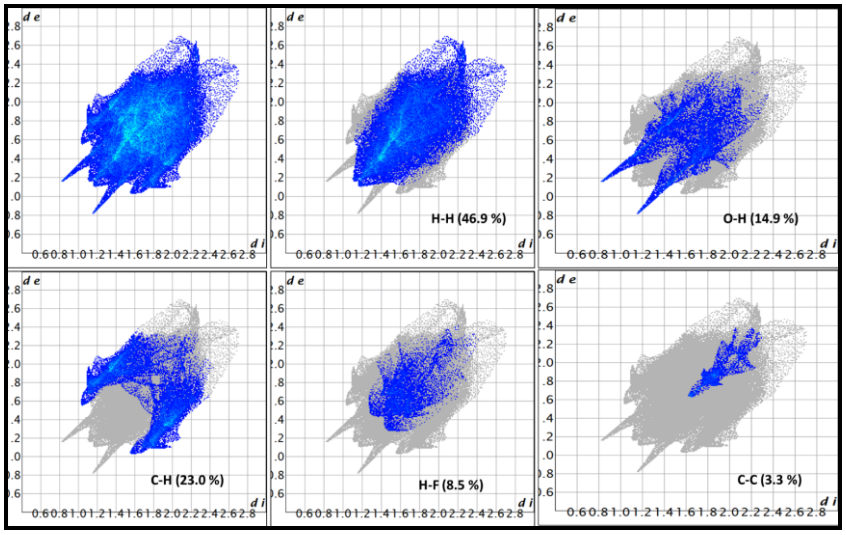

Figure 6A.31 *Hirshfeld finger print plots of* ***FMAPA***

Table 6A.8: *Intermolecular Hirshfeld inter-atomic interaction percentages*

Interaction	Contribution (%)
C-C	3.3
C-H/H-C	23.0
C-N/N-C	0.8
C-O/O-C	0.2
C-F/F-C	0.2
H-H	46.9

H-N/N-H	1.9
H-O	14.9
H-F/F-H	8.5
N-N/N-N	0.2

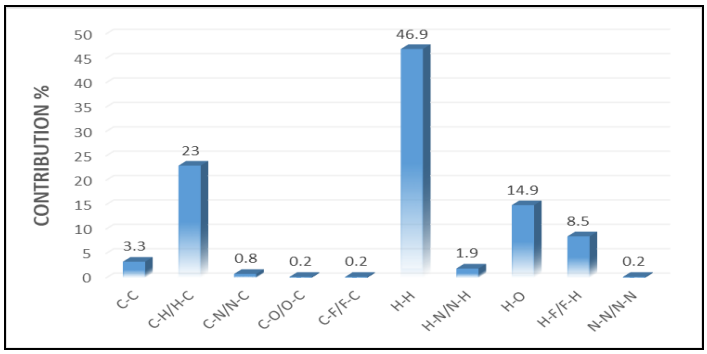

Figure 6A.32: *Relative contributions of different intermolecular contacts to the Hirshfeld surface area of* ***FMAPA***

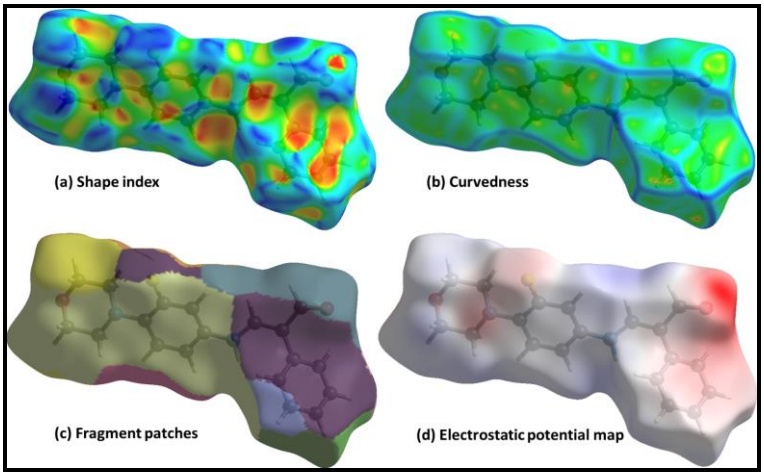

Figure 6A.33: *Hirshfeld surface maps of* ***FMAPA*** *represented by modes*

The presence of interaction is indicated by the pattern of neighboring red and blue triangles that are displayed on the shape index surfaces of **FMAPA** (**Figure 6A.33 (a**)) and the corresponding curvatures of the surfaces on the same side of the molecule through large and flat green regions on it (**Figure 6A.33 (b)).** The electrostatic potential generated by the HF/3-21G basis set is depicted with red representing negative electrostatic potential (hydrogen acceptors) and blue representing positive electrostatic potential (hydrogen donor) (**Figure 6A.33 (d)).**

The surface parameters of shape index and curvedness are used to determine the molecular arrangements in the crystal. The measures of shape index and curvedness describe the local shape in terms of principal curvatures. The flat regions on the curvedness **Figure 6A.33 (c)** plot reflect planar molecule stacking. The arrangement of red and blue triangles on the contour index map demonstrates the typical property of π-π interactions. The molecule is clearly stacked in a planar way since it has flat portions on the curvedness map.

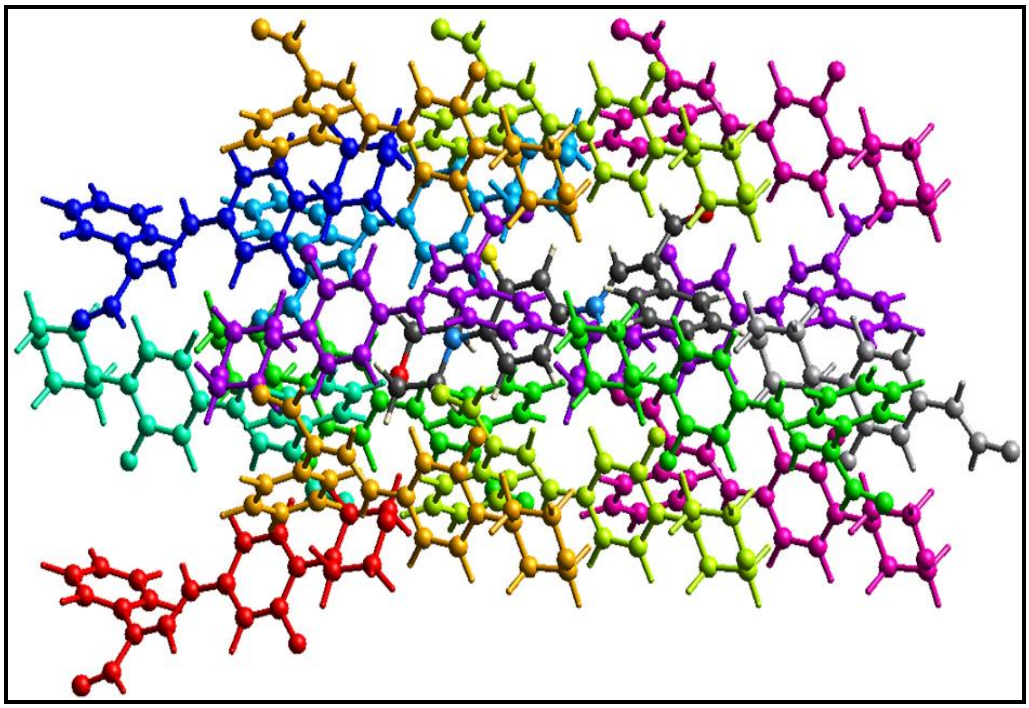

Figure 6A.34: *Pair-wise intermolecular interactions in* ***FMAPA*** *(viewed along the c axis)*

Table 6A.9: *Pair-wise intermolecular interaction energies of* ***FMAPA***

	N	Symop	R	Electron density	E_ele	E_pol	E_dis	E_rep	E_tot
	1	-x, -y, -z	15.89	HF/3-21G	-11.6	-1.0	-4.9	0.0	-16.9
	2	-x, y+1/2, -z+1/2	8.62	HF/3-21G	0.7	-0.4	-4.1	0.1	-3.2
	2	-x, y+1/2, -z+1/2	6.54	HF/3-21G	-9.9	-5.8	-38.9	16.6	-35.4
	2	x, -y+1/2, z+1/2	13.56	HF/3-21G	1.1	-0.7	-9.6	0.0	-7.9

1	x, -y+1/2, z+1/2	16.76	HF/3-21G	-2.0	-1.9	-8.8	0.0	-11.2
1	-x, -y, -z	10.11	HF/3-21G	-2.7	-1.4	-23.0	7.5	-18.3
1	-x, -y, -z	13.86	HF/3-21G	2.0	-0.2	-7.3	0.0	-4.7
2	x, y, z	6.22	HF/3-21G	-9.0	-3.6	-69.0	32.5	-47.2

Energy Model	k_ele	k_pol	k_disp	k_rep
CE-HF ... HF/3-21G electron densities	1.019	0.651	0.901	0.811
CE-B3LYP ... B3LYP/6-31G(d,p) electron densities	1.057	0.740	0.871	0.618

2	-x, y+1/2, -z+1/2	9.41	HF/3-21G	-44.3	-15.4	-29.4	35.2	-53.0

The scaling parameters for evaluated energies for HF/3-21G are k_{ele} = 1.019, k_{pol} = 0.651, k_{disp} = 0.901, and k_{rep} = 0.811; -75.7 kJmol^{-1}, -195 kJmol^{-1}, -30.4 kJmol^{-1}, and 91.9 kJmol^{-1}, respectively, are the energies of electrostatic, dispersion, polarization, and repulsion interactions. **Figure 6A.34** shows the molecular pair-wise interactions in the **FMAPA** crystal. The total energy is -197.8 kJmol^{-1}. The chemical pair-wise interaction energies are listed in **Table 6A.8.** R stands for the distance between the mean atomic locations. Dispersion energy dominates electrostatic energy. Molecular packing is depicted in **Figure 6A.35** along the a, b, and c axes, which correspond to coulomb energy (red), dispersion energy (green), and total energy (blue). The size of the cylinders in the energy frameworks represents molecular packing and the strength of the interaction energy[9].

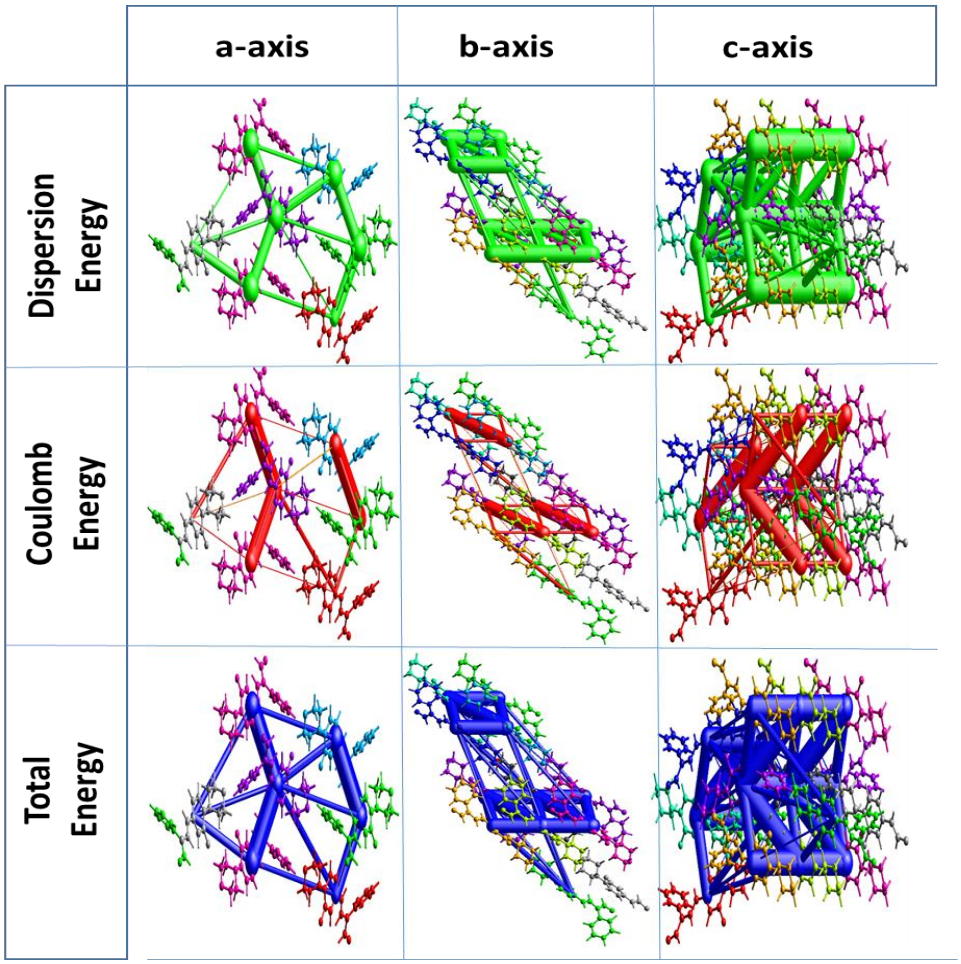

Figure 6A.35: *Crystallographic axis-wise modes of intermolecular energies in* ***FMAPA***

6A.8 Molecular Docking Studies of FMAPA and FMAMC:

EGFR-TK (pdb id: 1m17) belongs to the epidermal growth factor receptor family[10]. Excess EGFR expression results in anal cancer and epithelial malignancies of the neck and head. We chose the protein receptor EGFR as a target for molecular docking by the **FMAPA** and **FMAMC**.

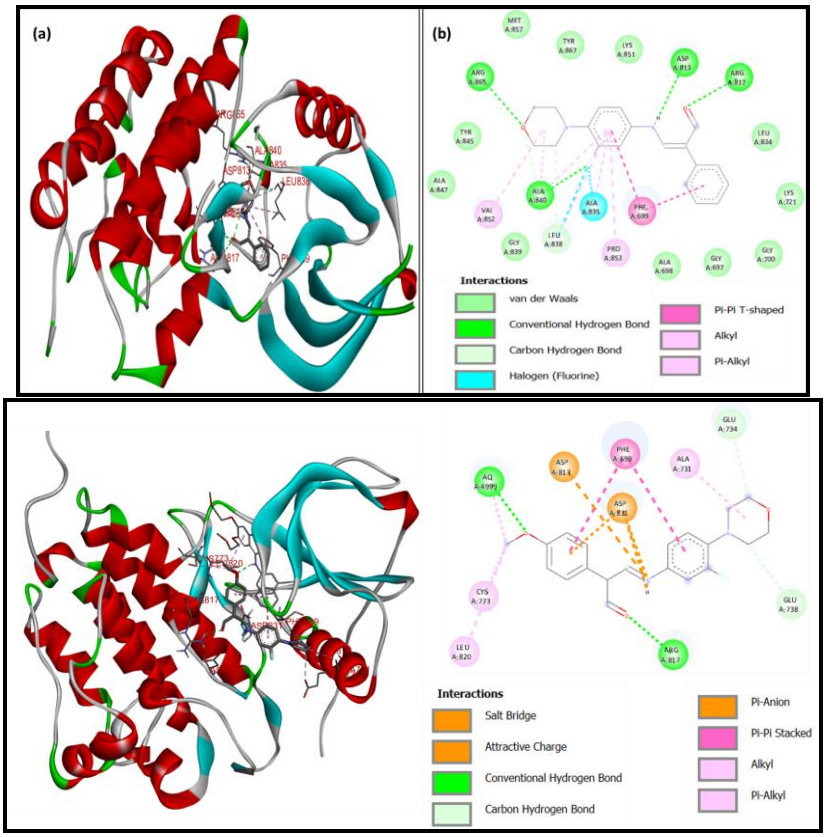

Figure 6A.36: *Molecular docking interactions of* ***FMAPA*** *and* ***FMAMC*** *with EGFR-TK protein; (a) 3D depiction of ligand-receptor binding interactions and (b) 2D representation of different forms of interactions with amino acid residues*

The molecule **FMAPA** has a binding energy of -8.7 kcal mol^{-1} and docks to the EGFR through eight hydrogen bonds with the protein amino acid residues of ARG817, ALA840, ARG865, ASP813, LEU838, there are two halogen interaction in the LEU838, ALA835 and eight hydrophobic interactions in the PHE699, ALA840, VAL852, ALA835, LEU838, PRO853 amino acid residues are shown in **Figure 6A.36.**

The molecule **FMAMC** has a binding energy of -8.3 kcal mol^{-1} and docks to the EGFR through, three electrostatic interactions with the protein amino acid residues of ASP831, ASP831 and five hydrogen bonding interactions with ARG817, GLU734, and GLU738. There are six hydrophobic interactions in the PHE699, ALA731, CYS773 and LEU820 amino acid residues, which are shown in **Figure 6A.36.**

PART B

SPECTRAL, SINGLE CRYSTAL XRD AND COMPUTATIONAL CHEMISTRY STUDIES OF FFMPMC AND FFMMMC

SECTION – B1

6B.1 Analytical Characterization of FFMPMC and FFMMMC:

Table 6B.1 shows the physical and analytical characteristics of the **FFMPMC** and **FFMMMC**. The data is stoichiometrically matched with the formulae shown in **Figure 6B.1.**

Table 6B.1: *Analytical data[#] of* ***FFMPMC*** and ***FFMMMC***

Compound	M.P (°C)	Molecular formula	Molecular weight	Elemental analysis*			
				%C	%H	%N	%O
FFMPMC	187-189	$C_{29}H_{30}F_2N_4O_2$	504.57	66.92 (67.05)	5.87 (5.95)	8.58 (8.72)	9.80 (9.87)
FFMMMC	166-168	$C_{29}H_{32}ClF_2N_4^+O_7^-$	622.03	55.84 (55.91)	5.19 (5.34)	8.79 (8.92)	17.84 (17.97)

[#] data in parenthesis are calculated ones; [*] data limited to integral values

6B.2 Mass Spectra of FFMPMC and FFMMMC:

Figure 6B.2 shows the mass spectra of the **FFMPMC** and **FFMMMC**. The molecular formulas of **FFMPMC** and **FFMMMC**, which are 505.24 and 535.25, respectively, match the M+1 base peak.

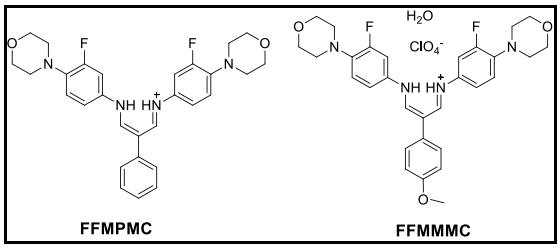

Figure 6B.1: *Structures of* ***FFMPMC*** *and* ***FFMMMC***

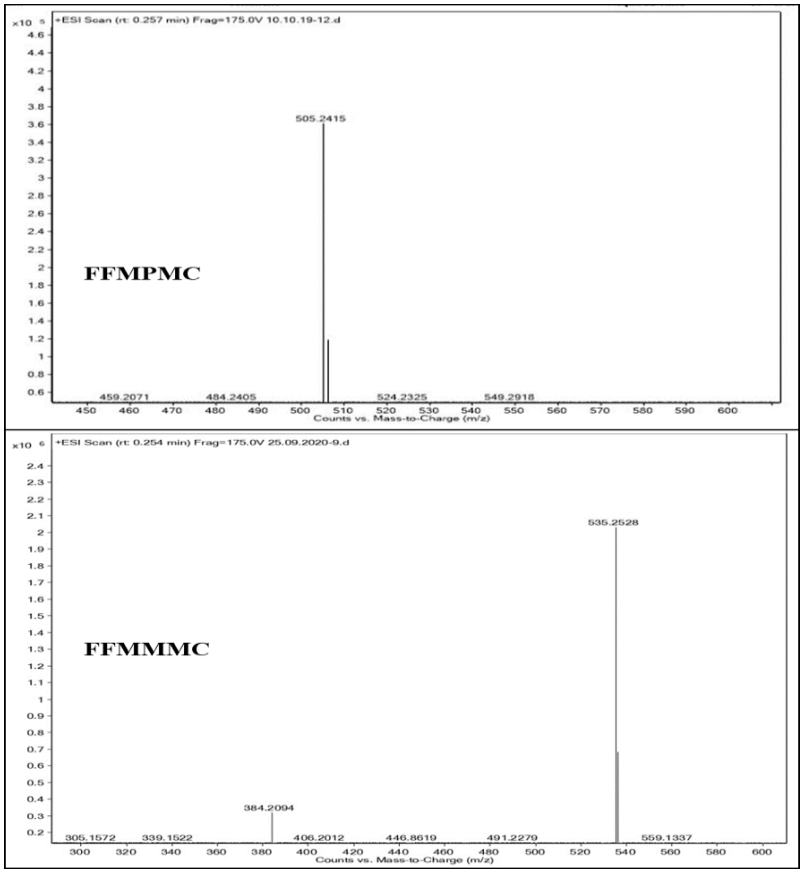

Figure 6B.2: *Mass Spectra of* ***FFMPMC*** *and* ***FFMMMC***

6B.3 IR Spectral Studies of FFMPMC and FFMMMC:

Figure 6B.3 shows the infrared spectra of **FFMPMC** and **FFMMMC**. **FFMPMC:** 3444 br (N-H), 3000-3065 s (=N-H in aromatic), 2860-2960 s (aliphatic C-H), 1605 s (C=N), 1515 s (=C-H in aromatic), 1112 s (C-O in morpholine). **FFMMMC:** 3444 br (N-H), 3000-3057 s (=N-H in aromatic), 2821-2980 s (aliphatic C-H), 1655 s (C=N), 1516 s (=C-H in aromatic), 1110 s (C-O in morpholine).

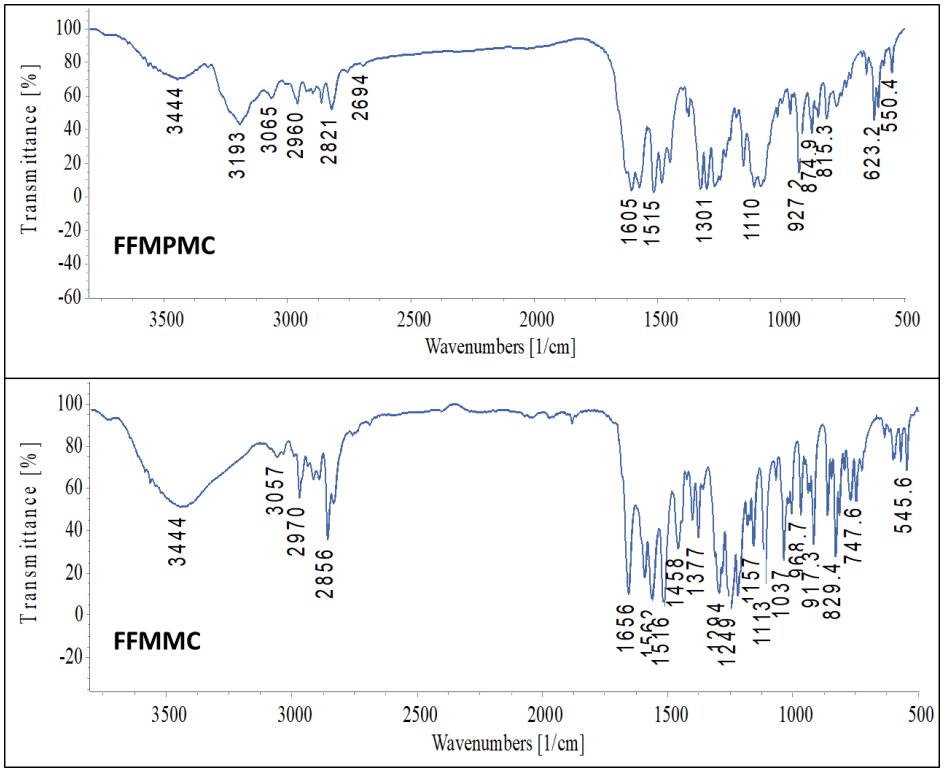

Figure 6B.3: *IR Spectra of* ***FFMPMC*** *and* ***FFMMMC***

6B.4 NMR Spectral Studies of FFMPMC and FFMMMC:

The ^{1}H NMR spectra of **FFMPMC** and **FFMMMC** is shown in **Figure 6B.4.** In the **FFMPMC** ^{1}H-NMR spectrum, imine CH=N- protons show chemical shift values of 8.71 and 10.85 ppm as a doublet. Chemical shift values for the remaining aromatic hydrogens range from 7.10 to 7.63 ppm. Eight morpholine ring protons show up together at 3.01-3.76 ppm. In the **FFMMMC** ^{1}H-NMR spectrum, imine CH=N- protons shows chemical shift values of 9.59 and 12.09 ppm as a doublet. Chemical shift values for the remaining aromatic hydrogens range from 7.26 to 6.82 ppm. Three methoxy protons and eight morpholine ring protons show up together at 3.88-3.83 ppm. Morpholine (CH_2 N-) protons appear in two chemical shift zones, 3.05 and 1.59 ppm.

The ^{13}C NMR spectra of **FFMPMC** and **FFMMMC** is shown in **Figure 6B.5.** In the **FFMPMC**, the imine C=N- carbons' spin-decoupled ^{13}C-NMR spectral line appears at 158.71 ppm and 153.42 ppm. Carbons of morpholine (-CH_2-N-) are shown at 55.85 and 50.91 ppm, while carbons of morpholine (-CH_2-O-) appear at 66.56 ppm. In the **FFMMMC**, the imine C=N- carbons' spin-decoupled ^{13}C-NMR spectral line appears at 164.79 ppm and 160.17 ppm. At 66.46

ppm, methoxy carbon (-O-CH_3) can be found. Carbons of morpholine (-CH_2-O-) are shown at 55.35 and 51.03 ppm, while carbons of morpholine (-CH_2-N-) appear at 49.31 and 39.59 ppm.

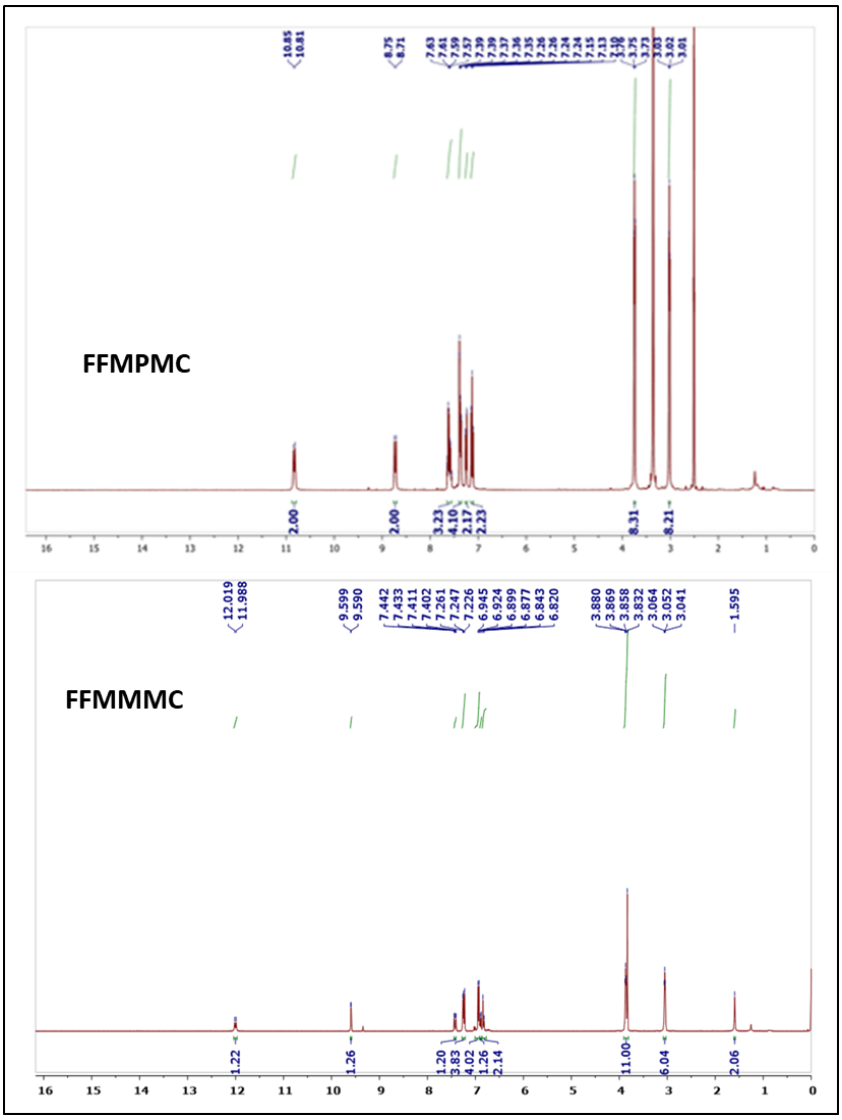

Figure 6B.4: *^{1}H-NMR Spectra of* ***FFMPMC*** *and* ***FFMMMC***

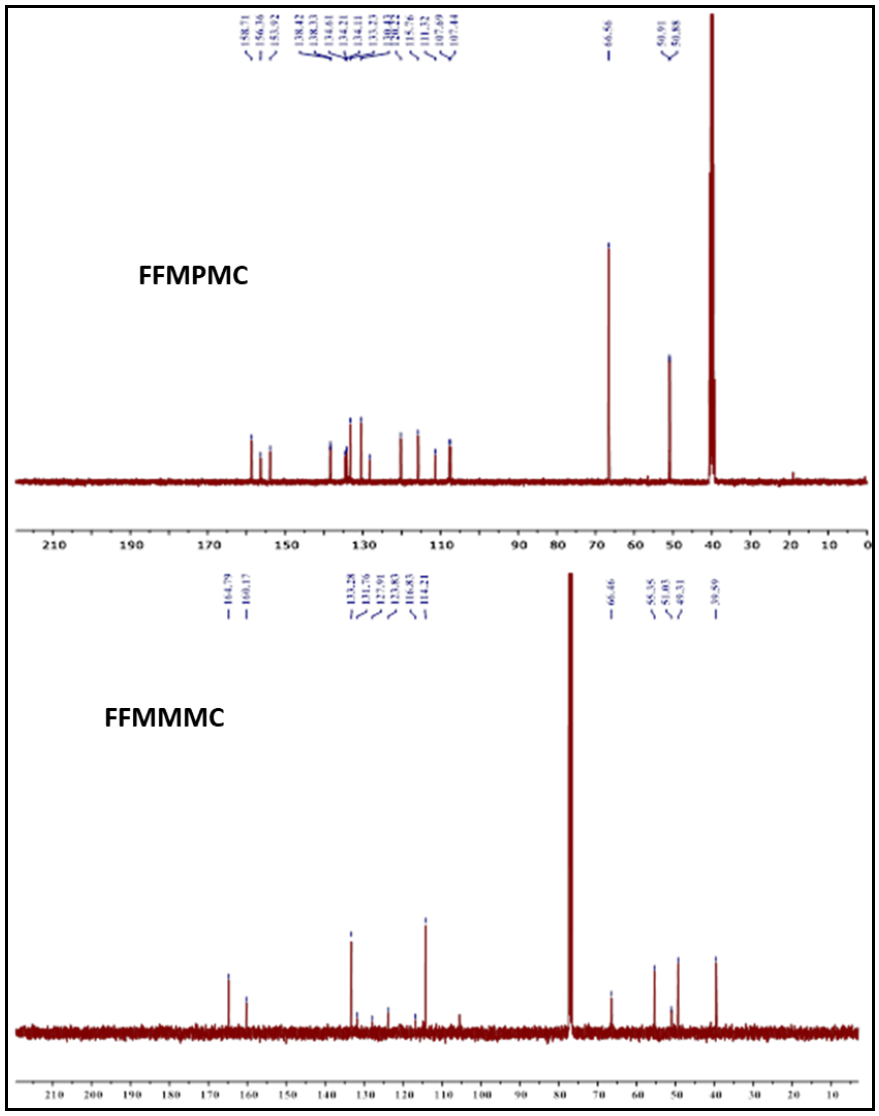

Figure 6B.5: *^{13}C-NMR Spectra of **FFMPMC** and **FFMMMC***

6B.5 Fluorescence Studies of FFMPMC and FFMMMC:

The **FFMPMC** and **FFMMMC** luminisence spectra are presented in **Figure 6A.5**. Green light emission provides broad emission peaks at 466 and 522 nm, respectively, which corresponds to electron transfer from the azomethelene group to the benzene ring via the single bond. The band gap energy was calculated to be around 2.69 and 2.37 eV for **FFMPMC** and **FFMMMC,** respectively. The reason that its absorption (excitation) and fluorescence (emission) peaks at ~500 nm are so close suggests that there is no inter-system crossing or molecular vibrational relaxation

process in the visible region. These powerful peaks can be used to analyse **FFMPMC** and **FFMMMC** photometrically.

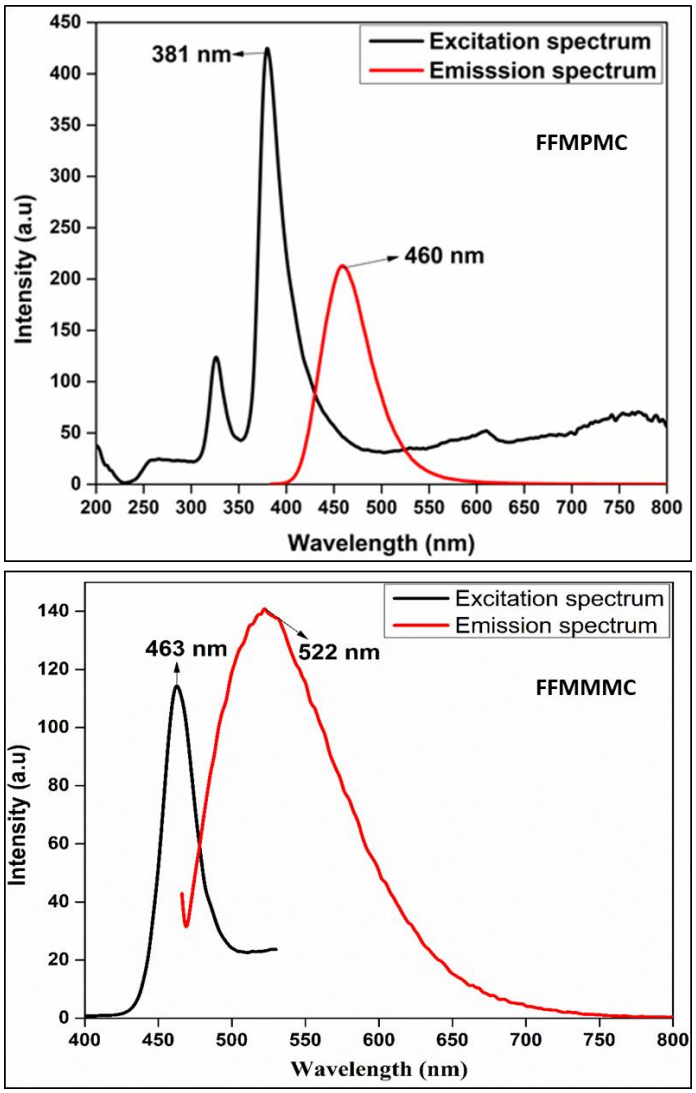

Figure 6B.6: *The solid state absorption (black) and emission (red) spectra of* ***FFMPMC*** *and* ***FFMMMC***

6B.6 Tautomerization and Potentiometric Titration of FFMPMC and FFMMMC:

Both **FFMPMC** and **FFMMMC** are found to exhibit tautomeric proton exchange equilibrium in aqueous media[11]. A generalized schematic is shown in **Scheme 6B.1.** In order to ascertain whether these Schiff bases act as amphoteric systems as shown in **Scheme 6B.1,** potentiometric pH titration was carried out[12].

In a 100 ml beaker, 5x 10^{-4} M of **FFMPMC** in DMSO (20 ml) was added after arranging a titration system with 0.07 M HCl in the burette. As HCl was added, a pH meter was used to keep a record of the pH of the solution. HCl was added in 0.5ml increments until the pH values plateaued. At several such compositions the uv-visible spectra were also recorded. The titration curve was drawn using the volume of HCl used and the pH for each addition of HCl. Using a 0.07 M NaOH solution, the same procedure was followed. **Figure 6B.7** shows the titration curves of **FFMPMC** with **NaOH** and **HCl.** The sigmoidal curves obtained from both titrations of ligand with HCl and NaOH gave an isosbestic point at 5.2 ml. The calculated pKa and pKb values of the ligand **FFMPMC** are 10.4 and 3.6.

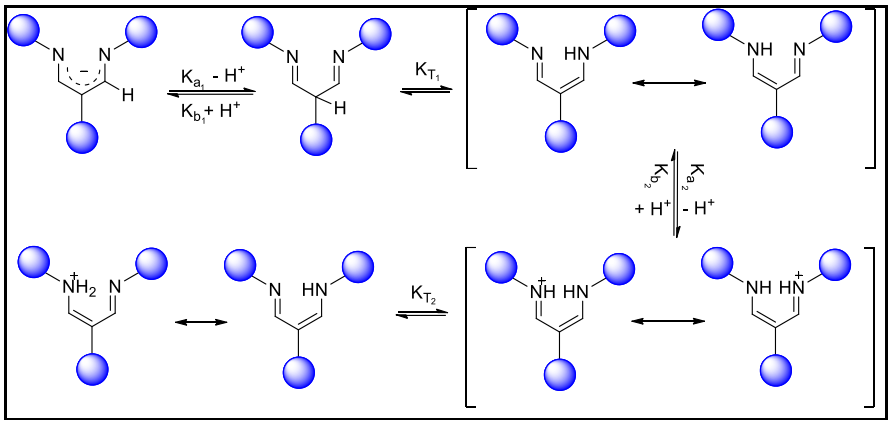

Scheme 6B.1: *Tautomeric structures of* ***FFMPMC*** *and* ***FFMMMC***

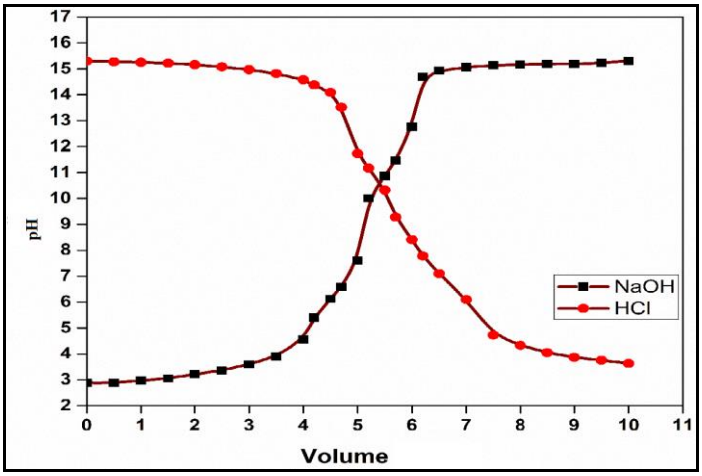

Figure 6B.7: *Acid-base pH metric titration curve for the titration of* ***FFMPMC*** *(5x10^{-4} M)*

6B.7 Crystal Structure Analysis of FFMMMC:

Figure 6B.8 shows the single crystal XRD structure of **FFMMMC.** We could not obtain single crystals for **FFMPMC** suitable for molecular structure determination. **FFMMMC** crystallizes in a centrosymmetric triclinic P_{-1} space group with two molecules in a one-unit cell. **Table 6B.2** has the relevant XRD data. **Figure 6B.9** shows a graph of reflection angle vs. intensity. The unit cell is presented in three different configurations along each of the three crystallographic axes in **Figure 6B.10**. Intermolecular hydrogen bonding is seen in **Figure 6B.11.**

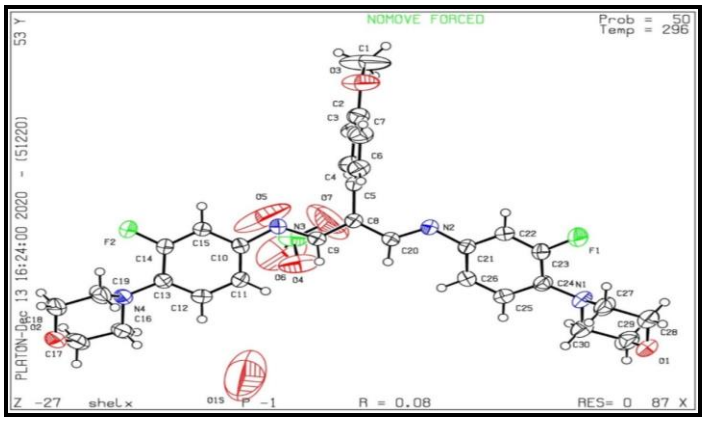

Figure 6B.8: *XRD- Platon diagram of* ***FFMMMC*** *with atom-numbering*

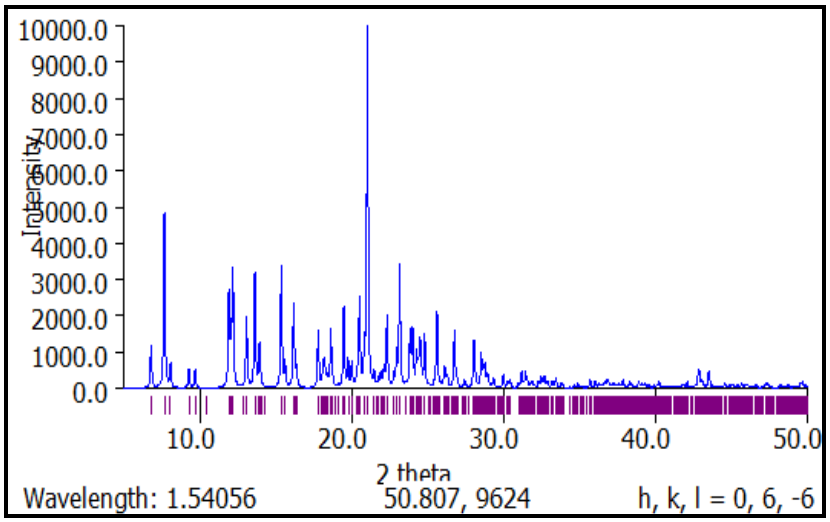

Figure 6B.9: *X-Ray diffraction intensity as a function of angle (^{o}) of reflection*

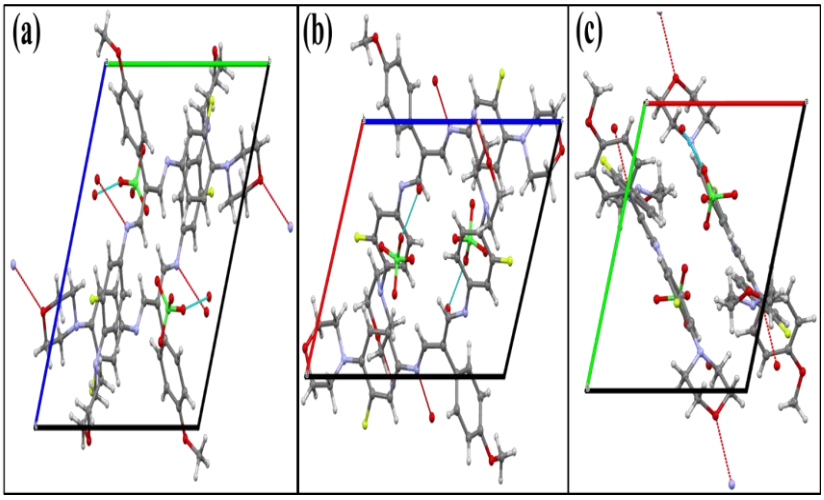

Figure 6B.10: *Unit cells of* ***FFMMMC (A)*** *and* ***FMMC (B)*** *seen along crystallographic* ***(a)*** *a-axis* ***(b)*** *b-axis* ***(c)*** *c-axis*

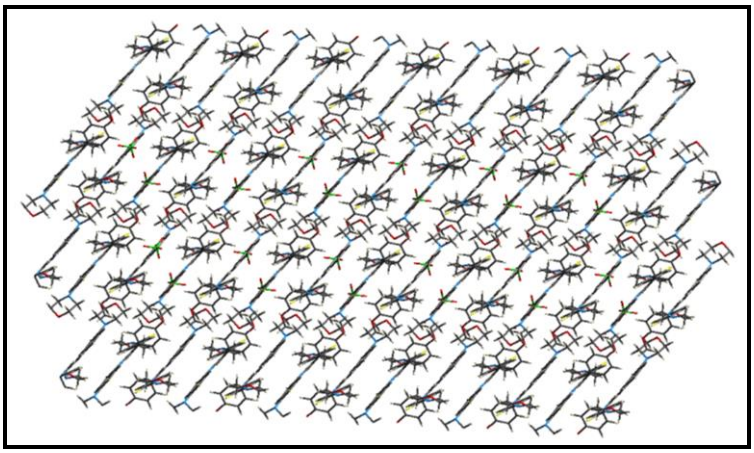

Figure 6B.11: *Crystal packing diagram of* ***FFMMMC*** *showing the two dimesitional layer structure with O-H…N intramolecular hydrogen bonding*

Table 6B.2: *X-ray crystallographic data of* ***FFMMMC***

CCDC	2181236
Empirical formula	$C_{30}H_{32}F_2N_4O_3$
Formula weight	534.59
color/shape	Orange needle
Temperature, K	296 K
Crystal system	*P*-1
Space group	Triclinic
Unit cell dimensions, Å	a = 10.1165(8); b = 12.6191(13); c = 14.9201(18)
	α = 107.643(5); β = 109.756(3); γ = 99.105(3)
Volume, $Å^3$	1634.5(3)
Z	2
Density, Mg/m^3	1.319
Absorption coefficient, mm^{-1}	0.182
Reflections collected/unique	13642/ 7315
θ range for data collections	1.570 – 28.377°
F (000)	676
Limiting indices	$-13 \leq h \leq 8$; $-16 \leq k \leq 16$; $-19 \leq l \leq 19$
Goodness-of-fit on F^2	1.027
Final R indices [$I > 2\sigma(1)$]	$R_1 = 0.0822$, $wR_2 = 0.2443$
R indices (all data)	$R_1 = 0.1390$, $wR_2 = 0.3011$
Largest diff. peak and hole ($eÅ^{-3}$)	0.735 and -0.457

SECTION-B2

6B.8 Correlation of the X-Ray Crystallographic and Computational Molecular Modelled Data of FFMMMC and FFMPMC:

The crystal structure of **FFMMMC** reveals that it is in a quaternary ammonium cationic form with a perchlorate counter anion. In **Scheme 6B.1,** the tautomer's of **FFMMMC** are shown. As a result, its structural characteristics in free molecular **FFMMC** and in protonated form are likely to differ in many structural and geometric parameters. We performed computational investigations on the molecule **FFMMMC** in its free form (gaseous state) in order to understand the quantum mechanical aspects and structural parameters of the molecule. The Austin Model-1 (AM1) semi-empirical method and the ChemSoft MM2 method that generates energy-minimized molecules by a force field Self-Consistent Field (SCF) approach, besides a structure from a more reliable and advanced density functional theory (DFT) applicable for many-electron and many-atom molecular systems, are employed to arrive at the structural features of **FFMMMC**. Similar calculations have been accomplished on the tautomers of the protonated form of it. The DFT method is taken as the more reliable one because it takes into consideration all those criteria of AM1 and MM2 besides various inter-electronic interactions through functional (rather than simple electronic wave functions), famously known as the B3LYP (Becke, 3-parameter, Lee–Yang–Parr) method. We compare the experimental single crystal XRD data with the molecular structure data obtained from various competing and progressing platforms, to correlate the geometry of **FFMMMC** in free and solid state forms. This experiment would also serve as evidence of the above-mentioned three computational approaches with regard to their consistency and usability.

Tables 6B.4, **6B.5** and **6B.6** display the bond lengths, bond angles, dihedral angles, and torsional angles generated from single crystal XRD studies of **FFMMMC**. Though the effect of the perchlorate ion is not considered in the modelled structures, the tabulated computational values are in good agreement with the results of experimental XRD data. Wherever any larger deviations are found, they are attributable to the reality that XRD studies are for a multi-molecular solid state material with intermolecular and interionic interactions, whereas the modelled data, particularly those from MM2 and AM1, are for an isolated cationic form. In these tables, the Klyne-Prelog nomenclature has been adopted such that s = syn, a = anti, p = peri-planar (0+300 and 180+300), and c = clinal.

A careful examination of **Table 6B.4** reveals that B3LYP's deviations from theoretically calculated bond lengths are quite small and, as expected, are in better agreement with empirical d ata than the other two methods used, MM2 and AM1.

Table 6B.5 displays important selected bond angles at various regions of the **FFMMMC.** Because of the 3-dimensional and all-single-bonded torsional and spanning nature of C-sp3, the bond angles, arrived at by modelling and those obtained from XRD studies, differ marginally. **Table 6B.6** shows a variation of dihedral angles. According to both computational and experimental data, the methoxy benzene moiety is nearly perpendicular to the remaining molecular skeleton. Many of the dihedral angles obtained by XRD correlate quite well with those calculated. The values acquired from the DFT/B3LYP appear to be in greater agreement with the experimental data than those generated from the other two platforms, namely, AM1 and MM2, in almost all situations of computational approaches, as expected. The dihedral angles of H_{11}-C_{11}-C_{12}-H_{12} and N_4-C_{13}-C_{14}-C_{15} are shifted from +sp to +ap using the AM1, MM2, and B3LYP methods, whereas the dihedral angles of C_7-C_2-C_3-H_3 and N_4-C_{13}-C_{14}-C_{15} are shifted from –ap to +ap. H_3-C_3-C_4-C_5 conformation +ap changed to –ap, while C_3-C_4-C_5-C_6 conformation +sp changed to –sp. H_{29A}-C_{29}-C_{30}-H_{30B} conformation +sc changed to –sc. In all approaches, the –sc conformation of H_{18B}-C_{18}-C_{19}-N_4 was transformed to +ac while the conformation –sc of C_6-C_5-C_8-C_{20} turned out to be +ac on B3LYP, to –sc on AM1, and to +sp on AM1. The conformation, +sp, of C_{20}-C_8-C_9-H_9 is found to be -sp on B3LYP but -ap on both AM1 and MM2 platforms, whereas the -*ap* of C_{20}-C_8-C_9-H_9 to +*ap* on both B3LYP and AM1 but to -*sp* on MM2 and the -*sp* of C_5-C_6-C_7-H_7 to +*ap* on B3LYP and AM1 but to +*sp* on MM2.

In **Table 6B.7** and **Table 6B.8** are placed a set of structural parameters of bond lengths, bond angles and dihedral angles excerpted from **Table 6B.4**, **Table 6B.5** and **Table 6B.6** at the core of the molecule shown in **Figure 6B.13**. Though in the gaseous state and as a solute in certain possible solvents, the molecule, **FFMMMC**¸ is expected to exhibit tautomeric equilibrium as mentioned in **Scheme 6B.1**, it would settle into the most stable form in the solid state, governed by many aspects, including intermolecular and interionic interactions. A few years back, a series of compounds with a core moiety similar to the one shown in **Figure 6B.13** were investigated theoretically on B3LYP simulation to evaluate the tautomeric equilibria in the gaseous state and in some selected solvents[13]**.** The results were compared to the experimental solid state structural

data of two synthesized compounds. Global minimized structures of **FFMMMC** ligand is depicted at **Figure 6B.12.** The numbering adaptation is shown in **Figure 6B.12** for subsequent reference in the discussion**.** To visualize the molecular disposition in space and to provide a 3D visual of it, the anaglyph picture and stereographic representation of the **FFMMMC** are given in **Figure 6B.13** and **Figure 6B.14**, respectively. Conformational analysis plots of **FFMMMC** are shown in **Figure 6B.15** through **Figure 6B.30**. The HOMO and LUMO molecular orbitals and their corresponding energies of **FFMMMC** are shown in **Figure 6B.31**. Despite the fact that the MOs' absolute energies are considerably different, the band gap between the HOMO and LUMO of **FFMMMC** in the AM1, B3LYP, and MM2 computational methods is around 0.19, 0.135, and 0.992 eV, respectively. **Table 6B.3** shows important molecular energy data obtained from three different computational platforms. A detailed look at the crystallographic data of **FFMMMC** indicates that all the carbon and nitrogen atoms are predominantly in their sp^2 hybridization, suggesting that the core moiety shown in **Figure 6B.31** is essentially planar.

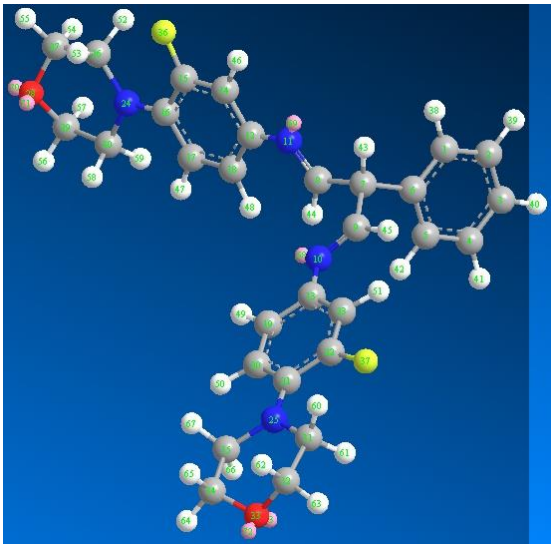

Figure 6B.12: *MM2-energy-minimized structure of* ***FFMPMC*** *(keto form)*

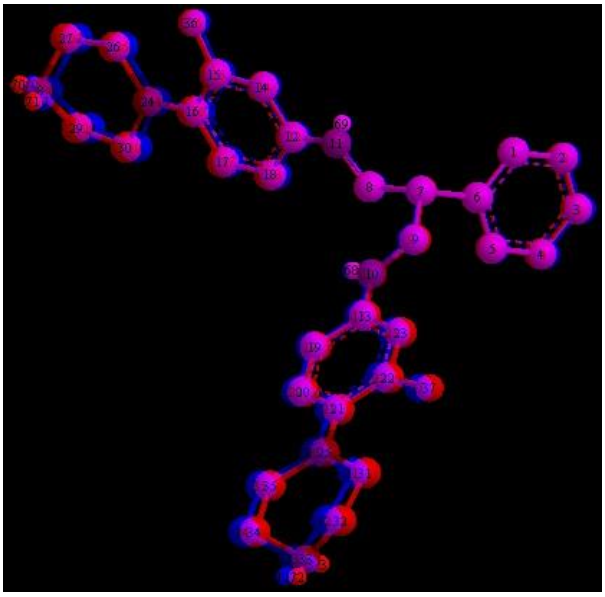

Figure 6B.13: *MM2-energy-minimized anaglyph structure of* ***FFMPMC*** *(keto form)*

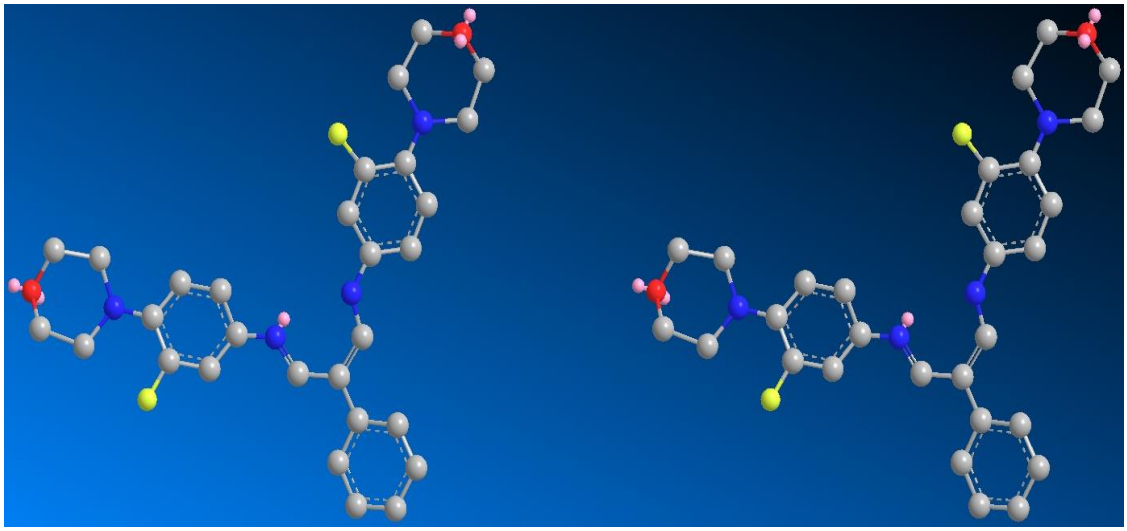

Figure 6B.14*: Stereographic projection of MM2-minimized structure of* ***FFMPMC*** *(enamine form) obtained from ChemDrawPro*

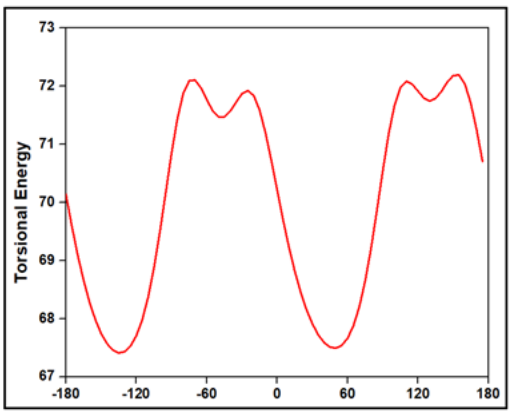

***Figure 6B.15**: Conformational analysis over C6-C7*

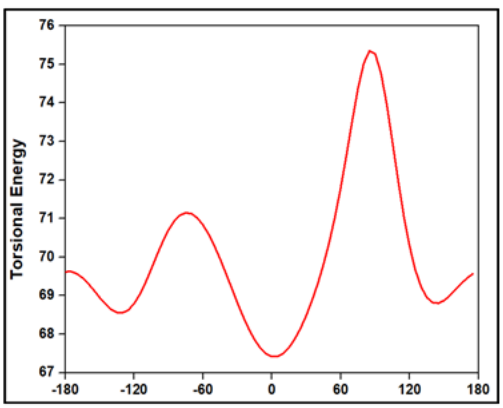

***Figure 6B.16**: Conformational analysis over C7-C9*

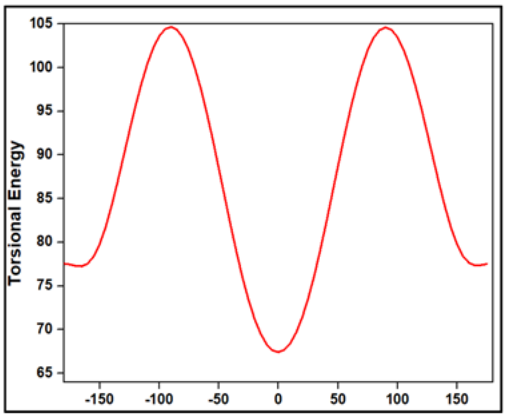

***Figure 6B.17**: Conformational analysis over N10-C13*

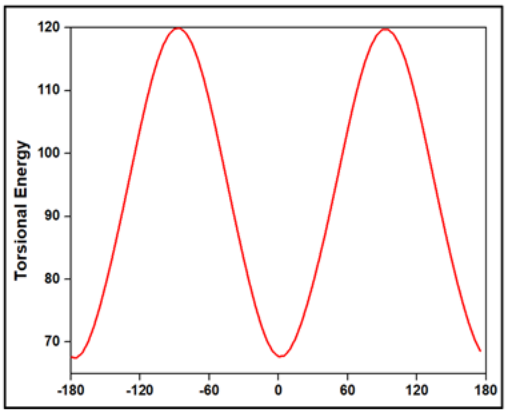

***Figure 6B.18**: Conformational analysis over C21-N25*

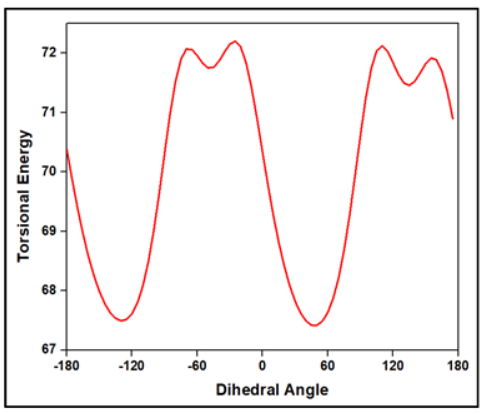

***Figure 6B.19:** Conformational analysis over C5-C6-C7-C9*

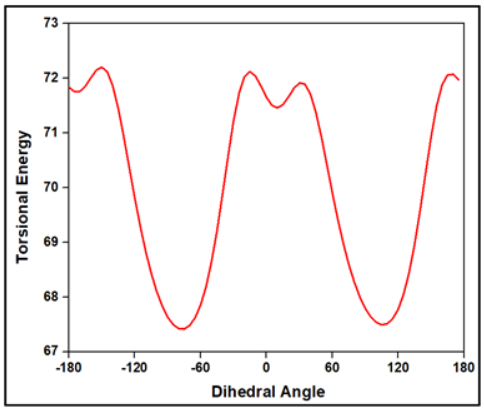

***Figure 6B.20:** Conformational analysis over C5-C6-C7-C8*

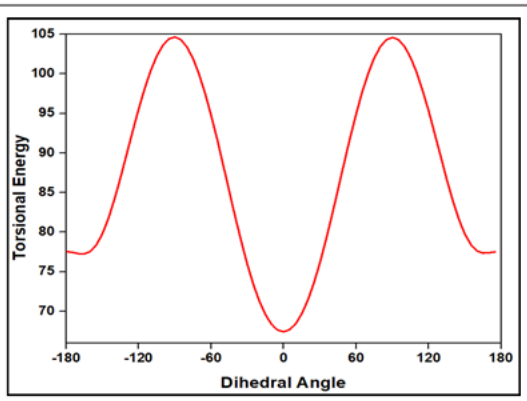

Figure 6B.21: *Conformational analysis over C9-N10-C13-C23*

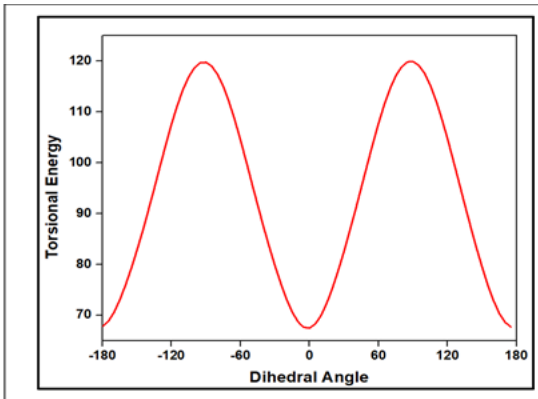

Figure 6B.22: *Conformational analysis over C22-C21-N25-C31*

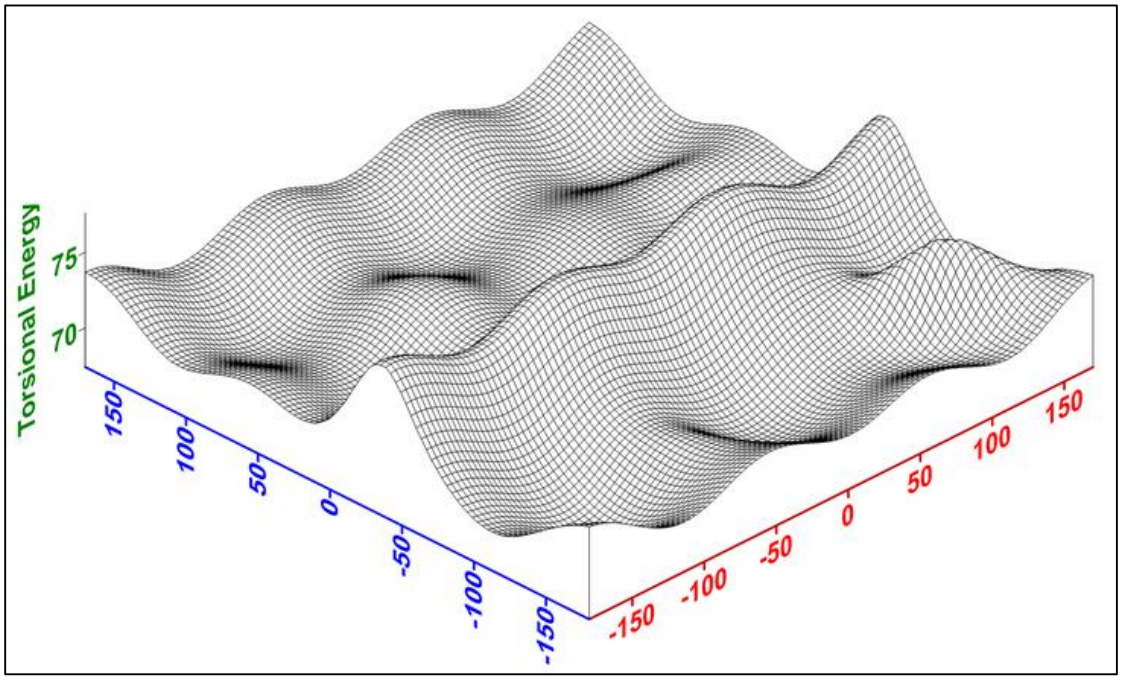

Figure 6B.23: *Double dihedral torsional energy Surfer plot of* ***FFMPMC*** *(keto form) C8-C7 (on axis shown in blue) and C7-C9 (on axis shown in red) bonds (Refer* ***Figure 6B.12*** *for numbering of the atoms)*

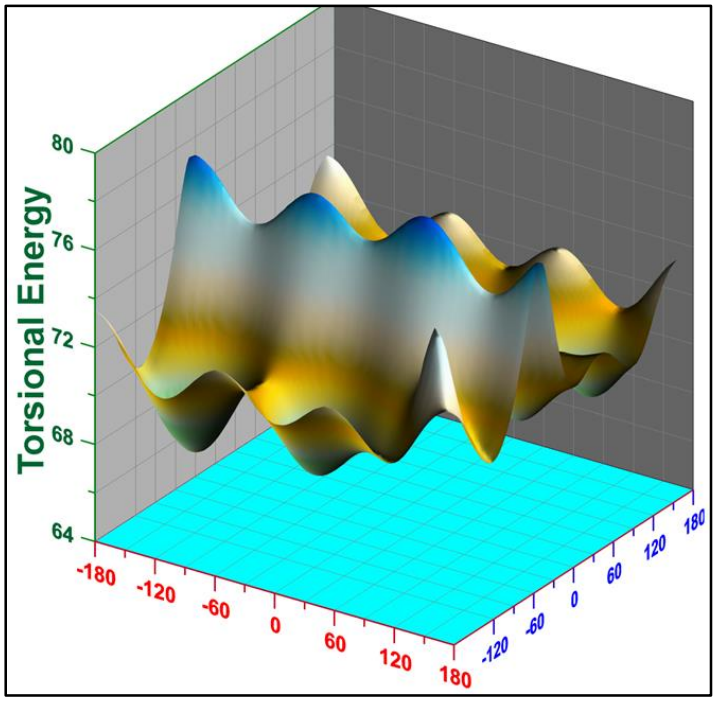

Figure 6B.24: *Double dihedral torsional energy Grapher plot of* ***FFMPMC*** *(keto form) C8-C7 (on axis shown in blue) and C7-C9 (on axis shown in red) bonds (Refer* ***Figure 6B.12*** *for numbering of the atoms)*

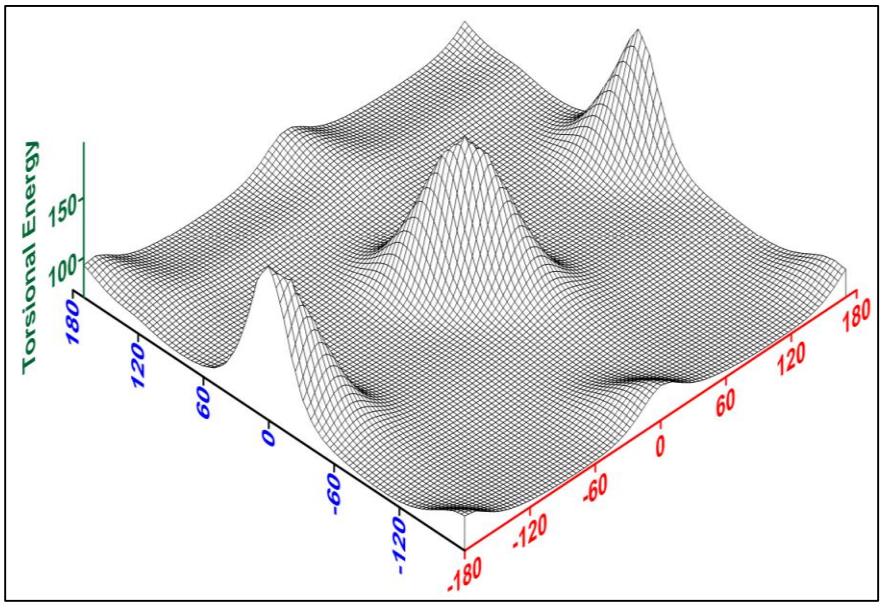

Figure 6B.25: *Double dihedral torsional energy Surfer plot of* ***FFMPMC*** *(keto form) C6-C7 (on axis shown in blue) and C7-C8 (on axis shown in red) bonds (Refer* ***Figure 6B.12*** *for numbering of the atoms)*

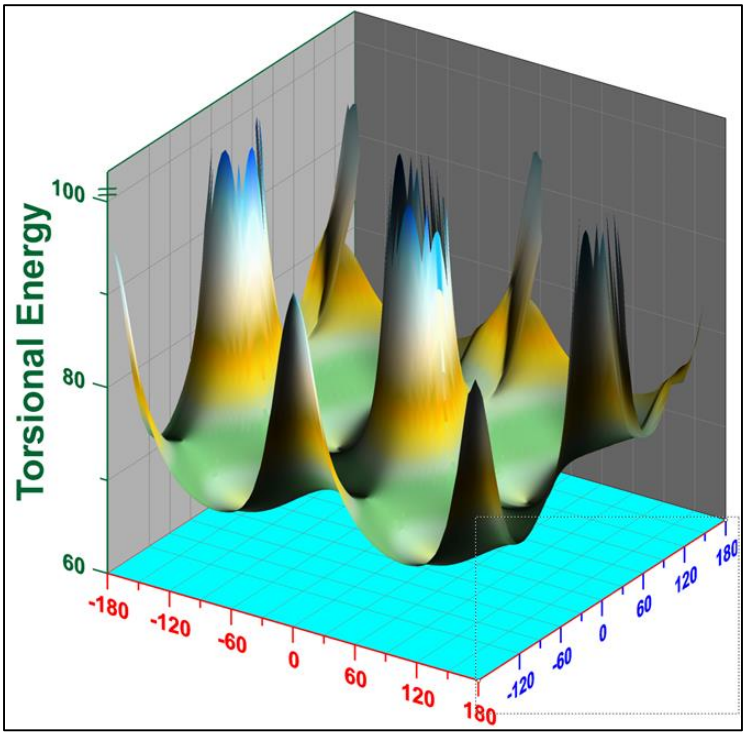

Figure 6B.26: *Double dihedral torsional energy Grapher plot of* ***FFMPMC*** *(keto form) C6-C7 (on axis shown in blue) and C7-C8 (on axis shown in red) bonds (Refer* ***Figure 6B.12*** *for numbering of the atoms)*

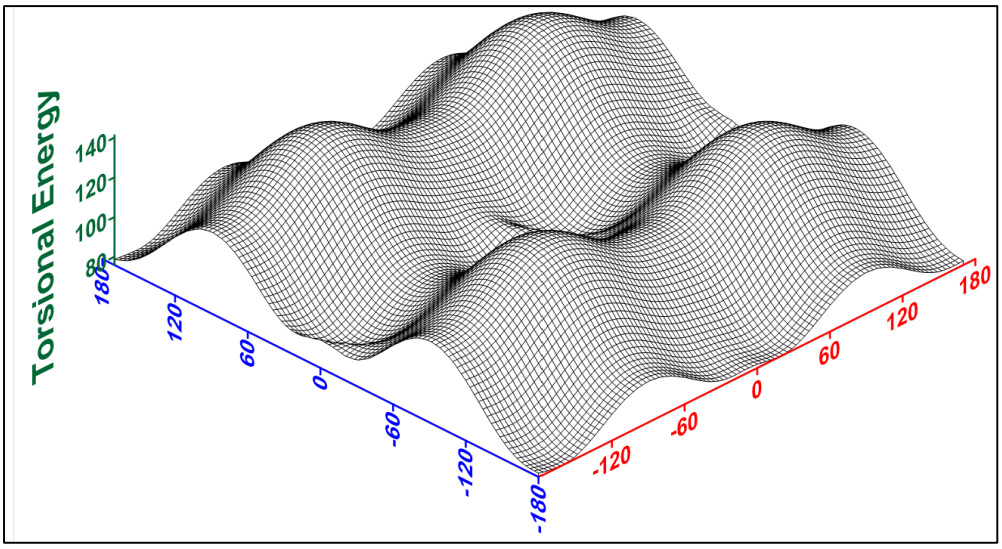

Figure 6B.27: *Double dihedral torsional energy Surfer plot of* ***FFMPMC*** *(keto form) C6-C7 (on axis shown in blue) and C7-C9 (on axis shown in red) bonds (Refer* ***Figure 6B.12*** *for numbering of the atoms)*

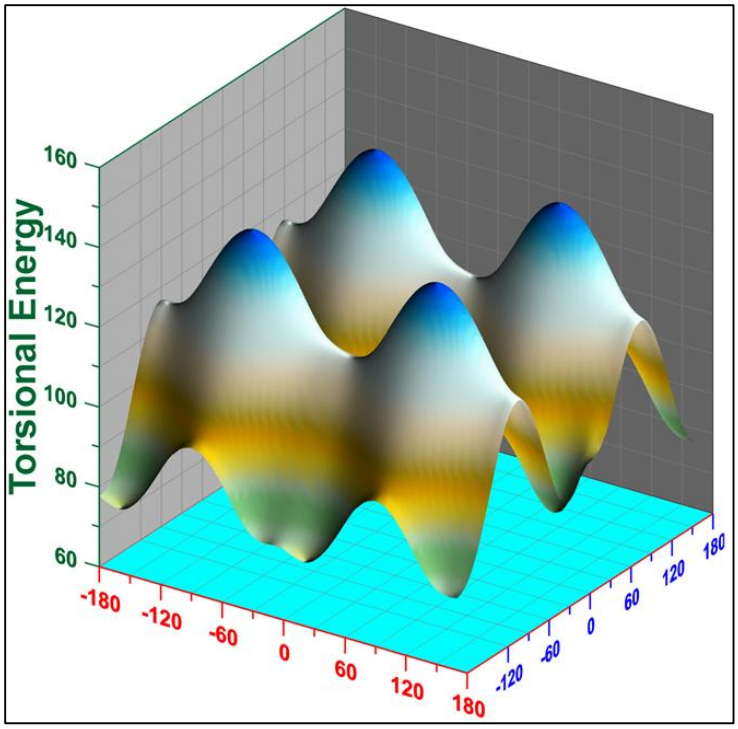

Figure 6B.28: *Double dihedral torsional energy Grapher plot of* ***FFMPMC*** *(keto form) C6-C7 (on axis shown in blue) and C7-C9 (on axis shown in red) bonds (Refer* ***Figure 6B.12*** *for numbering of the atoms)*

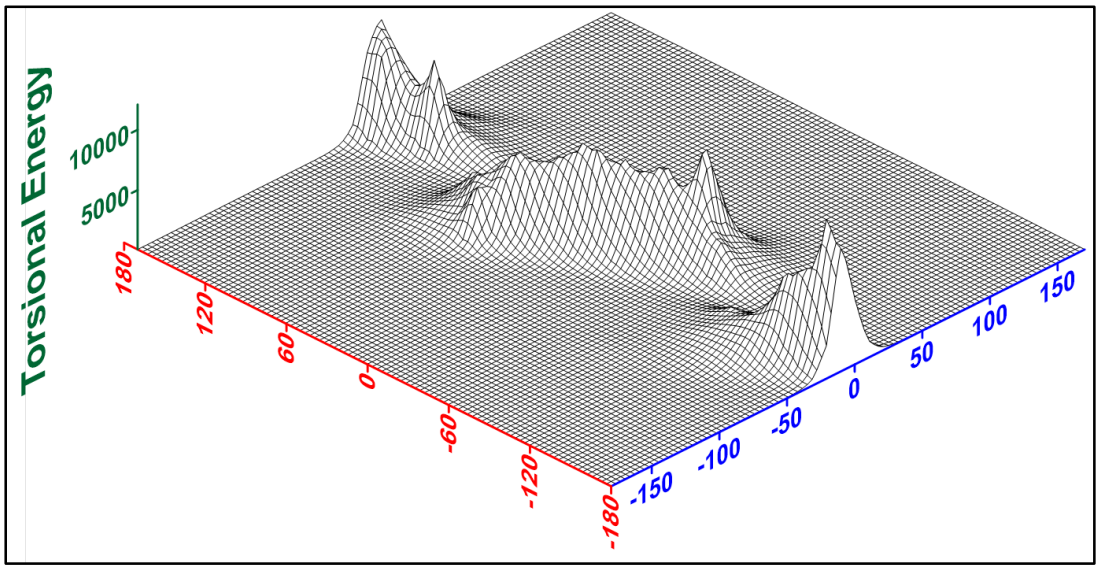

Figure 6B.29: *Double dihedral torsional energy Surfer plot of* ***FFMPMC*** *(enamine form) C8-N11 (on axis shown in red) and N11-C12 (on axis shown in blue) bonds (Refer* ***Figure 6B.12*** *for numbering of the atoms)*

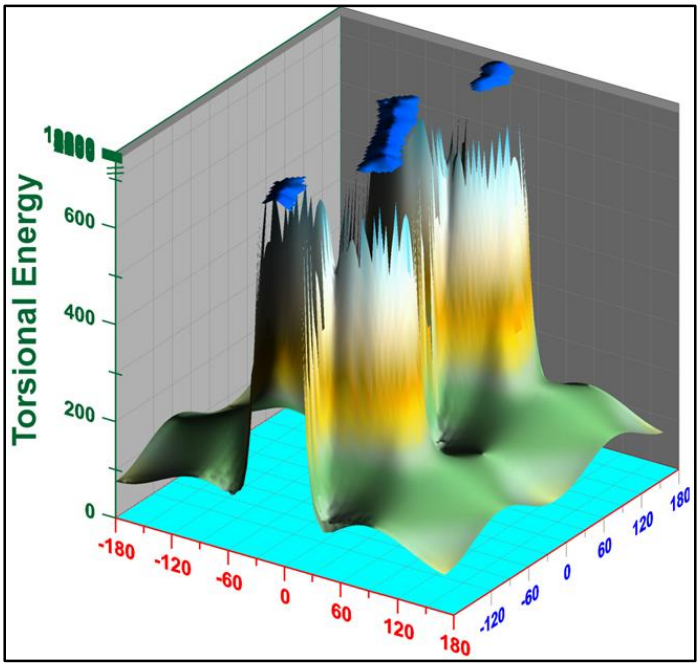

Figure 6B.30: *Double dihedral torsional energy Grapher plot of* ***FFMPMC*** *(enamine form) C8-N11 (on axis shown in blue) and N11-C12 (on axis shown in red) bonds (Refer* ***Figure 6B.12*** *for numbering of the atoms)*

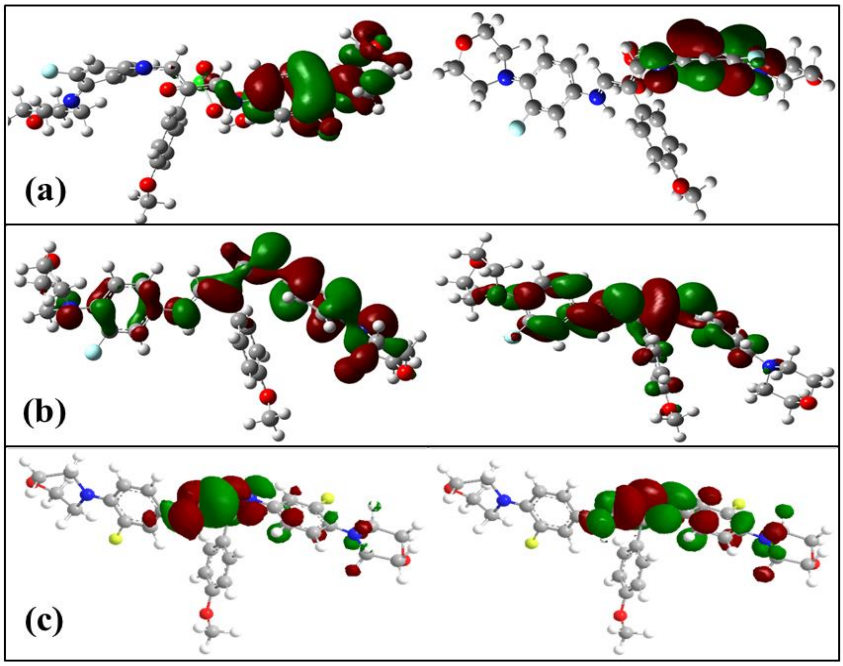

Figure 6B.31: *HOMO-LUMO orbitals of* ***FFMMMC*** *obtained from (a) AM1 (b) B3LYP (c) MM2*

Table 6B.3: *Important molecular energy data evaluated by AM1, B3LYP and MM2 calculations on* ***FFMMMC***

Parameter	**AM1**	**B3LYP**	**MM2**
E_{HOMO} (eV)	-0.393	-0.175	-1.300
E_{LUMO} (eV)	-0.203	-0.040	-0.308
I (eV) Ionization Potential	0.393	0.175	1.300
A (eV) Electron affinity	0.203	0.040	0.308
η (eV) Chemical hardness	0.095	0.067	0.496
μ (eV) Chemical potential	0.298	0.107	0.804
χ (eV) Electro negativity	-0.298	-0.107	-0.804
S (eV^{-1}) Global softness	5.263	7.463	1.008

Table 6B.4: *Comparative list of selected bond lengths(Å) of* ***FFMMMC***

Bond	Bond type	Bond lengths (Å)				Fractional Variation (Δ/XRD)		
		XRD	**AM1**	**MM2**	**B3LYP**	**AM1**	**MM2**	**B3LYP**
$H_{1A} – C_1$	$H–Csp^3$	0.960	1.093	1.113	1.098	-0.139	0.159	-0.144
$H_{1B} – C_1$	$H–Csp^3$	0.960	1.113	1.100	1.097	-0.159	-0.146	-0.143
$H_{1C} – C_1$	$H–Csp^3$	0.961	1.100	1.111	1.091	-0.145	-0.156	-0.135
$C_1 – O_3$	$Osp^3 – Csp^3$	1.369	1.452	1.409	1.418	-0.061	-0.029	-0.036
$C_2 – C_3$	$Csp^2–Csp^2$	1.356	1.405	1.345	1.404	-0.036	0.008	-0.035
$C_2 – C_7$	$Csp^2–Csp^2$	1.353	1.416	1.344	1.398	-0.047	0.007	-0.033
$C_2 – O_3$	$Osp^3 – Csp^2$	1.385	1.364	1.374	1.364	0.015	0.008	0.015
$C_7 – C_2$	$Csp^2–Csp^2$	1.383	1.412	1.345	1.407	-0.021	0.027	-0.017
$C_3 – H_3$	$Csp^2 –H$	0.931	1.087	1.102	1.085	-0.168	-0.184	-0.165

$C_3 – C_4$	$Csp^2–Csp^2$	1.406	1.393	1.344	1.386	0.009	0.044	0.014
$C_4 – H_4$	$Csp^3–H$	0.930	1.100	1.102	1.086	-0.183	-0.185	-0.168
$C_4 – C_5$	$Csp^2–Csp^2$	1.375	1.403	1.351	1.408	-0.020	0.017	-0.024
$C_5 – C_6$	$Csp^2–Csp^2$	1.380	1.410	1.350	1.401	-0.022	0.022	-0.015
$C_5 – C_8$	$Csp^2–Csp^2$	1.502	1.472	1.363	1.490	0.020	0.093	0.008
$C_6 – H_6$	$Csp^2–H$	0.929	1.092	1.100	1.087	-0.175	-0.184	-0.170
$C_6 – C_7$	$Csp^2–Csp^2$	1.383	1.385	1.342	1.398	-0.001	0.030	-0.011
$C_7 – H_7$	$Csp^2–H$	0.930	1.091	1.104	1.084	-0.173	-0.187	-0.166
$C_8 – C_9$	$Csp^2–Csp^2$	1.376	1.463	1.356	1.370	-0.063	0.015	0.004
$C_8 – C_{20}$	$Csp^2 – Csp^2$	1.390	1.357	1.357	1.464	0.024	0.024	-0.053
$C_9 – H_9$	$Csp^2–H$	0.931	1.118	1.096	1.085	-0.201	-0.177	-0.165
$C_9 – N_3$	$Csp^2 – Nsp^2$	1.323	1.321	1.273	1.363	0.002	0.038	-0.030
$C_{10} – C_{11}$	$Csp^3 – Csp^2$	1.376	1.405	1.341	1.401	-0.021	0.025	-0.018
$C_{10} – C_{15}$	$Csp^2 – Csp^2$	1.387	1.407	1.341	1.404	-0.014	0.033	-0.012
$C_{10} – N_3$	$Csp^2 – Nsp^2$	1.428	1.445	1.275	1.402	-0.012	0.107	0.018
$C_{11} – H_{11}$	$Csp^2 – H$	0.929	1.097	1.105	1.084	-0.181	-0.189	-0.167
$C_{11} – C_{12}$	$Csp^2 – Csp^2$	1.395	1.388	1.342	1.394	0.005	0.038	0.001
$C_{12} – H_{12}$	$Csp^2 – H$	0.930	1.103	1.098	1.084	-0.186	-0.181	-0.166
$C_{12} – C_{13}$	$Csp^2 – Csp^2$	1.374	1.413	1.353	1.403	-0.028	0.015	-0.021
$C_{13} – C_{14}$	$Csp^2 – Csp^2$	1.395	1.428	1.358	1.406	-0.024	0.027	-0.008
$C_{13} – N_4$	$Csp^2 – Nsp^3$	1.421	1.422	1.285	1.415	-0.001	0.096	0.004
$C_{14} – C_{15}$	$Csp^2– Csp^2$	1.373	1.389	1.346	1.382	-0.012	0.020	-0.007
$C_{14} – F_2$	$Csp^2– F$	1.354	1.332	1.323	1.353	0.016	0.023	0.001
$C_{15} – H_{15}$	$Csp^2 – H$	0.930	1.091	1.102	1.086	-0.173	-0.185	-0.168
$C_{16}– H_{16A}$	$Csp^3 – H$	0.970	1.114	1.115	1.100	-0.148	-0.149	-0.134

$C_{16} – H_{16B}$	$Csp^3 – H$	0.970	1.119	1.106	1.092	-0.154	-0.140	-0.126
$C_{16} – C_{17}$	$Csp^3 – C\ sp^3$	1.492	1.541	1.528	1.555	-0.033	-0.024	-0.042
$N_4 – C_{16}$	$Nsp^3 – Csp^3$	1.461	1.493	1.490	1.464	-0.022	-0.020	-0.002
$H_{17A} – C_{17}$	$H – Csp^3$	0.971	1.106	1.115	1.094	-0.139	-0.148	-0.127
$H_{17B} – C_{17}$	$H – Csp^3$	0.970	1.103	1.115	1.102	-0.137	-0.149	-0.136
$O_2 – C_{17}$	$Osp^3 – Csp^3$	1.420	1.439	1.402	1.417	-0.013	0.013	0.002
$C_{18} – H_{18A}$	$Csp^3 – H$	0.970	1.103	1.115	1.103	-0.137	-0.149	-0.137
$C_{18} – H_{18B}$	$Csp^3 – H$	0.970	1.105	1.115	1.094	-0.139	-0.149	-0.128
$C_{18} – C_{19}$	$Csp^3 – Csp^3$	1.498	1.544	1.529	1.550	-0.031	-0.021	-0.035
$C_{18} – O_2$	$Csp^3 – Osp^3$	1.422	1.439	1.402	1.426	-0.012	0.014	-0.003
$C_{19} – H_{19A}$	$Csp^3 – H$	0.970	1.108	1.116	1.091	-0.142	-0.151	-0.125
$C_{19} – N_4$	$Csp^3 – Nsp^3$	1.468	1.492	1.486	1.465	-0.016	-0.012	0.002
$C_{20} – H_{20}$	$Csp^2 – H$	0.930	1.115	1.095	1.097	-0.199	-0.177	-0.180
$C_{20} – N_2$	$Csp^2 – Nsp^3$	1.317	1.408	1.267	1.285	-0.069	0.038	0.024
$C_{21} – C_{22}$	$Csp^2 – Csp^2$	1.384	1.490	1.345	1.406	-0.077	0.028	-0.016
$C_{21} – C_{26}$	$Csp^2 – Csp^2$	1.397	1.492	1.343	1.402	-0.068	0.039	-0.004
$C_{21} – N_2$	$Csp^2 – Nsp^3$	1.417	1.288	1.271	1.417	0.091	0.103	0.000
$C_{22} – H_{22}$	$Csp^2 – Csp^2$	0.930	1.096	1.106	1.084	-0.178	-0.189	-0.166
$C_{22} – C_{23}$	$Csp^2 – Csp^2$	1.366	1.345	1.345	1.381	0.015	0.015	-0.011
$C_{23} – C_{24}$	$Csp^2 – Csp^2$	1.394	1.493	1.356	1.407	-0.071	0.027	-0.009
$C_{23} – F_1$	$Csp^2 – F$	1.362	1.327	1.325	1.358	0.026	0.027	0.003
$C_{24} – C_{25}$	$Csp^2 – Csp^2$	1.394	1.483	1.353	1.403	-0.064	0.029	-0.006
$C_{21} – N_2$	$Csp^2 – Nsp^3$	1.415	1.315	1.286	1.415	0.071	0.091	0.000
$C_{25} – H_{25}$	$Csp^2 – H$	0.930	1.094	1.101	1.084	-0.176	-0.184	-0.166
$C_{24} – N_1$	$Csp^2 – Nsp^3$	1.415	1.315	1.286	1.415	0.071	0.091	0.000

$C_{25} - C_{26}$	$Csp^2 - Csp^2$	1.375	1.339	1.343	1.394	0.026	0.023	-0.014
$C_{26} - H_{26}$	$Csp^2 - H$	0.931	1.105	1.102	1.085	-0.187	-0.184	-0.165
$C_{27} - H_{27A}$	$Csp^3 - H$	0.970	1.121	1.118	1.105	-0.156	-0.153	-0.139
$C_{27} - H_{27B}$	$Csp^3 - H$	0.970	1.110	1.116	1.090	-0.144	-0.151	-0.124
$C_{27} - C_{28}$	$Csp^3 - Csp^3$	1.502	1.547	1.529	1.526	-0.030	-0.018	-0.016
$C_{27} - N_1$	$Csp^3 - Nsp^3$	1.466	1.491	1.486	1.471	-0.017	-0.014	-0.003
$C_{28} - H_{28A}$	$Csp^3 - H$	0.970	1.105	1.115	1.094	-0.139	-0.149	-0.128
$C_{28} - H_{28B}$	$Csp^3 - H$	0.970	1.110	1.115	1.102	-0.144	-0.149	-0.136
$C_{28} - O_1$	$Csp^3 - Osp^3$	1.428	1.429	1.402	1.422	-0.001	0.018	0.004
$C_{29} - H_{29A}$	$Csp^3 - H$	0.970	1.108	1.115	1.094	-0.142	-0.149	-0.128
$C_{29} - H_{29B}$	$Csp^3 - H$	0.969	1.109	1.115	1.102	-0.144	-0.151	-0.137
$C_{29} - C_{30}$	$Csp^3 - Csp^3$	1.515	1.541	1.145	1.528	-0.017	0.244	-0.009
$C_{29} - O_1$	$Csp^3 - Osp^3$	1.422	1.436	1.402	1.412	-0.010	0.014	0.007
$C_{30} - H_{30A}$	$Csp^3 - H$	0.970	1.115	1.117	1.106	-0.149	-0.152	-0.140
$C_{30} - H_{30B}$	$Csp^3 - H$	0.971	1.124	1.118	1.095	-0.158	-0.151	-0.128
$C_{30} - N_1$	$Csp^3 - Nsp^3$	1.457	1.499	1.490	1.459	-0.029	-0.023	-0.001

Table 6B.5: *Comparative list of selected bond angles (°) of* ***FFMMMC***

Atomic String	Central Atom	XRD	B3LYP	AM1	MM2	Variation from XRD data (%)		
						B3LYP	**AM1**	**MM2**
H_{1A}-C_1-H_{1B}	Csp^3	109.5	109.1	112.3	111.9	0.37	2.56	2.19
H_{1A}-C_1-H_{1C}	Csp^3	109.5	109.2	110.8	108.2	0.27	1.19	1.19
H_{1A}-C_1-O_3	Csp^3	109.5	111.5	110.4	110.4	1.83	0.82	0.82
H_{1B}-C_1-H_{1C}	Csp^3	109.4	109.2	110.9	108.1	0.18	1.37	1.19
H_{1B}-C_1-O_3	Csp^3	109.4	111.5	110.4	107.8	1.92	0.91	1.46

H_{1B}-C_1-O_3	Csp^3	109.4	111.5	110.4	107.8	1.92	0.91	1.46
H_{1C}-C_1-O_3	Csp^3	109.4	105.9	101.4	110.3	3.20	7.31	0.82
C_3-C_2-O_3	Csp^2	123.2	115.7	125.9	126.0	6.09	2.19	2.27
C_7-C_2-O_3	Csp^2	115.2	124.8	112.6	119.3	8.33	2.26	3.56
C_2-C_3-H_3	Csp^2	120.5	118.4	121.3	120.4	1.74	0.66	0.08
C_2-C_3-C_4	Csp^2	119.0	120.3	118.7	122.3	1.09	0.25	2.77
C_2-C_3-C_4	Csp^2	119.0	120.3	118.7	122.3	1.09	0.25	2.77
H_3-C_3-C_4	Csp^2	120.5	121.1	119.9	117.3	0.50	0.50	2.66
C_3-C_4-H_4	Csp^2	119.6	119.3	119.4	114.2	0.25	0.17	4.52
C_3-C_4-C_5	Csp^2	120.8	121.3	120.5	123.6	0.41	0.25	2.32
H_4-C_4-C_5	Csp^2	119.6	119.3	119.9	122.1	0.25	0.25	2.09
C_4-C_5-C_6	Csp^2	117.8	117.5	120.0	113.4	0.25	1.87	3.74
C_4-C_5-C_8	Csp^2	122.3	121.0	120.1	122.8	1.06	1.80	0.41
C_6-C_5-C_8	Csp^2	119.9	121.4	119.8	123.8	1.25	0.08	3.25
C_5-C_6-H_6	Csp^2	119.2	119.3	119.7	122.6	0.08	0.42	2.85
C_5-C_6-C_7	Csp^2	121.7	121.8	120.2	123.2	0.08	1.23	1.23
H_6-C_6-C_7	Csp^2	119.2	118.7	119.9	114.1	0.42	0.59	4.28
C_2-C_7-C_6	Csp^2	119.2	119.5	119.0	122.9	0.25	0.17	3.10
C_2-C_7-H_7	Csp^2	120.4	121.1	119.1	118.2	0.58	1.08	1.83
C_6-C_7-H_7	Csp^2	120.4	121.1	119.1	118.2	0.58	1.08	1.83
C_6-C_7-H_7	Csp^2	120.4	119.3	121.8	118.9	0.91	1.16	1.25
C_5-C_8-C_9	Csp^2	122.6	120.4	119.4	119.0	1.79	2.61	2.94
C_5-C_8-C_{20}	Csp^2	121.8	124.5	124.7	122.8	2.22	2.38	0.82
C_9-C_8-C_{20}	Csp^2	115.6	114.8	115.6	118.2	0.69	0.00	2.25
C_8-C_9-H_9	Csp^2	117.1	119.2	117.4	120.7	1.79	0.26	3.07
C_8-C_9-N_3	Csp^2	125.9	125.7	122.5	127.3	0.16	2.70	1.11

H_9-C_9-N_3	Csp^2	117.0	114.9	119.7	111.9	1.79	2.31	4.36
C_{11}-C_{10}-C_{15}	Csp^2	119.5	118.3	120.9	115.8	1.00	1.17	3.10
C_{15}-C_{10}-N_3	Csp^2	116.7	118.0	118.8	126.9	1.11	1.80	8.74
C_{10}-C_{11}-H_{11}	Csp^2	120.4	120.9	121.2	120.3	0.42	0.66	0.08
C_{10}-C_{11}-C_{12}	Csp^2	119.2	120.4	119.6	121.3	1.01	0.34	1.76
H_{11}-C_{11}-C_{12}	Csp^2	120.4	118.6	119.1	118.4	1.50	1.08	1.66
C_{11}-C_{12}-H_{12}	Csp^2	118.4	118.5	118.5	113.0	0.08	0.08	4.56
C_{11}-C_{12}-C_{13}	Csp^2	123.2	122.4	121.9	124.2	0.65	1.06	0.81
H_{12}-C_{12}-C_{13}	Csp^2	118.4	119.0	119.4	122.9	0.51	0.84	3.80
C_{12}-C_{13}-C_{14}	Csp^2	115.4	115.4	116.2	113.6	0.00	0.69	1.56
C_{12}-C_{13}-N_4	Csp^2	124.9	125.4	123.1	121.5	0.40	1.44	2.72
C_{14}-C_{13}-N_4	Csp^2	119.6	119.1	120.1	124.9	0.42	0.42	4.43
C_{13}-C_{14}-C_{15}	Csp^2	123.4	123.5	123.1	122.5	0.08	0.24	0.73
C_{13}-C_{14}-F_2	Csp^2	119.0	118.7	120.3	123.6	0.25	1.09	3.87
C_{15}-C_{14}-F_2	Csp^2	117.6	117.7	116.4	113.9	0.09	1.02	3.15
C_{10}-C_{15}-C_{14}	Csp^2	119.3	119.7	117.9	122.7	0.34	1.17	2.85
C_{10}-C_{15}-H_{15}	Csp^2	120.3	121.5	121.5	120.6	1.00	1.00	0.25
H_{16A}-C_{16}-H_{16B}	Csp^3	108.3	106.9	105.5	110.0	1.29	2.59	1.57
H_{16A}-C_{16}-H_{17}	Csp^3	109.8	109.4	110.6	107.3	0.36	0.73	2.28
H_{16A}-C_{16}-N_4	Csp^3	109.9	108.8	106.1	108.3	1.00	3.46	1.46
H_{16B}-C_{16}-C_{17}	Csp^3	109.9	111.4	110.7	105.1	1.36	0.73	4.37
H_{16B}-C_{16}-C_{17}	Csp^3	109.9	109.4	110.3	105.1	0.45	0.36	4.37
H_{16B}-C_{16}-N_4	Csp^3	109.9	108.4	110.7	111.5	1.36	0.73	1.46
C_{17}-C_{16}-N_4	Csp^3	109.1	111.4	113.1	114.6	2.11	3.67	5.04
C_{16}-C_{17}-H_{17A}	Csp^3	109.3	110.6	112.6	110.5	1.19	3.02	1.10
C_{16}-C_{17}-H_{17B}	Csp^3	109.4	111.4	112.1	111.6	1.83	2.47	2.01

C_{16}-C_{17}-O_2	Csp^3	111.4	110.2	110.8	110.9	1.08	0.54	0.45
H_{17A}-C_{17}-H_{17B}	Csp^3	108.0	107.5	109.7	106.5	0.46	1.57	1.39
O_2-C_{17}-H_{17A}	Csp^3	109.4	106.4	110.9	107.8	2.74	1.37	1.46
O_2-C_{17}-H_{17B}	Csp^3	109.7	110.4	109.2	109.3	0.64	0.46	0.36
H_{18A}-C_{18}-H_{18B}	Csp^3	107.9	108.2	109.7	106.4	0.28	1.67	1.39
H_{18A}-C_{18}-C_{19}	Csp^3	109.3	110.3	116.7	110.6	0.91	6.77	1.19
H_{18A}-C_{18}-O_2	Csp^3	109.2	110.3	108.9	107.8	1.01	0.27	1.28
H_{18B}-C_{18}-C_{19}	Csp^3	109.3	111.1	112.6	111.6	1.65	3.02	2.10
O_2-C_{18}-H_{18B}	Csp^3	109.2	105.2	101.4	109.2	3.66	7.14	0.00
C_{19}-C_{18}-O_2	Csp^3	111.8	111.4	111.8	111.2	0.36	0.00	0.54
C_{18}-C_{19}-H_{19A}	Csp^3	109.8	110.7	110.1	104.7	0.82	0.27	4.64
C_{18}-C_{19}-N_4	Csp^3	109.5	110.3	112.1	114.8	0.73	2.37	4.84
H_{19A}-C_{19}-H_{19B}	Csp^3	108.3	107.0	105.6	110.7	1.20	2.49	2.22
H_{19A}-C_{19}-N_4	Csp^3	109.7	107.3	111.3	108.4	2.19	1.46	1.19
H_{19B}-C_{19}-N_4	Csp^3	109.7	110.1	106.6	111.0	0.36	2.83	1.19
C_8-C_{20}-H_{20}	Csp^2	117.0	112.5	121.0	118.4	3.85	3.42	1.20
C_8-C_{20}-N_2	Csp^2	126.0	133.7	127.9	127.7	6.11	1.51	1.35
H_{20}-C_{20}-N_2	Csp^2	117.1	113.6	111.0	113.9	2.99	5.21	2.73
C_{22}-C_{21}-C_{26}	Csp^2	118.6	117.8	112.7	115.0	0.67	4.97	3.04
C_{22}-C_{21}-N_2	Csp^2	119.0	118.5	119.2	116.3	0.42	0.17	2.27
C_{26}-C_{21}-N_2	Csp^2	122.4	123.1	127.6	128.7	0.57	4.25	5.15
C_{21}-C_{22}-H_{22}	Csp^2	120.4	120.5	118.5	119.0	0.08	1.58	1.16
C_{21}-C_{22}-C_{23}	Csp^2	119.2	120.0	116.4	123.6	0.67	2.35	3.69
H_{22}-C_{22}-C_{23}	Csp^2	120.4	119.4	125.0	117.4	0.83	3.82	2.49
C_{22}-C_{23}-C_{24}	Csp^2	124.5	123.4	120.6	122.1	0.88	3.13	1.93
C_{22}-C_{23}-F_1	Csp^2	117.1	117.9	121.7	114.1	0.68	3.93	2.56

C_{24}-C_{23}-F_1	Csp^2	118.4	118.6	117.5	123.8	0.17	0.76	4.56
C_{23}-C_{24}-C_{25}	Csp^2	114.9	115.6	111.4	113.4	0.61	3.05	1.31
C_{23}-C_{24}-N_1	Csp^2	120.9	120.1	126.4	124.9	0.66	4.55	3.31
C_{25}-C_{24}-N_1	Csp^2	124.1	124.1	121.8	121.6	0.00	1.85	2.01
C_{24}-C_{25}-H_{25}	Csp^2	118.9	119.3	118.7	122.4	0.34	0.17	2.94
C_{24}-C_{25}-C_{26}	Csp^2	122.3	122.0	118.1	124.6	0.25	3.43	1.88
H_{25}-C_{25}-C_{26}	Csp^2	118.8	118.5	123.0	113.0	0.25	3.54	4.88
C_{21}-C_{26}-C_{25}	Csp^2	120.5	120.9	119.3	121.3	0.33	1.00	0.66
C_{21}-C_{26}-H_{26}	Csp^2	119.7	119.3	118.0	122.1	0.33	1.42	2.01
C_{25}-C_{26}-H_{26}	Csp^2	119.8	119.7	122.5	116.6	0.08	2.25	2.67
H_{27A}-C_{27}-H_{27B}	Csp^3	108.1	108.2	106.4	110.7	0.09	1.57	2.41
H_{27A}-C_{27}-C_{28}	Csp^3	109.6	109.5	109.6	104.7	0.09	0.00	4.47
H_{27A}-C_{27}-N_1	Csp^3	109.6	109.2	108.3	111.0	0.36	1.19	1.28
H_{27B}-C_{27}-C_{28}	Csp^3	109.6	109.3	109.6	107.1	0.27	0.00	2.28
H_{27B}-C_{27}-N_1	Csp^3	109.6	110.7	113.5	108.4	1.00	3.56	1.09
C_{28}-C_{27}-N_1	Csp^3	110.3	109.5	109.2	114.8	0.73	1.00	4.08
C_{27}-C_{28}-H_{28A}	Csp^3	109.4	110.5	112.0	111.6	1.01	2.38	2.01
C_{27}-C_{28}-H_{28B}	Csp^3	109.4	109.4	111.1	111.5	0.00	1.55	1.92
C_{27}-C_{28}-O_1	Csp^3	111.3	111.5	109.9	111.2	0.18	1.26	0.09
H_{28A}-C_{28}-H_{28B}	Csp^3	108.0	108.8	109.9	110.6	0.74	1.76	2.41
O_1-C_{28}-H_{28A}	Csp^3	109.4	106.4	110.4	107.8	2.74	0.91	1.46
O_1-C_{28}-H_{28B}	Csp^3	109.4	110.0	102.9	109.2	0.55	5.94	0.18
H_{29A}-C_{28}-H_{29B}	Csp^3	108.1	108.7	109.4	106.5	0.56	1.20	1.48
H_{29A}-C_{29}-C_{30}	Csp^3	109.6	110.4	111.4	137.7	0.73	1.64	25.64
O_1-C_{29}-H_{29A}	Csp^3	109.4	106.5	111.2	109.3	2.65	1.65	0.09
H_{29B}-C_{29}-C_{30}	Csp^3	109.5	110.4	102.9	106.2	0.82	6.03	3.01

H_{29B}-C_{29}-O_1	Csp^3	109.4	110.1	102.9	107.8	0.64	5.94	1.46
C_{30}-C_{29}-O_1	Csp^3	110.8	111.5	111.6	104.3	0.63	0.72	5.87
C_{29}-C_{30}-H_{30B}	Csp^3	109.6	109.5	110.8	105.1	0.09	1.09	4.11
C_{29}-C_{30}-N_1	Csp^3	110.3	109.3	109.3	114.6	0.91	0.91	3.90
H_{30A}-C_{30}-H_{30B}	Csp^3	108.1	107.9	108.2	109.9	0.19	0.09	1.67
H_{30A}-C_{30}-N_1	Csp^3	109.6	112.2	108.5	111.5	2.37	1.00	1.73
H_{30B}-C_{30}-N_1	Csp^3	109.5	109.0	112.1	108.3	0.46	2.37	1.10
C_{24}-N_1-C_{27}	Nsp^3	114.5	116.1	124.9	120.5	1.40	9.08	5.24
C_{24}-N_1-C_{30}	Nsp^3	110.5	111.1	112.8	119.5	0.54	2.08	8.14
C_9-N_3-C_{10}	Nsp^2	124.2	127.8	122.8	133.4	2.90	1.13	7.41
C_{13}-N_4-C_{16}	Nsp^3	116.5	119.1	116.4	119.8	2.23	0.09	2.83
C_{13}-N_4-C_{19}	Nsp^3	114.7	116.3	116.3	120.6	1.39	1.39	5.14
C_{16}-N_4-C_{19}	Nsp^3	109.8	109.9	110.7	119.5	0.09	0.82	8.83
C_{28}-O_1-C_{29}	Osp^3	109.3	110.5	112.7	110.2	1.10	3.11	0.82
C_{17}-O_2-C_{18}	Osp^3	109.8	111.9	114.1	110.2	1.91	3.92	0.36
C_1-O_3-C_2	Osp^3	118.2	118.2	118.5	118.7	0.00	0.25	0.42

Table 6B.6: *Comparative list of selected torsional angles (°) of* ***FFMMMC***

Atomic String	XRD		B3LYP		AM1		MM2	
	Angle	(*)	Angle	(*)	Angle	(*)	Angle	(*)
H_{1A}-C_1-O_3-C_2	-17.4	*-sp*	+61.8	*+sc*	+62.0	*+sc*	+62.9	*+sc*
H_{1B}-C_1-O_3-C_2	-137.4	*-ac*	-179.3	*-ac*	+179.5	*+ap*	+26.7	*+sp*
H_{1C}-C_1-O_3-C_2	+102.7	*+ac*	-60.5	*-sc*	-62.8	*-sc*	+0.8	*+sp*
C_7-C_2-C_3-H_3	-178.6	*-ap*	-179.8	*-ap*	-179.5	*-ap*	+179.7	*+ap*
C_7-C_2-C_3-C_4	+1.5	*+sp*	+0.1	*+sp*	+0.2	*+sp*	+0.4	*+sp*
O_3-C_2-C_3-H_3	+0.3	*+sp*	+0.1	*+sp*	+0.4	*+sp*	-179.1	*-ap*

O_3-C_2-C_3-C_4	-179.6	*-ap*	-179.9	*-ap*	-179.9	*-ap*	+0.6	*+sp*
C_3-C_2-C_7-C_6	-0.1	*-sp*	-0.4	*-sp*	-0.3	*-sp*	+179.4	*+ap*
C_3-C_2-C_7-H_7	+180.0	*+ap*	-179.5	*-ap*	+179.6	*+ap*	+178.2	*+ap*
O_3-C_2-C_7-C_6	-178.9	*-ap*	+179.6	*+ap*	+179.7	*+ap*	+0.2	*+sp*
O_3-C_2-C_7-H_7	+1.0	*+sp*	+0.5	*+sp*	-0.3	*-sp*	+179.1	*+ap*
C_3-C_2-O_3-C_1	-8.5	*-sp*	+178.9	*+ap*	+0.8	*+sp*	-178.8	*-ap*
C_7-C_2-O_3-C_1	+170.4	*+ap*	-1.0	*-sp*	-179.2	*-ap*	-2.1	*-sp*
C_2-C_3-C_4-H_4	+178.2	*+ap*	+179.9	*+ap*	-178.7	*-ap*	+177.4	*+ap*
C_2-C_3-C_4-C_5	-1.7	*-sp*	+0.5	*+sp*	+0.4	*+sp*	+0.5	*+sp*
H_3-C_3-C_4-H_4	-1.7	*-sp*	-0.1	*-sp*	+1.0	*+sp*	-1.9	*-sp*
H_3-C_3-C_4-C_5	+178.4	*+ap*	-179.5	*-ap*	-179.8	*-ap*	-178.8	*-ap*
C_3-C_4-C_5-C_6	+0.3	*+sp*	-0.7	*-sp*	-1.0	*-sp*	-1.1	*-sp*
C_3-C_4-C_5-C_8	-176.7	*-ap*	-178.6	*-ap*	+179.0	*+ap*	+179.9	*+ap*
H_4-C_4-C_5-C_6	-179.6	*-ap*	+179.8	*+ap*	+178.1	*+ap*	-3.1	*-sp*
H_4-C_4-C_5-C_8	+3.4	*+sp*	+2.0	*+sp*	-1.7	*-sp*	+177.3	*+ap*
C_4-C_5-C_6-H_6	-178.8	*-ap*	+178.7	*+ap*	-179.0	*-ap*	-175.0	*-ap*
C_4-C_5-C_6-C_7	+1.2	*+sp*	+0.3	*+sp*	+0.9	*+sp*	+0.9	*+sp*
C_8-C_5-C_6-H_6	-1.8	*-sp*	-3.3	*-sp*	+0.8	*+sp*	+176.6	*+ap*
C_8-C_5-C_6-C_7	+178.3	*+ap*	+178.2	*+ap*	-179.2	*-ap*	-0.3	*-sp*
C_4-C_5-C_8-C_9	-82.8	*-sc*	+117.8	*+ac*	-70.5	*-ac*	+158.8	*+ap*
C_4-C_5-C_8-C_{20}	+98.6	*+ac*	-57.1	*-sc*	+103.4	*+ac*	-38.7	*-sc*
C_6-C_5-C_8-C_9	+100.3	*+ac*	-60.1	*-sc*	+109.5	*+ac*	-154.5	*-ap*
C_6-C_5-C_8-C_{20}	-78.3	*-sc*	+125.0	*+ac*	-76.4	*-sc*	+24.6	*+sp*
C_5-C_6-C_7-C_2	-1.4	*-sp*	+0.2	*+sp*	-0.2	*-sp*	+180.0	*+ap*
C_5-C_6-C_7-H_7	-1.3	*-sp*	+179.3	*+ap*	+179.8	*+ap*	+1.8	*+sp*
H_6-C_6-C_7-C_2	+178.6	*+ap*	-178.1	*-ap*	+179.7	*+ap*	+6.9	*+sp*
H_6-C_6-C_7-H_7	-1.3	*-sp*	+0.9	*+sp*	-0.2	*-sp*	+1.3	*+sp*
C_5-C_8-C_9-H_9	-178.5	*-ap*	-178.1	*-ap*	-176.7	*-ap*	+4.9	*+sp*
C_5-C_8-C_9-N_3	+1.4	*+sp*	+0.4	*+sp*	+9.2	*+sp*	-177.3	*-ap*
C_{20}-C_8-C_9-H_9	+0.2	*+sp*	-2.6	*-sp*	+8.8	*+ap*	-10.3	*-ap*
C_{20}-C_8-C_9-N_3	-179.9	*-ap*	+175.8	*+ap*	-165.2	*-ap*	+177.2	*+ap*
C_5-C_8-C_{20}-H_{20}	+176.9	*+ap*	+167.8	*+ap*	+178.1	*+ap*	-9.1	*-sp*

C_5-C_8-C_{20}-N_2	-3.1	*-sp*	-10.3	*-sp*	+0.1	*+sp*	+174.3	*+ap*
C_9-C_8-C_{20}-H_{20}	-1.8	*-sp*	-7.3	*-sp*	-7.7	*-sp*	+175.8	*+ap*
C_9-C_8-C_{20}-N_2	+178.2	*+ap*	+174.4	*+ap*	+174.1	*+ap*	-13.5	*-sp*
C_8-C_9-N_3-C_{10}	-176.6	*-ap*	+178.7	*+ap*	+166.4	*+ap*	-178.7	*-ap*
H_9-C_9-N_3-C_{10}	+3.4	*+sp*	-2.6	*-sp*	-7.4	*-sp*	-0.8	*-sp*
C_{15}-C_{10}-C_{11}-H_{11}	+177.6	*+ap*	+179.2	*+ap*	-179.2	*-ap*	+179.5	*+ap*
C_{15}-C_{10}-C_{11}-$C1_2$	-2.4	*-sp*	-1.1	*-sp*	+1.6	*+sp*	-0.3	*-sp*
N_3-C_{10}-C_{11}-H_{11}	-4.1	*-sp*	-0.4	*-sp*	+4.9	*+sp*	-0.2	*-sp*
N_3-C_{10}-C_{11}-C_{12}	+175.9	*+ap*	+179.3	*+ap*	-174.1	*-ap*	-180.0	*-ap*
C_{11}-C_{10}-C_{15}-C_{14}	+1.8	*+sp*	-0.8	*-sp*	-1.7	*-sp*	+0.3	*+sp*
C_{11}-C_{10}-C_{15}-H_{15}	-178.2	*-ap*	+179.8	*+ap*	+178.9	*+ap*	-179.5	*-ap*
N_3-C_{10}-C_{15}-C_{14}	-176.6	*-ap*	+178.7	*+ap*	+174.1	*+ap*	-180.0	*-ap*
N_3-C_{10}-C_{15}-H_{15}	+3.3	*+sp*	-0.4	*-sp*	-5.2	*-sp*	+0.2	*+sp*
C_{11}-C_{10}-N_3-C_9	-5.6	*-sp*	-12.4	*-sp*	-31.5	*-sc*	+0.1	*+sp*
C_{15}-C_{10}-N_3-C_9	+172.7	*+ap*	+167.9	*+ap*	+152.6	*+ap*	+179.7	*+ap*
C_{10}-C_{11}-C_{12}-H_{12}	-178.8	*-ap*	-176.7	*-ap*	+179.7	*+ap*	+179.4	*+ap*
C_{10}-C_{11}-C_{12}-C_{13}	+1.1	*+sp*	+2.4	*+sp*	+0.5	*+sp*	-0.3	*-sp*
H_{11}-C_{11}-C_{12}-H_{12}	+1.2	*+sp*	+2.9	*+sp*	+0.6	*+sp*	+179.6	*+ap*
H_{11}-C_{11}-C_{12}-C_{13}	-178.8	*-ap*	-177.9	*-ap*	-178.5	*-ap*	-0.2	*-sp*
C_{11}-C_{12}-C_{13}-C_{14}	+0.7	*+sp*	-1.5	*-sp*	-2.5	*-sp*	+0.8	*+sp*
C_{11}-C_{12}-C_{13}-N_4	+178.2	*+ap*	+175.9	*+ap*	+169.4	*+ap*	-179.9	*-ap*
H_{12}-C_{12}-C_{13}-C_{14}	-179.3	*-ap*	+177.5	*+ap*	+178.2	*+ap*	-178.8	*-ap*
H_{12}-C_{12}-C_{13}-N_4	-1.9	*-sp*	-4.9	*-sp*	-9.7	*-sp*	+0.4	*+sp*
C_{12}-C_{13}-C_{14}-C_{15}	-1.4	*-sp*	-0.5	*-sp*	+2.5	*+sp*	-0.8	*-sp*
C_{12}-C_{13}-C_{14}-F_2	+178.6	*+ap*	-179.5	*-ap*	-179.4	*-ap*	+178.9	*+ap*
N_4-C_{13}-C_{14}-C_{15}	-179.0	*-ap*	-178.1	*-ap*	-169.7	*-ap*	+180.0	*+ap*
N_4-C_{13}-C_{14}-F_2	+1.0	*+sp*	+2.7	*+sp*	+8.3	*+sp*	-0.3	*-sp*
C_{12}-C_{13}-N_4-C_{16}	-17.6	*-sp*	-20.7	*-sp*	-120.0	*-sp*	-2.1	*-sp*
C_{12}-C_{13}-N_4-C_{19}	+112.7	*+ac*	+114.6	*+ac*	+121.4	*+ac*	-178.6	*-ap*
C_{14}-C_{13}-N_4-C_{16}	+159.8	*+ap*	+156.7	*+ap*	+159.6	*+ap*	-4.2	*-sp*
C_{14}-C_{13}-N_4-C_{19}	-69.9	*-sc*	-67.9	*-sc*	-66.8	*-sc*	+1.7	*+sp*
C_{13}-C_{14}-C_{15}-C_{10}	+0.1	*+sp*	+1.7	*+sp*	-0.4	*-sp*	+0.3	*+sp*
C_{13}-C_{14}-C_{15}-H_{15}	-179.8	*-ap*	-178.9	*-ap*	+178.9	*+ap*	-179.9	*-ap*
F_2-C_{14}-C_{15}-C_{10}	-179.9	*-ap*	-179.2	*-ap*	-178.5	*-ap*	-1.2	*-sp*
F_2-C_{14}-C_{15}-H_{15}	+0.2	*+sp*	+0.1	*+sp*	+0.8	*+sp*	+179.6	*+ap*
H_{16A}-C_{16}-C_{17}-H_{17A}	-178.3	*-ap*	+97.4	*+ac*	+120.6	*+ac*	-145.3	*-ac*
H_{16A}-C_{16}-C_{17}-H_{17B}	-60.3	*-sc*	-22.1	*-sp*	-3.6	*-sp*	-34.8	*-sc*
H_{16A}-C_{16}-C_{17}-O_2	+60.8	*+sc*	-144.5	*-ac*	-126.1	*-ac*	+107.2	*+ac*
H_{16B}-C_{16}-C_{17}-H_{17A}	-59.2	*-sc*	-20.7	*-sp*	-3.6	*-sp*	-109.3	*-ac*

H_{16B}-C_{16}-C_{17}-H_{17B}	+58.7	+*sc*	-140.3	-*ac*	-120.3	-*ac*	-18.6	-*sp*
H_{16B}-C_{16}-C_{17}-O_2	+179.8	+*ap*	+97.2	+*ac*	+117.2	+*ac*	+28.1	+*sp*
N_4-C_{16}-C_{17}-H_{17A}	+61.2	+*sc*	-142.6	-*ac*	-120.4	-*ac*	-18.1	-*sp*
N_4-C_{16}-C_{17}-H_{17B}	+179.2	+*ap*	+97.8	+*ac*	+115.2	+*ac*	-106.7	-*ac*
N_4-C_{16}-C_{17}-O_2	-59.7	-*sc*	-24.6	-*sp*	-7.2	-*sp*	+144.6	+*ac*
H_{16A}-C_{16}-N_4-C_{13}	+69.9	+*sc*	-23.2	-*sp*	-149.4	-*ac*	+28.4	+*sp*
H_{16A}-C_{16}-N_4-C_{19}	-62.7	-*sc*	+82.7	+*sc*	+74.6	+*sc*	+90.3	+*ac*
H_{16B}-C_{16}-N_4-C_{13}	-49.2	-*sc*	-23.2	-*sp*	-35.6	-*sc*	+131.1	+*ac*
H_{16B}-C_{16}-N_4-C_{19}	+178.3	+*ap*	-161.1	-*ap*	-171.6	-*ap*	-68.8	-*sc*
C_{17}-C_{16}-N_4-C_{13}	-169.7	-*ap*	+100.1	+*ac*	+89.0	+*sc*	+12.4	+*sp*
C_{17}-C_{16}-N_4-C_{19}	+57.8	+*sc*	-37.7	-*sc*	-46.8	-*sc*	-170.3	-*ap*
C_{16}-C_{17}-O_2-C_{18}	+59.5	+*sc*	+66.0	+*sc*	+58.1	+*sc*	-67.6	-*sc*
H_{17A}-C_{17}-O_2-C_{18}	-61.4	-*sc*	-172.9	-*ap*	+178.1	+*ap*	-7.3	-*sp*
H_{17B}-C_{17}-O_2-C_{18}	-179.5	-*ap*	-56.5	-*sc*	-65.9	-*sc*	-25.0	-*sp*
H_{18A}-C_{18}-C_{19}-H_{19A}	-61.3	-*sc*	-28.8	-*sp*	-10.4	-*sp*	-104.5	-*ac*
H_{18A}-C_{18}-C_{19}-H_{19B}	+57.6	+*sc*	+89.9	+*sc*	-10.4	-*sp*	+145.5	+*ac*
H_{18A}-C_{18}-C_{19}-N_4	+178.1	+*ap*	-147.5	-*ac*	-134.5	-*ac*	+34.3	+*sc*
H_{18B}-C_{18}-C_{19}-H_{19A}	+56.6	+*sc*	-148.9	-*ac*	-18.0	-*sp*	+15.9	+*sp*
H_{18B}-C_{18}-C_{19}-H_{19B}	+175.5	+*ap*	-30.1	-*sc*	-134.5	-*ac*	-144.3	-*ac*
H_{18B}-C_{18}-C_{19}-N_4	-64.0	-*sc*	+92.3	+*ac*	+106.5	+*ac*	+106.2	+*ac*
O_2-C_{18}-C_{19}-H_{19A}	+177.6	+*ap*	+94.1	+*ac*	+111.8	+*ac*	+15.9	+*sp*
O_2-C_{18}-C_{19}-H_{19B}	-63.4	-*sc*	-147.1	-*ac*	-131.6	-*ac*	-29.9	-*sp*
O_2-C_{18}-C_{19}-N_4	+57.1	+*sc*	-24.6	-*sp*	-7.0	-*sp*	-147.1	-*ac*
H_{18A}-C_{18}-O_2-C_{17}	-179.3	-*ap*	+83.3	+*sc*	+73.4	+*sc*	-171.8	-*ap*
H_{18B}-C_{18}-O_2-C_{17}	+62.9	+*sc*	-160.0	-*ap*	-170.8	-*ap*	-56.6	-*sc*
C_{19}-C_{18}-O_2-C_{17}	-58.2	-*sc*	-39.5	-*sc*	-50.4	-*sc*	+66.9	+*sc*
C_{18}-C_{19}-N_4-C_{13}	+170.0	+*ap*	-75.3	-*sc*	-81.5	-*sc*	-174.2	-*ap*
C_{18}-C_{19}-N_4-C_{16}	-56.6	-*sc*	+63.8	+*sc*	+54.4	+*sc*	+5.3	+*sp*
H_{19A}-C_{19}-N_4-C_{13}	+49.4	+*sc*	+47.7	+*sc*	+42.3	+*sc*	+22.4	+*sp*
H_{19A}-C_{19}-N_4-C_{16}	-177.1	-*ap*	-173.0	-*ap*	+178.3	+*ap*	-29.5	-*sp*
H_{19B}-C_{19}-N_4-C_{16}	+64.0	+*sc*	-56.9	-*sc*	-66.8	-*sc*	-83.0	-*sc*
C_8-C_{20}-N_2-C_{21}	-174.0	-*ap*	-8.7	-*sp*	-75.3	-*sc*	-179.7	-*ap*
H_{20}-C_{20}-N_2-C_{21}	+6.1	+*sp*	+173.1	+*ap*	+106.4	+*ac*	-0.9	-*sp*
C_{26}-C_{211}-C_{22}-H_{22}	-178.4	-*ap*	-176.8	-*ap*	+145.2	+*ac*	-179.6	-*ap*
C_{26}-C_{21}-C_{22}-C_{23}	+1.7	+*sp*	+2.3	+*sp*	-35.9	-*sc*	+0.3	+*sp*
N_2-C_{21}-C_{22}-H_{22}	+3.4	+*sp*	-4.0	-*sp*	-41.5	-*sc*	-0.1	-*sp*
N_2-C_{21}-C_{22}-C_{23}	-176.5	-*ap*	+175.1	+*ap*	+137.3	+*ac*	+0.1	+*sp*
C_{22}-C_{21}-C_{26}-C_{25}	-0.4	-*sp*	-2.4	-*sp*	+35.2	+*sc*	+179.8	+*ap*
C_{22}-C_{21}-C_{26}-H_{26}	+179.5	+*ap*	+177.6	+*ap*	-145.7	-*ac*	+179.4	+*ap*

N_2-C_{21}-C_{26}-C_{25}	+177.7	+*ap*	-174.8	-*ap*	-137.5	-*ac*	-0.1	-*sp*
N_2-C_{21}-C_{26}-H_{26}	-2.4	-*sp*	+5.2	+*sp*	+41.6	+*sc*	-0.2	-*sp*
C_{22}-C_{21}-N_2-C_{20}	-162.3	-*ap*	+128.8	+*ac*	-165.6	-*ap*	+1.1	+*sp*
C_{26}-C_{21}-N_2-C_{20}	+19.6	+*sp*	-58.8	-*sc*	+6.5	+*sp*	+0.5	+*sp*
C_{21}-C_{22}-C_{23}-C_{24}	-1.0	-*sp*	-0.7	-*sp*	+0.8	+*sp*	+0.3	+*sp*
C_{21}-C_{22}-C_{23}-F_1	+177.1	+*ap*	+179.9	+*ap*	+177.2	+*ap*	-179.3	-*ap*
H_{22}-C_{22}-C_{23}-C_{24}	+179.1	+*ap*	+178.5	+*ap*	+179.5	+*ap*	-0.1	-*sp*
H_{22}-C_{22}-C_{23}-F_1	-2.8	-*sp*	-0.8	-*sp*	-4.0	-*sp*	+179.5	+*ap*
C_{22}-C_{23}-C_{24}-C_{25}	-1.1	-*sp*	-0.9	-*sp*	+35.5	+*sc*	-0.8	-*sp*
C_{22}-C_{23}-C_{24}-N_1	+176.6	+*ap*	-177.9	-*ap*	-138.2	-*ac*	+180.0	+*ap*
F_1-C_{23}-C_{24}-C_{25}	-179.1	-*ap*	+178.3	+*ap*	-140.9	-*ac*	+113.4	+*ac*
F_1-C_{23}-C_{24}-N_1	-1.5	-*sp*	+1.3	+*sp*	+45.2	+*sc*	-0.5	-*sp*
C_{23}-C_{24}-C_{25}-H_{25}	-177.7	-*ap*	-179.5	-*ap*	+145.6	+*ac*	-178.9	-*ap*
C_{23}-C_{24}-C_{25}-C_{26}	+2.4	+*sp*	+0.9	+*sp*	-36.4	-*sc*	+0.8	+*sp*
N_1-C_{24}-C_{25}-H_{25}	+4.7	+*sp*	-2.6	-*sp*	-40.2	-*sc*	+179.6	+*ap*
N_1-C_{24}-C_{25}-C_{26}	-175.1	-*ap*	+177.8	+*ap*	+137.7	+*ac*	-0.2	-*sp*
C_{23}-C_{24}-N_1-C_{27}	+63.7	+*sc*	-62.6	-*sc*	-1.9	-*sp*	-0.8	-*sp*
C_{23}-C_{24}-N_1-C_{30}	-165.2	-*ap*	+162.8	+*ap*	+174.2	+*ap*	+4.8	+*sp*
C_{25}-C_{24}-N_1-C_{27}	-118.9	-*ac*	+120.6	+*ac*	-175.1	-*ap*	+2.5	+*sp*
C_{25}-C_{24}-N_1-C_{30}	+12.2	+*sp*	-13.8	-*sp*	+1.1	+*sp*	-178.1	-*ap*
C_{24}-C_{25}-C_{26}-C_{21}	-1.8	-*sp*	+0.7	+*sp*	+1.8	+*sp*	-0.3	-*sp*
C_{24}-C_{25}-C_{26}-H_{26}	+178.4	+*ap*	-179.2	-*ap*	-177.2	-*ap*	+179.8	+*ap*
H_{25}-C_{25}-C_{26}-C_{21}	+178.4	+*ap*	-178.8	-*ap*	+179.6	+*ap*	+1.1	+*sp*
H_{25}-C_{25}-C_{26}-H_{26}	-1.5	-*sp*	+1.2	+*sp*	+0.6	+*sp*	-179.6	-*ap*
H_{27A}-C_{27}-C_{28}-H_{28A}	-178.5	-*ap*	+172.8	+*ap*	+173.8	+*ap*	-36.1	-*sc*
H_{27A}-C_{27}-C_{28}-H_{28B}	-57.8	-*sc*	+53.0	+*sc*	+50.4	+*sc*	-154.3	-*ap*
H_{27A}-C_{27}-C_{28}-O_1	+63.2	+*sc*	-65.1	-*sc*	-62.8	-*sc*	+83.6	+*sc*
H_{27B}-C_{27}-C_{28}-H_{28A}	-57.3	-*sc*	+54.3	+*sc*	+57.3	+*sc*	+107.9	+*ac*
H_{27B}-C_{27}-C_{28}-H_{28B}	+60.7	+*sc*	-65.5	-*sc*	-66.0	-*sc*	-146.2	-*ac*
H_{27B}-C_{27}-C_{28}-O_1	-178.3	-*ap*	+176.2	+*ap*	-179.4	-*ap*	-30.9	-*sc*
N_1-C_{27}-C_{28}-H_{28A}	+63.4	+*sc*	-65.5	-*sc*	-67.5	-*sc*	-34.6	-*sc*
N_1-C_{27}-C_{28}-H_{28B}	-178.5	-*ap*	+174.6	+*ap*	+169.0	+*ap*	+105.7	+*ac*
N_1-C_{27}-C_{28}-O_1	-57.5	-*sc*	+56.4	+*sc*	+55.7	+*sc*	-156.5	-*ap*
H_{27A}-C_{27}-N_1-C_{24}	+67.7	+*sc*	-71.7	-*sc*	-117.8	-*ac*	+125.2	+*ac*
H_{27A}-C_{27}-N_1-C_{30}	-66.3	-*sc*	+65.3	+*sc*	+65.6	+*sc*	-89.9	-*sc*
H_{27B}-C_{27}-N_1-C_{24}	-50.8	-*sc*	+47.5	+*sc*	+0.2	+*sp*	+24.1	+*sp*
H_{27B}-C_{27}-N_1-C_{30}	+175.2	+*ap*	-175.4	-*ap*	-176.2	-*ap*	+70.3	+*sc*
C_{28}-C_{27}-N_1-C_{24}	-171.6	-*ap*	+167.5	+*ap*	+122.8	+*ac*	+7.1	+*sp*
C_{28}-C_{27}-N_1-C_{30}	+54.4	+*sc*	-55.4	-*sc*	-53.7	-*sc*	+170.8	+*ap*

C_{27}-C_{28}-O_1-C_{29}	+60.3	+*sc*	-58.5	-*sc*	-61.4	-*sc*	+66.9	+*sc*
H_{28A}-C_{28}-O_1-C_{29}	-60.7	-*sc*	+63.1	+*sc*	+62.7	+*sc*	+6.8	+*sp*
H_{28B}-C_{28}-O_1-C_{29}	-178.7	-*ap*	-179.1	-*ap*	-179.9	-*ap*	+25.3	+*sp*
H_{29A}-C_{29}-C_{30}-H_{30A}	-60.3	-*sc*	-172.6	-*ap*	-172.1	-*ap*	-145.3	-*ac*
H_{29A}-C_{29}-C_{30}-H_{30B}	+58.2	+*sc*	-54.8	-*sc*	-53.8	-*sc*	-79.7	-*sc*
H_{29A}-C_{29}-C_{30}-N_1	+178.9	+*ap*	+64.6	+*sc*	+68.2	+*sc*	+157.7	+*ap*
H_{29B}-C_{29}-C_{30}-H_{30A}	+58.1	+*sc*	+64.8	+*sc*	+68.8	+*sc*	+32.2	+*sc*
H_{29B}-C_{29}-C_{30}-H_{30B}	+176.5	+*ap*	-52.9	-*sc*	-49.4	-*sc*	+142.6	+*ac*
H_{29B}-C_{29}-C_{30}-N_1	-62.7	-*sc*	-175.7	-*ap*	-169.0	-*ap*	-107.1	-*ac*
O_1-C_{29}-C_{30}-H_{30A}	+178.9	+*ap*	+65.2	+*sc*	+63.9	+*sc*	+33.1	+*sc*
O_1-C_{29}-C_{30}-H_{30B}	-62.6	-*sc*	-176.9	-*ap*	-177.7	-*ap*	+27.0	+*sp*
O_1-C_{29}-C_{30}-N_1	+58.1	+*sc*	-57.5	-*sc*	-55.6	-*sc*	+145.8	+*ac*
H_{29A}-C_{29}-O_1-C_{28}	+178.8	+*ap*	-62.6	-*sc*	-62.6	-*sc*	+36.5	+*sc*
H_{29B}-C_{29}-O_1-C_{28}	+60.7	+*sc*	+179.5	+*ap*	-179.7	-*ap*	-129.0	-*ac*
C_{30}-C_{29}-O_1-C_{28}	-60.2	-*sc*	+59.0	+*sc*	+61.4	+*sc*	+33.2	+*sc*
C_{29}-C_{30}-N_1-C_{24}	+172.4	+*ap*	-167.6	-*ap*	-122.7	-*ac*	+173.5	+*ap*
C_{29}-C_{30}-N_1-C_{27}	-54.6	-*sc*	+55.6	+*sc*	+53.9	+*sc*	-11.2	-*sp*
H_{30A}-C_{30}-N_1-C_{24}	+51.6	+*sc*	+71.6	+*sc*	+116.2	+*ac*	-124.4	-*ac*
H_{30A}-C_{30}-N_1-C_{27}	-175.4	-*ap*	-64.9	-*sc*	-67.1	-*sc*	+90.4	+*ac*
H_{30B}-C_{30}-N_1-C_{24}	-66.8	-*sc*	-47.9	-*sc*	-3.3	-*sp*	+134.1	+*ac*
H_{30B}-C_{30}-N_1-C_{27}	+66.2	+*sc*	+175.4	+*ap*	+173.3	+*ap*	-68.8	-*sc*
* The conformations were designated by Klyne-Prelog termsusing *s* = syn, *a* = anti, *p* = peri-planar (0 ± 30^0& 180 ± 30^0) and all other angles *c* = clinal, and + & - signs.								

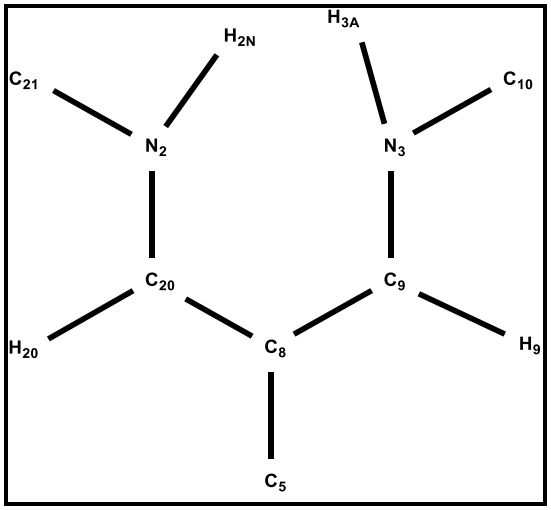

Figure 6B.32: *Core structure of* ***FFMMMC*** *molecule*

Table 6B.7: *Selected geometric and delocalization parameters for* ***FFMMMC***

PARAMETRES	**LEFT**		**RIGHT**		**|DIFFERENCE|**
Bond lengths	C_{21}-N_2	1.410	C_{10}-N_3	1.417	0.007
	N_2-H_{2N}	0.890	N_3-H_{3A}	0.860	0.03
	N_2-C_{20}	1.319	N_3-C_9	1.311	0.008
	C_{20}-H_{20}	0.929	C_9-H_9	0.931	0.002
	C_{20}-C_8	1.391	C_9-C_8	1.382	0.009
	C_8-C_5	1.495			
Bond angles	C_{21}-N_2-H_{2N}	118.0	C_{10}-N_3-H_{3A}	117.4	0.6
	C_{21}-N_2-C_{20}	124.7	C_{10}-N_3-C_9	125.2	0.5
	H_{2N}-N_2-C_{20}	117.0	H_{3A}-N_3-C_9	117.4	0.4
	N_2-C_{20}-C_8	126.2	N_3-C_9-C_8	126.3	0.1
	N_2-C_{20}-H_{20}	116.9	N_3-C_9-H_9	116.9	0
	H_{20}-C_{20}-C_8	116.9	H_9-C_9-C_8	116.8	0.1
	C_{20}-C_8-C_5	122.0	C_9-C_8-C_5	122.7	0.7
Dihedral angles	C_{21}-N_2-C_{20}-H_{20}	+5.9	C_{10}-N_3-C_9-H_9	+3.4	
	C_{21}-N_2-C_{20}-C_8	-174.1	C_{10}-N_3-C_9-C_8	-176.6	
	H_{2N}-N_2-C_{20}-H_{20}	+177.0	H_{3A}-N_3-C_9-H_9	-176.6	
	H_{2N}-N_2-C_{20}-C_8	-3.0	H_{3A}-N_3-C_9-C_8	+3.4	
	N_2-C_{20}-C_8-C_5	-2.0	N_3-C_9-C_8-C_5	+1.1	
	H_{20}-C_{20}-C_8-C_9	-1.3	H_9-C_9-C_8-C_{20}	+0.4	
	N_2-C_{20}-C_8-C_9	+178.7	N_3-C_9-C_8-C_{20}	-179.6	
	H_{20}-C_{20}-C_8-C_5	+178.0	H_9-C_9-C_8-C_5	-178.9	

Table 6B.8: *Sum of bond angles around selected atoms in* ***FFMMMC***

Around N_2	Angle 1	Angle 2	Angle 3	SUM
	H_{2N}-N_2-C_{21}	H_{21}-N_2-C_{20}	H_{2N}-N_2-C_{20}	
	118.0	124.7	117.0	359.7
Around N_3	H_{3A}-N_3-C_{10}	H_{3A}-N_3-C_9	C_{10}-N_3-C_9	
	117.4	117.4	125.2	360.0
Around C_{20}	H_{20}-C_{20}-C_8	N_2-C_{20}-C_8	N_2-C_{20}-H_{20}	
	116.9	126.2	116.9	360.0
Around C_9	N_3-C_9-H_9	N_3-C_9-C_8	C_8-C_9-H_9	
	116.9	126.3	116.8	360.0

Except the terminal zones, the central core structure of **FFMPMC** and **FFMMMC** is very similar. As we could not obtain a single crystal of the **FFMPMC**, we have attempted MM2 calculations on **FFMPMC** and calculated many of their structural parameters such as bond lengths, bond angles, and dihedral angles at some crucial moieties.

6B.9 Hirshfeld Surface Analysis:

Figure 6B.33 shows the Hirshfeld surface interaction diagram and fingerprint plots[14] of **FFMMMC.** The surfaces show d_{norm} in the range of -0.205 to 2.244 Å. Strong acceptor-donor intermolecular hydrogen bond interactions appear as prominent red color spots at C_{19}-$H_{19}O_3$, C_9-H_9----O_4, C_{20}-H_{20}----O_4, C_{30}-H_{30}----F_2, C_{15}-H_{15}----O_1, C_{12}-H_{12}----O_1, C_{30}-H_{30}----O_4 and C_{15}----C_{27}-H_{27}. The relative percent Hirshfeld surface area contributions of various intermolecular interatomic interactions are shown in **Table 6B.9**. This table and **Figure 6B.33** together suggest some H···H interactions as the strongest, with nearly 32.8% surface concentration. The O···H/ O···H contacts contribute to around 29% with two spikes at a de + di value of ~1.4 Å whereas the F···H/ H···F to about 8.7% with a de + di value of ~1.6 Å and the C···H/ H···C to about 15% with de + di value again of ~1.4 Å. The contributions of all other intermolecular interatomic interactions are less than 15%. **Figure 6B.34** shows the relative contributions of different intermolecular contacts to the Hirshfeld surface area of **FFMMMC**.

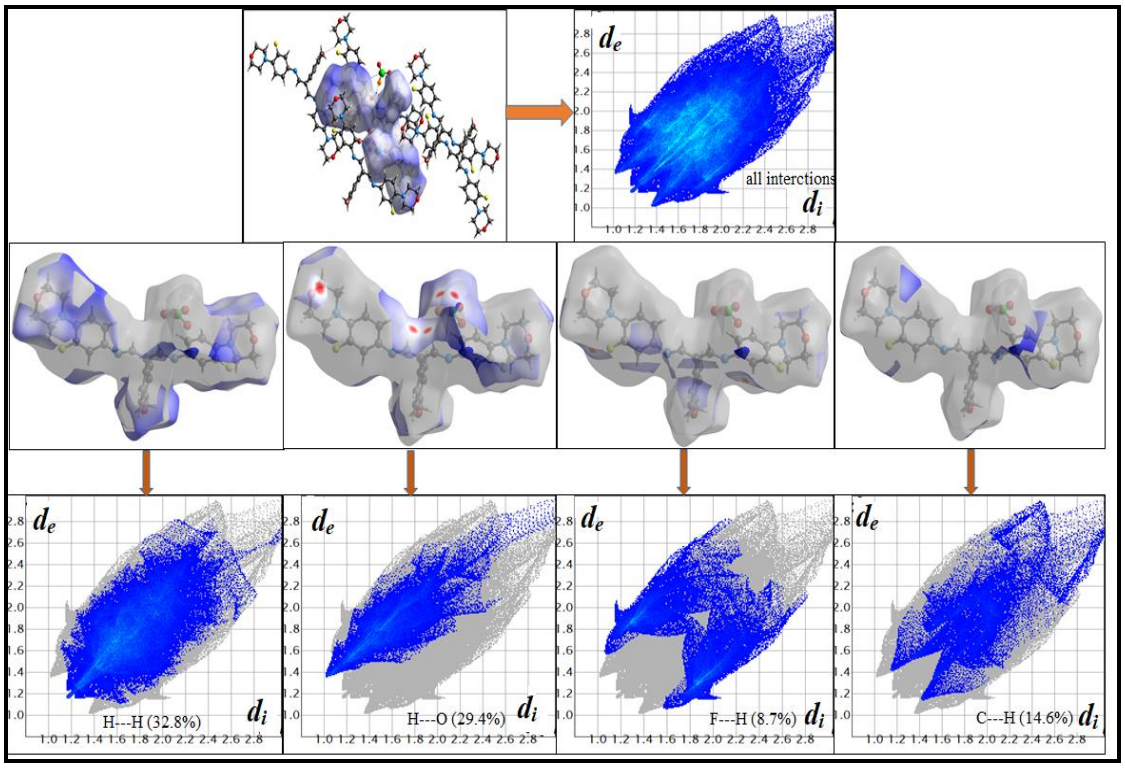

Figure 6B.33: *Hirshfeld finger print plots of* ***FFMMMC***

Table 6B.9: *Intermolecular Hirshfeld inter-atomic interaction percentages of* ***FFMMMC***

Interaction	Contribution (%)
C-C	1.1
C-H/H-C	14.6
C-N/N-C	0.2
C-O/O-C	1.8
C-F/F-C	1.4
H-H	32.8
H-N/N-H	3.5
H-O	29.5
H-F/F-H	8.7
N-O/N-O	2.7
O-F/F-O	1.8
O-H	29.5
O-O	1.9

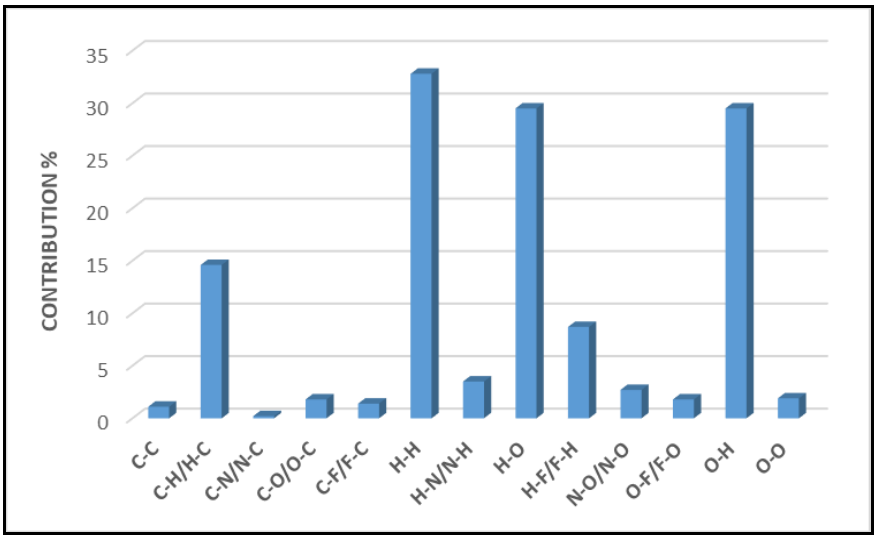

Figure 6B.34: *Relative contributions of different intermolecular contacts to the Hirshfeld surface area of* ***FFMMMC***

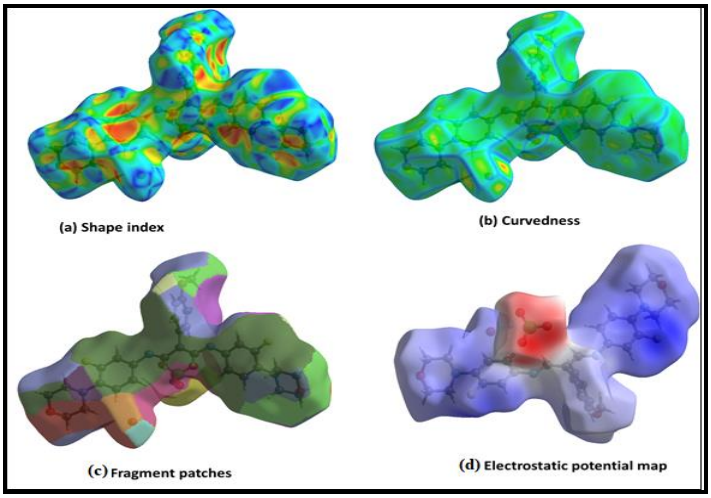

Figure 6B.35: *Hirshfeld surface maps of* ***FFMMMC*** *represented by modes*

The shape index, curvedness, fragment patch and electrostatic potential map surfaces are shown in **Figure 6B.35.** The pattern of nearby red and blue triangles on the shape index surfaces of **FFMMMC** and the corresponding curvatures of the surfaces on the same side of the molecule through wide and flat green patches on them show the presence of interaction[15]. The electrostatic potential created by the HF/3-21G basis set is shown in **Figure 6B.35 (d),** with red representing negative electrostatic potential (hydrogen acceptors) and blue representing positive electrostatic potential (hydrogen donors) (hydrogen donor).

The strength of the electronic contacts and their corresponding interaction energy are usually correlated with the Hirshfeld surface analyzed data. E_{ele} = - 65.9, E_{pol} = - 55.0, E_{dis} = - 288.9, E_{rep} = 115.5, E_{tot} = - 269.6 are the scale factors used to create energy frame works for HF-3-21G. These model energies show that dispersion energy plays a key role in crystal interactions. Individual energy components are shown as cylinders between the centroids of interacting molecular pairs in **Figure 6B.37**, corresponding to dispersion energy, coulomb energy, and total energy along the a, b, and c axes, respectively, while the relevant energies are listed in **Table 6B.10**. The cylindrical radii are represented as a proportionate measure of the strength of the interaction energies in the laddered bars, normalized to 100 with a minimum value of 5 kJ mol^{-1}.

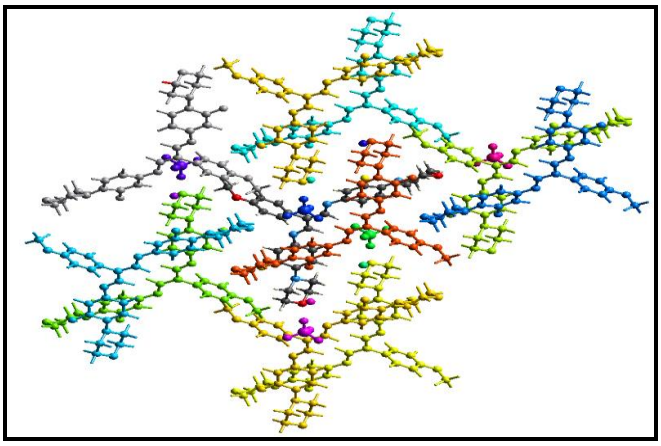

Figure 6B.36: *Pair-wise intermolecular interactions in* ***FFMMMC*** *(viewed along the c axis)*

Table 6B.10: *The molecular pair-wise interaction energies of* ***FFMMMC***

	N	Symop	R	Electron density	E_ele	E_pol	E_dis	E_rep	E_tot
	1	-x, -y, -z	13.16	HF/3-21G	0.0	-0.8	0.0	0.0	-0.5
	1	-x, -y, -z	5.48	HF/3-21G	-12.6	-3.4	-89.8	36.3	-66.4
	1	-x, -y, -z	5.46	HF/3-21G	-27.3	-8.3	-97.9	39.6	-89.4
	2	x, y, z	14.87	HF/3-21G	0.0	-5.6	0.0	0.0	-3.7
	1	-x, -y, -z	18.20	HF/3-21G	0.0	-1.1	0.0	0.0	-0.7

	2	x, y, z	14.92	HF/3-21G	0.0	-6.0	0.0	0.0	-3.9
	1	-x, -y, -z	12.11	HF/3-21G	0.0	-5.2	0.0	0.0	-3.4
	1	-	4.49	HF/3-21G	0.0	nan	0.0	0.0	nan
	1	-	3.60	HF/3-21G	0.0	0.0	0.0	0.0	0.0
	1	-	6.19	HF/3-21G	0.0	nan	0.0	0.0	nan
	1	-	4.77	HF/3-21G	-27.3	-8.3	-97.9	39.6	-89.4
	1	-x, -y, -z	13.07	HF/3-21G	0.0	-1.0	0.0	0.0	-0.6
	2	x, y, z	14.93	HF/3-21G	0.0	-0.2	0.0	0.0	-0.1
	1	-x, -y, -z	18.94	HF/3-21G	0.0	-0.9	0.0	0.0	-0.6
	1	-	6.22	HF/3-21G	1.3	-0.2	-3.3	0.0	-1.7
	1	-	9.84	HF/3-21G	0.0	-5.6	0.0	0.0	-3.7
	1	-	11.54	HF/3-21G	0.0	-0.8	0.0	0.0	-0.5
	1	-	10.48	HF/3-21G	0.0	-0.1	0.0	0.0	-0.1
	1	-	11.45	HF/3-21G	0.0	-0.0	0.0	0.0	-0.0
	1	-	8.11	HF/3-21G	0.0	-0.4	0.0	0.0	-0.3
	1	-	13.58	HF/3-21G	0.0	-6.0	0.0	0.0	-3.9
	1	-	12.71	HF/3-21G	0.0	-1.1	0.0	0.0	-0.7

Energy Model	k_ele	k_pol	k_disp	k_rep
CE-HF ... HF/3-21G electron densities	1.019	0.651	0.901	0.811
CE-B3LYP ... B3LYP/6-31G(d,p) electron densities	1.057	0.740	0.871	0.618

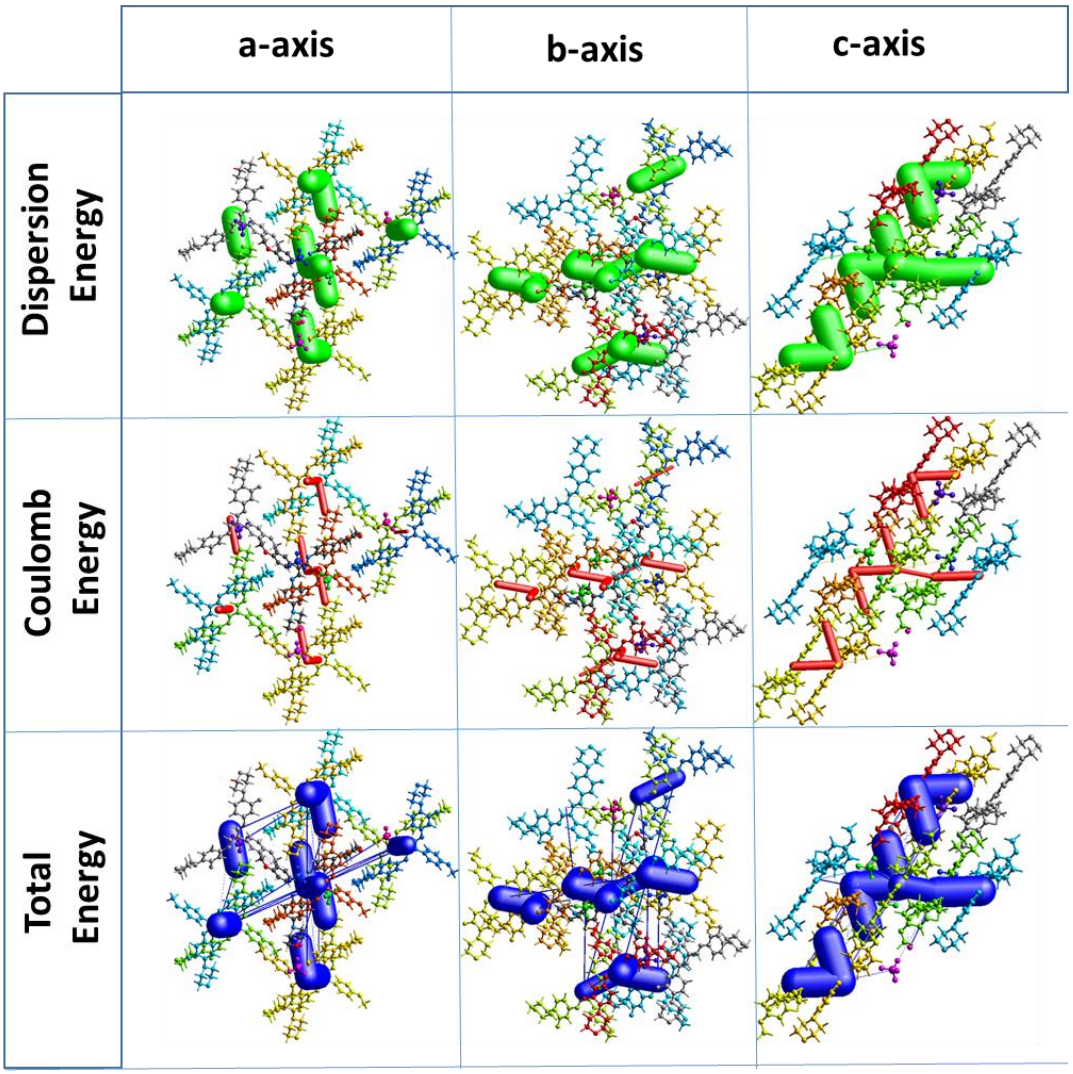

Figure 6B.37: *Crystallographic axis-wise modes of intermolecular energies in* ***FFMMMC***

6B.10 Molecular Docking Studies of FFMPMC and FFMMMC

EGFR-TK (pdb id: 1m17) belongs to the epidermal growth factor receptor family[16]. Excess EGFR expression results in anal cancer and epithelial malignancies of the neck and head. We chose EGFR as a target protein receptor for molecular docking by the cations of **FFMPMC** and **FFMMMC**.

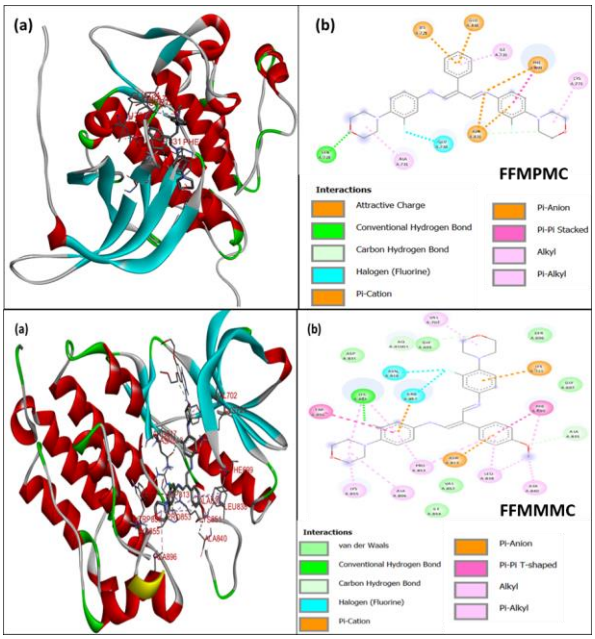

Figure 6B.38: *Molecular docking interactions of* ***FFMPMC*** *and* ***FFMMMC*** *with EGFR-TK protein; (a) 3D depiction of ligand-receptor binding interactions and (b) 2D representation of different forms of interactions with amino acid residues*

The cationic form of **FFMPMC** has a binding energy of -9.3 kcal mol^{-1} and docks to the EGFR through two hydrogen bonds with the amino acid residues of ASP-831 and SER-728. One halogen interaction with the protein amino acid residue of GLU-734 and seven electrostatic interactions with amino acid residues of ASP-831, LYS-721, PHE-699 and GLU-738. There are four hydrophobic interactions in the PHE-699, ALA-731, CYS-773 and ILE-735 amino acid residues, which are shown in **Figure 6B.25.**

The cationic form of **FFMMMC** has a binding energy of -9.8 kcal mol^{-1} and docks to the EGFR through three hydrogen bonds with the amino acid residues of LYS-851, ALA-835. Two halogen interactions with the protein amino acid residue of ARG-817, ASN-818 and three electrostatic interactions with amino acid residues of LYS-721, ARG-817, ASP-813. There are thirteen hydrophobic interactions in the PHE-699, TRP-856, VAL-702, ALA-840, LYS-851, LYS-855, ALA-896, LEU-838, PHE-699, PRO-853, LYS-851 amino acid residues are shown in **Figure 6B.25.**

References

(1). Fuchi, Y.; Sakuma, M.; Ohyama, K.; Hagihara, R.; Kohno, M.; Hamada, K.; Mizutani, A.; Karasawa, S. Selective Synthesis of Substituted Amino-Quinoline Derivatives by C-H Activation and Fluorescence Evaluation of Their Lipophilicity-Responsive Properties. *Scientific Reports* **2019**, *9* (1), 17723. https://doi.org/10.1038/s41598-019-53882-z.

(2). dos Santos, G. C.; Servilha, R. O.; de Oliveira, E. F.; Lavarda, F. C.; Ximenes, V. F.; da Silva-Filho, L. C. Theoretical-Experimental Photophysical Investigations of the Solvent Effect on the Properties of Green- and Blue-Light-Emitting Quinoline Derivatives. *Journal of Fluorescence* **2017**, 27 (5), 1709–1720. https://doi.org/10.1007/s10895-017-2108-0.

(3). Bairwa, D.; Raghavendra Rao, K.; Swain, D.; Guru Row, T. N.; Bhat, H. L.; Elizabeth, S. Potassium L-Ascorbate Monohydrate: A New Metal–Organic Nonlinear Optical Crystal. *Applied Physics B* **2021**, *127* (1), 9. https://doi.org/10.1007/s00340-020-07561-x.

(4). Blinder, S. M. Basic Concepts of SCF Theory. *American Journal of Physics*. 1965, p 431.

(5). Goldstein, E.; Allinger, N. L. Molecular Mechanics Calculations (MM2) on Aliphatic Nitriles. *Journal of Molecular Structure: THEOCHEM* **1989**, *188* (1–2), 149–157. https://doi.org/10.1016/0166-1280(89)85033-X.

(6). Saad, F. A. Elaborated Molecular Docking and DFT/B3LYP Studies for Novel Sulfa Drug Complexes, Spectral and Antitumor Investigations. *Journal of Thermal Analysis and Calorimetry* **2017**, *129* (1), 425–440. https://doi.org/10.1007/s10973-016-6017-2.

(7). Spackman, M. A.; Jayatilaka, D. Hirshfeld Surface Analysis. *CrystEngComm* **2009**, *11* (1), 19–32. https://doi.org/10.1039/B818330A.

(8). Carter, D. J.; Raiteri, P.; Barnard, K. R.; Gielink, R.; Mocerino, M.; Skelton, B. W.; Vaughan, J. G.; Ogden, M. I.; Rohl, A. L. Difference Hirshfeld Fingerprint Plots: A Tool for Studying Polymorphs. *CrystEngComm* **2017**, *19* (16), 2207–2215. https://doi.org/10.1039/C6CE02535H.

(9). Bhola, Y. O.; Socha, B. N.; Pandya, S. B.; Dubey, R. P.; Patel, M. K. Molecular Structure, DFT Studies, Hirshfeld Surface Analysis, Energy Frameworks, and Molecular Docking Studies of Novel (E)-1-(4-Chlorophenyl)-5-Methyl-N′-((3-Methyl-5-Phenoxy-1-Phenyl-1H-Pyrazol-4-Yl) Methylene)-1H-1, 2, 3-Triazole-4-Carbohydrazide. *Molecular Crystals and Liquid Crystals* **2019**, *692* (1), 83–93. https://doi.org/10.1080/15421406.2020.1721946.

(10). Westwood, M.; Joore, M.; Whiting, P.; van Asselt, T.; Ramaekers, B.; Armstrong, N.; Misso, K.; Severens, J.; Kleijnen, J. Epidermal Growth Factor Receptor Tyrosine Kinase (EGFR-TK) Mutation Testing in Adults with Locally Advanced or Metastatic Non-Small Cell Lung Cancer: A Systematic Review and Cost-Effectiveness Analysis. *Health Technology Assessment* **2014**, *18* (32), 1–165. https://doi.org/10.3310/hta18320.

(11). (a) Malik, P. K. Investigation on Tautomeric Equilibrium of Schiff Base in Mixed Binary

Solvent. **2010**, 24.

(b) Kluba, M.; Lipkowski, P.; Filarowski, A. Theoretical Investigation of Tautomeric Equilibrium in Ortho-Hydroxy Phenyl Schiff Bases. *Chemical Physics Letters* **2008**, *463* (4–6), 426–430. https://doi.org/10.1016/j.cplett.2008.08.076.

(c) Hureau, M.; Moissette, A.; Smirnov, K. A Spectroscopic Study of Tautomeric Equilibrium of Salicylideneaniline in ZSM-5 Zeolites. *Molecules* **2019**, *24* (4), 795. https://doi.org/10.3390/molecules24040795.

(d) M. Al-Saidi, H. Potentiometric Study of a New Schiff Base and Its Metal Ion Complexes: Preparation, Characterization and Biological Activity. *International Journal of Electrochemical Science* **2020**, *15* (11), 10785–10801. https://doi.org/10.20964/2020.11.06.

(12). M. Al-Saidi, H. Potentiometric Study of a New Schiff Base and Its Metal Ion Complexes: Preparation, Characterization and Biological Activity. *International Journal of Electrochemical Science* **2020**, *15* (11), 10785–10801. https://doi.org/10.20964/2020.11.06.

(13). Romero-Fernández, M. P.; Ávalos, M.; Babiano, R.; Cintas, P.; Jiménez, J. L.; Light, M. E.; Palacios, J. C. Pseudo-Cyclic Structures of Mono- and Di-Azaderivatives of Malondialdehydes. Synthesis and Conformational Disentanglement by Computational Analyses. *Org. Biomol. Chem.* **2014**, *12* (44), 8997–9010. https://doi.org/10.1039/C4OB01507J.

(14). Naghiyev, F. N.; Cisterna, J.; Khalilov, A. N.; Maharramov, A. M.; Askerov, R. K.; Asadov, K. A.; Mamedov, I. G.; Salmanli, K. S.; Cárdenas, A.; Brito, I. Crystal Structure and Hirshfeld Surface Analysis of Acetoacetanilide Based Reaction Products. *Molecules* **2020**, *25* (9), 2235. https://doi.org/10.3390/molecules25092235.

(15). Angeline Shirmila, D.; Reuben Jonathan, D.; Krishna Priya, M.; Laavanya, K.; Hemalatha, J.; Usha, G. Synthesis, Structure Determination, Molecular Interaction Analysis, Molecular Docking Studies, and Anticancer Activity Investigation of a Chalcone Derivative: (2E)-2-[(2,4-Dimethoxyphenyl)Methylidene]-3,4 Dihydronaphthalen-1(2H)-One. *Materials Today: Proceedings* **2022**, https://doi.org/10.1016/j.matpr.2022.04.479.

(16). Braut, T.; Krstulja, M.; Kujundžić, M.; Manestar, D.; Hadžisejdić, I.; Jonjić, N.; Grahovac, B.; Manestar, D. Epidermal Growth Factor Receptor Protein Expression and Gene Amplification in Normal, Hyperplastic, and Cancerous Glottic Tissue: Immunohistochemical and Fluorescent in Situ Hybridization Study on Tissue Microarrays. *Croatian Medical Journal* **2009**, *50* (4), 370–379. https://doi.org/10.3325/cmj.2009.50.370.

CHAPTER VII

SYNTHESIS AND SPECTRAL, ELECTROCHEMICAL, COMPUTATIONAL AND BIOLOGICAL STUDIES OF 2,2'-(((1E,3E)-2-PHENYLPROPANE-1,3-DIYLIDENE)-BIS-(AZANEYLYLIDENE))-DIBENZOIC ACID (PDBAD) AND ITS BIVALENT METAL COMPLEXES [M(PDBAD)X_2]

The studies of the tetradentate Schiff base ligand, 2,2'-((1E,3E)-2-phenylpropane-1,3-diylidene)-bis-(azaneylylidene)-dibenzoic acid **(PDBAD),** and its metal complexes with a variety of bivalent metal ions such as Zn(II), Cd(II), Co(II), Ni(II), Mn(II) and Cu(II) have been discussed in this chapter. All these have been characterized by using various analytical and spectroscopic methods. Additionally, voltammetric studies, molecular modeling has also been conducted. Biological activity studies like antimicrobial, antioxidant, antifungal, anti-malarial and antitumor capabilities have been tested for both **PDBAD** and **[M(PDBAD)X_2]** complexes. The condensation of 2-phenylmalonaldehyde with anthranilic acid yields this **PDBAD** Schiff base with a tetra dentate capability. The detailed synthesis of **PDBAD** and its metal complexes are presented in **Chapter II.** The studies suggest the structure of **PDBAD** and **[M(PDBAD)X_2]** as shown in **Figure 7A.1.**

This Chapter is divided into three parts, viz., **PART A**, **PART B**, and **PART C**.

Part A presents the results of the physical, analytical, spectroscopic, electrochemical and coordination chemistry studies of the **PDBAD** and its metal complexes, **[M(PDBAD)X_2].**

Part B shows results and discussion of the studies of the molecular modeling and protein molecular docking of the ligand and its metal complexes, many attempts have been made in vain to develop an analysis of **[Cu(PDBAD)]** or any of the **[M(PDBAD)X_2].**

Prat C describes the biological activity studies of the **PDBAD** ligand and its metal complexes.

PARTA

SPECTRAL, ELECTROCHEMICAL AND COORDINATION CHEMISTRY STUDIES OF PDBAD and [M(PDBAD)X_2]

7A.1 Analytical Characteristics of the PDBAD and [M(PDBAD)X_2]:

The physical and analytical characteristics of the **PDBAD** ligand and its metal complexes are shown in **Table 7A.1**. The structures of the chemical compounds match well with the results of the elemental analysis. **Figure 7A.1** shows the structures of **PDBAD** ligand and its metal complexes.

Table 7A.1: *Analytical data[#] of* ***PDBAD*** *and* ***[M(PDBAD)X_2]***

Compound	M.P (°C)	Molecular formula	Molecular weight	Elemental analysis*			
				%C	%H	%N	%O
PDBAD	195-197	$C_{23}H_{18}N_2O_4$	386	53.16 (71.49)	4.25 (4.70)	3.38 (7.25)	16.29 (16.56)
[Cu(PDBAD)]	240-242	$C_{23}H_{16}CuN_2O_4$	447	61.43 (61.67)	3.48 (3.60)	6.12 (6.25)	14.17 (14.29)
[Ni(PDBAD)]	275-277	$C_{23}H_{16}NiN_2O_4$	443	62.24 (62.35)	3.51 (3.64)	6.16 (6.32)	14.19 (14.44)
[Co(PDBAD)$(H_2O)_2$]	268-270	$C_{23}H_{20}CoN_2O_6$	479	57.63 (58.21)	4.21 (4.42)	5.84 (5.91)	20.03 (21.05)
[Mn(PDBAD)$(H_2O)_2$]	243-245	$C_{23}H_{20}MnN_2O_6$	475	58.11 (58.63)	4.24 (4.53)	5.89 (6.18)	20.19 (20.75)
[Zn(PDBAD)$(H_2O)_2$]	254-226	$C_{23}H_{20}ZnN_2O_6$	484	56.86 (57.12)	4.15 (4.33)	5.77 (5.93)	19.76 (19.92)

[#] data in parenthesis are calculated ones; [*] data limited to integral values

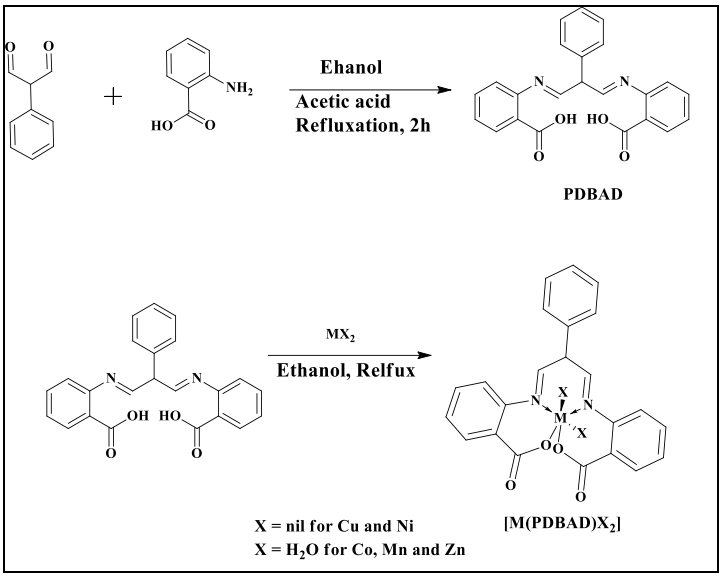

Figure 7A.1: *Schematic of the synthesis of* ***PDBAD*** *and* ***[M(PDBAD)X$_2$]***

7A.2 IR Spectral Studies:

The FTIR spectra of **PDBAD** ligand and its complexes show aliphatic C-H stretching frequencies in the range of 3000-3100 cm^{-1} (**Figures 7A.2–7A.7**). The **PDBAD** ligand's ν (C-N) stretching bands at 1575 and 1540 cm^{-1} decrease by ~20-60 cm^{-1} on complexation. Similarly, the **PDBAD** ligand's ν (C=O) stretching bands at 1683 and 1625 cm^{-1} decrease by ~30-90 cm^{-1} on complexation. The negative shift of these bands up on complexation is caused by the loss of the –C=N- and –C=O-tautomeric characters and it indicates the formation of metal complexes via the imine and carboxylic acid functional groups[1]**.** Important infrared spectral data are provided in **Table 7A.2.**

Table 7A.2: *IR data$^{\#}$ of* ***PDBAD*** *and* ***[M(PDBAD)X$_2$]***

Compounds		**IR spectral data (cm^{-1})$^{\#}$**			
	νC-H (aromatic)	**νCOO (str)**	**νC=N (sym)**	**νM-N**	**νM-O**
PDBAD	3068	1683, 1625	1575, 1540	-	-
[Cu(PDBAD)]	3095	1596, 1579	1549, 1496	530	437
[Ni(PDBAD)]	3098	1633, 1593	1494, 1459	576	449
[Co(PDBAD)(H$_2$O)$_2$]	3065	1592, 1556	1505, 1445	533	470

[Mn(PDBAD)(H$_2$O)$_2$]	3074	1597, 1578	1537, 1498	523	466
[Zn(PDBAD)(H$_2$O)$_2$]	3095	1611, 1586	1505, 1453	529	472

#, in KBr pellet

7A.3 Electronic Spectral Studies:

The electronic spectra of **PDBAD** ligand and its metal complexes are shown in **Figures 7A.8** through **Figure 7A.11**. The **PDBAD** ligand exhibits only two transitions at ~345 and 415 nm. The two peaks for **PDBAD** are attributed to $n\rightarrow\pi^*$ (of the carboxylic acid) and $\pi\rightarrow\pi^*$ (aromatic) transitions. The electronic spectra of **[M(PDBAD)X$_2$]** differ significantly from that of their ligand, **PDBAD.**

Table 7A.3 comprises the relevant electronic spectral data for **PDBAD** and **[M(PDBAD)X$_2$].** The weak broad band observed for **[Cu(PDBAD)]** at 735 nm is assigned to the $^2B_{1g} \rightarrow {}^2E_g$ d-d transition[2]**.** Whereas, shifting in $n\rightarrow\pi^*$ and $\pi\rightarrow\pi^*$ (aromatic) transitions indicate the formation of **[Cu(PDBAD)]** metal complex, furthermore, spectral data points to a square planar geometry. The bands observed for **[Ni(PDBAD)]** at ~ 517 and 633 nm are assigned to $^3T_1(F) \rightarrow {}^3T_1(P)$ and $^3T_1(F) \rightarrow {}^3A_2(F)$) d-d transitions, respectively, indicating that **[Ni(PDBAD)]** has a tetrahedral structure[3]**.** One band at 517 nm in the electronic spectra of **[Co(PDBAD)(H$_2$O)$_2$]** is attributed to the $^4A_2(F) \rightarrow {}^4T_1(P)$ d-d transition, implying tetrahedral geometry for **[Co(PDBAD)(H$_2$O)$_2$]**[4]**. [Mn(PDBAD)(H$_2$O)$_2$]** is a d^5 high spin system with spin and Laporte forbidden transitions[5]**. [Zn(PDBAD)(H$_2$O)$_2$]** has no d-d transitions, as expected for d^{10} systems.

Table 7A.3: *Physical, electronic spectral and magnetic data of* ***PDBAD*** *and* ***[M(PDBAD)(H$_2$O)$_2$]***

Compound	Color	Electronic spectral data λ (ε)*	μ_{eff} (BM)
PDBAD	Yellow	345 (13100); 415 (21600)	-
[Cu(PDBAD)]	Brown	291 (21570); 453 (16600); 735 (1630)	1.65
[Ni(PDBAD)]	Green	349 (35200); 397 (41000); 633 (2150)	2.42
[Co(PDBAD)(H$_2$O)$_2$]	Brown	332 (17000); 430 (6000); 517 (2000)	4.15
[Mn(PDBAD)(H$_2$O)$_2$]	Yellow	230 (4125); 280 (1125)	5.12
[Zn(PDBAD)(H$_2$O)$_2$]	Yellow	234 (3250); 259 (2985); 288 (2375); 320 (2000)	-

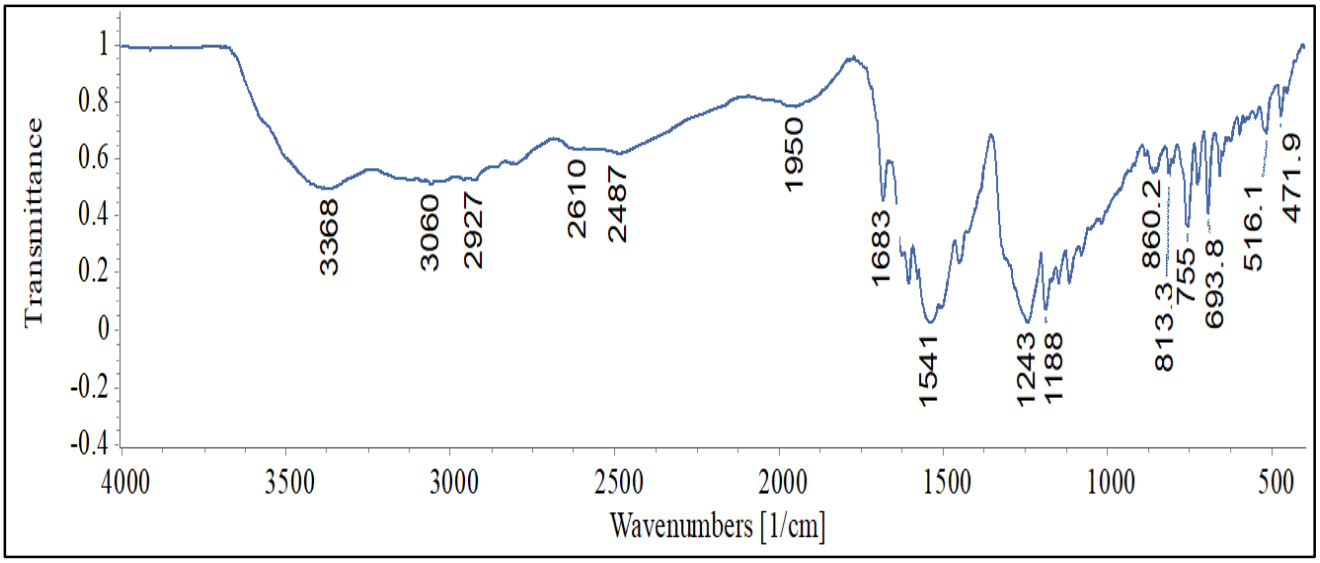

Figure 7A.2: *IR spectrum of* ***PDBAD***

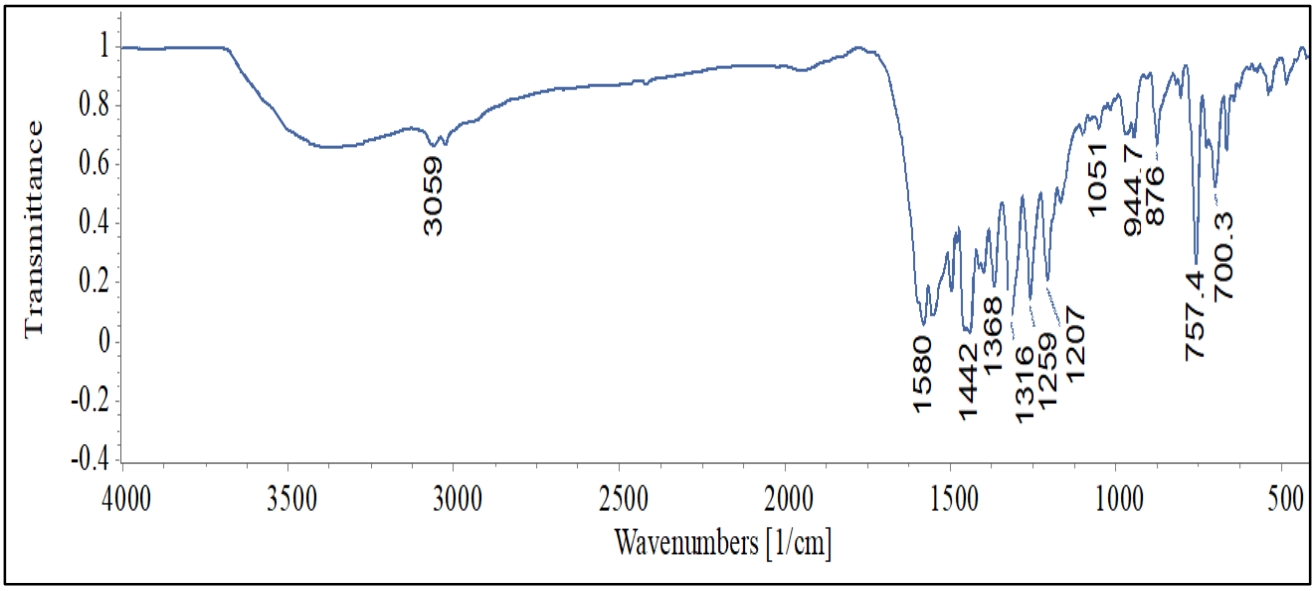

Figure 7A.3: *IR spectrum of* ***[Cu(PDBAD)]***

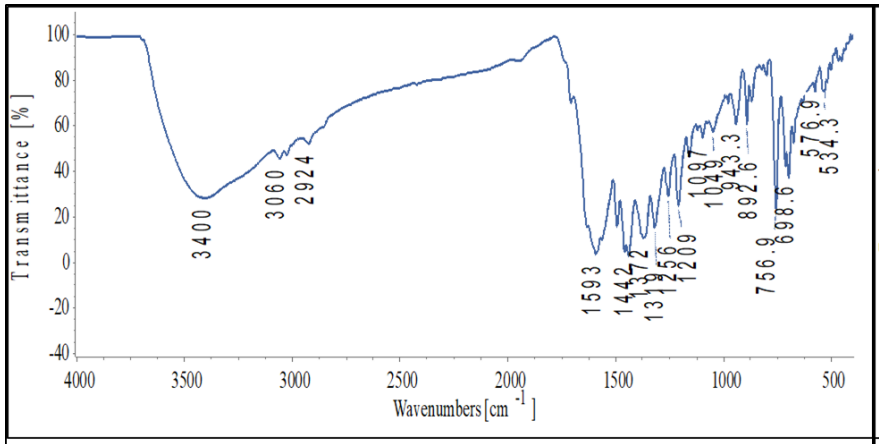

Figure 7A.4: *IR Spectrum of* ***[Ni(PDBAD)]***

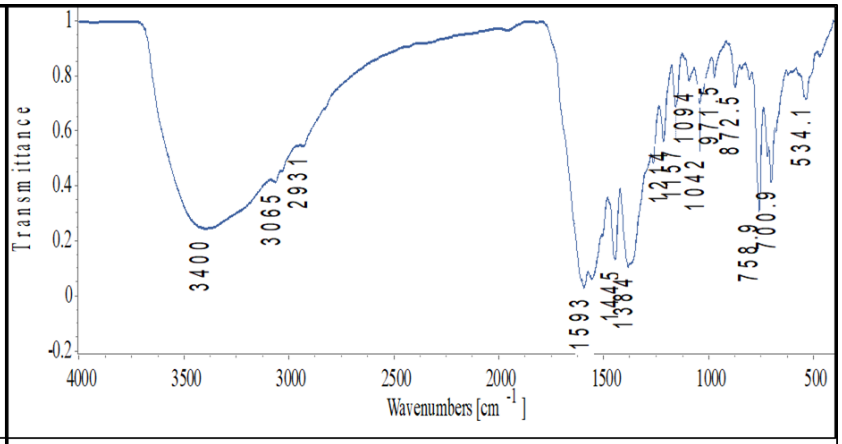

Figure 7A.5: *IR Spectrum of* ***[Co(PDBAD)(H$_2$O)$_2$]***

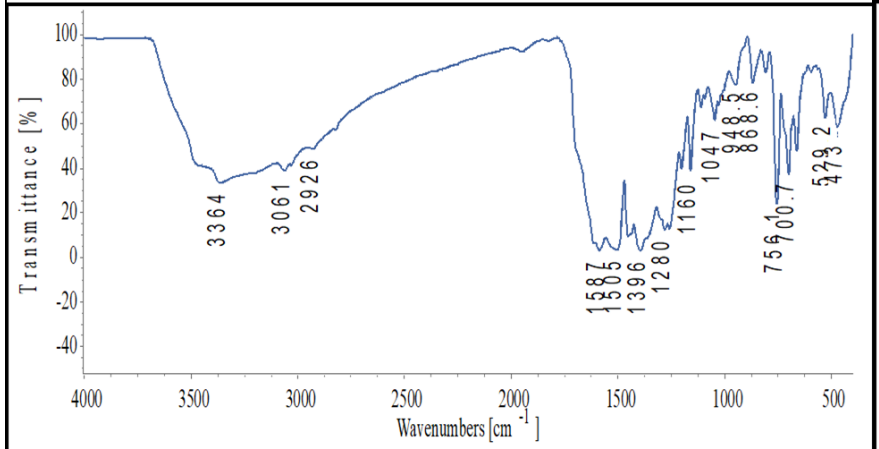

Figure 7A.6: *IR Spectrum of* ***[Mn(PDBAD)(H$_2$O)$_2$]***

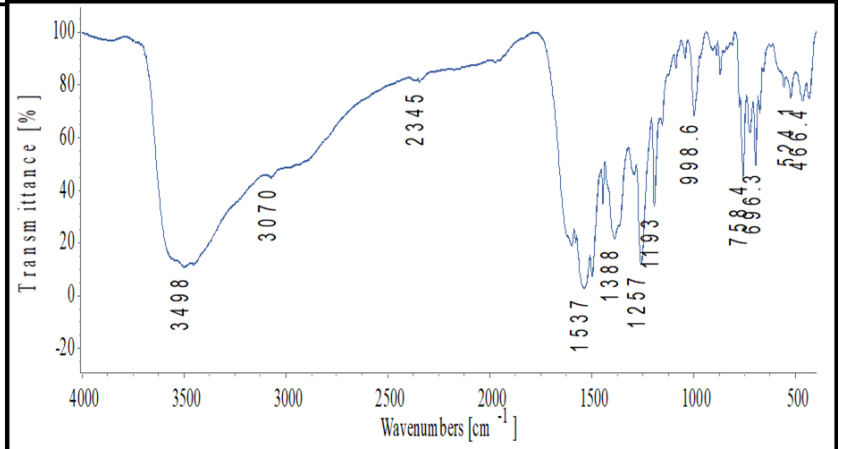

Figure 7A.7: *IR Spectrum of* ***[Zn(PDBAD)(H$_2$O)$_2$]***

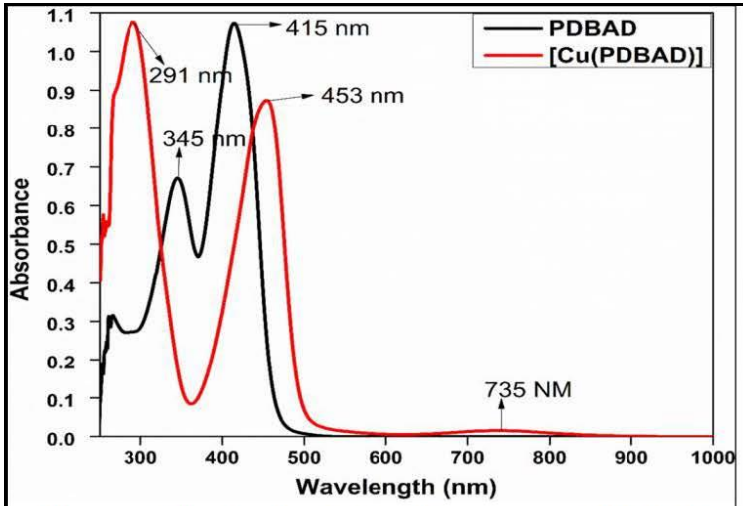

Figure 7A.8: *Overlay UV-Visible spectra of* ***PDBAD*** *and* ***[Cu(PDBAD)]***

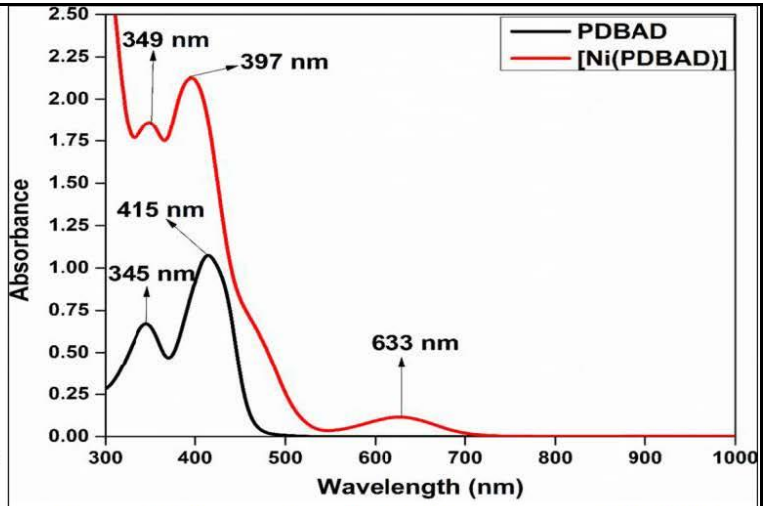

Figure 7A.9: *Overlay UV-Visible spectra of* ***PDBAD*** *and* ***[Ni(PDBAD)]***

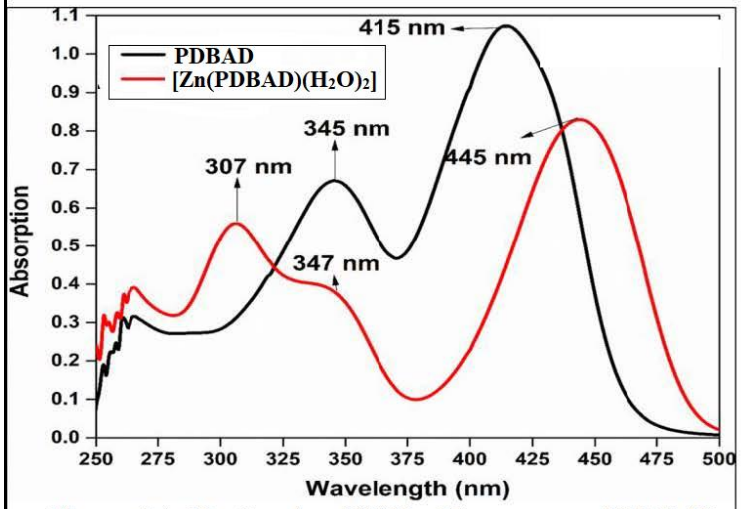

Figure 7A.10: *Overlay UV-Visible spectra of* ***PDBAD*** *and* ***[Zn(PDBAD)(H$_2$O)$_2$]***

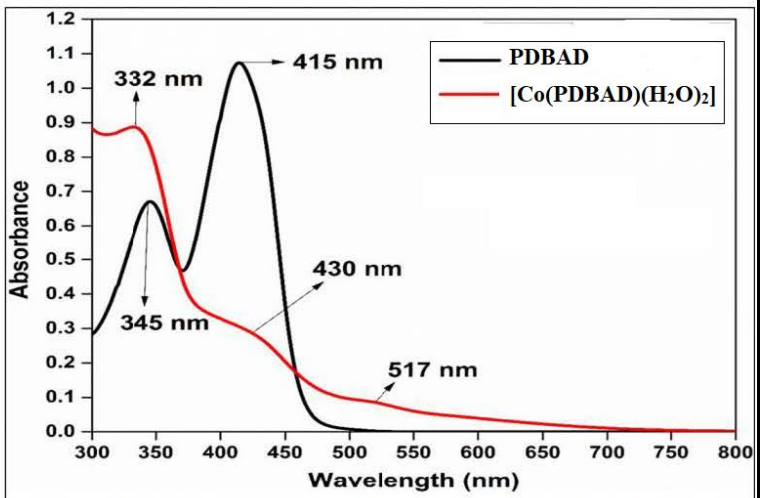

Figure 7A.11: *Overlay UV-Visible spectra of* ***PDBAD*** *and* ***[Co(PDBAD)(H$_2$O)$_2$]***

7A.4 Fluorescence Spectral Studies of PDBAD and [M(PDBAD)X_2]:

Figure 7A.12 represents the luminisence spectrum of **PDBAD.** The emission of green light, which corresponds to electron transfer from the azomethelene group to the benzene ring through the single bond, produces a broad emission peak at 421 nm[6]. The energy of the band gap was measured to be around 2.94 eV.

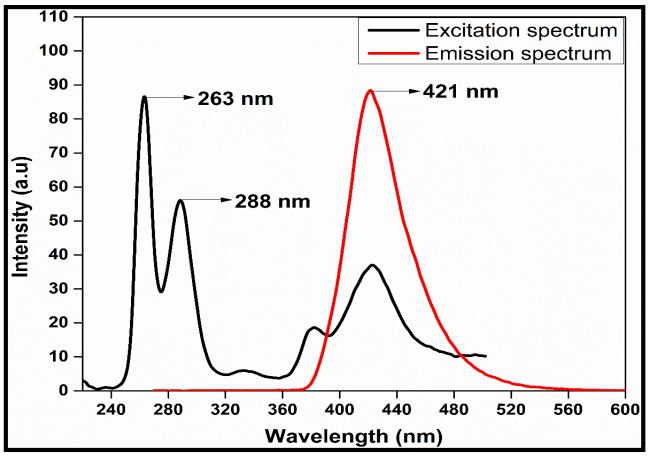

Figure 7A.12: *The solid state Absorption (black) and emission (red) spectra of* ***PDBAD***

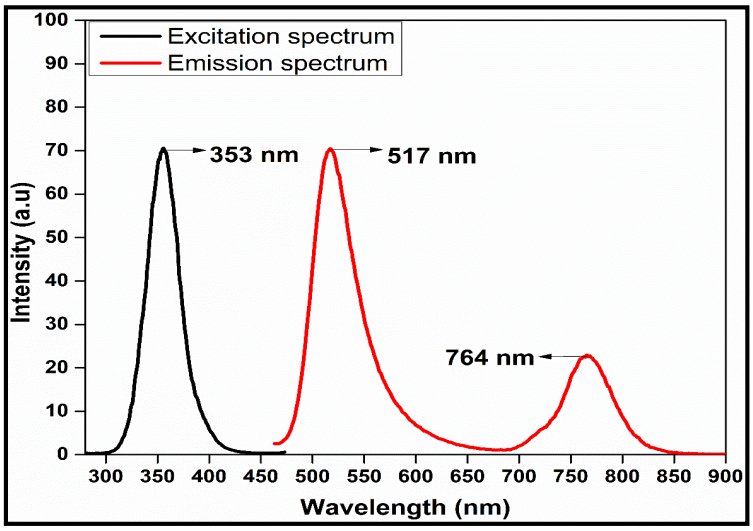

Figure 7A.13: *The solid state Absorption (black) and emission (red) spectra of [**Cu(PDBAD)**]*

Figures 7A.13 through **7A.17** show the fluorescence spectra of **[M(PDBAD)X_2]** for M = Cu, Mn, Ni, Zn, Co. The **[Cu(PDBAD)]** complex exhibits two emission bands at 517 and 764 nm

for an excitation wavelength of 288 nm. In the case of the **[Mn(PDBAD)(H$_2$O)$_2$]** complex, two emission bands are observed at 415 and 777 nm upon excitation at 356 nm. The **[Ni(PDBAD)]** complex exhibited three emission bands at 396, 520, and 755 nm for the excitation wavelength of 332 nm. The **[Zn(PDBAD)(H$_2$O)$_2$]** complex has a 511 nm emission band and a 487 nm excitation band. Similarly, for excitation with 372 nm the **[Co(PDBAD)(H$_2$O)$_2$]** complex exhibits two emission bands at 435 and 750 nm.

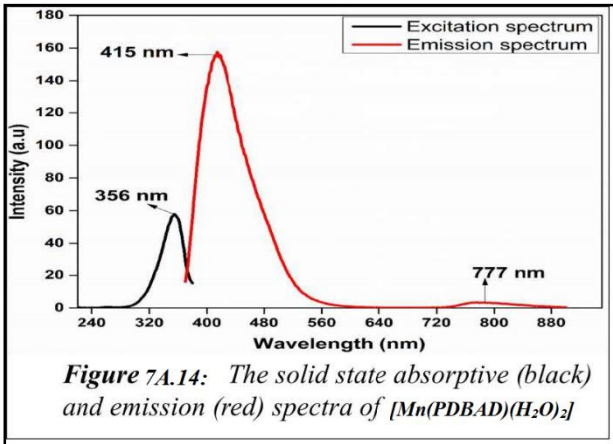

Figure 7A.14: *The solid state absorptive (black) and emission (red) spectra of* ***[Mn(PDBAD)(H$_2$O)$_2$]***

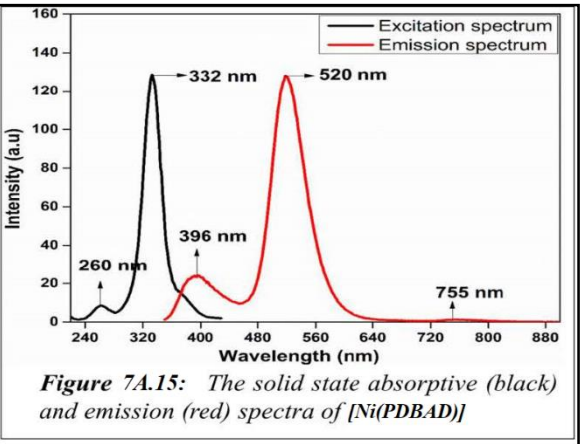

Figure 7A.15: *The solid state absorptive (black) and emission (red) spectra of* ***[Ni(PDBAD)]***

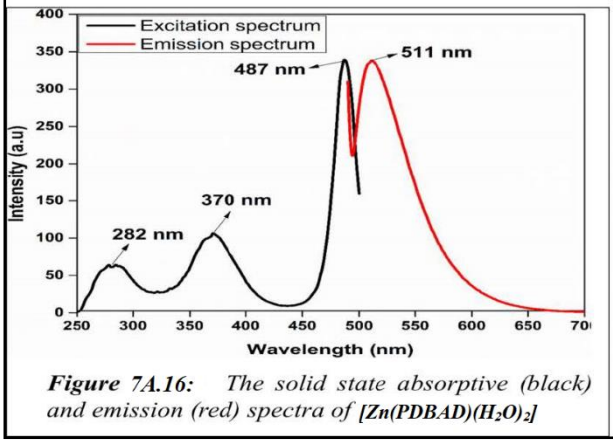

Figure 7A.16: *The solid state absorptive (black) and emission (red) spectra of* ***[Zn(PDBAD)(H$_2$O)$_2$]***

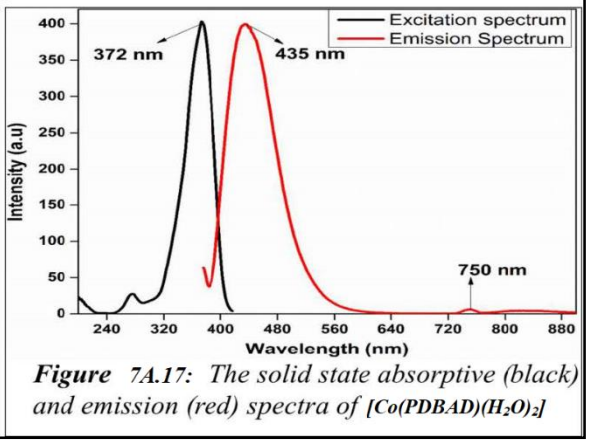

Figure 7A.17: *The solid state absorptive (black) and emission (red) spectra of* ***[Co(PDBAD)(H$_2$O)$_2$]***

7A.5 Fluorescence Spectrophotometric Titration of PDBAD Against Cu^{+2} ion (Job's Plot):

In order to find out the metal to ligand ratio (coordination number), a fluorescence spectrophotometric titration has been carried out for a fixed amount of **PDBAD** (titrand) against varied metal ion content (titrant) in a monovariation Job's Method at a fixed excitation wavelength of 353 nm[7]. **Figure 7A.19** shows the Job's plot of **PDBAD** against $CuCl_2$. This and Job's plot for other metal ions indicate the metal to ligand stoichiometry matching to the formulae, **[M(PDBAD)X$_2$]** (where X = nil for Cu^{+2} and Ni^{+2} but X = H_2O for Co^{+2}, Mn^{+2} and Zn^{+2}).

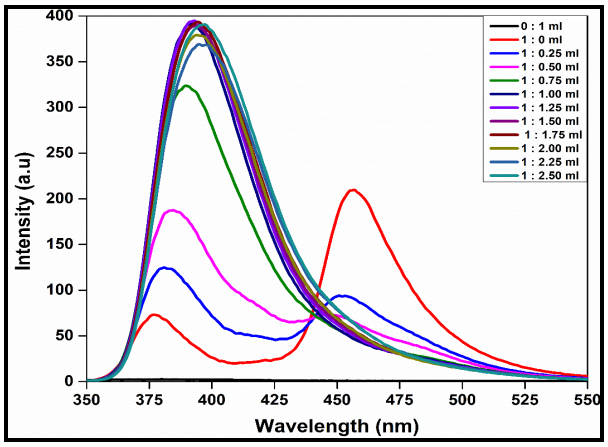

Figure 7A.18: *Spectrophotometric titration of* ***PDBAD*** *(c = 1x10^{-4} M) against* ***$CuCl_2$*** *(c = 1x10^{-4} M) with variation metal volume*

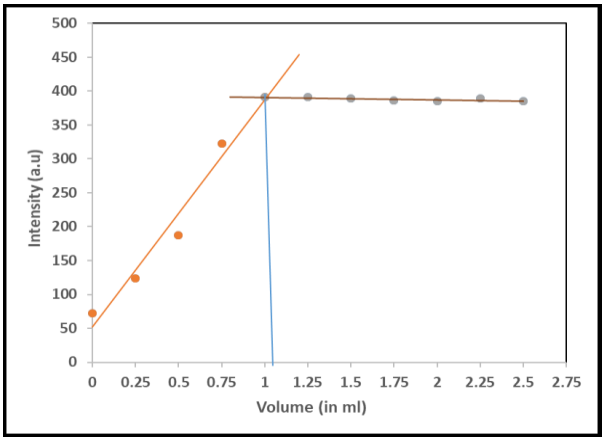

Figure 7A.19: *Monovariation Job's plot for the spectrophotometric titration of* ***PDBAD*** *(c = 1x10^{-4} M) against $CuCl_2$*

Based on the elemental analysis and the above mentioned Job's Plots, the structure of metal complexes are tentatively assisted as in **Figure 7A.1.**

7A.6 Electron Spin Resonance Spectroscopy of [Cu(PDBAD)]:

The polycrystalline state ESR spectrum of **[Cu(PDBAD)]** is shown in **Figure 7A.20**. A single broad peak centered at g = 2.101 is observed. From the simulated spectrum of **[Cu(PDBAD)]** the tensor values, $g_{\|}$ and $g_{\perp}$ are evaluated as 2.252 and 2.047, respectively. The presence of unpaired electrons in the d_{x2-y2} (ground state) orbital is discerned from the fact that $g_{\|}$

> $g_{\perp}$ > 2.0023, which also infers a square planar geometry to the Cu(II) center[8]**.** The fact that the g_{avg} value is lower than 2.3 means there is a covalent bond between the metal and the ligand.

The geometric parameter, G, also known as magnetic exchange interaction parameter and calculated by the following formula, is found out to be about 5.58. However, it is well known, as reported by Hathaway and Billing, that a value of G < 4 infers an appreciable magnetic interaction between adjacent metal centers in a solid state, whereas that of G > 4 is a negligible one[9]**.**

$$G = \frac{g_{\parallel} - 2.0023}{g_{\perp} - 2.0023} \qquad \textbf{(6.1)}$$

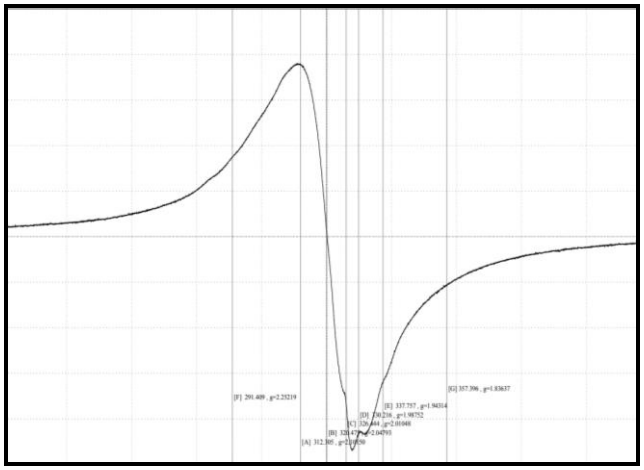

Figure 7A.20: *X-band electron spin resonance spectrum of* ***[Cu(PDBAD)]*** *in solid state*

The fact that the exchange interaction parameter value of complex **[Cu(PDBAD)]** is greater than 4 indicates that copper centers do not have spin exchange interaction, as in certain Schiff base square planar complexes and copper[10].

7A.7 Cyclic Voltammetric Studies of PDBAD and [M(PDBAD)X_2]:

Figures 7A.21 (a) shows the cyclic voltammogram (CV) of **PDBAD** ligand as a function of scan rate. Two anodic peaks at E_p = 0.85 and E_p = 0.96 V are observed with no corresponding cathodic peaks in the reverse scan. The CV then indicates an irreversible oxidation of **PDBAD** in consecutive electron transfer steps.

In **Figure 7A.21 (b)** is shown the relation between peak current, i_p and scan rate, ν. The linearity plot of i_p vs $\nu^{1/2}$ indicates that the electron transfer proceeds is diffusion controlled. **Figure 22 (b)** shows the linear sweep voltammogram (LSV) of **PDBAD B** varied concentrations. The anodic peak currents are found to be linear with the concentrations of the **PDBAD**. Thus LSV seems to serve as an electroanalytical tool for the analysis of **PDBAD.**

The cyclic voltammogram of **[Zn(PDBAD)(H$_2$O)$_2$]** shows one prominent oxidation at 0.67 V, attributed to ligand oxidation of azomethine groups (**Figure 7A.23 (a)**). The oxidation peak potentials are slightly negative when compared to the free ligand (E_{pa} = 23 mV) due to the coordination of the **PDBAD** ligand to the Zn(II) ion center. The electron charge transfers from metal to the ligand. In **Figure 7A.23(b)** is shown the effect of scan rate on the peak current. The linearity of the i_p with ν is indicative of diffusion-controlled electron transfer. **Figure 7A.24(a)** shows the LSV of **[Zn(PDBAD)(H$_2$O)$_2$]** with varied concentration whereas **Figure 7A.24(b)** shows the linearity of i_p of **[Zn(PDBAD)(H$_2$O)$_2$].** This plot suggests possible quantitative analysis of Zn ion by complexometric LSV.

The electron transfers coefficient (α_{na}) and heterogeneous electron transfer rate constant (k^o_h) have been evaluated from studies of the influence of concentration and scan rate on peak potentials[11]. The pertinent electrochemical data along with the diffusion coefficient (D) value are shown in **Table 7A.4.**

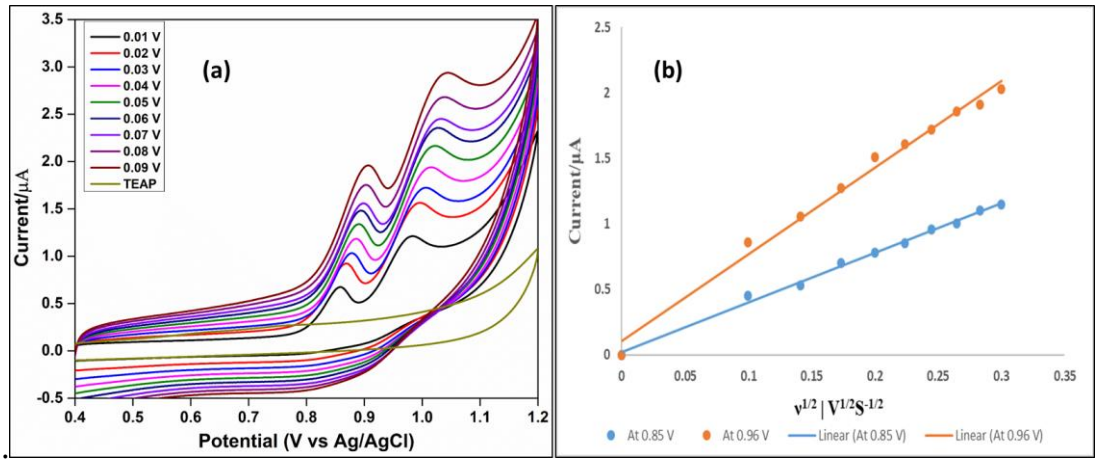

Figure 7A.21: (a) *Cyclic voltammogram of* ***PDBAD*** *(5x10^{-5} M) in DMSO at different scan rates* ***(b)*** *Effect of scan rate on the anodic current of* ***PDBAD***

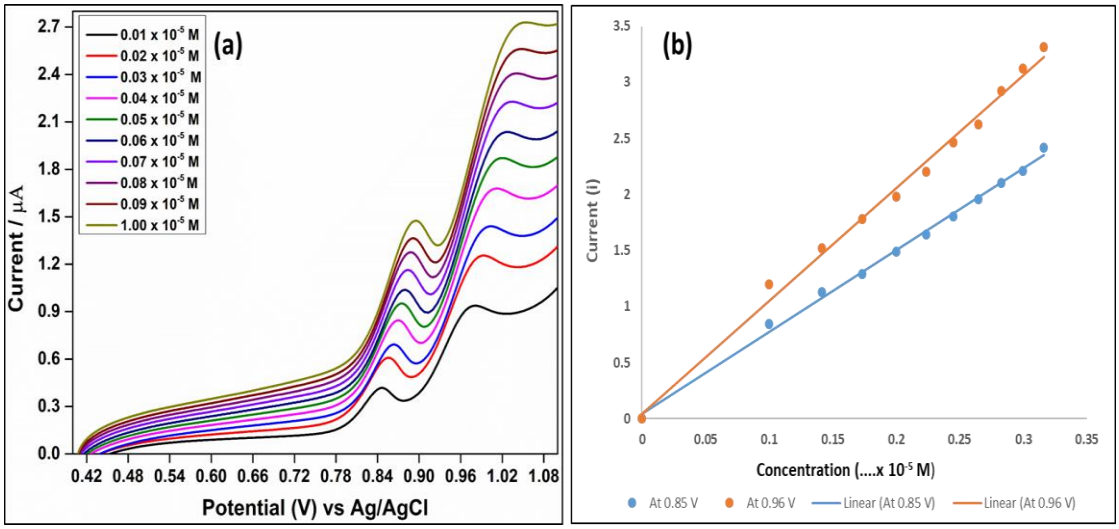

Figure 7A.22: (a) *LSV of* ***PDBAD*** *in DMSO at different concentrations* ***(b)*** *Variation of anodic and cathodic currents of* ***PDBAD*** *with respect to various concentration*

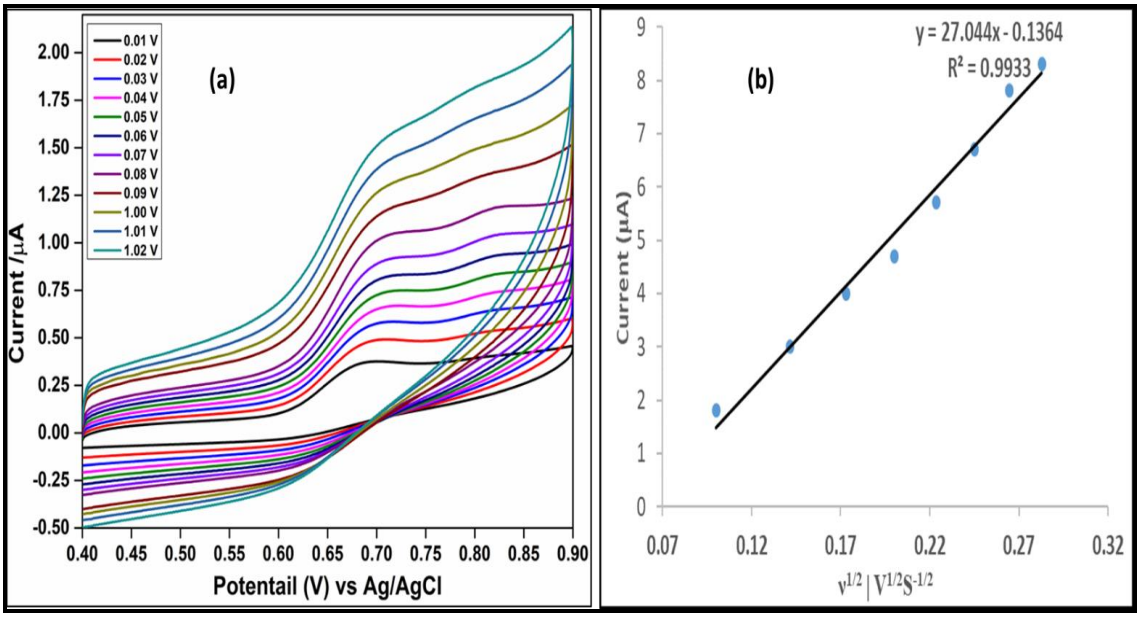

Figure 7A.23: (a) *Cyclic voltammogram of* ***[Zn(PDBAD)(H$_2$O)$_2$]*** *(5x 10^{-5} M) in DMSO at different scan rates* ***(b)*** *Effect of scan rate on the anodic current of* ***[Zn(PDBAD)(H$_2$O)$_2$]***

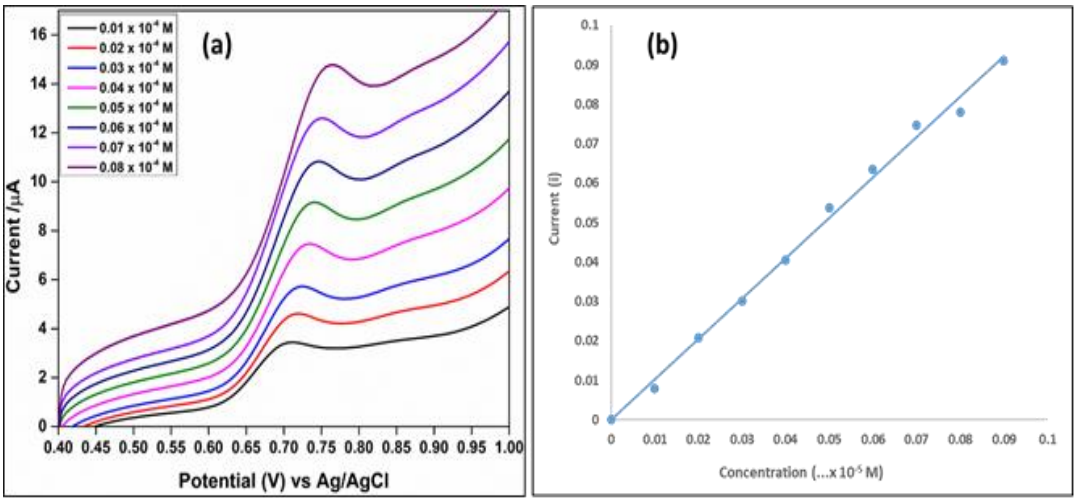

Figure 7A.24: (a) *LSV of* ***[Zn(PDBAD)(H$_2$O)$_2$]*** *(5x10^{-5} M) in DMSO at different scan rates* ***(b)*** *Effect of scan rate on the anodic current of* ***[Zn(PDBAD)(H$_2$O)$_2$]***

Table 7A.4: *Electrochemical data of* ***PDBAD*** *and* ***[Zn(PDBAD)(H$_2$O)$_2$]*** *various metal complexes in acetone medium*

Compound	**Parameters**		
	(D) in cm^2 s^{-1}	**(α_{na}) in cm^2 s^{-1}**	**k^o_h in cm^2 s^{-1}**
PDBAD	9.32 x 10^{-6}	0.34	5.22x 10^{-5}
[Zn(PDBAD)(H$_2$O)$_2$]	11.36 x 10^{-6}	0.66	10.13 x 10^{-5}

PART B

MOLECULAR MODELING AND MOLECULAR DOCKING STUDIES OF PDBAD AND ITS METAL COMPLEXES

7B.1 Molecular Modelling Studies of PDBAD and [M(PDBAD)X_2]:

Molecular modelling studies were used to determine the conformational visualization of the molecules in various forms in order to address the stability aspects of the **PDBAD** ligand and its metal complexes **[M(PDBAD)X_2].** The global energy minimized structures are calculated using the MM2 force field method with an RMS gradient of 0.01. In any structural analysis, the bond length, bond angles and torsional angles are some of the most essential structural factors. The ligand **PDBAD** as well as its complexes are being investigated. There is a great degree of consistency between the experimental and simulated results. **Figure 7B.1** shows the globally minimized structures of the **PDBAD** ligand. The numbering adaptation is shown in **Figure 7B.1** for subsequent reference in the discussion**. Figures 7B.2** and **7B.3** show the anaglyph image and stereographic depiction of the **PDBAD**, respectively, to view the molecule disposition in space and to provide a 3D visual of it. We have used computational methods for dihedral driving and double dihedral driving to undertake conformational analysis by torsion across the chosen single bonds. Conformational analysis plots of **PDBAD** are shown in **Figure 7B.4** through **Figure 7B.25**.

Quantum mechanical HOMO-LUMO orbital energy estimates were used to compute the expected gas-phase electronic transitions (**Figures 7B.26** through **Figure 7B.31**). **Table 7B.1** and **Table 7B.2** contain some of the important bond lengths, bond angles and torsional angles data of **[M(PDBAD)X_2]** obtained from MM2 calculations.

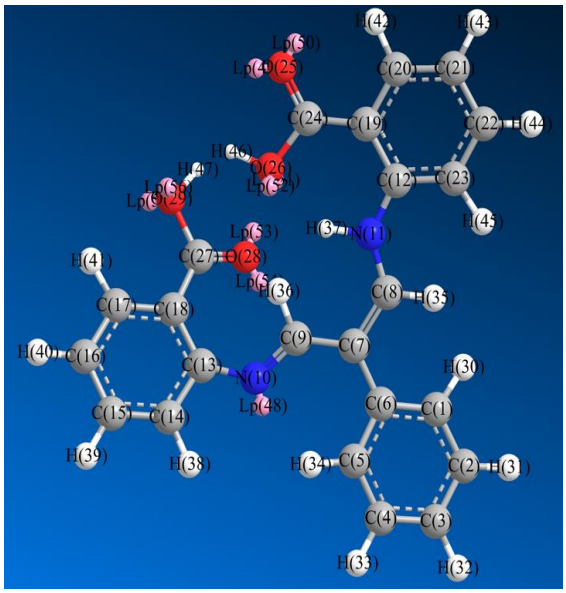

Figure 7B.1: *MM2-energy-minimized structure of* ***PDBAD*** *(enamine form)*

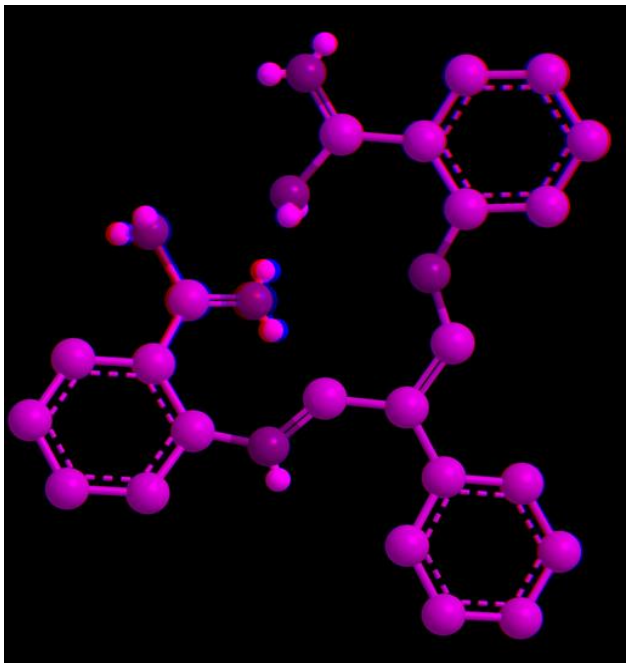

Figure 7B.2: *MM2-energy-minimized anaglyph structure of* ***PDBAD*** *(Enamine form)*

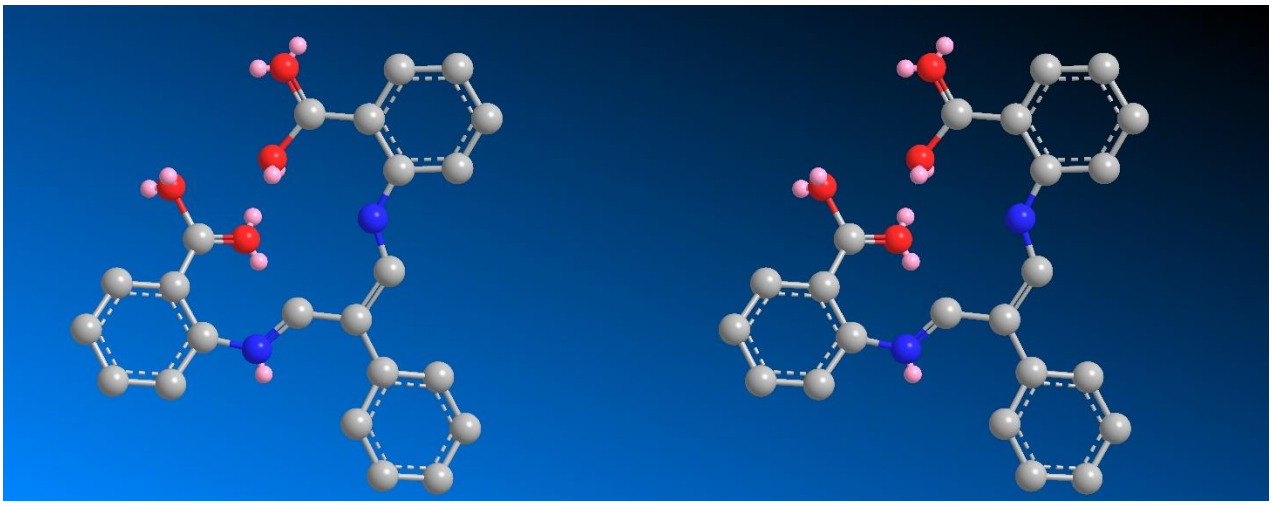

***Figure 7B.3**: Stereographic projection of MM2-minimized structure of **PDBAD** (enamine form) obtained from ChemDrawPro*

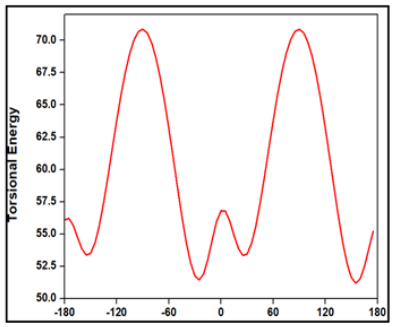

***Figure 7B.4:** Conformational analysis over C6-C7*

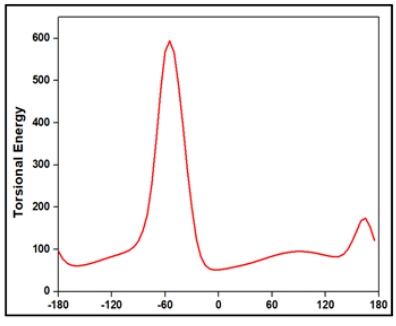

***Figure 7B.5:** Conformational analysis over C7-C9*

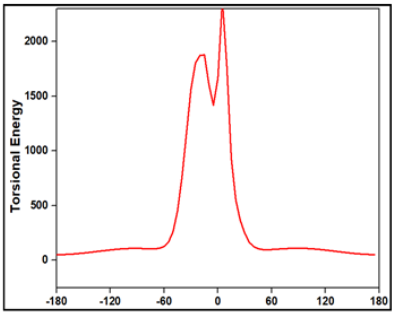

***Figure 7B.6:** Conformational analysis over C8-N11*

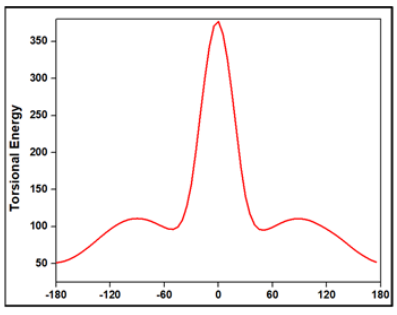

***Figure 7B.7:** Conformational analysis over N11-C12*

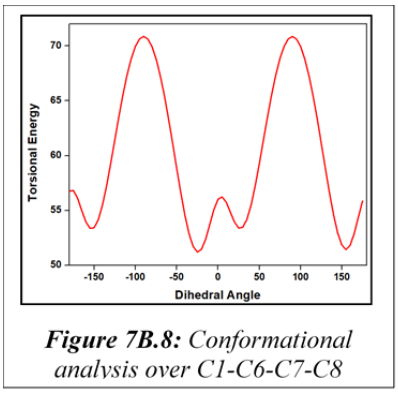

Figure 7B.8: *Conformational analysis over C1-C6-C7-C8*

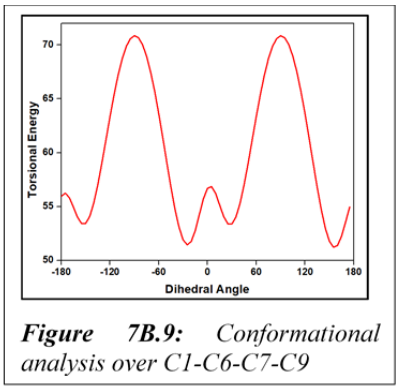

Figure 7B.9: *Conformational analysis over C1-C6-C7-C9*

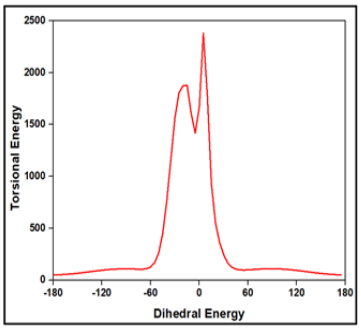

Figure 7B.10: *Conformational analysis over C7-C8-N11-C12*

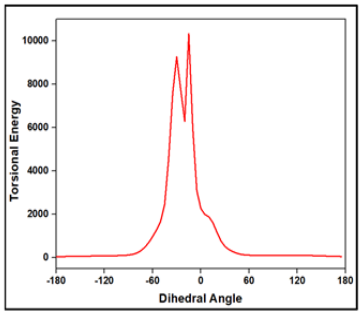

Figure 7B.11: *Conformational analysis over* C7-C9-N10-C13

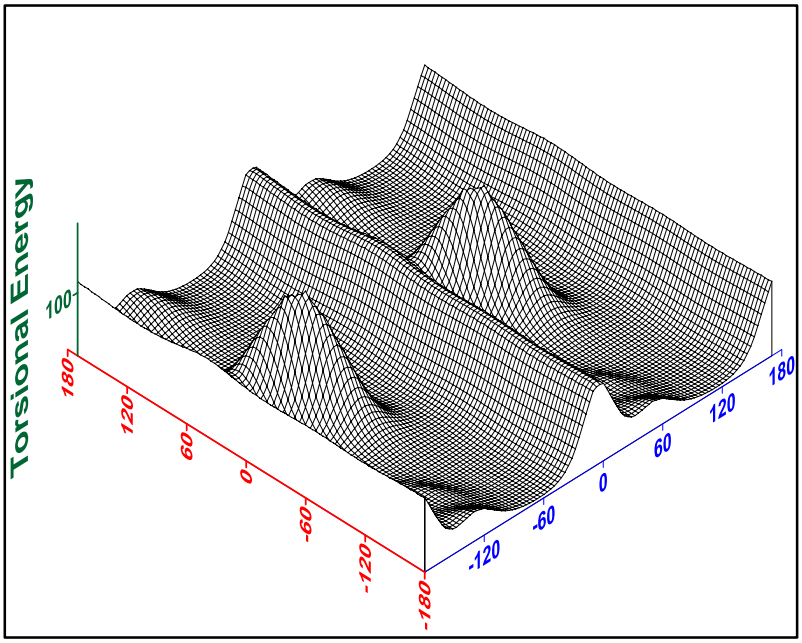

Figure 7B.12: *Double dihedral torsional energy Surfer plot of* ***PDBAD*** *(keto form) over C6-C7 (on axis shown in red) and C7-C9 (on axis shown in blue) bonds (Refer* ***Figure 7B.1*** *for numbering of the atoms)*

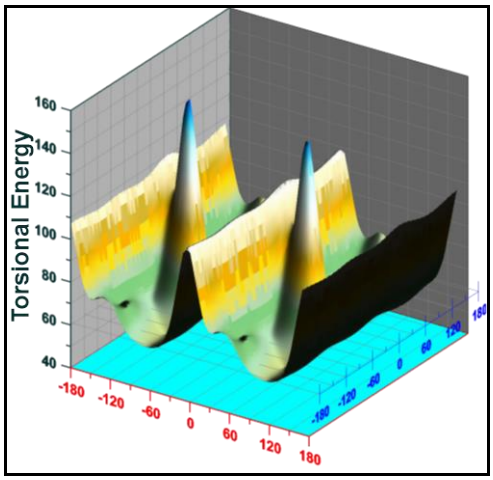

Figure 7B.13: *Double dihedral torsional energy Grapher plot of* ***PDBAD*** *(keto form) over C6-C7 (on axis shown in blue) and C7-C9 (on axis shown in red) bonds (Refer* ***Figure 7B.1*** *for numbering of the atoms)*

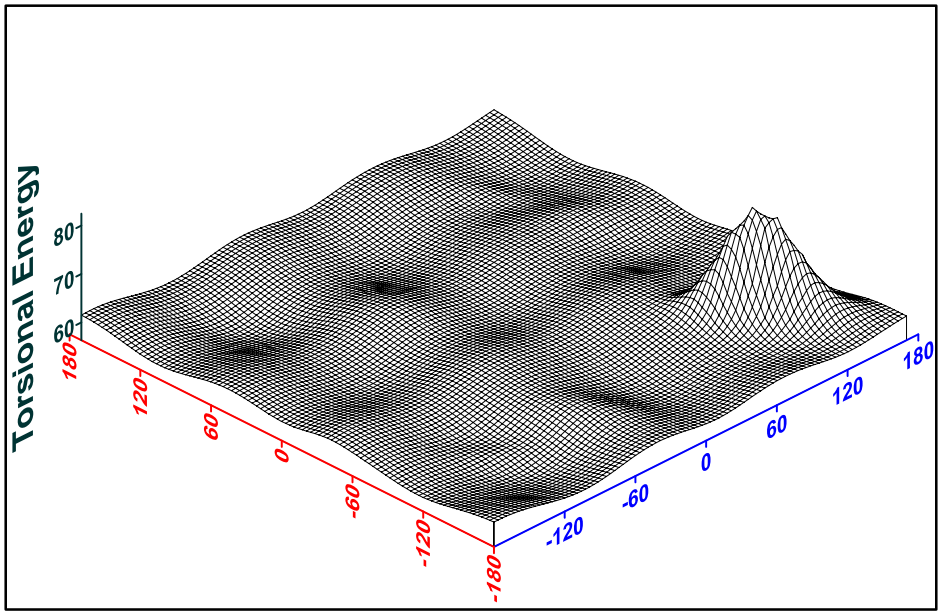

Figure 7B.14: *Double dihedral torsional energy Surfer plot of* ***PDBAD*** *(keto form) over C8-C7 (on axis shown in red) and C7-C9 (on axis shown in blue) bonds (Refer* ***Figure 7B.1*** *for numbering of the atoms)*

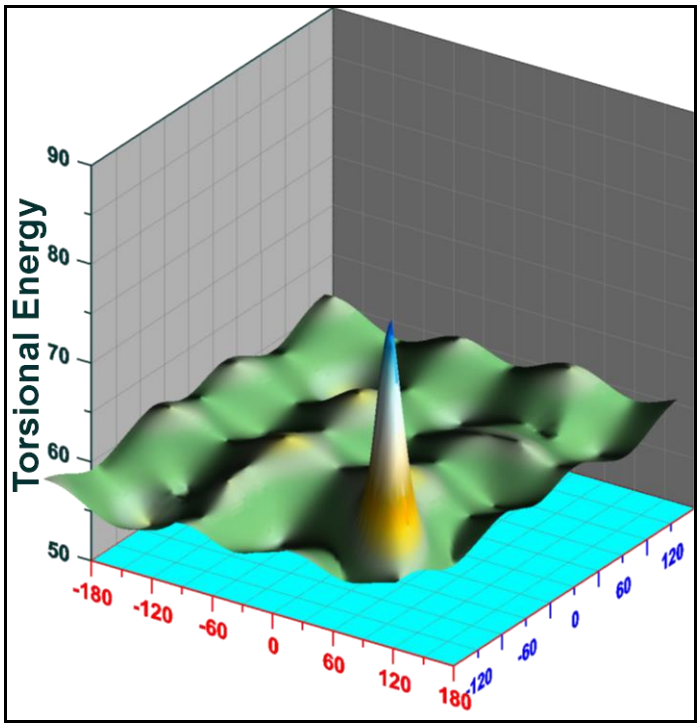

Figure 7B.15: *Double dihedral torsional energy Grapher plot of* ***PDBAD*** *(keto form) over C8-C7 (on axis shown in blue) and C7-C9 (on axis shown in red) bonds (Refer* ***Figure 7B.1*** *for numbering of the atoms)*

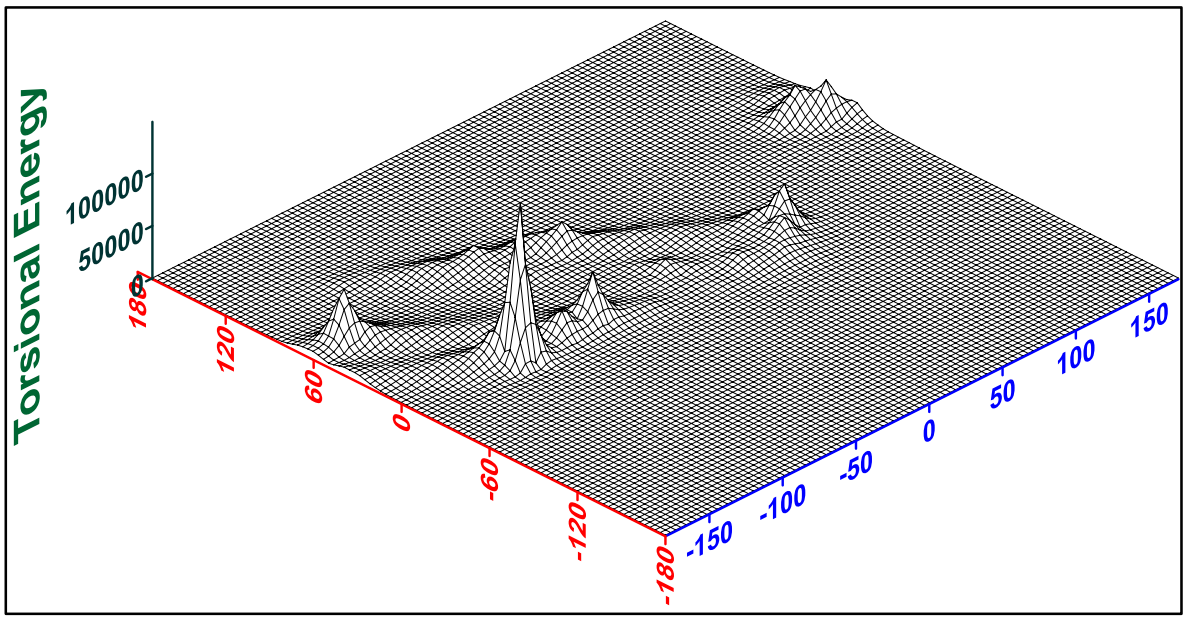

Figure 7B.16: *Double dihedral torsional energy Surfer plot of* ***PDBAD*** *(keto form) over C7-C8 (on axis shown in red) and C8-N11 (on axis shown in blue) bonds (Refer* ***Figure 7B.1*** *for numbering of the atoms)*

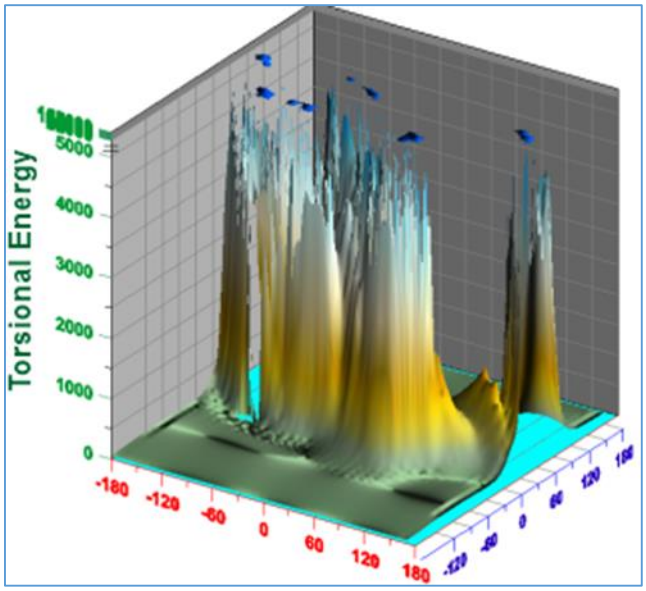

Figure 7B.17: *Double dihedral torsional energy Grapher plot of* ***PDBAD*** *(keto form) over C7-C8 (on axis shown in blue) and C8-N11 (on axis shown in red) bonds (Refer* ***Figure 7B.1*** *for numbering of the atoms)*

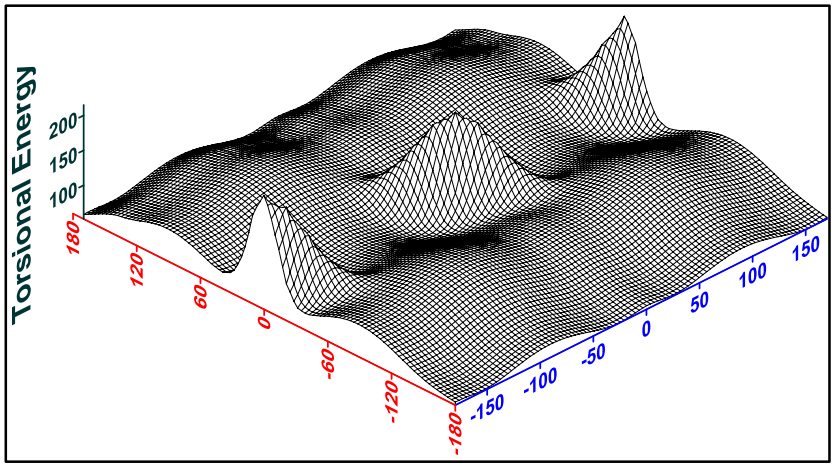

Figure 7B.18: *Double dihedral torsional energy Surfer plot of* ***PDBAD*** *(enamine form) over C7-C8 (on axis shown in red) and C8-N11 (on axis shown in blue) bonds (Refer* ***Figure 7B.1*** *for numbering of the atoms)*

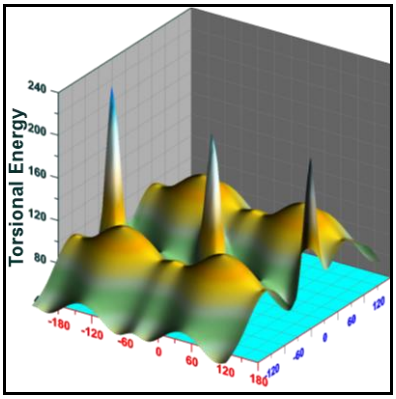

Figure 7B.19: *Double dihedral torsional energy Grapher plot of* ***PDBAD*** *(enamine form) over C7-C8 (on axis shown in blue) and C8-N11 (on axis shown in red) bonds (Refer* ***Figure 7B.1*** *for numbering of the atoms)*

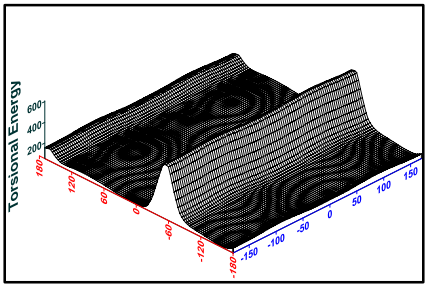

Figure 7B.20: *Double dihedral torsional energy Surfer plot of* ***PDBAD*** *(enamine form) over C6-C7 (on axis shown in red) and C7-N9 (on axis shown in blue) bonds (Refer* ***Figure 7B.1*** *for numbering of the atoms)*

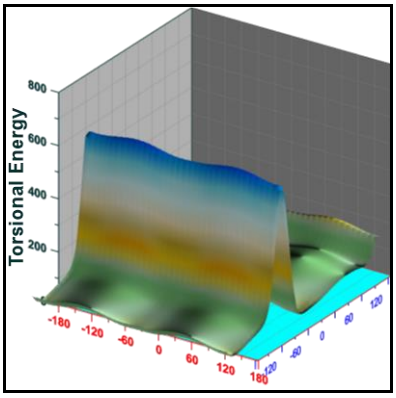

Figure 7B.21: *Double dihedral torsional energy Grapher plot of* ***PDBAD*** *(enamine form) over C7-C8 (on axis shown in blue) and C8-N11 (on axis shown in red) bonds (Refer* ***Figure 7B.1*** *for numbering of the atoms)*

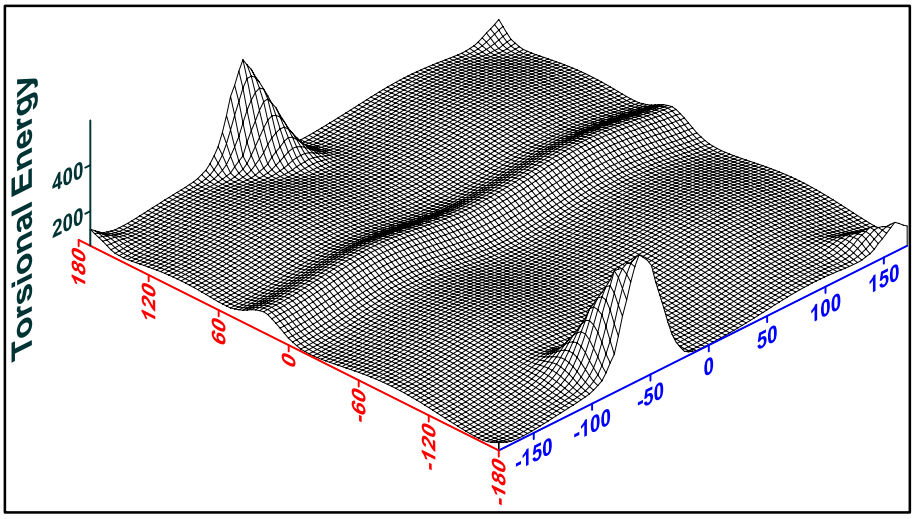

Figure 7B.22: *Double dihedral torsional energy Surfer plot of* ***PDBAD*** *(enamine form) over C8-C7 (on axis shown in red) and C7-C9 (on axis shown in blue) bonds (Refer* ***Figure 7B.1*** *for numbering of the atoms)*

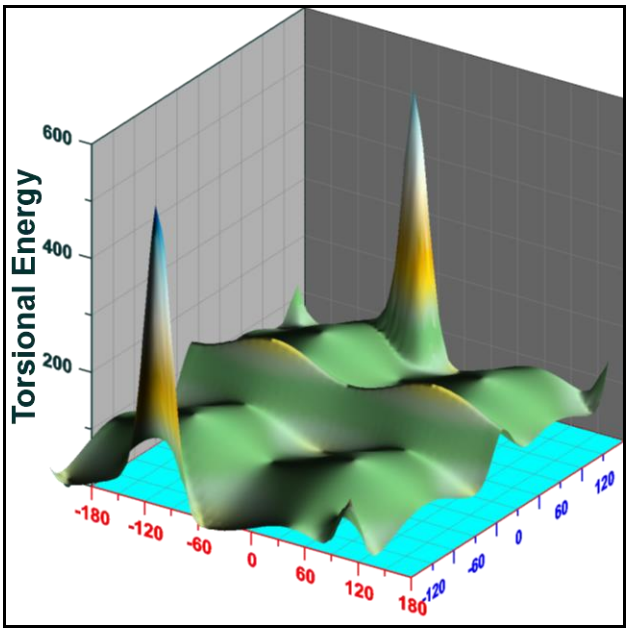

Figure 7B.23: *Double dihedral torsional energy Grapher plot of* ***PDBAD*** *(enamine form) over C8-C7 (on axis shown in blue) and C7-C9 (on axis shown in red) bonds (Refer* ***Figure 7B.1*** *for numbering of the atoms)*

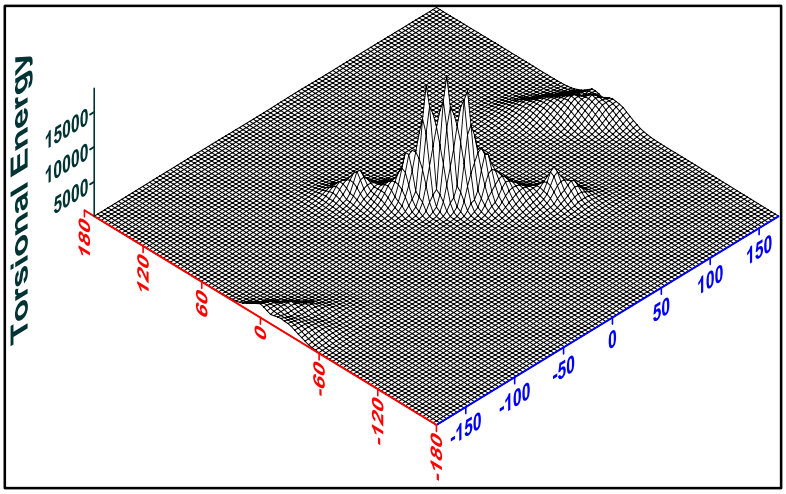

Figure 7B.24: *Double dihedral torsional energy Surfer plot of* ***PDBAD*** *(enamine form) over C7-C8 (on axis shown in red) and C8-N11 (on axis shown in blue) bonds (Refer* ***Figure 7B.1*** *for numbering of the atoms)*

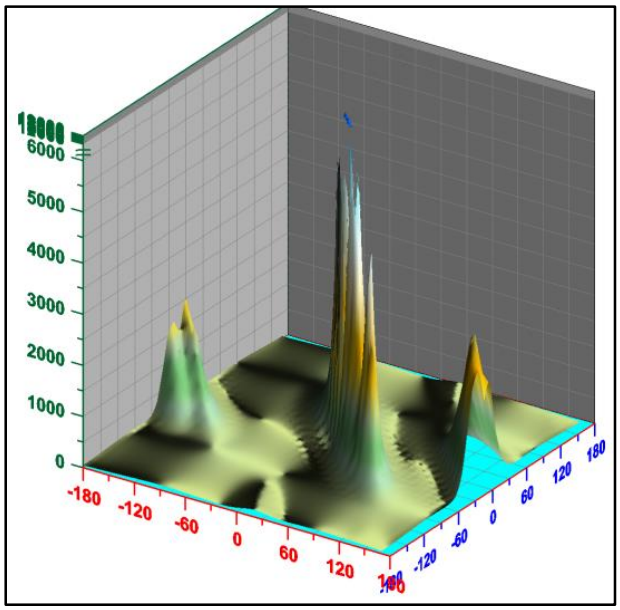

Figure 7B.25: *Double dihedral torsional energy Grapher plot of* ***PDBAD*** *(enamine form) over C7-C8 (on axis shown in blue) and C8-N11 (on axis shown in red) bonds (Refer* ***Figure 7B.1*** *for numbering of the atoms)*

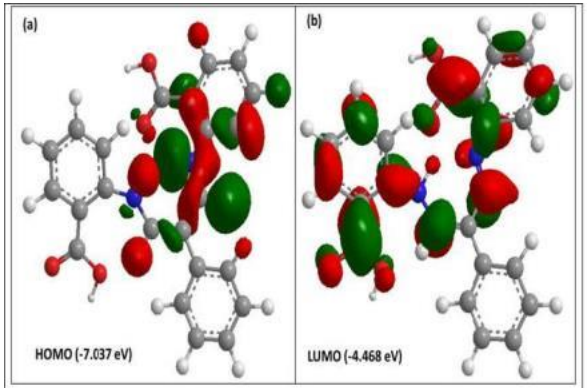

Figure 7B.26: ***HOMO*** *and* ***LUMO*** *molecular orbitals of* ***PDBAD***

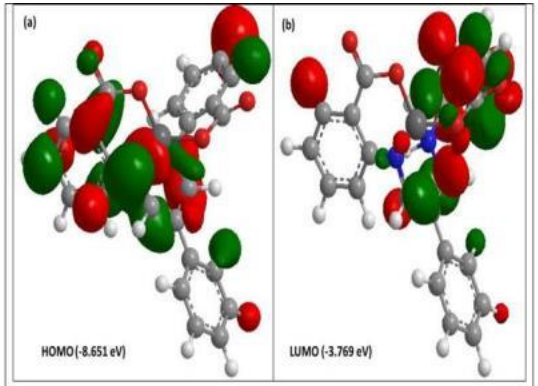

Figure 7B.27: ***HOMO*** *and* ***LUMO*** *molecular orbitals of* ***[Cu(PDBAD)]***

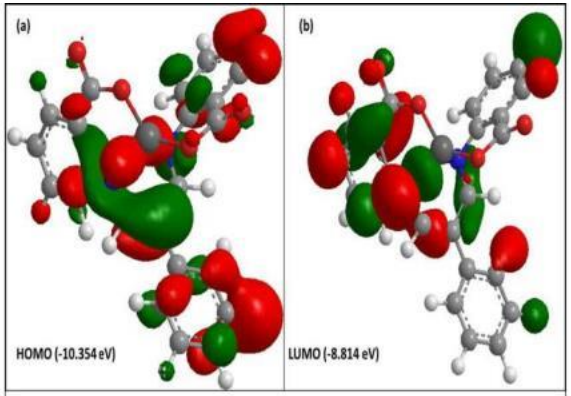

Figure 7B.28: ***HOMO and LUMO*** *molecular orbitals of* ***[Ni(PDBAD)]***

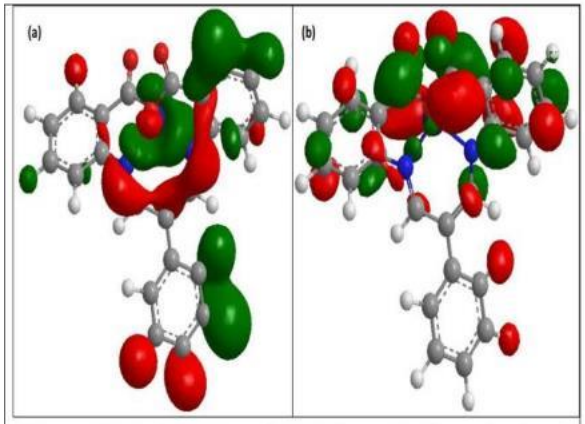

Figure 7B.29: ***HOMO*** *and* ***LUMO*** *molecular orbitals of* ***[Co(PDBAD)(H$_2$O)$_2$]***

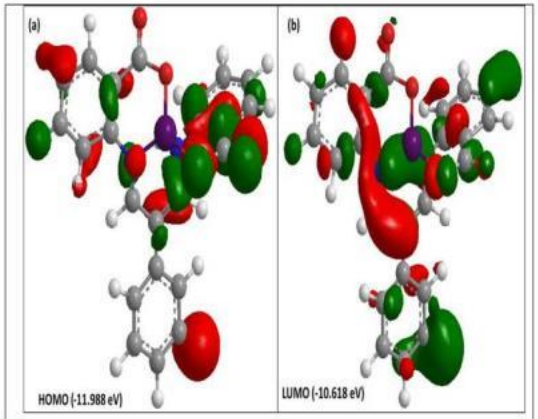

Figure 7B.30: ***HOMO*** *and* ***LUMO*** *molecular orbitals of* ***[Mn(PDBAD)$_2$(H$_2$O)$_2$]***

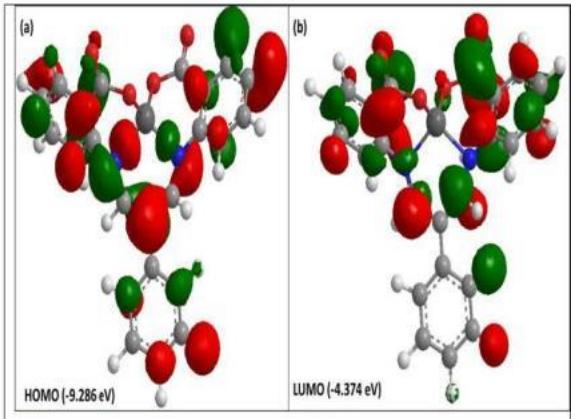

Figure 7B.31: ***HOMO*** *and* ***LUMO*** *molecular orbitals of* ***[Zn(PDBAD)(H$_2$O)$_2$]***

Table 7B.1: *Some of the important bond lengths and bond angles of* ***[M(PDBAD)X_2]***

Bond Lengths (Å)	**[Cu(PDBAD)]**	**[Ni(PDBAD)]**	**[Co(PDBAD)(H_2O)$_2$]**	**[Mn(PDBAD)(H_2O)$_2$]**	**[Zn(PDBAD)(H_2O)$_2$]**
C_6-C_7	1.360	1.369	1.369	1.360	1.364
C_7-C_8	1.364	1.359	1.358	1.353	1.361
C_7-C_9	1.350	1.361	1.357	1.347	1.356
C_9-N_{11}	1.277	1.286	1.287	1.288	1.281
C_8-N_{10}	1.286	1.271	1.273	1.284	1.276
N_{10}-M	1.312	1.804	1.832	1.838	1.929
N_{11}-M	1.844	1.801	1.832	1.870	1.929
N_{11}-C_{12}	1.284	1.295	1.292	1.285	1.286
N_{10}-C_{13}	1.286	1.275	1.280	1.289	1.274
C_{19}-C_{24}	1.377	1.382	1.380	1.383	1.388
C_{24}-O_{29}	1.219	1.219	1.225	1.222	1.220
C_{24}-O_{25}	1.385	1.391	1.478	1.379	1.394
O_{25}-M	1.806	1.774	0.748	1.794	1.890
O_{28}-M	1.812	1.763	0.713	1.801	1.894
O_{28}-C_{26}	1.382	1.380	1.466	1.383	1.384
C_{26}-O_{27}	1.220	1.221	1.266	1.219	1.220
C_{26}-C_{18}	1.378	1.384	1.376	1.368	1.382
Bond Angles (°)					
$C_1C_6C_7$	124.1	123.4	123.2	123.1	121.4
$C_5C_6C_7$	121.0	123.1	123.5	122.1	123.9
$C_6C_7C_8$	124.3	119.6	120.6	124.8	120.8
$C_6C_7C_9$	121.5	120.1	120.8	123.0	118.5
$C_7C_8N_{10}$	129.6	130.1	130.1	129.6	127.7
$C_7C_9N_{11}$	120.6	133.5	130.6	120.8	126.6
$C_8N_{10}M$	116.4	112.6	116.3	119.2	112.9
$C_9N_{11}M$	105.6	110.9	118.0	107.8	106.7
$C_8N_{10}C_{13}$	124.0	128.3	126.2	118.0	130.9

$C_9N_{11}C_{12}$	131.1	137.6	125.9	114.8	132.2
$N_{10}MN_{11}$	112.0	108.5	99.7	81.9	101.1
$N_{10}MO_{25}$	101.3	90.8	102.4	106.8	91.3
$C_{18}C_{26}O_{28}$	124.0	126.1	121.4	121.5	125.3
$O_{25}MO_{28}$	117.6	115.9	127.7	123.2	123.9
$C_{26}O_{28}M$	111.3	106.7	124.6	118.1	109.1
$C_{24}O_{25}M$	106.3	109.5	123.2	113.8	106.3
$O_{28}MN_{11}$	89.9	105.3	104.4	80.9	91.9
$C_{26}C_{18}C_{12}$	121.9	124.7	114.3	116.9	124.2
$C_{24}C_{19}C_{13}$	119.2	121.6	114.2	125.1	124.7

Table 7B.2: *Some of the important torsional angles of* ***[M(PDBAD)X_2]***

Torsional Angles (Å)	**Cu(PDBAD)**	**Ni(PDBAD)**	**[Co(PDBAD)(H_2O)$_2$]**	**[Mn(PDBAD)(H_2O)$_2$]**	**[Zn(PDBAD)(H_2O)$_2$]**
$H_{36}C_8N_{10}M$	-161.6	-168.6	-163.3	+168.2	-158.4
$C_7C_8N_{10}M$	+31.8	+23.0	+28.5	-10.1	+32.9
$C_7C_9N_{11}M$	+49.8	-173.1	+5.7	+70.3	+54.9
$H_{37}C_9N_{11}M$	+62.9	-179.4	+177.6	-113.1	-123.5
$C_8N_{10}MO_{25}$	-139.3	-138.0	-137.5	+123.6	-138.8
$C_8N_{10}MO_{28}$	+93.6	+101.8	+83.5	-29.5	+91.3
$C_{13}N_{10}MO_{25}$	+43.6	+71.5	+68.8	-24.5	+70.4
$C_{13}N_{10}MO_{28}$	-56.0	-48.7	-70.2	-177.7	-59.3
$C_{18}C_{26}O_{28}M$	+22.3	+28.3	+36.6	-32.4	+19.2
$C_{18}C_{12}N_{11}M$	-57.1	-24.1	-25.0	+57.5	-56.2
$N_{10}MO_{28}C_{26}$	-166.6	-167.8	-162.2	+132.4	-153.1
$N_{10}MO_{25}C_{24}$	-49.8	-53.6	-54.5	+15.2	-52.6
$N_{11}MO_{25}C_{24}$	-175.7	-165.1	-159.3	+94.5	-158.5
$N_{11}MO_{28}C_{26}$	-52.5	-46.3	-55.7	+58.6	-49.5
$O_{29}C_{24}O_{25}M$	+36.0	-152.1	-148.1	+176.2	-152.7
$O_{27}C_{26}O_{28}M$	-154.6	-152.8	-142.8	+145.7	-157.3

7B.2 Molecular Docking Studies of PDBAD and [M(PDBAD)X_2]:

For molecular protein docking studies with **PDBAD** and **[M(PDBAD)X_2],** we selected EGFR as a target protein receptor[12]. **Table 7B.3** comprises of the binding energies obtained from docking investigations. The binding energies of the ligand and complexes with the protein receptor EGFR (as shown in **Table 7B.3**) indicate that the ligand and complexes have a good affinity for the EGFR protein receptor. The docking tests also show that **[Mn(PDBAD)(H_2O)$_2$]** and **[Ni(PDBAD)]** have the lowest binding energies against EGFR, with a values of -11.4 kcal mol^{-1} and -9.8 kcal mol^{-1} respectively. **Figure 7B.32** – **Figure 7B.37** shows the molecular docking interaction diagrams of **PDBAD** and **[M(PDBAD)X_2].**

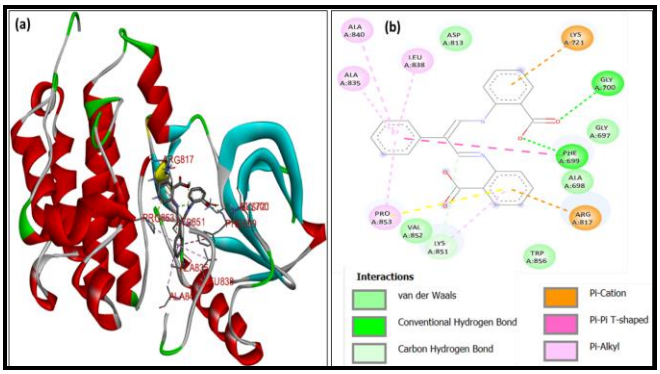

Figure 7B.32: *Molecular docking interactions of* ***PDBAD*** *with EGFR-TK protein; (a) 3D depiction of ligand-receptor binding interactions and (b) 2D representation of different forms of interactions with amino acid residues*

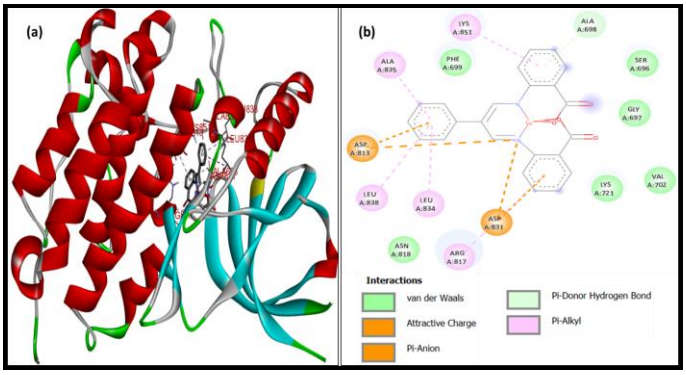

Figure 7B.33: *Molecular docking interactions of* ***[Cu(PDBAD)]*** *with EGFR-TK protein; (a) 3D depiction of ligand-receptor binding interactions and (b) 2D representation of different forms of interactions with amino acid residues*

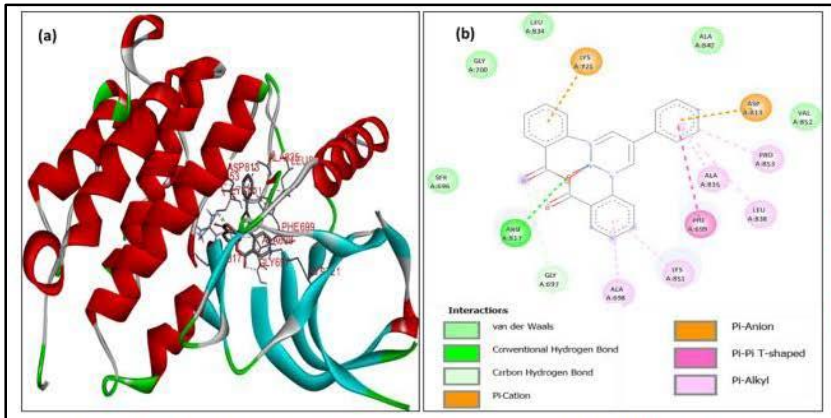

Figure 7B.34: *Molecular docking interactions of* ***[Ni(PDBAD)]*** *with EGFR-TK protein; (a) 3D depiction of ligand-receptor binding interactions and (b) 2D representation of different forms of interactions with amino acid residues*

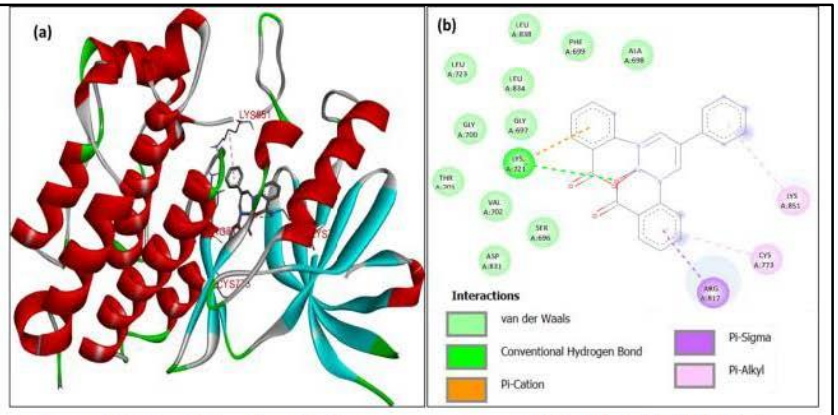

Figure 7B.35: *Molecular docking interactions of* ***[Co(PDBAD)(H$_2$O)$_2$]*** *with EGFR-TK protein; (a) 3D depiction of ligand-receptor binding interactions and (b) 2D representation of different forms of interactions with amino acid residues*

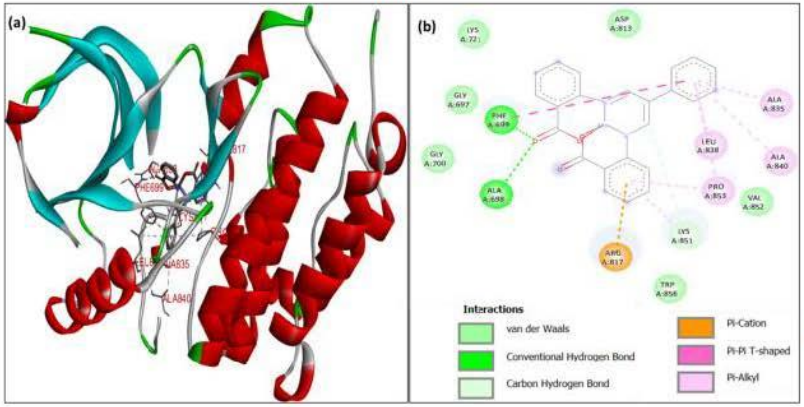

Figure 7B.36: *Molecular docking interactions of* ***[Mn(PDBAD)(H$_2$O)$_2$]*** *with EGFR-TK protein; (a) 3D depiction of ligand-receptor binding interactions and (b) 2D representation of different forms of interactions with amino acid residues*

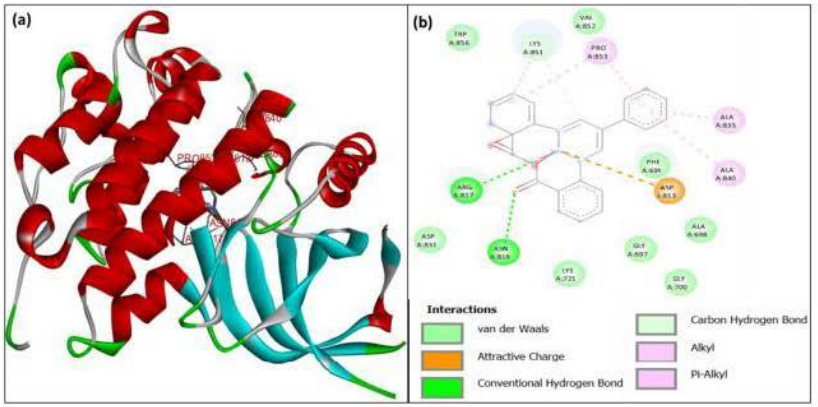

Figure 7B.37: *Molecular docking interactions of* ***[Zn(PDBAD)(H$_2$O)$_2$]*** *with EGFR-TK protein; (a) 3D depiction of ligand-receptor binding interactions and (b) 2D representation of different forms of interactions with amino acid residues*

The ligand **PDBAD** docks to the EGFR through a total of five hydrogen bond interactions with amino acid residues of PHE699, GLY700, and LYS851. Furthermore, it docks through two electrostatic interactions with LYS721, ARG817 and seven hydrophobic interactions with the amino acid residues of PHE699, ALA835, LEU838, ALA840, PRO853, LYS851 and PRO853.

The **[Ni(PDBAD)]** complex docks to the EGFR via a one-hydrogen bond interaction with the ALA698 protein amino acid residues., it docks through four electrostatic interactions with LYS721, ASP813 and six hydrophobic interactions with the amino acid residues of PHE699, ALA835, LEU838, PRO853, ALA698, LYS851.

The **[Cu(PDBAD)]** complex docks to the EGFR through one hydrogen bond interaction with the ALA698 protein amino acid residues. It also docks through four electrostatic interactions with ASP813, ASP831 and six hydrophobic interactions with the amino residues LEU834, ALA835, LEU838, ALA698, LYS851, and ARG817.

The **[Co(PDBAD)(H_2O)$_2$]** complex binds to the EGFR through one hydrogen bond interaction with the CYS773 protein amino acid residues, one electrostatic interaction with LYS721 and three hydrophobic interactions with ARG817, LYS851 and CYS773.

The **[Mn(PDBAD)(H_2O)$_2$]** complex exhibits three hydrogen bond interactions with amino acid residues of ALA698, PHE699 and LYS851. Furthermore, it binds through one electrostatic interaction with amino acid residue ARG817 and through seven hydrophobic interactions with PHE699, ALA835, LEU838, ALA840, PRO853, LYS851 and PRO853.

The **[Zn(PDBAD)(H_2O)$_2$]** complex docks to the EGFR through four hydrogen bond interactions with the protein amino acid residues of ARG817, ASN818 and LYS851. it binds through one electrostatic interaction with amino acid residue ASP813 and five hydrophobic interactions with the LYS851, PRO853, ALA835 and ALA840.

Table 7B.3: *Docking results of* ***PDBAD*** *and its metal complexes with the EGFR protein*

Compound	Binding energy (kcal mol^{-1})	No. of H-bonds	Proteins residues involved in the interactions
PDBAD	-8.4	5	ALA840, ALA835, LEU838, ASP813, LYS721, GLY700, GLY697, PHE699, ALA698, ARG817, TRP856, LYS851, VAL852, PRO853
[Cu(PDBAD)]	-10.2	1	ALA835, PHE699, LYS851, ALA698, SER696, GLY697, LYS721, VAL702, ASP831, ARG817, ASN818, LEU834, LEU838, ASP813, ALA835, PHE699, LYS851
[Ni(PDBAD)]	-10.7	2	GLY700, LEU834, LYS721, ALA840, ASP813, VAL852, PRO853, ALA835, LEU838, PHE699, LYS851, ALA698, GLY697, ARG817, SER696
[Co(PDBAD)$(H_2O)_2$]	-9.8	1	LYS721, ARG817, CYS773, LYS851, ALA698, PHE699, LEU838, LEU834, GLY697, GLY700, THR701, VAL702, SER696, ASP831
[Mn(PDBAD)$(H_2O)_2$]	-10.8	3	LYS721, GLY697, PHE699, GLY700, ALA698, ASP813, ARG817, TRP856, LYS851, PRO853, LEU838, ALA840, ALA835, PRO853, VAL852
[Zn(PDBAD)$(H_2O)_2$]	-10.4	4	TRP856, LYS851, VAL852, PRO853, ALA835, PHE699, ASP813, ALA840, ALA698, GLY697, GLY700, LYS721, ASN818, ASP831, ARG817

PART C

BIOLOGICAL ACTIVITY STUDIES OF PDBAD AND [M(PDBAD)X_2]

7C.1 *In vitro* Antimicrobial Activity:

The **PDBAD** ligand and its various Schiff base complexes were tested for microbiological activity against two gram-positive and two gram-negative bacteria along with streptomycin as a standard. **Table 7C.1** lists the results of the studies.

Table 7C.1: *Antibacterial activity MIC values of* ***PDBAD*** *and* ***[M(PDBAD)X_2]*** *(µg/ml)*

Compound	*S. aureus*	*B. subtilis*	*K.pneumoniae*	*E. coli*
[Cu(PDBAD)]	8.46	9.15	6.14	8.52
[Zn(PDBAD)(H_2O)$_2$]	6.23	8.42	13.26	14.35
[Ni(PDBAD)]	16.43	24.54	16.36	16.11
[Co(PDBAD)(H_2O)$_2$]	11.23	14.25	10.85	12.95
[Mn(PDBAD)(H_2O)$_2$]	18.12	24.63	12.21	17.83
PDBAD	60.26	55.63	61.42	74.97
Streptomycin	3.82	3.51	3.87	3.64

The results reveal that the ligand shows less activity against both gram negative and gram positive microorganisms. All the complexes exhibit moderate to good activity compared with both standards and ligands.

7C.2 *In vitro* Antioxidant Property:

The scavenging activity has been studied for the free radical *DPPH* (2,2-Diphenyl-1-picrylhydrazyl)[13]**.** The results are presented in **Table 7C.2.** The data indicate **[Co(PDBAD)(H_2O)$_2$]** and **[Cu(PDBAD)]** complexes have considerable antioxidant activity in the same order. Further, the ligand and the remaining complexes show good to moderate antioxidant activity **(Figure 7C.1).**

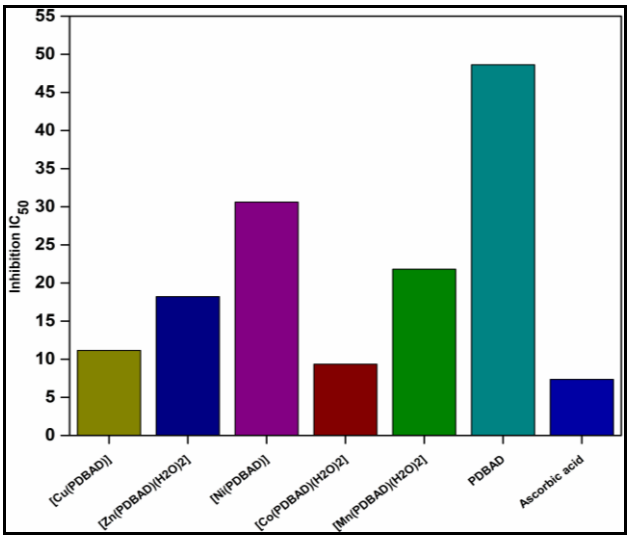

Figure 7C.1: *Histographical representation of the IC_{50} inhibition values of DPPH radical scavenging activity of* ***PDBAD*** *and* ***[M(PDBAD)X_2]***

Table 7C.2: *Anti-scavenging activity MIC values of* ***PDBAD*** *and* ***[M(PDBAD)X_2]*** *(µg/ml)*

Compound	IC_{50} (µM)
[Cu(PDBAD)]	11.15 ± 0.38
[Zn(PDBAD)$(H_2O)_2$]	18.22 ± 1.61
[Ni(PDBAD)]	30.62 ± 1.51
[Co(PDBAD)$(H_2O)_2$]	9.35 ± 1.24
[Mn(PDBAD)$(H_2O)_2$]	21.81 ± 1.22
PDBAD	48.63 ± 0.58
Ascorbic acid	7.35 ± 0.28

7C.3 *In vitro* Antifungal Activity:

In vitro antifungal activity studies of Schiff base ligand **(PDBAD)** and its complexes are investigated with the help of two fungal strains, *Asperegillusniger* and *pencilliumnotatum*, with ketoconazole drug as a standard. The results are provided in **Table 7C.3.** The anti-fungal activities of **[Ni(PDBAD)], [Co(PDBAD)$(H_2O)_2$]** and **[Cu(PDBAD)]** are reasonably closer to the standard for both the fungal strains.

Table 7C.3: *Antifungal activity MIC values of* ***PDBAD*** *and* ***[M(PDBAD)X_2]*** *(µg/ml)*

Compound	*Asperegillusniger*	*Pencilliumnotatum*
[Cu(PDBAD)]	4.92	7.25
[Zn(PDBAD)(H_2O)$_2$]	7.29	6.18
[Ni(PDBAD)]	3.25	4.65
[Co(PDBAD)(H_2O)$_2$]	4.31	5.72
[Mn(PDBAD)(H_2O)$_2$]	7.35	9.11
PDBAD	8.62	9.54
Ketoconazole	2.67	2.78

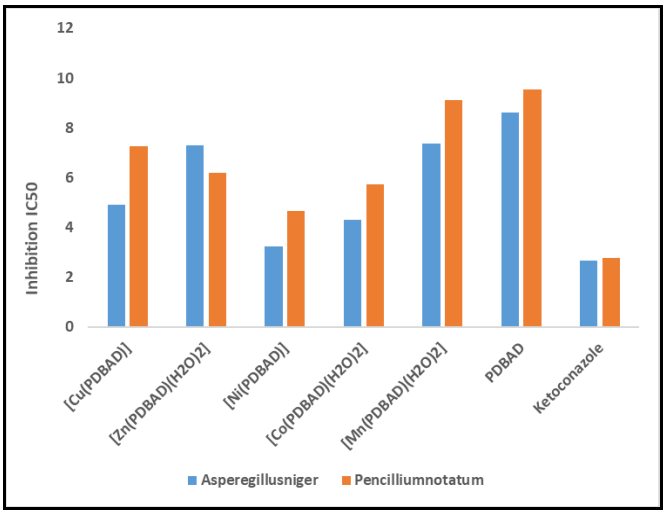

Figure 7C.2: *Histographical representation of the IC_{50} inhibition values of Asperegillusniger, Pencilliumnotatum antifungal activity of* ***PDBAD*** *and* ***[M(PDBAD)X_2]***

7C.4 *In vitro* Anticancer Activity:

The anticancer activity of **PDBAD** and its complexes was tested against three cancer cell lines, MCF-7, HepG-2 and HEK-293 by the MTT assay method with cisplatin as standard[14]. The results are presented in the **Table 7C.4**. From the results, only **[Mn(PDBAD)(H_2O)$_2$]** and **[Ni(PDBAD)]** complexes exhibit some promising results.

Table 7C.4: *Anticancer activity MIC values of* ***PDBAD*** *and* ***[M(PDBAD)X_2]*** *(µg/ml)*

Codes	MCF-7	HepG-2	HEK-293
[Cu(PDBAD)]	33.213 ± 0.991	43.48 ± 1.08	91.67 ± 1.11

[Zn(PDBAD)(H_2O)$_2$]	38.63 ± 1.36	32.26 ± 0.98	86.27 ±0.89
[Ni(PDBAD)]	25.59 ± 0.382	19.97 ± 0.359	ND
[Co(PDBAD)(H_2O)$_2$]	52.66 ± 1.325	58.12 ± 0.125	82.58 ± 1.29
[Mn(PDBAD)(H_2O)$_2$]	22.41 ± 0.361	17.39 ± 1.211	ND
PDBAD	79.24 ± 0.436	67.24 ± 1.39	ND
Cisplatin	10.56 ± 0.271	7.34 ± 0.18	ND

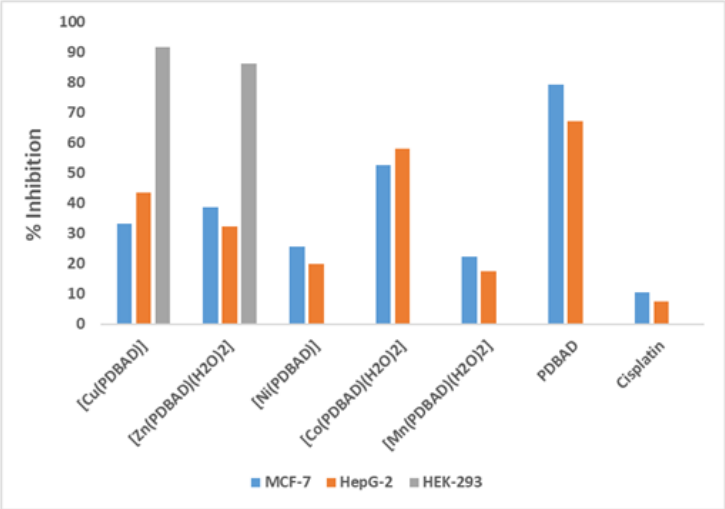

Figure 7C.3: *Histographical representation of % inhibition values of MCF-7, HepG-2, HEK-293 of cytotoxicity activity of* ***PDBAD*** *and its metal complexes*

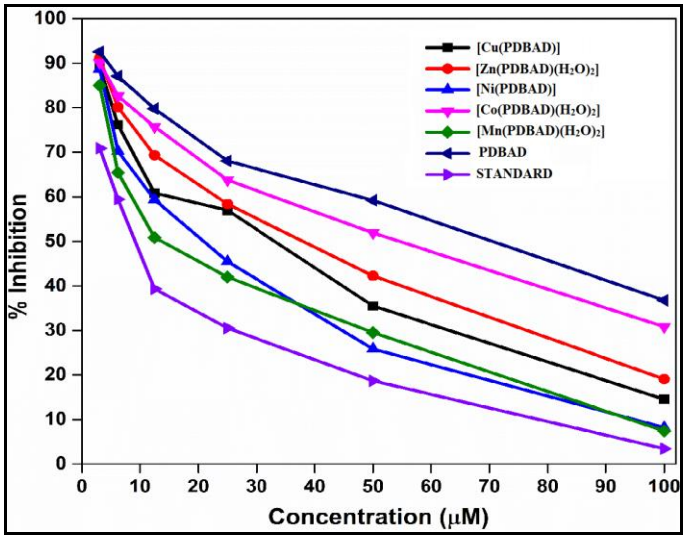

Figure 7C.4: *Cell viability assay; dose-response curves of* ***PDBAD*** *and its metal complexes with different concentrations on MCF7 cells*

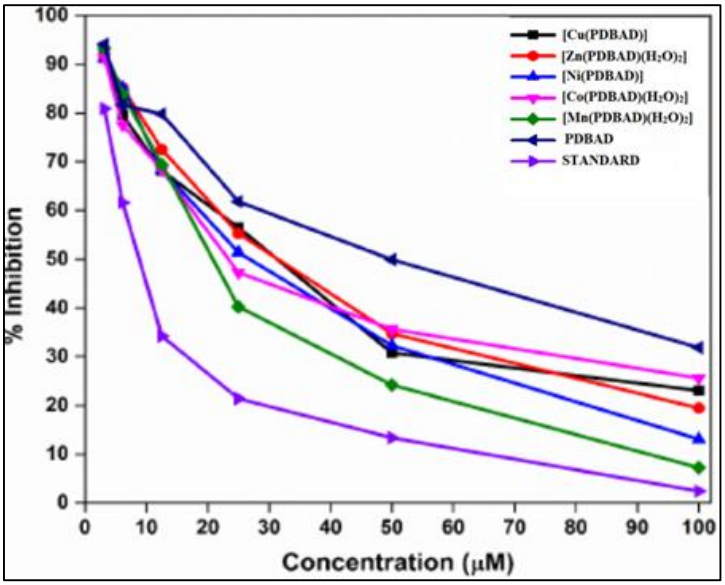

Figure 7C.5: *Cell viability assay; dose-response curves of* ***PDBAD*** *and its metal complexes with different concentrations on HepG-2 cells*

References

(1). (a) Hasan, M. R.; Hossain, M. A.; Salam, M. A.; Uddin, M. N. Nickel Complexes of Schiff Bases Derived from Mono/Diketone with Anthranilic Acid: Synthesis, Characterization and Microbial Evaluation. *Journal of Taibah University for Science* **2016**, *10* (5), 766–773. https://doi.org/10.1016/j.jtusci.2015.11.007.

(b) Navaneetham, N. S.; Kalyanasundaram, R.; Soundararajan, S. Lanthanide Chelate Complexes of Salicyloyl Hydrazide-Salicylaldehyde Schiff Base (SHSASB) and Anthranilic Acid-Salicylaldehyde Schiff Base (AASASB). *Inorganica Chimica Acta* **1985**, *110* (3), 169–173. https://doi.org/10.1016/S0020-1693(00)82303-8.

(2). (a) Ammal P, R.; Prasad, A. R.; Joseph, A. Synthesis, Characterization, in Silico, and in Vitro Biological Screening of Coordination Compounds with 1,2,4-Triazine Based Biocompatible Ligands and Selected 3d-Metal Ions. *Heliyon* **2020**, *6* (10), e05144. https://doi.org/10.1016/j.heliyon.2020.e05144.

(b) Pahonţu, E.; Ilieş, D. C.; Shova, S.; Oprean, C.; Păunescu, V.; Olaru, O. T.; Rădulescu, F. Ş.; Gulea, A.; Roşu, T.; Drăgănescu, D. Synthesis, Characterization, Antimicrobial and Antiproliferative Activity Evaluation of Cu(II), Co(II), Zn(II), Ni(II) and Pt(II) Complexes with Isoniazid-Derived Compound. *Molecules* **2017**, *22* (4), 1–17. https://doi.org/10.3390/molecules22040650.

(3). Abdul-Ghani, A. J.; Khaleel, A. M. N. Synthesis and Characterization of New Schiff Bases Derived from N (1)-Substituted Isatin with Dithiooxamide and Their Co(II), Ni(II), Cu(II), Pd(II), and Pt(IV) Complexes. *Bioinorganic Chemistry and Applications* **2009**, *2009*, 1–12. https://doi.org/10.1155/2009/413175.

(4). Al-Zaidi, B. H.; Hasson, M. M.; Ismail, A. H. New Complexes of Chelating Schiffbase: Synthesis, Spectral Investigation, Antimicrobial, and Thermal Behavior Studies. *Journal of Applied Pharmaceutical Science* **2019**, *9* (4), 45–57. https://doi.org/10.7324/JAPS.2019.90406.

(5). J. Althaher, L. Synthesis and Characterization of Mn(II), Co(II), Ni(II), Cu(II), Zn(II), and Hg(II) Complexes with [(N-(N-Benzilidin Aminoethyl) Iodomethylene Dithiocarbamate]. *Rafidain Journal of Science* **2013**, *24* (7), 25–33. https://doi.org/10.33899/rjs.2013.77813.

(6). Jayabharathi, J.; Jayamoorthy, K.; Thanikachalam, V. Synthesis, Photophysical and Electroluminescent Properties of Green Organic Light Emitting Devices Based on Novel Iridium Complexes Containing Benzimidazole Ligands. *Journal of Organometallic Chemistry* **2014**, *761*, 74–83. https://doi.org/10.1016/j.jorganchem.2014.03.002.

(7). (a) Patra, L.; Das, S.; Gharami, S.; Aich, K.; Mondal, T. K. A New Multi-Analyte Fluorogenic Sensor for Efficient Detection of Al 3+ and Zn 2+ Ions Based on ESIPT and CHEF Features. *New Journal of Chemistry* **2018**, *42* (23), 19076–19082. https://doi.org/10.1039/C8NJ03191F.

(b) Salem, H. Spectrofluorimetric, Atomic Absorption Spectrometric and Spectrophotometric Determination of Some Fluoroquinolones. *American Journal of Applied Sciences* **2005**, *2* (3), 719–729. https://doi.org/10.3844/ajassp.2005.719.729.

(8). (a) Nishida, Y.; Hayashida, K.; Sumita, A.; Kida, S. Electronic Structures of Square Planar Cobalt(II), Nickel(II) and Copper(II) Complexes with Some N4-Macrocyclic Ligands [1]. *Inorganica Chimica Acta* **1978**, *31* (C), 19–23. https://doi.org/10.1016/S0020-1693(00)94974-0.

(b) Krishnan, V. G. Anion and Symmetry Effects in the ESR Spectra of Copper Complexes. *Journal of Molecular Structure* **1979**, *55* (C), 89–97. https://doi.org/10.1016/0022-2860(79)80186-6.

(9). (a) Packianathan, S.; Kumaravel, G.; Raman, N. DNA Interaction, Antimicrobial and Molecular Docking Studies of Biologically Interesting Schiff Base Complexes Incorporating 4-Formyl- N , N -Dimethylaniline and Propylenediamine. *Applied Organometallic Chemistry* **2017**, *31* (3), e3577. https://doi.org/10.1002/aoc.3577.

(b) Tabassum, S.; Afzal, M.; Al–Lohedan, H.; Zaki, M.; Khan, R. A.; Ahmad, M. Synthesis and Structure Elucidation of New Open Cubane Tetranuclear [Cu II 4] Cluster: Evaluation of the DNA/HSA Interaction and PBR322 DNA Cleavage Pathway and Cytotoxicity. *Inorganica Chimica Acta* **2017**, *463*, 142–155. https://doi.org/10.1016/j.ica.2017.04.031.

(10). Ramadevi, P.; Singh, R.; Prajapati, A.; Gupta, S.; Chakraborty, D. Cu(II) Complexes of Isoniazid Schiff Bases: DNA/BSA Binding and Cytotoxicity Studies on A549 Cell Line. *Advances in Chemistry* **2014**, *2014*, 1–14. https://doi.org/10.1155/2014/630575.

(11). (a) Schundelmeier, S.; Speiser, B.; Bettinger, H. F.; Einholz, R. (Electro)Chemical Oxidation of 6,13-Bis[Tri(Isopropyl)Silylethynyl]Pentacene to Its Radical Cation and Dication. *ChemPhysChem* **2017**, *18* (16), 2266–2278. https://doi.org/10.1002/cphc.201700435.

(b) Blandón-Naranjo, L.; Hoyos-Arbeláez, J.; Vázquez, M. V.; Della Pelle, F.; Compagnone, D. NADH Oxidation onto Different Carbon-Based Sensors: Effect of Structure and Surface-Oxygenated Groups. *Journal of Sensors* **2018**, *2018*, 1–9. https://doi.org/10.1155/2018/6525919.

(12). Wieduwilt, M. J.; Moasser, M. M. The Epidermal Growth Factor Receptor Family: Biology Driving Targeted Therapeutics. *Cellular and Molecular Life Sciences* **2008**, *65* (10), 1566–1584. https://doi.org/10.1007/s00018-008-7440-8.

(13). Kedare, S. B.; Singh, R. P. Genesis and Development of DPPH Method of Antioxidant Assay. *Journal of Food Science and Technology* **2011**, *48* (4), 412–422. https://doi.org/10.1007/s13197-011-0251-1.

(14). Mirmalek, S. A.; Jangholi, E.; Jafari, M.; Yadollah-Damavandi, S.; Javidi, M. A.; Parsa, Y.; Parsa, T.; Salimi-Tabatabaee, S. A.; Kolagar, H. G.; Jalil, S. K.; Alizadeh-Navaei, R. Comparison of in Vitro Cytotoxicity and Apoptogenic Activity of Magnesium Chloride and Cisplatin as Conventional Chemotherapeutic Agents in the MCF-7 Cell Line. *Asian Pacific Journal of Cancer Prevention* **2016**, *17* (sup3), 131–134. https://doi.org/10.7314/APJCP.2016.17.S3.131.

SUMMARY AND SCOPE FOR FURTHER WORK

Summary

The Thesis, entitled, "***Synthesis, Structural Characterization by X-Ray Diffractometry and Biological Studies of Some Nitrogenous Compounds and Their Correlations with Computational Modelling***", deals with the synthesis and characterization of a few selected nitrogenous organic compounds along with their molecular structure determination by single crystal XRD and correlation of the structural parameters with those obtained by molecular modeling of these compounds and their bivalent metal complexes. Both, ligands and their complexes have been exposed to molecular docking on some biomolecules and were tested for possible anti-fungal, anti-bacterial, anti-cancer and anti-oxidant *in vitro* applications.

Chapter I introduces the importance of nitrogenous organic compounds with a special emphasis on Schiff bases, dithiocarbammates, quinolinium compounds, etc. and their metal complexes. The contemporary research on the correlation of empirical molecular structural studies by XRD and those obtained from advanced computational modeling, is highlighted with examples. The Chapter concludes with the Scope and objectives.

Chapter II, entitled, **'Materials and Methods'**, describes the procedures of the synthesis and characterization of the compounds studied. **Part A** of this Chapter deals with the synthesis of the compounds and their metal complexes whereas **Part B** the details of characterization of the compounds by various methods. Introduction to current computational chemistry procedures and some of the instrumental methods are also provided.

In **Chapter III**, entitled, **Spectral, Electrochemical, Molecular Modelling, Protein Docking and Biological Activity Studies of Fluoxetine Dithiocarbamate (FLXDTC) and Its Bivalent Metal Complexes**, and divided into 3 Parts, the details of investigations of a dithiocarbammate ligand, **FLXDTC**, along with its bivalent metal complexes are presented. The studies indicate the formation **M(FLXDTC)$_2$** complex [M = Zn(II), Cd(II), Co(II), Ni(II), Mn(II) and Cu(II)]. **Cu(FLXDTC)$_2$** takes additional $CuCl_2$ to result in the formation of **Cu$_2$(FLXDTC)$_2$Cl$_2$** kind binuclear complex with sulfur atom bridges Molecular docking studies and antimicrobial, antioxidant, antifungal, anti-malarial and antitumor capabilities have been tested for both **FLXDTC** and **M(FLXDTC)$_2$** complexes. The biological activity studies of **FLXDTC** ligand and its metal complexes are also described.

The title of **Chapter IV**, is "**Synthesis and Spectral, Electrochemical, Single Crystal X-Ray Diffractometric, Computational Chemistry and Biological Studies of 1-(((3-Fluoro-4-morpholinophenyl)-imino)methyl)-napthalen-2-ol (FMIMN) and Its Bivalent Metal Complexes"**. The characterization of the **FMIMN**, and it metal complexes is discussed in its **Part A.** It is found that **FMIMN** crystallizes in the $P_{21/n}$ monoclinic space group.

Conformational analysis, evaluation of structural parameters, HOMO-LUMO orbital energies, single and double dihedral analysis, etc. by molecular modelling, molecular docking studies on the EGFR protein, and so on are placed in **Part B**. The comparison of XRD data with those by computational analysis is presented and discussed. There is an excellent agreement of the computationally evaluated data with the empirical data obtained by single crystal XRD data. The biological activity studies of ligand and its metal complexes are presented in **Part C**. In general, the activities of the complexes were found to be better than those of **FMIMN**. **Zn(FMIMN)$_2$** shows better antimicrobial activity while **Cd(FMIMN)$_2$** a promising anticancer activity.

Chapter V is titled as, **Synthesis, Characterization and Single Crystal X-Ray Diffractometric, Computational Chemistry and Biological Studies of a Pair of Phenyl Quinolinium Salts.** Two novel organic molecules, viz., 7-fluoro-6-morpholino-3-phenylquinolin-1-ium **(FMPC)** and 7-fluoro-3-(4-methoxyphenyl)-6-morpholinoquinolin-1-ium chloride **(FMMC)** salts have been synthesized and characterized by various spectroscopic techniques and by single crystal XRD studies. Both **FMPC** and **FMMC** crystallize in their centrosymmetric monoclinic $P_{21/c}$ space groups. The crystal structure analysis data and molecular modelling studies on the platforms of AM1, MM2 and B3LYP calculations and the data have been correlated with the XRD data. The computationally evaluated data are found to be in excellent agreement with the empirical single crystal XRD data. Hirshfeld surface analysis and energy frame work calculations, carried on **FMPC** and **FMMC**, reveal some interesting hydrogen bond intermolecular interactions.

These new heterocyclic compounds exhibit certain level of anti-cancer property as proven from the MTT assaying. These studies are presented systematically in Part A and Part B of this Chapter.

In **Chapter VI**, entitled, **Spectral Characterization, and Single Crystal X-Ray Diffractometric, Computational and Biological Studies of Mono- and Di-Aza Derivatives of a Pair of Malonaldehydes**, studies of 2-phenylmalonaldehyde and 2-(4-methoxyphenyl)-malonaldehyde, each possessing two terminal aldehyde groups and potential candidates of tautomerism have been presented in this Chapter.

Single crystals could be generated only for (Z)-3-((3-fluoro-4-morpholinophenyl)amino)-2-phenylacrylaldehyde **(FMAPA)**, with one of the carbonyl groups converted to azomethine, and 3-fluoro-N-((1E,2Z)-3-((3-fluoro-4-morpholinophenyl)amino)-2-(4-methoxyphenyl)allylidene)-4-morpholinobenzenaminium **(FFMMMC)**, with both the carbonyl groups converted to azomethines whereas we could not obtain single crystals of 3-fluoro-N-((1Z,3E)-3-((3-fluoro-4-morpholinophenyl)imino)-2-phenylprop-1-en-1-yl)-4-morpholinobenzenaminium **(FFMPMC)** and (Z)-3-((3-fluoro-4-morpholinophenyl)amino)-2-(4-methoxyphenyl)acrylaldehyde **(FMAMA)**. **FMAPA** crystallizes in a centrosymmetric monoclinic P21/c space group but with four molecules in one-unit cell whereas **FFMMMC** crystallizes in a centrosymmetric triclinic P_{-1} space group with only two molecules in a one-unit cell. **Section 1** of **Part A** (**Section A1**) deals with the spectral, single crystal XRD studies, molecular structural determination of **FMAPA** and

FMAMA, while **Section 2** of this Part (**Section A2**) discusses the computational chemistry of the same along with their protein docking studies. Similarly, **Section 1** of **Part B** (**Section B1**) and **Section 2** of **Part B** (**Section B2**) covers the corresponding bis-derivatives of dialdehyde viz. FFMPMC and FFMMMC. The XRD molecular structural data of **FMAPA** and **FFMPMC** obtained through single crystal XRD studies have been compared with the molecular modelled structural of all the four compounds in this Chapter. Finally, this Chapter presents briefly the biological applications of the title compounds.

In the last, **Chapter VII**, entitled, **Synthesis and Spectral, Electrochemical, Computational and Biological Studies of 2,2'-(((1E,3E)-2-Phenylpropane-1,3-diylidene)-bis-(azaneylylidene))-dibenzoic Acid (PDBAD) and Its Bivalent Metal Complexes [M(PDBAD)X_2],** the studies of the Schiff base ligand, 2,2'-(((1E,3E)-2-phenylpropane-1,3-diylidene)bis(azaneylylidene))-dibenzoic acid **(PDBAD)**, along with those of its complexes of some bivalent metal ions such as Zn(II), Cd(II), Co(II), Ni(II), Mn(II) and Cu(II) are described. The studies propose the formation **[M(PDBAD)X_2]** type complexes due to the tetradentate nature of the ligand. Biological activity like antimicrobial, antioxidant, antifungal, anti-malarial and antitumor capabilities has been tested for both **PDBAD** and **[M(PDBAD)X_2]** kind of complexes along with molecular docking studies. While **PART A** describes the characterization of the **PDBAD**, **PART B** molecular modelling and protein molecular docking studies and **PART C** is for the biological activity studies of **PDBAD** and **[M(PDBAD)X_2]**.

Scope for Further Work

The kind of organic skeletons of the compounds that I have synthesized and studied are very common in many of the functional materials and pharmaceuticals. Most of these heterocyclic compounds defy crystallization for the determination of their exact molecular structure. Our studies have suggested how Density Functional Theoretical (DFT) molecular modeling gave structural parameters found to be very close to the ones determined by single crystal X-Ray Diffractometry (XRD). More and more such recent studies need to pile up to form a heap of organic and coordination compounds that have a wide variety of inherent structural motifs with tables of correlations between the computational parameters and the X-Ray Diffractometric data.

Like the Heat Charts, CCDC, CODATA, ASTM, CRC Handbook, etc, one such database of molecular structural correlations with empirical X-Ray Crystallographic data may soon be compiled so as to enable chemists and materials scientists to confidently arrive at the molecular structural parameters to those compounds that are unable to be crystallized. In the regime of Quantitative Structure Activity Relationships (QSARs), it is important to have such charts aplenty.

With constant theoretical refinements taking place in Quantum Mechanics, more reliable computational modeling platforms are likely to be developed that may bring the expected XRD data much more closely to the computational data and vice versa.

Molecular Docking to other physiologically decisive macromolecules, biomolecules, proteins, nucleosides, cell-organelle, metallo-enzymes in the light of the correlation charts of XRD data and computational data may open new vistas in pharmaceutics and biotechnological applications.

Publications Arising from the Work Presented in This Thesis:

1. ***Synthesis, characterization, molecular structure determination by single crystal X-ray diffraction, and Hirshfeld surface analysis of 7-fluoro-6-morpholino-3-phenylquinolin-1-ium chloride salt and computational studies of its cation***.
   Dhananjay Rao Thandra, Ramachandraiah Allikayala* *Journal of Molecular Structure* 2022, **1250**, 131701**.** https://doi.org/10.1016/j.molstruc.2021.131701.

2. ***Synthesis, spectral studies, molecular structure determination by single crystal X-ray diffraction of (E)-1-(((3-fluoro-4-morpholinophenyl)imino)methyl)napthalen-2-ol and computational studies by Austin model-1(AM1), MM2 and DFT/B3LYP***.
   Dhananjay Rao Thandra, Rajeshwar Rao Bojja, Ramachandraiah Allikayala* *SN Applied Sciences* 2020, **2**, 2523-3971**,** https://doi.org/10.1007/s42452-020-03525-0.

3. ***Synthesis and spectral, electrochemical, protein-docking and biological studies of fluoxetine dithiocarbamate and its bivalent metal complexes.***
   Dhananjay Rao Thandra, Venkata Bharat Nishtala, Ramachandraiah Allikayala*, *Chemistry Africa* 2021, **4**, 777-789, https://doi.org/10.1007/s42250-021-00283-3

4. Two or Three More Papers Worth Material is Yet to be Published.

Conferences and Workshops Attended to Present Papers from the Work Presented in This Thesis:

1. Modified Redox Functionalization of Optically Active Drug Molecules by Dithiocarbamate Adduction and Bivalent Metal Ion Complexation.
   Dhananjay Rao Thandra and Ramachandraiah Allikayala
   International Conference on Advanced Functional Materials (ICAFM-2017) organized by Rajive Gandhi University of Knowledge Technologies Basar, Telangana, 18th-20th, December 2017.
2. A One Week Faculty Development Workshop on TEACHING AND LEARNING CHEMICAL SPECTROSCOPY THROUGH HANDS-ON EXPERIENCE organized by

Department of Chemistry in association with Teaching Learning Centre, National Institute of Technology Warangal, 11^{th}-16^{th} October, 2017.

3. Synthesis and Characterization of the Sodium Salts of 4,4′ - Dithiocarbamates of Some 4,4′ - Diaminobiphenyls

   Dhananjay Rao Thandra and Ramachandraiah Allikayala

   Telangana Academy of Sciences (TSSC-2018) organized by National Institute of Technology Warangal, 22^{nd}-24^{th}, December 2018.

4. Synthesis, Characterization and Molecular Docking Biological Studies of the Coordination Compounds of Fluoxetine Dithiocarbamate with Some Bivalent Metal Ions, **M(FLXDTC)$_2$**.

   Dhananjay Rao Thandra and Ramachandraiah Allikayala

   Telangana Academy of Sciences (TSSC-2018) organized by National Institute of Technology Warangal, 22^{nd}-24^{th}, December 2018.

5. Synthesis and Characterization of the Sodium Salts of 4,4′ - Dithiocarbamates of Some 4,4′ - Diaminobiphenyls

   Dhananjay Rao Thandra and Ramachandraiah Allikayala

   Telangana Academy of Sciences (TSSC-2018) organized by National Institute of Technology Warangal, 22^{nd}-24^{th} December, 2018.

6. Synthesis, Characterization of Fluoxetine Dihiocarbamate and Spectrophotometric, Electrochemical Assay.

   Dhananjay Rao Thandra and Ramachandraiah Allikayala

   Telangana Academy of Sciences (TSSC-2018) organized by National Institute of Technology Warangal, 22^{nd}-24^{th} December, 2018.

7. Modified Redox Functionalization of Optically Active Drug Molecules by Dithiocarbamate Adduction and Bivalent Metal Ion Complexation.

   Dhananjay Rao Thandra and Ramachandraiah Allikayala

   International Workshop and Symposium on Green Chemistry and Technology (IWSGCT-18) organized by P.G. Department of Chemistry, Govt. Dungar College (Re accredited with 'A' Grade by NAAC) Bikaner - 334 001 (INDIA) In association with - Green Chemistry Network Centre, University of Delhi; Royal Society of Chemistry, London (North India section), 15^{th}-17^{th} October, 2018.

8. Synthesis and Characterization of the Sodium Salts of 4,4′ - Dithiocarbamates of Some 4,4′ - Diaminobiphenyls.

   Dhananjay Rao Thandra and Ramachandraiah Allikayala

   National Conference on Emerging Trends in Instrumental Methods of Chemical Analysis (ETIMCA-2019) organized by Department of Chemistry, National Institute of Technology Warangal, 30th-31st January, 2019.

9. Synthesis and Characterization of μ-Oxalato and μ-Azido bis-Biphenyl Bridged Tetranuclear Complexes as Supramolecular Cavitands.

   T. Sarojini, **T. Dhanajaya Rao**, D. Prabhakarachary, and A. Ramachandraiah

   International Conference on Advances in Chemical Sciences and Technologies (ACST-2019) held at Department of Chemistry, NIT Warangal, 23rd-25th September, 2019.

10. Synthesis and Spectral, Electrochemical and Spectroelectrochemical Characterization of a Schiff base Derived from 2-Phenylmalonaldehyde and 4,4'- Diaminobiphenyls.

    T. Dhanajaya Rao and A. Ramachandraiah

    International Conference on Advances in Chemical Sciences and Technologies (ACST-2019) held at Department of Chemistry, NIT Warangal, 23rd-25th September, 2019.

11. Three-Day Online International Conference on "Conventional and Digital methods in Chemical Education" organized by Department of Chemistry, National Institute of Technology Warangal, 29th-31st July, 2021.

12. International Workshop on "Supporting Chemistry Research with modern DFT (Density Functional Theory): Software, Techniques, and Applications organized by Department of Chemistry, Smt. S. S. Patel Nootan Science & Commerce College, Visnagar, Dist. Mehsana. Gujarat, India, 5th-16th February 2021.

BIO-DATA

Thandra Dhananjay Rao

Contact Address
Lab No. 603,
Department of Chemistry
National Institute of Technology Warangal
Warangal, 506004, Telangana

E-mail: dhanu.chem41@gmail.com
Contact No. 9550949439

Academic Qualification

July 2016-present **: Research Scholar (PhD Student)**

Under the supervision of **Prof. A. Ramachandraiah (HAG, Retd.)** Department of Chemistry, National Institute of Technology Warangal, Telangana, India

Thesis Title: 'Synthesis, Structural Characterization by X-Ray Diffractometry and Biological Studies of Some Nitrogenous Compounds and Their Correlations with Computational Modelling'

September 2010-april 2016 **: Integrated MSc Chemistry**

Chaitanya Post Graduated College (Deemed to be University),

Kishanpura, Hanamkonda, Warangal, 506001

Percentage of Marks: **86.54 (First class with Distinction)**

May 2008-March 2010 **: Intermediate (Mathematics, Physics, Chemistry)**

Board of Intermediate Education, Andhra Pradesh, India

Percentage of Marks: **90.70 (First class with Distinction)**

June 2007-March 2008 **: Secondary School Certificate (High School)**

Board of Secondary Education, Andhra Pradesh, India

Percentage of Marks: **90.00 (First Class with Distinction)**

Personal Details:

- Name : Thandra Dhananjay Rao
- Father's Name : Narasimha Rao
- Mother's Name : Savithri
- Date of Birth : 05-12-1991
- Gender : Male
- Marital Status : not married
- Nationality : Indian

- Languages Known : Telugu, English, Hindi

Achievements:

- Qualified Telangana State Eligibility Test **(TS-SET)** 2017 for Assistant Professor/Lectureship in the subject of **Chemical Sciences**.
- Qualified Graduated Aptitude Test in Engineering **(GATE)** 2016.

Technical Skills:

- Experience in utilizing the software – Microsoft Office, ChemDraw, surfer, origin, CrystalExplorer, AutoDock/Vina etc.
- Experience in MENDELEY Desktop.

Expertise in Instrumental Techniques:

- Electrochemical Impedance Analyzer, Zahner-Elektrik (IM6e), GmbH, Germany
- Electrochemical Workstation, Sinsil CHI 619D
- UV-Visible Spectrophotometers, Analytica Jena Specord 205 and Schimadzu 1601
- UV-Visible-NIR Agilent cary 5000
- Thermoscientific UV-Visible Spectrophotometer Evolution 600 Instrument
- Analytika F96pro Fluorescence Spectrophotometer
- FTIR Spectrophotometer, PerkinElmer 100s
- Differential Scanning Calorimetry, Q10 TA instruments, USA
- Jeol FA-100, X-band ESR Spectrometer
- Agilent ICPOES 720 series
- BioLogic MOS-500 CD and ORD spectrophotometer
- Other small instruments relevant for materials characterization and analysis

Research Interest:

- Computational and Modelling studies
- Synthesis of Organic and Inorganic compounds
- Spectral and electrochemical analysis

Other Capabilities:

- Capable of carrying out both collaborative and independent research
- Motivated strong ethics and providing efficient service
- Very good interpersonal and communication skills along with management skills
- Good experience in writing technical papers, presentation, and reports
- Worked with many post graduate students for their projects